

AWARD NUMBER:
W81XWH-12-1-0607

TITLE:
Emotion Regulation Training for Treating Warfighters with Combat-Related PTSD Using Real-Time fMRI and EEG-Assisted Neurofeedback

PRINCIPAL INVESTIGATOR:
Jerzy Bodurka

CONTRACTING ORGANIZATION:
Laureate Institute for Brain Research
Tulsa, OK 74136

REPORT DATE:
December 2017

TYPE OF REPORT:
Final

PREPARED FOR: U.S. Army Medical Research and Materiel Command Fort Detrick, Maryland
21702-5012

DISTRIBUTION STATEMENT: Approved for Public Release; Distribution Unlimited

The views, opinions and/or findings contained in this report are those of the author(s) and should not be construed as an official Department of the Army position, policy or decision unless so designated by other documentation.

REPORT DOCUMENTATION PAGE			<i>Form Approved</i> <i>OMB No. 0704-0188</i>		
Public reporting burden for this collection of information is estimated to average 1 hour per response, including the time for reviewing instructions, searching existing data sources, gathering and maintaining the data needed, and completing and reviewing this collection of information. Send comments regarding this burden estimate or any other aspect of this collection of information, including suggestions for reducing this burden to Department of Defense, Washington Headquarters Services, Directorate for Information Operations and Reports (0704-0188), 1215 Jefferson Davis Highway, Suite 1204, Arlington, VA 22202-4302. Respondents should be aware that notwithstanding any other provision of law, no person shall be subject to any penalty for failing to comply with a collection of information if it does not display a currently valid OMB control number. PLEASE DO NOT RETURN YOUR FORM TO THE ABOVE ADDRESS.					
1. REPORT DATE December 2017		2. REPORT TYPE Final		3. DATES COVERED 30Sep2012-29Sep2017	
4. TITLE AND SUBTITLE Emotion Regulation Training for Treating Warfighters with Combat-Related PTSD Using Real-Time fMRI and EEG-Assisted Neurofeedback.				5a. CONTRACT NUMBER	
				5b. GRANT NUMBER W81XWH-12-1-0607	
				5c. PROGRAM ELEMENT NUMBER	
6. AUTHOR(S) Jerzy Bodurka E-Mail: jbodurka@laureateinstitute.org				5d. PROJECT NUMBER	
				5e. TASK NUMBER	
				5f. WORK UNIT NUMBER	
7. PERFORMING ORGANIZATION NAME(S) AND ADDRESS(ES) Laureate Institute for Brain Research 6655 S. Yale Ave, Tulsa, OK 74137				8. PERFORMING ORGANIZATION REPORT NUMBER	
9. SPONSORING / MONITORING AGENCY NAME(S) AND ADDRESS(ES) U.S. Army Medical Research and Materiel Command Fort Detrick, Maryland 21702-5012				10. SPONSOR/MONITOR'S ACRONYM(S)	
				11. SPONSOR/MONITOR'S REPORT NUMBER(S)	
12. DISTRIBUTION / AVAILABILITY STATEMENT Approved for Public Release; Distribution Unlimited					
13. SUPPLEMENTARY NOTES					
14. ABSTRACT PTSD is a chronic and disabling condition. Neurocircuitry-based models of PTSD emphasize dysregulation of the amygdala, which is involved in the regulation of PTSD-relevant emotions. We are utilizing real-time functional magnetic resonance imaging neurofeedback (rtfMRI-nf) training with concurrent electroencephalography (EEG) recordings to directly target and modulate the emotion regulation neurocircuit. By using multimodal data, we proposed to determine which EEG signals/leads correlated with clinical improvement associated with the rtfMRI-nf training and to develop stand-alone EEG neurofeedback training. Difficult recruitment was the main reason behind the two-years (no cost extension) delayed study schedule. Data analysis indicates amygdala training with concurrent EEG recordings in a combat-related PTSD population is feasible, tolerated well, and resulted in improvements in PTSD symptoms. The training enhanced functional connectivity between the amygdala and the prefrontal cortex in PTSD, and also resulted in increased hippocampus volume associated with PTSD symptom reductions. We identified the variations in frontal upper alpha EEG asymmetry (FEA) during the rtfMRI-nf amygdala training as a promising measure of PTSD severity and treatment response. We determined the feasibility of the stand-alone EEG-only neurofeedback training protocol based on in combat-related PTSD.					
15. SUBJECT TERMS PTSD; amygdala; fMRI; EEG; real-time fMRI neurofeedback; simultaneous EEG-fMRI; emotion regulation					
16. SECURITY CLASSIFICATION OF:	17. LIMITATION OF ABSTRACT	18. NUMBER OF PAGES 56	19a. NAME OF RESPONSIBLE PERSON USAMRMC		
a. REPORT U	b. ABSTRACT U	c. THIS PAGE U	UU		19b. TELEPHONE NUMBER

Table of Contents

	<u>Page</u>
1. Introduction	4
2. Keywords	4
3. Body	4
4. Key Research Accomplishments	42
5. Reportable Outcomes	44
6. Conclusions	49
7. References	51
8. Appendices	55
9. Supporting data	56

1. INTRODUCTION:

Our *main objective* was to determine whether rtfMRI- and rtEEG-assisted neurofeedback emotion regulation training protocols can reduce the symptoms of combat-related post-traumatic stress disorder (PTSD), a chronic and disabling psychiatric condition. Individuals with PTSD suffer from the dysregulation of several types of emotion, including fear, anxiety, anger, and depression [1–4]. Neurocircuit models of PTSD emphasize the role of the amygdala and its reciprocal interactions with the ventromedial prefrontal cortex (vmPFC) [5–9]. To advance understanding of the treatment of combat-related PTSD, the current state-of-the-art research aimed at testing ways to modulate the functions of the emotion circuit implicated in PTSD. We utilized recent advances in real-time functional magnetic resonance imaging neurofeedback (rtfMRI-nf) to target and modulate amygdala activity [10–11]. This technique measures neuronal activity with sufficiently high temporal resolution that information from the amygdala is immediately available to form a feedback loop. In parallel with rtfMRI-nf, we obtained simultaneous measurement of electroencephalography (EEG) signals, which directly reflect brain activity in the cerebral cortex [12]. By using the multimodal imaging data, we can determine which EEG signals/leads or their combination specifically predict or correlate with clinical improvement that has been associated with the rtfMRI-nf training [11,13–17]. This knowledge will enable to establish a translational path toward the development of stand-alone real-time EEG neurofeedback (rtEEG-nf) training for emotion regulation, which can facilitate the widespread implementation of the treatment approach due to the high portability and relatively low cost of EEG systems.

2. KEYWORDS:

Combat-related PTSD, fMRI, EEG, emotions, amygdala, neurofeedback

3. BODY

3.1 RESEARCH ACCOMPLISHMENTS SPECIFIC TO STUDY AIMS.

We have developed novel methodological approaches to improved EEG and fMRI data analysis described below in the novel data analysis methods section. Further, we have developed data processing pipelines to accomplish the study aims. We conducted data analysis for Aim #1, including the following: i) validating whether Veterans with PTSD can tolerate well and use rtfMRI-nf training to enhance their control of the hemodynamic response of the amygdala, and to further assess specificity of this training; ii) evaluating whether the training procedure resulted in PTSD symptom reductions, and iii) evaluating possible sustained neuroplastic changes induced by the procedure. For Aim #2 data analysis included the following: i) performing EEG analysis to investigate EEG correlates of the rtfMRI-nf procedure and identify EEG features suitable for a stand-alone EEG-nf training protocol, and ii) conducting EEG exploratory analyses focusing on temporally independent EEG microstates. For Aim #3 —although we have not yet reached the intended recruitment target— we conducted preliminary analyses to examine the feasibility of EEG-nf based on frontal asymmetry in the EEG alpha band. Descriptions of the above analyses follow below.

A) Real-time fMRI neurofeedback training of amygdala activity with simultaneous EEG in Veterans with combat-related PTSD

A1. Introduction

We report the results from the first controlled emotion regulation study in Veterans with combat-related PTSD utilizing rtfMRI-nf of amygdala activity. The study included three rtfMRI-nf training sessions wherein brain activity was simultaneously monitored via electroencephalography (EEG) and fMRI. We analyzed effects of

A2.2 Participants

Participants provided written informed consent as approved by the IRB. They met the *Diagnostic and Statistical Manual of Mental Disorders-Fourth Edition Text Revision* (DSM-IV-TR) (American Psychiatric Association, 2000) criteria for PTSD. All the subjects were male and had PTSD related to combat trauma as their primary diagnosis. They received monetary compensation for their participation in the study.

Participants were randomly assigned to either the experimental group (EG) or the control group (CG) at approximately a 2:1 ratio and they were blinded to group status. During the rtfMRI-nf training sessions (visits 4, 5, 6), the EG was provided with rtfMRI-nf based on BOLD activity of the LA [11]. The CG was provided with

control rtfMRI-nf based on BOLD activity of a brain region, presumably not involved in emotion processing [11]. Selection of the target regions for rtfMRI-nf is described in detail below.

Table 1 reports main characteristics of the EG and CG groups. After excluding participants with severe head motions, in the EG, 20 participants completed the first rtfMRI-nf session (visits 1-4), and

Table 1	Experimental group (EG)		Control group (CG)	
Measure	Started mean (SD)	Completed mean (SD)	Started mean (SD)	Completed mean (SD)
Participants	20	15	11	8
Age	31 (6)	31 (5)	34 (8)	37 (8)
CAPS	51.3 (13.9)	40.6 (17.9)	57.0 (24.1)	53.8 (22.3)
PCL-M	44.7 (10.8)	36.3 (11.9)	47.2 (17.8)	40.5 (19.6)
HDRS	16.8 (5.8)	11.1 (5.5)	14.7 (8.6)	11.1 (5.8)
MADRS	20.7 (8.9)	13.9 (10.0)	17.1 (12.9)	14.3 (9.4)

15 of them completed the whole study (visits 1-8, Fig. A1A). In the CG, 11 subjects completed the first rtfMRI-nf session, and 8 of them completed the whole study. There were no significant group differences in age, CAPS, PCL-M, HDRS, or MADRS ratings at baseline.

A2.3 Experimental protocol

The experimental protocol for each rtfMRI-nf session (Fig. A1B) was like the one we employed previously in rtfMRI-nf studies with healthy participants [11] and MDD patients [17,36]. Prior to each rtfMRI-nf session, a participant was given detailed instructions that included an overview of the experiment and an explanation of each experimental task. The participant was asked to think of and write down three happy autobiographical memories, keeping them private. It was suggested that the participant use those three memories at the beginning of the rtfMRI-nf training to evaluate their effects, and then explore various other happy autobiographical memories as the training progressed to enhance happy emotion and improve rtfMRI-nf performance.

Each rtfMRI-nf session included seven fMRI runs (Fig. A1B), and each run lasted 8 min and 46 s. During the initial and final Rest runs, participants were asked to relax and rest while looking at a fixation cross. The five task runs – the Practice run, Run 1, Run 2, Run 3, and the Transfer run – consisted of alternating 40-s long blocks of Happy Memories, Count, and Rest conditions (Fig. A1B). The real-time GUI display screens for these conditions are shown schematically in Fig. A1C. Each condition was specified by visual cues that included a colored square with the condition name at the center of the screen and a text line at the top of the screen. For the Happy Memories condition blocks, participants were instructed to feel happy by evoking and contemplating happy autobiographical memories while simultaneously trying to raise the variable-height red rtfMRI-nf bar on the screen to the target level of the blue bar (Fig. A1C, left). The red bar height was updated every 2 s, and was also indicated by the red numeric value shown above the bar (Fig. A1C, left). For the Count condition blocks, the subjects were instructed to mentally count back from 300 by subtracting a given integer as shown on the screen (Fig. A1C, middle). For the Rest condition blocks, participants were asked to rest and let their minds wander while looking at the screen (Fig. A1C, right).

During the four rtfMRI-nf runs (Practice, Runs 1-3), participants performed the three experimental tasks as indicated by the GUI display screens shown in Fig. A1C. The target level for the rtfMRI-nf (blue bar in Fig. A1C, left) was fixed during each run, but was raised in a linear fashion across the four nf runs. It was set to 0.5%, 1.0%, 1.5%, and 2.0% for the Practice run, Runs 1-3, respectively (see Fig. A3A below). During the Practice run, participants were given an opportunity to become familiar with (or refresh knowledge of) the rtfMRI-nf procedure and to consider the emotional impact of the three happy autobiographical memories they had prepared. During the Transfer run, the participants performed the same tasks as during the preceding nf runs, except that no bars were shown on the screen during the Happy Memories conditions, and the text line read “As Happy as possible”. The Transfer run was included to evaluate whether participants’ learned ability to control BOLD activity of the target ROI generalized beyond the actual rtfMRI-nf training when the nf information was no longer provided. The Count conditions involved counting back from 300 by subtracting 3, 4, 6, 7, and 9 for the Practice run, Runs 1-3, and the Transfer run, respectively. After each experimental run with the Happy Memories task, a participant was asked to verbally rate his performance on a scale from 0 (*not at all*) to 10 (*extremely*) by answering two questions: “How successful were you at recalling your happy memories?” and “How happy are you right now?”.

A2.4 Regions of interest

The rtfMRI-nf procedure was based on the target region-of-interest (ROI) approach we employed previously [11,17]. Two target ROIs were defined as 14-mm diameter spheres in the stereotaxic array of Talairach and Tournoux [37]. The target ROI centered at $(-21, -5, -16)$ in the left amygdala (LA) region (Fig. A2A) was used for the EG. The target ROI centered at $(-42, -48, 48)$ in the left horizontal segment of the intraparietal sulcus (LHIPS) region (Fig. A2B) was used for the CG. The specified ROI centers were selected based on quantitative meta-analyses of functional neuroimaging studies investigating the role of the amygdala in emotion processing [38] or the role of the HIPS in number processing [39]. During the experiment, these target ROIs were transformed from the Talairach space to each participant’s individual fMRI (EPI) image space and used to provide rtfMRI-nf signal depending on the group. For offline fMRI data analysis, the left amygdala (LA) and the right amygdala (RA) ROIs (Fig. A2C) were defined anatomically as the amygdala regions specified in the Talairach-Tournoux brain atlas in AFNI [40].

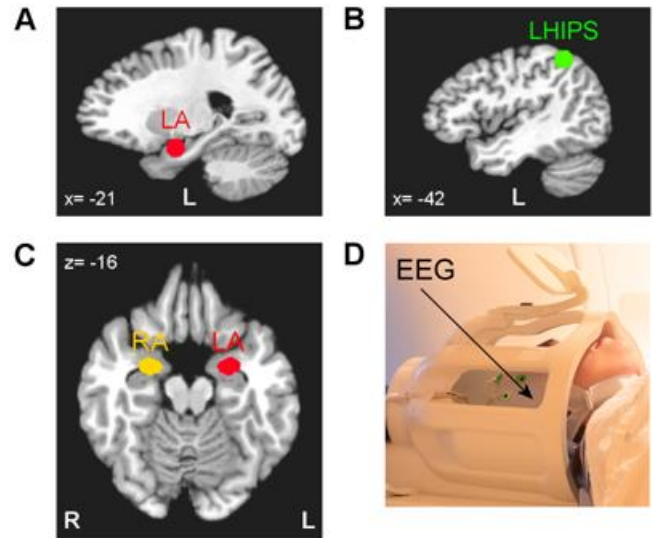


Figure A2. A-C) ROIs selection; D) EEG-fMRI.

A2.5 Data acquisition

All experiments were conducted on the General Electric Discovery MR750 3T MRI scanner with a standard 8-channel receive-only head coil (Fig. A2D). A single-shot gradient echo EPI sequence with FOV/slice=240/2.9 mm, $TR/TE=2000/30$ ms, flip angle=90°, 34 axial slices per volume, slice gap=0.5 mm, SENSE $R=2$ in the phase encoding (anterior-posterior) direction, acquisition matrix 96×96, sampling bandwidth=250 kHz, was employed for fMRI. Each fMRI run lasted 8 min 46 s and included 263 EPI volumes (the first three EPI volumes were excluded to allow the fMRI signal to reach a steady state and were excluded from data analysis). Physiological pulse oximetry and respiration waveforms were recorded simultaneously with fMRI. The EPI images were reconstructed into a 128×128 matrix, resulting in 1.875×1.875×2.9 mm³ fMRI voxels. A T1-weighted 3D MPRAGE sequence with FOV/slice=240/1.2 mm, $TR/TE=5.0/1.9$ ms, $TD/TI=1400/725$ ms, flip

angle=10°, 128 axial slices per slab, SENSE $R=2$, acquisition matrix 256×256, sampling bandwidth=31.2 kHz, scan time=4 min 58 s, was used for structural imaging. It provided high-resolution anatomical brain images with 0.94×0.94×1.2 mm³ voxels.

EEG recordings were performed simultaneously with fMRI (Fig. A2D) using a 32-channel MR-compatible EEG system from Brain Products, GmbH. The EEG system clock was synchronized with the MRI scanner 10 MHz clock using the Brain Products' SyncBox device. EEG data were acquired with 0.2 ms temporal and 0.1 μ V measurement resolution (16-bit 5 kS/s sampling) in 0.016-250 Hz frequency band with respect to FCz reference. All technical details of the EEG-fMRI system configuration and data acquisition were reported previously [41]. Similar to our recent study [17], the EEG recordings in the present work were passive, i.e. no EEG information was used in real time as part of the experimental procedure.

A2.6 Real-time data processing

The rtfMRI-nf was implemented using the custom real-time fMRI system utilizing real-time functionality of AFNI [40] as described previously [11]. A high-resolution MPRAGE anatomical brain image and a short EPI dataset (5 volumes) were acquired prior to each rtfMRI-nf session. The last volume in the EPI dataset was used as a reference EPI volume defining the subject's individual EPI space. The LA and LHIPS target ROIs, defined in the Talairach space (Fig. A2A,B) were transformed to the individual EPI space using the MPRAGE image data. The resulting ROIs in the EPI space contained approximately 140 voxels each. During the subsequent fMRI runs (Fig. A1B), the AFNI real-time plugin was used to perform volume registration of each acquired EPI volume to the reference EPI volume (motion correction) and export mean values of fMRI signals for these ROIs in real time. The custom developed GUI software was used to further process the exported fMRI signal values and display the ongoing rtfMRI-nf information (Fig. A1C). The rtfMRI signal for each Happy Memories condition was computed as a percent signal change relative to the baseline obtained by averaging fMRI signal values for the preceding Rest condition block (Fig. A1B). A moving average of the current and two preceding rtfMRI signal values was computed to reduce effects of fMRI noise and physiological artifacts [11]. This average value was used to set the height of the red rtfMRI-nf bar (Fig. A1C) every TR=2 s.

A2.7 fMRI data analysis

Our analysis focused on the first neurofeedback training session (Visit 4) to evaluate and understand effect of rtfMRI-nf in neurofeedback-naïve PTSD individuals before examining effects across multiple sessions. Offline analysis of the fMRI data was performed in AFNI as described in detail in *Supplementary material* (S1.1). The analysis involved fMRI pre-processing with despiking, cardiorespiratory artifact correction [42], slice timing correction, and volume registration. A general linear model (GLM) analysis with Happy Memories and Count block-stimulus conditions was applied to the preprocessed fMRI data. Average GLM-based fMRI percent signal changes were computed for the LA and RA ROIs, shown in Fig. A2C.

A2.8 fMRI connectivity analysis

Analysis of fMRI functional connectivity for the LA as the seed region was performed within the GLM framework. The fMRI data were bandpass filtered between 0.01 Hz and 0.08 Hz. The six fMRI motion parameters were similarly filtered. The LA ROI (Fig. A2C) was transformed to each subject's individual high-resolution anatomical image space, and then to the individual EPI image space. The LA ROI in the EPI space included ~100 voxels. In addition, 10-mm-diameter ROIs were defined within the left and right frontal white matter (WM) and within the left and right ventricle cerebrospinal fluid (CSF). These ROIs were defined using individual high-resolution anatomical brain maps and similarly transformed. The resulting ROIs in the individual EPI space were used as masks to obtain average time courses for the LA, left and right WM, and left and right CSF regions. The GLM-based functional connectivity analysis was conducted for each task run using the

3dDeconvolve AFNI program. The -censor option was used to restrict the analysis to the Happy Memories condition blocks in each run. The GLM model included the time course of the LA ROI as the stimulus (seed) regressor. Nuisance covariates included five polynomial terms, time courses of the six fMRI motion parameters (together with the same time courses shifted by one TR), time courses of the left and right WM and CSF ROIs to reduce physiological noise [43], and step functions to account for the breaks in the data between the Happy Memories condition blocks. Each GLM analysis provided R^2 -statistics and t -statistics maps for the stimulus regressor term, which we used to compute the correlation coefficient for each voxel. The correlation coefficient maps were Fisher r -to- z normalized, transformed to the Talairach space, and re-sampled to $2 \times 2 \times 2$ mm³ isotropic voxel size. The resulting individual LA functional connectivity maps were spatially smoothed (5 mm FWHM) and submitted to group analyses.

Group analysis of fMRI connectivity for one task run (e.g., the Practice run) was performed using the 3dttest++ AFNI program. The analysis included three covariates: the CAPS ratings, the HDRS ratings, and the average individual fMRI connectivity of the LA with central white matter. The last covariate accounted for residual spurious LA connectivity effects caused, for example, by head motion. The central white matter mask was defined using the standard AFNI white matter mask in the Talairach space (TT_wm), that was re-sampled to $2 \times 2 \times 2$ mm³ voxels, subjected to three-step erosion, and limited to $15 < z < 35$ mm slab. The individual-subject LA connectivity values for the same run were averaged within this mask to yield a single covariate value for each subject. Centering of the three covariates was performed within the 3dttest++ program by subtraction of their means. The LA fMRI connectivity vs CAPS correlation effect was the main effect of interest. The statistical results were corrected for multiple comparisons by controlling the family-wise-error (FWE).

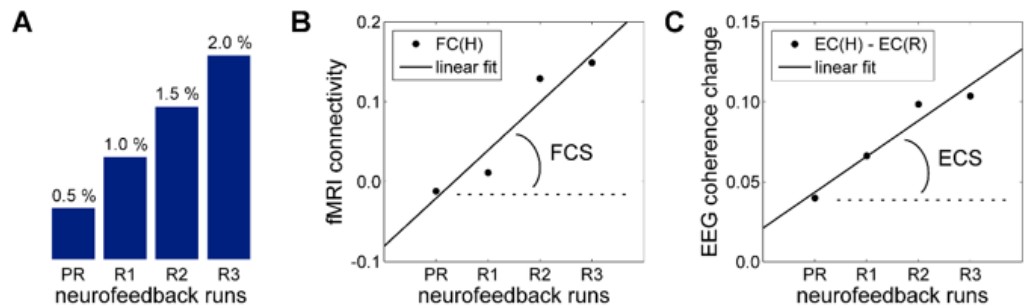


Figure A3. Analyses of linear trends in functional connectivity measures across neurofeedback runs. A) The target level for the rtfMRI-nf (blue bar in Fig. A1C) was raised in a linear fashion across the four rtfMRI-nf runs (Practice, Runs 1-3) in each neurofeedback session. B) Definition of the fMRI connectivity slope (FCS). It is defined, for each fMRI voxel, as a slope of a linear trend in fMRI connectivity with the seed ROI across the Happy Memories conditions in the four rtfMRI-nf runs. C) Definition of the EEG coherence slope (ECS). It is defined, for each pair of EEG channels, as a slope of a linear trend in upper alpha EEG coherence changes between the Rest and Happy Memories conditions across all rtfMRI-nf runs.

Analysis of fMRI connectivity enhancement across the four neurofeedback runs was conducted as follows. An fMRI connectivity slope (FCS) was defined for each voxel as a slope of a linear trend in fMRI connectivity with the LA seed ROI across the Happy Memories conditions in the four rtfMRI-nf runs (Practice, Run 1, Run 2, Run 3), as illustrated in Fig. A3B. The LA fMRI connectivity maps in the Talairach space for the four rtfMRI-nf runs were concatenated, and the 3dTfitter AFNI program was used to carry out a voxel-wise linear trend analysis, yielding the FCS map for each subject. Group analysis on the FCS data was performed using the 3dttest++ AFNI program. The analysis included three covariates: CAPS ratings, HDRS ratings, and the average individual LA FCS for central white matter. The last covariate was computed using the same white matter mask as described above, and accounted for spurious LA connectivity trends across the four runs. The FCS vs CAPS correlation effect and the mean FCS effect were the main effects of interest. The statistical results were corrected for multiple comparisons by controlling the FWE as explained above.

A2.9 EEG data analysis

Offline analysis of EEG data, acquired simultaneously with fMRI, was performed using BrainVision Analyzer 2.1 software (Brain Products, GmbH) as described in detail in *Supplementary material* (S1.2). Removal of EEG

artifacts was based on the average artifact subtraction and independent component analysis [44,45]. Channel Cz was selected as a new reference, and FCz was restored as a regular channel. Following the artifact removal, data from 29 EEG signal channels were down sampled to 8 ms temporal resolution. The upper alpha EEG band was defined individually for each participant as [IAF...IAF+2] Hz, where IAF is the individual alpha peak frequency. The IAF was determined by inspection of average EEG spectra for the occipital and parietal EEG channels across the Rest condition blocks in the four rtfMRI-nf runs (Fig. A1B).

A2.10 EEG coherence analysis

EEG coherence analysis was conducted separately for the Rest and Happy Memories conditions in each of the four rtfMRI-nf runs (Fig. A1B). The analysis included a segmentation with 4.096 s intervals (with exclusion of bad intervals, see S1.2), a complex FFT with 0.244 Hz spectral resolution, and the Coherence transform implemented in the Analyzer 2.1. A coherence value for signals from two EEG channels at a given frequency was computed as the squared magnitude of their cross spectrum value normalized by their power spectrum values at the same frequency ('magnitude-squared coherence' method). An average coherence value for the upper alpha band [IAF...IAF+2] Hz was then computed for each channel pair.

Analysis of EEG coherence enhancement across the four neurofeedback runs was performed as follows. An EEG coherence slope (ECS) was defined for each channel pair as a slope of a linear trend in the upper alpha EEG coherence changes between the Rest and Happy Memories conditions across the four rtfMRI-nf runs (Practice, Run 1, Run 2, Run 3), as illustrated in Fig. A3C. Analysis of partial correlations between the ECS values and the CAPS ratings, controlling for HDRS ratings, was performed using the partialcorr function in MATLAB. To alleviate the multiple comparisons problem, average ECS values were computed for previously defined groups of fronto-temporal EEG channels [17], and their partial correlations with the CAPS ratings were evaluated.

A2.11 Statistical tests

Inferential statistical analyses were performed in IBM SPSS Statistics 20. Correction for multiple comparisons was based on controlling the false discovery rate (FDR q), which was computed by applying the 3dFDR AFNI program to a column of uncorrected p -values from multiple tests. Partial correlation analyses were conducted using MATLAB Statistics toolbox.

Table 2	Initial mean (SD)	Final mean (SD)	Change t-score#	Change p-value [q]
Rating				
Experimental group (EG, n=15)				
CAPS	54.9 (13.6)	40.6 (17.9)	-3.69	0.0024 [0.004]*
Reexperiencing symptoms	11.1 (5.8)	9.1 (6.6)	-1.56	0.142 [0.142]
Avoidance symptoms	21.8 (7.4)	14.0 (9.4)	-3.78	0.0020 [0.004]*
Hyperarousal symptoms	22.0 (4.7)	17.5 (7.2)	-2.54	0.024 [0.030]*
HDRS	17.3 (6.5)	11.1 (5.5)	-4.61	0.0004 [0.002]*
Control group (CG, n=8)				
CAPS	62.3 (20.9)	53.8 (22.3)	-1.75	0.124 [0.207]
Reexperiencing symptoms	15.8 (6.3)	13.5 (8.4)	-1.41	0.203 [0.254]
Avoidance symptoms	24.6 (11.5)	18.0 (13.1)	-1.95	0.092 [0.207]
Hyperarousal symptoms	21.9 (4.6)	22.3 (4.5)	0.30	0.776 [0.776]
HDRS	16.8 (8.5)	11.1 (5.8)	-2.28	0.056 [0.207]
# $t(14)$ for the EG, $t(7)$ for the CG; * FDR $q < 0.05$ for the five tests.				

A3. Results

A3.1 Psychological measures

Changes in PTSD severity and comorbid depression severity for the PTSD Veterans who completed the study are reported in Table 2. The initial and final CAPS ratings were assessed during visits 2 and 8, respectively (Fig. A1A). The initial and final HDRS ratings were determined during visits 3 and 7, respectively. The participants in the EG showed a significant reduction in the total CAPS ratings after the study (EG: $t(14)=-3.69$, $p<0.0024$, $q<0.004$), with significant reductions in sub-scores for avoidance symptoms (EG: $t(14)=-3.78$, $p<0.0020$, $q<0.004$) and hyperarousal symptoms (EG: $t(14)=-2.54$, $p<0.024$, $q<0.030$). The EG participants also exhibited a significant reduction in the HDRS ratings (EG: $t(14)=-4.61$, $p<0.0004$, $q<0.002$).

The participants in the CG also showed a nonsignificant reduction in total CAPS ratings (CG: $t(7)=-1.75$, $p<0.124$, $q<0.207$). The corresponding reductions in avoidance symptoms (CG: $t(7)=-1.95$, $p<0.092$, $q<0.207$) and HDRS ratings (CG: $t(7)=-2.28$, $p<0.056$, $q<0.207$) were also nonsignificant.

In the EG, 12 participants out of 15 (80%) demonstrated clinically meaningful reductions in CAPS ratings (by 10 points or more). In the CG, 3 subjects out of 8 (or 38%) showed clinically meaningful CAPS reductions. However, no significant difference in the CAPS rating changes (final vs initial) was observed between the two groups (EG vs CG: $t(21)=-0.90$, $p<0.377$). Similarly, the HDRS rating changes (final vs initial) showed no significant group difference (EG vs CG: $t(21)=-0.22$, $p<0.825$).

A3.2 Amygdala BOLD activity

Figure A4 shows results of the offline fMRI activation analysis for the LA and RA ROIs (Fig. A2C). The results are for the first rtfMRI-nf session (visit 4; EG: $n=20$; CG: $n=11$). The LA BOLD activity levels for the Happy Memories conditions for the EG (H vs R, Fig. A4A, left) were significant for Run 3 (R3: $t(19)=3.03$, $p<0.007$, $q<0.035$) and for the Transfer run (TR: $t(19)=2.63$, $p<0.017$, $q<0.042$). There was no significant difference in the LA activity between these two runs (TR vs R3: $t(19)=-1.33$, $p<0.199$). The RA BOLD activity levels for the EG (H vs R, Fig. A4A, right) were significant for Run 3 (R3: $t(19)=3.04$, $p<0.007$, $q<0.034$) and trended toward significance after correction for the Transfer run (TR: $t(19)=2.24$, $p<0.037$, $q<0.093$). Similar to the LA, there was no significant difference in the RA activity between these two runs (TR vs R3: $t(19)=-1.16$, $p<0.259$). For the CG, BOLD activity levels for either the LA or the RA were not significant (Fig. A4B). To compare the neurofeedback effects between the EG and CG groups, we examined average individual BOLD activity levels across the three rtfMRI-nf training runs (Runs 1-3). For the average LA BOLD activity levels, Levene's test for

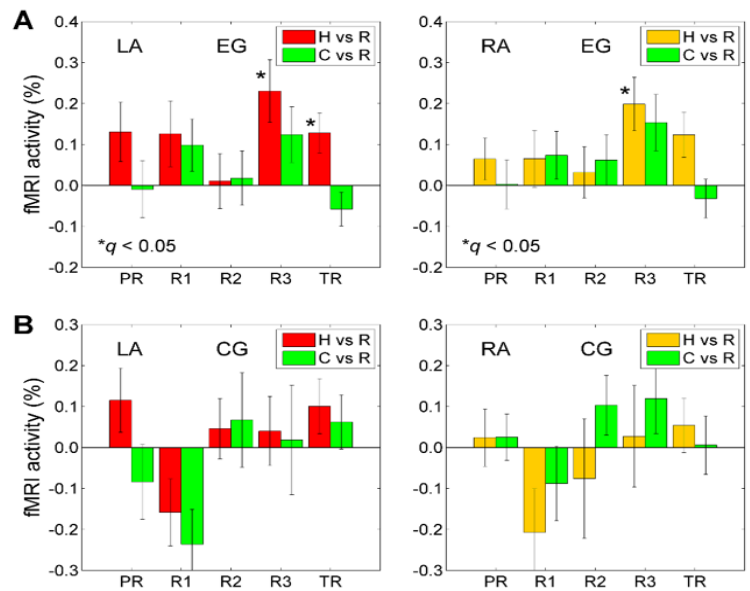


Figure A4. BOLD activity of the amygdala during the 1st rtfMRI-nf session.

A) Average fMRI percent signal changes for the left amygdala (LA, left) and the right amygdala (RA, right) ROIs for the experimental group (EG). Each bar represents a mean GLM-based fMRI percent signal change for the corresponding ROI with respect to the Rest baseline for the Happy Memories (H vs R) or Count (C vs R) conditions in a given run, averaged across the group. The error bars are standard errors of the means (sem) for the group averages. Significance of the H vs R results is specified after FDR correction for testing the data for five runs. B) Corresponding average fMRI percent signal changes for the control group (CG).

equality of variances suggested that variances differed between the groups ($F=4.79$, $p<0.037$). An independent-samples t -test with Welch-Satterthwaite adjustment indicated that the average LA BOLD activity levels were significantly higher for the EG than for the CG ($t(28.18)=2.38$, $p<0.024$, equal variances not assumed). For the average RA BOLD activity levels, variances did not differ between the groups ($F=0.14$, $p<0.908$). The difference in the average RA BOLD activity levels between the EG and the CG trended toward significance ($t(29)=1.76$, $p<0.088$).

A3.3 Amygdala Connectivity during Practice

All fMRI connectivity and EEG coherence results reported below correspond to the first rtfMRI-nf session (Fig. A1A, visit 4). The initial CAPS ratings (visit 2) and initial HDRS ratings (visit 3) were used in partial correlation analyses. Figure A5 shows whole-brain group statistical maps of the correlation between the LA fMRI connectivity during Happy Memories conditions in the Practice run and CAPS ratings for the EG. Data from $n=19$ EG participants were included in the analysis. One outlier EG participant, whose initial CAPS rating was much higher (CAPS=95) than the rest of the EG subjects, was excluded from the analysis to avoid biasing the group results. One outlier EG participant, whose initial CAPS rating was much higher (CAPS=95) than the rest of the EG subjects, was excluded from the analysis to avoid biasing the group results. The group statistical maps in Fig. A5 were thresholded at $t=\pm 2.95$ (uncorr. $p<0.01$) and clusters containing at least 75 voxels (FWE corr. $p<0.05$) are shown in the figure.

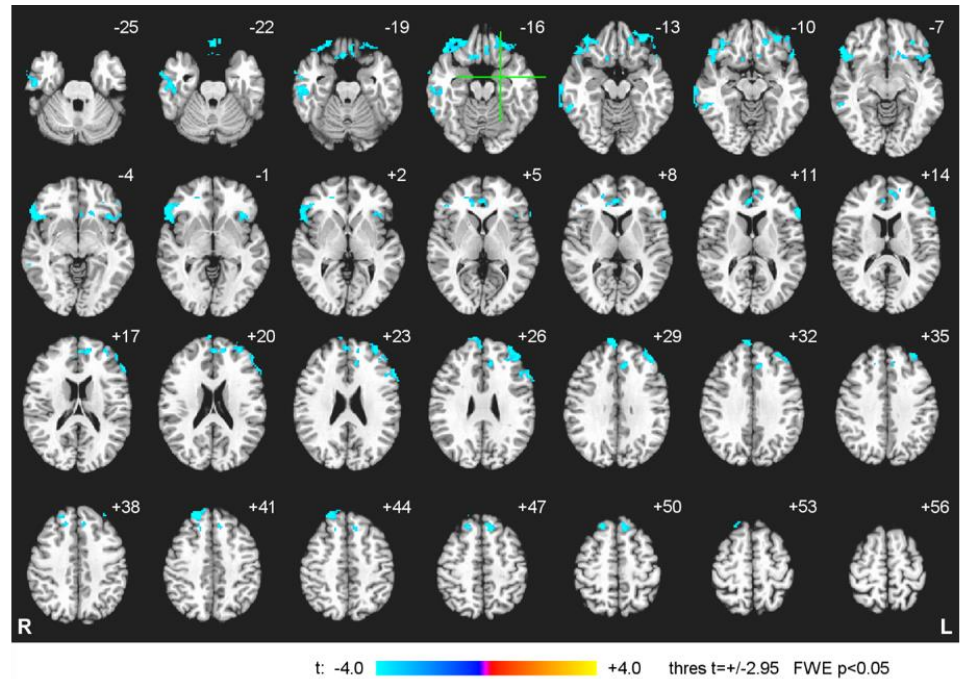


Figure A5. Statistical maps of the correlation between the fMRI connectivity of the left amygdala (LA) during the Happy Memories conditions in the Practice run and PTSD severity (CAPS) for the experimental group (EG). The correlation is a voxel-wise partial correlation with CAPS ratings controlled for comorbid depression severity (HDRS) ratings and average individual LA connectivity with white matter. The maps are FWE corrected and projected onto the standard anatomical template (Talairach), with 3 mm slice. The number adjacent to each slice indicates the z coordinate in mm. Peak t -statistics values for the correlation effect and the corresponding cluster properties are specified in Table 3.

Table 3.					
Region	Laterality	x, y, z (mm)	t-score	Size (voxels)	
Frontal Lobe					
Lateral orbitofrontal cortex (BA 47)	R	51, 23, -8	-9.50	646	
Dorsolateral prefrontal cortex (BA 9)	L	-33, 51, 24	-5.45	306	
Lateral orbitofrontal cortex (BA 11)	L	-31, 41, -11	-6.77	288	
Medial frontal polar cortex (BA 9)	R	9, 61, 30	-6.91	252	
Ventrolateral prefrontal cortex (BA 45)	L	-55, 21, 12	-6.85	188	
Dorsolateral prefrontal cortex (BA 8)	R	21, 43, 42	-6.70	181	
Superior frontal gyrus (BA 8)	L	-7, 31, 48	-5.62	158	
Medial orbitofrontal cortex (BA 11)	R	1, 33, -22	-5.55	125	
Medial orbitofrontal cortex (BA 11)	R	5, 20, -20	-7.34	84	
Temporal Lobe					
Middle temporal gyrus (BA 21)	R	67, -19, -12	-5.98	325	
Middle temporal gyrus (BA 20)	R	57, -43, -12	-5.94	92	
Limbic Lobe					
Anterior cingulate cortex (BA 24)	R	3, 37, 9	-5.76	127	
Sub-lobar Regions					
Insula (BA 13)	L	-35, 21, 0	-4.79	144	

Notations: BA – Brodmann areas; L – left; R – right; x, y, z – Talairach coordinates; FWE corrected $p<0.05$ (Size – cluster size, minimum 75 voxels for uncorr. $p<0.01$).

The cluster properties are described in Table 3. The results in Fig. A5 and Table 3 demonstrate that, at the beginning of the training, fMRI connectivity with the LA showed *negative* correlations with PTSD severity for many prefrontal brain regions, particularly the LOFC, the MOFC, the rACC, and the DLPFC. For the CG, the correlations during the Practice run are similar to those for the EG in Fig. A5.

The negative correlation effects mapped in Fig. A5 are illustrated in Figure A6. Note that several other regions exhibited *positive* correlations between their fMRI connectivity with the LA and CAPS ratings, but the corresponding clusters were not large enough to survive the whole-brain FWE correction. For example, these regions included the left caudate at (-19, -25, 20) ($t=5.21$, 62 vox.), the right mediodorsal nucleus (MD) of the thalamus at (3, -16, 15) ($t=5.46$, 26 voxels), the right amygdala at (25, -7, -20) ($t=5.00$, 24 voxels), the right precuneus (PCun, BA 39) at (27, -57, 31) ($t=4.24$, 22 voxels), the left precuneus (BA 7) at (-25, -61, 31) ($t=4.24$, 22 voxels). The correlation effects for the R MD and the R PCun are also illustrated in Fig. A6.

A3.4 Amygdala connectivity enhancement

Figure A7 exhibits whole-brain group statistical maps of the correlation between the LA fMRI connectivity slope (FCS) across Happy Memories conditions in the four rtfMRI-nf runs (Fig. A3B) and CAPS ratings. The results are for the same EG participants ($n=19$) as in Figs. A5 and A6. The maps in Fig. A7 were thresholded at $t=\pm 2.95$ (uncorr. $p<0.01$) and clusters containing at least 81

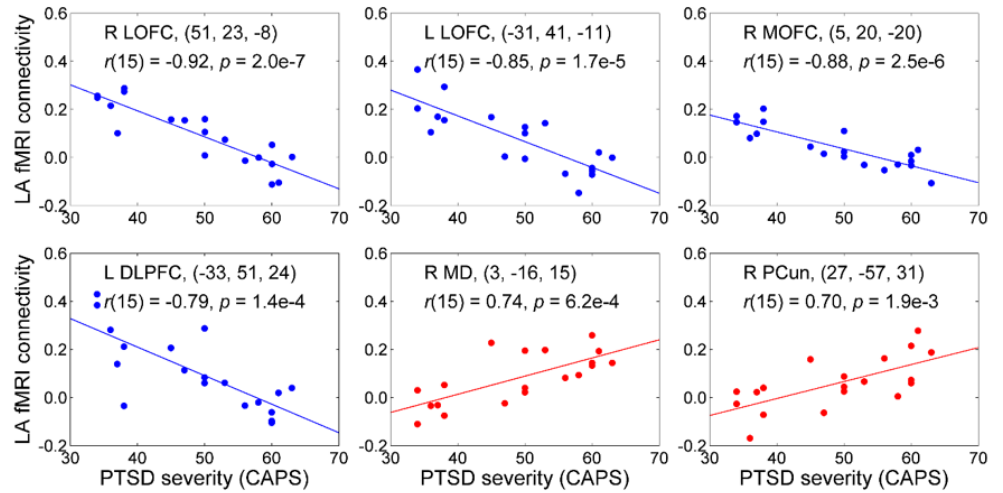


Figure A6. The correlation effects between the LA fMRI connectivity during the Happy Memories conditions in the Practice run and PTSD severity (CAPS) for the EG. Each plot shows an average correlation effect for a 10-mm diameter ROI centered at a specified location. The correlation is a partial correlation with CAPS ratings controlled for HDRS ratings and average individual LA connectivity with white matter ($n=19$, $df=15$). The results for the R LOFC, L LOFC, R MOFC, and L DLPFC correspond to those reported in Fig. A5 and Table 3. The results for the R MD and R PCun are included to illustrate existence of positive correlations between the LA fMRI connectivity and PTSD severity. Abbreviations: LOFC – lateral orbitofrontal cortex, MOFC – medial orbitofrontal cortex, DLPFC – dorsolateral prefrontal cortex, MD – mediodorsal nucleus of the thalamus, PCun – precuneus.

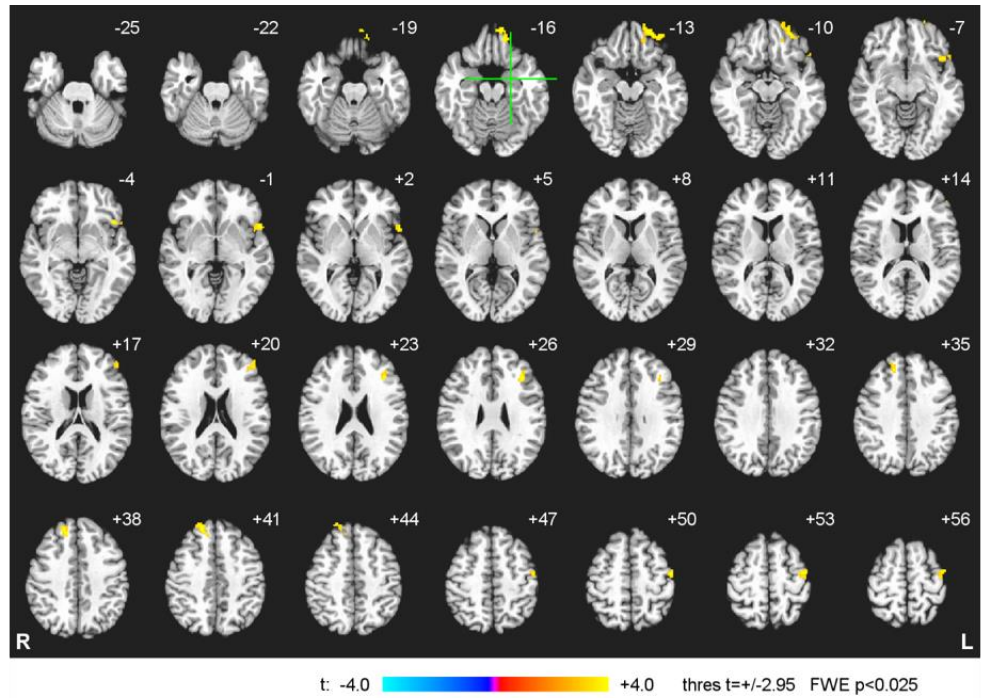


Figure A7. Statistical maps of the correlation between the fMRI connectivity slope (FCS) for the LA and PTSD severity (CAPS) for the experimental group (EG). The correlation is a voxel-wise partial correlation with CAPS ratings controlled for comorbid depression severity (HDRS) ratings and average individual LA FCS for white matter. The maps are FWE corrected and projected onto the TT_N27 template, with 3 mm separation between axial slices (numbers adjacent to slices indicate the z coordinate in mm). The green crosshairs mark the center of the LA target ROI. Peak t -statistics values for the correlation effect and the corresponding cluster properties are specified in Table 4.

voxels (FWE corr. $p < 0.025$) are shown in the figure. The cluster properties are specified in Table 4. The table also includes statistical results for the mean FCS effect, thresholded and clustered in the same way (FWE corr. $p < 0.025$, to account for testing the two effects). The mean FCS effect was obtained in the same group analysis and corresponds to the mean values of the covariates (CAPS ratings, HDRS ratings, LA FCS for white matter). The results in Fig. A7 and Table 4 demonstrate that the fMRI connectivity enhancement (FCS) with the LA during the training exhibited *positive* correlations with PTSD severity for several prefrontal regions, including the LOFC and the DLPFC. The left DLPFC also showed a significant fMRI connectivity enhancement with the LA that was independent of the CAPS and HDRS variability (the mean FCS effect, Table 4). For the CG, no significant positive FCS vs CAPS correlations or mean FCS effects were found within the PFC.

The positive correlation effects mapped in Fig. A7 are illustrated in Figure A8. Note that several other regions that showed negative correlations in Figs. A5 and A6 exhibited positive correlations between the FCS and CAPS, but the corresponding clusters did not survive the whole-brain FWE correction. For example, these regions included the right LOFC at (55, 25, -1) ($t = 5.22$, 68 voxels), the left MOFC at (-1, 39, -15) ($t = 3.99$, 25 voxels). Furthermore, some regions showed *negative* correlations between the FCS and CAPS, such as the right precuneus/posterior cingulate at (23, -62, 25) ($t = -3.71$, 39 voxels). The correlation effects for these regions are also illustrated in Fig. A8.

A3.5 EEG coherence enhancement

Figure A9 demonstrates correlations between the EEG coherence slope (ECS) for the upper alpha EEG band across the four rtfMRI-nf runs (Fig. A3C) and CAPS ratings for the EG. The EEG recordings were conducted simultaneously with fMRI (Fig. A2D). Data from 18 EG participants were included in the ECS vs CAPS correlation analysis, with the same outlier excluded as described above along with a second participant whose data were excluded due to excessive EEG-fMRI artifacts. According to Fig. A9A, the ECS exhibited positive correlations ($r(15) > 0$, $p < 0.05$, uncorr.) with CAPS ratings for many EEG channel pairs, particularly those involving frontal and left temporal (T7) EEG channels. (Negative correlations, $r(15) < 0$, did not reach the $p < 0.05$ statistical threshold). This correlation effect is illustrated in Fig. 9B for one channel pair.

Table 4.	Region	Laterality	x, y, z (mm)	t-score	Size (voxels)
FCS vs CAPS correlation effect					
	Lateral orbitofrontal cortex (BA 11)	L	-23, 47, -12	5.19	219
	Dorsolateral prefrontal cortex (BA 9)	R	15, 37, 39	4.65	116
	Dorsolateral prefrontal cortex (BA 9)	L	-35, 25, 26	5.45	110
	Lateral orbitofrontal cortex (BA 47)	L	-43, 17, -6	4.69	106
	Precentral gyrus (BA 4)	L	-49, -11, 50	5.76	84
Mean FCS effect					
	Dorsolateral prefrontal cortex (BA 9)	L	-55, 9, 30	4.68	250
	Inferior temporal gyrus (BA 20)	L	-55, -37, -16	6.35	93
	Superior temporal gyrus (BA 22)	R	55, -7, -2	4.64	81
Notations: BA – Brodmann areas; L – left; R – right; x, y, z – Talairach coordinates; FWE corrected $p < 0.025$ (Size – cluster size, minimum 81 voxels for uncorr. $p < 0.01$).					

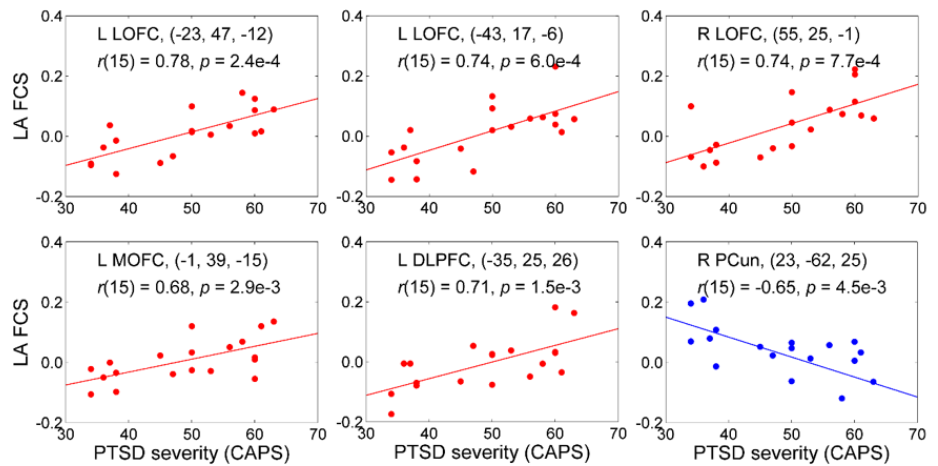


Figure A8. Illustration of the correlation effects between the LA FCS and PTSD severity (CAPS) for the EG. Each plot shows an average correlation effect for a 10-mm diameter ROI centered at a specified location. The correlation is a partial correlation with CAPS ratings controlled for HDRS ratings and average individual LA FCS for white matter ($n = 19$, $df = 15$).

Following our previous work [17], we defined average ECS for 10 pairs of fronto-temporal EEG channels on the left, ECS(L), and for 10 corresponding channel pairs on the right, ECS(R), as detailed in Fig. A9C,D. The ECS(L) demonstrated a significant *positive* correlation with CAPS ratings (Fig. A9C). The average ECS laterality, ECS(L)–ECS(R), showed a positive correlation with CAPS that trended toward significance (Fig. A9E).

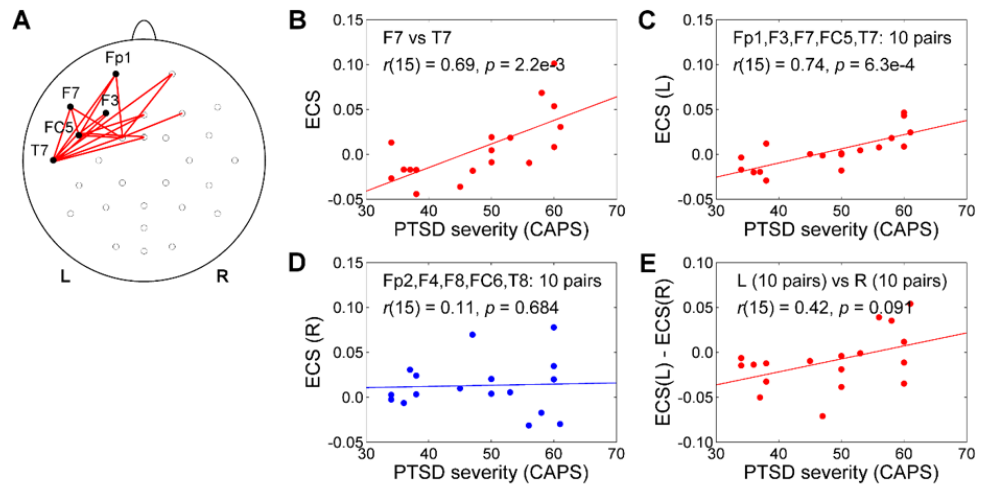


Figure 9. Correlation between the EEG coherence slope (ECS) in the upper alpha band and PTSD severity (CAPS) for the experimental group (EG). The correlation for each EEG channel pair (or average across multiple channel pairs) is a partial correlation with CAPS ratings controlled for comorbid depression severity (HDRS) ratings ($n=18$, $df=15$). A) Red segments denote EEG channel pairs for which the ECS vs CAPS correlations are positive ($r(15)>0$, $p<0.05$, uncorr.). B) Example of such correlation for one channel pair. C) Significant correlation between the ECS(L), i.e. the average ECS for 10 pairs of fronto-temporal EEG channels on the left, and CAPS ratings. D) Lack of correlation between the ECS(R), i.e. the average ECS for 10 pairs of corresponding fronto-temporal EEG channels on the right, and CAPS ratings. E) Correlation between the average ECS laterality, ECS(L)–ECS(R), and CAPS ratings.

A. Discussion

The EG participants who completed the first rtfMRI-nf training session ($n=20$) were able to significantly increase LA BOLD activity during the Happy Memories conditions in Run 3 and in the Transfer run. This suggests participants gradually learned to upregulate LA activity as the training progressed. Importantly, the LA BOLD activity levels averaged across the three rtfMRI-nf training runs (Runs 1-3) were significantly higher for the EG than for the CG. However, the PTSD patients in the EG only achieved mean LA activity levels for individual runs in the range from 0.1% to 0.2% (Fig. A4A). This is lower than the 0.2% to 0.3% mean LA activity range for MDD patients who followed the same protocol in our previous study [17].

Functional connectivity of the LA during the Happy Memories conditions in the Practice run of the first rtfMRI-nf session served as an estimate of the task-specific LA connectivity at the beginning of the training. During this run, the participants were exposed to the rtfMRI-nf for the first time and did not yet know how to effectively control the rtfMRI-nf signal. The results in Fig. A5 and Table 3 demonstrate negative correlations between the LA fMRI connectivity and the initial CAPS ratings for many prefrontal regions, including the LOFC (BA 47, 11), MOFC (BA 11), DLPFC (BA 9, 8), VLPFC (BA 45), medial frontopolar cortex (BA 9), and rACC (BA 24). These results are consistent with the PFC hypoactivity pattern previously observed among people with PTSD [46-48]. At the same time, the LA connectivity with several brain regions, including the right amygdala, the right MD, and the bilateral precuneus (BA 39, 7), exhibited positive, though smaller, correlations with the CAPS ratings (Sec. 3.3, Fig. A6). Parietal regions, including the precuneus and the inferior parietal lobule, are known to be hyperactive together with the amygdala in PTSD [46-48]. Our results suggest that fMRI connectivity between the amygdala and regions of the autobiographical memory recall system (MD, precuneus) is increased in PTSD not only during recollection of traumatic events, but also during retrieval of happy autobiographical memories.

The main result of the present work was the observation of the significant *positive* correlations between PTSD severity and the LA fMRI connectivity enhancement (FCS) for several PFC regions during the rtfMRI-nf training. This positive FCS vs CAPS correlation effect is observed for the left LOFC (BA 47, 11), bilateral DLPFC (BA 9), and left precentral gyrus (BA 4) for the EG (Fig. A7, Table 4). Positive, though less robust, correlation effects were also observed for the right LOFC (BA 47) and the left MOFC (BA 11), as illustrated in

Fig. A8. Such positive correlations suggested that the patients with more severe PTSD (higher CAPS ratings) showed more positive changes in the LA connectivity with these PFC regions as the rtfMRI-nf training progressed. For the right precuneus, the corresponding LA connectivity changes were more negative (Fig. A8). Therefore, the results in Figs. A7 and A8 demonstrate correction (at least partial) of the LA fMRI connectivity deficiencies specific to PTSD and evident in Figs. A5 and A6. Furthermore, the EG participants exhibited a significant mean FCS effect in the left DLPFC (BA 9) (Table 4). This effect indicated a significant fMRI connectivity enhancement between the LA and the left DLPFC across the rtfMRI-nf runs, independent of the PTSD and depression severity (and corresponding to the mean CAPS and HDRS ratings for the EG). This finding is generally consistent with the positive group-average fMRI connectivity changes between the amygdala and the DL/DMPFC during the rtfMRI-nf task reported by Nicholson [49].

EEG recordings performed simultaneously with fMRI allowed us to investigate electrophysiological correlates of the rtfMRI-nf training. We examined variations in EEG coherence, which is an EEG measure of functional connectivity, across the four rtfMRI-nf runs. The average enhancement in upper alpha EEG coherence for the fronto-temporal EEG channels on the left, ECS(L), significantly correlated with PTSD severity for the EG (Fig. A9C). Note that this positive ECS vs CAPS correlation effect is directly related to the positive FCS vs CAPS correlation effect in Fig. A7 and Table 4. Indeed, four out of five clusters in Fig. A7 appear within the left PFC. Stronger functional connectivities among these PFC regions and the LA likely result in stronger coherences for EEG signals measured above these regions. Importantly, the enhancements in functional connectivity that accompany the rtfMRI-nf training may therefore be observable in both fMRI and EEG domains.

Our study demonstrated that rtfMRI-nf of amygdala activity to enhance emotion regulation ability may be beneficial to Veterans with combat-related PTSD. Our fMRI and EEG results independently suggest that the rtfMRI-nf training has the potential to correct the amygdala-PFC functional connectivity deficiencies specific to PTSD. The most significant PTSD-specific enhancements in fMRI connectivity between the LA and the PFC were observed for the LOFC and DLPFC regions, which are parts of the EF/ER system. Because activities of these cortical regions can be probed using EEG, EEG-nf based on frontal EEG asymmetry in alpha band may complement the rtfMRI-nf of the amygdala.

B) Correlation between amygdala BOLD activity and frontal EEG asymmetry in PTSD

B. Introduction

In separate analyses to establish a neurofeedback target for Aim #3 of the study (i.e., stand-alone EEG neurofeedback) we investigated the connection between frontal EEG asymmetry and BOLD activity during the rtfMRI-nf training in PTSD by performing EEG-fMRI correlation analysis for the first neurofeedback visit. EEG acquired during an rtfMRI-nf procedure allows investigation of electrophysiological correlates of the rtfMRI-nf training [17]. Frontal EEG asymmetry (FEA) at rest has been shown to inversely correlate with PTSD severity [50]. FEA changes during emotional stimuli have been shown to reflect PTSD patients' response to CBT treatment [51]. We hypothesized that temporal correlation between frontal EEG asymmetry and BOLD activity of the amygdala would be enhanced during the rtfMRI-nf task compared to a control task. In addition, we expected that FEA changes during a happy emotion induction task with rtfMRI-nf targeting the left amygdala (LA) [11,17] provide information about the PTSD patients' individual response to the emotion regulation training. Our analysis confirmed this hypothesis and provided new insights into functional deficiencies in PTSD.

B. Methods

Twenty male patients with combat-related PTSD have completed this ongoing study in the experimental group. The study included 8 sessions (Fig. A1, in section A above): an initial psychological assessment, an initial

Clinician-Administered PTSD Scale (CAPS) evaluation, an MRI session with an emotional Stroop task, three rtfMRI-nf training sessions with simultaneous EEG, a repeat MRI session, and a final CAPS evaluation. Out of a cohort of 20 subjects used for these analyses, 15 completed training and have CAPS change scores. Severity of co-morbid depression was assessed using the Hamilton Depression Rating Scale (HDRS). Other experimental details are included in Study overview in section A above. The EEG-fMRI correlation analysis was performed as described in detail in [17].

To estimate FEA changes during training conditions (Happy, Count, Rest, Fig. A1, in section A above), time-frequency analysis was conducted using a continuous wavelet transform. The upper alpha EEG band was defined for each subject as $[IAF...IAF+2]$ Hz, where IAF is the individual alpha peak frequency. Frontal EEG asymmetry was defined as either $\ln(P(F4))-\ln(P(F3))$ or $\ln(P(F8))-\ln(P(F7))$, where P is EEG power in the upper alpha band. The time course of frontal EEG asymmetry was used to define two terms for the psychophysiological interaction (PPI) analysis: correlation and interaction.

The [EEG-asymmetry-based regressor] \times [Happy-Count] interaction term described the difference in temporal correlations of the frontal EEG asymmetry (convolved with the HRF) and BOLD activity between the Happy and Count conditions. The PPI analysis was conducted within the GLM framework for all brain voxels [17].

B. Results

The PPI interaction effect for the frontal EEG asymmetry $\ln(P(F4))-\ln(P(F3))$, averaged within the LA ROI (Fig. B1A), was positive and significant for the last rtfMRI-nf run (R3) and exhibited a significant linear trend across the nf runs. This means that temporal correlation between the frontal EEG asymmetry and the LA BOLD activity was significantly enhanced during the Happy condition with rtfMRI-nf compared to the Count condition. Similar PPI effects were observed for the $\ln(P(F8))-\ln(P(F7))$ asymmetry (Fig. B1B).

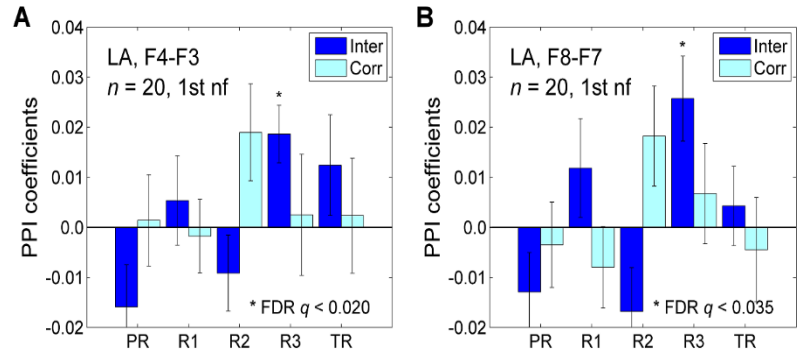


Figure B1. Enhancement in temporal correlation between frontal EEG asymmetry and BOLD activity of the left amygdala (LA) during the rtfMRI-nf training. A) Average PPI coefficients for the LA ROI corresponding to frontal EEG asymmetry $\ln(P(F4))-\ln(P(F3))$. B) Average PPI coefficients corresponding to frontal EEG asymmetry $\ln(P(F8))-\ln(P(F7))$. See [1].

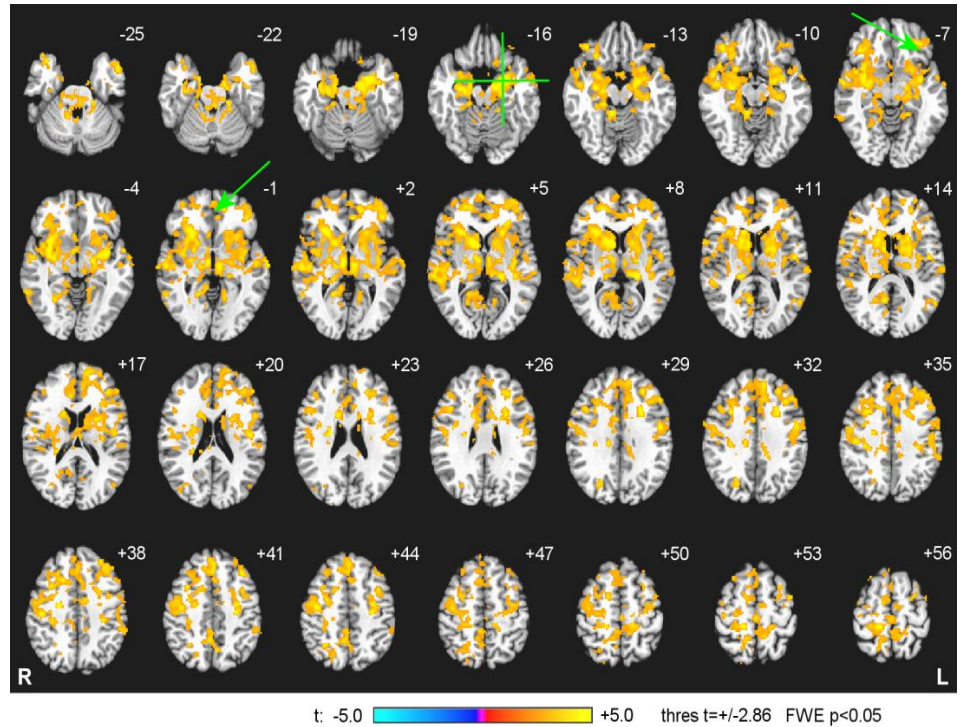


Figure B2. Group statistical map of the PPI interaction effect corresponding to frontal EEG asymmetry $\ln(P(F8))-\ln(P(F7))$. The green crosshairs mark the center of the LA target ROI. The green arrows point to regions (LOFC and rACC) for which the PPI interaction effects in PTSD are substantially weaker than in MDD. See [17].

The whole-brain PPI interaction map (Fig. B2) is generally consistent with the PPI interaction map reported previously for MDD patients [17]. However, the PPI interaction effect is considerably weaker (Fig. B2) for the left lateral orbitofrontal cortex (LOFC) and the left rostral anterior cingulate cortex (rACC).

Session-to-session variations in the average (across four rtfMRI-nf runs) individual Happy vs Rest FEA changes significantly correlated with the corresponding variations in CAPS ratings (Fig. B3A) and HDRS ratings (Fig. B3B). Our interpretation of these results is illustrated in Fig. B3C. A multiple regression analysis for Δ FEA vs Δ CAPS and Δ HDRS showed a significant main effect ($F(2,12)=14.7$, $p<0.001$). Partial correlation Δ FEA vs Δ CAPS controlling for Δ HDRS: $r(12)=0.71$, $p<0.004$. Partial correlation Δ FEA vs Δ HDRS controlling for Δ CAPS: $r(12)=0.58$, $p<0.031$.

B. Discussion

Our results demonstrated that frontal EEG asymmetry provides relevant information about the participants' emotional/motivational states during the rtfMRI-nf training not only in MDD [17], but also in PTSD. The average individual FEA changes during the rtfMRI-nf task are sensitive to severity of PTSD symptoms. Frontal EEG asymmetry can be used to indirectly probe activity of the amygdala and the related network by means of EEG. The weak PPI interaction effects for the LOFC and rACC (Fig. B2) can be attributed to the fact that activities of these regions are strongly affected by PTSD symptoms. The session-to-session variations in the FEA changes provide a measure of an individual response to emotion regulation training, reflecting reduction in both PTSD severity (CAPS) and co-morbid depression severity (HDRS). The partial correlation analyses suggest that variations in CAPS ratings and variations in HDRS ratings have essentially independent effects on the observed variations in the FEA changes. Our results indicated that the FEA variations associated with the rtfMRI-nf training can serve as a measure of treatment response in PTSD, and serves as good candidate for the neurofeedback signal for EEG only neurofeedback training.

C) Individual differences in the effect of the real-time fMRI amygdala neurofeedback emotional training in combat-related PTSD

C. Introduction

In this analysis, we addressed individual differences in the left amygdala (LA) rtfMRI-nf training effect to elucidate the critical factors of training success and treatment effect. Investigating such individual differences should help to classify patients who are responsive to the rtfMRI-nf treatment and those who are not, which is necessary to develop effective individualized treatment.

C. Methods

This analysis included thirty-six male combat Veterans with PTSD (age 21-48, mean=32, SD=7 years) participated in three rtfMRI-nf neurofeedback training sessions (see Study overview, section A for details). Three subjects and four subjects dropped out at the second and the third session, respectively. Each session

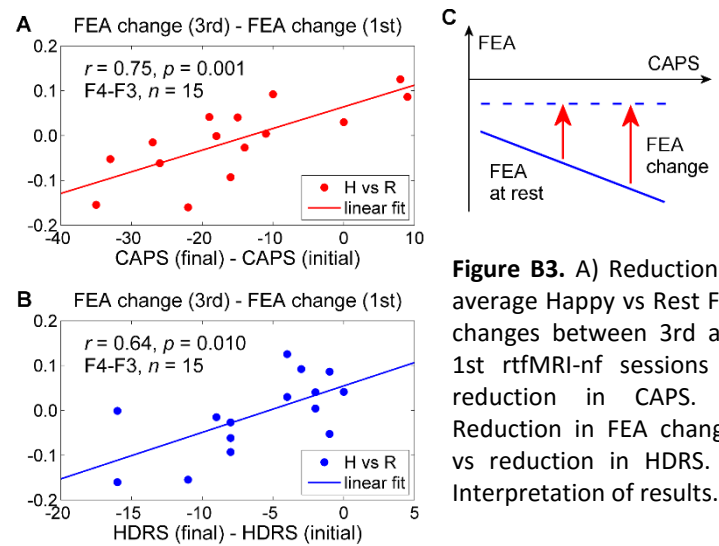


Figure B3. A) Reduction in average Happy vs Rest FEA changes between 3rd and 1st rtfMRI-nf sessions vs reduction in CAPS. B) Reduction in FEA changes vs reduction in HDRS. C) Interpretation of results.

was separated by an 11-day interval on average. Participants were randomly divided into active (N=25) and sham (N=11) feedback groups.

Functional images were processed with the Analysis of Functional NeuroImages (AFNI, <https://afni.nimh.nih.gov/>) software package. Pre-processing included physiological noise correction (RETROICOR/RVT regression), slice-timing correction, head motion alignment, normalization to MNI152 template brain with Advanced Normalization Tools (ANTs, <http://stnava.github.io/ANTs/>), smoothing with 6mm-FWHM Gaussian kernel, and scaling to percent change. Further noise reduction was applied in a general linear model (GLM) analysis by regressing out three principal components of ventricle signals, local white matter average signal (ANATICOR), motion parameters and their temporal derivative, and 4th-order polynomial for modeling slow signal fluctuations. The GLM analysis also included regressors of happy and count blocks (box-car time course convolved with hemodynamic response function), respectively, and event-related response at onset of every block. No significant difference in mean age or mean head motion between groups was observed for the analyzed subjects.

LA response during the happy block was extracted by beta-value of the fitted happy block regressor in the GLM analysis. Group analysis was performed with linear mixed-effect model (LME) analysis to examining the effects of training runs (continuous values of 0 to 3 for Practice, Run 1, Run 2, and Run 3, respectively), sessions (factor variable of #1, #2 and #3), and groups (active, sham) on happy block response in LA ROI. The statistical analyses were performed with R Statistical Computing Language and Environment. We also performed LME analysis for all voxels in the brain to investigate the rtfMRI-nf training effect in the whole brain. The whole-brain statistical map was thresholded with $p < 0.001$ voxel-wise, then with cluster-size corrected $p < 0.01$. Cluster-extent threshold was evaluated with improved autocorrelation function of spatial smoothness of fMRI signals [54].

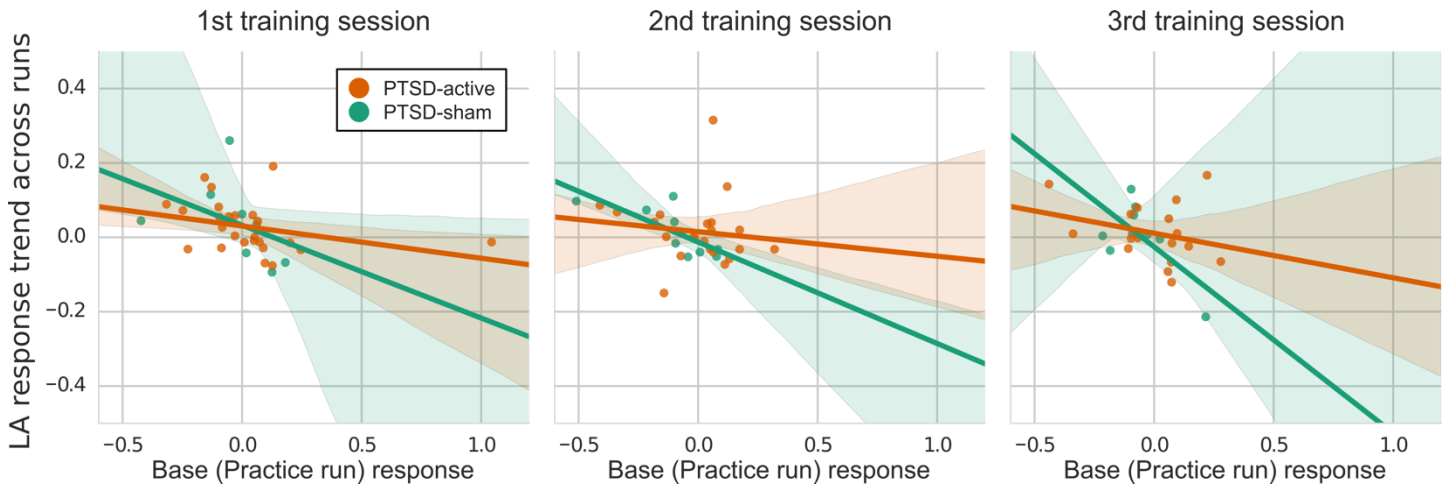


Figure C1. Correlations between baseline amygdala signal and training slope [17] across runs in each training session.

C. Results

The LME analysis showed no significant effect of the run ($p=0.108$) and the session ($p=0.790$). The training slope analysis, which has been introduced in section A above and reported previously [17], indicated that LA response trend across runs was correlated with baseline LA response (at Practice run in the feedback session #1). Fig. C1 shows the correlation between the baseline signal and training slope across runs in each session. The plot indicates a negative correlation between the baseline LA signal and slope of LA signal across training runs. We confirmed this association by performing LME analysis with the additional fixed effect of baseline LA signal. The analysis showed significant main effect of baseline signal ($p=0.004$).

We further examined the relationship between the individual variability of training effect and baseline symptoms and symptom change after the sessions. Baseline LA response was not correlated with any baseline symptom score. Training slope in LA signal was negatively correlated with baseline CAPS subscale C (avoidance and numbing symptoms). For symptom change, however, no significant correlation with LA baseline signal or training slope was found.

The whole brain analysis by LME revealed significant training effect at bilateral anterior insula, the precentral, and the postcentral regions, as well as the right ventrolateral prefrontal, the right medial dorsal frontal, anterior cingulate cortex (ACC), the right supramarginal, and the right inferior temporal regions. A significant training effect was also seen in the left prefrontal area (Fig. C2). These regions showed decreased response across training runs. The decrease in the ACC response was significantly correlated with a decrease in CAPS total score ($p=0.035$ for PTSD-active and $p=0.089$ for PTSD-sham, Fig.C3) and CAPS C subscale (avoidance and numbing) symptom ($p=0.030$ for PTSD-active and $p=0.063$ for PTSD-sham, Fig.C3).

C. Discussion

Training in self-regulating LA activity during positive autobiographical memory recall with rtfMRI-nf was effective to reduce symptoms of PTSD

group. While rtfMRI-nf training could increase LA response, there was no consistent increasing trend across multiple runs and sessions. We found, however, that LA response trend associated with baseline LA response. This individual variability might be due to ceiling LA activation for some PTSD patients. In contrast, while it has been indicated in MDD that patients have hypoactive LA activity to positively valenced stimuli compared to healthy controls [55], hyperactive amygdala has been reported for PTSD in emotional tasks [48] and in resting-state [56]. This suggests the current treatment strategy with rtfMRI-nf to increase LA activity was most effective for subtypes of PTSD patients with hypoactive amygdala response to positive memory recall.

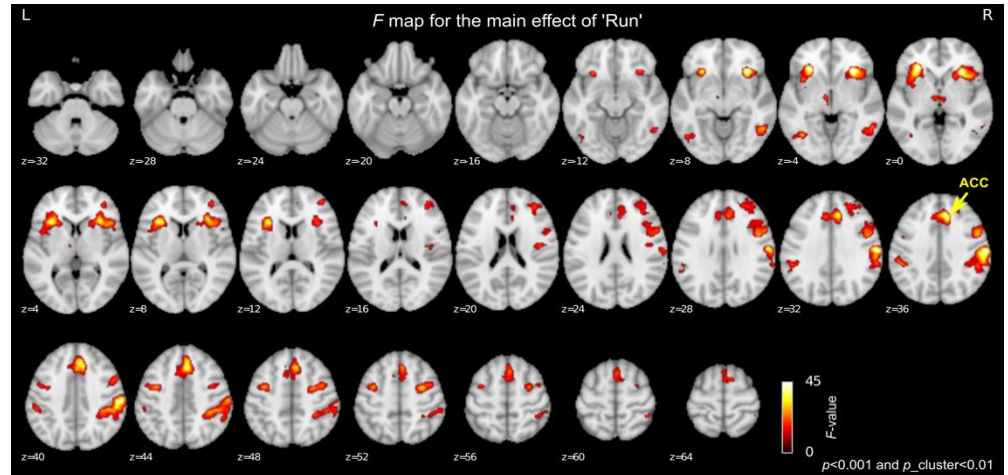


Figure C2. Regions with significant main effect of run in the LME analysis – the whole brain analysis.

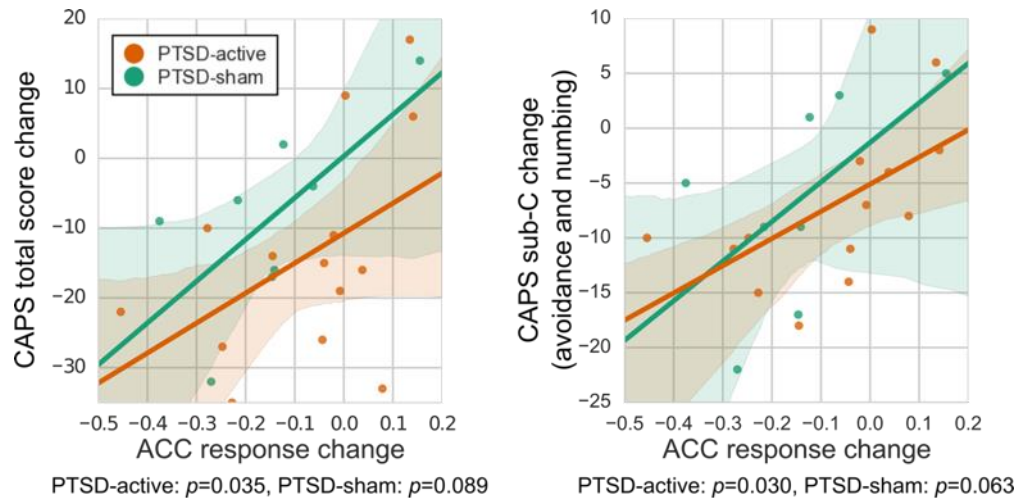


Figure C3. The ACC hemodynamic response associations with CAPS total score (left plot) and CAPS sub-C changes related to avoidance and numbing (right plot).

While the baseline LA activity could predict the training effect, symptom relief after the sessions was not associated with LA activity change. This suggests that symptom reduction might not be directly mediated by LA activity modulation, but by other regions that are co-modulated during the training. In the whole-brain analysis we found significant training effect across runs and sessions in the salience network regions including anterior insula and anterior cingulate cortex (ACC), whose response decreased across training. Furthermore, there was a significant association between PTSD symptom reduction and the decrease in the ACC response. These indicate that rtfMRI-nf training effect was not limited to the feedback target region (i.e. LA), but the training could affect other brain regions. The result suggests that the observed PTSD symptom reduction could be mediated by the co-activated brain regions (i.e. ACC).

D) Connectome-wide investigation of altered resting-state functional connectivity in war Veterans with and without PTSD

D. Introduction

Altered resting-state functional connectivity in PTSD suggests neuropathology of the disorder. While seed-based fMRI connectivity analysis is often used for the studies, such analysis requires defining a seed location *a priori*, which restricts search scope and could bias findings toward presupposed areas. Recently, a comprehensive exploratory voxel-wise connectivity analysis, the connectome-wide association approach, has been introduced using multivariate distance matrix regression (MDMR) for resting-state functional connectivity analysis [58]. The current analysis performed a connectome-wide investigation of resting-state functional connectivity for combat Veterans with and without PTSD compared to non-trauma-exposed healthy controls using MDMR.

D. Methods

Thirty-nine male combat Veterans with PTSD and 22 male combat Veterans without PTSD (Veterans control, VC) participated in the resting-state fMRI. In addition, 28 age-matched non-trauma-exposed healthy males who had participated in another study [59] were employed as non-trauma-exposed healthy controls (NC). Four PTSD and 4 VC participants were excluded from the analysis due to excessive head motion (more than 40 censored time points). There was no significant age difference between the groups.

The resting-state session took place prior to any task sessions. During the resting-state fMRI, participants were instructed not to move and to relax and rest while looking at a fixation cross on the screen. A single-shot gradient-recalled echo-planar imaging (EPI) sequence with sensitivity encoding (SENSE) was used for fMRI. The resting fMRI run time was 6 min 50 s (205 volumes).

AFNI was used for fMRI image processing. Physiological noise reduction with RETROICOR/RVT, slice-timing and motion correction, nonlinear warping to the MNI template brain with the Advanced Normalization Tools (ANTs) software (<http://stnava.github.io/ANTs/>), spatial smoothing (4mm-FWHM), and scaling to percent change were applied to resting-state fMRI data. Noise in signal time-course was removed by regressing out three principal components of ventricle signal, local white matter average signal (ANATICOR), motion parameters, and low-frequency fluctuation and censoring volumes with large head motion.

MDMR analysis was applied to investigate connectome-wide resting-state connectivity alteration between PTSD, VC, and NC groups. We followed the procedure introduced in Shehzad et al. (2014)[48] for the MDMR analysis. In each voxel, a connectivity map from that voxel to all other voxels was made with Pearson's correlations between signal time-courses of the voxels. The dependent variable of MDMR is a distance matrix of the connectivity maps between subjects. The distance of the maps between subjects was calculated with Euclidean distance of Fisher's z-transformed connectivity maps. The MDMR analysis evaluates the association

between the distance matrix (dissimilarities of connectivity maps across subjects) and the predictor variables in the design matrix. The design matrix included two columns of group factors for PTSD and VC as well as columns of age and motion size as nuisance variables as well as all 1s for the intercept. Statistical tests were performed with a 10,000-repetition permutation test. MDMR statistical map indicates that a whole-brain connectivity pattern at a voxel is altered between the groups. However, it does not show which specific connectivity is altered. To elucidate which voxel-by-voxel connectivity was altered between the groups, post-hoc seed-based connectivity analysis was performed for the significant regions of the MDMR statistical map.

D. Results

Figure D1 shows the thresholded map for the main effect of group in the MDMR analysis (cluster-size $p < 0.05$). Peak locations of the clusters with significant effect (cluster-size $p < .05$) were used as seeds for post-hoc seed-based connectivity analysis. Post-hoc analysis revealed significantly altered connectivity for PTSD compared to NC. Those included decreased connectivity between the left parahippocampal seed and the bilateral fusiform gyrus, middle occipital, middle temporal, and the posterior cingulate areas. Decreased connectivity for PTSD was also seen between the left medial frontal (supplementary motor area; SMA) seed and the anterior cingulate and the left anterior insula regions. Multiple left lateral prefrontal seeds also showed decreased connectivity for PTSD with salience network (SN) regions.

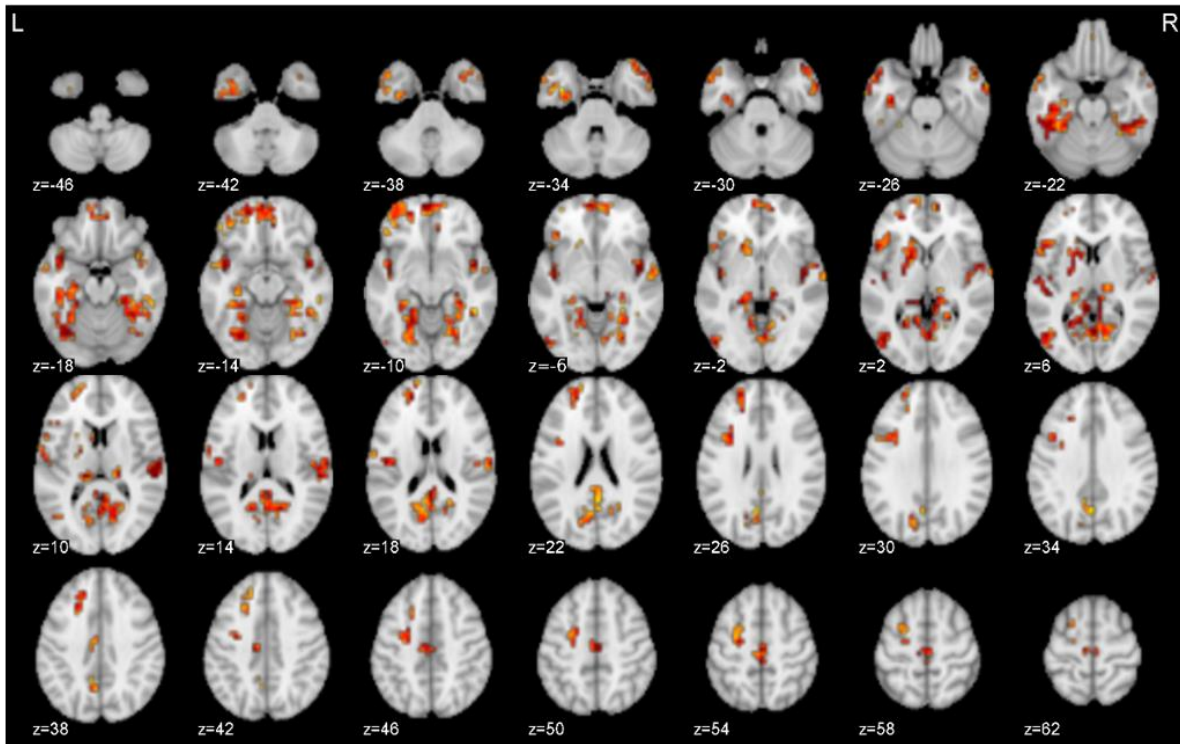


Figure D1. The MDMR statistics map for the main effects of group

Increased functional connectivity for PTSD was seen between the left insula seed and the right middle cingulate region. Connectivity between the right parahippocampal seed and the right anterior insula was negatively correlated with CAPS and PCL-M. Connectivity between the ventromedial prefrontal cortex (vmPFC) seed and the left middle frontal region was negatively correlated with CAPS scores.

The VC group also had significantly altered connectivity compared to NC. Those included decreased connectivity between the left superior frontal seed and the posterior default mode network areas, between the left middle frontal seed and the left postcentral region, between the right transverse temporal seed and the precuneus, and between the left superior temporal seed and the precuneus. Significantly increased connectivity in VC was seen between the left posterior insula seed and the right posterior insula, right lingual,

and right cuneus regions and between the left posterior insula and the right postcentral, right middle frontal, right middle temporal, right posterior cingulate, left superior parietal, right inferior frontal, right precuneus, and right thalamus. No significant connectivity differences between the PTSD and VC groups were found in the post-hoc analysis.

D. Discussion

The decreased connectivity between the lateral prefrontal regions and the salience network regions in PTSD was consistent with previous reports that indicated lowered emotion-regulation function in these regions. The decreased connectivity between the parahippocampal gyrus and visual cortex supported the dual representation theory of PTSD, which suggests dissociation between sensory and contextual memory representations in PTSD. The theory also supposes that the precuneus is a region that triggers retrieval of sensory memory of traumatic events. The decreased connectivity at the precuneus for VC might be associated with suppressing such a process. The current results did not show significant differences between the PTSD and VC groups. We note that this result does not necessarily indicate that PTSD and VC groups had the same connectivity patterns but limited sensitivity of MDMR analysis could affect the non-significant result.

E) Real-time fMRI amygdala neurofeedback positive emotional training normalized resting-state functional connectivity in combat Veterans with and without PTSD: a connectome-wide investigation

E. Introduction

The effect of neurofeedback training on resting-state functional connectivity warrants investigation as changes in spontaneous brain activation could reflect the association between sustained symptom relief and brain alteration. We have identified abnormal PTSD connectivity at the baseline session by a data-driven, connectome-wide approach using a multivariate distance matrix regression (MDMR) analysis [58] (section D). The current study examined the real-time fMRI neurofeedback (rtfMRI-nf) training effect on these abnormal connectivities using longitudinal linear mixed-effect model analysis. In addition, a longitudinal MDMR analysis was performed to examine connectome-wide neurofeedback training effects beyond those associated with effects on abnormal baseline connectivity.

E. Methods

Thirty PTSD and 17 VC participants completed 3 sessions of rtfMRI-nf training and the post-training resting-state scan session. PTSD participants were randomly assigned to the experimental group (PTSD-exp) where they received left amygdala rtfMRI-nf (N=21) or to the control group (PTSD-ctrl) where they received rtfMRI-nf from the left horizontal segment of the intraparietal sulcus (N=9). All VC participants were in the experimental group (VC-exp). Participants with excessive head motion (more than 40 censored volumes) were excluded from the analysis. Three PTSD and three VC participants who completed the post-training-session were excluded from the analysis.

We examined the changes in the abnormal connectivity identified in the previous connectome-wide analysis. The same resting-state fMRI protocol and image processing as in the previous analysis were used. The rtfMRI-nf training effect was examined by linear mixed-effect (LME) model analysis for longitudinal design. The LME model included fixed effects of session (baseline, post-training), group (PTSD-exp, PTSD-ctrl, VC-exp), session by group interaction, age, and motion size and a random effect of the subject on intercept. This analysis was done for the abnormal connectivity identified in the baseline analysis as well as for the left amygdala (LA) connectivity. We also performed a longitudinal MDMR analysis for a comprehensive investigation of the training effect that was not limited to the abnormal connectivity at baseline. The longitudinal MDMR included the connectivity maps before and after the training for each subject. The distance matrix of these maps was the dependent variable in the MDMR. This design matrix included session, group (PTSD-exp,

PTSD-ctrl, VC-exp), session by group interaction, age, and motion size. In addition, subject-wise factor variables were included in the design matrix. These regressors had 1 at a pair of a same subject's samples and 0 for the others. This could regress out subject-wise average effect, so that the longitudinal analysis could find the session and the group effect on within-subject connectivity difference.

E. Results

The PTSD group had significantly lower connectivity between the left amygdala and the left ventrolateral prefrontal cortex (vIPFC) than the NC group at baseline (Fig. E1). This connectivity was significantly increased after the training only for the PTSD-exp group ($t(29)=2.554$, corrected $p=0.047$). This connectivity change, however, was not significantly associated with symptom change. Abnormal resting-state connectivity for combat Veterans with and without PTSD was normalized after the training. Hypoconnectivity between the supplementary motor area (SMA) and the dorsal anterior cingulate cortex (dACC) in the PTSD group compared to the NC group at baseline was significantly increased after training only for the PTSD-exp group ($t(29)=2.770$, corrected $p=0.028$), and this connectivity increase was significantly associated with a decrease of PCL-M in the PTSD-exp group (Fig. E2, right plot, $t(15)=-3.092$, corrected $p=0.007$). Hypoconnectivity between the left superior frontal region and the precuneus and the supramarginal gyrus in the VC group compared to

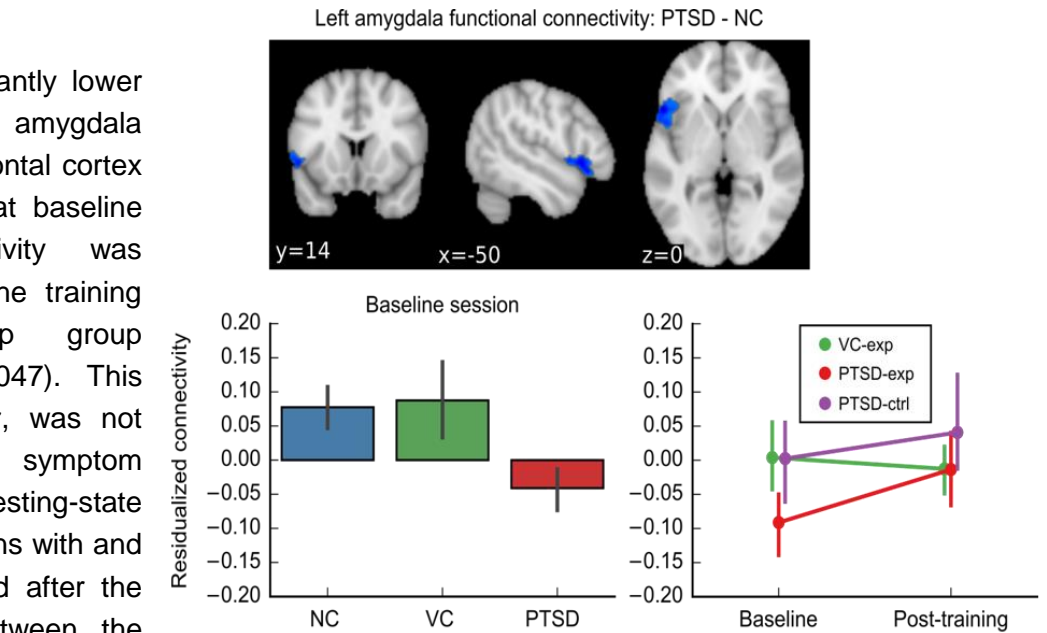


Figure E1. The region with significantly lower functional connectivity from the left amygdala ROI at the baseline session and its change between the sessions.

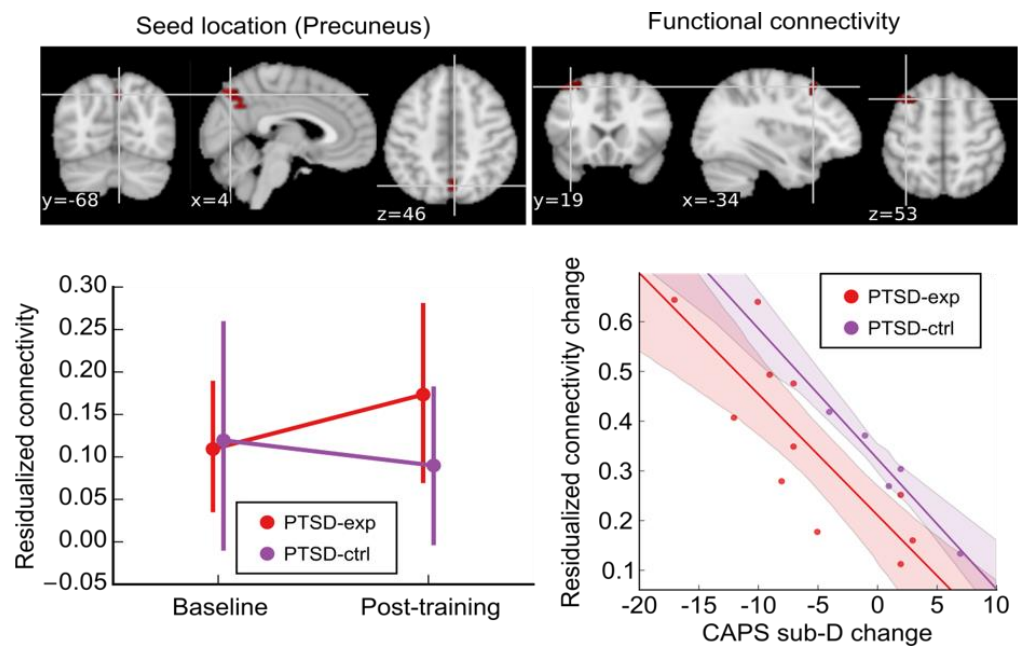


Figure E2. Training effect on resting-state functional connectivity identified with longitudinal MDMR.

the NC group at baseline was significantly increased after training only for the VC-exp group ($t(29)=3.518$, corrected $p=0.004$). The hyperconnectivity in bilateral insula regions for the VC was significantly decreased after training for the VC-exp group. Training effect on resting-state functional connectivity identified with longitudinal MDMR analysis is shown on Fig. E2. Longitudinal MDMR analysis revealed a connectivity change

between the precuneus and the left superior frontal cortex (Fig. E2). The increase of this connectivity was associated with a decrease in hyperarousal symptoms (CAPS Criterion D subscale).

E. Discussion

Comprehensive investigation of training effects on resting-state functional connectivity revealed that changes in connectivity were observed in left amygdala connectivity as well as in the SMA, ACC, insula, precuneus, and prefrontal regions. These changes were in the direction of normalizing abnormal connectivity for both PTSD and VC groups. Connectivity increases between the SMA and the dACC and between the precuneus and the left superior frontal gyrus were associated with decreases in PTSD symptoms measured by PCL-M and CAPS sub-D, respectively. These results indicated that the rtfMRI-nf training effect was not limited to a feedback target region and symptom relief could be mediated by brain modulation in several regions other than a feedback target area.

The connectivity changes observed in this study might involve correcting emotion representation and memory retrieval. Such an effect could be promoted by positive emotion enhancement training rather than suppressing or reappraising negative emotions. Ellard et al. (2017) [60] indicated that amygdala-vIPFC connectivity was increased during emotion acceptance and decreased during emotion suppression among people with anxiety disorders. They also showed that dACC activation was increased during emotion acceptance. Many rtfMRI-nf treatment studies have focused on suppressing abnormal activity. However, promoting positive emotional experience might help correct abnormal emotion representation and could have the same, if not more of, a therapeutic effect in treating the biological underpinnings of dysregulated emotion and mood disorder symptoms.

F) Real-time fMRI amygdala neurofeedback training lowers PTSD symptoms with hippocampus volume increase

F. Introduction

Emerging evidence suggests the utility of real-time fMRI neurofeedback (rtfMRI-nf) in symptom reduction due to normalizing aberrant functional and resting-state brain activations. However, its effect on brain structure is not clear. This study examined the rtfMRI-nf training effects on anatomical brain structures in a cohort of combat Veterans with posttraumatic stress disorder (PTSD). Participants underwent rtfMRI-nf training to increase left amygdala (LA) activity during positive autobiographical memory recall. We focused on the changes in hippocampus volume because hippocampus structural abnormalities are frequently reported in PTSD [61]. We hypothesized that LA rtfMRI-nf training during positive memory recall could affect hippocampus volume, and that volume changes would be associated with PTSD symptom reduction.

F. Methods

Thirty combat Veterans with PTSD completed three sessions of rtfMRI-nf emotional training and the pre- and post-training anatomical MRI scans. The participants were randomly divided into an experimental group (PTSD-exp, N=21), who received a neurofeedback (nf) signal from the LA and a control group (PTSD-ctrl, N=9), who received nf signal from a brain region (the left horizontal segment of the intraparietal sulcus) putatively not involved in processing emotions. Participants were instructed to retrieve positive autobiographical memories while attempting to increase the nf signal presented on a screen.

Structural T1-weighted MRI (MPRAGE) scans were performed about one week before and after the rtfMRI-nf visits. The following parameters were used: FOV = 240×192 mm, matrix = 256×256, 120 axial slices, slice thickness = 0.9 mm, 0.9375×0.9375×0.9 mm³ voxel volume, TR = 5 ms, TE = 2.0 ms, R = 2, flip angle = 8°, delay time = 1400 ms, inversion time = 725 ms, sampling bandwidth = 31.2 kHz, scan time = 5 min 40 s. The

mean interval between the pre- and post-training structural scans was 42 days (SD=12 days). PTSD symptoms were measured with the Clinician-Administered PTSD Scale (CAPS) for DSM-IV [62] about one week before and after the structural MRI scan.

FreeSurfer 6.0 (<http://surfer.nmr.mgh.harvard.edu/fswiki/FreeSurferWiki>) was used to process MRI images. The longitudinal processing pipeline [63] was used and volumes in the hippocampus and its subfields [64] were evaluated. Linear mixed-effect model (LME) analysis was used to test fixed effects of sessions (pre, post), group (PTSD-exp, PTSD-ctrl), laterality (left, right), and their interactions as well as age and estimated total intracranial volume (eTIV) as covariates. Power-proportion correction [65] was applied to the eTIV covariate. Random effect of subject on intercept was included in the model. We also performed LME analysis for the changes in volumes with fixed effects of group, symptom change, laterality, their interactions, age, and eTIV, and a random effect of subject on intercept.

F. Results

PTSD symptom significantly decreased after the training only for the PTSD-exp group (with significant session effect on CAPS total score in PTSD-exp group $t[21]=3.816$, $p=0.002$; and no significant effect in PTSD-ctrl group $t[21]=1.770$, $p=0.172$). No significant effect of the session and its interaction were found on hippocampal volumes when no symptom change was included in the analysis. When the change in CAPS score was included in the model, the PTSD-exp group showed a significant association between the symptom change and volume change in the CA1 ($F[1,19]=5.4991$, $p=0.030$) and the parasubiculum ($F[1,19]=7.724$, $p=0.012$) hippocampus regions (Fig. F1).

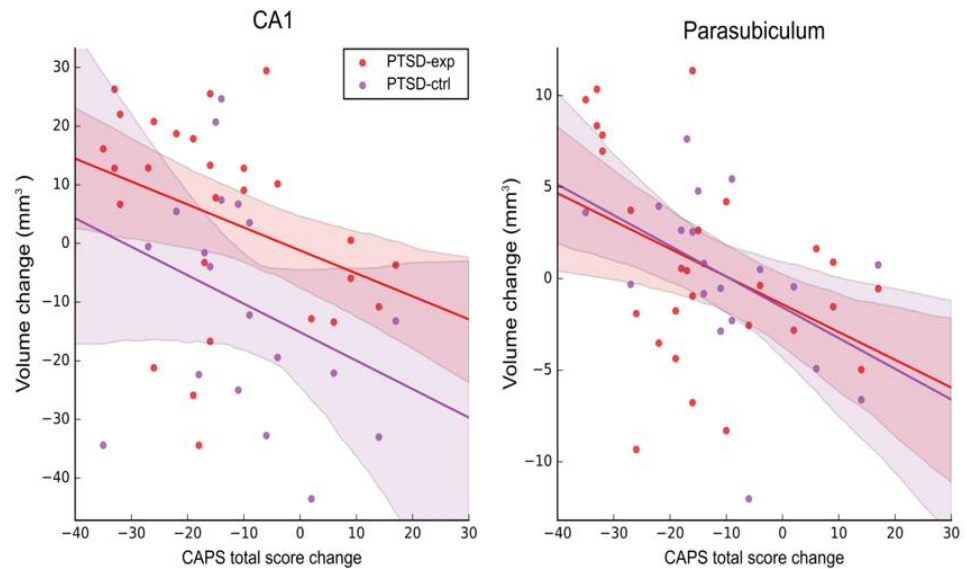


Figure F1. Association between hippocampus subfields (CA1 and parasubiculum) volume change and PTSD symptom (CAPS total score) change due to rtfMRI-nf training.

F. Discussion

rtfMRI-nf training to increase left amygdala activity during positive memory recall had a significant treatment effect to reduce PTSD symptoms. This symptom reduction was positively associated with the hippocampus volume increase, specifically in the CA1 and the parasubiculum regions, such that participants with a greater decrease in PTSD symptoms had more increase in the volumes. While smaller hippocampus volume has been reported for PTSD [61], the current result suggests that rtfMRI-nf LA emotional training provides PTSD symptom relief and recovers such atrophy.

G) Effects of rtfMRI amygdala neurofeedback on anxious reactivity to individualized reminders of a traumatic event

G. Introduction

The amygdala is thought to play a key role in both identifying salient cues in the environment (such as reminders of a traumatic event) and regulating emotional responses to those cues [66,67]. Accordingly, we continue to examine the hypothesis that people with PTSD receiving the rtfMRI-nf training will evidence a

greater reduction in emotional reactivity to traumatic event-specific stimuli presented via the well-established script-driven imagery paradigm (outside the MRI environment) compared to people with PTSD who receive sham feedback. This hypothesis is based on data from other laboratories and on our preliminary data demonstrating that amygdala hyperresponsivity in PTSD arises during the presentation of either traumatic stimuli or trauma-unrelated negatively-valenced stimuli, relative to neutral stimuli [66-73].

G. Methods

Forty-six male combat Veterans, 29 with PTSD (age 21–48) and 17 without PTSD (Veterans control, VC; age 22–55) completed the script-driven imagery procedure [73]. Of Veterans with PTSD, 20 completed the rtfMRI procedure with neurofeedback about amygdala activity (EX) and 9 completed the procedure with feedback provided from the intraparietal region (SHAM). Participants first worked with a trained experimenter to develop an individualized, 30-sec script that described their worst combat experience from the first-person perspective. A researcher then audio-recorded the script and presented the participant with the script outside of the scanner environment twice; once before and once after the rtfMRI procedure. Participants rated state levels of anxiety after each traumatic event script presentation using a 0 (*none*) to 10 (*extreme*) scale. In order to examine changes in anxious reactivity to the script-driven imagery procedure as a function of rtfMRI training, a repeated measures ANOVA was conducted with group (EX, SHAM, VC) entered as a fixed factor and post-script ratings made before and after the rtfMRI training entered as the repeated measure.

G. Results

Results indicated that the hypothesized group by anxiety rating interaction was trending toward statistical significance [Wilks Lambda = 0.915, $F(2, 43) = 2.01$, $p = 0.14$, partial $\eta^2 = 0.085$]. Fig. G1 illustrates the pattern of anxiety ratings as a function of group and script.

To more specifically examine anxious reactivity among participants with PTSD, an ANCOVA was conducted comparing the EX and SHAM groups with pre-rtfMRI anxiety ratings entered as a covariate and post-rtfMRI ratings entered as a dependent variable.

Here, after accounting for significant variance associated with pre-rtfMRI training anxiety

ratings [$F(1, 26) = 58.08$, $p < 0.001$, partial $\eta^2 = 0.691$], the difference in post-training anxiety ratings between the EX ($m = 4.40$, $SD = 2.23$) and SHAM ($m = 5.44$, $SD = 2.78$) groups was trending toward statistical significance [$F(1, 26) = 3.36$, $p = 0.078$, partial $\eta^2 = 0.115$].

G. Discussion

Results regarding the effects of the rtfMRI procedure on anxious reactivity to individualized traumatic event cues remain promising yet did not reach statistical significance. However, trends in the data are encouraging. Examination of Fig. G1 suggests that both experimental groups completing amygdala-focused training reported a decrease in anxiety elicited by the script procedure after completing the neurofeedback training, whereas participants completing the procedure with sham feedback reported an increase in anxiety. Given the relatively small sample size for detecting effects of an experimental manipulation on self-reported emotional

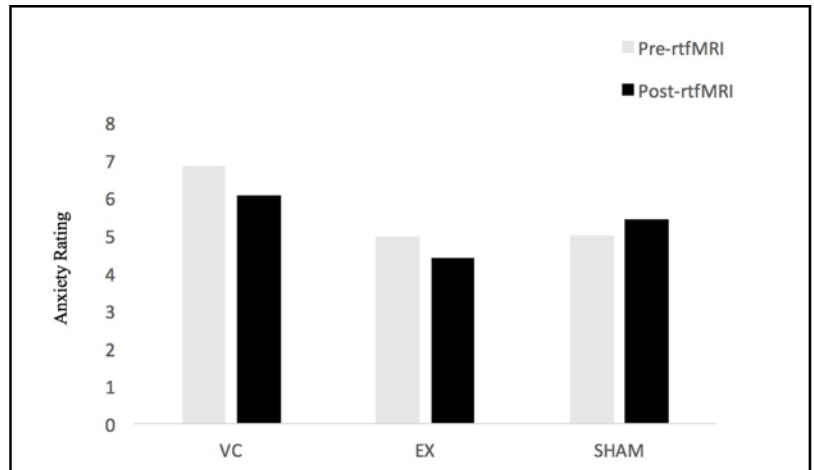


Figure G1. Self-reported anxiety ratings made after presentation of personalized traumatic event script-driven imagery both before and after rtfMRI-nf training. VC= Veterans controls without PTSD who completed rtfMRI-nf left amygdala training; EX= Veterans with PTSD who completed rtfMRI-nf left amygdala training; SHAM= Veterans with PTSD who completed rtfMRI-nf intraparietal region (HIPS, sham) training.

reactivity, these results suggest the amygdala-focused rtfMRI-nf procedure may indeed hold promise for reducing a key feature of PTSD: exaggerated emotional reactivity to traumatic event cues.

H) Tracking Resting State Connectivity Dynamics in Veterans with PTSD

H. Introduction

Resting state functional connectivity (RSFC) refers to correlations in hemodynamic activity levels among different brain regions, suggesting synchronization of neural activation of those regions during rest [74]. The activities of the resting brain, measured by blood-oxygenation-level-dependent (BOLD) functional magnetic resonance imaging (fMRI), reveals spontaneous and low-frequency (<0.1Hz) fluctuations that are temporally correlated and spatially organized into functional networks, collectively termed the “resting state networks” (RSNs) [75,76]. The alterations in two specific networks may underlie PTSD: the default mode network (DMN) [77-82], and the salience network (SN) [83,84]. Most studies examining integrity of network connectivity associated with PTSD have focused on civilian trauma; however, less is known about the effect of combat-related trauma. To date, only a few studies have examined network-level alternations in combat-related PTSD yet the findings have been elusive. Conflicting results of these studies have largely depended on the selection of a control group. Alterations in resting state networks, or connectivity, have been reported in PTSD compared to non-trauma-exposed controls [83], or a combination of trauma-exposed and non-trauma-exposed controls [85,86]. Combining both combat-exposed and civilian healthy controls obfuscates understanding if PTSD-related differences are specific to PTSD or due to combat exposure or even being in the military more generally. In this regard, a study by [87] examined details in three groups, i.e. Veterans with combat-related PTSD, combat-exposed controls without PTSD and never-traumatized healthy controls, and compared their resting state functional connectivity. Differences associated with PTSD were only observed in comparison with the civilian control, but not in comparison with combat-exposed Veterans. Thus, it remains unclear whether abnormality of resting state networks is best attributed to military status, combat exposure, or PTSD.

The goal of the current study was to test whether RSFC differs between combat-exposed Veterans with, as compared to without, PTSD. This method allows for ruling out the effects of being in the military generally, and combat exposure specifically. We employed a novel multimodal imaging approach using simultaneous electroencephalography (EEG) and fMRI to study activity in the resting state networks. The measurement of neural activity via fMRI, as done in prior work, is relatively limited in terms of understanding temporal dynamics of neural activity because the BOLD signal relies on a relatively slow hemodynamic response. In contrast, EEG is much more sensitive to the temporal dynamics of neural activity because it captures fast neuronal events that evolve on the scale of milliseconds. Neuroimaging with integrated and combined EEG-fMRI has been suggested to offer new insights in the study of functional connectivity because it offers both high spatial resolution of fMRI and the high temporal resolution of EEG [88]. To examine resting state network activity, a new method by Yuan et al. 2012 [89] has demonstrated that temporal independent EEG microstates (EEG-ms) can be obtained from resting state EEG acquired concurrently with fMRI. It was further showed that EEG-ms form direct electrophysiological signatures to the canonical resting state networks measured by resting state fMRI in both spatial and temporal domains [89,90]. This study examined EEG-ms associated with the resting state networks of relevance to PTSD — default mode network and the salience network. We proposed a new strategy to quantify the fast temporal dynamics of DMN, and SN functional connectivity in terms of EEG-ms occurrence rate. We hypothesized to observe abnormalities in the electrophysiological signatures of the two resting state networks, default-mode network and salience network, between the PTSD group and the combat control group.

H. Methods

Simultaneous EEG and fMRI data were from 36 Veterans with combat-related PTSD and 20 combat-exposed Veterans (combat-exposed controls, CEC) with eyes open in a resting state. Demographic and clinical characteristics are shown in Table H1.

Table H1. Participants demographics and clinical characteristics	PTSD (n=36)	CEC (n=20)
Age (Mean \pm SD Years)	32.0 \pm 7.0	34.0 \pm 9.0
PCL-M(Mean \pm SD) ***	42.9 \pm 14.6	18.3 \pm 2.2
CAPS(Mean \pm SD) ***	54.0 \pm 18.5	4.7 \pm 5.1
HARS (Mean \pm SD) ***	15.3 \pm 6.2	2.6 \pm 3.5
SHAPS(Mean \pm SD) ***	29.9 \pm 5.7	23.5 \pm 5.8
HDRS (Mean \pm SD) ***	14.3 \pm 5.6	2.6 \pm 3.7
MADRS (Mean \pm SD)***	17.2 \pm 8.2	2.1 \pm 3.8

*** significant difference between PTSD and CEC groups at $p < 0.001$

Abbreviations: PTSD: post-traumatic stress disorder; CEC: combat exposed controls; CAPS: Clinician Administered PTSD Scale; PCL-M: the PTSD checklist, military version. HARS: Hamilton Anxiety Rating Scale; HDRS: Hamilton depression rating scale; SHAPS: Snaith-Hamilton pleasure scale; MADRS: Montgomery-Asberg depression rating scale; SD: standard deviation.

BOLD fMRI RSNs were derived from preprocessed imaging data using spatial independent component analysis (ICA) separately for PTSD and CEC groups. The default mode network, anterior salience network and posterior salience network were selected out of all RSNs by comparing to those reported in [91]. The difference between groups was assessed using a two-sample unpaired t test. After correcting the MRI and cardioballistic artifacts, temporal independent EEG microstates (EEG-ms) were derived using the method described in [89]. We have identified temporal independent EEG-ms for each participant, and then obtained CEC and PTSD group results. The DMN, SN-related EEG-ms were selected by choosing one EEG-ms of correlated time course with BOLD fMRI DMN and/or SNs. The complete time courses of DMN, SNs-related

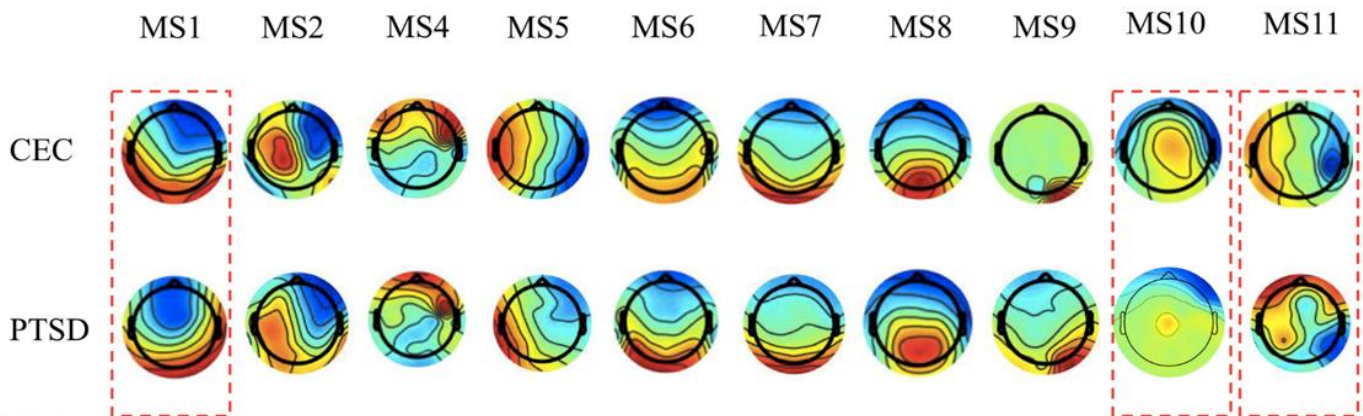


Figure H1. EEG microstates identified in CEC and PTSD groups. The pairs of microstates in dashed lines (MS1, M10, and MS11) show distinct features between HC and PTSD groups.

EEG-ms were obtained by back-projection and determined via a winner-take-all approach. The occurrence rate of DMN, SNs-related EEG-ms were calculated per each subject then compared across groups and against the clinical ratings.

H. Results

Figure H1 shows two sets of ten identified EEG microstates for both CEC (upper row), and PTSD (lower row) groups. Nine out of the ten microstates highly resemble those found in our previous study in [89]. A unique

microstate MS11 was identified in the current study, featuring a bilateral pattern with sources originated from the junction of posterior and temporal areas.

As the dynamics of the temporal independent microstates were reconstructed from EEG time series, it allows us to examine their signatures at a millisecond time scale. Among these EEG-ms, three microstates demonstrated distinctive differences in their fast evolving dynamics. EEG-ms that differ across both patient groups are marked by dashed lines in Fig. H1. The occurring frequencies of these three microstates are significantly different between HC and PTSD groups. To further explore the neuronal substrates of these three signature microstates, the temporal dynamics of the microstates were compared with the time courses of BOLD signals after convolving with impulse hemodynamic response function.

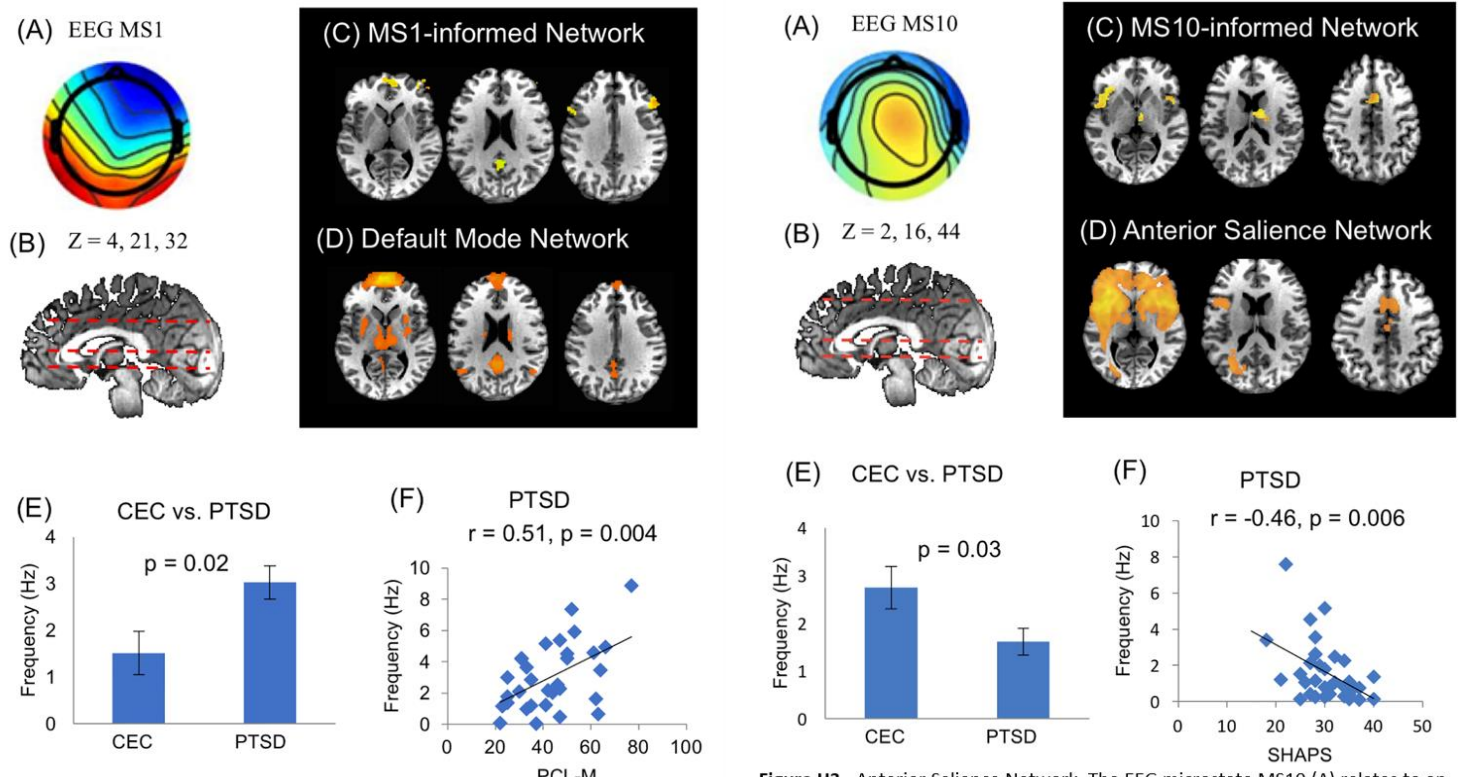


Figure H2. Dorsal Default Mode Network. The EEG microstate MS1 (A) relates to an EEG-informed Network (C) which resembles the fMRI dorsal Default Mode Network (D), showing at positions $z=4, 21$ and 32 (B). (E) Occurring frequency of microstate MS1 differs between CEC and PTSD groups ($p = 0.02$). (F) In all thirty-six PTSD individuals, the occurring frequency of microstate MS1 is positively correlated to the score of symptom severity measured by PCL-M ($r = 0.51, p = 0.004$).

Figure H3. Anterior Salience Network. The EEG microstate MS10 (A) relates to an EEG-informed network (C) which resembles the fMRI Anterior Salience Network (D), showing at positions $z=2, 16$ and 44 (B). (E) Occurring frequency of microstate MS10 differs between CEC and PTSD groups ($p = 0.03$). (F) In the PTSD individuals, the occurring frequency of microstate MS10 is inversely correlated to the score of hedonic tone measured by the Snaith-Hamilton Pleasure Scale (SHAPS) ($r = -0.46, p = 0.006$).

Regions where BOLD and EEG microstate time series are correlated were identified using a general linear model. The dorsal default model network (dDMN) was therefore identified associated with one of the EEG microstate, MS1 (Fig. H2). Importantly, the occurring frequency of the dDMN-associated EEG microstates shows distinctive temporal dynamics between CEC and PTSD groups (i.e., higher in the PTSD group). Moreover, the occurring frequency of the EEG-ms was also linearly related to the scores of PCL-M scores in the PTSD group, indicating that more severe PTSD symptoms are associated with faster dynamics of the DMN network. Two other microstates MS 10 and MS11, were also found to be associated with distinctive dynamics between PTSD and CEC groups. Interestingly, both MS10 and MS11 identified a similar insular network, including bilateral insular, the cingulate cortex and the medial temporal cortex. MS10 (Fig. H3) appears to engage the anterior salience network (SN) that includes the anterior insular, dorsal anterior

cingulate/paracingulate cortex, and the medial thalamus. By the way of comparison, MS11 (Fig. H4) is related to the posterior insular network that includes the posterior insular region and dorsal anterior cingulate cortex.

However, the temporal dynamics of MS10 and MS11 show importantly different characteristics. For MS11, the PTSD group showed significantly higher occurring frequency than the control group, whereas for microstate MS 10, the PTSD group showed lower occurring frequency. Furthermore, the dynamics of MS10 was found to negatively correlate with SHAPS scores across the individual subjects, which assess hedonic experience or positive valence. Therefore, in the PTSD group, participants with higher level of hedonic tone are associated with lower occurrence frequency of the anterior insular network. The dynamics of MS11 did not show any significant linear trend between the occurring frequency and the level of symptoms ($p > 0.05$ for both PCL-M and SHAPS scores).

H. Discussion

We investigated and compared the electrophysiological signatures of hemodynamic RSNs in male Veterans with and without combat related PTSD. To our knowledge, this is the first examination of resting state networks in PTSD using a multimodal concurrent EEG-fMRI approach and also controls for combat exposure. We proposed a new strategy to integrate EEG and fMRI by quantifying the fast temporal dynamics associated with the resting state networks. Results show that in three fMRI derived resting state networks, namely DMN as well as anterior and posterior SNs networks, the temporal dynamics as characterized and measured by EEG, differ as a function of PTSD. The electrophysiological correlates – temporal independent EEG microstates associated with the DMN and anterior and posterior SNs - show aberrant occurrence frequency in PTSD. In particular, the occurring frequency of the DMN is higher in PTSD and positively correlated with the score of PTSD severity. In contrast, the occurring frequency of the anterior SN is lower in PTSD and negatively correlated with the score of hedonic tone or degree of pleasantness.

Multiple brain regions have been depicted in the imaging studies of PTSD, as patterns of activations during tasks of symptom provocation. Hyperactivity of limbic brain regions (e.g., amygdala, insula) and the hypo-activity of brain areas involved in emotional regulation (e.g., ventromedial prefrontal cortex (vmPFC), dorsal anterior cingulate cortex (dACC)) were observed, suggesting insufficient top-down modulation of limbic regions (especially the amygdala) by the prefrontal cortex [4,92,93]. In addition, resting state fMRI imaging has gained recent interests in the investigation of the neurobiological mechanism of PTSD, as the disease manifests itself as re-experiencing of the traumatic events, accompanied by lasting symptom of avoidance and hyperarousal at resting state. While the activation patterns of the PTSD-implicated regions have been examined extensively in

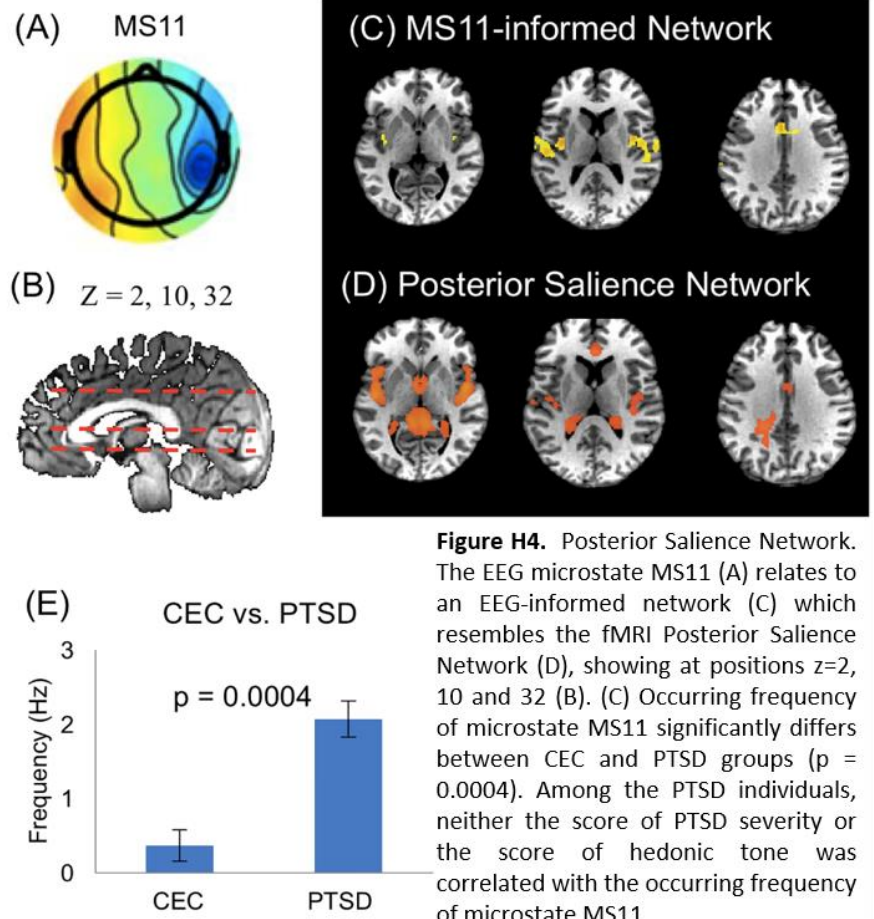


Figure H4. Posterior Saliency Network. The EEG microstate MS11 (A) relates to an EEG-informed network (C) which resembles the fMRI Posterior Saliency Network (D), showing at positions $z=2, 10$ and 32 (B). (C) Occurring frequency of microstate MS11 significantly differs between CEC and PTSD groups ($p = 0.0004$). Among the PTSD individuals, neither the score of PTSD severity or the score of hedonic tone was correlated with the occurring frequency of microstate MS11.

the past, patterns of connectivity between these regions are also investigated, which could shed important new information on the neural basis of PTSD, and on mechanisms of PTSD symptom development. Results suggested *increased* occurrence frequency of DMN-related electrophysiological states in the Veterans with PTSD as compared to the Veteran controls. The EEG microstate MS1 was observed to be the electrophysiological correlates of regions including the precuneus, the medial prefrontal gyrus (MPFC) and the bilateral dorsal lateral PFC, which constitutes the key nodes of the DMN [94]. The precuneus is involved in autobiographical memory and is also related to self-referential processing [95-97]. Furthermore, precuneus activity has been related to trauma memory generalization [98], and flashbacks [99]. Thus, alterations in the precuneus are associated with PTSD and may potentially be related to altered memory- and self-referential processes, such as memory deficits, intrusions or flashbacks. These findings altogether suggest that the DMN is disturbed in PTSD.

Our observation regarding *increased* DMN temporal dynamics is in line with previous task-based studies of PTSD patients which report increased connectivity within DMN-related regions [83]. An analysis of the whole brain RSFC network topology associated with combat-related PTSD revealed the abnormally increased connectivity of the precuneus within the DMN [85]. Furthermore, our investigation extended prior work by examining the DMN using a multimodal approach and showed increased temporal dynamics within the PTSD group. Moreover, the temporal dynamics in PTSD appear positively correlated with PTSD severity. As PTSD severity increased, the occurrence of electrophysiological states (e.g. EEG-ms) associated with the DMN were higher, suggesting a neuroimaging metric that has potential as a biomarker of symptom severity.

The salience network [100] has also been another focus in the neuroimaging studies of PTSD. The SN consists of dorsal anterior cingulate (dACC) and orbital frontoinsula cortices with robust connectivity to subcortical and limbic structures. Further delineation of the salience network resulted in two sub-networks, the anterior SN and the posterior SN [91]. Studies of SN has suggested it plays in detecting and orienting to salient stimuli [101-102], emotional control [100], cognitive control [103], and error processing [104]. In particular, the intrinsic functional connectivity of the dACC node of the SN has been associated with anxiety ratings in the healthy population [100]. Alterations in the SN that is associated with PTSD, however, have been investigated in a limited number of studies. The insula and amygdala have been found to be hyperactive in PTSD [46,82] and are involved in the SN [101]. Reduced ACC resting state functional connectivity with the thalamus, amygdala, posterior cingulate cortex (PCC)/precuneus, and prefrontal regions has been reported in PTSD versus non-trauma-exposed controls [83,85], trauma-exposed controls [84,103] or both [85,86]. As discussed above, using a control group of non-trauma-exposed civilian or a combination of combat-exposed and non-combat-exposed controls raises methodological concerns and limits the interpretation of the findings.

Our results found distinct PTSD-related signatures for the anterior SN and the posterior SN. The microstate MS10 was observed to be the electrophysiological correlate of the anterior SN, which includes the anterior insular, dorsal anterior cingulate/paracingulate cortex, and the medial thalamus. In contrast, MS11 is related to the posterior insular network that includes the posterior insular region and dACC. The delineation of anterior and posterior SN has been documented in data-driven studies of resting-state fMRI data [91] and tractography-based studies of diffusion tensor imaging data [103]. However, the functional relevance of the subnetworks of the SN is not yet clear. Our study compared the temporal dynamics of the EEG microstates associated with the anterior and posterior SN: *decreased* temporal dynamics in the anterior SN, yet increased dynamics in the posterior SN, were observed in PTSD. These results may suggest an antagonist relationship between the anterior and posterior SN in PTSD. More interestingly, the dynamics of the anterior SN is related to the hedonic tone of the participants. The PTSD group was found to have significantly higher hedonic tone than the controls, and correspondingly the PTSD participants show a significantly lower occurrence frequency EEG-ms associated with anterior SN. In line with the group-level finding, at an individual level, the higher the score of

hedonic tone is, the less frequently the anterior SN EEG-ms occurs. These results suggest that activity of the SN is disturbed in among people with PTSD while at rest, and are consistent with work documenting abnormal functioning of the emotion regulation network in this population.

Moreover, the SN is thought to be critically involved in switching between exogenous and endogenous attentional states and regulating the balance between DMN and central-executive network (CEN) activity [104]. Therefore, in addition to being among the three most well-established intrinsically connected brain networks, the DMN, SN and CEN appear to be inherently related to (and interconnected with) one another. Our studies showed evidence supporting an orchestra relationship between DMN and SN, particularly in the domain of temporal dynamics. Whereas the temporal dynamics of DMN become more frequent in PTSD, the states of the anterior SN go on an opposite, diminishing direction. Interestingly, the exaggerated DMN dynamics are positively associated with the severity of PTSD symptoms whereas the diminishing states of the anterior SN are negatively associated with the hedonic tone across PTSD individuals. Moreover, the posterior SN has been also delineated in our findings, having an antagonistic role than the anterior SN. Although the states of the posterior SN show higher occurrence frequency in the PTSD than the CEC group, it remains still unclear about the functional underpinning of the posterior SN.

In summary, this study showed differences in the default mode network, anterior and posterior salience networks, comparing Veterans with combat-related PTSD to combat-exposed Veteran controls without PTSD. The occurrence frequency of the EEG microstates associated with the default mode network was higher in PTSD than control, and positively associated with the severity of PTSD symptoms. The occurrence frequency of the electrophysiological state associated with the anterior salience network was lower in PTSD than control, and negatively associated with the hedonic tone in PTSD participants. Our findings contribute new information to our understanding neural mechanisms of PTSD, and further suggest that a disruption in emotion generation and regulation circuits play a crucial role and contribute to the pathophysiology of PTSD.

I) EEG-only neurofeedback training feasibility in combat-related PTSD

I. Introduction

We have developed a stand-alone EEG-only neurofeedback (EEG-nf) training protocol for emotion-regulation training and applied it to Veterans with combat-related PTSD. The procedure design was based on the insights we gained from the experiments utilizing the rtfMRI-nf of the amygdala with simultaneous EEG recordings (Sections A-D). After conducting an exploratory data analysis on collected multimodal rtfMRI-nf and simultaneously recorded EEG data, we selected an EEG signal feature for stand-alone EEG neurofeedback experiments. The analysis revealed that variations in frontal upper alpha EEG asymmetry during the rtfMRI-nf amygdala regulation training as a promising measure of PTSD severity and treatment response, and therefore is a promising EEG-nf target (Section B).

I. Methods

The experimental setup for the EEG-nf training is shown in Figure I1. Hardware includes: i) main Linux workstation to control the entire procedure by means of a custom developed and integrated real-time software system; ii) windows laptop for collecting EEG and physiological data and sending those data in real-time to the main computer via a TCP/IP socket; ii) peripheral devices: 64-channel EEG system two BrainAmp MR plus



Figure I1. Experimental setup for EEG-nf.

amplifiers from Brain Products, GmbH and a 64-channel EEG cap from EasyCap, a module for physiological GSR (galvanic skin response) and respiration measurements, utilizing a BrainAmp ExG amplifier with GSR and respiration belt sensors from Brain Products, GmbH, mechanical keyboard response device for ecStroop task, joystick for AAT, headphones and volume control for the script-driven imagery procedure [SDIP], and a mobile cart for performing the experimental tasks. The main computer received the EEG data and used them to generate the EEG-nf signal, which was displayed to a participant by a custom GUI software. All the EEG-nf equipment used was MR compatible, and the entire EEG-nf procedure could be performed during fMRI if needed. In addition, we implemented the ecStroop, SDIP, and AAT tasks in Python programming language and all tasks were integrated with controlling software running on the main Linux workstation.



Figure 12. Experimental protocol for one EEG-nf session.

The experimental protocol for one EEG-nf session is illustrated in Figure I2. The protocol was very similar to the procedure we used previously for the rtfMRI-nf experiments targeting the left amygdala (Sections A-D). For EEG-nf, the red variable-height neurofeedback bar represented the difference in the target asymmetry (A) values between a current Happy Memories condition and the Rest baseline computed for the preceding 40-s long Rest condition block. In addition, the height of the EEG-nf bar was updated every 1 s.

Visit 1	Visit 2	Visit 3	Visit 4	Visit 5	Visit 6	Visit 7	Visit 8	Visit 9 (optional)
Screening/doctor (may be split into 2 visits)	Consent/baseline assessment (may be combined with visit 1)	Baseline scans	Neurofeedback #1	Neurofeedback #2 (5-9 days after visit 4)	Neurofeedback #3 (5-9 days after visit 5)	Follow-up scans (5-9 days after visit 6)	Follow-up assessments (can be combined with visit 7)	Post-sham neurofeedback
SCID screening visit Doctor visit	Consent CAPS Script development TAS ECS BIS/BAS Word selection VAS	HAM-D MADRS HAM-A PCL-M SHAPS BDI POMS VAS	HAM-D MADRS HAM-A PCL-M SHAPS BDI POMS VAS	HAM-D MADRS HAM-A PCL-M SHAPS BDI POMS VAS	HAM-D MADRS HAM-A PCL-M SHAPS BDI POMS VAS	HAM-D MADRS HAM-A PCL-M SHAPS BDI POMS VAS	CAPS	HAM-D MADRS HAM-A PCL-M SHAPS BDI POMS VAS
		EEG prep Resting state Behavioral tasks • ecStroop • SDIP • AAT	Neurofeedback education EEG prep Neurofeedback POMS VAS Post-NF Questionnaire	EEG prep Neurofeedback POMS VAS Post-NF Questionnaire	EEG prep Neurofeedback POMS VAS Post-NF Questionnaire	EEG prep Resting state Behavioral tasks • ecStroop • SDIP • AAT		EEG prep Neurofeedback POMS VAS Post-NF Questionnaire

Key
Clinician ratings
Self-assessments
EEG prep
Behavioral testing by lab

Figure 13: Phase 3 visit schedule. SCID=Structured Clinical Interview for DSM-IV, CAPS=Clinician-Administered PTSD Scale, TAS=Toronto Alexithymia Scale, ECS=Emotional Contagion Scale, BIS/BAS=Behavioral Inhibition System/Behavior Avoidance System, HAM-D=Hamilton Rating Scale for Depression, MADRS=Montgomery-Åsberg Depression Rating Scale, HAM-A=Hamilton Rating Scale for Anxiety, PCL-M=PTSD Checklist-Military Version, SHAPS=Snaith-Hamilton Pleasure Scale, BDI=Beck Depression Inventory, POMS=Profile of Mood States, VAS=Visual Analog Scales, ecStroop=Emotional Counting Stroop, SDIP=Script-Driven Imagery Procedure, AAT=Approach-Avoidance Task.

The entire EEG-nf neurofeedback emotional training protocol (Phase 3) included eight visits, as detailed in Figure I3. Visits 2 and 8 involved the initial and final PTSD severity (CAPS) assessments, respectively. Visit 3 involved the ecStroop, SDIP, and AAT procedures performed with simultaneous EEG recordings, as well as

resting EEG measurements. Visits 4, 5, and 6 were the three EEG-nf training sessions. Visit 7 included the same procedures with simultaneous EEG as Visit 3.

I. Results.

Seventeen participants completed the 1st EEG-nf session (visit 4), and sixteen of them completed the 3rd EEG-nf session (visit 6). Only the results for the 1st EEG-nf session are reported here. Most of the subjects were able to successfully upregulate the frontal EEG asymmetry during the Happy Memories conditions (relative to the Rest conditions) using the EEG-nf. Three participants (out of 17) showed negative asymmetry changes across the four nf runs and were classified as non-

responders. Figure I4 shows mean group results for the 1st EEG-nf session ($n=14$) from the offline EEG data analysis. The results need to be considered preliminary, because the EEG analysis involved exclusion of bad intervals (characterized by large muscle and eye movement artifacts), but did not involve EEG artifact removal by means of independent component analysis (ICA). The shorthand notation 'F4-F3' stands for the normalized frontal EEG asymmetry $FEA = \ln(P(F4)) - \ln(P(F3))$ for the alpha band [7.5...12.5] Hz with the standard reference (FCz). As illustrated in Fig. I4, the mean Happy vs Rest FEA changes were positive for each of the five task runs, and significant ($p < 0.05$, uncorr.) for the Practice run (PR) and Run 2 (R2).

The FEA changes averaged across the four EEG-nf runs (PR, R1, R2, R3) for each participant were also significant: $t(13) = 2.31$, $p < 0.038$. These results demonstrate that the implemented EEG-nf procedure is effective and allows successful upregulation of the FEA. Significance of the FEA results can be expected to improve after a more accurate EEG artifact removal by means of ICA.

(This work is currently in progress). To evaluate variations in alpha EEG activity across the brain, we conducted an EEG source analysis using the exact low-resolution electromagnetic tomography (eLORETA), implemented in the LORETA-KEY software (KEY Institute for Brain-Mind Research, Switzerland). The analysis was applied to the same 64-channel EEG data ($n=14$), transformed to the common average reference. It involved computation of EEG cross spectra separately for the Happy Memories with EEG-nf conditions and for the Rest conditions across the four nf runs (PR, R1, R2, R3).

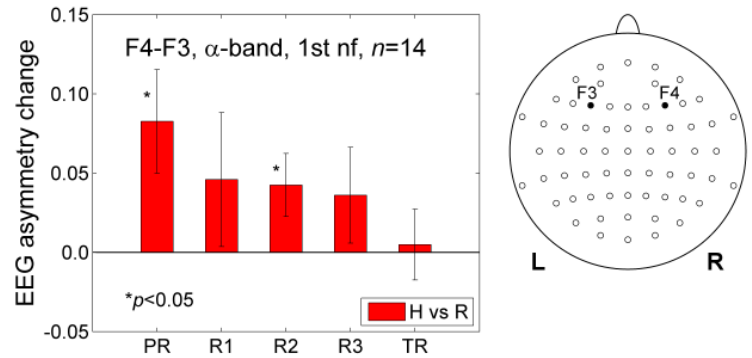
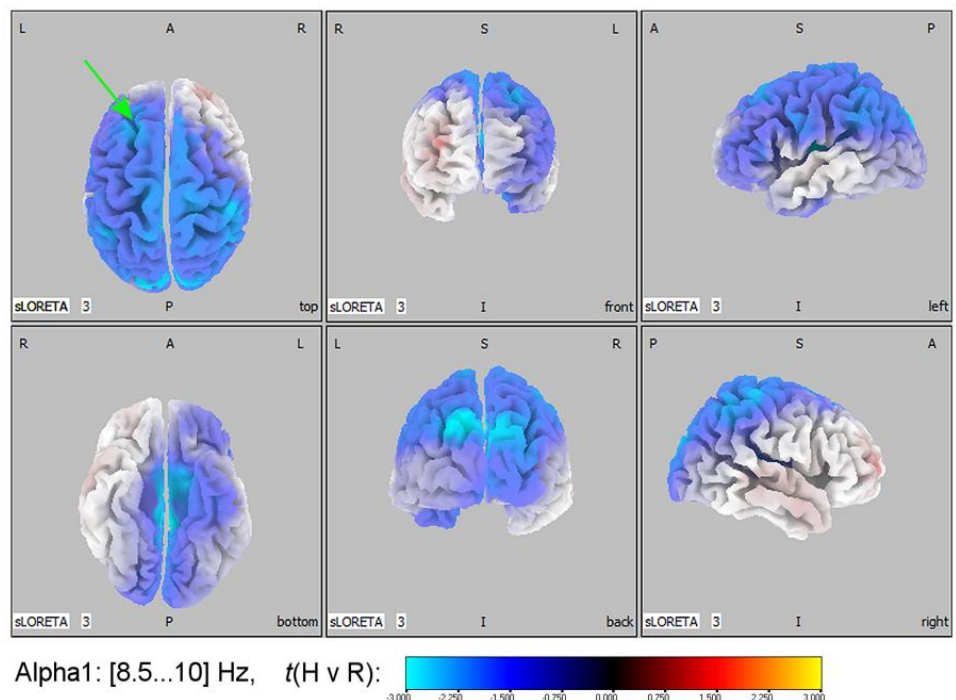


Figure I4. Changes in frontal EEG asymmetry during the EEG-nf task relative to Rest.

Figure I5. Changes in the lower alpha (α_1) EEG activity during the EEG-nf task relative to Rest.

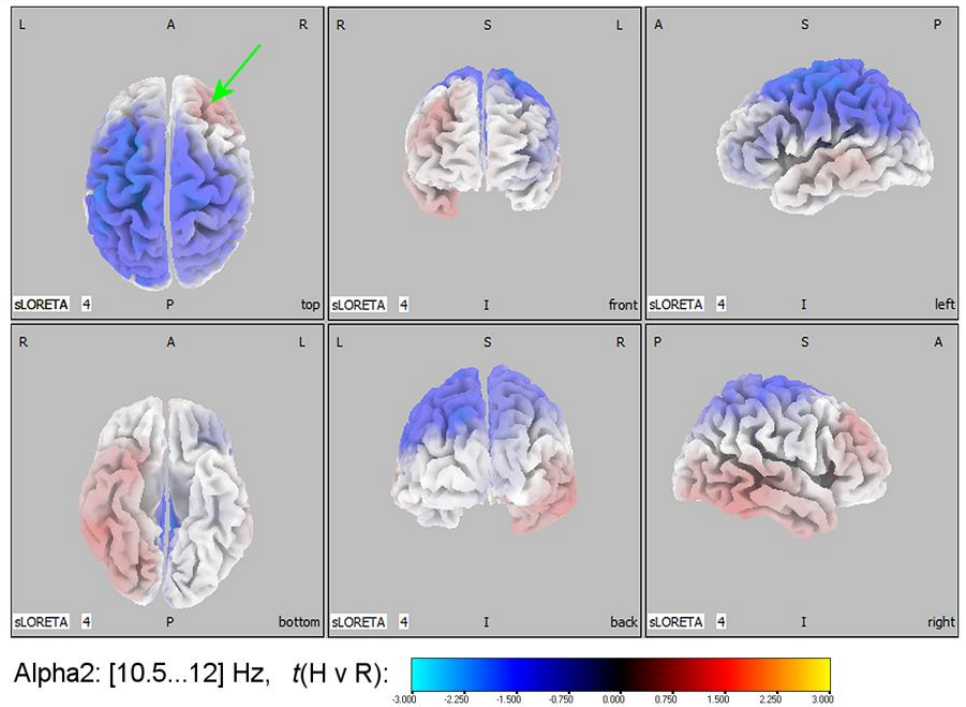


The cross spectra were calculated for the lower alpha band, α_1 [8.5...10] Hz, and the upper alpha band, α_2 [10.5...12] Hz, as defined in the LORETA-KEY software.

The current source density for each band was then obtained using the eLORETA transform. Group analysis involved voxel-wise comparison of log-transformed current density values between the Happy Memories and Rest conditions. It included a correction for multiple comparisons as implemented in the LORETA-KEY software. Figure I5 shows changes in the lower alpha (α_1) EEG current density between the EEG-nf task and the Rest task. Hemispheric asymmetry is clearly visible for the prefrontal cortex. A pronounced reduction in the α_1 current density is observed for the left prefrontal regions with the maximum reduction in the left DLPFC (BA 8, green arrow).

Figure I6 shows changes in the upper alpha (α_2) EEG current density between the same tasks. A more pronounced increase in the α_2 current density can be seen for the right prefrontal regions with the maximum increase in the right DLPFC (BA 9, green arrow). Thus, upregulation of the target FEA measure using the EEG-nf is accompanied by *both* the increase in localized alpha activity for the right DLPFC (underneath F4) *and* the reduction in localized alpha activity for the left DLPFC (underneath F3). Importantly, the deep temporal lobe regions show current density variations similar to those for the corresponding left/right DLPFC (Figs. I5,I6) suggesting similar activity modulations for the left/right amygdala.

Figure 6. Changes in the upper alpha (α_2) EEG activity during the EEG-nf task relative to Rest.



I. Discussion

Our preliminary EEG-nf results demonstrate the effectiveness of the selected EEG-nf procedure in Veterans with and without PTSD. Performance of the EEG-nf task is accompanied by activation (lower alpha) of the left DLPFC and de-activation (higher alpha) of the right DLPFC. Both effects are beneficial to PTSD patients according to the literature [51, 105]. Normalization of frontal EEG asymmetry may conceivably lead to a reduction in severity of PTSD symptoms, as suggested by our experimental results on EEG effects of the rtfMRI-nf. Further analyses of our 64-channel EEG data, together with the physiological data (GSR, respiration, heart rate) and the psychological assessment measures (Fig. I3), promise to extend these promising preliminary results.

3.2 PROBLEMS IN ACCOMPLISHING STUDY TASKS

Difficult and challenging recruitment is the main reason behind the study delay schedule by two years. We therefore requested on Jun 30, 2015 a twelve months extension and later on August 2, 2016 a second twelve-month, no-cost extension (beyond the original project completion date of Sep 29, 2015), which was approved. During the fourth year of the project period we have completed Phase 1 of the study (i.e., real-time fMRI

neurofeedback [rtfMRI-nf] and EEG data collection) targeting Aim #1: *Establish rtfMRI-nf training feasibility with concurrent EEG recordings in a combat-related PTSD population*. We have already met and exceeded project Milestone #2: fMRI/EEG data collection of 8 subjects per group (control: Veterans with no PTSD; neurofeedback, sham: Veterans with PTSD). Data analysis indicates (as described below) rtfMRI-nf amygdala training with concurrent EEG recordings in a combat-related PTSD population is feasible. In parallel we have also developed the rtfMRI-nf and rtEEG-nf software (Milestone #3) for the purpose of Aim #2: *Develop a stand-alone rtEEG neurofeedback training protocol for PTSD*. We identified the variations in frontal upper alpha EEG asymmetry during the rtfMRI-nf amygdala training as a promising measure of PTSD severity and treatment response. This EEG signal feature is suitable for developing a stand-alone EEG neurofeedback training protocol (Milestones # 4-7). We have finished preparation (Milestone #8) and conducted data collection for Phase 3 of the project and Aim #3: *EEG-only neurofeedback training feasibility in combat-related PTSD*. The Phase 3 subject visit schedule is shown in Figure 1 below. We have not reached intended recruitment targets for Phase 3 of the study, however collected data indicates EEG-nf training feasibility. However larger number of subjects would be necessary to ensure clinical efficacy of EEG-nf based on frontal EEG asymmetry beyond our pilot observation. Below we included comprehensive descriptions of the study recruitment efforts and activities during this award, as well as achieved recruitments target.

3.3 PARTICIPANT RECRUITMENTS

Recruitment proved to be very challenging for this protocol, despite our best and very substantial efforts. In October 2012, we began implementing our agreed upon recruitment strategy with the Jack C. Montgomery Veterans Administration (VA) Medical Center (Muskogee, OK and Tulsa clinic). The plan included both passive and active recruitment strategies at the local VA behavior health centers. Upon further investigation, active recruitment strategies were not feasible due to VA regulations, so passive recruitment strategies were continued, using VA clinicians to provide information about a study to patients. Passive recruitment methods were not fruitful and referrals from the VA did not materialize, despite several meetings and many efforts to collaborate. We developed an extensive and creative outreach program in attempt to reach Veterans. Approvals from Western Institutional Review Board and the USAMRMC Office of Research Protection, Human Research Protection Office were obtained in February 2013 to begin active recruitment. After obtaining approval, we utilized specific media outlets to introduce our study and provide information to the Veteran population about research initiatives and needs. Media resources that have been utilized include 9 advertisements on 6 different local radio stations, Facebook, Craigslist, commercial slots in Tulsa movie theaters, and local newspaper ads. The Community Service Council (CSC) was engaged on March 19th, 2013. This effort yielded contacts with Carla Tanner and Jim Lyall who host monthly Veteran's Initiative meetings for Veteran service providers. Beginning in April of 2013, recruitment efforts included attending the initiative meetings monthly, for a total of 6 (April-September) meetings sponsored by the local Veterans Initiative Council. Each month, meetings were comprised of 20-30 local and federal Veteran service providers and groups. We constructed packets of pamphlets and brochures reviewed them with service providers during these monthly meetings. Recruitment efforts were expanded to the Mental Health Association, Tulsa (MHAT). In April of 2013, our recruitment project staff attended and presented at an event called "Crisis: Opportunity for Change." In addition to presenting, a recruitment and information dissemination table was manned by our recruitment-focused staff and study pamphlets were handed out throughout the duration of the event; approximately 50 pieces of literature were provided to service providers. Recruitment efforts also extended to local law enforcement and attorneys. Our staff met with the Tulsa Police Department and presented information on our target population and provided a box of 50 pamphlets for distribution to Veteran officers.

During that same time, an attorney from Legal Aid Services of Oklahoma was provided a packet of 75 fliers for the study. Also in April, our recruitment for the current study extended to media outlets; an interview with project staff was aired on KWGS, the local public radio station, to provide exposure and information about the study. Beginning in May of 2013, our recruitment efforts yielded a new relationship with Brookhaven Psychiatric Hospital. Each month our recruitment-focused staff attended meetings and provided approximately 235 pieces of study focused literature to various social workers, mental health counselors, psychologists, and physicians. On May 7th, a meeting was held with psychotherapist Daniel Morris of Human Skills and Resources. Approximately 100 brochures were provided for clinicians and clients. Recruitment efforts were also extended to psychiatrists at the Laureate Psychiatric Clinic and Hospital (LPCH). On May 28th, 2013, we hosted our first recruitment oriented luncheon for the psychiatrists and physicians of LPCH. Study brochures were given out. These luncheons continued through September. We also engaged Family and Children Services; introductory conversations were made and pamphlets mailed for distribution to clients.

In order to engage Veterans more directly, in June of 2013, recruitment-focused staff participated in the US Army National Guard's 30 Day Yellow Ribbon Event in Jenks, Oklahoma. A display table was set up and manned for the duration of the event. Approximately 100 packets of information were distributed. During that same month, recruitment efforts aimed to engage the larger community in learning about our research during the Tulsa Tough athletic event. During the month of July, we sought to continue to engage new community organizations. Each month thereafter, fliers and pamphlets were distributed to gyms, Physical Therapy of Tulsa, Neurosurgery Associates, and ear/nose/throat specialists. On July 13-14, 2013, our recruitment staff attended the 60 Day Yellow Ribbon Event held by the US Army National Guard in Tulsa. Primary activities involved welcoming Veterans and discussing our research project as well as providing informational materials to potential participants and their loved ones. Approximately 130 packets of information were distributed. Also, on July 21, 2013, Muskogee VA held its Welcome Home event at the (Bank of Oklahoma) BOK Center in downtown Tulsa and recruitment staff set up two display tables and dispersed information as well as key chains and cell phone holders with our institute's logo to serve as a reminder of the PTSD research being conducted. In the month on August 2013, recruitment efforts included providing a tour of our institute to the News on 6 crew. Our interview and presentation aired on KOTV on August 22, 2013 during the 5:00pm and 10:00pm time slots. On August 27, 2013, we welcomed the Attorney General and formally presented information about our research study and our goals. In September, 2013, recruitment staff attended the Soul Wounds Veterans' ceremony at All Souls Unitarian Church in Tulsa. With permission, our staff placed study brochures on tables in the lobby areas and provided information to attendees. On September 19, 2013, recruitment forged a new partnership with the Veteran Advisory Council and presented information about our research study, target population and recruitment needs; pamphlets were distributed to approximately 43 community Veteran service providers. Recruitment-focused staff presented before The University of Tulsa Student Veteran Association. On September 26, 2013, recruitment staff attended a meeting at a local (Veterans of Foreign Wars) VFW and distributed study brochures to Veterans. On September 26, 2013, recruitment efforts included a table set up and information distribution at the Zarrow Mental Health Symposium. September 26-30, 2013, recruitment-oriented staff tended a table at the Tulsa State Fair.

For the second year (October 2013 through October 2014), LIBR recruitment staff developed methods of regular outreach in the community for the study. Recruitment efforts included attending events in the community such as mental health events and events that were targeted towards the study population. Staff continued to engage with community organizations in already established ongoing partnership with our institution. In July 2014, aiming to further improve our most effective recruitment tools, recruitment staff rewrote the radio advertisements and redesigned the brochures. We contacted the popular radio stations and

have been in ongoing communication with them through September 2014. Results from each radio ad were collected and compared. In August 2014, in an effort to further validate local station genres, recruitment ran ads on airways that were reevaluated as promising. We aired 15 total spots during weekday and weekend drive-times with a result of 6 newly established calls. We looked into a higher ranked rock station via the Arbitrends rankings, running 18 spots over three days with a return of 2 calls. In September 2014, in order to reach out to a broader population, recruitment staff contacted a Spanish radio station. Negotiations of price were made with KBEZ and Clear Channel radio for a PTSD ad running for 42 spots from the over six days. We established 4 new calls from this series. Beginning in October 2014, we also began airing radio ads on two radio stations in the Oklahoma City area. Our recruitment efforts included an on-going monthly relationship with certain medical and Veteran organizations such as the Veterans Initiative, Family and Children Services, Veteran's Advisory Council, and Laureate Psychiatric Clinic and Hospital. Starting in January, staff also began meeting with local physicians' offices, apartment complexes, motorcycle shops, and gun stores, in order to arrange for distribution of recruitment materials. In August 2014, we obtained permission and distributed recruitment materials on tables, cork boards, and information booths at the student unions on the Tulsa campuses of the University of Oklahoma and Oklahoma State University. Permission was also obtained to distribute materials at the University of Tulsa student union. During the month of October 2014 alone LIBR placed over 400 pamphlets, flyers, and business cards at local apartments, gyms, laundry facilities, liquor stores, colleges, and technology schools. Recruitment staff reached out to the psychological health director at the 138th fighter wing in Tulsa, the psychological health director at the OKC National Guard, and the Rolling Thunder event coordinator.

During the third year of the grant (October 2014 through October 2015) radio advertising continued to be our most successful recruitment effort. We ran 28 ads on 9 different radio stations across multiple genres (country, rock, hip-hop, top 40, and contemporary hits) and two metropolitan areas (Oklahoma City and Tulsa). Radio stations were chosen based on previous success as well as Nielson ratings procured during the last year. We also found that advertisements run during patriotic holidays (e.g. Independence Day) seem to be especially effective.

Beginning in October 2014, in order to help with recruitment, LIBR decided to have Veterans who were excluded from the study participate in a LIBR-funded single-visit version of the study. We have also continued our community outreach efforts during the last year. We have an on-going monthly relationship with certain medical and Veteran organizations such as the Veterans Initiative, Family and Children Services, Veteran's Advisory Council, and Laureate Psychiatric Clinic and Hospital. In November of 2014, LIBR had an open house for the community. The open house allowed professionals in the community, including the VA, to come to LIBR and learn about ongoing research studies. We have also provided tours and study information specifically for staff of Veteran and mental health organizations, including the Coffee Bunker (a local organization that provides a gathering place for Veterans and their families), the Wounded Warriors (a program that provides hyperbaric oxygen therapy to Veterans to treat TBI and PTSD), and the Mental Health Association of Tulsa. Our recruitment staff was able to obtain a list of zip codes where many Veterans reside. Staff attended community organizations in those areas to build partnerships that will help with recruitment.

During the fourth year of the grant (October 2015 through September 2016) radio advertising continued to be our most successful recruitment effort. We ran 15 ads for a total of 1221 ad spots on 4 different radio stations across multiple genres (country, rock, hip-hop, and contemporary hits) in the Tulsa area. This year we also aired a television ad for the study. The advertisement aired on the local FOX station as well as the local MyNetworkTV station. There were a total of 290 ad spots over 19 days in June. We have also continued

running advertisements on Facebook on a quarterly basis. These advertisements reach up to 200,000 individual accounts and target both male and female users to maximize the number of both direct and indirect referrals. We have also continued our community outreach efforts during the last year. LIBR staff participated in the PURPOSE 2.2 Run/Walk, an event to raise awareness of Veteran suicide, on April 30, 2016. LIBR also promoted the study at a number of events throughout the year, including the North Tulsa Neighborhood Summit (August 27, 2016) and the Zarrow Symposium (September 28-30, 2016). We have an on-going monthly relationship with certain medical and Veteran organizations such as the Veterans Initiative, Family and Children Services, Veteran's Advisory Council, and Laureate Psychiatric Clinic and Hospital. We also continued our efforts directly targeting recruiting patients/potential participants from Family and Children Services monthly and the Laureate Psychiatric Clinic and Hospital weekly.

During the fifth year of the grant (October 1, 2016 through June 30, 2017) radio advertising continued to be our most successful recruitment effort. We ran 1 ad with 70 ad spots on the Tulsa-area active rock station. LIBR staff members participated in monthly on-air interviews the hip-hop station, which is the highest rated station for minority listeners in the Tulsa area according to Arbitron. This time we also once again aired a television ad for the study. The advertisement aired on the local FOX station as well as the local MyNetworkTV station. There were a total of 316 ad spots over the month of October. We have also continued running advertisements on Facebook on a quarterly basis. These advertisements reach up to 200,000 individual accounts and target both male and female users to maximize the number of both direct and indirect referrals. During January and February, LIBR recruitment staff attended the Oklahoma State University Tulsa Vendor Days events to promote the current study as well as the other LIBR studies. LIBR recruitment staff attended a number of Veteran-focused events during the preceding quarter to promote the study, distribute printed material, and answer questions. These events included the Tulsa Oklahoma Veterans Project Easter Egg Hunt (April 8), local comedy club The Looney Bin's "Ha Ha's for Vets" (April 19), and the Brian "Bucky" Utter Memorial Golf Tournament in Broken Arrow, OK supporting BRRX4Vets (May 12). LIBR recruitment also visited 8 local schools (universities, community colleges, and technical schools) to distribute recruitment materials. Other general LIBR recruitment events included the Tulsa Roots Music Global Bash (April 15), National Trails Day (June 3), and Tulsa Tough (June 9-11). On May 31st Dr. Bodurka and members of the LIBR administration met with leaders from the local VFW (Post 577). We have an on-going monthly relationship with certain medical and Veteran organizations such as the Veterans Initiative, Family and Children Services, Veteran's Advisory Council, and Laureate Psychiatric Clinic and Hospital. Each month, our recruitment-focused staff attended meetings and provided presentations as well as provided study-focused literature to various social workers, mental health counselors, psychologists, and physicians. These recruitment efforts included meetings and presentations with selected clinicians who work directly with the target population. We also continued our efforts directly targeting recruiting patients/potential participants from Family and Children Services monthly and the Laureate Psychiatric Clinic and Hospital weekly.

In summary, considerable institutional support including but not limited to staff time and marketing efforts were committed over five years in an effort to enroll Veterans, this is a challenging group to recruit for multiple complicated reasons.

3.4 ENROLLMENT INFORMATION FOR 2013-2017

During the first year of the study, October 1, 2012 through September 30, 2013, we received 61 calls regarding the study. Sixteen Veterans enrolled in the study 11 of those Veterans completed at least one fMRI scan, six completed at least one session of the fMRI neurofeedback session. Two Veterans completed the study.

In October 2014 LIBR had received 300 phone calls since the study began. During the second year of the study, 85 were consented to the screening assessment. Out of the 85 screens, 46 were eligible, 23 consented to the study and 17 completed the study.

Beginning in January of 2015, LIBR began using a new system for storing subject data. The new system is paperless and made it easier to track subjects and to facilitate the intake of Veterans who contact LIBR through streams other than our study focused recruitment efforts. Between January and October of 2015, 210 Veterans completed the LIBR phone screening, 32 consented to the study and 19 Veterans completed the study.

During the fourth year of the study, we completed phase 1, began to recruit exclusively for the phase 3 of the study, and rewrote some of the advertising material to align with the participation criteria for the EEG-only experiments.

Between October 1, 2015 and September 30, 2016, 414 Veterans contacted LIBR. During this time, 3 Veterans were consented to phase 1 and 2 Veterans completed phase 1, bringing the total enrolled in Phase 1 74 and the total who completed phase 1 to 40. For Phase 3, 8 consented to the study and 4 completed the study.

During the fifth year of the study we recruited exclusively for phase 3. 216 Veterans contacted LIBR, 18 consented for the study and 11 completed the study, for a total of 26 subjects enrolled in phase 3 and 15 completed.

The study target enrollment for Phase 1 was 72 Veterans, and Phase 3 was 72 Veterans. The table below summarized the study Phase 1 and Phase 3 enrollments:

	Phase 1 (rtfMRI-nf with EEG)	Phase 2 (stand-alone EEG-nf)
Contacted	985	630
Enrolled	74 (target 72)	26 (target 72)
Completed the study all visits	40	15

The demographic for the PTSD Veteran enrollment goes as follows: 100 % were male subjects, 70 % Caucasian, 13% American Indian, 0% Asian, 3% Black/African American, 12% more than one race, and 2% Hawaiian/Pacific Islander.

3.5 RECOMMENDED CHANGES OR FUTURE WORK

A) Duration of the training and sustainability of the training effect

We observed significant PTSD symptom reduction due to the rtfMRI-nf positive emotional training and this symptom reduction continued across training sessions. However, consistent training effect on the LA activity modulation was seen only in the first training session. This suggests that continuing symptom reduction might be due to a sustained effect of the first training session and the following training sessions might not have contributed to the treatment effects. In the future study, we should investigate necessary training duration to obtain treatment effect and also how long such effect is sustained.

B) Non-invasive rtfMRI-nf modulation of other regions than amygdala to alleviate PTSD symptoms

The discrepancy between the training effect on the LA activity and symptom change also suggests that symptom relief might be mediated by brain modulation other than the LA activity. In fact, our analysis in section

C, D, and E indicated that the changes in LA activity and resting-state connectivity changes were not associated with symptom change. The analysis revealed that the training effect was not limited in the LA region and the activation reduction in the salience network regions (Fig. C2) and increased resting-state functional connectivity at the precuneus were significantly correlated with symptom reduction. The rtfMRI-nf training that directly targets this activity or connectivity might be more effective to alleviate PTSD symptoms. As there were individual variabilities in the training effect and symptom reduction (section C), the future study needs to elucidate which region's modulation is most effective for what type of patient. Personalized, non-invasive modulation with rtfMRI-nf and concurrent EEG recording and determination of the neural interactions within the brain circuit relevant to positive emotion experience, memory retrieval and approach motivation can lead to novel and more efficient clinical targets for treatment of PTSD.

C) EEG neurofeedback positive emotion regulation training during concurrent fMRI in PTSD.

Our preliminary of the frontal EEG asymmetry in alpha band (FEA) EEG neurofeedback (EEG-nf) results demonstrate the effectiveness of the selected EEG-nf procedure in Veterans with and without PTSD. Performance of the EEG-nf task was accompanied by activation (lower alpha) of the left dorsolateral prefrontal cortex (DLPFC) and de-activation (higher alpha) of the right DLPFC. Both effects are beneficial to PTSD patients according to the literature [51, 105]. Therefore normalization of FEA may conceivably lead to a reduction in severity of PTSD symptoms, as suggested by our experimental results on EEG effects of the rtfMRI-nf (section A, B). However further data collection, and analysis 64-channel EEG data, together with the physiological data (GSR, respiration, heart rate) and the psychological assessment measures would be required to fully validate. In addition, conducting FEA-base EEG-nf with concurrent fMRI recording would even further established EEG-nf modulation association with: (a) amygdala, DLPFC, and ACC, precuneus BOLD activities, (b) PTSD symptoms improvements. Developing and validating the EEG-only neurofeedback with fMRI can lead to portable and affordable fMRI-verified EEG-based interventions for depression.

4. KEY RESEARCH ACCOMPLISHMENTS

- Real-time fMRI neurofeedback amygdala positive emotional training is feasible in Veterans with combat related PTSD, and all study participants tolerate this procedure well, with no adverse effects.
- Veterans with PTSD can learn to self-regulate their amygdala BOLD responses during recall of positive autobiographical memories.
- The rtfMRI-nf training of the left amygdala resulted in statistically and clinical significant improvements in PTSD (CAPS, PCL-M) and depression (HRSD) symptoms. Significant reductions in PTSD and depression symptoms were seen in Veterans with PTSD in the experimental group but not in controls.
- Functional connectivity between the amygdala and the left dorsolateral prefrontal cortex as well as the orbitofrontal cortex was enhanced during the rtfMRI-nf and this enhancement positively correlated with PTSD severity, reversing connectivity deficiencies specific to PTSD.
- The rtfMRI-nf training resulted in left-lateralized EEG coherence enhancement, indicating increased coherent neuronal activity in the left fronto-temporal regions and suggesting therapeutic potential and a beneficial increase in approach motivation. Such increase is more pronounced in patients with more severe PTSD.
- Modulation of BOLD LA activity during the neurofeedback procedure was accompanied by changes in frontal EEG asymmetry (FEA) in the upper alpha band (right vs. left electrodes, more positive FEA) consistent with more approach-oriented responses and traits as well as more positive emotions.

- Reduction in CAPS ratings was associated with reduction in the average FEA changes during the rtfMRI-nf task, indicating that variations in FEA during rtfMRI-nf training might independently provide valuable information about PTSD severity and treatment response.
- FEA was identified as a promising target for EEG-only neurofeedback training among Veterans with combat-related PTSD.
- Individual variability in response to the training exists. Only the PTSD patients with low baseline left amygdala (LA) activity showed significant increase of LA activity across the training sessions, suggesting increased LA activity was most effective for subtypes of PTSD patients with hypoactive amygdala response to positive memory recall.
- PTSD symptom relief after the sessions was not associated with LA activity change. We found many regions that showed a rtfMRI-nf training effect. Decreasing activity in salience network regions across sessions was significantly associated with symptom reduction.
- Novel connectome-wide functional connectivity analysis of Veterans with and without PTSD and matched healthy controls conducted before the neurofeedback training revealed reduced connectivity between the lateral prefrontal regions and the salience network regions in PTSD.
- The decreased connectivity between the parahippocampal gyrus and visual cortex supported the dual representation theory of PTSD, which suggests dissociation between sensory and contextual memory representations in PTSD. The theory also supposes that the precuneus is a region that triggers retrieval of sensory memory of traumatic events. The decreased connectivity at the precuneus for Veterans without PTSD might be associated with suppressing such a process.
- The rtfMRI-nf training effect was not limited to a feedback target region and symptom relief could be mediated by brain modulation in several regions other than a feedback target area.
- Longitudinal connectome-wide analysis revealed neurofeedback training effects on resting state functional connectivity. Training affected both the left amygdala and the supplementary motor area (SMA), anterior cingulate cortex (ACC), insula, precuneus and prefrontal regions connectivities. These changes normalized aberrant connectivities for both Veterans with and without PTSD. Connectivity increases between the SMA and the dACC and between the precuneus and the left superior frontal gyrus were associated with a decrease in PTSD symptoms measured by PCL-M and CAPS sub-D, respectively.
- The symptom reduction due to rtfMRI-nf left amygdala positive emotional training was positively associated with the hippocampus volume increase, specifically in the CA1 and the parasubiculum regions, such that participants with a greater decrease in PTSD symptoms had more increase in the volumes, suggesting recovery from hippocampus atrophy specific to PTSD.
- The rtfMRI-nf training procedure resulted in trends toward reducing anxious reactivity to individualized traumatic event cues presented via a script-driven imagery procedure, although the trend has not yet reached statistical significance.
- We have discovered temporal independent EEG microstates in individuals with combat related PTSD and found microstates that differ between Veterans with and without PTSD symptoms. The occurrence frequency/rate of the EEG-ms which was associated with BOLD dorsal default mode, and salience networks, statistically differentiates PTSD and healthy Veterans groups and positively correlates with PTSD symptom severity.
- The occurrence rate of the EEG microstates associated with the dorsal default mode network was higher in PTSD than control, and positively associated with the severity of PTSD symptoms. The occurrence rate of the electrophysiological state associated with the anterior salience network was lower in PTSD than control, and negatively associated with the hedonic tone in PTSD participants.

- Real-time frontal EEG asymmetry in the alpha band EEG neurofeedback training during recalling positive emotions is feasible in Veterans with combat related PTSD, and all study participants tolerate this procedure well, with no adverse effects.
- EEG-nf positive emotional training has beneficial effect for Veterans with PTSD by normalizing frontal EEG asymmetry in alpha band through activation (lower EEG alpha power) of the left dorsolateral prefrontal cortex (DLPFC) and de-activation (higher EEG alpha power) of the right DLPFC.

5. REPORTABLE OUTCOMES

5.1 SUBMITTED MANUSCRIPTS

Peer-Reviewed Scientific Journals:

- 1) Misaki, M., Barzigar, N., Zotev, V., Phillips, R., Cheng, S., Bodurka, J. (2015). Real-time fMRI processing with physiological noise correction - Comparison with off-line analysis. *J Neurosci Methods* 256, 117-121. (pdf copy is attached)
- 2) Wong, C.K., Zotev, V., Misaki, M., Phillips, R., Luo, Q., Bodurka, J. (2016) Automatic EEG-assisted retrospective motion correction for fMRI (aE-REMCOR). *Neuroimage*. 129:133-47. doi: [10.1016/j.neuroimage.2016.01.042](https://doi.org/10.1016/j.neuroimage.2016.01.042). (pdf copy is attached)
- 3) Mayeli A, Zotev V, Refai H, Bodurka J. (2016) Real-time EEG artifact correction during fMRI using ICA. *J Neurosci Methods*. 2016 Sep 30;274:27-37. doi: 10.1016/j.jneumeth.2016.09.012. (pdf copy is attached)
- 4) Misaki, M., Phillips, R., Zotev, V., Wong, C.K., Wurfel, B., Krueger, F., Feldner M., Bodurka, J. (2017) Connectome-wide investigation of altered resting-state functional connectivity in war Veterans with and without posttraumatic stress disorder. *Neuroimage: Clinical* 17:285-296. doi: 10.1016/j.nicl.2017.10.032. (pdf copy is attached)
- 5) Wong, C.K., Luo, Q., Zotev, V., Phillips, R., Chan, K.W.C, Bodurka, J. Automatic cardiac cycle determination directly from EEG-fMRI data by multi-scale peak detection method. *Journal of Neuroscience Method* (2017, revised under review; pdf copy is attached)
- 6) Yuan, H., Phillips, R., Wong, C.K., Zotev, V., Misaki, M., Wurfel, B.E., Krueger, F., Feldner, M., Bodurka, J. Tracking resting state connectivity dynamics in Veterans with PTSD. *Neuroimage: Clinical* (2017, revised under review; pdf copy is attached).
- 7) Zotev, V., Phillips, R., Misaki, M., Wong, C.K., Wurfel, B.E., Krueger, F., Feldner, M., Bodurka, J., Real-time fMRI neurofeedback training of amygdala activity with simultaneous EEG in Veterans with combat-related PTSD. *Neuroimage: Clinical* (2017, revised under review; pdf copy is attached).
- 8) Misaki, M., Phillips, R., Zotev, V., Wong, C.K., Wurfel, B., Krueger, F., Feldner M., Bodurka, J., Real-time fMRI amygdala neurofeedback positive emotional training normalized resting-state functional connectivity in combat Veterans with and without PTSD: a connectome-wide investigation. *Neuroimage: Clinical* (2017, revised under review; pdf copy is attached).
- 9) Rahmani, B., Wong, C.K., Norouzzadeh, P., Bodurka, J., McKinney, B.A., Dynamical Hurst analysis identifies EEG channel differences between PTSD and healthy controls. *PLOS One* (2017, revised under review; pdf copy is attached).

5.2 CONFERENCE ABSTRACTS

- 1) Barzigar, N., Misaki, M., Zotev, V., Yuan, H., Phillips, R., Chang, S., Bodurka, J., (2014). Real-time image preprocessing and physiological noise correction for fMRI. Poster presented at the 20th Annual Meeting of the Organization for Human Brain Mapping, Hamburg, Germany, In Conf. Proc. 2031.
- 2) Wong, C.K., Zotev, V., Yuan, H., Bodurka, J. (2014). Cardiac cycle detection in EEG with residual MRI gradient artifact by multiple-scale peak detection. Poster presented at the 20th Annual Meeting of the Organization for Human Brain Mapping, Hamburg, Germany, In Conf. Proc. 3470.
- 3) Yuan, H., Wong, C.K., Phillips, R., Zotev, V., Misaki, M., Feldner, M., Bodurka, J. (2014). Default mode changes in Veterans with PTSD after real-time fMRI neurofeedback training of amygdala. Poster presented at

- the 20th Annual Meeting of the Organization for Human Brain Mapping, Hamburg, Germany, In Conf. Proc. 1402.
- 4) Wong, C.K., Zotev, V., Yuan, H., Misaki, M., Phillips, R., Luo, Q., Bodurka, J. (2015). An automatic EEG-assisted retrospective motion correction for fMRI (aE-REMCOR). Poster presented at the 23rd Annual Meeting of the International Society of Magnetic Resonance in Medicine, Toronto, Canada. In: Proc. Intl. Soc. Magn. Reson. Med. 23, 2562.
 - 5) Zotev, V., Phillips, R., Misaki, M., Wong C., Wurfel, B., Meyer, M., Krueger, F., Feldner, M., Bodurka, J. (2015) Real-time fMRI neurofeedback with simultaneous EEG in combat-related PTSD: identification of EEG measures of PTSD severity and treatment response. Poster presented at the 23rd Annual Meeting of the International Society of Magnetic Resonance in Medicine, Toronto, Canada. In: Proc. Intl. Soc. Magn. Reson. Med. 23, 1366.
 - 6) Phillips, R., Zotev, V., Young, K., Masaya, M., Wong, C.K., Wurfel, B., Meyer, M., Krueger, F., Feldner, M., Bodurka, J. (2015). Amygdala connectivity after real-time fMRI neurofeedback emotional training in combat-related PTSD. Poster presented at the 23rd Annual Meeting of the International Society of Magnetic Resonance in Medicine, Toronto, Canada. In: Proc. Intl. Soc. Magn. Reson. Med. 23, 1360.
 - 7) Yuan, H., Phillips, R., Zotev, V., Misaki, M., Wong, C., Wurfel, B., Meyer, M., Krueger, F., Feldner, M., Bodurka, J. (2015) Role of ACC in fMRI neurofeedback training of amygdala in Veterans with PTSD. Poster presented at the 21st Annual Meeting of the Organization for Human Brain Mapping Honolulu, USA, In Conf. Proc. 1024.
 - 8) Zotev, V., Phillips, R., Misaki, M., Wong, C., Wurfel, B., Meyer, M., Krueger, F., Feldner, M., Bodurka, J. (2015) rtfMRI neurofeedback with concurrent EEG in combat-related PTSD: EEG measures of treatment response. Poster presented at the 21st Annual Meeting of the Organization for Human Brain Mapping Honolulu, USA, In Conf. Proc. 1025.
 - 9) Mayeli, A., Zotev, V., Refai, H., Bodurka, J. (2015) ICA-based automatic artifacts detection and removal from EEG data recorded simultaneously with fMRI. Poster presented at the 21st Annual Meeting of the Organization for Human Brain Mapping Honolulu, USA, In Conf. Proc. 1831.
 - 10) Yuan, H., Phillips, R., Zotev, V., Misaki, M., Wong, C., Wurfel, B., Meyer, M., Krueger, F., Feldner, M., Bodurka, J. (2015) Tracking resting state connectivity dynamics in Veterans with PTSD: new insights from EEG-fMRI. Poster presented at the 21st Annual Meeting of the Organization for Human Brain Mapping Honolulu, USA, In Conf. Proc. 1931.
 - 11) Zotev, V., Phillips, R., Misaki, M., Wong, C.K., Wurfel, B., Meyer, M., Krueger, F., Feldner, M., Bodurka, J. (2015). Evaluation of rtfMRI Neurofeedback Training Effects in Combat-related PTSD Using Simultaneous EEG. Poster presented at the 24th Annual Meeting of the International Society of Magnetic Resonance in Medicine, Singapore. In: Proc. Intl. Soc. Magn. Reson. Med. 24, 280
 - 12) Mayeli, A., Zotev, V., Refai, H., Bodurka, J. (2016). Real-time ICA-based artifact correction of EEG data recorded during functional MRI. E-poster presented at the 24th Annual Meeting of the International Society of Magnetic Resonance in Medicine, Singapore. In: Proc. Intl. Soc. Magn. Reson. Med. 24, 3773
 - 13) Wong, C.K., Zotev, V., Misaki, M., Phillips, R., Luo, Q., Bodurka, J. (2016). Automatic EEG-assisted retrospective head motion correction improves rs-fMRI connectivity analysis. Poster presented at the 24th Annual Meeting of the International Society of Magnetic Resonance in Medicine, Singapore. In: Proc. Intl. Soc. Magn. Reson. Med. 24, 3774
 - 14) Wong, C.K., Zotev, V., Misaki, M., Phillips, R., Luo, Q., Bodurka, J. (2016). Support vector machine classification of head motion independent components from EEG-fMRI. Poster presented at the 22nd Annual Meeting of the Organization for Human Brain Mapping, Geneva, Switzerland. In: Conf. Proc. 1811.
 - 15) Phillips, R., Zotev, V., Young, K., Misaki, M., Wong, C.K., Wurfel, B., Meyer, M., Krueger, F., Feldner, M., Bodurka, J. (2016). Changes in Amygdala Connectivity During Multiple Visits of Real-Time fMRI Neurofeedback Training. Poster presented at the 22nd Annual Meeting of the Organization for Human Brain Mapping, Geneva, Switzerland. In: Conf. Proc. 3951.
 - 16) Zotev, V., Phillips, R., Misaki, M., Wong, C.K., Wurfel, B., Meyer, M., Krueger, F., Feldner, M., Bodurka, J. (2016). Evaluation of rtfMRI Neurofeedback Training Effects in Combat-related PTSD Using Simultaneous EEG. Poster presented at the 22nd Annual Meeting of the Organization for Human Brain Mapping, Geneva, Switzerland. In: Conf. Proc. 1082.

- 17) Rahmani, B., Wong, C.K., Norouzzadeh, P., Bodurka, J., McKinney, B. (2016). Dynamical Hurst analysis of EEG signal discriminates between PTSD and healthy controls. Poster presented at the 22nd Annual Meeting of the Organization for Human Brain Mapping, Geneva, Switzerland. In: Conf. Proc. 1756.
- 18) Misaki, M., Phillips, R., Zotev, V., Wong, C.K., Wurfel, B., Kruger, F., Feldner, M., Bodurka, J. (2017). Connectome-wide exploration of altered resting state connectivity in combat Veterans with and without PTSD and real-time fMRI neurofeedback training effect on abnormal connectivity. Poster presented at the 25th Annual Meeting of the International Society of Magnetic Resonance in Medicine, Honolulu, USA, In: Proc. Intl. Soc. Magn. Reson. Med. 25, 4213.
- 19) Wong, C.K., Luo, Q., Zotev, V., Phillips, R., Bodurka, J. Multi-scale peak detection method for an automatic cardiobalistic artifact period determination directly from EEG-fMRI data. (2017) Poster presented at the 25th Annual Meeting of the International Society of Magnetic Resonance in Medicine, Honolulu, USA, In: Proc. Intl. Soc. Magn. Reson. Med. 25, 5414.
- 20) Zotev, V., Phillips, R., Misaki, M., Wong, C.K., Wurfel, B., Meyer, M., Kruger, F., Feldner, M., Bodurka, J. (2017). Real-time fMRI neurofeedback of the amygdala enhances amygdala-orbitofrontal connectivity and lateralized EEG coherence in Veterans with combat-related PTSD. In: Proc. Intl. Soc. Magn. Reson. Med. 25, 512.
- 21) Misaki, M., M., Phillips, R., Zotev, V., Wong, C.K., Wurfel, B., Kruger, F., Feldner, M., Bodurka, J. (2017). Altered resting-state connectivity in PTSD and real-time fMRI neurofeedback training effect. Poster presented at the Annual Meeting of the Organization for Human Brain Mapping OHBM2017, Vancouver, Canada. In: Conf. Proc. 1084.
- 22) Wong, C.K., Zotev, V., Phillips, R., Misaki, M., Bodurka, J. (2017). Toward real-time head motion correction for EEG-fMRI: EEG-derived motion components classification. Poster presented at the Annual Meeting of the Organization for Human Brain Mapping OHBM2017, Vancouver, Canada. In: Conf. Proc. 1108.
- 23) Zotev, V., Phillips, R., Misaki, M., Wong, C.K., Wurfel, B., Meyer, M., Kruger, F., Feldner, M., Bodurka, J. (2017). Real-time fMRI neurofeedback of the amygdala enhances amygdala-orbitofrontal connectivity in combat-related PTSD. Poster presented at the Annual Meeting of the Organization for Human Brain Mapping OHBM2017, Vancouver, Canada. In: Conf. Proc. 2620.
- 24) Misaki, M., Zotev, V., Phillips, R., Wong, C.K., Kruger, F., Feldner, M., Bodurka, J. (2017). Individual difference in the effect of amygdala neurofeedback emotional training in combat-related PTSD. Poster presented at the Real-time functional imaging and neurofeedback conference 2017, Nara, Japan, In: Conf. Proc. 31.
- 25) Misaki, M., Phillips, R., Zotev, V., Wong, C.K., Wurfel, B., Kruger, F., Feldner, M., Bodurka, J. Whole brain effect of real-time fMRI amygdala neurofeedback emotional training and its association with PTSD symptom reduction. (2017, under review, submitted to Joint Annual Meeting of the International Society of Magnetic Resonance in Medicine and European Society of Magnetic Resonance in Medicine and Biology, June 2018, Paris, France).
- 26) Misaki, M., Phillips, R., Zotev, V., Wong, C.K., Wurfel, B., Kruger, F., Feldner, M., Bodurka, J. A connectome-wide investigation of the longitudinal effect of real-time fMRI amygdala neurofeedback emotional training on resting-state connectivity in combat Veterans with PTSD. (2017, under review, submitted to Joint Annual Meeting of the International Society of Magnetic Resonance in Medicine and European Society of Magnetic Resonance in Medicine and Biology, June 2018, Paris, France).
- 27) Zotev, V., Phillips, R., Misaki, M., Wong, C.K., Wurfel, B., Meyer, M., Kruger, F., Feldner, M., Bodurka, J. EEG correlates of real-time fMRI neurofeedback of the amygdala in combat-related PTSD evaluated using eLORETA. (2017, under review, submitted to Joint Annual Meeting of the International Society of Magnetic Resonance in Medicine and European Society of Magnetic Resonance in Medicine and Biology, June 2018, Paris, France).
- 28) Wong, C.K., Luo, Q., Zotev, V., Phillips, R., Chan, K.W.C., Bodurka, J. Improved cardiobalistic artifact waveform for artifact correction with direct cardiac cycle detection from EEG-fMRI data. (2017, under review, submitted to Joint Annual Meeting of the International Society of Magnetic Resonance in Medicine and European Society of Magnetic Resonance in Medicine and Biology, June 2018, Paris, France).
- 29) Wong, C.K., Luo, Q., Zotev, V., Phillips, R., Chan, K.W.C., Bodurka, J. Direct cardiobalistic cycle measurement from EEG-fMRI data improves artifact removal template. (2017, under review, submitted to Annual Meeting of the Organization for Human Brain Mapping OHBM2018, June 2018, Singapore).

30) Misaki, M., Mulyana, B., Phillips, R., Zotev, V., Wong, C.K., Wurfel, B., Kruger, F., Feldner, M., Bodurka, J. Real-time fMRI amygdala neurofeedback training lowers PTSD symptoms with hippocampus volume increase. (2017, under review, submitted to Annual Meeting of the Organization for Human Brain Mapping OHBM2018, June 2018, Singapore).

5.3 PRESENTATIONS

- 1) Bodurka, J. (2014). Emotional regulation training for treating warfighters with combat-related PTSD using real-time fMRI and EEG-assisted neurofeedback. Progress report presented at the MOMRP PTSD Biomarkers IPR annual meeting, Ft. Detrick, MD.
- 2) Feldner, M. T. (2014). *Preliminary Evidence for the Efficacy of Real-Time fMRI Neurofeedback in the Treatment of PTSD*. Lecture presented to the College Student Interest Group in Neurology (CO-SIGN) at the University of Arkansas.
- 3) Phillips, R., Zotev, V., Yuan, H., Young, K., Wong, C.K., Wurfel, B., Krueger, F., Feldner, M., Bodurka, J., Self-regulation of amygdala activation with real-time fMRI neurofeedback in combat-related PTSD. (2014). In: Proc. Intl. Soc. Magn. Reson. Med. 22, 252.
- 4) Bodurka, J. (2015). Emotional regulation training of amygdala using real-time fMRI and EEG-assisted neurofeedback in combat-related PTSD. Talk (seminar) at the 31st Annual Meeting of the International Society for Traumatic Stress Studies, New Orleans, Louisiana, USA.
- 5) Bodurka, J. (2015). Emotional regulation training with real-time fMRI neurofeedback of the amygdala and simultaneous EEG measurements. Talk (key note) at the Neuroscience Symposium, Central Institute for Mental Health, Mannheim, Germany.
- 6) Bodurka, J. (2015). Emotional regulation training for treating warfighters with combat-related PTSD using real-time fMRI and EEG-assisted neurofeedback. Progress report presented at the MOMRP PTSD Biomarkers IPR annual meeting, Ft. Detrick, MD.
- 7) Bodurka, J. (2016). Emotion Regulation Training with Real-Time fMRI Neurofeedback of the Amygdala and Concurrent EEG Recordings in Combat-Related PTSD. Talk at the 13th Annual Meeting of the Society for Brain Mapping and Therapeutics, Miami, Florida, USA
- 8) Bodurka, J. (2016). Advances in multimodal MRI and EEG Imaging for studying the human brain. Talk (invited first inaugural speaker of the Stephenson School of Biomedical Engineering seminar series), Oklahoma University, Norman, Oklahoma, USA.
- 9) Bodurka J. (2016). Emotion Regulation Training of Amygdala using Real-time fMRI and EEG-assisted Neurofeedback. Talk (seminar) at the 22nd Annual Meeting of Organization for Human Brain Mapping, Geneva, Switzerland.
- 10) Bodurka J. (2017). Real-time fMRI neurofeedback amygdala emotional regulation training with concurrent EEG recordings. Mount Sinai Translational and Molecular Imaging Institute Seminar Series, New York, USA.
- 11) Bodurka J. (2017). Non-invasive brain neuromodulation with real-time fMRI neurofeedback amygdala emotional regulation training and concurrent EEG recordings. Center for Brain Health, The University of Texas at Dallas, Seminar Series, Dallas, TX, USA.
- 12) Bodurka J. (2017). Real-time fMRI neurofeedback modulation of amygdala hemodynamic activity improves the approach motivation deficiencies in depression and PTSD. Talk at the 15th Annual Meeting of the Society for Brain Mapping and Therapeutics, Los Angeles, California, USA
- 13) Bodurka J. (2018). Real-time fMRI amygdala neurofeedback emotional training effects and its association with PTSD symptoms reductions. Invited talk at the 16th Annual Meeting of the Society for Brain Mapping and Therapeutics, Los Angeles, California, USA

5.4 METHODS DEVELOPMENT

1) Misaki, M., Barzigar, N., Zotev, V., Phillips, R., Cheng, S., Bodurka, J. (2015). Real-time fMRI processing with physiological noise correction - Comparison with off-line analysis. J Neurosci Methods 256, 117-121. – pdf file with this publication is attached.

We have developed a real-time fMRI processing system with a dedicated graphic processing unit (GPU) for intensive whole-brain fMRI data processing in real-time. The system implements all of image processing that

are used in an off-line analysis including physiological noise correction. It can complete whole-brain GLM analysis with more than 100,000 voxels and more than 250 volumes in less than 300ms.

2) Wong CK, Zotev V, Misaki M, Phillips R, Luo Q, Bodurka J. (2016) Automatic EEG-assisted retrospective motion correction for fMRI (aE-REMCOR). *Neuroimage*. 129:133-47. doi: [10.1016/j.neuroimage.2016.01.042](https://doi.org/10.1016/j.neuroimage.2016.01.042). – pdf file with this publication is attached.

We have development of an enhanced an automated implementation of EEG-assisted retrospective motion correction (E-REMCOR), which utilizes EEG motion artifacts to correct the effects of head movements in simultaneously acquired fMRI data on a slice-by-slice basis – aE-REMCOR. The aE-REMCOR algorithm, implemented in MATLAB, enables automated preprocessing of the EEG data, ICA decomposition, and, importantly, automatic, computer-based identification of motion-related ICs. The aE-REMCOR is capable of substantially reducing head motion artifacts in fMRI data.

3) Mayeli A, Zotev V, Refai H, Bodurka J. (2016) Real-time EEG artifact correction during fMRI using ICA. *J Neurosci Methods*. 2016 274:27-37. doi: 10.1016/j.jneumeth.2016.09.012. – pdf file with this publication is attached.

We have developed and implemented improved, real-time ICA-based EEG artifact corrections method during simultaneous EEG-fMRI experiments.

4) Wong, C.K., Luo, Q., Zotev, V. Phillips, R., Chan, K.W.C, Bodurka, J. Automatic cardiac cycle determination directly from EEG-fMRI data by multi-scale peak detection method. *Journal of Neuroscience Method* (2017, revised under review) – pdf file with the revised manuscript is attached.

We developed a better algorithms for artifact suppression in EEG data acquired simultaneously with fMRI, by improved method for automatic period detection of cardioballistic artifacts in EEG-fMRI data. The proposed algorithm achieves a higher and better detection accuracy of the artifact occurrence on a large EEG dataset in EEG-fMRI, and importantly without using the ECG recordings. It virtually eliminates the need of ECG for BCG artifact removal. Importantly, it can be applied retrospectively on the large EEG-fMRI data sets already acquired.

5) Misaki, M., Phillips, R., Zotev, V., Wong, C.K., Wurfel, B., Krueger, F., Feldner M., Bodurka, J., Real-time fMRI amygdala neurofeedback positive emotional training normalized resting-state functional connectivity in combat Veterans with and without PTSD: a connectome-wide investigation. *Neuroimage: Clinical* (2017, revised under review) – pdf file with manuscript is attached.

We have developed novel longitudinal multivariate distance matrix regression (MDMR) analysis to investigate and identify the rtfMRI-nf left amygdala training effect on whole-brain voxel-by-voxel resting state connectivity in Veterans with and without PTSD.

6) Rahmani, B., Wong, C.K., Norouzzadeh, P., Bodurka, J., McKinney, B.A., Dynamical Hurst analysis identifies EEG channel differences between PTSD and healthy controls. *PLOS One* (2017, revised under review). – pdf file with the revised manuscript is attached.

We employed a time-dependent Hurst analysis to identify EEG signals (channels or electrodes) that differentiate between healthy controls and combat-related PTSD subjects, and can lead to simplified diagnostic application of the EEG. Results indicate that F3 electrode may be a useful channel for diagnostic applications of Hurst exponents in distinguishing PTSD and healthy subjects.

7) Yuan, H., Phillips, R., Wong, C.K., Zotev, V., Misaki, M., Wurfel, B.E., Krueger, F., Feldner, M., Bodurka, J. Tracking resting state connectivity dynamics in Veterans with PTSD. *Neuroimage: Clinical* (2017, revised under review) – pdf file with the revised manuscript is attached.

Novel multimodal approach to study abnormal brain resting state connectivity dynamics in PTSD: novel insights from simultaneous EEG and fMRI. This novel analysis approach uses temporal independent EEG microstates (EEG-ms) to study PTSD abnormalities in default mode and salience networks activity temporal dynamics.

5.5 EMPLOYMENT, RESEARCH, TRAINING OPPORTUNITIES SUPPORTED BY THIS AWARD

Laureate institute for Brain Research (LIBR, Tulsa, OK) was the primary research site for all human research conducted in this award. The following individuals were involved in conducted research on this award: Drs. Jerzy Bodurka (Principal Investigator, LIBR), Vadim Zotev (Co-Investigator (Co-I), LIBR), Masaya Misaki (Co-I,

LIBR), Mathew Feldner (Co-I, University of Arkansas (UA), Fayetteville, AK), Frank Krueger (Co-I, George Mason University (GMU), Fairfax, VA), Chung-Ki Wong (Post-doctoral fellow, LIBR), Han Yuan (Post-doctoral fellow, LIBR); Mathew Mayer MD, (Co-I, psychiatrist, LIBR); Raquel Phillips (B.S., research coordinator, LIBR), and Lisa Kinyon (MS, LPC, psychiatric interviewer, LIBR). In addition as part of centralized clinical assessment team (see below), clinical interviews were conducted by LIBR certified psychiatrists including MDs Brent Wurfel, and William Yates. Medical monitor for the study was Michael Dubriwny MD (psychiatrist, Laureate Psychiatric Clinic and Hospital, Tulsa, OK). In addition the following graduate students have training opportunities to learn about i) PTSD, ii) advance neuroimaging techniques such real-time fMRI neurofeedback, iii) multimodal simultaneous EEG-rtfMRI imaging, iv) neuroimaging data analysis: Ahmad Mayeli, Nafise Barzigar, Ben Mulyana (master of sciences, graduate students from University of Oklahoma, Tulsa graduate college), Bahareh Rahmani, (Ph.D., graduate student from University of Tulsa), Sergey Chernyak (Ph.D. graduate student from GMU).

In addition for the purpose of this award, with LIBR institutional support, i) centralized clinical assessment with certified psychiatrists coverage and recruitment infrastructure was established, and expanded; ii) advance multimodal brain imaging capabilities were established, expanded and maintained; iii) computing and data storage infrastructure were expanded, and maintained. In addition, a new human brain imaging capacity was established: a stand-alone 64-channel EEG, galvanic skin-conductance (GSR), respiratory, cardiac waveforms recording station and advance computer stimulus delivery system, capable to conduct advance neurofeedback experiments.

The synergy between neuroscientists, psychiatrists, computational neuroscientists, clinical psychologists and physicists resulted in development and advances in several data analytic multimodal statistical approaches for the data generated. At subcontractor institutions, the partnership has also been very valuable for the work being done at the University of Arkansas. Continued research collaboration between Dr. Feldner and the Dr. Bodurka's LIBR research team resulted in new knowledge contributions to understanding PTSD and related neurobiological functioning. In addition, it has promoted the education of advanced undergraduate and graduate students at the University of Arkansas. Dr. Feldner has disseminated information about the neurobiology of PTSD, treatment of combat-related PTSD, and more specifically the rtfMRI-nf procedure examined in this project to these groups via lectures and invited presentations to various student groups. Similarly, Dr. Feldner has presented portions of this research to the Veterans Healthcare System of the Ozarks via annual presentations to the faculty and interns involved in treating PTSD at this local VA. Finally, it has continued to influence Dr. Feldner's research program, by extending his laboratory-based translational work that focuses on better understanding PTSD in order to develop enhanced treatments by facilitating adoption of increasingly neurobiologically-focused assessments, including the type of EEG-measured prefrontal asymmetry examined in this project. Finally collaboration research experiences gained through this award contributed to a successful full professorship evaluation of Dr. Feldner who is now Professor, and Director of Psychological Clinic at the Department of Psychological Science at the University of Arkansas. This award and collaborations resulted in George Mason University administrative support and improvements to Dr. Krueger lab computational infrastructure for help with computationally intense aspects of the award, and through collaboration with LIBR and UA helped in development of novel neuroimaging analysis approaches. The research, mentor, and collaboration experiences gained through this award contributed to a successful tenure-track evaluation of Dr. Krueger who is now an Associate Professor at the School of System Biology at GMU. Dr. Krueger has also disseminated information about the neurobiology of, and novel treatment strategies for PTSD, via lectures and invited presentations to various student groups. The reward further gave LIBR, UA, and GMU more visibility regarding performing cutting-edge research in the field of clinical neuroscience with

focus on better understanding pathophysiology of PTSD and researching a novel technology-assisted intervention.

6. CONCLUSION

Recruitment of Veterans formed the major challenge for this study, and has resulted in data collection delays and two years no-cost extension was necessary to reach most of study goals. During the study, we secured substantial institutional support for our very substantial recruitment efforts to further increase our recruitment campaign focused on the Veteran population in Oklahoma. Those recruitments efforts (as summarized in this report) improved subject enrollment rate and also resulted in raising awareness of combat-related PTSD and our research efforts to understand better pathophysiology of this costly disease and our thrust to research novel intervention. Although we have not reach intended recruitment targets especially for EEG-only neurofeedback (EEG-nf) training, the collected data indicated EEG-nf training feasibility in combat related PTSD.

This research established and showed real-time fMRI-nf emotional training with concurrent EEG recording in a combat-related PTSD population. This procedure was tolerated well without any adverse effects. Veterans with PTSD can learn to self-regulate their left amygdala (LA) BOLD responses during recall of positive autobiographical memories. The rtfMRI-nf training of the left amygdala resulted in statistically and clinical significant improvements in PTSD (CAPS, PCL-M) and depression (HRSD) symptoms. Significant reductions in PTSD and depression symptoms were seen in Veterans with PTSD in the experimental group who received LA feedback but not in controls who received feedback for another brain region not involved in emotion regulation.

Analyses were conducted to examine the effects of the rtfMRI procedure on task response. The main result of the present work is the observation of the significant *positive* correlations between PTSD severity and the LA fMRI connectivity enhancement (FCS) for several PFC regions during the rtfMRI-nf training. Results demonstrated that rtfMRI-nf of amygdala activity to enhance emotion regulation ability may be beneficial to Veterans with combat-related PTSD. Our fMRI and EEG results independently suggest that the rtfMRI-nf training has the potential to correct the amygdala-prefrontal cortex (PFC) functional connectivity deficiencies specific to PTSD. The most significant PTSD-specific enhancements in fMRI connectivity between the LA and the PFC were observed for the lateral orbitofrontal cortex (LOFC) and dorsolateral prefrontal cortex (DLPFC) regions, which are parts of the executive function and emotion regulation system. Because activities of these cortical regions can be probed using EEG, EEG-nf based on frontal EEG asymmetry in alpha band may complement the rtfMRI-nf of the amygdala. Indeed, our results also indicate that the FEA variations associated with the rtfMRI-nf training can serve as a measure of treatment response in PTSD, and serves as good candidate for the neurofeedback signal for EEG only neurofeedback training. Comparably, training in self-regulating LA activity during positive autobiographical memory recall with rtfMRI-nf was effective to reduce symptoms of PTSD group. Since this effect was significant only for the active group, LA signal feedback was more effective than only practicing positive autobiographical memory recall as was done in the sham neurofeedback situation. The training effect on LA activity, however, was not seen for all participants. The strategy of using rtfMRI-nf to increase LA activity was most effective for subtypes of PTSD patients with a hypoactive amygdala response to positive memory recall. While baseline LA activity could predict the training effect, symptom relief after the sessions was not associated with LA activity change. This suggests that symptom reduction might not be directly mediated by LA activity modulation, but by other regions that are co-modulated during the training.

Analyses were also conducted to examine resting state functional connectivity in PTSD. A connectome-wide investigation of resting-state functional connectivity using MDMR suggested decreased connectivity between the lateral prefrontal regions and the salience network regions in PTSD, which is consistent with previous reports that indicated lowered emotion-regulation function in these regions. Next, comprehensive investigation of rtfMRI-nf training effects on resting-state functional connectivity revealed that changes in connectivity were observed both in left amygdala connectivity as well as in the supplementary motor area (SMA), anterior cingulate cortex (ACC), insula, precuneus, and prefrontal regions. These changes were in the direction of normalizing abnormal connectivity for both PTSD and Veterans control (VC) groups. Connectivity increases between the SMA and the dACC and between the precuneus and the left superior frontal gyrus were associated with a decrease in PTSD symptoms measured by PCL-M and CAPS sub-D, respectively. These results indicated that the rtfMRI-nf training effect was not limited to a feedback target region and symptom relief could be mediated by brain modulation in several regions other than a feedback target area. Moreover, a multi-modal analysis of fMRI-derived resting state networks demonstrated that the occurring frequency of EEG microstates in the dorsal default mode network (DMN) is higher in PTSD and positively correlated with the score of PTSD severity. In contrast, the occurring frequency of the anterior salience network (SN) is lower in PTSD and negatively correlated with the score of hedonic tone or degree of pleasantness. These findings contribute new information to our understanding neural mechanisms of PTSD, and further suggest that a disruption in emotion generation and regulation circuits play a crucial role and contribute to the pathophysiology of PTSD.

In addition, and importantly the rtfMRI-nf left amygdala positive emotional training had a significant treatment effect to reduce PTSD symptoms. This symptom reduction was positively associated with the hippocampus volume increase, specifically in the CA1 and the parasubiculum regions, such that participants with a greater decrease in PTSD symptoms had more increase in the volumes, suggesting recovery from hippocampus atrophy specific to PTSD.

Collectively, these results have significantly advanced understanding of the neurobiology of PTSD and offer promising targets for real-time EEG neurofeedback-assisted interventions.

7. REFERENCES

1. Diagnostic and Statistical Manual of Mental Disorders (DSM-IV) (American Psychiatric Association, 2000).
2. Milliken, C. S., Auchterlonie, J. L. & Hoge, C. W. Longitudinal assessment of mental health problems among active and reserve component soldiers returning from the Iraq war. *Jama* 298, 2141-8, (2007).
3. Kessler, R. C. Posttraumatic stress disorder: the burden to the individual and to society. *J Clin Psychiatry* 61 Suppl 5, 4-12; discussion 13-4, (2000).
4. Rauch, S. L., Shin, L. M. & Phelps, E. A. Neurocircuitry models of posttraumatic stress disorder and extinction: human neuroimaging research--past, present, and future. *Biol Psychiatry* 60, 376-82 (2006).
5. Shin, L. M., Rauch, S. L. & Pitman, R. K. Amygdala, medial prefrontal cortex, and hippocampal function in PTSD. *Ann N Y Acad Sci* 1071, 67-79, (2006).
6. Protopopescu, X. et al. Differential time courses and specificity of amygdala activity in posttraumatic stress disorder subjects and normal control subjects. *Biol Psychiatry* 57, 464-73 (2005).
7. Rauch, S. L. et al. Exaggerated amygdala response to masked facial stimuli in posttraumatic stress disorder: a functional MRI study. *Biol Psychiatry* 47, 769-76, (2000).
8. Sergerie K, Chochol C, Armony JL. The role of the amygdala in emotional processing: a quantitative meta-analysis of functional neuroimaging studies. *Neurosci Biobehav Rev*. 32(4):811-30, (2008).
9. Shin, L. M. et al. A functional magnetic resonance imaging study of amygdala and medial prefrontal cortex responses to overtly presented fearful faces in posttraumatic stress disorder. *Arch Gen Psychiatry* 62, 273-81, (2005).
10. deCharms, R. C. Applications of real-time fMRI. *Nat Rev Neurosci* 9, 720-729, (2008).
11. Zotev, V., Krueger, F., Phillips, R., Alvarez, R. P., Simmons, W. K., Bellgowan, P., Drevets, W. C., Bodurka, J. Self-regulation of amygdala activation using real-time fMRI neurofeedback. *PLoS ONE* 6(9), e24522,

- (2011).
12. Mulert, C., Lemieux, L. (Eds) EEG-FMRI: Physiological basis, Technique and Applications. Springer (2010).
 13. Allen, J.J.B., Harmon-Jones, E., Cavender, J.H., Manipulation of frontal EEG asymmetry through biofeedback alters self-reported emotional responses and facial EMG. *Psychophysiology* 38, 685–693, (2001).
 14. Gordon, E., Palmer, D.M., Cooper, N., EEG alpha asymmetry in schizophrenia, depression, PTSD, panic disorders, ADHD and conduct disorder. *Clinical EEG and Neuroscience* 41, 178-183, (2010).
 15. Harmon-Jones, E, Gable, P.A., Peterson, C. K. The role of asymmetric frontal cortical activity in emotion-related phenomena: a review and update. *Biol. Psychol* 84(3), 451-462, (2010).
 16. Yuan, H., Zotev, V., Phillips, R., Drevets, W.C., Bodurka, J. Spatiotemporal dynamics of the brain at rest – exploring EEG microstates as electrophysiological signatures of BOLD resting state networks. *Neuroimage* 60(4), 2062-2072, (2012).
 17. Zotev, V., Yuan, H., Misaki, M., Phillips, R., Young, K.D., Feldner, M.T. Bodurka J. Correlation between amygdala BOLD activity and frontal EEG asymmetry during real-time fMRI neurofeedback training in patients with depression. *NeuroImage Clinical* 2016 11:224-238
 18. Oldfield, R.C., 1971. The assessment and analysis of handedness: the Edinburgh inventory. *Neuropsychologia* 9, 97-113.
 19. Maxwell, M.E., 1992. Family Interview for Genetic Studies (FIGS). National Institute of Mental Health, Washington, DC.
 20. Fagerström, K.O., 1978. Measuring degree of physical dependency to tobacco smoking with reference to individualization of treatment. *Addict. Behav.* 3, 235-241.
 21. Hollingshead, A.B., 1975. Four factor index of social status. Yale University, Department of Sociology.
 22. Rush, A.J., Carmody, T.J., Reimnitz, P.E., 2000. The Inventory of Depressive Symptomatology (IDS): clinician (IDS-C) and self-report (IDS-SR) ratings of depressive symptoms. *Int. J. Methods Psychiatr. Res.* 9, 45-59.
 23. Hamilton, M., 1960. A rating scale for depression. *J. Neurol. Neurosurg. Psychiatry* 23, 56-62.
 24. Blake, D.D., Weathers, F.W., Nagy, L.M., Kaloupek, D.G., Klauminzer, G., Charney, D.S., Keane, T.M., 1990. A clinician rating scale for assessing current and lifetime PTSD: the CAPS-1. *Behav. Ther.* 13, 187-188.
 25. Weathers, F.W., Keane, T.M., Davidson, J.R.T., 2001. Clinician-Administered PTSD Scale: a review of the first ten years of research. *Depress. Anxiety* 13, 132-156.
 26. Bagby, R.M., Parker, J.D.A., Taylor, G.J., 1994. The twenty-item Toronto Alexithymia Scale – I. Item selection and cross-validation of the factor structure. *J. Psychosom. Res.* 38, 33-40.
 27. Doherty, R.W., 1997. The emotion contagion scale: a measure of individual differences. *J. Nonverb. Behav.* 21, 131-154.
 28. Whalen, P.J., Bush, G., Shin, L.M., Rauch, S.L., 2006. The emotional counting Stroop: a task for assessing emotional interference during brain imaging. *Nat. Protocols* 1, 293-296.
 29. Pitman, R.K., Orr, S.P., Foa, D.F., de Jong, J.B., Claiborn, J.M., 1987. Psychophysiological assessment of posttraumatic stress disorder imagery in Vietnam combat Veterans. *Arch. Gen. Psychiatry* 44, 970-975.
 30. Hopper, J.W., Frewen, P.A., Sack, M., Lanius, R.A., van der Kolk, B.A., 2007. The Responses to Script-Driven Imagery Scale (RSDI): assessment of state posttraumatic symptoms for psychobiological and treatment research. *J. Psychopathol. Behav. Assess.* 29, 249-268.
 31. Montgomery, S.A., Asberg, M., 1979. A new depression scale designed to be sensitive to change. *Br. J. Psychiatry* 134, 382-389.
 32. Weathers, F.W., Huska, J., Keane, T.M., 1991. The PTSD Checklist Military Version (PCL-M). National Center for PTSD, Boston, MA.
 33. Hamilton, M., 1959. The assessment of anxiety states by rating. *Br. J. Med. Psychol.* 32, 50-55.
 34. Snaith, R.P., Hamilton, M., Morley, S., Humayan, A., Hargreaves, D., Trigwell, P., 1995. A scale for the assessment of hedonic tone: the Snaith-Hamilton Pleasure Scale. *Br. J. Psychiatry* 167, 99-103.
 35. McNair, D.M., Lorr, M., Droppleman, L.F., 1971. Profile of Mood States. Educational and Industrial Testing Service, San Diego.
 36. Young, K.D., Siegle, G.J., Zotev, V., Phillips, R., Misaki, M., Yuan, H., Drevets, W.C., Bodurka, J., 2017. Randomized clinical trial of real-time fMRI amygdala neurofeedback for major depressive disorder: effects on symptoms and autobiographical memory recall. *Am. J. Psychiatry* 174, 748-755.
 37. Talairach, J., Tournoux, P., 1988. Co-Planar Stereotaxic Atlas of the Human Brain. Thieme Medical Publishers, New York.
 38. Sergerie, K., Chochol, C., Armony, J.L., 2008. The role of the amygdala in emotional processing: a quantitative meta-analysis of functional neuroimaging studies. *Neurosci. Biobehav. Rev.* 32, 811–830.

39. Dehaene, S., Piazza, M., Pinel, P., Cohen, L., 2003. Three parietal circuits for number processing. *Cogn. Neuropsychol.* 20, 487–506.
40. Cox, R.W., 1996. AFNI: software for analysis and visualization of functional magnetic resonance neuroimages. *Comput. Biomed. Res.* 29, 162-173.
41. Zotev, V., Yuan, H., Phillips, R., Bodurka, J., 2012. EEG-assisted retrospective motion correction for fMRI: E-REMCOR. *NeuroImage* 63, 698-712.
42. Glover, G.H., Li, T.Q., Ress, D., 2000. Image-based method for retrospective correction of physiological motion effects in fMRI: RETROICOR. *Magn. Reson. Med.* 44, 162-167.
43. Jo, H.J., Saad, Z.S., Simmons, W.K., Milbury, L.A., Cox, R.W., 2010. Mapping sources of correlation in resting state fMRI, with artifact detection and removal. *NeuroImage* 52, 571-582.
44. Bell, A.J., Sejnowski, T.J., 1995. An information-maximization approach to blind separation and blind deconvolution. *Neural Comput.* 7, 1129-1159.
45. McMenamin, B.W., Shackman, A.J., Maxwell, J.S., Bachhuber, D.R.W., Koppenhaver, A.M., Greischar, L.L., Davidson, R.J., 2010. Validation of ICA-based myogenic artifact correction for scalp and source-localized EEG. *NeuroImage* 49, 2416-2432.
46. Etkin, A., Wager, T.D., 2007. Functional neuroimaging of anxiety: a meta-analysis of emotional processing in PTSD, social anxiety disorder, and specific phobia. *Am. J. Psychiatry* 164, 1476-1488.
47. Lanius, R.A., Bluhm, R., Lanius, U., Pain, C., 2006. A review of neuroimaging studies in PTSD: heterogeneity of response to symptom provocation. *J. Psychiat. Res.* 40, 709-729.
48. Patel, R., Spreng, R.N., Shin, L.M., Girard, T.A., 2012. Neurocircuitry models of posttraumatic stress disorder and beyond: a meta-analysis of functional neuroimaging studies. *Neurosci. Biobehav. Rev.* 36, 2130-2142.
49. Nicholson, A.A., Rabellino, D., Densmore, M., Frewen, P.A., Paret, C., Kluetsch, R., Schmahl, C., Théberge, J., Neufeld, R.W.J., McKinnon, M.C., Reiss, J., Jetly, R., Lanius, R.A., 2017. The neurobiology of emotion regulation in posttraumatic stress disorder: amygdala downregulation via real-time fMRI neurofeedback. *Hum. Brain. Mapp.* 38, 541-560.
50. Kemp, A.H., 2010. Disorder specificity despite comorbidity: resting EEG alpha asymmetry in major depressive disorder and post-traumatic stress disorder. *Biological Psychology*, 85, 350-354.
51. Rabe, S. 2008. Changes in brain electrical activity after cognitive behavioral therapy for posttraumatic stress disorder in patients injured in motor vehicle accidents. *Psychosomatic Medicine*, 70, 13-19.
52. Young, K.D., Zotev, V., Phillips, R., Misaki, M., Yuan, H., Drevets, W.C., Bodurka, J., 2014. Real-time FMRI neurofeedback training of amygdala activity in patients with major depressive disorder. *PLoS ONE* 9, e88785.
53. Misaki, M., Phillips, R., Zotev, V., Wong, C.K., Wurfel, B., Krueger, F., Feldner M., Bodurka, J. (2017) Connectome-wide investigation of altered resting-state functional connectivity in war Veterans with and without posttraumatic stress disorder. *Neuroimage: Clinical* 17:285-296.
54. Cox, R.W., Chen, G., Glen, D.R., Reynolds, R.C., Taylor, P.A., 2017. FMRI Clustering in AFNI: False-Positive Rates Redux. *Brain Connect* 7, 152-171.
55. Victor, T.A., Furey, M.L., Fromm, S.J., Ohman, A., Drevets, W.C., 2010. Relationship between amygdala responses to masked faces and mood state and treatment in major depressive disorder. *Arch Gen Psychiatry* 67, 1128-1138.
56. Wang, T., Liu, J., Zhang, J., Zhan, W., Li, L., Wu, M., Huang, H., Zhu, H., Kemp, G.J., Gong, Q., 2016. Altered resting-state functional activity in posttraumatic stress disorder: A quantitative meta-analysis. *Sci Rep* 6, 27131.
57. Ochsner, K.N., Silvers, J.A., Buhle, J.T., 2012. Functional imaging studies of emotion regulation: a synthetic review and evolving model of the cognitive control of emotion. *Ann N Y Acad Sci* 1251, E1-24.
58. Shehzad, Z., Kelly, C., Reiss, P.T., Cameron Craddock, R., Emerson, J.W., McMahon, K., Copland, D.A., Castellanos, F.X., Milham, M.P., 2014. A multivariate distance-based analytic framework for connectome-wide association studies. *Neuroimage* 93 Pt 1, 74-94.
59. Misaki, M., Suzuki, H., Savitz, J., Drevets, W.C., Bodurka, J., 2016. Individual Variations in Nucleus Accumbens Responses Associated with Major Depressive Disorder Symptoms. *Sci Rep* 6, 21227.
60. Ellard, K.K., Barlow, D.H., Whitfield-Gabrieli, S., Gabrieli, J.D., Deckersbach, T., 2017. Neural Correlates of Emotion Acceptance Versus Worry or Suppression in Generalized Anxiety Disorder. *Soc Cogn Affect Neurosci.*
61. Logue, M.W., van Rooij, S.J., Dennis, E.L., Davis, S.L., Hayes, J.P., Stevens, J.S., Densmore, M., Haswell, C.C., Ipser, J., Koch, S.B., 2017. Smaller Hippocampal Volume in Posttraumatic Stress Disorder: A Multi-Site ENIGMA-PGC Study. *Biological Psychiatry* (in press, <https://doi.org/10.1016/j.biopsych.2017.09.006>).
62. Blake, D., Weathers, F., Nagy, L., Kaloupek, D., Charney, D., Keane, T., 1995. Clinician-Administered

PTSD Scale for DSM-IV (CAPS-DX). National Center for Posttraumatic Stress Disorder, Behavioral Science Division, Boston VA Medical Center, Boston, MA.

63. Reuter, M., Schmansky, N.J., Rosas, H.D., Fischl, B., 2012. Within-subject template estimation for unbiased longitudinal image analysis. *Neuroimage* 61, 1402-1418.
64. Iglesias, J.E., Augustinack, J.C., Nguyen, K., Player, C.M., Player, A., Wright, M., Roy, N., Frosch, M.P., McKee, A.C., Wald, L.L., Fischl, B., Van Leemput, K., 2015. A computational atlas of the hippocampal formation using ex vivo, ultra-high resolution MRI: Application to adaptive segmentation of in vivo MRI. *Neuroimage* 115, 117-137.
65. Liu, D., Johnson, H.J., Long, J.D., Magnotta, V.A., Paulsen, J.S., 2014. The power-proportion method for intracranial volume correction in volumetric imaging analysis. *Front Neurosci* 8, 356.
66. Cisler, J. M., Olatunji, B. O., Feldner, M. T., & Forsyth, J. P. 2010. Emotion regulation and the anxiety disorders: An integrative review. *Journal of Psychopathology and Behavioral Assessment*, 32, 68-82.
67. Phelps, E. A. & LeDoux, J. E. Contributions of the amygdala to emotion processing: from animal models to human behavior. 2005. *Neuron* 48, 175-87, (2005).
68. Davis, M. & Whalen, P. J. 2001. The amygdala: vigilance and emotion. *Mol Psychiatry* 6, 13-34.
69. Driessen, M. et al. 2004. Posttraumatic stress disorder and fMRI activation patterns of traumatic memory in patients with borderline personality disorder. *Biol Psychiatry* 55, 603-11.
70. Feldner, M. T., Monson, C. M., & Friedman, M. J. 2007. A critical analysis of approaches to targeted PTSD prevention: Current status and theoretically-derived future directions. *Behavior Modification*, 31, 80-116.
71. Shin, L. M., Rauch, S. L. & Pitman, R. K. 2006. Amygdala, medial prefrontal cortex, and hippocampal function in PTSD. *Ann N Y Acad Sci* 1071, 67-79.
72. Liberzon, I. et al. 1999. Brain activation in PTSD in response to trauma-related stimuli. *Biol Psychiatry* 45, 817-26.
73. Pitman, R. K., Orr, S. P., Foa, D. F., de Jong, J. B., & Claiborn, J. M. 1987. Psychophysiologic assessment of posttraumatic stress disorder imagery in Vietnam combat Veterans. *Archives of General Psychiatry* 44, 970-975.
74. Greicius, M.D., Supekar, K., Menon, V., Dougherty R.F. 2009. Resting-state functional connectivity reflects structural connectivity in the default mode network. *Cereb Cortex* 19(1):72-78.
75. Biswal, B., Yetkin, F.Z., Haughton, V.M., Hyde, J.S. 1995. Functional connectivity in the motor cortex of resting human brain using echo-planar MRI. *Magn. Reson. Med.* 34:537-541.
76. Fox, M.D. and Raichle, M.E., 2007. Spontaneous fluctuations in brain activity observed with functional magnetic resonance imaging. *Nature Reviews Neuroscience* 8:700-711.
77. Bluhm, R.L., Williamson, P.C., Osuch, E.A., Frewen, P.A., Stevens, T.K., Boksman, K., Neufeld, R.W., Théberge, J., Lanius, R.A. 2009. Alterations in default mode network connectivity in posttraumatic stress disorder related to early-life trauma. *J. Psychiatric Neurosci* 34(3):187-194.
78. Daniels, J.K., Frewen, P., McKinnon, M.C., Lanius, R.A., Default mode alterations in posttraumatic stress disorder related to early-life trauma: a developmental perspective. 2011. *J Psychiatry Neurosci.* 36:56-9.
79. Shin, L.M., Lasko, N.B., Macklin, M.L., Karpf, R.D., Milad, M.R., Orr, S.P., Goetz, J.M., Fischman, A.J., Rauch, S.L., Pitman, R.K.. 2009. Resting metabolic activity in the cingulate cortex and vulnerability to posttraumatic stress disorder. *Arch Gen Psychiatry.* 66:1099-107.
80. Lanius, R.A., Bluhm, R.L., Coupland, N.J., Hegadoren, K.M., Rowe, B., Theberge, J., Neufeld, R.W., Williamson, P.C., Brimson, M. 2010. Default mode network connectivity as a predictor of post-traumatic stress disorder symptom severity in acutely traumatized subjects. *Acta Psychiatr Scand.* 121:33-40.
81. Lui, S., Huang, X., Chen, L., Tang, H., Zhang, T., Li, X., Li, D., Kuang, W., Chan, R.C., Mechelli, A., Sweeney, J.A., Gong, Q. 2009. High-field MRI reveals an acute impact on brain function in survivors of the magnitude 8.0 earthquake in China. *Proc Natl Acad Sci U S A.* 106:15412-15417;
82. Shin, L.M., Liberzon, I., 2010. The neurocircuitry of fear, stress, and anxiety disorders. *Neuropsychopharmacol.* 35:169-191.
83. Daniels, J.K., McFarlane, A.C., Bluhm, R.L., Moores, K.A., Clark, C.R., Shaw, M.E., Williamson, P.C., Densmore, M., Lanius, R.A. 2010. Switching between executive and default mode networks in posttraumatic stress disorder: alterations in functional connectivity. *J Psychiatry Neurosci.* 35:258-66.
84. Sripada, R.K., King, A.P., Garfinkel, S.N., Wang, X., Sripada, C.S., Welsh, R.C., Liberzon, I. 2012. Altered resting-state amygdala functional connectivity in men with posttraumatic stress disorder. *J. Psychiatry Neurosci.* 37(4):241-249.
85. Kennis, M., Rademaker, A.R., van Rooij, S.J., Kahn, R.S., Geuze, E. 2015. Resting state functional connectivity of the anterior cingulate cortex in Veterans with and without post-traumatic stress disorder. *Hum Brain Mapp* 36(1):99-109.

86. Sripada, R.K., King, A.P., Welsh, R.C., Garfinkel, S.N., Wang, X., Sripada, C.S., Liberzon, I. 2012a. Neural dysregulation in posttraumatic stress disorder: evidence for disrupted equilibrium between salience and default mode brain networks. *Psychosom Med.* 74(9):904-911.
87. DiGangi, J.A., Tadayyon, A., Fitzgerald, D.A., Rabinak, C.A., Kennedy, A., Klumpp, H., Rauch, S.A., Phan, K.L. 2016. Reduced default mode network connectivity following trauma. *Neurosci Lett* 615:37-43.
88. He, B.J., Snyder, A.Z., Zempel, J.M., Smyth, M.D., Raichle, M.E., 2008. Electrophysiological correlates of the brain's intrinsic large-scale functional architecture. *Proc. Natl. Acad. Sci.* 105:16039-16044.
89. Yuan H., Zotev V., Phillips R., Drevets W.C., Bodurka J., 2012. Spatiotemporal dynamics of the brain at rest — Exploring EEG microstates as electrophysiological signatures of BOLD resting state networks. *Neuroimage* 60:2062–2072.
90. Yuan, H., Ding, L., Zhu, M., Zotev, V., Phillips, R., Bodurka, J., 2016. Reconstructing Large-Scale Brain Resting-State Networks from High-Resolution EEG: Spatial and Temporal Comparisons with fMRI. *Brain Connect* 6(2):122-35.
91. Shirer, W. R., Ryali, S., Rykhlevskaia, E., Menon, V., and Greicius, M. D. 2012. Decoding subject-driven cognitive states with whole-brain connectivity patterns. *Cereb. Cortex* 22:158–165.
92. Liberzon, I., Sripada, C.S., 2007. The functional neuroanatomy of PTSD: a critical review. *Prog. Brain Res.* 167:151–169.
93. Pitman, R.K., Rasmusson, A.M., Koenen, K.C., Shin, L.M., Gilbertson, M.W., Milad, M.R., Liberzon, I. 2012. Biological studies of post-traumatic stress disorder. *Nat Rev Neurosci* 13(11):769-787.
94. Buckner, R.L., Andrews-Hanna, J.R., Schacter, D.L. 2008. The brain default network: anatomy, function, and relevance to disease. *Ann NY Acad Sci* 1124:1-38.
95. Lou, H.C., Luber, B., Crupain, M., Keenan, J.P., Nowak, M., Kjaer, T.W., Sackeim, H.A., Lisanby, S.H. 2004. Parietal cortex and representation of the mental Self. *Proc Acad Sci USA* 101(17):6827-6832.
96. Cavanna, A.E., Trimble, M.R. 2006. The precuneus: a review of its functional anatomy and behavioral correlates. *Brain* 129(3): 564–583.
97. Yuan, H., Young, K.D., Phillips, R., Zotev, V., Misaki, M., Bodurka, J. 2014. Resting-state functional connectivity modulation and sustained changes after real-time functional magnetic resonance imaging neurofeedback training in depression. *Brain Connect* 4(9):690-701.
98. Hayes, J.P., LaBar, K.S., McCarthy, G., Selgrade, E., Nasser, J., Dolcos, F., Morey, R.A., 2011. Reduced hippocampal and amygdala activity predicts memory distortions for trauma reminders in combat-related PTSD. *J. Psychiatr. Res.* 45(5):660–669.
99. Whalley, M.G., Kroes, M.C.W., Huntley, Z., Rugg, M.D., Davis, S.W., Brewin, C.R., 2013. An fMRI investigation of posttraumatic flashbacks. *Brain Cogn.* 81 (1):151–159.
100. Seeley, W.W., Menon, V., Schatzberg, A.F., Keller, J., Glover, G.H., Kenna, H., Reiss, A.L., Greicius, M.D. 2007. Dissociable intrinsic connectivity networks for salience processing and executive control. *J Neurosci* 27(9):2349-2356.
101. Cauda, F., D'Agata, F., Sacco, K., Duca, S., Geminiani, G., Vercelli, A. 2011. Functional connectivity of the insula in the resting brain. *Neuroimage.* 55:8–23.
102. Yin, Y., Jin, C., Hu, X., Duan, L., Li, Z., Song, M., Chen, H., Feng, B., Jiang, T., Jin, H., Wong, C., Gong, Q., Li, L., 2011. Altered resting-state functional connectivity of thalamus in earthquake-induced posttraumatic stress disorder: a functional magnetic resonance imaging study. *Brain Res.* 1411:98–107.
103. Figley TD, Bhullar N, Courtney SM, Figley CR. 2015. Probabilistic atlases of default mode, executive control and salience network white matter tracts: an fMRI-guided diffusion tensor imaging and tractography study. *Front Hum Neurosci.* 9:585.
104. Bressler, S. L., and Menon, V. 2010. Large-scale brain networks in cognition: emerging methods and principles. *Trends Cogn. Sci.* 14:277–290.
105. Meyer, T., Smeets, T., Giesbrecht, T., Quaedflieg, C.W., Smulders, F.T., Meijer, E.H., Merckelbach, H.L. 2015. The role of frontal EEG asymmetry in post-traumatic stress disorder. *Biol Psychol* 108:62-77.

8. APPENDICES

The published papers and submitted manuscripts under reviewed pdf copies are attached:

- 1) Misaki, M., Barzigar, N., Zotev, V., Phillips, R., Cheng, S., Bodurka, J., entitled: Real-time fMRI processing with physiological noise correction - Comparison with off-line analysis. published in *J Neurosci Methods* 2015 256, 117-121.

- 2) Wong, C.K, Zotev, V., Misaki, M., Phillips, R., Luo, Q., Bodurka, J. entitled: Automatic EEG-assisted retrospective motion correction for fMRI (aE-REMCOR); published in Neuroimage. 2016 129:133-47. doi: [10.1016/j.neuroimage.2016.01.042](https://doi.org/10.1016/j.neuroimage.2016.01.042).
- 3) Mayeli A, Zotev V, Refai H, Bodurka J., entitled: Real-time EEG artifact correction during fMRI using ICA; published in J Neurosci Methods. 2016 274:27-37. doi: 10.1016/j.jneumeth.2016.09.012.
- 4) Misaki, M., Phillips, R., Zotev, V., Wong, C.K., Wurfel, B., Krueger, F., Feldner M., Bodurka, J. entitled: Connectome-wide investigation of altered resting-state functional connectivity in war Veterans with and without posttraumatic stress disorder: published in Neuroimage: Clinical 2017 17:285-296. doi: 10.1016/j.nicl.2017.10.032.
- 5) Wong, C.K., Luo, Q., Zotev, V. Phillips, R., Chan, K.W.C, Bodurka, J. Automatic cardiac cycle determination directly from EEG-fMRI data by multi-scale peak detection method; revision under review Journal of Neuroscience Method 2017.
- 6) Yuan, H., Phillips, R., Wong, C.K., Zotev, V., Misaki, M., Wurfel, B.E., Krueger, F., Feldner, M., Bodurka, J., entitled: Tracking resting state connectivity dynamics in Veterans with PTSD; revision under review Neuroimage: Clinical 2017.
- 7) Zotev, V., Phillips, R., Misaki, M., Wong, C.K., Wurfel, B.E., Krueger, F., Feldner, M., Bodurka, J., entitled: Real-time fMRI neurofeedback training of amygdala activity with simultaneous EEG in Veterans with combat-related PTSD; revision in progress Neuroimage: Clinical 2017.
- 8) Misaki, M., Phillips, R., Zotev, V., Wong, C.K., Wurfel, B., Krueger, F., Feldner M., Bodurka, J., entitled: Real-time fMRI amygdala neurofeedback positive emotional training normalized resting-state functional connectivity in combat Veterans with and without PTSD: a connectome-wide investigation; revision under review Neuroimage: Clinical 2017.
- 9) Rahmani, B., Wong, C.K., Norouzzadeh, P., Bodurka, J., McKinney, B.A., entitled: Dynamical Hurst analysis identifies EEG channel differences between PTSD and healthy controls; revision under review in: PLOS One 2017.

9. SUPPORTING DATA:

Nothing to report.



Computational Neuroscience
Short communication

Real-time fMRI processing with physiological noise correction – Comparison with off-line analysis



Masaya Misaki^{a,*}, Nafise Barzigar^{a,b}, Vadim Zotev^a, Raquel Phillips^a, Samuel Cheng^b, Jerzy Bodurka^{a,c,**}

^a Laureate Institute for Brain Research, Tulsa, OK, USA

^b Department of Electrical and Computer Engineering, University of Oklahoma, Tulsa, OK, USA

^c College of Engineering, University of Oklahoma, Tulsa, OK, USA

HIGHLIGHTS

- A comprehensive real-time fMRI processing system was demonstrated.
- The system includes intensive processing steps comparable to off-line analysis.
- Comprehensive whole brain data analysis can be done in real-time with a PC.
- A number of available samples need to be considered in real-time GLM.

ARTICLE INFO

Article history:

Received 9 June 2015

Received in revised form 27 August 2015

Accepted 30 August 2015

Available online 4 September 2015

Keywords:

Real-time fMRI processing
Image processing
Physiological noise correction
Functional connectivity
Neurofeedback

ABSTRACT

Background: While applications of real-time functional magnetic resonance imaging (rtfMRI) are growing rapidly, there are still limitations in real-time data processing compared to off-line analysis.

New methods: We developed a proof-of-concept real-time fMRI processing (rtfMRIp) system utilizing a personal computer (PC) with a dedicated graphic processing unit (GPU) to demonstrate that it is now possible to perform intensive whole-brain fMRI data processing in real-time. The rtfMRIp performs slice-timing correction, motion correction, spatial smoothing, signal scaling, and general linear model (GLM) analysis with multiple noise regressors including physiological noise modeled with cardiac (RETROICOR) and respiration volume per time (RVT).

Results: The whole-brain data analysis with more than 100,000 voxels and more than 250 volumes is completed in less than 300 ms, much faster than the time required to acquire the fMRI volume. Real-time processing implementation cannot be identical to off-line analysis when time-course information is used, such as in slice-timing correction, signal scaling, and GLM. We verified that reduced slice-timing correction for real-time analysis had comparable output with off-line analysis. The real-time GLM analysis, however, showed over-fitting when the number of sampled volumes was small.

Comparison with existing methods: Our system implemented real-time RETROICOR and RVT physiological noise corrections for the first time and it is capable of processing these steps on all available data at a given time, without need for recursive algorithms.

Conclusions: Comprehensive data processing in rtfMRI is possible with a PC, while the number of samples should be considered in real-time GLM.

© 2015 Elsevier B.V. All rights reserved.

1. Introduction

Real-time functional magnetic resonance imaging (rtfMRI), first introduced by Cox et al. (1995), is a process that uses functional MRI to evaluate brain activation and displays the processed image while keeping pace with data acquisition. While applications of rtfMRI are growing rapidly (Sulzer et al., 2013), there are still limitations in real-time data processing compared to off-line analysis. One

* Corresponding author.

** Corresponding author at: Laureate Institute for Brain Research, Tulsa, OK, USA.
Tel.: +1 918 502 5101; fax: +1 918 502 5135.

E-mail addresses: mmisaki@laureateinstitute.org (M. Misaki),
jbodurka@laureateinstitute.org (J. Bodurka).

limitation is that real-time image processing must be at least as fast as the time required to acquire and reconstruct a single brain volume. Another limitation is data availability. In a real-time analysis, the data sample is incrementally acquired so that processes utilizing time-course information cannot be the same as those used in off-line analysis.

Here, we demonstrated that computational time does not limit real-time processing with a current state-of-the-art personal computer (PC). We implemented a proof-of-concept rtfMRI processing (rtfMRIp) system that allows comprehensive real-time processing (RTP) on all available data at a given time, including adapted slice-timing and signal scaling, motion corrections, spatial smoothing, and RETROICOR (Glover et al., 2000) and RVT (Birn et al., 2008), the first instance of real-time physiological noise corrections with general linear model (GLM) analysis. RETROICOR and RVT are computationally intensive physiological noise correction methods that can evaluate variable noise effect voxel-wise, which is more flexible than global signal or white matter and cerebrospinal fluid average signal regression. Here we showed that they could be done in real time. We also verified that time-course analyses in slice-timing correction adapted for real-time processing could output comparable results with off-line analysis. The limitation in rtfMRIp was GLM analysis with a small number of samples. The more noise regressors used for correction, the longer we needed to wait before obtaining a reliable brain activation estimate.

2. Method

2.1. Real-time fMRI processing system (rtfMRIp)

The rtfMRIp system was implemented on a General Electric MR750 3 Tesla MRI scanner equipped with a custom-developed real-time fMRI system (Bodurka and Bandettini, 2008). See [Supplementary Fig. 1](#) for detailed system configuration. The RTP software was written in C code as an extension of an existing real-time plugin for AFNI (Cox, 1996) and runs on a Linux (Ubuntu 12.04) real-time processing (RP) computer (dual Intel Xeon (E5-2670) CPUs (8 cores), 128 GB RAM, and an NVIDIA Tesla K20X GPU with 2688 cores and 6 GB memory). The GPU was used only in the GLM analysis. The original real-time plugin features real-time image communication, motion correction, and data saving functions. We extended plugin functionalities by adding multi-threading to run multiple image processing tasks including slice timing, motion corrections, spatial smoothing, signal scaling, and regression with motion, slow drift, and physiological noise corrections. Cardiac waveforms were measured with a pulse oximeter, and respiration signal was measured with a pneumatic belt. Sampling rate of these signals was 200 Hz, which was down-sampled to 40 Hz by averaging five consecutive samples to reduce noise.

2.2. Real-time processing (RTP)

The initial few volumes are ignored to allow fMRI signal to reach a steady state. First, the slice-timing correction was performed by interpolating and resampling the time-course data at shifted time points. In the off-line analysis, either spline, Fourier, or Sinc interpolation is used. In RTP, however, available data points are restricted to past and current time, so high-order interpolation cannot be used. For RTP adaptation, we used resampling with linear and cubic interpolation. The linear method uses only the current and one past data points to interpolate, so it can be applied in RTP without modification. Cubic interpolation uses two points from the past, the current, and one future point to interpolate. We introduced a pseudo future point with the same value as the current one to perform the cubic interpolation. After the slice-timing correction,

volume registration and spatial smoothing were performed. We used the same code that was implemented in the original AFNI source code.

Voxel-wise signal normalization by converting each signal time course to the percent change relative to average signal was applied to the smoothed image. To normalize the signal, we used a fixed number of initial volumes to estimate the average signal, and this initial average is used for scaling all the subsequent time points. The number of volumes to wait before estimating the average is equal to the number of regressors in the GLM analysis. Since the GLM analysis requires a larger number of samples than the number of regressors, regression can only start once a sufficient number of samples have been acquired.

Once enough data had been acquired, the GLM analysis was performed. Polynomial regressors, 12 motion parameters (shift in x, y, and z directions, yaw, roll, and pitch rotations and their temporal derivatives), 8 RETROICOR (4 Fourier series basis functions each for cardiac and respiration) (Glover et al., 2000), and 5 RVT (Birn et al., 2008) regressors were included in the design matrix. The RETROICOR and RVT calculation was implemented in C (based on the AFNI's RetroTS.m MATLAB script). The RetroTS function read cardiac and respiration signal recorded since the start of the scan and calculated 4 cardiac and 4 respiration RETROICOR regressors. The phase of these regressors corresponded to the sample time of the first slice (the aligned time in the slice timing correction). Additionally 5 RVT regressors were also computed.

Every time a new volume was received, the data was incrementally copied to a pre-assigned memory location. The regressors of the motion parameters were also incrementally added. Updates of the RETROICOR, RVT, and polynomial regressors were not incremental, but all the vectors were re-calculated at every volume. Since the RETROICOR and RVT processes include frequency analysis for noise reduction and extracting peak points, recalculating whole estimates with an increased number of samples can improve the estimate of the regressor. This update, however, disables the use of the recursive regression method (Bagarinao et al., 2003) because the design matrix for the past data was changed. Recursive regression is useful to reduce computational time, but the current implementation demonstrated that computational time did not restrict running a full GLM analysis. The polynomial order was determined by the length of scan at the time of the regression. The order of the polynomial is calculated as $1 + \text{int}(d/150)$, where d is the scan duration in seconds (default in AFNI's 3dDeconvolve). All the column vectors in the design matrix were normalized to unit variance at every update.

The GLM analysis was performed using the quadratic least square (QLS) solving (SGELS) routine in LAPACK (Linear Algebra Package). This routine solves the $Y = BX$ equation to find B while minimizing the squared difference between Y and BX . We used the Intel Math Kernel Library (Intel® Math Kernel Library 11.0) for solving this on the CPU and CULA (Humphrey et al., 2010) on the GPU. These high performance libraries enabled fast computation for large-scale data composed of whole-brain voxels. The QLS solution (beta value) was used to regress out the noise components to obtain the residual volume, $r = y - Bx$. While the entire history of the collected data is used to run the regression analysis, the residual volume was calculated only for the current volume since only the current estimate of brain activation is needed in a real-time application.

2.3. System evaluation

We used resting-state fMRI data (14 healthy subjects) from a previous study (Zotef et al., 2011) for evaluating the developed rtfMRIp system. The gradient-echo EPI data were acquired in a resting-state session with eyes open and fixated on a cross on

the screen (TR/TE = 2000/30 ms, flip angle = 90°, SENSE acceleration = 2, 34 axial slices, FOV = 240 mm, 96 × 96 matrix reconstructed to 128 × 128 resulting in 1.9 × 1.9 × 2.9 mm³ voxel volume, and 263 volumes). The fMRI data of this scan, and corresponding cardiac and respiratory signals, were fed to the rtfMRIp using Dimon software to simulate an experimental session. We also evaluated the rtfMRIp system during actual fMRI scanning (same MRI scanner, same EPI parameters except the number of slices = 41 and 225 volumes). Eight healthy volunteers (age 21–32 years, 5 females) performed a resting-state scan. The study was approved by the Western IRB and the subjects gave informed consent to participate.

Processing time was calculated from when the system received a volume to when the processed volume was saved on a disk, which did not include the time of image reconstruction on the scanner or data transfer from the MRI host computer to the real-time processing computer (less than 1 s). In the simulation, the computation time evaluation was performed with and without using the GPU for GLM analysis. In the actual experiment, four subjects were processed with the GPU and the other four subjects were processed without the GPU.

Comparison between the real-time image processing and the off-line data analysis was performed for the slice-timing correction, signal scaling, and GLM analysis. Only the simulated experiment data were used in these evaluations to test multiple settings of real-time analysis. For the slice-timing correction, on-line linear and cubic corrections were compared with off-line Fourier correction. AFNI's 3dTshift command was used for the off-line analysis. For the signal scaling, we evaluated how quickly the temporal average converged during a scan using correlation between the spatial patterns of the average up to each time and the average of all time points.

For the GLM analysis, output of real-time GLM analysis was compared with that of off-line analysis using AFNI tools. In the off-line analysis, slice-timing correction was applied with 3dTshift with the Fourier method. Motion correction was done by registering volumes to the first volume. Smoothing with a 4 mm-FWHM Gaussian kernel was applied to the registered images. The signal values were scaled to percent change relative to the mean across time in each voxel. Twelve motion parameters (shift in x, y, and z directions; yaw, roll, and pitch rotations; and their temporal derivatives), 8 RETROICOR (4 basis functions each for cardiac and respiration), 5 RVT, and 4th-order polynomial regressors were included in the design matrix of the regression analysis. We used 3dREMLfit for the GLM in the off-line analysis. This command performed autocorrelation noise correction, which was not implemented in the real-time processing. The real-time processing used the same parameters as in the off-line analysis except for the slice-timing correction, signal scaling, and regression. On-line cubic interpolation was used for the real-time slice-timing correction in this evaluation.

3. Results

3.1. Processing time

Fig. 1 shows image processing time on the RP computer for the simulated real-time experiment (left) and for the actual real-time experiment (right). Regression analysis began at 27th volume. The graph shows mean processing time (bold lines) and standard error of mean across subjects (thin lines). The processing time for the first (27th) and the last volumes were excluded from the plot since they took an extra-long time due to initialization and closing processes. The mean number of voxels within the mask was 105,394 (SD = 7308) for the simulation dataset, 129,561 (SD = 9693) for the

real-time experiment without GPU, and 132,956 (SD = 21,809) for the real-time experiment with GPU.

3.2. Comparisons with off-line processing

Mean correlation coefficients between the output of the real-time and off-line (FFT interpolation) slice-timing corrections across subjects in each slice were calculated for both linear and cubic real-time interpolations. Even at the longest interpolation size (1.0 s), the mean correlation was higher than 0.95 (Supplementary Fig. 2), and cubic interpolation showed slightly better correlation with the off-line FFT processing than linear interpolation, though the difference was not significant. Regarding the scaling factor, we noted that correlation between the spatial pattern scaled by average until the time of each volume in real-time and that scaled by average of all volumes slowly converged with time (Supplementary Fig. 3).

Fig. 2A shows the correlation between the outputs of the real-time and off-line processing after the regression. Thirteen RETROICOR and RVT regressors and 12 motion regressors were included in the regression. The red line is drawn by fitting a function; $y = a(1 - \exp(-(t - b)/\tau))$, where t is the number of volumes, b is a shift of time, τ is a time constant, and a is a scaling factor. Fig. 2B shows the signal standard deviation within a brain in the real-time processed output. The small standard deviation of the residual image at early volumes indicates that over-fitting happened due to there being an insufficient number of samples to fit multiple regressors. The time course of standard deviation was similar to that of the correlation between the real-time and off-line processing outputs, suggesting that over-fitting made the output of the real-time processing less reliable compared to the off-line analysis. The same analysis was performed with the fewer regressors by excluding physiological noise regressors (Fig. 2C and D) and further excluding the six motion derivative regressors (Fig. 2E and F). Using fewer regressors shortened the time to converge the correlation between the real-time and off-line outputs.

4. Discussion

We have developed a proof-of-concept real-time fMRI processing system (rtfMRIp) and showed that computationally intensive fMRI processing could be done in real time with a PC equipped with a dedicated GPU. Current rtfMRIp implementation includes slice-timing correction, motion correction, spatial smoothing, signal scaling, and GLM analysis with motion parameters, polynomial regressors, and the first real-time implementation of physiological noise correction with RETROICOR and RVT regressors. These processing steps could be completed in less than 300 ms with more than 250 volumes for a whole brain with more than 100,000 voxels. While this is the first demonstration of intensive real-time fMRI data processing comparable to off-line analysis, computation time will no longer be a prohibitive factor in the further development of rtfMRIp capabilities in the near future.

Aside from computation time, RTP requires several different approaches compared to off-line processing in time-course data analysis. For slice-timing correction, reduced alternative methods for real-time processing could output comparable results with off-line processing. We note that performance of low-order interpolation in the slice-timing correction depends on the length of TR, and this correction might not be necessary for a short TR. Nevertheless, we included this process to demonstrate that it could be implemented in rtfMRIp if necessary. For signal scaling, spatial pattern of scaled signal in real time was not the same as in off-line analysis due to the difference of scaling factor. This could be critical when a multi-voxel pattern analysis (MVPA) is used for neurofeedback. Another normalization (e.g. Lee et al., 2015) should be applied

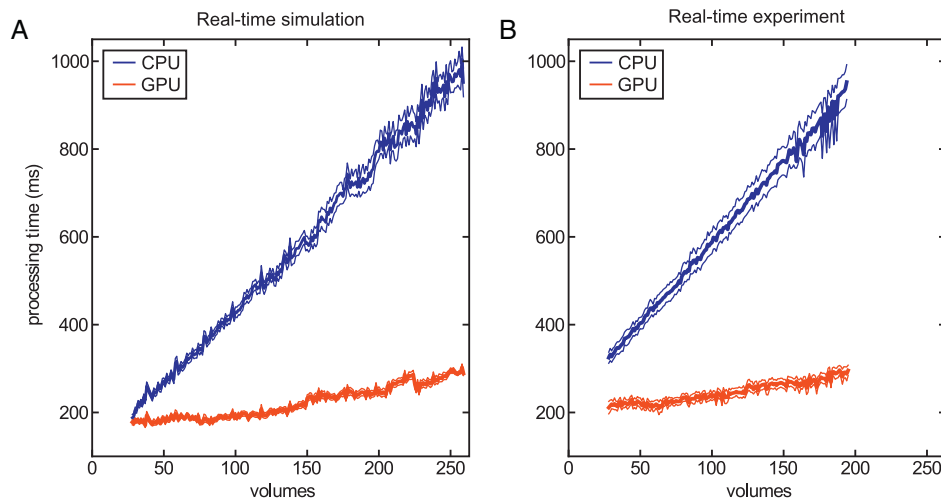


Fig. 1. Computation time of real-time image processing without GPU (CPU: blue lines) and with GPU (red lines) for the regressions. The bold lines and thin lines indicate mean processing time and its standard error across subjects, respectively. (For interpretation of the references to color in text, the reader is referred to the web version of this article.)

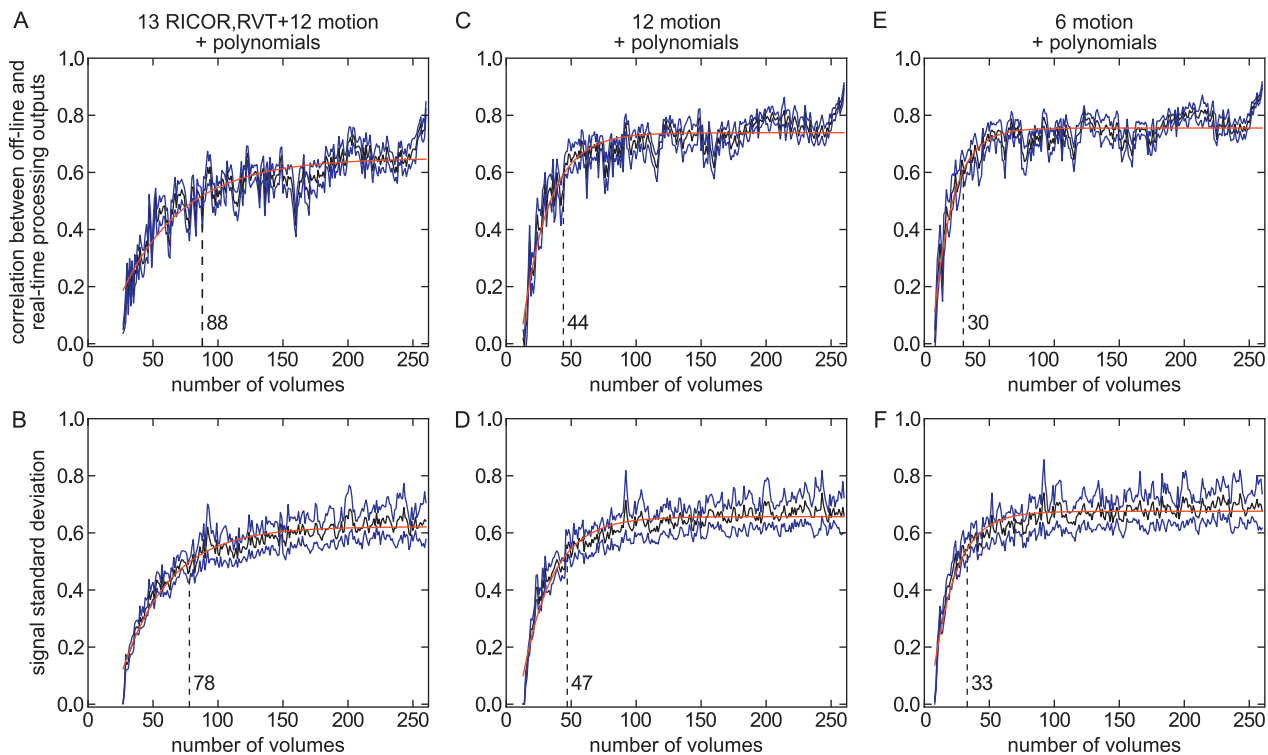


Fig. 2. (A) Comparisons between the real-time processed image and off-line processed image after the GLM analysis. The thick black line shows mean correlation between the real-time and off-line processed images at each volume, and the thin blue lines show standard error. The red line shows a fitted function line. The dotted vertical line indicates the time point where the fitted line reached 80% of the correlation at the last volume. (B) Time course of signal standard deviation within a brain in the real-time processed image. Conventions are the same as A. (C and D) Same plot as A and B excluding RETROICOR and RVT regressors. (E and F) Same plot as A and B excluding RETROICOR, RVT, and motion derivative regressors. (For interpretation of the references to color in text, the reader is referred to the web version of this article.)

when MVPA is used in real time. We also note that the scaling does not affect the temporal pattern of signal change. Since updating the scaling factor at every volume could induce artificial signal fluctuation in the scaled time course, a fixed scaling factor should be used when a voxel-wise analysis is used.

For the GLM analysis, certain number of samples must be collected for the RTP output to converge, and time to converge was longer when a larger number of noise regressors were used. We do not have a fundamental solution for the problem of GLM convergence time other than simply waiting. This could limit an rtfMRI

application, for example in a neurofeedback experiment. If one used a simple block design and brain activation is assumed to be large enough compared to noise, there is no need to include many noise regressors and neurofeedback could be started earlier. However, if one wants to use functional connectivity for a neurofeedback signal, physiological noise suppression should be included in RTP, resulting in a longer wait time before a reliable estimation of functional connectivity (with better noise suppression) is available. One must carefully balance the trade-off between thorough noise correction and early availability of neurofeedback signal.

We note that the presented system is neither necessarily an optimal implementation of rtfMRIp nor the aim of this report to propose a computationally optimal implementation. Rather, we aim to demonstrate that modern PC technology has already given us the freedom to implement computationally intensive processing. Hinds et al. (2011) have already presented a similar approach for rtfMRIp, in which the noise model was regressed out from fMRI data by incremental GLM analysis. They, however, did not implement slice-timing correction, signal scaling, or spatial smoothing and the processed region was restricted to within an ROI. Our system implemented all of these processing steps for whole-brain data, in addition to real-time implementation of RETROICOR and RVT physiological noise correction. Such comprehensive real-time fMRI analysis has not been demonstrated before. Our results indicated that this computationally heavy processing can be realized in real-time fMRI even without a supercomputer facility but with a commonly available PC.

The current report focused on real-time fMRI image processing before showing a feedback signal. An application of our system to neurofeedback experiment was demonstrated in Misaki et al. (2015). While processing step selection could vary depending on the purpose of experiment, we showed that multi-step and computationally intense the whole-brain fMRI preprocessing, including GLM analysis, can now be conducted with all available data at a given time, in real time. The current results will increase the possibility of rtfMRI application, such as feedback of connectivity measures, which requires physiological noise correction, and MVPA, which requires whole brain signal to evaluate feedback signal.

Acknowledgements

This research was supported by the Laureate Institute for Brain Research and the William K. Warren Foundation and in part by W81XWH-12-1-0697 award from the U.S. Department of Defense.

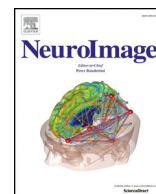
Source code of the extension of AFNI real-time system reported in the paper is available upon request.

Appendix A. Supplementary data

Supplementary data associated with this article can be found, in the online version, at <http://dx.doi.org/10.1016/j.jneumeth.2015.08.033>.

References

- Bagarinao E, Matsuo K, Nakai T, Sato S. Estimation of general linear model coefficients for real-time application. *Neuroimage* 2003;19:422–9.
- Birn RM, Smith MA, Jones TB, Bandettini PA. The respiration response function: the temporal dynamics of fMRI signal fluctuations related to changes in respiration. *Neuroimage* 2008;40:644–54.
- Bodurka J, Bandettini PA. Real-time software for monitoring MRI scanner operation. In: 14th Annual Meeting of the Organization for Human Brain Mapping; 2008. p. S85.
- Cox RW. AFNI: software for analysis and visualization of functional magnetic resonance neuroimages. *Comput Biomed Res* 1996;29:162–73.
- Cox RW, Jesmanowicz A, Hyde JS. Real-time functional magnetic resonance imaging. *Magn Reson Med* 1995;33:230–6.
- Glover GH, Li TQ, Ress D. Image-based method for retrospective correction of physiological motion effects in fMRI: RETROICOR. *Magn Reson Med* 2000;44:162–7.
- Hinds O, Ghosh S, Thompson TW, Yoo JJ, Whitfield-Gabrieli S, Triantafyllou C, Gabrieli JDE. Computing moment-to-moment BOLD activation for real-time neurofeedback. *Neuroimage* 2011;54:361–8.
- Humphrey JR, Price DK, Spagnoli KE, Paolini AL, Kelmelis EJ. CULA: hybrid GPU accelerated linear algebra routines. In: SPIE Defense and Security Symposium (DSS); 2010.
- Lee D, Jang C, Park HJ. Multivariate detrending of fMRI signal drifts for real-time multiclass pattern classification. *Neuroimage* 2015;108:203–13.
- Misaki M, Suzuki H, Luo Q, Wong CK, Phillips R, Zotev V, Bodurka J. Hyperscan real-time fMRI neurofeedback for studying interacting individuals. In: 21st Annual Meeting of the Organization for Human Brain Mapping; 2015. p. 4431.
- Sulzer J, Haller S, Scharnowski F, Weiskopf N, Birbaumer N, Blefari ML, Bruehl AB, Cohen LG, DeCharms RC, Gassert R, Goebel R, Herwig U, LaConte S, Linden D, Luft A, Seifritz E, Sitaram R. Real-time fMRI neurofeedback: progress and challenges. *Neuroimage* 2013;76:386–99.
- Zotev V, Krueger F, Phillips R, Alvarez RP, Simmons WK, Bellgowan P, Drevets WC, Bodurka J. Self-regulation of amygdala activation using real-time fMRI neurofeedback. *PLoS ONE* 2011;6:e24522.



Automatic EEG-assisted retrospective motion correction for fMRI (aE-REMCOR)



Chung-Ki Wong^a, Vadim Zotev^a, Masaya Misaki^a, Raquel Phillips^a, Qingfei Luo^a, Jerzy Bodurka^{a,b,c,*}

^a Laureate Institute for Brain Research, Tulsa, OK, USA

^b College of Engineering, University of Oklahoma, Norman, OK, USA

^c Center for Biomedical Engineering, University of Oklahoma, Norman, OK, USA

ARTICLE INFO

Article history:

Received 1 September 2015

Accepted 20 January 2016

Available online 27 January 2016

Keywords:

Motion correction

Motion artifacts

E-REMCOR

fMRI

EEG

EEG-fMRI

ICA

ABSTRACT

Head motions during functional magnetic resonance imaging (fMRI) impair fMRI data quality and introduce systematic artifacts that can affect interpretation of fMRI results. Electroencephalography (EEG) recordings performed simultaneously with fMRI provide high-temporal-resolution information about ongoing brain activity as well as head movements. Recently, an EEG-assisted retrospective motion correction (E-REMCOR) method was introduced. E-REMCOR utilizes EEG motion artifacts to correct the effects of head movements in simultaneously acquired fMRI data on a slice-by-slice basis. While E-REMCOR is an efficient motion correction approach, it involves an independent component analysis (ICA) of the EEG data and identification of motion-related ICs. Here we report an automated implementation of E-REMCOR, referred to as aE-REMCOR, which we developed to facilitate the application of E-REMCOR in large-scale EEG-fMRI studies. The aE-REMCOR algorithm, implemented in MATLAB, enables an automated preprocessing of the EEG data, an ICA decomposition, and, importantly, an automatic identification of motion-related ICs. aE-REMCOR has been used to perform retrospective motion correction for 305 fMRI datasets from 16 subjects, who participated in EEG-fMRI experiments conducted on a 3 T MRI scanner. Performance of aE-REMCOR has been evaluated based on improvement in temporal signal-to-noise ratio (TSNR) of the fMRI data, as well as correction efficiency defined in terms of spike reduction in fMRI motion parameters. The results show that aE-REMCOR is capable of substantially reducing head motion artifacts in fMRI data. In particular, when there are significant rapid head movements during the scan, a large TSNR improvement and high correction efficiency can be achieved. Depending on a subject's motion, an average TSNR improvement over the brain upon the application of aE-REMCOR can be as high as 27%, with top ten percent of the TSNR improvement values exceeding 55%. The average correction efficiency over the 305 fMRI scans is 18% and the largest achieved efficiency is 71%. The utility of aE-REMCOR on the resting state fMRI connectivity of the default mode network is also examined. The motion-induced position-dependent error in the DMN connectivity analysis is shown to be reduced when aE-REMCOR is utilized. These results demonstrate that aE-REMCOR can be conveniently and efficiently used to improve fMRI motion correction in large clinical EEG-fMRI studies.

© 2016 The Authors. Published by Elsevier Inc. This is an open access article under the CC BY-NC-ND license (<http://creativecommons.org/licenses/by-nc-nd/4.0/>).

1. Introduction

Head motion has been recognized as a major source of artifacts in fMRI data since early days of fMRI (e.g. Cox and Hyde, 1997; Friston et al., 1995, 1996; Hajnal et al., 1994; Jiang et al., 1995). In task fMRI, motion-induced artifacts often correlate with experimental tasks (Hajnal et al., 1994), leading to inaccurate estimates of BOLD activity levels and reduced significance of fMRI findings. This issue is particularly important for frontal and prefrontal brain regions that usually exhibit the largest motions. In resting-state fMRI, head movements introduce

systematic changes in estimated fMRI functional connectivity strength across the brain (Power et al., 2012; Van Dijk et al., 2012). Such spurious changes can lead to incorrect interpretations of the functional connectivity results on the group level if the data is ineffectively preprocessed (Power et al., 2012; Saad et al., 2013; Gotts et al., 2013; Jo et al., 2013). The traditional fMRI motion correction approach bases on spatial co-registration of 3D fMRI volumes (e.g. Friston et al., 1995; Cox and Jesmanowicz, 1999). Despiking at the beginning of the preprocessing pipeline further attenuates the fMRI motion effect (Jo et al., 2013; Satterthwaite et al., 2013). The traditional approach implicitly assumes that all motion occurs between the volume acquisitions (Cox and Hyde, 1997). Thus, it cannot adequately take into account effects of faster intra-volume movements (Beall and Lowe, 2014). It has been suggested that a slice-based fMRI motion correction can be superior to the

* Corresponding author at: Laureate Institute for Brain Research, Tulsa, OK, USA.
E-mail address: jbodurka@laureateinstitute.org (J. Bodurka).

Selection algorithm for motion ICs

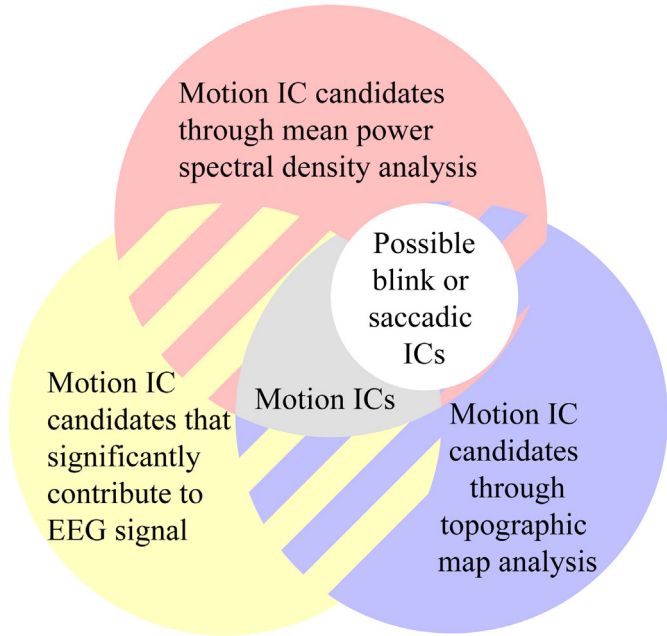


Fig. 1. The sketch of the automatic identification of ICs through the analyses of the mean power spectral density, topographic map, and contribution to the EEG signal. Possible blink and saccade ICs are removed from the motion ICs selection.

traditional volume registration approach (Beall and Lowe, 2014; Zotev et al., 2012).

Multimodal brain imaging, combining fMRI with simultaneous EEG recordings (e.g. Mulert and Lemieux, 2010), offers new exciting opportunities for fMRI motion correction. Simultaneous EEG–fMRI combines the advantages of the high temporal resolution of EEG and the high spatial resolution of fMRI. While the artifact on the fMRI data can be minimized with the use of MR-compatible EEG system, introduction of fMRI environment related artifacts to the EEG data is inevitable. In particular, cardioballistic and motion artifacts are exacerbated inside an MR scanner. These artifacts can be reduced with designated hardware setup (Bonmassar et al., 2002; Masterton et al., 2007), or corrected effectively by independent component analysis (Srivastava et al., 2005; Mantini et al., 2007).

Recently, we introduced a method for EEG-assisted retrospective motion correction of fMRI data (E-REMCOR) that employs the EEG array as a sensitive motion detector in addition to recording neuronal activity (Zotev et al., 2012). In this method, voltage artifacts induced in the EEG array leads due to head motion in a strong uniform magnetic field of an MRI scanner are used to define regressors describing rotational head movements with millisecond temporal resolution. E-REMCOR makes it possible to regress out the effects of rapid head movements from unprocessed fMRI data on a slice-by-slice basis prior to volume registration. Thus, E-REMCOR complements both the traditional fMRI volume registration approach, which performs better for slower head motions, and the RETROICOR method for slice-specific correction of fMRI cardiorespiratory artifacts (Glover et al., 2000). E-REMCOR does not require any specialized equipment (beyond the

EEG–fMRI instrumentation) and can be applied retrospectively to any existing EEG–fMRI dataset.

Application of E-REMCOR involves an independent component analysis (ICA) of EEG data and identification of independent components (ICs) corresponding to different head motions. This process requires a close examination of the EEG recordings and a careful evaluation of the IC properties. Therefore, an automation of E-REMCOR to enable a robust and efficient motion correction without human supervision is desirable. In this paper, we describe such an automation extension of E-REMCOR, which we refer to as aE-REMCOR. We explicitly detail the quantitative criteria that effectively distinguish the different motion ICs. We also evaluate its performance for a large number of EEG–fMRI datasets. An improved automatic fMRI motion correction afforded by aE-REMCOR would provide an additional incentive for recording EEG during fMRI, and thus encourage a broader use of simultaneous EEG–fMRI. It would also greatly benefit large clinical studies by improving fMRI data quality and reducing numbers of subjects excluded due to excessive motion.

2. Methods

2.1. E-REMCOR

The aE-REMCOR method is an automation extension of E-REMCOR. E-REMCOR is based on the observation that voltage artifacts (electromotive force, EMF) induced in EEG leads due to rigid-body movements of the head in the uniform magnetic field of an MRI scanner can be analytically related to time derivatives of real-time rotational head motion parameters (Zotev et al., 2012). Definition of the high-temporal-resolution E-REMCOR regressors is independent of the fMRI pulse sequence properties. The MR artifacts are removed from the EEG data by means of the average artifact subtraction (Allen et al., 2000) before the EEG data are used for E-REMCOR.

Application of E-REMCOR for fMRI motion correction includes three steps. First, an independent component analysis (ICA, e.g. Bell and Sejnowski, 1995; Makeig et al., 1997) is performed for the EEG data:

$$V_i(t) = \sum_{j=1}^N b_{ij} F_j(t) + \varepsilon_i(t), \quad i = 1 \dots N. \quad (1)$$

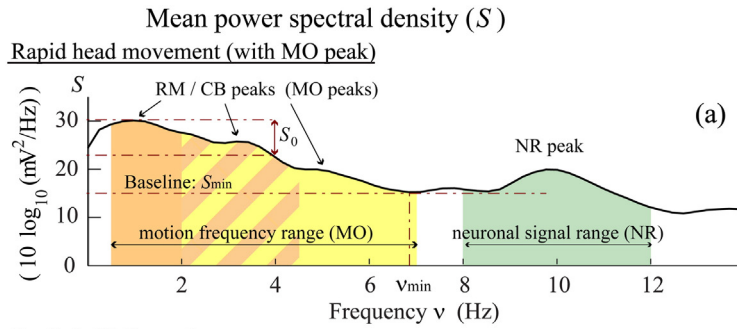
Here, $\{V_i(t)\}$ are signals from N EEG channels, $\{F_j(t)\}$ are the corresponding independent components (ICs), $\{b_{ij}\}$ are elements of the ICA back-projection matrix, and $\varepsilon_i(t)$ is an error term also including the i th-channel's Gaussian noise. The ICs $F_k(t)$, $k = 1 \dots K$, approximating random-motion and/or cardioballistic (CB) artifacts $V_{EMF}^{(i)}(t)$ are

$$V_{EMF}^{(i)}(t) \approx \sum_{k=1}^K b_{ik} F_k(t), \quad i = 1 \dots N, K \leq N. \quad (2)$$

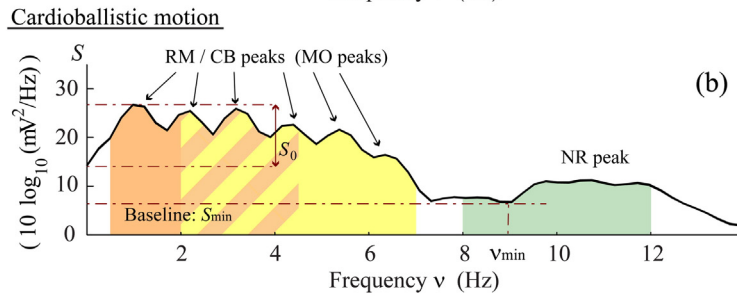
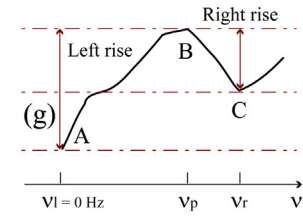
The identification criteria for the random head motion are outlined in Zotev et al., 2012. The quantitative classification of the criteria for the random head motion, together with the cardioballistic motions caused by cardiac pulsations, will be detailed in the following sections.

Second, each motion-related IC $F_k(t)$ is band-pass filtered from 0.1 to 20 Hz and integrated over time (with constant $\Delta t = 0.4$ s) to yield two E-REMCOR regressors, $R_1^{(k)}(t)$ and $R_2^{(k)}(t)$, having the same temporal

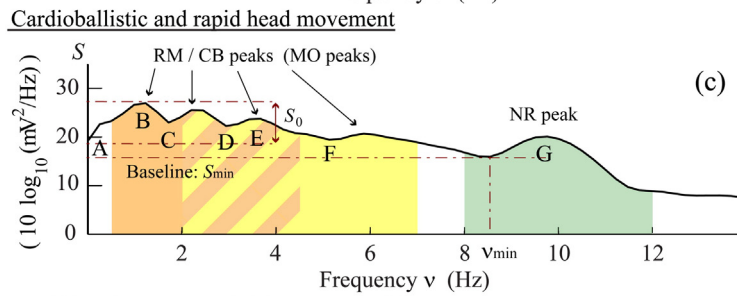
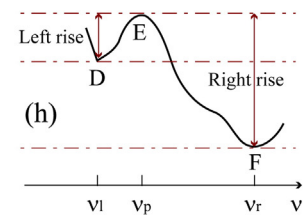
Fig. 2. (a)–(f) The mean power spectral density of (a) a rapid head movement IC; (b) a cardioballistic motion IC; (c) a mixture of cardioballistic motion and rapid head movement IC; (d) another rapid head movement IC with reflection points in the RM range; (e) a blink IC; (f) a saccade IC. (g)–(h): The rises of peaks B and E in (c) from their neighboring left and right minima when the neighboring right minimum is below 8 Hz. (i)–(j): The rises of the NR peaks G and K in (c) and (e). (k): The rise of the reflection points in (d). In (a)–(f), S_0 is the difference between the maximum and minimum spectrum power below 4 Hz. Motion frequency range (MO) refers to the combined frequency range of RM and CB. RM, CB and MO peaks stand for the peaks found in the RM, CB and MO frequency ranges respectively. In (g)–(h), the peak rise is defined as the average of the left and right rises. In (i), the peak rise is the power difference between the peak G and the minimum between F and G. In (j), the peak rise is the power difference between the peak K and the minimum value between J and K. In (k), the rise of the reflection point H is the power difference between H and I, and the rise of the reflection point I is the power difference between I and J ($v = 4.5$ Hz).



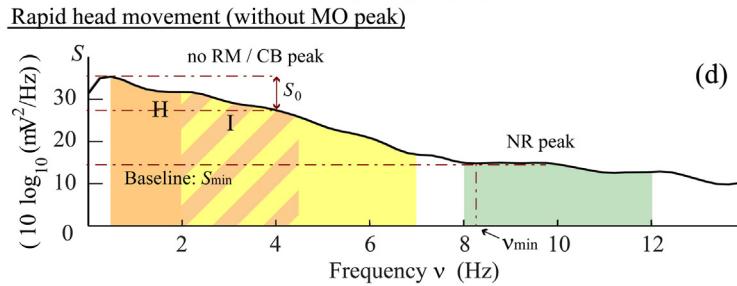
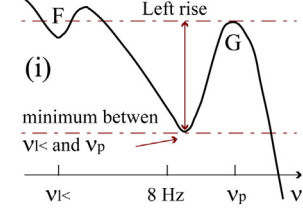
Rise of peak B in Fig. (c)



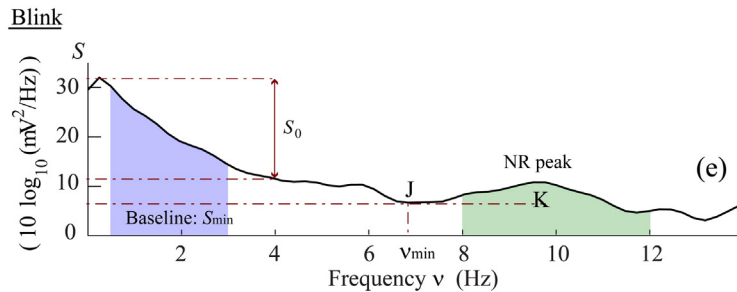
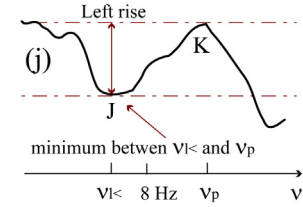
Rise of peak E in Fig. (c)



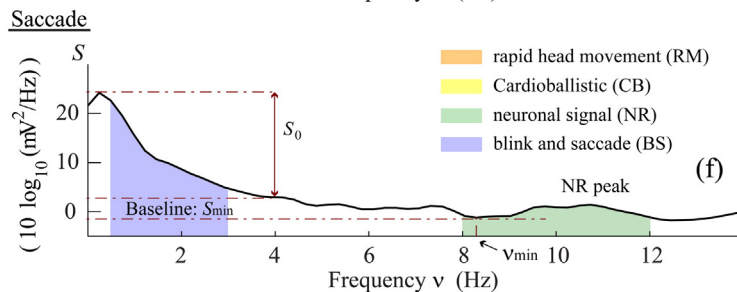
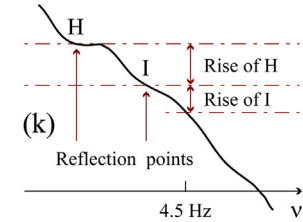
Rise of peak G in Fig. (c)



Rise of peak K in Fig. (e)



Reflection points in Fig. (d)



resolution as the EEG data:

$$R_1^{(k)}(t) = \int_{t-\Delta t}^t F_k(\tau) d\tau, \text{ and } R_2^{(k)}(t) = \int_0^{t-\Delta t} F_k(\tau) d\tau. \quad (3)$$

Third, the E-REMCOR regressors are sub-sampled to match the acquisition times $\{t_s\}$ for each slice in the fMRI dataset and linearly detrended. Correction of motion artifacts in the unprocessed fMRI data is performed by means of a linear regression procedure (with fit coefficients $\{\beta\}$ and a linear regressor R_L) applied to each fMRI voxel's time course:

$$S_{\text{fMRI}}(t_s) = \beta_0 + \beta_1 R_L(t_s) + \sum_{k=1}^K [\beta_{k1} R_1^{(k)}(t_s) + \beta_{k2} R_2^{(k)}(t_s)] + \varepsilon(t_s). \quad (4)$$

Thus, the E-REMCOR motion correction is performed on a slice-by-slice basis, and can be applied simultaneously with RETROICOR. It is usually followed by the standard fMRI data processing with slice-time adjustment and volume registration to correct effects of slower head motions.

The purpose of aE-REMCOR is to automate and streamline the practical use of E-REMCOR for large datasets and/or groups of subjects. We developed an advanced algorithm for automatic identification of motion-related ICs, Eq. (2). The algorithm automatically characterizes and recognizes the special features of the motion artifacts imposed on the mean power spectral density, topographic map, and EEG signal contribution of the ICs as described in detail below. In the previous work, the motion ICs were prepared with Brain Products, GmbH's Analyzer 2 proprietary software. The current automation procedure is implemented in MATLAB, together with the MR artifact removal, the ICA decomposition, and the IC integration, Eq. (3). The final motion correction step, Eq. (4), is performed for fMRI data in AFNI (Cox, 1996; Cox and Hyde, 1997) using the 3dTfitter AFNI program.

2.2. Data acquisition

The study was conducted at the Laureate Institute for Brain Research. The research protocol was approved by the Western Institutional Review Board (IRB). Eleven PTSD patients and five healthy controls (mean age 31 ± 8 years, all male) participated in the study. The study included three EEG-fMRI scanning sessions. Each session lasted for about two hours and was separated approximately one week apart. In each session, there were five real time fMRI neurofeedback (rtfMRI-nf) training scans (Zotev et al., 2011) and two resting scans immediately before and after the rtfMRI-nf training scans. In this study, the scans with missing fMRI slice markers, or mismatched EEG and fMRI scan numbers were not considered, giving a total of 305 scans in the analysis, which includes 219 rtfMRI-nf training scans and 86 resting scans.

The experimental procedure and data acquisition parameters were the same as described in Zotev et al., 2012. The EEG-fMRI experiments were conducted on a GE Discovery MR750 3 T MRI scanner with a standard 8-channel receive-only head coil. A single-shot gradient-echo EPI sequence with Sensitivity Encoding (SENSE) was employed for fMRI. The following EPI imaging parameters were used: repetition time $TR = 2000$ ms, echo time $TE = 30$ ms, FOV = 240 mm, 34 axial slices per volume, slice thickness = 2.9 mm, slice gap = 0.5 mm, 96×96 acquisition matrix, SENSE acceleration factor $R = 2$, flip angle = 90° , sampling bandwidth = 250 kHz. Each fMRI run lasted 8 min 46 s. Three EPI volumes (6 s) were excluded from the data analysis to allow the fMRI signal to reach steady state. The EPI images were reconstructed into a 128×128 matrix, so the resulting fMRI voxel size was $1.875 \times 1.875 \times 2.9$ mm³. Physiological pulse oximetry and respiration waveforms were also simultaneously acquired with fMRI. The EEG recordings were performed simultaneously with fMRI using a 32-channel MR-compatible EEG system from Brain Products GmbH. The EEG signals

were acquired with 16-bit 5 kS/s sampling providing 0.2 ms temporal and 0.1 μ V measurement resolution. The signals were measured relative to the standard reference (FCz) and were hardware-filtered between 0.016 Hz (10 s time constant) and 250 Hz during the acquisition.

2.3. EEG preprocessing and ICA

The EEG data, together with the information about event markers and MRI slice markers, are loaded in MATLAB using the EEGLAB (Delorme and Makeig, 2004) command `pop_loadbv()`. The MRI slice markers are used to label the time period of the concurrent EEG and fMRI measurements. Because the MR artifacts are strictly periodic with the fMRI repetition time TR , they are efficiently removed from the EEG data using the average artifact subtraction. The EEG data are then low-pass filtered at 40 Hz and downsampled to 250 S/s (4 ms sampling interval). Band-rejection filters (1 Hz bandwidth) are applied to remove harmonics of the fMRI slice selection frequency, 17 Hz, as well as the AC power line artifact at 60 Hz, and a vibration artifact at 26 Hz.

The ICA is performed on the preprocessed EEG data using the Infomax algorithm (Bell and Sejnowski, 1995) implemented in EEGLAB (binica, Delorme and Makeig, 2004) to separate 31 ICs for $N = 31$ EEG channels. The ICs related to head motions, Eq. (2), are identified automatically. The selected ICs are bandpass filtered from 0.1 to 20 Hz to exclude both the slowly and fast varying contributions that may be unrelated to head motion (such as EEG instrumentation drifts). The ICs are then used to define E-REMCOR regressors, Eq. (3).

2.4. Automatic identification of motion ICs

In aE-REMCOR, the ICs corresponding to head motions are identified automatically. An IC is recognized as motion-related if its mean power spectral density, topographic map, and contribution to the EEG signal manifest certain features that are generally observed for motion ICs. Note that our original work on E-REMCOR focused on correction of artifacts corresponding to random head movements so CB artifacts were removed from the EEG data using the average artifact subtraction (Allen et al., 1998). In the present paper, the CB artifacts are included in the analysis together with the random-motion artifacts. The reason is that a certain type of head motion can contribute to both random and cardioballistic head movements, so the two kinds of artifacts are not entirely independent and may be hard to separate (Zotev et al., 2012). The inclusion of CB artifacts makes the E-REMCOR procedure more flexible, but it does not, in general, eliminate the need for RETROICOR.

The aE-REMCOR automation algorithm is illustrated in Fig. 1. ICs related to rapid head motion and cardioballistic motions are recognized when the criteria in the analyses of mean power spectral density, topographic map, and EEG signal contribution are simultaneously satisfied. Eye blink ICs and saccadic ICs are also identified in addition to the head motion ICs to ensure proper separation of head movement and eye movement artifacts. The IC classification parameters used in this paper are determined empirically across 305 EEG-fMRI scans from 16 subjects. The three sections below describe the quantification of the characteristics and the identification of the motion ICs through the analyses of mean power spectral density (Section 2.5), topographic map (Section 2.6), and EEG signal contribution (Section 2.7).

2.5. Motion IC identification through power spectral density analysis

To better understand the physical origins of the ICs, the mean power spectral density of each IC is analyzed. In aE-REMCOR, the mean power spectral density (S) is computed using the MATLAB function `pwelch()` over time windows of 2.048 s length with 1.024 s overlap (512 and 256 data points with 4 ms sampling). The spectral resolution ($\Delta\nu$) is 0.244 Hz. Fig. 2 shows some typical spectra for the ICs related to motions, blink and saccade. Geometrically, the spectrum has a negative convexity feature at frequency ν when its second derivative at ν is less than zero

($S''(v) < 0$). For the mean power spectral density of the ICs corresponding to rapid head movement, it is observed for the frequency range of 0.5–4.5 Hz that there is either a spectral peak or a negative convexity feature without a spectral peak. For the ICs corresponding to the cardioballistic (CB) motions, obvious spectral peaks are observed in 2–7 Hz part of the spectrum. To categorize the physical origin of an IC, the spectrum is divided into different frequency ranges (Figs. 2(a)–(f)): rapid head movement (RM: 0.5–4.5 Hz), cardioballistic motion (CB: 2–

7 Hz), blink and saccade (BS: 0.5–3 Hz), and neuronal alpha activity (NR: 8–12 Hz). The BS and NR frequency ranges are examined so that possible blink and saccade ICs, as well as ICs corresponding to EEG alpha activity, can be identified and excluded from the motion IC candidates. The spectrum beyond 12 Hz is not considered in the analysis. Technical details of the automatic analysis of IC spectra are described in the Supplementary materials (Section S1, Tables S1–S3).

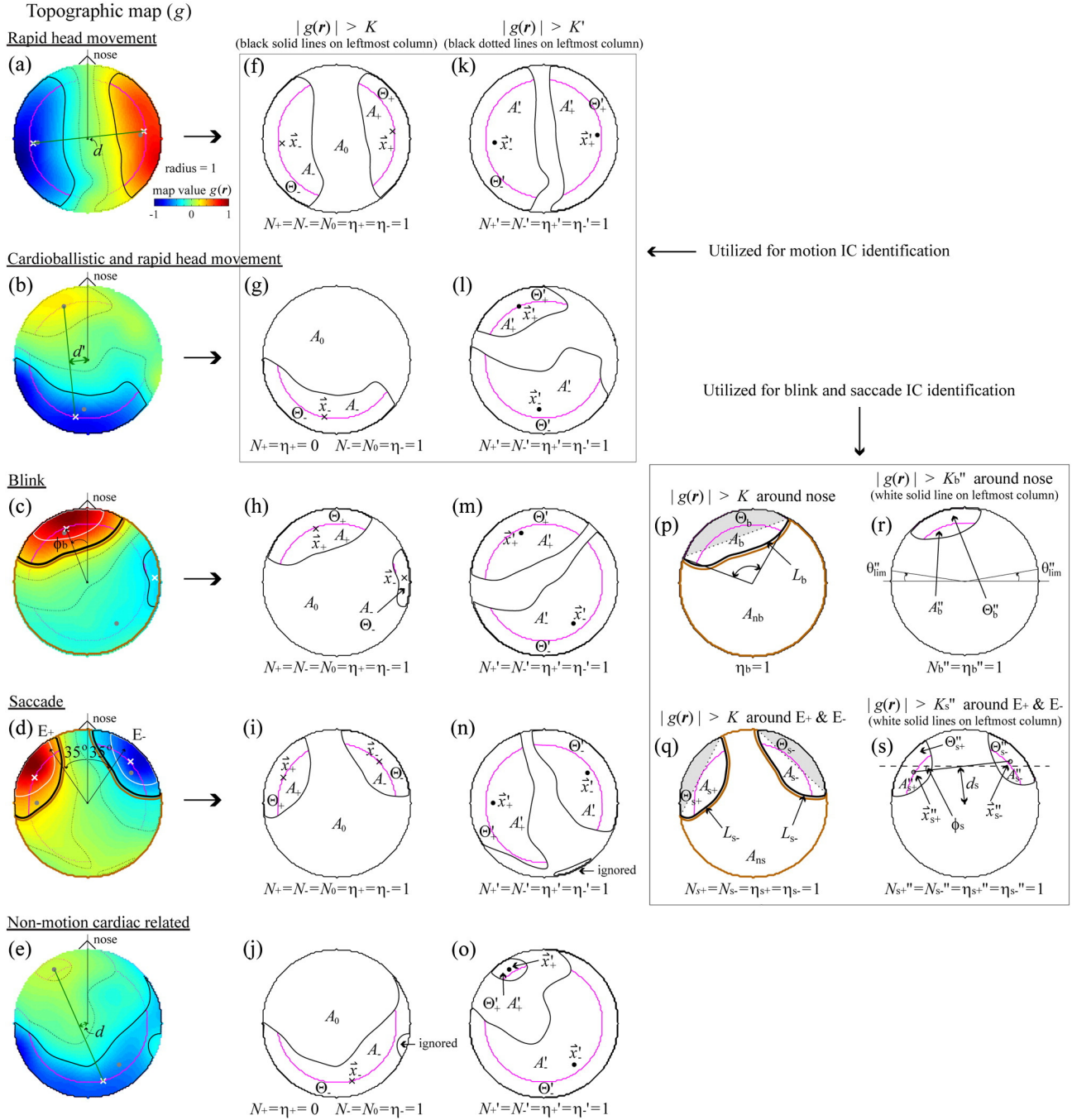


Fig. 3. The topographical maps for (a) the IC corresponding to rapid head movement in Fig. 2(a); (b) the IC mixture of rapid head movement and cardioballistic motion in Fig. 2(c); (c) the blink IC in Fig. 2(e); (d) the saccade IC in Fig. 2(f); (e) the example of a non-motion cardiac-related IC. The map boundary with width 0.2 is marked with magenta lines. In (a)–(e), the primary polarity regions ($|g(r)| > K$) are enclosed in black solid lines and the geometrical centers are marked with white crosses. The secondary polarity regions ($|g(r)| > K'$) are enclosed in black dotted lines and the centers are marked with gray dots. Here $(K, K') = (0.3, 0.1)$ are the threshold values. (f)–(j) plot the primary polarity regions of (a)–(e) explicitly with the geometrical centers marked as \mathbf{x}_{\pm} . (k)–(o) plot the secondary polarity regions of (a)–(e) explicitly with the geometrical centers marked as \mathbf{x}'_{\pm} . (p)–(q) show the primary polarity regions around the positions of the nose in (c) and E_{\pm} in (d) respectively. The points E_{\pm} are defined at a distance 0.9 from the origin and at an angle 35° from the vertical line joining the origin and the nose. (r)–(s) show the central regions enclosed in white solid lines around the positions of the nose in (c) and E_{\pm} in (d). (f)–(g) and (k)–(l) are utilized in the identification of motion ICs. (p)–(s) are utilized in the blink and saccade ICs identification. In (r), the two angles $\theta_{lim}'' = 10^\circ$ from the horizontal line are the extension limit of the central region in the topography of a blink IC. Other symbols are defined in Section S2.1.

2.6. Motion IC identification through topographic map analysis

The spatial projection of an IC contribution onto the EEG channel space forms the IC topographic map (Fig. 3(a)–(e)). The topographic map of an IC is computed by spatially interpolating the corresponding column of the ICA back-projection matrix $\{b_{ij}\}$ in Eq. (1) using the MATLAB function `griddata()`. When the head undergoes a simple rigid-body rotation in the uniform magnetic field of the MRI scanner, spurious conductive contours on the opposite sides of the EEG array typically experience magnetic flux changes of opposite signs, giving bilateral opposite polarities for EEG channels on the opposite sides of the EEG array (Zotev et al., 2012). In principle, the IC contributions for such opposite-side EEG channels should be of the same order of magnitude, so that the topographic map remains bipolar if a sufficiently high magnitude threshold is applied. In practice, bilateral opposite polarities with asymmetric magnitudes are often observed in an IC mixture of random and CB motions. Examples of topographic maps for motion ICs with symmetric and asymmetric magnitudes are shown in Figs. 3(a) and (b). It should be noted that not all cardiac-related ICs (McMenamin et al., 2010) can be used for E-REMCOR, but only those that are clearly cardiobalistic in nature. For example, cardiac beats can be accompanied by deformations of the soft padding underneath the subject's head causing deformations of the EEG leads for the occipital EEG channels. The resulting artifacts have periodicity of the cardiac activity and unilateral topography, but their relation to the rigid-body head motion parameters is indirect and nonlinear. An example of the non-motion cardiac-related IC is shown in Fig. 3(e).

In aE-REMCOR, topographic maps of various ICs are analyzed automatically with certain requirements for IC polarity regions, including positions of the polarity regions, minimum region areas and arc region areas (Fig. 3(f)–(s)). Possible blink or saccade ICs are also identified by

their topographic properties in addition to the motion IC candidates. Technical details of the automatic analysis of IC topographies are described in the Supplementary materials (Section S2, Tables S4–S5).

2.7. Motion IC identification through analysis of EEG signal contribution

Rapid and random head movements produce prominent spikes with durations of no less than tens of milliseconds in the EEG signal time courses, particularly for the electrodes near the edges of the EEG array. Similar spikes are evident in the time courses of the corresponding motion-related ICs. Removing the contributions of such motion-related ICs from the EEG data reduces the spikes significantly. Cardiobalistic (CB) motions also produce signal spikes, which, however, are distributed more evenly across the EEG signal time course. Removal of the cardiobalistic IC contributions leads to a steady signal reduction at the CB peak positions. EEG signals without the contribution of a particular IC, which we denote $V_i'(t)$, can be obtained using Eq. (1) with the corresponding column of the back-projection matrix $\{b_{ij}\}$ set to zero. The signal reduction after the removal of a selected IC is thus equal to the time course of that IC times the spatial projection constant for a given EEG channel.

In aE-REMCOR, the signal reduction at the i -th electrode ($|V_i(t) - V_i'(t)|$) after the removal of a particular IC is evaluated for the time periods corresponding to rapid head movements and/or cardiac beats. This approach is illustrated in Fig. 4. To identify a motion IC candidate, signal reduction criteria should be satisfied for a minimum number of EEG electrodes located close to the edges of the EEG array. Technical details of the automatic analysis of IC contributions are described in the Supplementary materials (Section S3, Tables S6–S8).

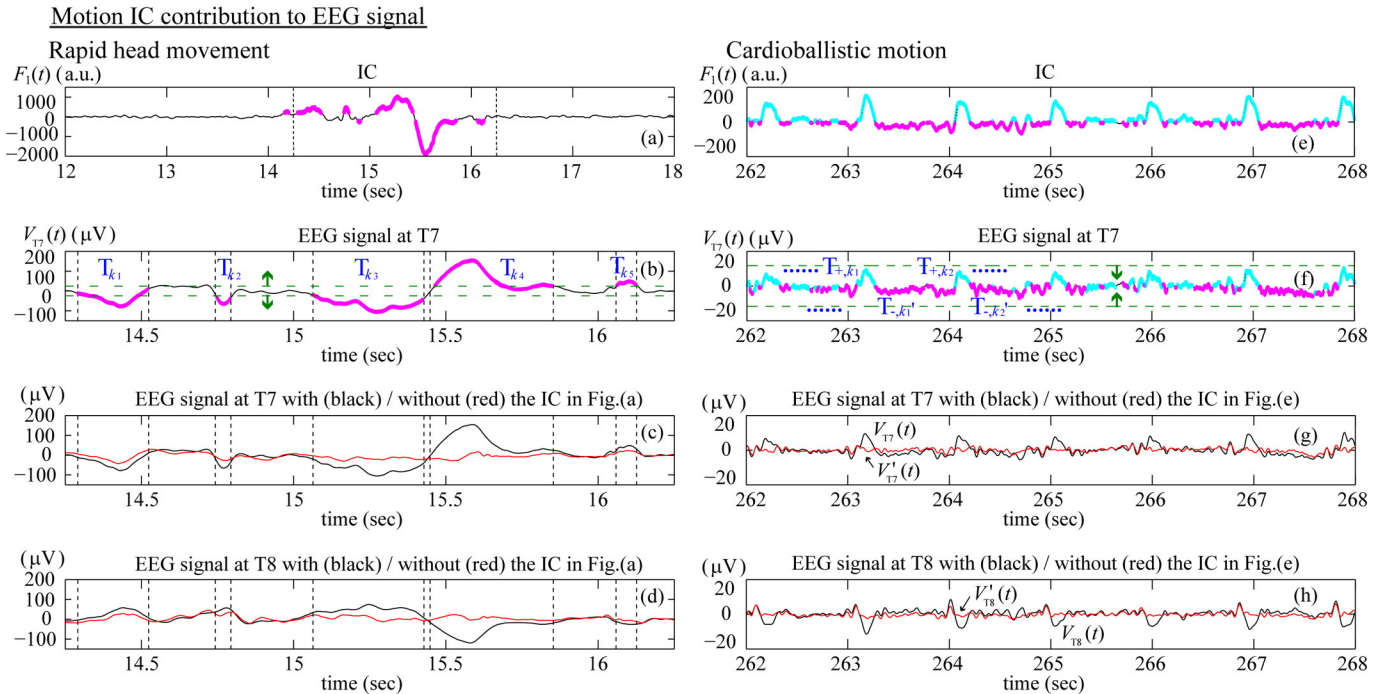


Fig. 4. (a) The time course of the rapid head movement IC, $F_1(t)$, shown previously in Figs. 2(a) and 3(a). (b) The time course of the signal measured at electrode T7 ($V_{T7}(t)$). (c)–(d) The time courses of the signal measured at electrode T7 and T8 before (black) and after (red) the removal of the IC in (a). (e) The time course of the cardiobalistic motion IC shown in Figs. 2(b) and 7(c). (f) The time course of the signal measured at electrode T7 ($V_{T7}(t)$). (g)–(h) The time courses of the signal measured at electrode T7 and T8 before (black) and after (red) the removal of the IC in (e). The dotted lines in (a) indicate the time period in (b). In (a), the magenta line segments indicate the time periods when $F_1(t)$ is larger (smaller) than the threshold value $F_{1,0} + 4\sigma_{F1}$ ($F_{1,0} - 4\sigma_{F1}$). In (b), the green dashed lines plot the threshold values $V_{T7,0} \pm 4\sigma_{T7}$. Each magenta line segment (T_k) in (b) represents the examination time period for the rapid head movement IC when the extremum of $V_{T7}(t)$ during the indicated period in (a) is greater than $V_{T7,0} + 4\sigma_{T7}$ or smaller than $V_{T7,0} - 4\sigma_{T7}$. In (e), cyan and magenta line segments indicate the time periods when $F_1(t)$ is larger (smaller) than $F_{1,0} + 0.1\sigma_{F1}$ ($F_{1,0} - 0.1\sigma_{F1}$). In (f), the green dashed lines plot the threshold values $V_{T7,0} \pm 4\sigma_{T7, \min}(\tau = 10 \text{ s})$. Here $F_{1,0}$, σ_{F1} , $V_{T7,0}$, σ_{V7} and $\sigma_{V7, \min}$ are defined in Eqs. (S4), (S5) and (S7). Each cyan (or magenta) line segment T_{+k} (T_{-k}) in (f) indicates the examination time period for the cardiobalistic motion IC when the signal at T7 during the indicated period in (e) is bounded by the threshold values $V_{T7,0} \pm 4\sigma_{T7, \min}(\tau = 10 \text{ s})$.

2.8. Analysis of aE-REMCOR performance

A set of EEG based motion regressors are constructed by time integrating the selected motion ICs (Eq.(3)). These regressors are utilized to correct for head movements in the fMRI dataset on a slice-by-slice basis using AFNI 3dTfitter (Eq.(4)). The correction performance of aE-REMCOR on the fMRI dataset is examined using temporal signal-to-noise ratio (TSNR), motion parameters of the brain voxels, and improvement in the resting state fMRI (rs-fMRI) connectivity analysis. The maximum displacements of the voxels for each brain volume, the root mean square difference between an fMRI volume and the 1st volume, and the motion parameters (displacements dS, dL, dP in the superior–inferior, left–right and posterior–anterior directions, and rotation angles yaw, pitch and roll about the above directions) are estimated

by AFNI 3dvolreg. For each scan, the above motion parameters with and without aE-REMCOR application are evaluated.

The temporal signal-to-noise ratio of an fMRI image is given by (Bodurka et al., 2007)

$$\text{TSNR}(\mathbf{r}) = \text{mean}(S_{\text{fMRI}}(\mathbf{r}, n), n = 1, \dots, N_{\text{fMRI}}) / \text{std}(S_{\text{fMRI}}(\mathbf{r}, n), n = 1, \dots, N_{\text{fMRI}}), \quad (5)$$

where $S_{\text{fMRI}}(\mathbf{r}, n)$ is the signal magnitude at the position \mathbf{r} in the n^{th} brain volume of the fMRI dataset, and N_{fMRI} is the total number of the brain volume. The improvement of the TSNR(\mathbf{r}) between the fMRI datasets with and without aE-REMCOR application ($\Delta\text{TSNR}(\mathbf{r})$), and the average

The automatic results of aE-REMCOR with identified motion ICs in a scan with moderate head movements

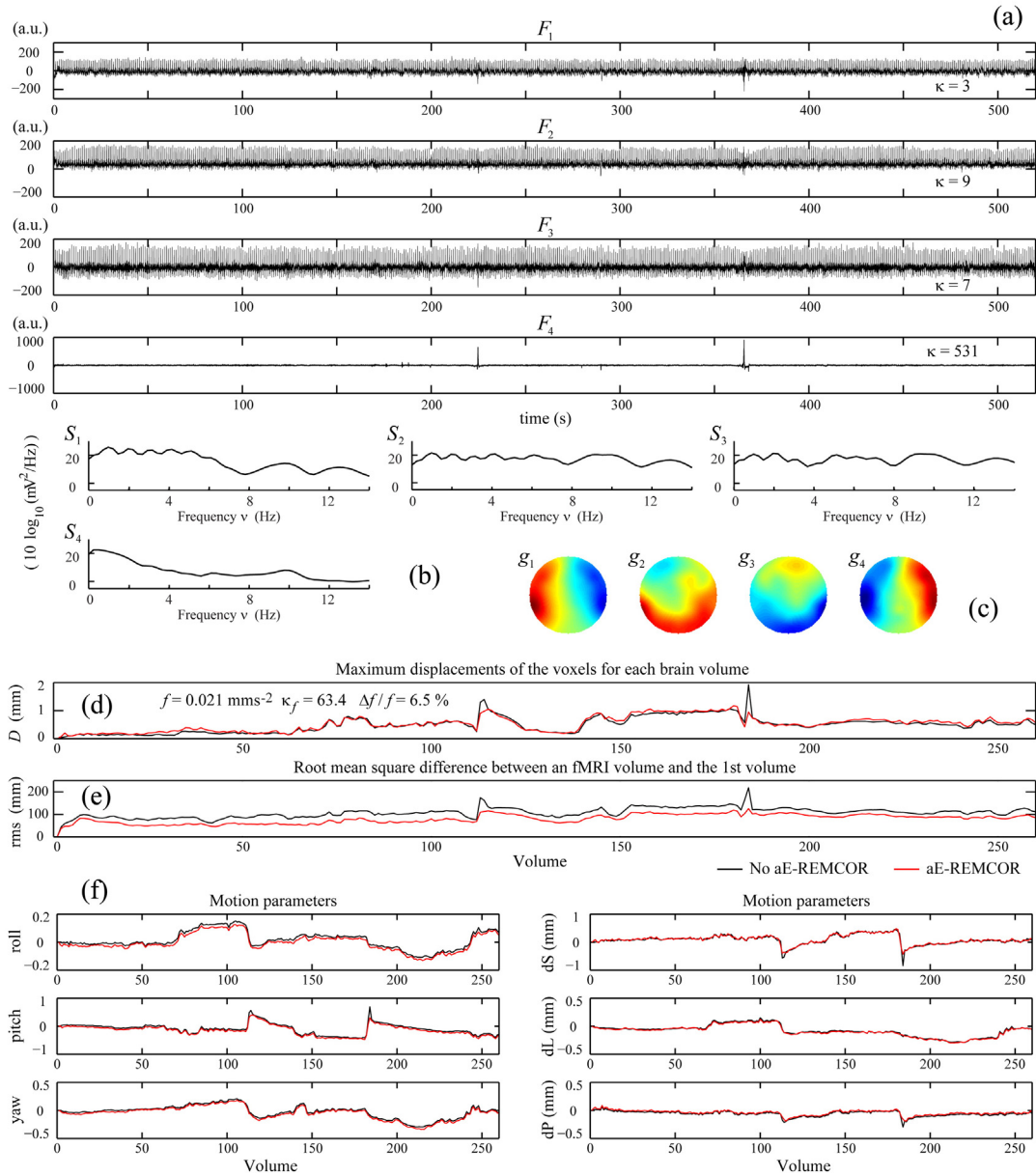


Fig. 5. The automatic results of aE-REMCOR with identified motion ICs in a scan with moderate rapid head movements. (a) The time courses, (b) spectra, (c) topographic maps of the identified motion IC. (d) The maximum displacement of the voxels (D) for each brain volume. (e) The root mean square difference (rms) between an fMRI volume and the 1st volume. (f) The rotation angles roll, pitch, yaw and the displacements along the superior (dS), left (dL) and posterior (dP) directions calculated by AFNI 3dvolreg. (g) The ΔTSNR plots on the slices of the brain along the axial direction without volume registration (upper plot) and with volume registration (lower plot). In (d)–(f), the results with and without aE-REMCOR are respectively plotted in red and black lines.

The automatic results of aE-REMCOR with identified motion ICs in a scan with moderate head movements

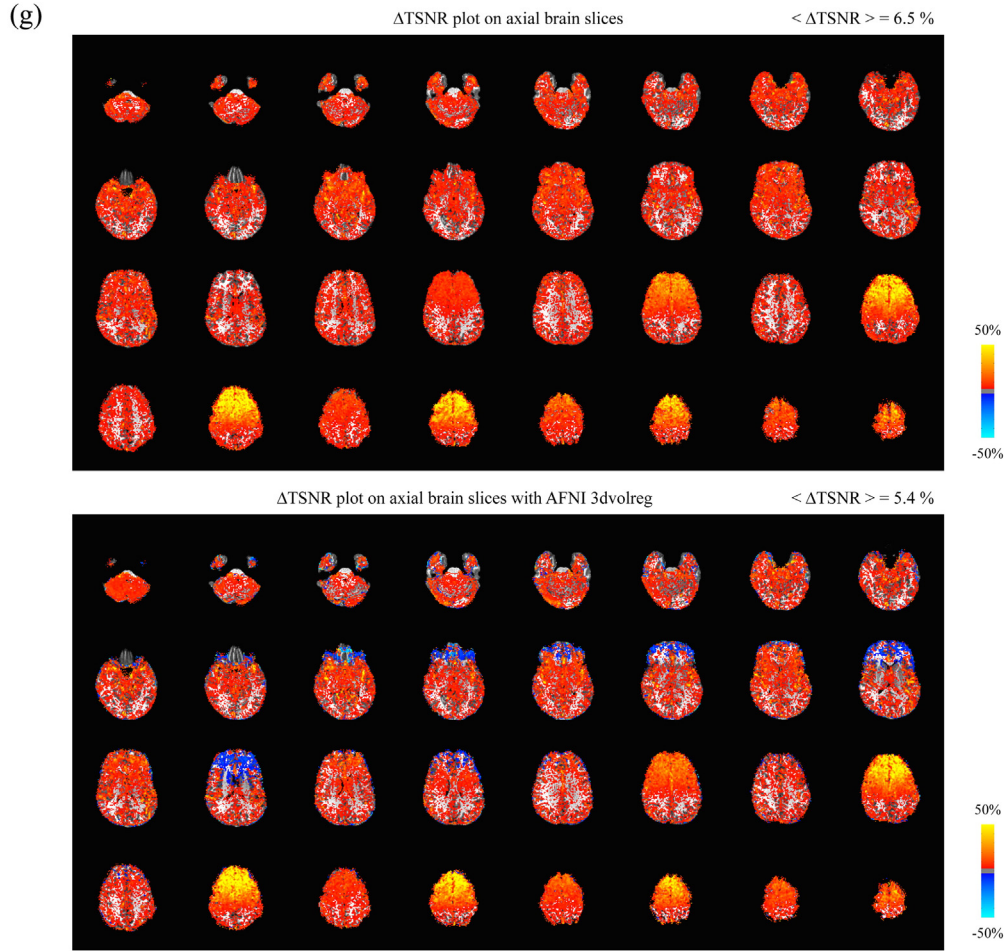


Fig. 5 (continued).

of $\Delta\text{TSNR}(\mathbf{r})$ over the brain.

$$\langle \Delta\text{TSNR} \rangle = \text{mean}(\Delta\text{TSNR}(\mathbf{r}), \mathbf{r} \in \text{whole volume of the brain}) \quad (6)$$

are examined for each scan. To understand the combined effects of aE-REMCOR and the standard fMRI preprocessing procedure, ΔTSNR and $\langle \Delta\text{TSNR} \rangle$ are also evaluated with the volume registration using AFNI 3dvolreg applied to both the original and aE-REMCOR corrected datasets.

In the rs-fMRI connectivity analysis, we compared the seed-based (posterior cingulate cortex) default-mode network (DMN) connectivity results performed with and without aE-REMCOR. When aE-REMCOR was applied, it was employed before the fMRI preprocessing steps: slice-timing correction, volume registration, and Talairach coordinate registration (Talairach and Tournoux, 1998). Then the fMRI data was spatially blurred to 4-mm FWHM and temporally bandpass filtered at 0.01–0.08 Hz to reduce the effect of low-frequency drift and high-frequency noise (Biswal et al., 1995; Lowe et al., 1998). The rs-fMRI connectivity of the DMN was examined in 86 resting scans using GLM-based correlation analysis (Friston, 2005; Van Dijk et al., 2010). A spherical seed ROI with radius 5 mm was centered at the posterior cingulate cortex (PCC) (Talairach coordinate: (0, −51, 22) (Van Dijk et al., 2010)). Nuisance covariates included cerebrospinal fluid signal, white matter signal, and the 6 rigid body motion parameters (dS, dL, dP, yaw, pitch and roll). We evaluated the correlation and the correlation difference of the data with and without aE-REMCOR. We also quantified the correlation changes in medial prefrontal cortex (mPFC: (0, 49, 2)),

lateral parietal cortex (LatPar-L: (−45, −60, 32), LatPar-R: (43, −60, 29)), and hippocampal formation (HF-L: (−22, −19, −15), HF-R: (22, −19, −15)) of the DMN (Van Dijk et al., 2010).

3. Results

3.1. Automatic identified motion ICs

Figs. 5–7 show the automatic results of aE-REMCOR with identified motion ICs from scans with examples of moderate, significant and little rapid head movements respectively. In each figure, the time courses, spectra, and topographic maps of the selected motion IC, as well as the motion information acquired with AFNI 3dvolreg and the TSNR improvement, are plotted. For the scan shown in Fig. 5, four motion ICs are identified. The first three ICs are identified as cardioballistic motion ICs and the fourth is identified as the rapid head movement IC (Supplementary Table S9). In this scan, the two kinds of motions are well separated in the selected motion ICs with little mixing of the other components. However, such a well separation of components is not always the case with the ICA, especially when there are significant motions during the scan.

Fig. 6 shows the results from a scan with significant subject motions. For this scan, five motion ICs are identified. The 1st, 2nd, 4th and 5th IC ($F_1(t)$, $F_2(t)$, $F_4(t)$, $F_5(t)$) are identified as the rapid head movement ICs, and the 3rd IC ($F_3(t)$) is identified as the cardioballistic motion IC. The spectra, and topographic maps of the 1st and 3rd ICs are shown previously in Figs. 2(a), 3(a) and 2(c), 3(b). The time course of the 1st IC is

shown in Fig. 4(a). In the time course of $F_3(t)$, in addition to the obvious spikes caused by the rapid head movements, distinct cardiac pulses are also observed (Fig. 6(h)). Indeed $F_3(t)$ is a significant mixture of cardiobalistic motion and rapid head movement components due to the incomplete separation of the ICA. Thus a more accurate

interpretation about the identification algorithm on the random head and cardiobalistic motions in Supplementary Table S9 is that the algorithm actually estimates the dominant component of the IC, instead of distinguishing each IC with only one physical origin.

The automatic results of aE-REMCOR with identified motion ICs in a scan with severe head movements

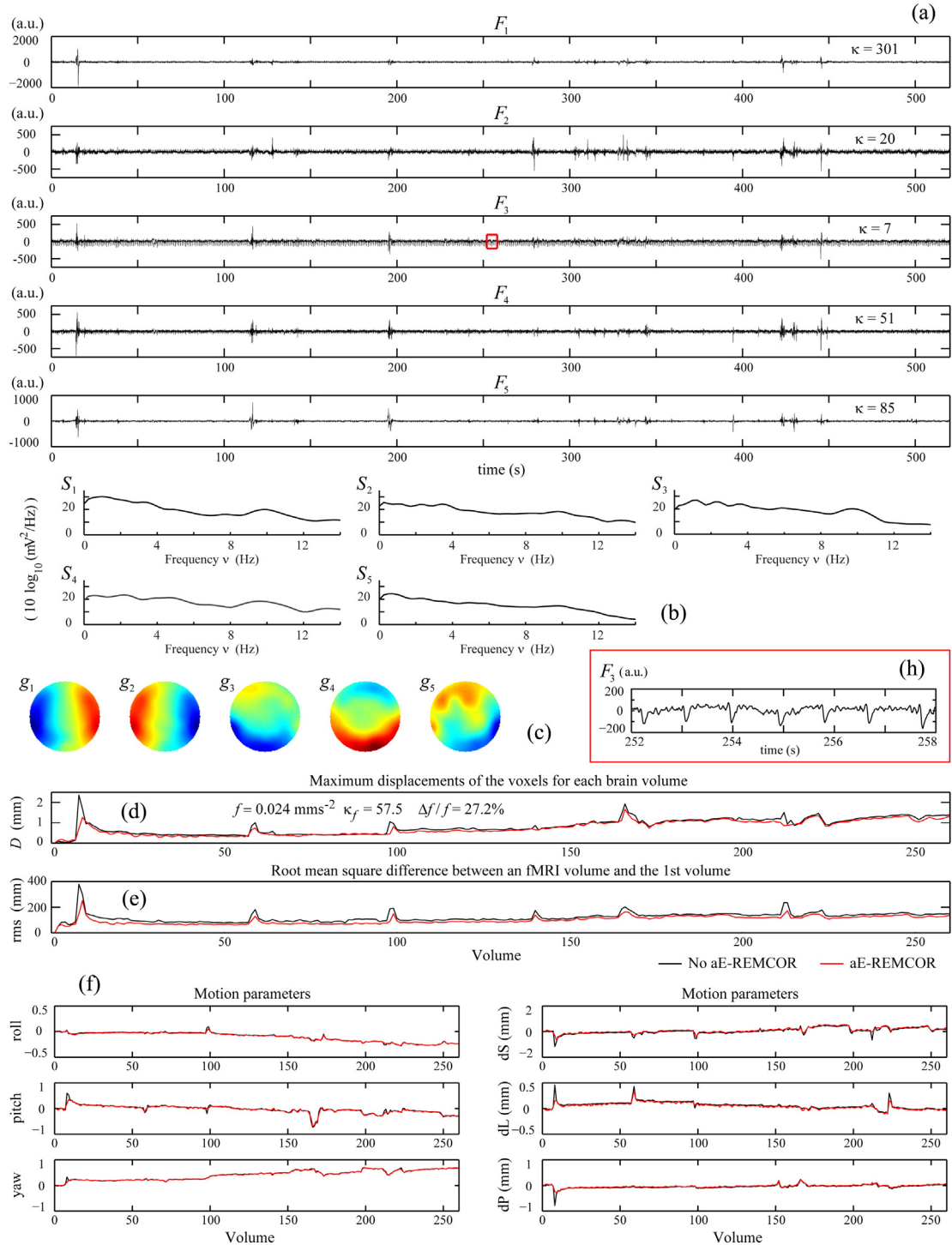


Fig. 6. The automatic results of aE-REMCOR with identified motion ICs in a scan with severe rapid head movements. (a) The time courses, (b) spectra, (c) topographic maps of the identified motion IC. (d) The maximum displacement of the voxels (D) for each brain volume. (e) The root mean square difference (rms) between an fMRI volume and the 1st volume. (f) The rotation angles roll, pitch, yaw and the displacements along the superior (dS), left (dL) and posterior (dP) directions calculated by AFNI 3dvolreg. (g) The ΔTSNR plots on the slices of the brain along the axial direction without volume registration (upper plot) and with volume registration (lower plot). (h) The close-up of the red box in (a). In (d)–(f), the results with and without aE-REMCOR are respectively plotted in red and black lines.

The automatic results of aE-REMCOR with identified motion ICs in a scan with severe head movements

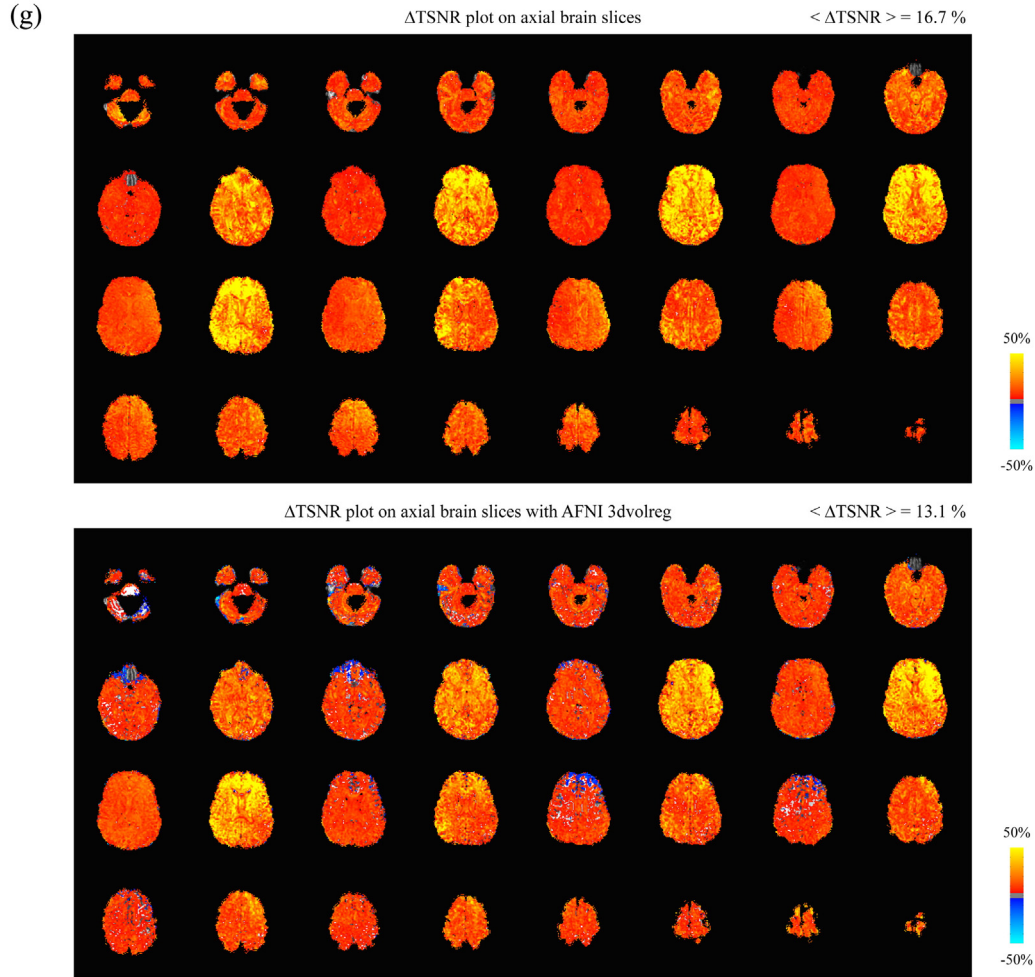


Fig. 6 (continued).

3.2. TSNR improvement

The ΔTSNR with and without the volume registration using AFNI 3dvolreg are plotted on the slices of the brain along the axial direction in Figs. 5(g) and 6(g). The figures show that larger ΔTSNR are obtained on the brain edge regions, as these areas are affected the most by the rapid head movement. Also, the motion correction in a particular time period gives similar ΔTSNR pattern in alternative slices, since with the SENSE acceleration factor = 2 used for the fMRI image acquisition, the first half of the interleaved images are acquired in one time period, and the remaining half of the interleaved images are acquired in the other time period. In Figs. 5(g) and 6(g), the average improvements of the TSNR over the brain ($\langle \Delta\text{TSNR} \rangle$) without volume registration are 6.5% and 16.7% (5.4% and 13.1% with volume registration). The corresponding top 10th percentile of ΔTSNR without volume registration reaches over 14.3% and 33.9% (14.6% and 28.2% with volume registration).

Fig. 7 shows the results from a scan with little subject motion. For this scan, one IC is identified as the cardioballistic motion IC. No significant improvement is observed in TSNR (Fig. 7(g)), and $\langle \Delta\text{TSNR} \rangle$ without volume registration is increased by 1.1% (1.4% with volume registration). While aE-REMCOR is shown to be capable of substantially removing head movements in the fMRI dataset in Figs. 5 and 6, it does not necessarily improve much the image quality for the scan with little head movements as the motion artifact in the fMRI data is small. Since a larger $\langle \Delta\text{TSNR} \rangle$ can be obtained in the scans with more severe motions, it is thus expected that the efficiency of aE-REMCOR depends on the motion severity.

Figs. 5(d)–(f), 6(d)–(f) and 7(d)–(f) show the maximum displacement of the voxels for each brain volume (D), the root mean square difference between an fMRI volume and the 1st volume (rms), and the motion parameters (roll, pitch, yaw, dS, dL, dP) calculated by AFNI 3dvolreg. The spikes in D , rms and the motion parameters indicate the occurrences of the rapid head movements. With the application of aE-REMCOR, the spikes in Figs. 5(d)–(f) and 6(d)–(f) are significantly reduced, and the fluctuations in Fig. 7 (d)–(f) are also slightly smoothed.

3.3. Efficiency of aE-REMCOR

The rapid change in the magnitude of the maximum displacements of the voxels for each brain volume (Figs. 5(d), 6(d) and 7(d)) can be used to characterize the severity of the head movements for the examination of the efficiency of aE-REMCOR. To measure the fluctuations of the maximum displacement for the brain voxels (D), the second derivative $d^2D(n)/dn^2$ is calculated, where n is the number index of the brain volume. The head movement severity is defined by the average magnitude of the second derivative over the entire scan, and is given by

$$f = \text{mean} \left(\left| d^2D(n)/dn^2 \right| / (\Delta t)^2, n = 1, \dots, N_{\text{fMRI}} \right). \quad (7)$$

Here $\Delta t = 2$ s is the time interval between the acquisitions of two consecutive brain volumes, which is equal to the repetition time of the fMRI scan. The motion severities with and without the application of

The automatic results of aE-REMCOR with identified motion ICs in a scan with little head movements

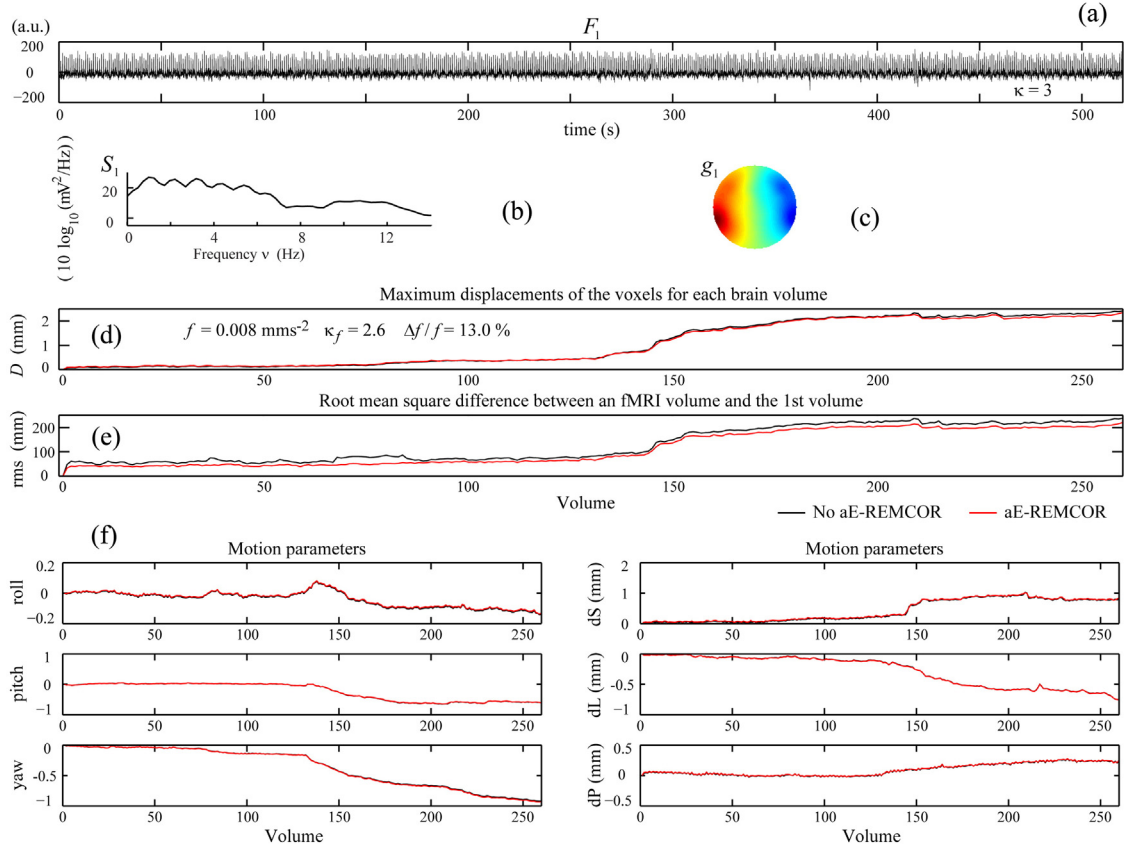


Fig. 7. The automatic results of aE-REMCOR with identified motion ICs in a scan with little head movements. (a) The time courses, (b) spectra, (c) topographic maps of the identified motion IC. (d) The maximum displacement of the voxels (D) for each brain volume. (e) The root mean square difference (rms) between an fMRI volume and the 1st volume. (f) The rotation angles roll, pitch, yaw and the displacements along the superior (dS), left (dL) and posterior (dP) directions calculated by AFNI 3dvolreg. (g) The ΔTSNR plots on the slices of the brain along the axial direction without volume registration (upper plot) and with volume registration (lower plot). In (d)–(f), the results with and without aE-REMCOR are respectively plotted in red and black lines.

aE-REMCOR are denoted by f' and f respectively. Note that the motion severity f signifies the fast changing spiky features of D instead of the slowly varying components. It can be interpreted as the average acceleration of the head motions during the scan. Thus a larger f usually indicates occasional or prolonged period of rapid head movements during the scan. To distinguish these two situations, the kurtosis of $d^2D(n)/dn^2$ is calculated:

$$\kappa_f = \text{kurtosis}\left(d^2D(n)/dn^2/(\Delta t)^2, n = 1, \dots, N_{\text{fMRI}}\right). \quad (8)$$

Kurtosis is a measure of non-Gaussianity. For prolonged period of rapid head movements, the distribution of $d^2D(n)/dn^2$ tends to become more Gaussian by the Central Limit Theorem, giving a small κ_f and a large f . The occasional rapid head movements, on the other hand, will give rise to a large κ_f and a moderate f . Finally, a small κ_f and a small f indicate the absence of significant head motions.

The aE-REMCOR was applied to 305 fMRI scans. The average improvement $\langle\Delta\text{TSNR}\rangle$ is plotted against f in Fig. 8(a), (c), and the improvements $\Delta\text{TSNR}(\mathbf{r})$ at the upper (blue dots) and lower (red dots) 10th percentile are plotted in Fig. 8(b), (d). It should be noted that a larger $\langle\Delta\text{TSNR}\rangle$ can usually be achieved in the scans with large f and κ_f . In other words, a higher aE-REMCOR efficiency can be obtained when there are severe head movements during the scan. With aE-REMCOR, the largest average improvement over the brain $\langle\Delta\text{TSNR}\rangle$ goes up to 27%, and the corresponding top 10% of the ΔTSNR reaches over 55%. The average $\langle\Delta\text{TSNR}\rangle$ over the scans with prolonged ($f > 0.10$) and occasional ($\kappa_f > 40$) rapid head movements in Fig. 8(a) are 13.7% and 7.7%

(9.1% and 5.2% in Fig. 8(c)). This shows a higher correction performance in scans with prolonged rapid head movements than in scans with occasional rapid head movements. In most cases when the subjects have no significant motion (small f and κ_f), $\langle\Delta\text{TSNR}\rangle$ increases slightly by a few percent, indicating the effectiveness of aE-REMCOR in removing the cardioballistic motions in the fMRI dataset.

The decrease in the motion severity $\Delta f = f - f'$, which quantifies the smoothing of the fluctuations in D after motion correction, is another measure of the efficiency of the aE-REMCOR. For instance, if aE-REMCOR removes all traces of motions, the maximum displacement of the voxels for all brain volumes ($D(n)$, $n = 1, \dots, N_{\text{fMRI}}$), and hence f , vanishes. In this limit, $\Delta f/f = 1$. In the other extreme, if the EEG based regressors fail to carry any motion information, f' can be any number larger than f depending on the performance of AFNI 3dTfitter. In this case, $\Delta f/f \leq 0$. In reality, there is an upper limit for the efficiency ratio $\Delta f/f$. The ratio is smaller than one as D is unlikely to be zero after the motion correction because of the noise and inaccurate representation of motions in the EEG data and also the fMRI data. Fig. 9(a) plots Δf against f for the 305 scans, and Fig. 9(b) plots the efficiency ratio $\Delta f/f$. Similar to the TSNR analysis, a higher efficiency ratio $\Delta f/f$ can usually be achieved when there are severe head movements during the scan (large f). The maximum efficiency of the current aE-REMCOR algorithm can be approximated by the bounding slope of the plot, which is about 74%. The average efficiency over the 305 scans is 18%, and the maximum efficiency over the scans is 71%. aE-REMCOR is shown to be capable of improving the TSNR and reducing the motion severity in scans with rapid head movements and cardioballistic motions. Nevertheless one should be cautious in using 3dTfitter for cardioballistic motion correction in

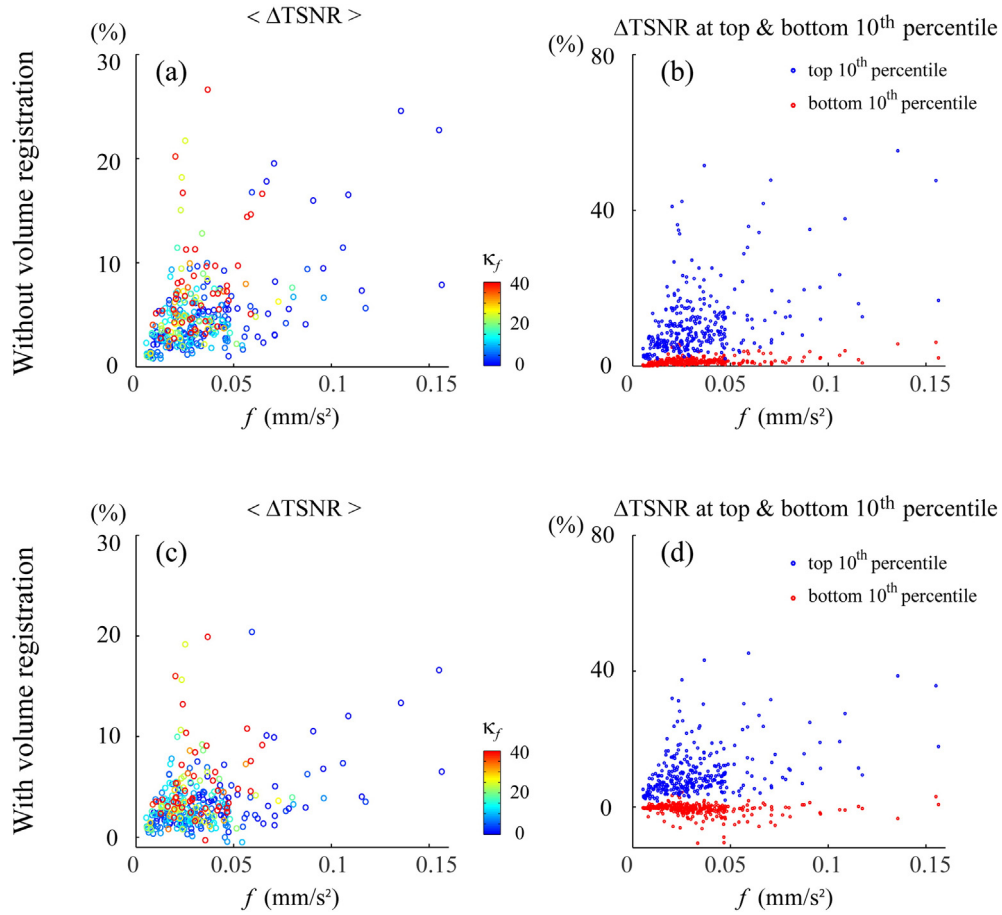


Fig. 8. The plots of (a), (c) the average improvement $\langle \Delta \text{TSNR} \rangle$ against the motion severity f ; (b), (d) the ΔTSNR at the upper (blue dots) and lower (red dots) 10th percentile against f . The ΔTSNR in (a)–(b) are calculated without volume registration. The ΔTSNR in (c)–(d) are calculated with volume registration (AFNI 3dvolreg). The color used in (a) and (c) is scaled to the kurtosis of the second derivative of the maximum displacement D defined in Eq. (8).

experiments with small signal-to-noise ratio, as any inefficient motion correction will introduce relatively significant overcorrection in the fMRI images.

3.4. rs-fMRI connectivity analysis.

The utility of aE-REMCOR to improve the rs-fMRI connectivity of the default mode network (DMN) is examined with the seed-based correlation analysis in this section. The motion severity parameters f and κ_f

for the resting scans are summarized in Fig. 10. These parameters are used to choose the scanning group with occasional rapid head movements ($\kappa_f > 40$: the 7 scans in red circle) and the scanning group with prolonged period of rapid head movements ($f > 0.10$: the 4 scans in blue circle).

Fig. 11(a)–(b) plot the rs-fMRI DMN correlation maps for the scan previously shown in Fig. 6. Stripes are observed in Fig. 11(a) for the correlation map without aE-REMCOR. The stripes can be seen clearly in the correlation difference (Fig. 11(c)). This stripe pattern originates

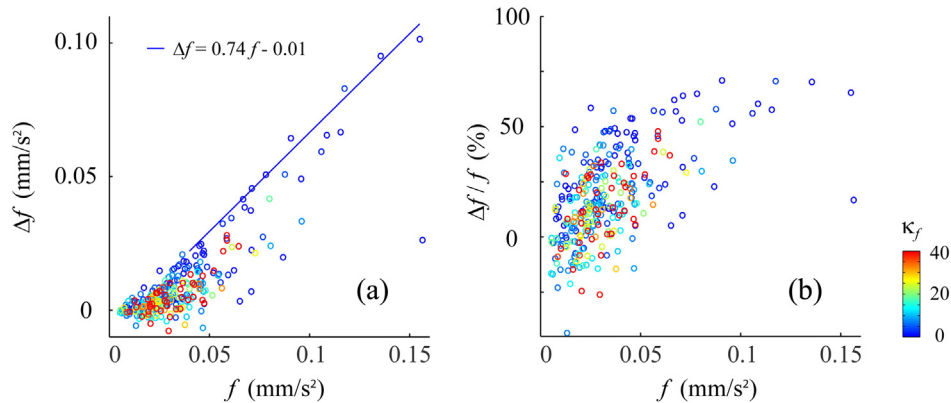


Fig. 9. The plots of (a) Δf against the motion severity f ; (b) the efficiency ratio $\Delta f/f$ against f . The color used in (a) and (b) is scaled to the kurtosis of the second derivative of the maximum displacement D defined in Eq. (8).

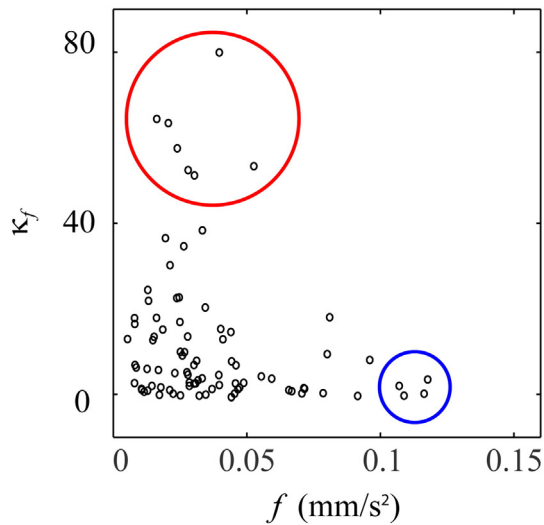


Fig. 10. The summary of the motion severity parameters f and κ_f in resting scans. The scans with $\kappa_f \geq 40$ and $f \geq 0.1$ to be used in the rs-fMRI connectivity analysis in Figs. 11(d)–(f) are enclosed in red and blue lines.

from the motion-induced signal loss in neighboring imaging slices as discussed in Section 3.2. When aE-REMCOR is applied, the contrast of the stripes reduces (Fig. 11(b)). Fig. 11(d)–(f) plot the group correlation differences in scans with occasional ($\kappa_f > 40$), prolonged ($f > 0.10$), and both kinds of rapid head movements ($\kappa_f > 40$ or $f > 0.10$). Similar motion-induced stripes with a lower contrast can be observed. The group correlation maps of the DMN for all resting scans are plotted in Fig. 11(g) and (h). The corresponding group correlation difference ((h) - (g)) is shown in Fig. 11(i). When all the 86 resting scans are considered, the motion-induced stripes disappear (Fig. 11(i)). This shows the reduced significance of motion artifacts on the DMN connectivity when sufficient scans with little head motion are considered. Nevertheless, when the entire group of subjects exhibits significant rapid head movements, slice-by-slice fMRI motion correction is particularly important to improve the accuracy of the rs-fMRI connectivity analysis. The centers of the ROIs in posterior cingulate cortex (PCC), medial prefrontal cortex (mPFC), lateral parietal cortex (LatPar-L, LatPar-R) and hippocampal formation (HF-L, HF-R) of the DMN are marked with crosshairs in Fig. 11. The correlation difference at a given ROI is denoted by $\Delta C(\text{ROI's name})$. The correlation difference, its percentage change relative to the original correlation value without aE-REMCOR, and the p -value are calculated for different scanning groups. For all scanning groups, a slight correlation decrease is observed at the seed ROI: for $\kappa_f > 40$, $\Delta C(\text{PCC}) = -0.017$ (-2.2% , $p = 0.004$); for $f > 0.10$, $\Delta C(\text{PCC}) = -0.004$ (-0.7% , $p = 0.213$); for $\kappa_f > 40$ or $f > 0.10$, $\Delta C(\text{PCC}) = -0.012$ (-1.7% , $p = 0.003$); for all resting scans, $\Delta C(\text{PCC}) = -0.003$ (-0.4% , $p = 0.018$). For the group with $\kappa_f > 40$, a large correlation change is found at the hippocampal formation $\Delta C(\text{HF-R}) = 0.019$ (60.4% , $p = 0.018$). When all the resting scans are considered, $\Delta C(\text{mPFC}) = 0.002$ (1.1% , $p = 0.451$), $\Delta C(\text{LatPar-L}) = -0.007$ (-3.3% , $p = 0.018$), $\Delta C(\text{LatPar-R}) = -0.004$ (-2.1% , $p = 0.174$), $\Delta C(\text{HF-L}) = 0.006$ (8.8% , $p = 0.027$), and $\Delta C(\text{HF-R}) = 0.008$ (12.6% , $p = 0.005$). The changes are statistically significant in PCC, LatPar-L, HF-L, and HF-R.

4. Discussions

In this paper, automatic categorization algorithms were developed to provide quantitative descriptions and analyses on the features observed in the mean power spectral density, topographic map and signal contribution of an identified IC in the EEG data acquired simultaneously

with fMRI. The algorithm aims to mimic the manual selection of the ICs related to head movements by adequately choosing the features that are commonly observed in the motion ICs. The effectiveness of the algorithm can be measured by its accuracy of reproducing the manual selection. From the examination of a total of 9455 ICs in 305 scans, there were 1045 true identification of motion ICs (TP), 8370 true identification of non-motion ICs (TN), 9 false identification of motion ICs (FP), and 31 false identification of non-motion ICs (FN), giving a precision $P_{IC} = TP/(TP + FP) = 99.15\%$, recall $R_{IC} = TP/(TP + FN) = 97.12\%$, and F-score $= 2P_{IC}R_{IC}/(P_{IC} + R_{IC}) = 98.12\%$.

The present categorization algorithm is utilized to select the motion ICs for the purpose of correcting head motions on slice-by-slice basis in the fMRI dataset. While the selected cardiobalistic motion ICs manifest distinct cardiac pulses in each cycle, they are insensitive to the improper positioning of electrocardiogram (ECG) and are less sensitive to head motions when compared to the ECG. Thus there is an advantage in utilizing the selected cardiobalistic motion ICs for applications like cardiac period and arrhythmia detections.

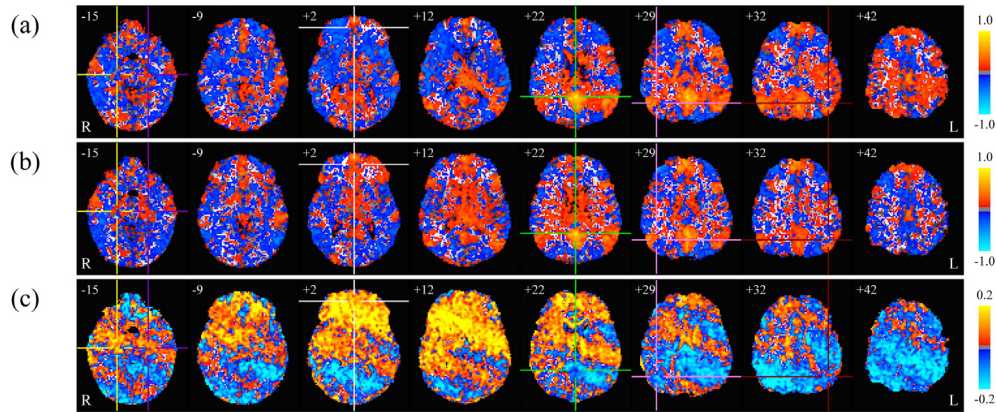
The developed automatic algorithm can also be utilized to preprocess the EEG data when it is applied in a reverse manner to remove, instead of to select, the identified rapid head movement ICs, cardiobalistic motion ICs, and possible blink and saccade ICs from the EEG data. For the current purpose of motion ICs selection, a cardiobalistic IC with exceedingly large power at high harmonic frequencies in the mean power spectral density or insignificantly small EEG signal contribution is not considered. For the purpose of preprocessing the EEG data, ICs related to cardiobalistic artifact with large power at high harmonic frequencies and small signal contribution should also be selected for removal. With the preprocessed EEG data, further identification, such as for the alpha rhythm of the neuronal signal, is possible when the features of the mean power spectral density, topographic map and signal contribution are adequately chosen and the parameters are properly adjusted.

Currently parameters are determined empirically based on the commonly observed features in 305 scans from 16 subjects in a 3 T MRI scanner. The parameters may need to be adjusted when other than 3 Tesla MRI field strengths are used or more datasets are available. Given a huge amount of data, the identifications of motions will benefit from more systematic approaches, like logistic regression or support vector machine modeling. Nevertheless, the current automatic algorithm provides basic tools to understand the properties of the motion related ICs, the potential and limitation of the ICA, and the efficiency of the motion correction in the fMRI datasets with the EEG based regressors.

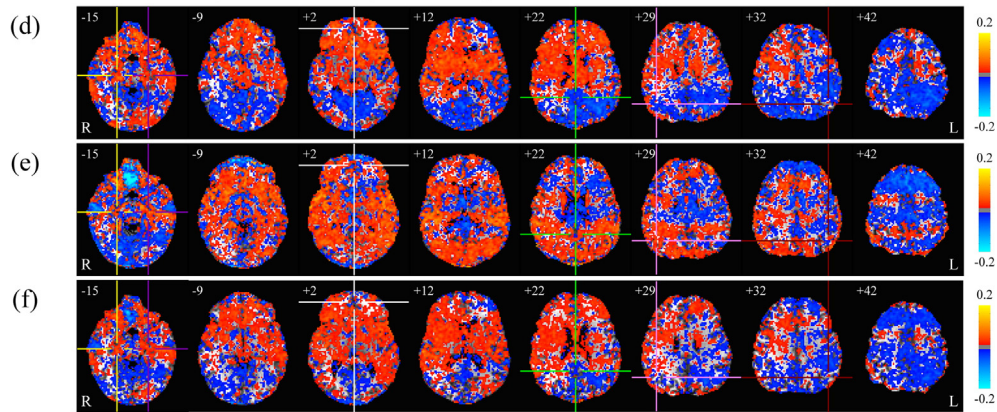
The calculations are carried out in a workstation with dual Intel® Xeon® CPU E5-2620 at 2.00GHz and 16GB memory. No explicit parallelization was implemented in the MATLAB code. The computation time of the ICA increases with the requested number of ICs, and the computation time of the motion correction procedures in AFNI increases with the number of selected motion ICs and the size of the image. Consider an fMRI dataset with 260 brain volumes, 34 axial slices per volume and an image matrix 128×128 , and an EEG dataset with 31 ICs and 5 identified as motion ICs, the computation times (and percentage) of the main motion correction procedures are 13.9 s (2.3%) for the EEG data preprocessing, 137.5 s (22.4%) for the ICA, 8.6 s (1.4%) for the spectrum analysis, 3.9 s (0.6%) for the topography analysis, 31.9 s (5.2%) for the signal contribution analysis, 228 s (37.1%) for the AFNI regressors calculations in BRIK format, and 191.4 s (31.1%) for the AFNI 3dtfitter calculations. It should be noted that the computation times of the ICA and AFNI dominate the whole process. Thus their speeds critically determine the possibility of the aE-REMCOR in real-time application. Since the three motion IC identification analyses can be performed independently and simultaneously for each IC, the computation speed can be improved by parallelizing the algorithm. For the motion correction of the fMRI data in AFNI, the calculations, in principle, can also be sped up by parallelizing the algorithm with the use of graphic processing unit (GPU) (Misaki et al., 2015).

Resting state functional connectivity of default mode network

For the resting scan shown in Fig. 6



For the resting scans with significant rapid head movements



For all resting scans

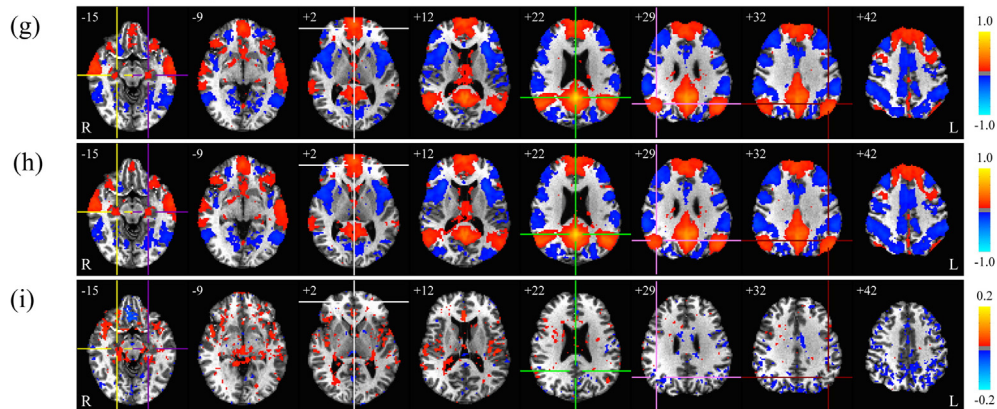


Fig. 11. Resting state connectivity of the default mode network (DMN). (a)–(b): Correlation map without and with aE-REMCOR for the scan with significant rapid head movements shown in Fig. 6. (c): Correlation difference ((b)–(a)). (d)–(f): Group correlation difference for the scans with occasional rapid head movements ($rs_T \geq 40$), prolonged rapid head movements ($f \geq 0.1$), and both ($rs_T \geq 40$ or $f \geq 0.1$). (g)–(h): Group correlation map without and with aE-REMCOR for all the 86 resting scans. (i): Group correlation difference for all the resting scans ((h)–(g)). The centers of the ROI in PCC (0, –52, 22), mPFC (0, 49, 2), LatPar-L (–45, –60, 32), LatPar-R (43, –60, 29), HF-L (–22, –19, –15) and HF-R (22, –19, –15) of the DMN are respectively marked with green, white, maroon, pink, purple and yellow crosshairs. Indicated next to each slice image is the z-coordinate of the slice. For the group analysis in (g)–(i), uncorrected $p < 0.05$ is used.

5. Conclusions

An automatic EEG-assisted retrospective motion correction (aE-REMCOR) method that utilizes EEG data to correct for head movements in fMRI on a slice-by-slice basis is reported. The aE-REMCOR automatically preprocesses and analyzes the EEG data, identifies the independent components (ICs) corresponding to head motions, and constructs the EEG based regressors with the identified motion ICs. The entire

automatic procedure is carried out in MATLAB. The motion artifacts in the fMRI images are corrected with the motion regressors in AFNI.

The automatic identification of the motion ICs is achieved by recognizing the special features of the motion artifacts imposed on the mean power spectral density, topographic map, and EEG signal contribution of the ICs. An automatic algorithm for the motion IC identification is developed. The algorithm is shown to be capable of identifying the ICs related to rapid head movements and cardioballistic motions, and also

the dominant component in the mixture of them when the ICA fails to separate the different motion components completely.

The aE-REMCOR is applied to 305 fMRI scans from 16 subjects in a 3 T MRI scanner. The results show that aE-REMCOR is capable of substantially removing head motions in fMRI images. With aE-REMCOR, the spikes and fluctuations of the motion parameters induced by the head movements are significantly reduced and smoothed. In particular, when there are significant rapid head movements during the scan, a large temporal signal-to-noise ratio (TSNR) improvement and high correction efficiency can be achieved. Depending on the subject's motion, the average TSNR improvement over the brain with aE-REMCOR goes up to 27% with the largest 10% of the TSNR improvement reaches over 55%. In the efficiency analysis for the motion correction, the average correction efficiency over the 305 scans is 18% and the largest achieved efficiency is 71%. It is observed from the results that the highest possible motion correction efficiency with the current aE-REMCOR algorithm is bounded by approximately 74%. The utility of aE-REMCOR on the fMRI connectivity of the default mode network (DMN) is examined in 86 resting scans. The motion-induced position-dependent error in the DMN connectivity analysis is shown to be reduced when aE-REMCOR is utilized. The results also show the importance of slice-by-slice fMRI motion corrections to improve the accuracy of rs-fMRI connectivity analysis when the entire group of subjects exhibits significant rapid head motions. The achieved automation procedure warrants its use in large clinical EEG and fMRI studies, and provides incentive for conducting simultaneous EEG & fMRI.

Acknowledgments

This work was supported by the U.S. Department of Defense grant W81XWH-12-1-0607.

Appendix A. Supplementary data

Supplementary data to this article can be found online at <http://dx.doi.org/10.1016/j.neuroimage.2016.01.042>.

References

- Allen, P.J., Polizzi, G., Krakow, K., Fish, D.R., Lemieux, L., 1998. Identification of EEG events in the MR scanner: the problem of pulse artifact and a method for its subtraction. *NeuroImage* 8, 229–239.
- Allen, P.J., Josephs, O., Turner, R., 2000. A method for removing imaging artifact from continuous EEG recorded during functional MRI. *NeuroImage* 12, 230–239.
- Beall, E.B., Lowe, M.J., 2014. SimPACE: generating simulated motion corrupted BOLD data with synthetic-navigated acquisition for the development and evaluation of SLOMOCO: a new, highly effective slice-wise motion correction. *NeuroImage* 101, 21–34.
- Bell, A.J., Sejnowski, T.J., 1995. An information-maximization approach to blind separation and blind deconvolution. *Neural Comput.* 7, 1129–1159.
- Biswal, B., Yetkin, F.Z., Haughton, V.M., Hyde, J.S., 1995. Functional connectivity in the motor cortex of resting human brain using echo-planar MRI. *Med. Res. Med.* 34, 537–541.
- Bodurka, J., Ye, F., Petridou, N., Murphy, K., Bandettini, P.A., 2007. Mapping the MRI voxel volume in which thermal noise matches physiological noise – implications for fMRI. *NeuroImage* 34, 542–549.
- Bonmassar, G., Purdon, P.L., Jääskeläinen, I.P., Chiappa, K., Solo, V., Brown, E.N., Belliveau, J.W., 2002. Motion and ballistocardiogram artifact removal for interleaved recording of EEG and EPs during MRI. *NeuroImage* 16, 1127–1141.
- Cox, R.W., 1996. AFNI: software for analysis and visualization of functional magnetic resonance neuroimages. *Comput. Biomed. Res.* 29, 162–173.
- Cox, R.W., Hyde, J.S., 1997. Software tools for analysis and visualization of fMRI data. *NMR Biomed.* 10, 171–178.
- Cox, R.W., Jesmanowicz, A., 1999. Real-time 3D image registration for functional MRI. *Magn. Reson. Med.* 42, 1014–1018.
- Delorme, A., Makeig, S., 2004. EEGLAB: an open source toolbox for analysis of single-trial EEG dynamics including independent component analysis. *J. Neurosci. Methods* 134, 9–21.
- Friston, K.J., Ashburner, J., Frith, C.D., Poline, J.B., Heather, J.D., Frackowiak, R.S.J., 1995. Spatial registration and normalization of images. *Hum. Brain Mapp.* 2, 165–189.
- Friston, K.J., Williams, S., Howard, R., Frackowiak, R.S.J., Turner, R., 1996. Movement-related effects in fMRI time-series. *Magn. Reson. Med.* 35, 346–355.
- Friston, K.J., 2005. Models of brain function in neuroimaging. *Annu. Rev. Psychol.* 56, 57–87.
- Glover, G.H., Li, T.Q., Ress, D., 2000. Image-based method for retrospective correction of physiological motion effects in fMRI: RETROICOR. *Magn. Reson. Med.* 44, 162–167.
- Gotts, S.J., Saad, Z.S., Jo, H.J., Wallace, G.L., Cox, R.W., Martin, A., 2013. The perils of global signal regression for group comparisons: a case study of Autism Spectrum Disorders. *Front. Hum. Neurosci.* 7 (Article 356).
- Hajnal, J.V., Myers, R., Oatridge, A., Schwieso, J.E., Young, I.R., Bydder, G.M., 1994. Artifacts due to stimulus correlated motion in functional imaging of the brain. *Magn. Reson. Med.* 31, 283–291.
- Jiang, A., Kennedy, D.N., Baker, J.R., Weisskoff, R.M., Tootell, R.B.H., Woods, R.P., Benson, R.R., Kwong, K.K., Brady, T.J., Rosen, B.R., Belliveau, J.W., 1995. Motion detection and correction in functional MR imaging. *Hum. Brain Mapp.* 3, 224–235.
- Jo, H.J., Gotts, S.J., Reynolds, R.C., Bandettini, P.A., Martin, A., Cox, R.W., Sadt, Z.S., 2013. Effective preprocessing procedures virtually eliminate distance-dependent motion artifacts in resting state fMRI. *J. Appl. Math.* 935154 (2013).
- Lowe, M.J., Mock, B.J., Sorenson, J.A., 1998. Functional connectivity in single and multislice echoplanar imaging using resting-state fluctuations. *NeuroImage* 7, 119–132.
- Makeig, S., Jung, T.P., Bell, A.J., Ghahremani, D., Sejnowski, T.J., 1997. Blind separation of auditory event-related brain responses into independent components. *Proc. Natl. Acad. Sci. U. S. A.* 94, 10979–10984.
- Mantini, D., Perrucci, M.G., Cugini, S., Ferretti, A., Romani, G.L., Del Gratta, C., 2007. Complete artifact removal for EEG recorded during continuous fMRI using independent component analysis. *NeuroImage* 34, 598–607.
- Masterton, R.A.J., Abbott, D.F., Fleming, S.W., Jackson, G.D., 2007. Measurement and reduction of motion and ballistocardiogram artefacts from simultaneous EEG and fMRI recordings. *NeuroImage* 37, 202–211.
- McMenamin, B.W., Shackman, A.J., Maxwell, J.S., Bachhuber, D.R.W., Koppenhaver, A.M., Greischar, L.L., Davidson, R.J., 2010. Validation of ICA-based myogenic artifact correction for scalp and source-localized EEG. *NeuroImage* 49, 2416–2432.
- Misaki, M., Barzagar, N., Zotev, V., Phillips, R., Cheng, S., Bodurka, J., 2015. Real-time fMRI processing with physiological noise correction – comparison with off-line analysis. *J. Neurosci. Methods* 256, 117–121.
- Mulert, C., Lemieux, L. (Eds.), 2010. EEG-fMRI: Physiological Basis, Technique, and Applications. Springer-Verlag, Berlin Heidelberg.
- Power, J.D., Barnes, K.A., Snyder, A.Z., Schlaggar, B.L., Petersen, S.E., 2012. Spurious but systematic correlations in functional connectivity MRI networks arise from subject motion. *NeuroImage* 59, 2142–2154.
- Saad, Z.S., Reynolds, R.C., Jo, H.J., Gotts, S.J., Chen, G., Martin, A., Cox, R.W., 2013. Correcting brain-wide correlation differences in resting-state fMRI. *Brain Connect.* 3, 339–352.
- Srivastava, G., Crottaz-Herbette, S., Lau, K.M., Glover, G.H., Menon, V., 2005. ICA-based procedures for removing ballistocardiogram artifacts from EEG data acquired in the MRI scanner. *NeuroImage* 24, 50–60.
- Satterthwaite, T.D., Elliott, M.A., Gerraty, R.T., Ruparel, K., Loughhead, J., Calkins, M.E., Eickhoff, S.B., Hakonarson, H., Gur, R.C., Gur, R.E., Wolf, D.H., 2013. An improved framework for confound regression and filtering for control of motion artifact in the preprocessing of resting-state functional connectivity data. *NeuroImage* 64, 240–256.
- Talairach, J., Tournoux, P., 1998. Co-Planar Stereotaxic Atlas of the Human Brain. Thieme Medical Publishers, New York.
- Van Dijk, K.R.A., Hedden, T., Venkataraman, A., Evans, K.C., Lazar, S.W., Buckner, R.L., 2010. Intrinsic functional connectivity as a tool for human connectomics: theory, properties, and optimization. *J. Neurophysiol.* 103, 297–321.
- Van Dijk, K.R.A., Sabuncu, M.R., Buckner, R.L., 2012. The influence of head motion on intrinsic functional connectivity MRI. *NeuroImage* 59, 431–438.
- Zotev, V., Krueger, F., Phillips, R., Alvarez, R.P., Simmons, W.K., Bellgowan, P., Drevets, W.C., Bodurka, J., 2011. Self-regulation of amygdala activation using real-time fMRI neurofeedback. *PLoS One* 6, e24522.
- Zotev, V., Yuan, H., Phillips, R., Bodurka, J., 2012. EEG-assisted retrospective motion correction for fMRI: E-REMCOR. *NeuroImage* 63, 698–712.



Real-time EEG artifact correction during fMRI using ICA



Ahmad Mayeli^{a,b}, Vadim Zotev^a, Hazem Refai^b, Jerzy Bodurka^{a,c,d,*}

^a Laureate Institute for Brain Research, Tulsa, OK, USA

^b Department of Electrical and Computer Engineering, University of Oklahoma, Tulsa, OK, USA

^c Stephenson School of Biomedical Engineering, University of Oklahoma, Norman, OK, USA

^d Biomedical Engineering Center, University of Oklahoma, Norman, OK, USA

HIGHLIGHTS

- A real-time method based on ICA (rtICA) is proposed to remove artifacts from EEG data acquired simultaneously with fMRI.
- The rtICA effectively reduces ocular, motion, BCG, muscle and residual MR artifacts and retrieves EEG signals.
- The rtICA method following the rtAAS outperforms the rtAAS for removing artifacts in real time.
- The rtICA revealed reliable artifact suppression results for further applications of real-time multimodal EEG-fMRI.

ARTICLE INFO

Article history:

Received 18 July 2016

Received in revised form 8 September 2016

Accepted 29 September 2016

Available online 30 September 2016

Keywords:

Real-time artifact correction

fMRI

EEG

EEG-fMRI

Real-time ICA

ABSTRACT

Background: Simultaneous acquisition of EEG and fMRI data results in EEG signal contamination by imaging (MR) and ballistocardiogram (BCG) artifacts. Artifact correction of EEG data for real-time applications, such as neurofeedback studies, is the subject of ongoing research. To date, average artifact subtraction (AAS) is the most widespread real-time method used to partially remove BCG and imaging artifacts without requiring extra hardware equipment; no alternative software-only real time methods for removing EEG artifacts are available.

New methods: We introduce a novel, improved approach for real-time EEG artifact correction during fMRI (rtICA). The rtICA is based on real time independent component analysis (ICA) and it is employed following the AAS method. The rtICA was implemented and validated during EEG and fMRI experiments on healthy subjects.

Results: Our results demonstrate that the rtICA employed after the rtAAS can obtain 98.4% success in detection of eye blinks, 4.4 times larger INPS reductions compared to RecView-corrected data, and effectively reduce motion artifacts, as well as imaging and muscle artifacts, in real time on six healthy subjects.

Comparison with existing methods: We compared our real-time artifact reduction results with the rtAAS and various offline methods using multiple evaluation metrics, including power analysis. Importantly, the rtICA does not affect brain neuronal signals as reflected in EEG bands of interest, including the alpha band.

Conclusions: A novel real-time ICA method was proposed for improving the EEG quality signal recorded during fMRI acquisition. The results show substantial reduction of different types of artifacts using real-time ICA method.

© 2016 The Author(s). Published by Elsevier B.V. This is an open access article under the CC BY-NC-ND license (<http://creativecommons.org/licenses/by-nc-nd/4.0/>).

1. Introduction

Electroencephalography (EEG) and functional Magnetic Resonance Imaging (fMRI) are widely used, noninvasive, and safe techniques for detecting and characterizing changes in brain states and their relation to brain activity (Ritter and Villringer, 2006). The

techniques complement each other well because of high temporal resolution of EEG data and high spatial resolution of fMRI data (Niazy et al., 2005). Furthermore, because EEG is a direct measure of brain activity and fMRI is an indirect measure, simultaneous EEG-fMRI measurements can aid in cross validation. However, recording EEG inside the MRI scanner and during fMRI acquisition suffers from several safety and technical challenges (Kruggel et al., 2000). A major problem is the presence of artifacts in EEG data, such as MR or imaging artifacts and also ballistocardiogram (BCG) artifacts. BCG and imaging artifacts appear in the EEG signal as a result of the sig-

* Corresponding author at: Laureate Institute for Brain Research, Tulsa, OK, USA.
E-mail address: jbodurka@laureateinstitute.org (J. Bodurka).

nal being recorded inside MRI scanner and during fMRI acquisition respectively (Niazy et al., 2005). Other types of artifacts, such as muscle and ocular artifacts can be present in EEG data regardless if the EEG is recorded inside or outside the MRI scanner (Mantini et al., 2007; McMenamin et al., 2010).

The average artifact subtraction method (AAS) (Allen et al., 1998, 2000) is commonly used to remove BCG and imaging artifacts. To date, it is the most widespread real-time method used to partially remove such artifacts. The AAS method is based on the repetitive pattern of imaging and BCG artifacts, and it generates an artifact template to subtract it from the EEG signal. Even though the AAS can effectively reduce BCG and imaging artifacts, some residual artifacts remain when this algorithm is applied to raw EEG data in both real time and offline (Niazy et al., 2005). High quality, modern MRI scanner gradient controllers together with synchronization of MRI and EEG system clocks enable generation of accurate and reproducible templates of gradient artifacts, and allow for AAS template subtraction that has proven extremely successful (Laufs, 2012). However, temporal variability of BCG artifact makes removal of BCG artifact using the AAS less efficient. While the AAS has proven successful for reducing BCG and, especially, imaging artifacts, the method does not remove ocular, motion, and muscle artifacts. Instead, ICA has been widely used in offline analysis as an alternative for attenuating residual imaging and BCG artifacts, and other artifacts (e.g., Mantini et al., 2007; McMenamin et al., 2010; Srivastava et al., 2005; Wong et al., 2016; Zotev et al., 2016). A variety of ICA-based methods (e.g., FastICA, extended Infomax, Robust ICA, JADE, and SOBI) have been utilized for this purpose. More recently, Hsu et al. (2016) demonstrated that online recursive ICA algorithms are fast enough for real-time EEG source separation. However, they did not suggest any automatic algorithm for identifying artifacts among sources in their study.

Problems associated with EEG artifacts have led to the development of a number of alternative methods for removing fMRI environment and regular physiological artifacts. Niazy et al. (2005) suggested a novel method, namely optimal basis set (OBS), for generating BCG artifact templates. They used principal component analysis (PCA) for capturing temporal variations in artifacts and regressing BCG artifacts from EEG data. The result is superior performance over the AAS for removing BCG artifacts, with fewer residual artifacts remaining. This method has recently been adopted for real-time artifact correction (Wu et al., 2016). Like the rtAAS, this method can only remove BCG and imaging artifacts and the application of this method is obscured when the accuracy of R-peak detection is low due to ECG data distortion. Furthermore, since muscle and especially ocular and motion artifacts often have greater amplitudes compared to neural activity and higher or similar amplitude to BCG artifacts, the interaction of motion, muscle and ocular artifacts on BCG artifact template needs to be investigated further (Wu et al., 2016). Kim et al. (2004) proposed a combination of wavelet-based de-noising with adaptive filtering as post-processing to increase the AAS performance. Likewise, adaptive noise cancellation was suggested as a preprocessing step for the OBS (Niazy et al., 2005). PCA has also been used for removing BCG and imaging artifacts in studies reported in Negishi et al. (2004) and Bénar et al. (2003). Wavelet transform, followed by ICA, has proven to be a useful method for removing artifacts (Akhtar et al., 2012; Zhou and Gotman, 2004).

Several researchers utilized reference signals for removing BCG artifacts (Bonmassar et al., 2002; Dunseath and Alden, 2010; Luo et al., 2014; Masterton et al., 2007; van der Meer et al., 2016). Bonmassar et al. (2002) utilized a piezoelectric motion sensor to estimate motion artifact noise. Correlation between motion sensor and EEG signal was used to design the Kalman filter for removing BCG artifacts. Masterton et al. (2007) introduced a wire-loop-based method for correction of motion and BCG artifacts. Dunseath and

Alden (2010) suggested using reference electrodes attached to a conductive reference layer for recording artifacts and further removing noise from EEG data. Although these methods appear beneficial for reducing artifacts, they are not yet widely used. Unfortunately, these methods require hardware modification and additional equipment, which makes them complicated and more expensive to implement (Jorge et al., 2015). Furthermore, some of these methods require complicated and time consuming calculations, which make them less suitable for real-time applications.

Real-time imaging and BCG artifact correction techniques were used in several simultaneous EEG and fMRI studies (Becker et al., 2011; Cavazza et al., 2014; Zich et al., 2015; Zotev et al., 2014). The AAS implemented in real time in the RecView software (Brain Products GmbH, Gilching, Germany) was used in all of these studies for reducing BCG and imaging artifacts. Developing new real-time algorithms for removing EEG artifacts would make real-time analysis of multimodal EEG-fMRI signals more feasible and thus open many new research opportunities to study human brain function.

In this work, a novel real-time EEG artifact correction approach during fMRI (rtICA) is developed. The rtICA is a real-time ICA-based algorithm for reducing BCG and imaging artifacts, in addition to motion, ocular, and muscle EEG artifacts, and to improve EEG data quality acquired during fMRI. Imaging and BCG artifacts are first reduced using the BrainVision RecView software in real time prior to applying the rtICA (rtAAS + rtICA). The following section provides a more detailed description of our proposed rtICA method. Since the EEG activity is changing during time and in different conditions, instead of comparing EEG data recorded during fMRI acquisition and outside MRI scanner, we preferred to compare the performance of the rtAAS + rtICA for removing artifacts with RecView-corrected data and EEG data after applying different offline artifact corrections. Finally, we discuss results and improvement of the EEG data quality. A preliminary report of portions of this work was presented in Mayeli et al. (2015).

2. Methods

2.1. Data acquisition

The study was conducted at the Laureate Institute for Brain Research with research protocol approved by the Western Institutional Review Board (IRB). All participants provided written informed consent and received financial compensation for participation.

The rtAAS + rtICA artifact removal method has been tested on six healthy subjects (mean age: 36 ± 14 years, three females). Four resting EEG-fMRI runs were conducted; each run lasted 8 min 40 s. The participants were instructed to relax and rest with eyes closed for two runs, and then keep their eyes open and fixed on a cross for an additional two runs. Sequence runs with eyes-closed and eyes-open was balanced to eliminate fatigue factor (Yuan et al., 2013).

MR images were acquired via a General Electric Discovery MR750 whole-body 3 T MRI scanner with a standard 8-channel, receive-only head coil array. For fMRI acquisition, a single-shot gradient-recalled EPI sequence with Sensitivity Encoding (SENSE) was employed. The EPI sequence was custom modified to ensure that the repetition time TR was exactly 2000 ms (with $1 \mu\text{s}$ accuracy) and further enabling accurate correction of MR artifacts in EEG data, recorded simultaneously with fMRI. EPI imaging had the following parameters: FOV = 240 mm, slice thickness = 2.9 mm, slice gap = 0.5 mm, 34 axial slices per volume, 64×64 acquisition matrix, echo time TE = 30 ms, SENSE acceleration factor R = 2, flip angle = 90° , sampling bandwidth = 250 kHz. The fMRI run time was 8 min 40 s. For allowing the fMRI signal to reach

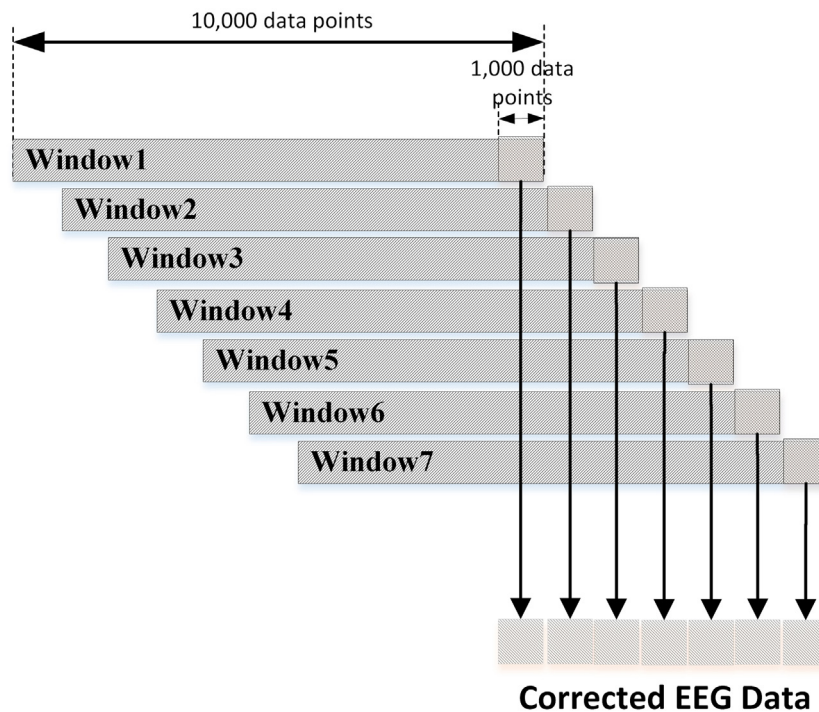


Fig. 1. Proposed data processing procedure suitable for real-time implementation. SOBI was applied on the whole 10,000 point sliding window, but the correction was only performed on the final 1000 pts.

steady state, three EPI volumes (6 s) were added at the beginning of the run and were excluded from data analysis. The fMRI voxel size was $3.75 \times 3.75 \times 2.9 \text{ mm}^3$. For acquiring anatomical image, a T1-weighted magnetization-prepared rapid gradient-echo (MPRAGE) sequence with SENSE was used. The MPRAGE sequence had the following parameters: FOV=240 mm, axial slices per slab = 128, slice thickness = 1.2 mm, image matrix size = 256×256 , TR/TE = 5.0/1.9 ms, SENSE factor R = 2, flip angle = 10° , delay time TD = 1400 ms, inversion time TI = 725 ms, sampling bandwidth = 31.2 kHz, scan time = 4 min 58 s.

EEG signals were recorded simultaneously with fMRI via a 32-channel MR-compatible EEG system from Brain Products GmbH. The EEG cap included 32 electrodes, arranged according to the international 10–20 system. One electrode was placed on the subject's back for recording the ECG signal. A Brain Products' SyncBox device was used to synchronize the EEG system clock with the 10 MHz MRI scanner clock. EEG acquisition temporal resolution was 0.2 ms (i.e., 16-bit 5 kS/s sampling), and measurement resolution was 0.1 μV . EEG signals were hardware filtered throughout the acquisition in a frequency band between 0.016 and 250 Hz. Brain Products' RecView software was used to monitor EEG data acquisition in real time and to reduce imaging and BCG artifacts before streaming to the rICA module.

2.2. Second order blind identification

Second order blind identification (SOBI) (Belouchrani et al., 1997) takes advantage of temporal correlations in the source activities. It calculates second order statistics–covariance matrices–which are later diagonalized. The SOBI differs from other blind separation algorithms by its robustness, the low number of tunable parameters requiring adjustment, and convergence speed, which is the most important reason for choosing this ICA algorithm for this study. Table 1 presents the average computation time required for ICA decomposition of 40 s 22-channel data using different ICA algorithms, computed by averaging the execution

Table 1

Average computation time (s) for 40 s (10,000 data points) 22-channel data using different ICA algorithms.

	Time(s)
Infomax	13.56 ± 1.23
JADE	2.96 ± 1.28
FastICA	6.74 ± 4.54
SOBI	0.71 ± 0.10

time for 3 subjects during an 8 min and 40 s resting state run. The ICA computations were performed on MATLAB 2012. The ICA MATLAB codes available in EEGLAB toolbox and their default values for ICA convergence were utilized. Among the presented four algorithms, SOBI has the lowest averaged time and standard deviation. Based on Klemm et al. (2009) study comparing ICA algorithms, the SOBI has been shown to provide some of the best-quality results in separating EEG data and artifacts.

2.3. Proposed ICA data processing suitable for real-time implementation

The proposed data processing procedure suitable for real-time implementation is shown in Fig. 1 (Mayeli et al., 2015). To obtain reliable and stable results from ICA decomposition, data submitted to the algorithm should be at least a multiple k of n^2 , where n is the number of channels and k may need to be 20 or larger (Onton et al., 2006). For instance, given 31-channel data and $k=20$, data samples will be at least 19,220. At a sampling rate of 250 S/s, data window duration is approximately 80 s. In this study, 22 channels were selected to increase algorithm speed, as opposed to performing ICA on all channels. When $n=22$ and $k=20$, the number of data points submitted to ICA should be more than 9680 – rounded up to 10,000 – data points. The selected channels, shown in Fig. 2, include all the available frontal EEG channels, because EEG activity over the frontal and prefrontal brain regions is relevant to emotion regulation and is used for neurofeedback studies (Cavazza et al.,

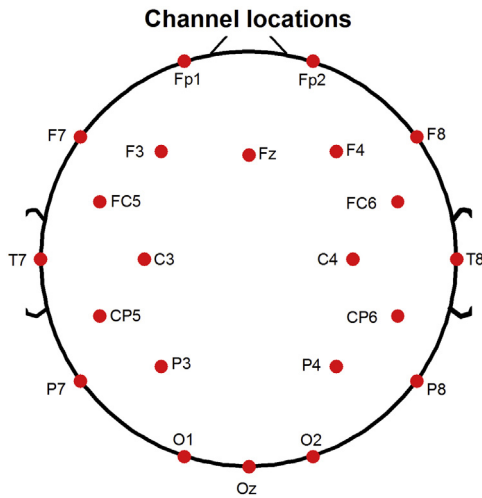


Fig. 2. Selected 22 channels for ICA decomposition.

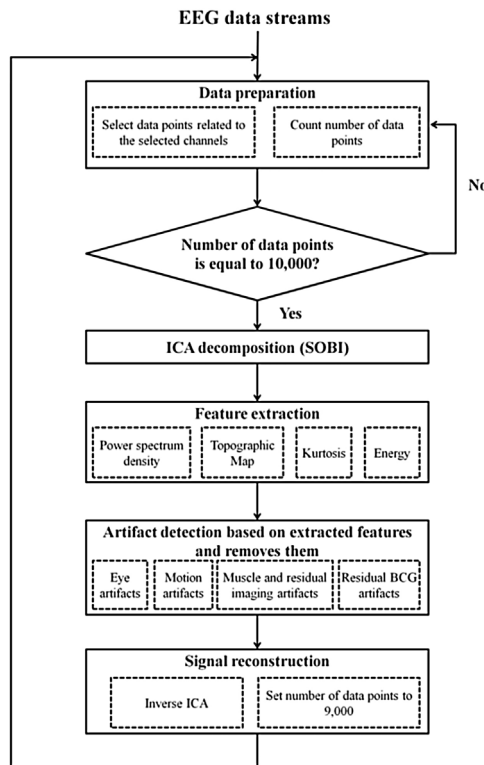


Fig. 3. rtAAS + rtICA flowchart.

2014; Zotev et al., 2014, 2016). Occipital electrodes (i.e. O1, O2 and Oz), which are important for investigating human visual evoked potential, were selected for ICA decomposition as well (Becker et al., 2008, 2011). The other channels were selected based on two criteria. First, since the BCG artifacts mostly exhibit bipolar properties, we selected symmetric channels for ICA decomposition. Second, the channels which are contaminated with artifacts and have common artifacts with occipital or frontal electrodes (e.g. channels T1 and T2 are affected by muscle artifacts) were selected. These selected channels and number of channels can be changed based on the application of real-time EEG-fMRI study and number of EEG system electrodes.

Fig. 3 offers a detailed flow diagram description of the rtAAS + rtICA process. The SOBI algorithm was implemented in the following way. The RecView software was utilized to reduce imag-

ing and BCG artifacts from the 32-channel EEG data in real time, and then to down-sample data to 250 S/s from 5000 S/s. RecView output data were exported in 8 ms blocks (i.e., two data points per block for all channels). The number of data points is first initialized to zero. During preprocessing, newly arriving data points are counted. Since this scheme requires 23 channels (i.e., 22 EEG channels plus 1 ECG electrode) for ICA decomposition, data points related to these channels are selected. ICA decomposition commences when total number of data points reaches 10,000. Four features (power spectrum density, topographic map, kurtosis, energy) are extracted from the last 1000 data points of each independent component (IC). Based on extracted features and defined thresholds, a maximum of 12 ICs for various types of artifacts are considered (i.e., a maximum of three components for ocular, three for motion, three for muscle and residual imaging artifact, and three components for BCG artifact). The number of ICs identified as artifacts was limited to prevent losing any brain activity. After subtracting artifactual ICs, inverse ICA reconstructs EEG data, and the number of data points is set to 9000. This procedure is repeated for each 1000 data samples received.

An example application of real-time EEG acquisition is EEG neurofeedback. Frontal EEG asymmetry is a promising target for EEG neurofeedback aimed at training emotion regulation, as confirmed by recent simultaneous EEG-fMRI studies (Cavazza et al., 2014; Zotev et al., 2014, 2016). When used as a real-time target for EEG neurofeedback, frontal EEG asymmetry in a specific EEG band is defined as Zotev et al. (2014):

$$A = \frac{P(F3) - P(F4)}{P(F3) + P(F4)} \quad (1)$$

where P is the EEG power for a given channel in a specific EEG band such as high-beta or alpha bands. Frontal EEG asymmetry in the alpha EEG band is defined with the opposite sign (Cavazza et al., 2014; Zotev et al., 2016).

2.4. Automatic IC classification

Various features are extracted from ICs and used to classify ICs as brain activity and artifacts. The first is the topographic map of each independent component, which indicates scalp map projection of selected components (i.e., each component primarily affecting a specific portion of the brain and can be determined using an ICA mixture matrix). The values of the topographic map were normalized to unity using inverse ICA matrices. The second feature is IC energy. The energy of a discrete time signal of x is defined by:

$$E_x \triangleq \sum_{n=-\infty}^{\infty} |x[n]|^2 \quad (2)$$

Kurtosis can also be used for separating artifacts and it is a measure of data distribution (i.e., peakedness or flatness) that can be calculated using the following equation:

$$\text{kurt}(x) = E\{x^4\} - 3(E\{x^2\})^2 \quad (3)$$

The final feature is power spectral density of IC calculated via the Fast Fourier Transform (FFT) to indicate distribution of signal power in frequency domain. For detecting eye, motion and residual BCG artifacts, the spectrum in the range between 0.5 and 40 Hz was normalized to the range of 0–1 and for detecting muscle and residual MR artifact, the spectrum in the range between 0.5 and 60 Hz was normalized to the unity.

The EEG data were recorded from three healthy female subjects (mean age: 26 ± 6 years) and three male subjects (mean age: 29 ± 9 years) diagnosed with combat related post-traumatic stress disorder (PTSD) across a neurofeedback experiment (3640 s) and were used to define a reliable threshold for each feature and to avoid removing brain activity instead of artifacts (Zotev et al., 2014).

Table 2

The summary of the identification of the ICs based on energy, kurtosis, topographic features and spectrum characteristics.

Types of Artifacts	Energy	Kurtosis	Topographic Features	Spectral Characteristics
Eye Artifacts	$>10^8$	>6	Prefrontal region (Fp1 and Fp2) with a larger threshold value of 28%	Normalized power between 0.5 and 3 Hz >0.22
Residual BCG Artifacts	–	–	Bipolar with the threshold value of larger than 0.25 AND Occipital region with a smaller threshold value of 14%	Normalized power between 2 and 7 Hz >0.18 AND Normalized power between 7 and 12 Hz <0.12
Muscle and Residual Imaging Artifacts	–	–	Unipolar	Normalized power between 30 and 60 Hz >0.68 AND Normalized power between 7 and 12 Hz <0.07
Motion Artifacts	$>10^9$	>15	Bipolar with the threshold value of 0.2	Normalized power between 0.5 and 4.5 Hz >0.26

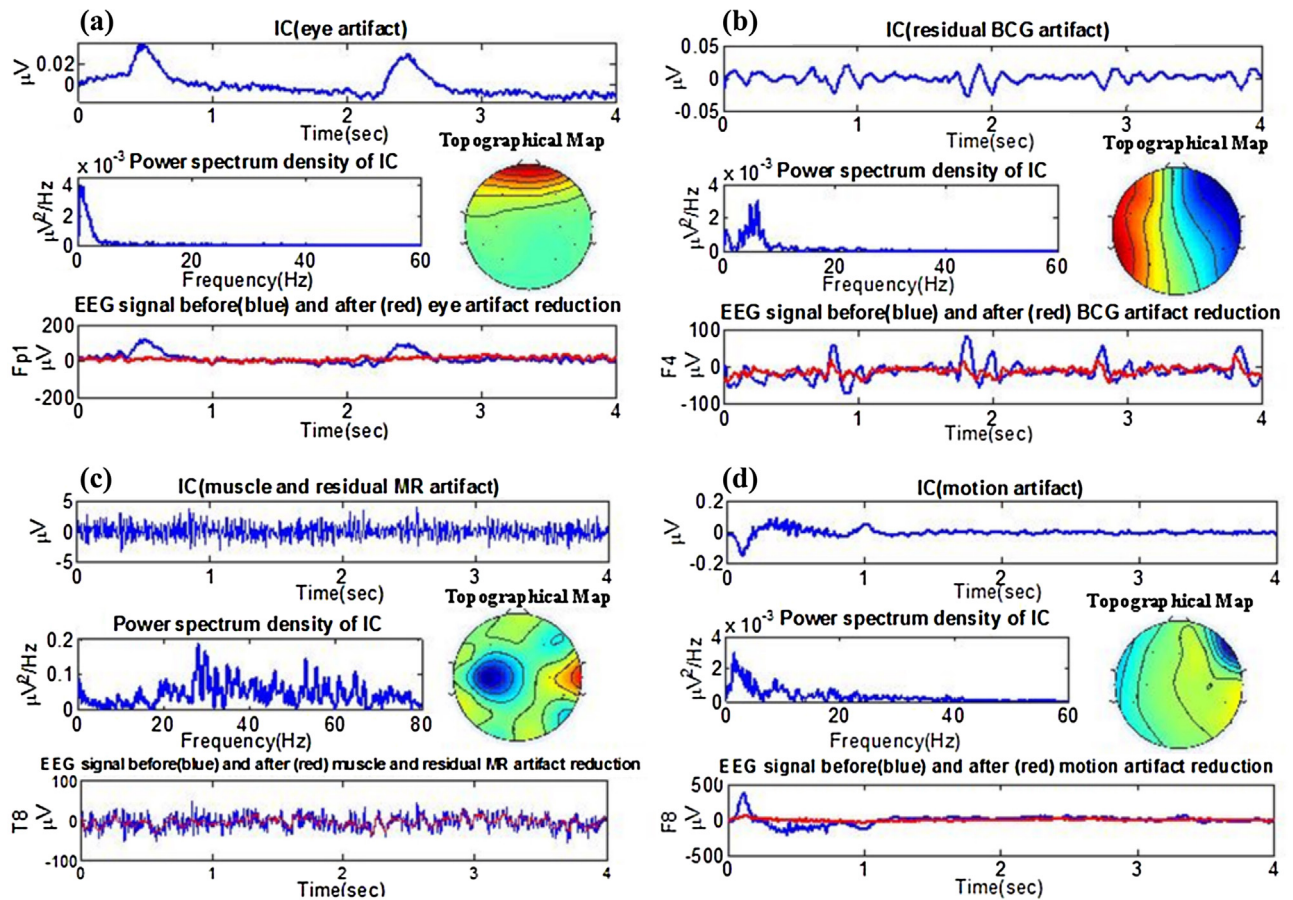
**Fig. 4.** Automatic (a) eye artifact, (b) residual BCG artifact, (c) residual MR and Muscle artifact and (d) motion artifact detection and results of removing them from EEG data.

Table 2 summarizes real-time classification criteria for each type of artifacts being detected including numerical threshold values for kurtosis, energy, topographic features and spectral characteristics. The described criteria are preliminary and need further optimization. Fig. 4 shows an overview of automatic artifact IC identification.

2.4.1. Eye artifact detection

Eye movement and blinking produces an electrical potential at a magnitude larger than brain activity. Due to eye proximity, ocular artifacts mostly affect frontal pole electrodes (i.e. channels Fp1 and Fp2), although they can propagate across much of the head and distort brain signals. Ocular artifacts are characterized by strong spatial projection in the prefrontal area, either shows high loadings

at the most anterior sites for eye blinks or manifests as an anterior dipole for saccades, high energy and low-frequency peaks (between 0.5 and 3 Hz) in the frequency domain (McMenamin et al., 2010; Wong et al., 2016). Based on such features, ocular artifacts can be easily detected among different ICs.

2.4.2. Residual BCG artifacts detection

BCG artifacts are extremely problematic in EEG due to their overlap with frequency range of normal neural activity. Although the RecView is often used to partially remove BCG artifacts, remaining residual artifacts can obscure the EEG signal because: (1) ECG signal recorded via chest or back electrodes during fMRI contains artifacts that can make reliable R-peak detection difficult (Luo et al.,

2014); and (2) AAS algorithm assumes pulse waveform with a highly reproducible pattern within a given time interval. In this way, subtracting average waveform from contaminated EEG can appropriately remove BCG artifacts. Notably, this assumption has not been proven (Kim et al., 2004). To reduce such artifacts, IC features (e.g., high relative power of theta band activity between 2 and 7 Hz) related to BCG artifacts can be leveraged (Wong et al., 2016). Furthermore, topographical maps corresponding to residual BCG artifacts exhibit primarily bipolar properties (Zotev et al., 2012). The bipolar properties could be appear in right side of head (i.e. channels F8, FC6, C4, CP6, P8 and T8) and left side of head (i.e. channels F8, FC6, C4, CP6, P8 and T8) or frontal (i.e. Fp1, Fp2, F7, F3, Fz, F4, and F8) and posterior (i.e. P7, P3, P4, P8, O1, Oz, and O2) sides of the head. BCG artifacts contain fairly large peaks, as shown in Fig. 4(b) and have high energy. Removing such ICs effectively reduces BCG artifacts.

2.4.3. Muscle and residual imaging artifacts detection

Although the RecView is used to reduce imaging and BCG artifacts before applying ICA, some residual artifacts remain. Residual imaging and muscle artifacts are primarily distinguished based on power spectra with broad peaks at higher frequencies (i.e., higher than regular EEG signal) (McMenamin et al., 2010). Because such artifacts could appear in the beta band, only ICs with high frequency activity at 30 Hz and higher are considered muscle and imaging artifacts (See Fig. 4(c)). After reducing such artifacts, most sharp spikes with high amplitudes are removed from the EEG signal.

2.4.4. Motion artifact detection

Head, body, or electrode movement artifacts are easily recognized offline as a result of their large amplitude. Intervals containing these artifacts can be excluded without difficulty, given that such activity does not occur frequently for most subjects. Real-time analysis of such data is difficult because of the random nature of motion artifacts. Motion artifact ICs are characterized by high kurtosis values (of the order of 10–1000), intense low-frequency activity (0.5–4.5 Hz) and bipolar topographies similar to BCG artifacts with different threshold values (Wong et al., 2016; Zotev et al., 2012). Because of the large magnitude of the random-motion artifacts, they may appear across multiple ICs in the ICA decomposition. Removing movement artifacts may remove some brain activity as well. To prevent this, the number of IC-detected movement artifacts is limited to only those components with very large energy and kurtosis, as well as those with low frequency activity. Fig. 4(d) shows IC identified as motion artifacts, as well as the outcomes after removing them.

2.5. Implementation

The proposed algorithm was implemented in MATLAB (MathWorks Inc., Natick, MA) for offline testing. The SOBI algorithm, implemented in EEGLAB (Delorme and Makeig, 2004) was used for ICA decomposition.

For real-time implementation, software code was written in Python programming language as an add-on module for simultaneous rtfMRI-EEG neurofeedback system as described in Zotev et al. (2014). Real-time ICA decomposition of RecView-corrected EEG data was added to the EEG client software for removing artifacts from signals before performing Math modules and integrating EEG and fMRI. This processing module was named “eeg_rtica”. Module outputs were saved to files in real time for further comparison with RecView-corrected data and offline methods.

2.6. Offline procedure for removing artifacts for evaluating rtAAS + rtICA algorithm

The BrainVision Analyzer 2 software (Brain Products GmbH, Germany) was used for offline analysis of the EEG data recorded simultaneously with fMRI. Different studies show that ICA following either the AAS or the OBS algorithms can successfully remove residual artifacts (Debener et al., 2008; Mantini et al., 2007; Zotev et al., 2014, 2016). Accordingly, for this study we primarily used this method as a reference to evaluate the rtAAS + rtICA performance and compare it with others. The procedure for offline EEG artifact removal using the AAS, filtering and ICA (AAS + Filtering + ICA) is the following. First, imaging artifacts were removed using the AAS method (Allen et al., 2000). EEG signals were then down-sampled to 250 S/s. Next, band-rejection filters (1 Hz bandwidth) were used for removing fMRI slice selection fundamental frequency (17 Hz) and its harmonics, vibration noise (26 Hz), and AC power line noise (60 Hz). These band-rejection filters should be selected based on the MRI scanner and sequence properties. For removing signals unrelated to brain activity, EEG data were bandpass filtered from 0.1 to 80 Hz (48 dB/octave). For detecting R-peaks more easily, ECG data were bandpass filtered from 0.1 to 12 Hz. Subsequently, BCG artifacts were removed using the AAS (Allen et al., 1998). A template of BCG artifacts from 21 cardiac periods of preceding data for each channel was used to create a template for removing BCG artifact using the AAS. Notably, R-peak detection is required for generating the BCG template. This can be accomplished automatically in the BrainVision Analyzer 2 software, with subsequent visual inspection to correct incorrectly positioned R-peak markers. After applying the AAS for reducing BCG artifacts, the Infomax algorithm (Bell and Sejnowski, 1995) was used for ICA decomposition. We chose the Infomax as ICA algorithm since this method is widely used for separating artifacts from EEG data and has been proven to be among the most reliable ICA methods for removing EEG artifacts (Nakamura et al., 2006; Vanderperren et al., 2010). However, we did not use this method for our rtICA implementation, because the Infomax is too slow for our real-time application (Klemm et al., 2009). ICA was performed on 31 channels, resulting in 31 ICs. The topographic map, power spectrum density, time course signal, energy value, and kurtosis value were used for detecting and removing artifactual ICs. Afterwards, EEG signal was reconstructed using inverse ICA. Furthermore, we compared the performance of the rtAAS + rtICA with two other offline artifact correction methods, consisting of removing imaging artifacts using the AAS, reducing imaging artifacts using AAS and other artifacts by means of our proposed automatic ICA-based method (this method was implemented offline, but it can be applied real-time as well). Finally, the rtAAS + rtICA results were compared with the RecView-corrected EEG data with imaging and BCG artifacts reduced in real time using the AAS.

2.7. Evaluation measures

Various evaluation metrics were used to determine the ability of the rtAAS + rtICA to reduce EEG artifacts (and, more importantly, preserve brain activity) and to compare its efficiency with that of offline correction.

2.7.1. The percentages of corrected eye blinks detected

To evaluate the algorithm performance for detecting eye blinks, EEG data were manually inspected to detect eye blinks and compare results to automatically detected eye blinks using the rtICA.

2.7.2. Power spectral density

To evaluate the rtAAS + rtICA performance given non-ideal conditions, we computed power spectral density (PSD) for all 22 EEG

Table 3
Eye blink detection results for 6 healthy subjects during eyes open resting state runs.

	Number of Eye Blinks Detected	True Number of Eye Blinks	Percentage of Eye Blinks Detected
Subject 1	190	193	98.45%
Subject 2	245	250	98.57%
Subject 3	82	84	97.62%
Subject 4	143	145	98.62%
Subject 5	71	75	94.67%
Subject 6	427	430	98.66%

channels before and after applying different artifact correction methods.

2.7.3. INPS reduction

To quantify changes and corrected improvements of BCG artifacts, the following Normalized Power Spectrum ratio (INPS) was computed as (Srivastava et al., 2005; Tong et al., 2001):

$$INPS = \frac{\sum_{i=1}^N PSD_i^{before \text{ BCG reduction}}}{\sum_{i=1}^N PSD_i^{after \text{ BCG reduction}}} \quad (4)$$

where N is the number of harmonics of ECG and PSD_i is the power spectral density of the i th ECG harmonic.

2.7.4. Power reduction in motion traces

Motion artifacts affect power spectrum significantly. To determine the efficiency of the rtAAS + rtICA for reducing such artifacts, we compared the power between 0.488 and 40.039 Hz using different algorithm in traces which were contaminated with motion artifacts.

3. Results

Fig. 5 shows a 4 s long segment of RecView-corrected EEG data (i.e., 22 channels) acquired simultaneously with fMRI, as well as the same trace of raw EEG recordings after removing imaging artifacts, rtAAS + rtICA corrected signal, AAS for imaging artifacts and automatic ICA corrected EEG data, and, finally, the clean EEG data using the proposed offline procedure.

Fig. 6 shows 22 ICs retrieved from RecView-corrected data with SOBI using equivalent traces presented in Fig. 5. In this example, IC 2, 5, and 6 were identified as eye artifact; IC 1, 3, and 7 were classified as residual BCG artifact; and IC22 were determined as a vibration noise at 26 Hz.

Table 3 shows the number of eye blinks detected using automatic rtICA method, as well as the number of actual blinks. Also detailed is the percentage of correctly detected eye blinks for the second and fourth runs (i.e. eyes open runs) for the six healthy subjects. The results demonstrate that rtICA effectively removes eye blink artifacts. Accurately detected eye blinks for all subjects were more than 94%.

Fig. 7 compares the performance of the BrainVision rtAAS, the rtAAS + rtICA and the offline methods in terms of INPS ratio. The INPS ratios for artifact correction methods were computed with respect to the EEG data obtained after removing imaging artifacts via offline AAS.

Fig. 8 demonstrates that, for most subjects, the rtAAS could not reduce effects of motion artifact on power value. However, the rtAAS + rtICA and the offline automatic ICA can reduce power during motion traces and can make it approximate the power value based on the offline AAS + Filtering + ICA artifact correction. The rtICA can significantly reduce effect of motion artifacts in all subjects.

Fig. 9 provides an example of the power spectral density of EEG data for a subject during eyes closed run using various artifact removal algorithms and shows that the rtAAS + rtICA can effectively

reduce artifacts in different EEG frequency bands without affecting the neuronal alpha and beta activities.

Finally, Fig. 10 illustrates the power in several EEG bands before and after artifact correction. From Fig. 10(a), it can be observed that, for all subjects, the RecView-corrected EEG data have the highest power value in the delta frequency band when compared to the rtAAS + rtICA and two other artifact correction methods. The rtAAS + rtICA and offline automatic ICA methods reduce this power and make it approximate the EEG data after using the AAS + Filtering + ICA artifact correction. Notably, the delta power reflected mostly ocular and motion artifacts. Fig. 10(b) demonstrates theta power of corrected EEG data using a number of algorithms. BCG artifacts affect the theta band power. Again, the rtAAS + rtICA can reduce artifacts more effectively than only the rtAAS and the offline automatic ICA. Muscle and residual imaging artifacts primarily affect amplitude of power spectrum in the beta frequency band. It is critical that the rtICA algorithm not mistakenly remove brain activity, a significant portion of which is reflected in the alpha band power, shown in Fig. 10(c). The figure illustrates that even though the alpha power value was reduced using the rtAAS + rtICA and offline automatic ICA, the value does not dip below alpha power using the offline AAS + Filtering + ICA artifact correction. This amount serves as our reference for nearly-artifact-free EEG data. Furthermore, Fig. 10(c) and (d) demonstrate that without the rtAAS, the rtICA performs poorly when used to reduce effects of artifacts on the alpha and beta frequency bands. From Fig. 10(d), we can observe that the rtAAS + rtICA could more effectively reduce such artifacts when compared to the performance of the rtAAS and rtICA.

4. Discussion

Few methods have been developed for real-time removal of BCG and imaging artifacts from EEG data recorded during fMRI. This has limited the application of real-time EEG-fMRI systems. We propose a novel algorithm based on ICA for attenuating all types of artifact in EEG data acquired during fMRI scans. The proposed real-time ICA method can further be utilized for any application requiring real-time ICA decomposition.

Although the rtAAS is supposed to reduce BCG artifacts, we can see in Fig. 7 that the average INPS value is less than zero for two subjects when using the rtAAS. Averaging the INPS among six subjects shows 4.4 times larger INPS reduction was achieved by using rtAAS + rtICA compared to rtAAS. For subject 1, the enormous amount of motion artifacts prevents the RecView from performing well. Furthermore, the ECG signal from subjects 1 and 4 are severely distorted, which makes detecting R-peak and creating accurate BCG artifact template in real time impossible. Except for subject 4, INPS reduction by the rtAAS + rtICA and offline automatic ICA is comparable with that of the AAS + Filtering + ICA method. The poor performance of the rtAAS + rtICA in terms of INPS for subject 4 could be the result of the low performance of the rtAAS.

Eye blink, motion and muscle artifacts are problematic and obscure the EEG signal quality significantly, but so far, there is no robust real-time method for removing such artifacts. The results of removing such artifacts in Table 3, Figs. 8 and 10(d) show that the rtICA can substantially reduce effects of these artifacts on EEG signal.

Based on evaluation metrics, the rtAAS + rtICA has superior performance when compared to the rtAAS and the rtICA. One reason for this phenomenon is that either the ICA or AAS might not effectively reduce BCG and imaging artifacts for some subjects. Thus, both methods complement each other when removing imaging, BCG, and other artifacts.

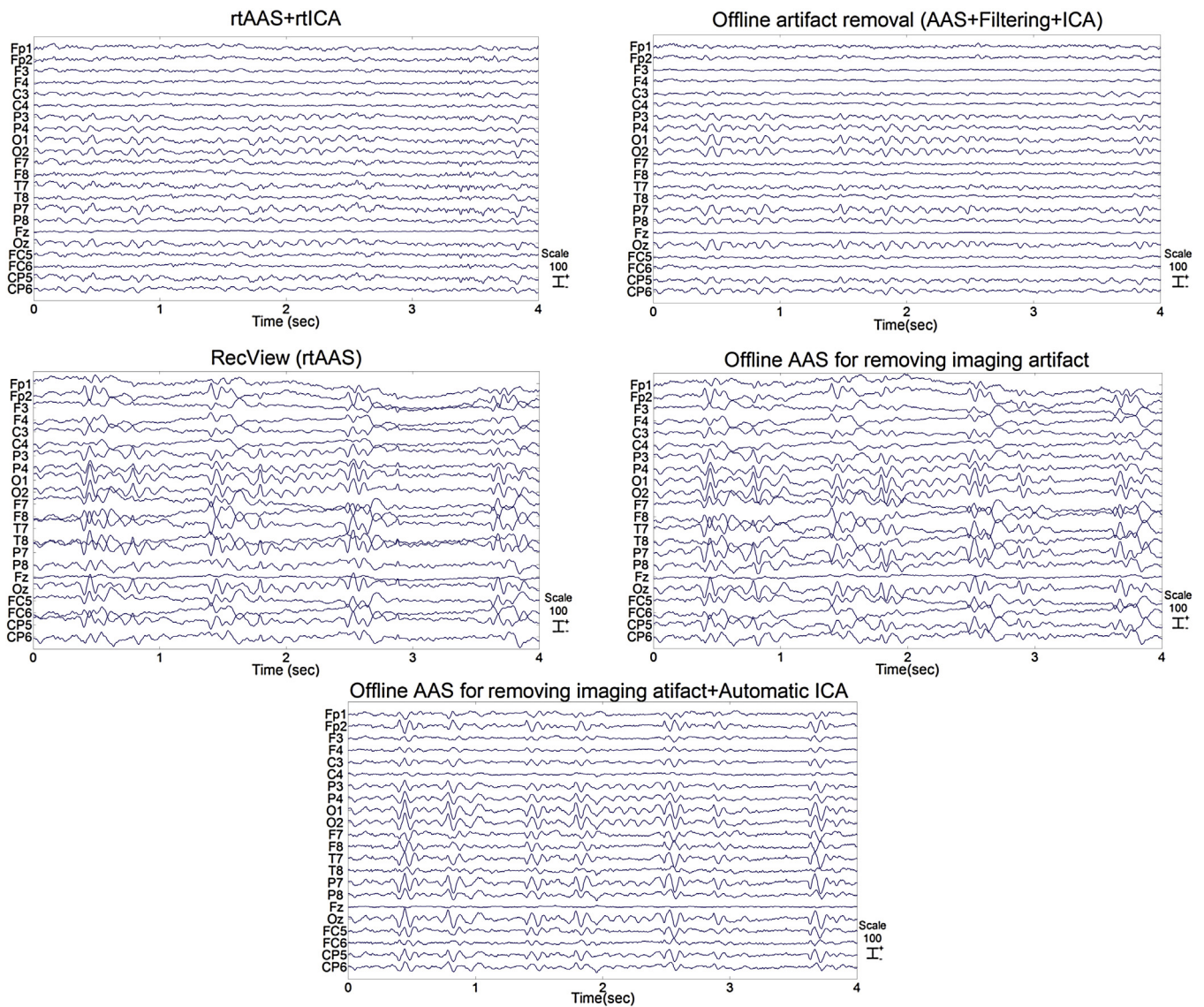


Fig. 5. Representative 4-s example traces of EEG data recorded during fMRI acquisition (subject 4 during eyes open run) after applying different offline and real-time artifact correction methods.

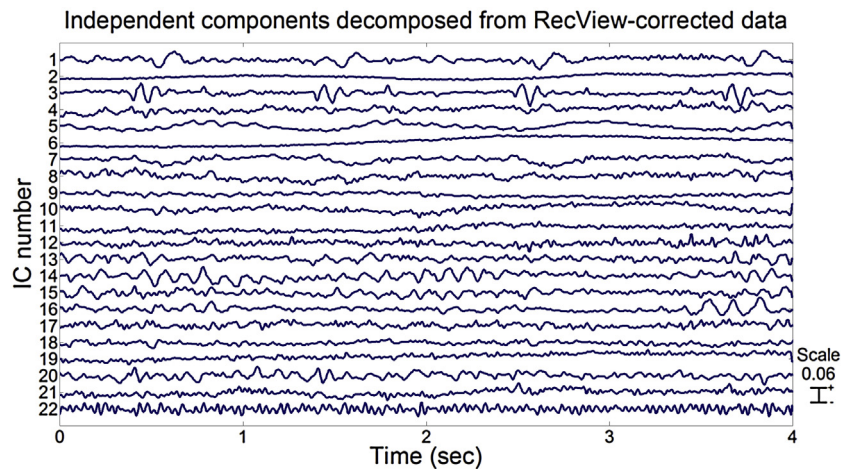


Fig. 6. 22 ICs decomposed from 22 channels RecView-corrected EEG data (the same trace as Fig. 5) using rtICA in real time.

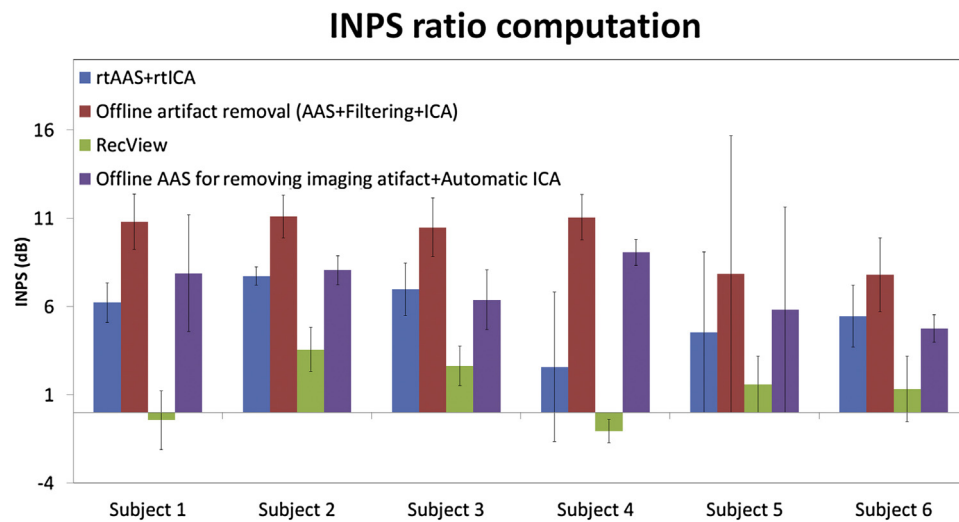


Fig. 7. INPS Reduction for all channels using different artifact correction methods versus the EEG data after removing imaging artifacts.

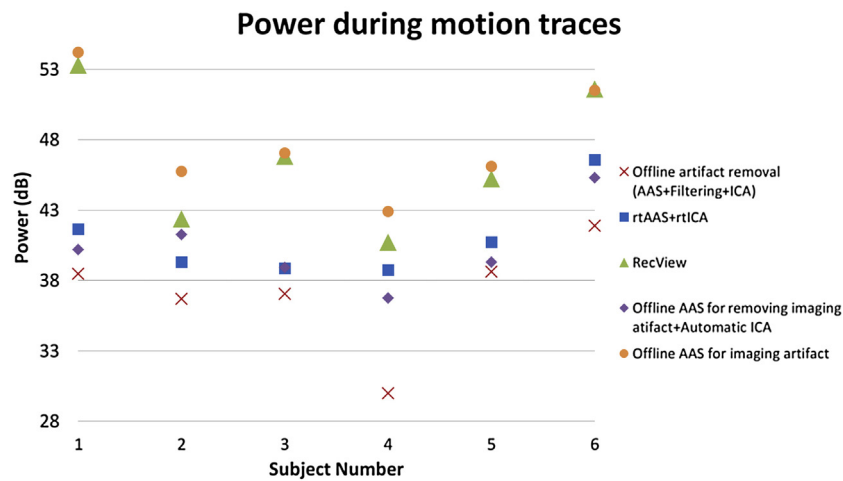


Fig. 8. Compression of power during motion traces using AAS + rtICA, RecView and offline artifact correction methods with power without any correction (EEG data after applying AAS for imaging artifact correction).

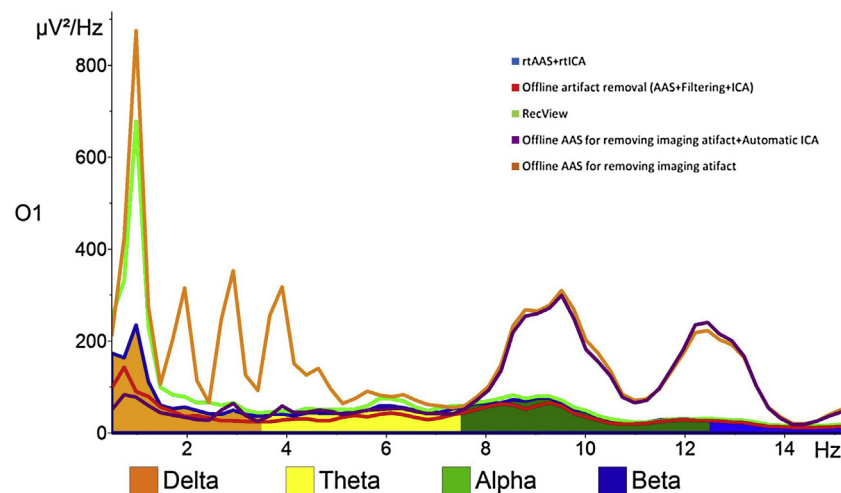


Fig. 9. An example of power spectral density of electrode O1 (for subject 2) during eyes-closed runs using different artifact removal algorithms.

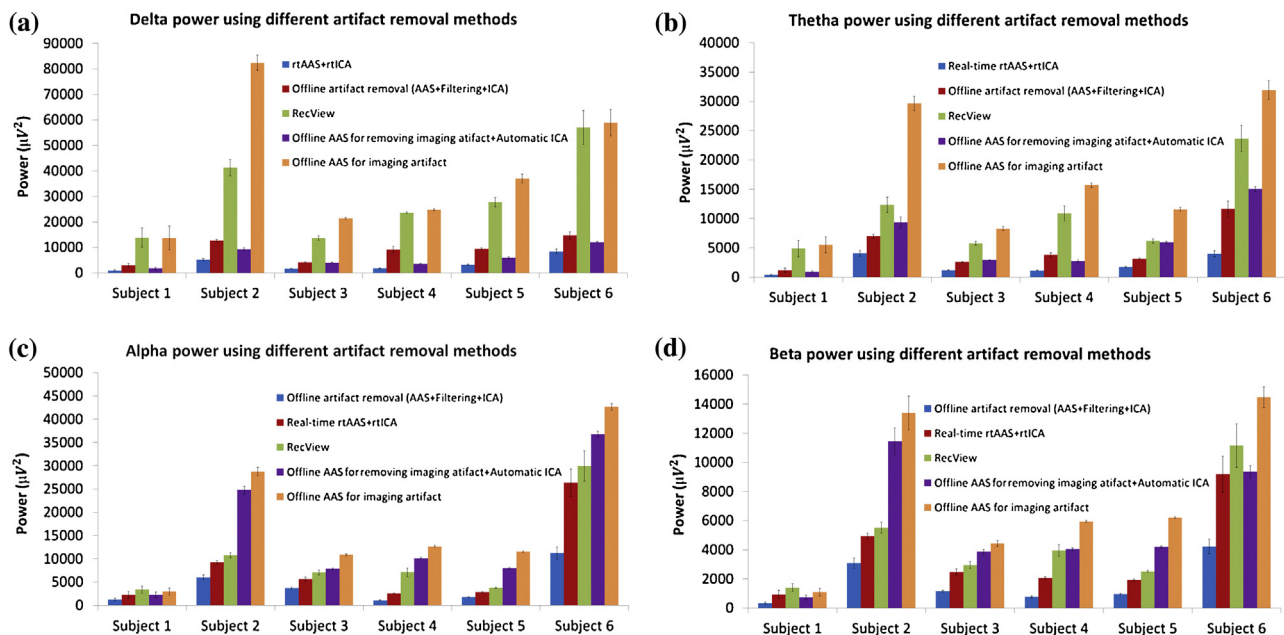


Fig. 10. The impact of different artifact correction on EEG power in (a) delta (b) theta (c) alpha and (d) beta frequency bands. Bar heights represent averages across channels, and error bars represent the standard error across ICA windows. Results are shown for all 6 subjects using average data from all 22 channels and all 4 resting state runs.

It is likely that our proposed real-time technique might not perform as efficiently as offline artifact detection techniques. Admittedly, several factors can lessen the method efficiency and can be further optimized. The most important factor is the accuracy of the real-time IC classification that separates various artifacts from the ICs describing neuronal activity. The classification criteria and numerical threshold settings used in this work will need to be optimized and refined further. For instance, recording test data before starting the actual experiment and using the test data as an input for a machine learning algorithm for classifying brain activity and artifact ICs may improve the efficiency of the method. Using mutual information appears helpful in this regard (Abbasi et al., 2015; Liu et al., 2012). Another important factor is the algorithm speed. When the algorithm is implemented in MATLAB, less than 1 s is required for removing artifacts from 4 s of EEG data; between 2 s and 4 s is required for this when running our stand-alone and proof-of-concept software implementation written in Python. Performing the ICA decomposition using the SOBI requires the greatest amount of time. Thus, implementing this particular code (i.e., ICA decomposition using the SOBI) in Cython (Behnel et al., 2011) or assisting C might aid in speeding up the algorithm. By increasing the method speed, we can apply ICA on 31 channels instead of 22 channels. This could improve the performance of the method for artifact correction. The recent study demonstrates that Online Recursive ICA (ORICA) can be successfully implemented in real time for source separation, but more investigations are needed to evaluate the ORICA efficiency for distinguishing ICs related to artifacts from brain activities (Hsu et al., 2016). Even though still there are opportunities to speed up the algorithm, the method can be used for real-time neurofeedback application and real-time monitoring of brain activity since the rtICA updates EEG results in the comparable time with fMRI (which is equal to TR).

5. Conclusion

Recording EEG during fMRI acquisition leads to EEG data contamination with large fMRI environment artifacts. Most EEG-fMRI studies have reduced artifacts offline; however only a few have involved real-time correction. We have introduced ICA-based real-

time EEG artifact correction during fMRI. This novel approach was successfully implemented and improved real-time EEG artifacts detection and removal during fMRI on all 6 healthy subjects. The proposed algorithm can be effectively implemented for various applications that require a real-time EEG signal with artifacts suppressed (e.g., neurofeedback and online monitoring of brain activity). Our work represents an important first step towards a wider use of ICA methods in real-time EEG-fMRI applications, such as determining the (functional) neural correlates of the EEG rhythms used in rtEEG neurofeedback and rtfMRI data.

Acknowledgment

This work was supported by the U.S. Department of Defense grant W81XWH-12-1-0607.

References

- Abbasi, O., Dammers, J., Arrubla, J., Warbrick, T., Butz, M., Neuner, I., Shah, N.J., 2015. Time-frequency analysis of resting state and evoked EEG data recorded at higher magnetic fields up to 9.4 T. *J. Neurosci. Methods* 255, 1–11.
- Akhtar, M.T., Mitsuhashi, W., James, C.J., 2012. Employing spatially constrained ICA and wavelet denoising for automatic removal of artifacts from multichannel EEG data. *Signal Process.* 92, 401–416.
- Allen, P.J., Polizzi, G., Krakow, K., Fish, D.R., Lemieux, L., 1998. Identification of EEG events in the MR scanner: the problem of pulse artifact and a method for its subtraction. *Neuroimage* 8, 229–239.
- Allen, P.J., Josephs, O., Turner, R., 2000. A method for removing imaging artifact from continuous EEG recorded during functional MRI. *Neuroimage* 12, 230–239.
- Bénar, C.G., Aghakhani, Y., Wang, Y., Izenberg, A., Al-Asmi, A., Dubeau, F., Gotman, J., 2003. Quality of EEG in simultaneous EEG-fMRI for epilepsy. *Clin. Neurophysiol.* 114, 569–580.
- Becker, R., Ritter, P., Villringer, A., 2008. Influence of ongoing alpha rhythm on the visual evoked potential. *Neuroimage* 39, 707–716.
- Becker, R., Reinacher, M., Freyer, F., Villringer, A., Ritter, P., 2011. How ongoing neuronal oscillations account for evoked fMRI variability. *J. Neurosci.* 31, 11016–11027.
- Behnel, S., Bradshaw, R., Citro, C., Dalcin, L., Seljebotn, D.S., Smith, K., 2011. Cython: the best of both worlds. *Comput. Sci. Eng.* 13, 31–39.
- Bell, A.J., Sejnowski, T.J., 1995. An information-maximization approach to blind separation and blind deconvolution. *Neural Comput.* 7, 1129–1159.
- Belouchrani, A., Abed-Meraim, K., Cardoso, J.-F., Moulines, E., 1997. A blind source separation technique based on second-order statistics. *IEEE Trans. Signal Process.* 45, 434–444.

- Bonmassar, G., Purdon, P.L., Jääskeläinen, I.P., Chiappa, K., Solo, V., Brown, E.N., Belliveau, J.W., 2002. Motion and ballistocardiogram artifact removal for interleaved recording of EEG and EPs during MRI. *Neuroimage* 16, 1127–1141.
- Cavazza, M., Aranyi, G., Charles, F., Porteous, J., Gilroy, S., Klovatch, I., Jackont, G., Soreq, E., Keynan, N.J., Cohen, A., Raz, G., Hendler, T., 2014. Towards empathic neurofeedback for interactive storytelling. *OpenAccess Ser. Inform.* 41, 42–60.
- Debener, S., Mullinger, K.J., Niazy, R.K., Bowtell, R.W., 2008. Properties of the ballistocardiogram artifact as revealed by EEG recordings at 1.5, 3 and 7 T static magnetic field strength. *Int. J. Psychophysiol.* 67, 189–199.
- Delorme, A., Makeig, S., 2004. EEGLAB: an open source toolbox for analysis of single-trial EEG dynamics including independent component analysis. *J. Neurosci. Methods* 134, 9–21.
- Dunseath, W.J.R., Alden, T.A., 2010. Apparatus and method for acquiring a signal. U.S. Patent 7715894.
- Hsu, S., Mullen, T.R., Jung, T., Cauwenberghs, G., 2016. Real-time adaptive EEG source separation using online recursive independent component analysis. *IEEE Trans. Neural Syst. Rehabil. Eng.* 24, 309–319.
- Jorge, J., Grouiller, F., Gruetter, R., Van Der Zwaag, W., Figueiredo, P., 2015. Towards high-quality simultaneous EEG-fMRI at 7 T: detection and reduction of EEG artifacts due to head motion. *Neuroimage* 120, 143–153.
- Kim, K.H., Yoon, H.W., Park, H.W., 2004. Improved ballistocardiographic artifact removal from the electroencephalogram recorded in fMRI. *J. Neurosci. Methods* 135, 193–203.
- Klemm, M., Hauelsen, J., Ivanova, G., 2009. Independent component analysis: comparison of algorithms for the investigation of surface electrical brain activity. *Med. Biol. Eng. Comput.* 47, 413–423.
- Kruggel, F., Wiggins, C.J., Herrmann, C.S., von Cramon, D.Y., 2000. Recording of the event-related potentials during functional MRI at 3.0 T field strength. *Magn. Reson. Med.* 44, 277–282.
- Laufs, H., 2012. A personalized history of EEG-fMRI integration. *Neuroimage* 62, 1056–1067.
- Liu, Z., de Zwart, J.A., van Gelderen, P., Kuo, L.W., Duyn, J.H., 2012. Statistical feature extraction for artifact removal from concurrent fMRI-EEG recordings. *Neuroimage* 59, 2073–2087.
- Luo, Q., Huang, X., Glover, G.H., 2014. Ballistocardiogram artifact removal with a reference layer and standard EEG cap. *J. Neurosci. Methods* 233, 137–149.
- Mantini, D., Perrucci, M.G., Cugini, S., Ferretti, A., Romani, G.L., Del Gratta, C., 2007. Complete artifact removal for EEG recorded during continuous fMRI using independent component analysis. *Neuroimage* 34, 598–607.
- Masterton, R.A.J., Abbott, D.F., Fleming, S.W., Jackson, G.D., 2007. Measurement and reduction of motion and ballistocardiogram artefacts from simultaneous EEG and fMRI recordings. *Neuroimage* 37, 202–211.
- Mayeli, A., Zotev, V., Refai, H., Bodurka, J., 2015. An automatic ICA-based method for removing artifacts from EEG data acquired during fMRI in real time. *IEEE 41st Annual Northeast Biomedical Engineering Conference (NEBEC)*.
- McMenamin, B.W., Shackman, A.J., Maxwell, J.S., Bachhuber, D.R.W., Koppenhaver, A.M., Greischar, L.L., Davidson, R.J., 2010. Validation of ICA-based myogenic artifact correction for scalp and source-localized EEG. *Neuroimage* 49, 2416–2432.
- Nakamura, W., Anami, K., Mori, T., Saitoh, O., Cichocki, A., Amari, S., 2006. Removal of ballistocardiogram artifacts from simultaneously recorded EEG and fMRI data using independent component analysis. *IEEE Trans. Biomed. Eng.* 53, 1294–1308.
- Negishi, M., Abildgaard, M., Nixon, T., Constable, R.T., 2004. Removal of time-varying gradient artefacts during continuous fMRI. *Clin. Neurophysiol.* 115, 2181–2192.
- Niazy, R.K., Beckmann, C.F., Iannetti, G.D., Brady, J.M., Smith, S.M., 2005. Removal of fMRI environment artifacts from EEG data using optimal basis sets. *Neuroimage* 28, 720–737.
- Onton, J., Westerfield, M., Townsend, J., Makeig, S., 2006. Imaging human EEG dynamics using independent component analysis. *Neurosci. Biobehav. Rev.* 30, 808–822.
- Ritter, P., Villringer, A., 2006. Simultaneous EEG-fMRI. *Neurosci. Biobehav. Rev.* 30, 823–838.
- Srivastava, G., Crottaz-Herbette, S., Lau, K.M., Glover, G.H., Menon, V., 2005. ICA-based procedures for removing ballistocardiogram artifacts from EEG data acquired in the MRI scanner. *Neuroimage* 24, 50–60.
- Tong, S., Bezerianos, A., Paul, J., Zhu, Y., Thakor, N., 2001. Removal of ECG interference from the EEG recordings in small animals using independent component analysis. *J. Neurosci. Methods* 108, 11–17.
- van der Meer, J.N., Pampel, A., Van Someren, E.J., Ramautar, J.R., van der Werf, Y.D., Gomez-Herrero, G., Lepsien, J., Hellrung, L., Hinrichs, H., Möller, H.E., Walter, M., 2016. Carbon-wire loop based artifact correction outperforms post-processing EEG/fMRI corrections—a validation of a real-time simultaneous EEG/fMRI correction method. *Neuroimage* 125, 880–894.
- Vanderperren, K., De Vos, M., Ramautar, J.R., Novitskiy, N., Mennes, M., Asseconci, S., Vanrumste, B., Stiers, P., Van den Bergh, B.R., Wagemans, J., Lagae, L., Sunaert, S., Van Huffel, S., 2010. Removal of BCG artifacts from EEG recordings inside the MR scanner: a comparison of methodological and validation-related aspects. *Neuroimage* 50, 920–934.
- Wong, C.K., Zotev, V., Misaki, M., Phillips, R., Luo, Q., Bodurka, J., 2016. Automatic EEG-assisted retrospective motion correction for fMRI (aE-REMCOR). *Neuroimage* 129, 133–147.
- Wu, X., Wu, T., Zhan, Z., Yao, L., Wen, X., 2016. A real-time method to reduce ballistocardiogram artifacts from EEG during fMRI based on optimal basis sets (OBS). *Comput. Methods Progr. Biomed.* 127, 114–125.
- Yuan, H., Zotev, V., Phillips, R., Bodurka, J., 2013. Correlated slow fluctuations in respiration, EEG, and BOLD fMRI. *Neuroimage* 79, 81–93.
- Zhou, W., Gotman, J., 2004. Removal of EMG and ECG artifacts from EEG based on wavelet transform and ICA. *Conference Proceedings. IEEE Engineering in Medicine and Biology Society*, 392–395.
- Zich, C., Debener, S., Kranczioch, C., Bleichner, M.G., Gutberlet, I., De Vos, M., 2015. Real-time EEG feedback during simultaneous EEG-fMRI identifies the cortical signature of motor imagery. *Neuroimage* 114, 438–447.
- Zotev, V., Yuan, H., Phillips, R., Bodurka, J., 2012. EEG-assisted retrospective motion correction for fMRI: E-REMCOR. *Neuroimage* 63, 698–712.
- Zotev, V., Phillips, R., Yuan, H., Misaki, M., Bodurka, J., 2014. Self-regulation of human brain activity using simultaneous real-time fMRI and EEG neurofeedback. *Neuroimage* 85, 985–995.
- Zotev, V., Yuan, H., Misaki, M., Phillips, R., Young, K.D., Feldner, M.T., Bodurka, J., 2016. Correlation between amygdala BOLD activity and frontal EEG asymmetry during real-time fMRI neurofeedback training in patients with depression. *Neuroimage: Clin.* 11, 224–238.



Connectome-wide investigation of altered resting-state functional connectivity in war veterans with and without posttraumatic stress disorder

Masaya Misaki^a, Raquel Phillips^a, Vadim Zotev^a, Chung-Ki Wong^a, Brent E. Wurfel^{a,b}, Frank Krueger^c, Matthew Feldner^d, Jerzy Bodurka^{a,e,*}

^a Laureate Institute for Brain Research, Tulsa, OK, United States

^b Laureate Psychiatric Clinic and Hospital, Tulsa, OK, United States

^c School of Systems Biology, George Mason University, Fairfax, VA, United States

^d Dept. of Psychological Science, University of Arkansas, Fayetteville, AR, United States

^e Stephenson School of Biomedical Engineering, University of Oklahoma, Norman, OK, United States

ARTICLE INFO

Keywords:

Posttraumatic stress disorder
Resting-state functional connectivity
Multivariate distance-based matrix regression
Connectome-wide association study
fMRI

ABSTRACT

Altered resting-state functional connectivity in posttraumatic stress disorder (PTSD) suggests neuropathology of the disorder. While seed-based fMRI connectivity analysis is often used for the studies, such analysis requires defining a seed location *a priori*, which restricts search scope and could bias findings toward presupposed areas. Recently, a comprehensive exploratory voxel-wise connectivity analysis, the connectome-wide association approach, has been introduced using multivariate distance matrix regression (MDMR) for resting-state functional connectivity analysis. The current study performed a connectome-wide investigation of resting-state functional connectivity for war veterans with and without PTSD compared to non-trauma-exposed healthy controls using MDMR.

Thirty-five male combat veterans with PTSD (unmedicated), 18 male combat veterans without PTSD (veterans control, VC), and 28 age-matched non-trauma-exposed healthy males (NC) participated in a resting-state fMRI scan. MDMR analysis was used to identify between-groups differences in regions with altered connectivity. The identified regions were used as a seed for post-hoc functional connectivity analysis.

The analysis revealed that PTSD patients had hypoconnectivity between the left lateral prefrontal regions and the salience network regions as well as hypoconnectivity between the parahippocampal gyrus and the visual cortex areas. Connectivity between the ventromedial prefrontal cortex and the middle frontal gyrus and between the parahippocampal gyrus and the anterior insula were negatively correlated with PTSD symptom severity. VC subjects also had altered functional connectivity compared to NC, including increased connectivity between the posterior insula and several brain regions and decreased connectivity between the precuneus region and several other brain areas.

The decreased connectivity between the lateral prefrontal regions and the salience network regions in PTSD was consistent with previous reports that indicated lowered emotion-regulation function in these regions. The decreased connectivity between the parahippocampal gyrus and visual cortex supported the dual representation theory of PTSD, which suggests dissociation between sensory and contextual memory representations in PTSD. The theory also supposes that the precuneus is a region that triggers retrieval of sensory memory of traumatic events. The decreased connectivity at the precuneus for VC might be associated with suppressing such a process.

1. Introduction

Posttraumatic stress disorder (PTSD) is one of the most prevalent mental disorders for war veterans. A screening for mental health problems by the US military suggested 9.8% of veterans returning from Iraq, 4.7% from Afghanistan, and 2.1% from other locations were at risk of PTSD (Hoge et al., 2006). Several studies have suggested a

biological basis for PTSD (Pitman et al., 2012 for review), including neuroimaging studies (e.g., Hayes et al., 2012; Lanius et al., 2006; Liberzon and Sripada, 2008; Patel et al., 2012). Nonetheless, ongoing research is needed to better understand the complex neurobiological abnormalities that underlie this costly and chronic condition.

One of the types of neuroimaging studies that is providing abundant insights into the neuropathology of intrinsic brain activity in PTSD is

* Corresponding author at: Laureate Institute for Brain Research, Tulsa, OK, United States.
E-mail address: jbodurka@laureateinstitute.org (J. Bodurka).

<http://dx.doi.org/10.1016/j.nicl.2017.10.032>

Received 4 April 2017; Received in revised form 18 October 2017; Accepted 28 October 2017

Available online 31 October 2017

2213-1582/ © 2017 The Authors. Published by Elsevier Inc. This is an open access article under the CC BY-NC-ND license (<http://creativecommons.org/licenses/by-nc-nd/4.0/>).

resting-state functional magnetic resonance imaging (rsfMRI), which measures blood oxygenation level dependent (BOLD) signal while a subject does not perform any explicit task. This includes studies using voxel-wise resting-state signal measurement such as amplitude of low-frequency fluctuation (ALFF) (Zou et al., 2008) and regional homogeneity (ReHo) (Zang et al., 2004). Meta-analyses of these studies combined with positron emission tomography (PET) studies (Koch et al., 2016; Wang et al., 2016) showed that PTSD patients had increased resting-state signal fluctuation or activity in the amygdala and the parahippocampal gyrus and decreased fluctuation or activity in the superior frontal gyrus and the middle frontal gyrus, although there is significant variability across studies. Decomposition of spatial coactivation patterns, such as independent component analysis (ICA), was also used in an rsfMRI study (Calhoun and Adali, 2012). Although ICA is typically employed to extract the spatial pattern of a functional network, it can also be used to evaluate connectivity with a dual regression technique (Filippini et al., 2009), in which correlations between the global network (independent component) time-course and voxel-wise time-courses are examined. Tursich et al. (2015) indicated that the connectivity of the salience network (SN) with the posterior insula and the superior temporal gyrus were negatively correlated with hyperarousal symptoms in PTSD. Graph analysis for resting-state connectivity (Fornito et al., 2013) was also employed in an rsfMRI study of PTSD (Lei et al., 2015), indicating that the resting-state functional network for PTSD shifted toward small-worldization with increased centrality in the default-mode network (DMN) and the SN.

Another commonly employed measure of rsfMRI is functional connectivity (Friston, 1994), which evaluates the correlation of signal time-courses between a seed region and other brain regions. Seed-based connectivity analyses also showed aberrant resting-state connectivity for PTSD. Brown et al. (2014) indicated increased connectivity between the basolateral amygdala and the anterior cingulate cortex (ACC), dorsal ACC, and dorsomedial prefrontal cortex as well as decreased connectivity between the amygdala and the left inferior frontal gyrus for PTSD patients compared to trauma-exposed controls. Zhang et al. (2016) found decreased connectivity between the ventral anterior insula and the ACC, and between the right posterior insula and the left inferior parietal lobe and the postcentral gyrus. Kennis et al. (2015) showed decreased connectivity between the caudal ACC and the precentral gyrus and between the perigenual ACC and the superior medial frontal gyrus and middle temporal gyrus.

These findings suggest several converging regions of pathological resting-state activity or connectivity for PTSD such as hyperactivity and increased connectivity in the SN regions, including the amygdala, anterior insula, and ACC, and hypoactivity and decreased connectivity in the prefrontal emotion-regulation areas including lateral prefrontal regions and dorsal and ventral medial prefrontal regions. Deficits in emotion regulation function due to hyperactive and hyperconnected SN and its hypoconnectivity with lateral prefrontal regions are thought to underlie the hyperarousal symptoms of PTSD (Fonzo et al., 2010; Lanius et al., 2006; Zhu et al., 2015).

A limitation of previous functional connectivity studies, however, is that seed-based resting-state connectivity analysis requires the a priori definition of a seed location. This restricts the scope of investigation to relations with the presupposed seed area and could bias findings toward the seed area. In particular, a priori predictions about the functioning of regions implicated in emotion regulation may have resulted in the overrepresentation of these regions in our current understanding of resting state functional connectivity in PTSD. Indeed, abnormal brain functioning in PTSD is not limited to the emotion regulation network. Task-based fMRI studies have suggested abnormal functioning in regions implicated in attention and working memory (Aupperle et al., 2012) as well as memory representation (Brewin, 2011; Whalley et al., 2013), such as the medial temporal and posterior brain regions including hippocampal, parietal, and occipital areas. Those low-level sensorimotor regions are rarely identified as seeds for functional connectivity

analyses in studies of PTSD. While voxel-wise whole-brain investigations of resting-state activity with ALFF, ReHo, and PET (Bonne et al., 2003; Kohn et al., 2014; Wang et al., 2016) often suggested altered resting-state activity in the sensorimotor, visual cortex, and hippocampal/parahippocampal areas, these measures did not elucidate functional connectivity of the regions. Connectivity analysis using ICA also does not capture region-by-region functional connectivity. Instead, it analyzes connectivity between a global brain network and a voxel-wise signal.

To complement these analyses, and to resolve the limitation of seed-based connectivity analysis, yet another rsfMRI analysis has been proposed: a connectome-wide approach that investigates comprehensive voxel-wise connectivity alterations (Shehzad et al., 2014). This approach utilizes a multivariate distance matrix regression (MDMR) analysis (Anderson, 2001) and can examine voxel-wise connectivity alterations in the whole brain without a priori seed definition. Satterthwaite et al. (2015) applied this analysis to major depressive disorder (MDD), PTSD, and female healthy control subjects and found that decreased connectivity between the amygdala and the dorsolateral prefrontal cortex, ACC, and anterior insula correlated with depression symptom severity. They also showed that elevated connectivity between the amygdala and the ventromedial prefrontal cortex correlated with anxiety symptom severity.

The aim of this study was to examine altered resting-state connectivity of male war veterans with and without PTSD and male age-matched non-trauma-exposed healthy controls using a connectome-wide approach. We expected connectome-wide investigation of altered resting-state functional connectivity to reveal a comprehensive view of the neuropathology of intrinsic brain functional connectivity among people with PTSD without bias introduced via hypothesis testing.

In addition to examining veterans with combat-related PTSD, we also examined altered resting-state connectivity among combat veterans without PTSD. While a population with trauma experience without PTSD has often been considered a control group for understanding atypical functioning among people with PTSD, several studies have demonstrated atypical brain activation in this group compared to non-trauma-exposed people. For example, war-deployed soldiers who did not develop PTSD showed lowered midbrain activation in a working memory task and decreased connectivity between the midbrain region and the prefrontal cortex compared to non-deployed soldiers (van Wingen et al., 2012). Meta-analysis of region-wise resting-state brain activation (Patel et al., 2012) indicated higher prefrontal activity among trauma-exposed people without PTSD compared to non-trauma-exposed controls. A resting-state functional connectivity analysis with an ACC seed (Kennis et al., 2015) also indicated that war veterans without PTSD had a different pattern of resting-state connectivity compared to civilian controls. The differences include decreased connectivity between the caudal ACC and the precentral gyrus and between the perigenual ACC and the superior medial frontal and the middle temporal gyrus, and increased connectivity between the rostral ACC and precentral and middle frontal regions. These data suggest that war veterans without PTSD could have altered intrinsic brain activation compared to both people with PTSD and non-trauma-exposed controls. Importantly, altered brain functioning in PTSD and trauma-exposed controls may not be incremental. Trauma-exposed controls without PTSD could have a specific brain alteration that does not exist in PTSD, which may function as an adaptive change to trauma exposure or as a protective factor that reduces the likelihood of developing PTSD subsequent to trauma exposure. The current study, therefore, employed three groups of male subjects: war veterans with PTSD (unmedicated), war veterans without PTSD, and age-matched non-trauma-exposed healthy controls. The study examined comprehensive connectome-wide differences in resting-state functional connectivity between these groups.

Table 1

Demographic characteristics of war veterans with PTSD, war veterans without PTSD (veteran controls; VC), and non-trauma-exposed healthy controls (NC). CAPS score was not available for two PTSD and two VC subjects. PCL-M score was not available for one PTSD and two VC subjects. MADRS score was not available for one PTSD and one VC subjects. Mean \pm SD for each group and statistics for the difference between the groups are shown except for age and head motion. Both age and head motion were not significantly different between groups with ANOVA ($F(2,78) = 1.39$, $p = 0.260$ for age and $F(2,78) = 1.29$, $p = 0.281$ for motion).

	PTSD	VC	NC	PTSD - VC	PTSD - NC	VC - NC
Number of participants	35	18	28			
Age	31.9 \pm 7.1	33.4 \pm 9.5	29.0 \pm 11.0			
(range)	21–48	22–55	19–53			
CAPS	55.2 \pm 18.4	4.8 \pm 4.9	NA	$t(47) = 10.73$ $p < 0.001$		
PCL-M	48.0 \pm 14.2	19.6 \pm 2.6	NA	$t(48) = 7.87$ $p < 0.001$		
MADRS	20.4 \pm 9.6	1.4 \pm 1.8	1.5 \pm 1.9	$t(76) = 9.87$ $p < 0.001$	$t(76) = 11.43$ $p < 0.001$	$t(76) = -0.04$ $p = 0.999$
HAM-A	18.2 \pm 7.8	1.9 \pm 1.5	2.2 \pm 2.5	$t(76) = 10.17$ $p < 0.001$	$t(76) = 11.67$ $p < 0.001$	$t(76) = 0.14$ $p = 0.989$
Motion (average FD)	0.06 \pm 0.03	0.07 \pm 0.02	0.05 \pm 0.02			

Abbreviations: CAPS: Clinician-Administered PTSD Scale, PCL-M: PTSD Checklist - military version, MADRS: Montgomery-Asberg Depression Scale, HAM-A: Hamilton Anxiety Rating Scale, FD: frame-wise displacement of fMRI images (mm/volume), NA: not available.

2. Material and methods

2.1. Participants

Thirty-nine male combat veterans with PTSD and 22 male combat veterans without PTSD (veterans control, VC) participated in the resting-state fMRI scan as part of a neurofeedback training study (to be published separately). In addition, 28 age-matched non-trauma-exposed healthy males who had participated in another study (Misaki et al., 2016) were employed as non-trauma-exposed healthy controls (NC). Four PTSD and 4 VC participants were excluded from the analysis due to excessive head motion (> 40 censored time points, see below). Table 1 shows numbers of analyzed participants and mean ages for each group. There was no significant age difference between the groups. The study was approved by the Western Institutional Review Board, Puyallup, WA. All procedures with human subjects were conducted according to the code of ethics of the World Medical Association (Declaration of Helsinki) for experiments involving humans. All subjects gave written informed consent to participate in the study and received financial compensation.

The psychiatric diagnosis was established according to Diagnostic and Statistical Manual of Mental Disorders, Fourth Edition, Text Revision (American Psychiatric Association, 2000) criteria using both the Structured Clinical Interview for DSM-IV Disorders (First et al., 1996) administered via a trained clinical interviewer and an unstructured interview with a psychiatrist. Exclusion criteria included serious suicidal ideation, psychosis, major medical or neurological disorders, general MRI exclusions, and exposure to psychotropic medications or to any medication likely to influence cerebral function or blood flow within three weeks (8 weeks for fluoxetine). Two VC subjects endorsed a history of alcohol abuse, one VC subject endorsed a history of alcohol dependence, one VC subject endorsed a history of major depressive disorder (MDD), and one VC subject endorsed a history of alcohol abuse and major depressive disorder. These morbidities for VC were fully remitted at study time. Additional exclusion criteria applied to the NC were history of war deployment or current or past personal or family (i.e., first-degree relative) history of axis I psychiatric conditions, as assessed using the Family Interview for Genetics Studies (FIGS).

2.2. Symptom measurement

PTSD symptoms were measured with the Clinician-Administered PTSD Scale (CAPS) for DSM-IV (Blake et al., 1995) and the PTSD Checklist - Military Version (PCL-M) (Weathers et al., 1993). The CAPS

is a well-established semi-structured clinical interview that is used to determine the presence of traumatic event exposure, characteristics of the traumatic event, and frequency and severity of PTSD symptoms and diagnoses. The CAPS has excellent psychometric properties including convergent and discriminant validity, test-retest and interrater reliability, and internal consistency (Weathers et al., 2001). The CAPS was administered by research staff trained to mastery in administration of the interview. The PCL-M is a 17-item questionnaire that was used to measure DSM-IV-defined PTSD symptom severity (American Psychiatric Association, 2000). Subjects indicate the degree to which they have been bothered by each symptom in the past week on a 1 (*not at all bothered*) to 5 (*extremely bothered*) scale. The PCL-M has shown strong convergent and divergent validity (Blanchard et al., 1996; Ruggiero et al., 2003).

Depression and anxiety symptoms were also measured with the Montgomery-Asberg Depression Rating Scale (MADRS) (Montgomery and Asberg, 1979) and the Hamilton Anxiety Scale (HAM-A) (Hamilton et al., 1976), respectively. The MADRS and HAM-A are well-established measures of the severity of depressive symptoms and anxiety symptoms with adequate psychometric properties (Jiang and Ahmed, 2009; Maier et al., 1988; Montgomery and Asberg, 1979; Reimherr et al., 2010). Table 1 includes mean symptom scores for each group.

2.3. MRI measurement

The resting-state session took place prior to any task sessions. During the resting-state fMRI, participants were instructed not to move and to relax and rest while looking at a fixation cross on the screen. Magnetic resonance imaging was conducted on a whole-body 3 T MR750 MRI scanner (GE Healthcare, Milwaukee, WI) equipped with 32-channel receive-only head array coils (GE Healthcare, Nova Medical, Wilmington, MA). A single-shot gradient-recalled echo-planar imaging (EPI) sequence with sensitivity encoding (SENSE) was used for fMRI. In the study for veterans, the EPI imaging parameters were TR = 2000 ms, TE = 30 ms, FA = 90°, FOV = 240 mm, 34 axial slices with 2.9 mm thickness with 0.5 mm gap, matrix = 96 \times 96, SENSE acceleration factor R = 2. The EPI images were reconstructed into a 128 \times 128 matrix resulting 1.875 \times 1.875 \times 3.4 mm³ voxel volume. The resting fMRI run time was 6 min 50 s (205 volumes). In the study for NC subjects, the EPI imaging parameters were TR = 2000 ms, TE = 25 ms, FA = 75°, FOV = 240 mm, 34 axial slices with 2.9 mm thickness without gap, matrix = 96 \times 96, SENSE acceleration factor R = 2. The EPI images were reconstructed into a 128 \times 128 matrix resulting in 1.875 \times 1.875 \times 2.9 mm³ voxel volume. The resting fMRI run time was 7 min 30 s (225 volumes). We used only the first 205

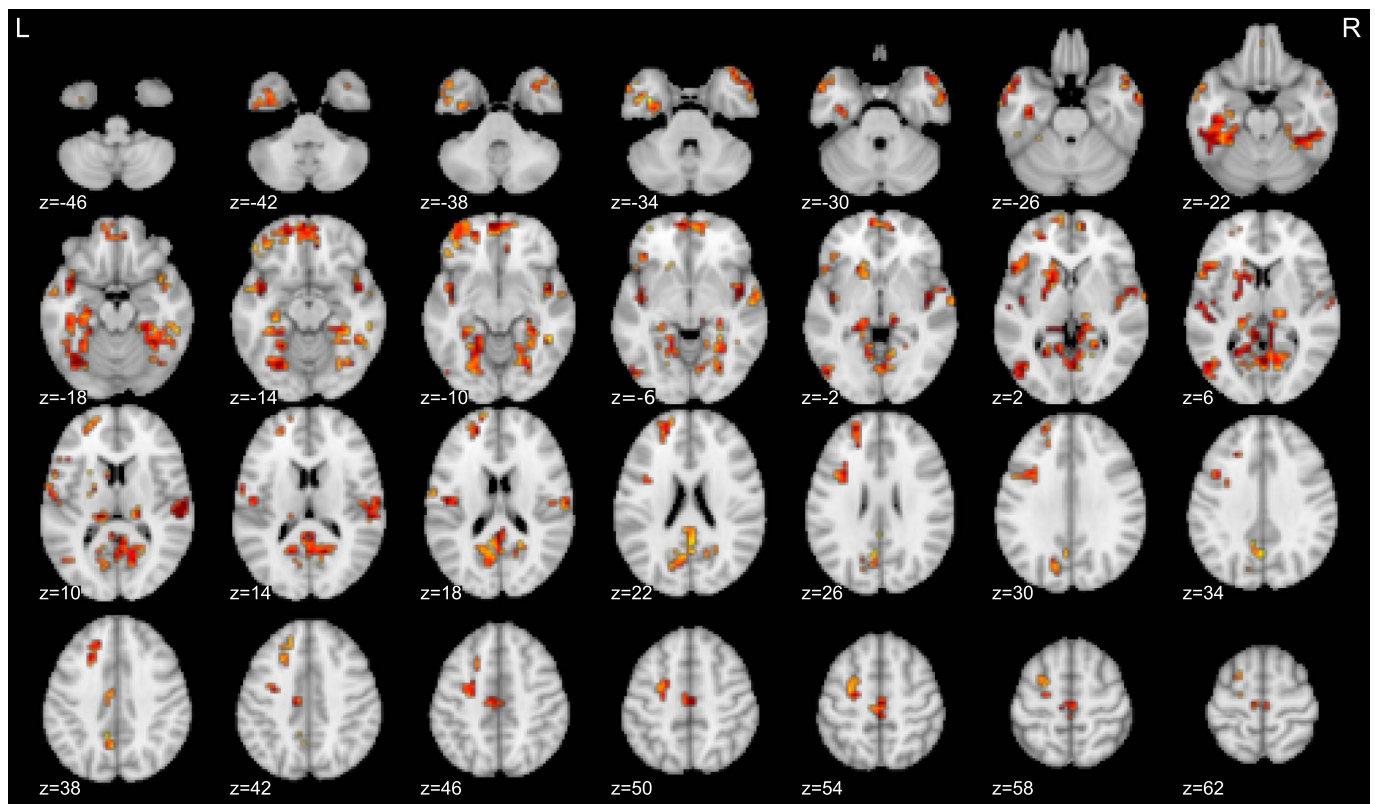


Fig. 1. MDMR pseudo- F value map for the main effect of groups (PTSD, VC, NC) thresholded with voxel-wise $p < 0.005$ and cluster-size $p < 0.05$.

volumes for the analysis to equate the number of volumes between the studies. Physiological pulse oximetry and respiration waveforms were simultaneously recorded (40 Hz) in both studies. A photoplethysmograph with an infrared emitter placed under the pad of a participant's finger was used for pulse oximetry, and a pneumatic respiration belt was used for respiration measurements.

To provide anatomical reference for fMRI data, T1-weighted MRI images were acquired with a magnetization-prepared rapid gradient-echo (MPRAGE) sequence. The following parameters were used: FOV = 240×192 mm, matrix = 256×256 , 120 axial slices, slice thickness = 0.9 mm, $0.9375 \times 0.9375 \times 0.9$ mm³ voxel volume, TR = 5 ms, TE = 2.0 ms, $R = 2$, flip angle = 8°, delay time = 1400 ms, inversion time = 725 ms, sampling bandwidth = 31.2 kHz, scan time = 5 min 40 s.

2.4. MRI image processing

Analysis of Functional NeuroImages (AFNI) software (<http://afni.nimh.nih.gov/afni/>) was used for imaging analysis. We utilized the afni_proc.py command to make a data processing script and used default parameters of this command except where noted. Initial five volumes were excluded from analysis. Outlier time points were replaced with interpolation (despike). RETROICOR (Glover et al., 2000) was applied to remove respiration- and cardiac-induced noise in the BOLD signal. Physiological fluctuations correlated with low-frequency changes in respiration depth were regressed out from the BOLD signal using respiration volume per time (RVT) correction (Birn et al., 2008). Slice-timing differences were corrected by aligning to the first slice. Motion correction was applied by aligning all functional volumes to the first volume. Nonlinear warping to the MNI template brain with resampling to 2 mm³ voxels was done with the Advanced Normalization Tools (ANTs) software (Avants et al., 2008) (<http://stnava.github.io/ANTs/>). We used the non-linearly aligned and averaged MNI152 brain provided with the FSL package (<https://fsl.fmrib.ox.ac.uk/fsl/fslwiki/>)

as a template. Spatial smoothing (4 mm FWHM) and scaling to percent change were applied to the data.

Further noise reduction was applied by regressing out three principal components of the ventricle signal, local white matter average signal (ANATICOR) (Jo et al., 2010), 12 motion parameters (3 shift and 3 rotation parameters with their temporal derivatives), and low-frequency fluctuation (3rd-order polynomial model) from the signal time course. White matter and ventricle masks were extracted using FreeSurfer 5.3 (<http://surfer.nmr.mgh.harvard.edu/>) from the anatomical image of individual subject and then warped to the normalized fMRI image space. Any fMRI time point with large motion (> 0.25 mm frame-wise displacement (FD)) along with the following point was censored within the regression (Power et al., 2015). FD was calculated as the root sum of squared temporal differences of six motion parameters.

2.5. Effect of scan parameter difference

Since fMRI scan parameters between the veteran groups (PTSD and VC) and the NC group were different, we examined signal difference between the groups specifically in their spatial smoothness and temporal signal to noise ratio (TSNR). It has been indicated that variable spatial smoothness and TSNR are major sources of inter-scanner variability in activation estimation of fMRI (Friedman and Glover, 2006; Friedman et al., 2006). We reasoned that if these properties were similar between the groups, connectivity difference between the groups could not be attributed to scan parameters difference. Spatial smoothness was evaluated using AFNI 3dFWHMx for the processed image after noise components were regressed out. Smoothness estimates were restricted to brain voxels that were covered by all subjects and censored volumes were excluded from the estimation. TSNR was defined as the mean signal divided by the temporal standard deviation for each voxel. TSNR was calculated for functional images before applying regression and censored volumes were excluded. We used the median TSNR in

Table 2

Peak locations of significant clusters for the main effect of groups in the MDMR analysis. Local maximum positions at least 30 mm apart from each other were extracted from significant clusters. Cluster-size *p*-values were evaluated by permutation test with 10,000 random permutations.

Peak location (MNI, mm)			Brain region	Pseudo- <i>F</i>	Cluster size (4 mm ³ voxel)	Cluster-size <i>p</i> -value
x	y	z				
12	−28	−2	R Thalamus	2.545	520	0.0001
−28	−68	−14	L Fusiform	2.377		
4	−68	2	R Lingual	2.335		
−36	−16	−26	L Parahippocampal	2.18		
44	−40	−22	R Fusiform	2.176	146	0.0014
24	−52	2	R Parahippocampal	1.915		
−4	60	−10	L vmPFC (BA11)	2.341	127	0.0020
−20	48	18	L Superior Frontal (BA10)	2.077	54	0.0100
−16	12	6	L Lenticular Nucleus	2.188		
−8	−20	62	L SMA	2.252	50	0.0120
56	4	−34	R Middle Temporal	2.171	49	0.0124
−44	−8	−6	L Insula	3.564	48	0.0126
−24	0	46	L Middle Frontal (BA6)	2.083	46	0.0138
−52	20	2	L Inferior Frontal (BA47)	2.088	44	0.0155
56	−24	10	R Transverse Temporal (BA41)	2.937	41	0.0173
−52	−76	−6	L Inferior Temporal/ Middle Occipital	2.216	38	0.0211
44	−8	−2	R Insula	2.69	36	0.0236
−48	−24	6	L Superior Temporal	2.177	34	0.0252
−32	12	26	L Middle Frontal (BA44)	1.988	30	0.0330
−52	8	−26	L Middle Temporal	2.051	28	0.0382
56	0	2	R Superior Temporal	1.984	26	0.0438
−24	28	34	L Superior Frontal (BA9)	1.927	26	0.0438

Abbreviations: L: left, R: right, BA: Brodmann area, vmPFC: ventromedial prefrontal cortex, SMA: supplementary motor area.

gray matter voxels. Friedman and Glover (2006) indicated that by covarying this measure during regression analysis one could eliminate significant effect of inter-scanner variability on activation estimation. We used Welch's two-tailed *t*-test to examine group difference of the mean smoothness in x, y, and z directions and the median TSNR in gray matter voxels.

2.6. MDMR analysis

MDMR analysis (Anderson, 2001; Shehzad et al., 2014) was applied to investigate comprehensive voxel-wise resting-state connectivity alteration between PTSD, VC, and NC groups. The processed resting-state fMRI image was down-sampled to 4 mm³ voxels. In order to avoid mixing noise outside the brain, we applied an anatomical brain mask to the functional image before resampling. Since we had already applied local white matter signal and ventricle signal regression at preprocessing, masking these regions was not applied at resampling. This down-sampling process was necessary because the whole-brain voxel-wise connectivity matrix in the original resolution was computationally too large for current hardware. To further reduce data size, only the voxels in gray matter regions were extracted from the down-sampled image. The gray matter mask was extracted from the MNI152 template brain provided with FSL. This masking resulted in extracting 18,693 voxels that were subject to the MDMR analysis.

We followed the procedure introduced in Shehzad et al. (2014) for the MDMR analysis, which is briefly reproduced here. MDMR is a mass voxel-wise analysis as it is performed for each voxel independently. Unlike a seed-based analysis that has many correlation statistics for one voxel, MDMR has a single multivariate omnibus statistic for each voxel.

In each voxel, a connectivity map from that voxel to all other voxels was made with Pearson's correlations between signal time-courses of the voxels. The dependent variable of MDMR is a distance matrix of the connectivity maps between subjects. The distance of the maps between subject *i* and *j*, (*d_{ij}*) was calculated with Euclidean distance of Fisher's *z*-transformed connectivity maps. The MDMR analysis evaluates the association between the distance matrix (dissimilarities of connectivity maps across subjects) and the predictor variables in the design matrix, *X*, using a pseudo-*F* value statistic, $F = \frac{tr(HG)/(m-1)}{tr[(I-H)G]/(n-m)}$, where $H = X(X^T X)^{-1} X^T$ is the hat matrix that maps response values (*G*) to the fitted value space, *m* is the number of columns in *X*, and *tr* is the trace of matrix. *G* is the mean-centered distance matrix as $G = CAC$, where $C = (I - \frac{1}{n} 11^T)$, $A = (-\frac{1}{2} d_{ij}^2)$, *n* is the number of subjects, *I* is the *n* × *n* identity matrix and 1 is a vector of *n* 1's. In the current study, the design matrix *X* included two columns of group factors for PTSD and VC, in which 1 indicated PTSD and 0 others, and 1 indicated VC and 0 others, respectively. This coding means that NC is a reference group and the effects of PTSD and VC relative to NC were evaluated. *X* also included columns of age and motion size (average FD) as nuisance variables as well as all 1's for the intercept.

Individual effect of regressors was estimated using a partial design matrix. Hat matrix with effects of no interest regressors was subtracted from the full hat matrix as $H_I = H - H_N$, where $H_N = X_N(X_N^T X_N)^{-1} X_N^T$, and *X_N* is a design matrix only with age, motion, and intercept columns. Pseudo-*F* value for the sum of the effect of interest, namely the main effect of the group difference, was then calculated as $F_I = \frac{tr(H_I G)/(m_I)}{tr[(I-H_I)G]/(n-m)}$, where *m_I* (= 2) is the number of effect of interest regressors.

Statistical tests for the pseudo-*F* value were performed with a permutation test. Nuisance regressors in the permutation test need to be handled differently from the regressors of interest because effect of interest should be evaluated after excluding nuisance effects. We used the Smith procedure (Winkler et al., 2014), in which regressors of interest were orthogonalized with regard to nuisance regressors and then the orthogonalized regressors of interest were permuted randomly. 10,000 random permutations were performed in the analysis.

These procedures were repeated for all voxels as a seed, and pseudo-*F* values (with respective *p*-values) were mapped onto the brain to make a statistical parametric map. We used a computationally efficient method introduced by Shehzad et al. (2014), in which evaluations for all voxels of all permutations were performed in one-time matrix multiplication. The MDMR statistical map was thresholded with voxel-wise *p* < 0.005, and then with cluster-size corrected *p* < 0.05. Cluster-size corrected *p*-value was evaluated with the same permutation procedure as the voxel-wise evaluation to avoid inflated false positive rate (Eklund et al., 2016).

2.7. Post-hoc seed-based analysis

MDMR statistical map indicates that a whole-brain connectivity pattern at a voxel is altered between the groups. However, it does not show which specific connectivity is altered. To elucidate which voxel-by-voxel connectivity was altered between the groups, post-hoc seed-based connectivity analysis was performed for the significant regions of the MDMR statistical map. Note that this analysis was performed only for a post-hoc investigation and restricted to the regions with significant MDMR statistics so that we could avoid multiple testing problems across seed-based analyses that could arise if we picked arbitrary regions for seed-based analysis.

The post-hoc analysis was performed with the original resolution whole-brain functional images (not restricted to gray matter). Seed regions were placed at peak locations of the significant clusters in the MDMR statistical map of the group main effect. Peak coordinates in each significant cluster separated by at least 30 mm were extracted. Seed area was a 6 mm-radius sphere centered at the peak coordinates of

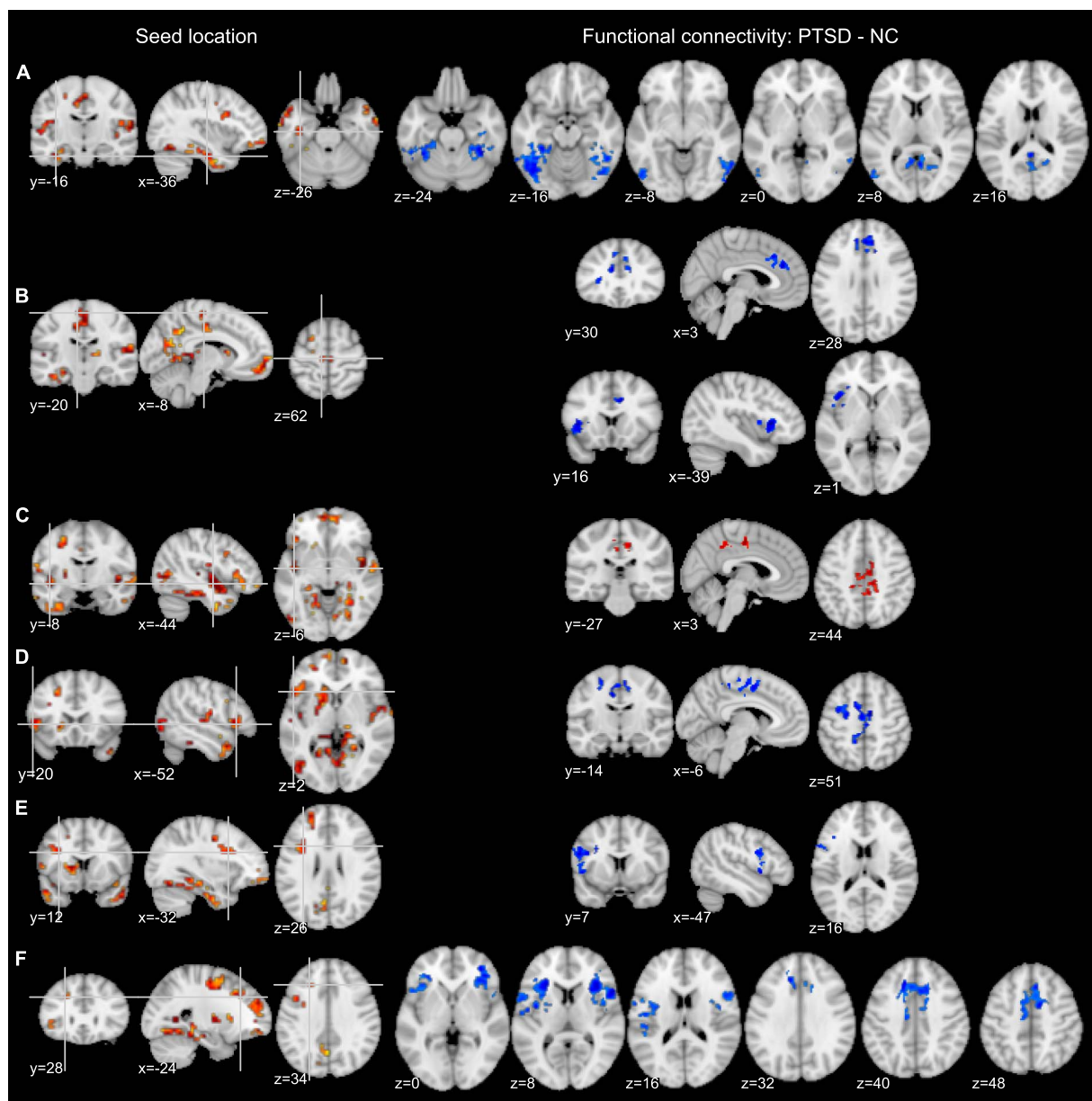


Fig. 2. Seed locations (indicated by crosshair) on the MDMR statistical map (left) and t -value maps of the regions with significantly (voxel-wise $p < 0.005$ and cluster-size-corrected $p < 0.016$) altered connectivity (right) for PTSD compared to NC (non-trauma-exposed controls) in post-hoc analysis. Connectivity alteration for PTSD was found for seed locations at the left parahippocampal gyrus (A), left SMA (supplementary motor area) (B), left insula (C), left inferior frontal gyrus (D), left middle frontal gyrus (E), and left superior frontal gyrus (F).

the MDMR statistical map. Average signal time-course of the seed area was used as a reference signal to calculate correlations with other voxels. Fisher's z -transformation was applied to the correlation coefficient to make a connectivity map for each subject. Voxel-wise general linear model analysis was performed for the connectivity map with the same design matrix as the MDMR analysis. t -value maps of each group contrast, PTSD-NC, VC-NC, and PTSD-VC, were calculated and thresholded with voxel-wise $p < 0.005$ and cluster-size corrected $p < 0.016$ for multiple testing of three groups. Cluster-size corrected p -value was evaluated with the permutation test (10,000 permutations) using the Smith procedure (Winkler et al., 2014).

3. Results

CAPS, PCL-M, MADRS and HAM-A were significantly higher for the PTSD group compared to the VC and NC groups, and not significantly different between the VC and NC groups. Amount of head motion

(average FD) was not significantly different between groups (Table 1). Spatial smoothness and TSNR of functional images were not significantly different between the veterans and NC groups. Mean spatial smoothness was 5.28 mm for veterans and 5.27 mm for NC ($t(56.859) = 0.331$, $p = 0.742$). Mean gray matter median TSNR was 127.2 for veterans and 123.3 for NC ($t(56.915) = 0.64$, $p = 0.525$).

Fig. 1 shows the thresholded map of pseudo- F value for the main effect of group in the MDMR analysis. Peak locations of the clusters with significant effect (cluster-size $p < 0.05$) are shown in Table 2. These peak locations were used as seeds for post-hoc seed-based connectivity analysis.

Fig. 2 shows seed locations and regions with significant functional connectivity alteration for the PTSD compared to NC groups. Supplementary table S1 shows peak locations in significant clusters of altered connectivity in PTSD-NC comparison at post-hoc analysis. Significantly decreased connectivity for PTSD was seen between the left parahippocampal seed and the bilateral fusiform gyrus, middle occipital,

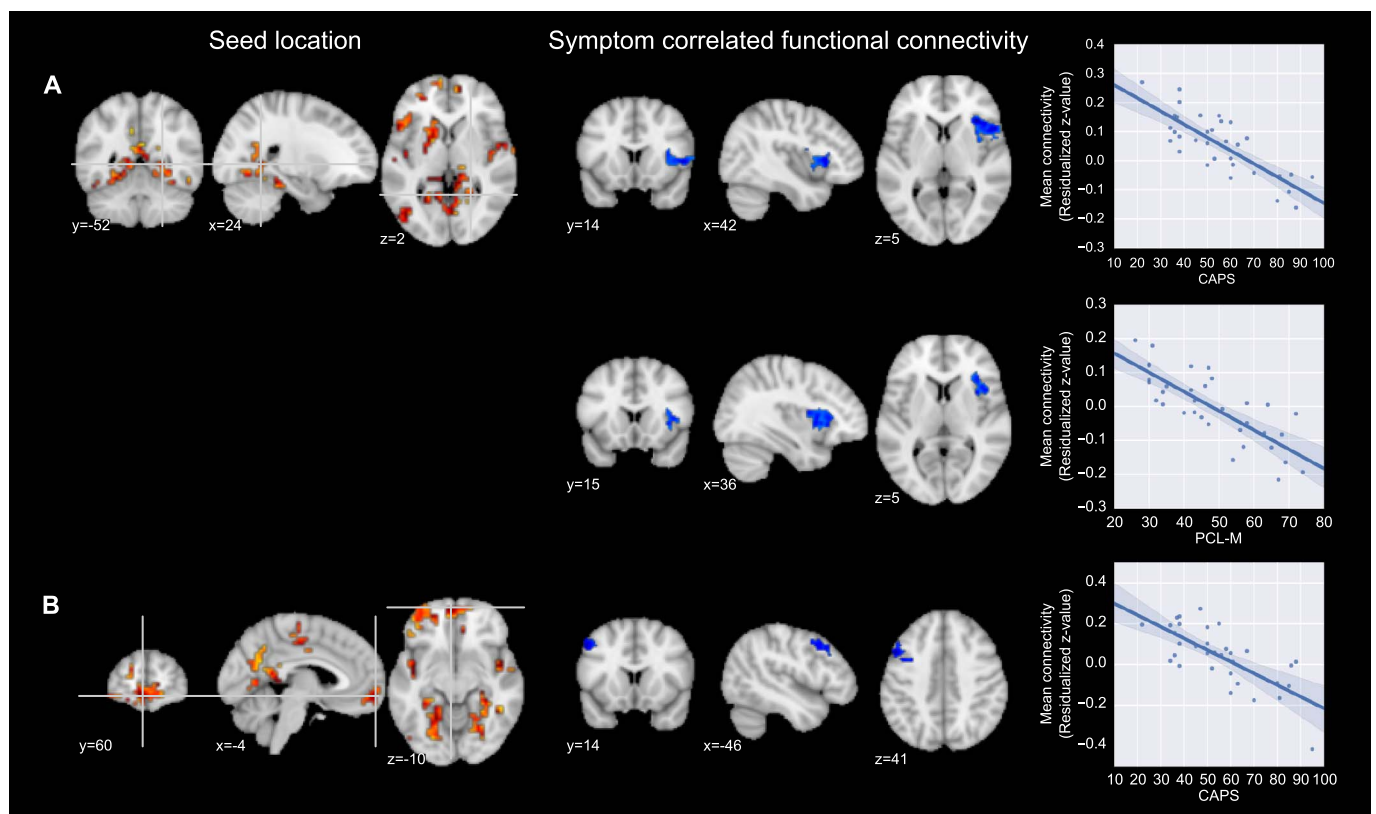


Fig. 3. Seed locations (indicated by crosshair) on the MDMR statistical map (left) and *t*-value maps of the regions with significant symptom-correlated connectivity (middle) among subjects with PTSD (voxel-wise $p < 0.005$ and cluster-size-corrected $p < 0.05$). Functional connectivity correlated with PTSD symptoms (CAPS and PCL-M) was found for seed locations at the right parahippocampal gyrus (A) and the left ventromedial prefrontal cortex (vmPFC) (B). Right panel shows symptom association with mean connectivity (z-value residualized with regard to age and motion covariates) in the regions shown in the maps (middle) with fitted line and its 95% confidence interval. CAPS: Clinician-Administered PTSD Scale, PCL-M: PTSD Checklist - Military Version.

middle temporal, and the posterior cingulate areas (Fig. 2A). Decreased connectivity for PTSD was also seen between the left medial frontal (supplementary motor area; SMA) seed and the anterior cingulate and the left anterior insula regions (Fig. 2B). Multiple left lateral prefrontal seeds showed decreased connectivity for PTSD including between the left inferior frontal seed and the right SMA and the left middle frontal region (Fig. 2D), between the left middle frontal seed and the left inferior frontal and the left superior temporal regions (Fig. 2E), and between the left superior frontal seed and the SMA, anterior cingulate, anterior insula, and inferior frontal regions (Fig. 2F). These hypo-connected regions (Fig. 2F) overlapped with salience network (SN) regions (Menon and Uddin, 2010). Increased functional connectivity for PTSD was seen between the left insula seed and the right middle cingulate region (Fig. 2C).

Correlations between symptom severity and functional connectivity alterations were also examined among people with PTSD for the seed locations in Table 2. The design matrix of this analysis included symptom scores instead of the group factor, along with age and motion covariates. The same permutation procedure used in the post-hoc analysis of group comparisons was used here. Fig. 3 shows seed locations and regions with connectivity significantly (voxel-wise $p < 0.005$ and cluster-size $p < 0.05$) correlated with PTSD symptom scores (CAPS, PCL-M). Peak locations of the significant clusters in Fig. 3 are shown in Supplementary Table S2. Connectivity between the right parahippocampal seed and the right anterior insula was negatively correlated with CAPS and PCL-M (Fig. 3A). Connectivity between the ventromedial prefrontal cortex (vmPFC) seed and the left middle frontal region was negatively correlated with CAPS scores (Fig. 3B). As a complementary analysis, we also examined the connectivity correlation with depression (MADRS) and anxiety (HAM-A) scores for PTSD

(Supplementary Fig. S1). Similar to CAPS and PCL-M, MADRS and HAM-A were negatively correlated with functional connectivity between the right parahippocampal seed and the right anterior insula (Supplementary Fig. S1A). Additionally, connectivity between the left insula and the left middle frontal gyrus was negatively correlated with MADRS and HAM-A (Supplementary Fig. S1B), and connectivity between the left middle frontal and the right inferior parietal regions was negatively correlated with MADRS scores (Supplementary Fig. S1C).

Fig. 4 shows seed locations and regions with significant functional connectivity alteration in the VC compared to NC group. Supplementary table S3 shows peak locations in significant clusters of altered connectivity in the post-hoc VC–NC comparison. Significantly decreased connectivity for VC was seen between the right lingual seed and the medial prefrontal area (Fig. 4A), between the left superior frontal seed and the posterior default mode network areas including the precuneus, posterior cingulate, and the right inferior parietal regions (Fig. 4B), between the left middle frontal seed and the left postcentral region (Fig. 4D), between the right transverse temporal seed and the precuneus (Fig. 4E), and between the left superior temporal seed and the precuneus (Fig. 4G). Significantly increased connectivity was seen between the left posterior insula seed and the right posterior insula, right lingual, and right cuneus regions (Fig. 4C) and between the left posterior insula and the right postcentral, right middle frontal, right middle temporal, right posterior cingulate, left superior parietal, right inferior frontal, right precuneus, and right thalamus.

No significant connectivity differences between the PTSD and VC groups were found in the post-hoc analysis. This could be due to the presence of remitted morbidities in the VC group, such as alcohol abuse, alcohol dependence, and major depressive disorder. We examined associations of these morbidity histories in the VC group with the

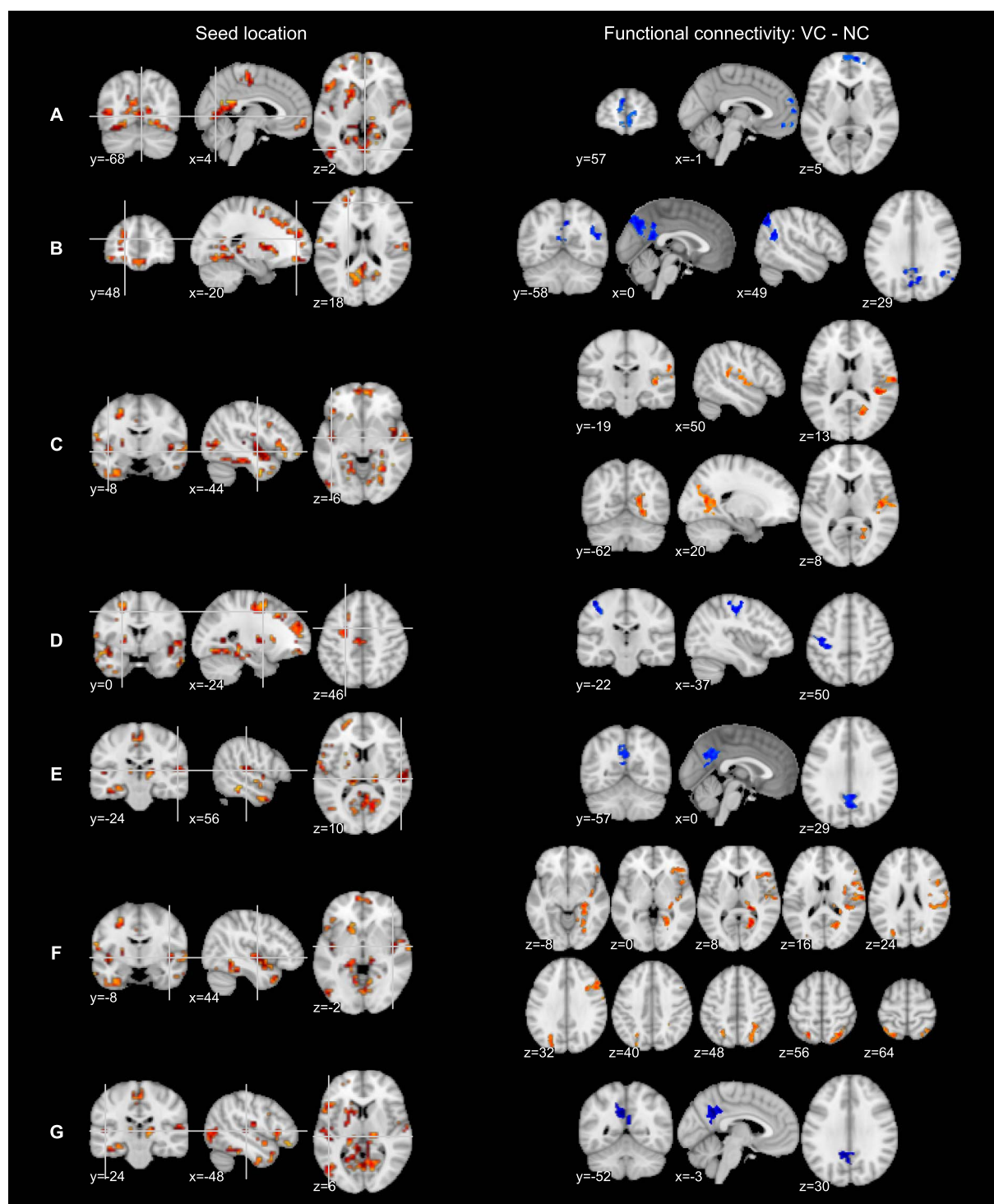


Fig. 4. Seed locations (indicated by crosshair) on the MDMR statistical map (left) and t -value maps of the regions with significantly (voxel-wise $p < 0.005$ and cluster-size-corrected $p < 0.016$) altered connectivity (right) for VC (veteran controls) compared to NC (non-trauma-exposed controls) in post-hoc analysis. Connectivity alteration for VC was found for seed locations at the left lingual gyrus (A), left superior frontal gyrus (B), left insula (C), left middle frontal gyrus (D), right transverse temporal gyrus (E), right insula (F), and left superior temporal gyrus (G).

connectivity alterations in Supplementary Figs. S2 and S3. Box plots of these figures show distribution of mean connectivity in the regions with significant alteration for PTSD (Supplementary Fig. S2) and VC (Supplementary Fig. S3) compared to NC. Supplementary Fig. S3 indicates that connectivity differences between VC and NC were not driven by the subjects with remitted morbidity. Supplementary Fig. S2 indicates that connectivity for VC tended to be in between PTSD and NC either with or without remitted morbidity, although variability in the

VC group could be increased by remitted morbidity. We further performed the same MDMR and post-hoc analyses excluding VC subjects with morbidity histories. This analysis, however, still did not show a significant connectivity difference between the PTSD and VC groups.

4. Discussion

Connectome-wide analysis of altered resting-state functional

connectivity for war veterans revealed decreased connectivity for PTSD patients in lateral frontal, SMA, and SN regions, as well as decreased connectivity between the parahippocampal and the visual cortex areas. PTSD symptom severity was negatively correlated with connectivity between the right parahippocampal gyrus and the right anterior insula and between the left vmPFC and the left middle frontal gyrus in people with PTSD. The analysis also revealed altered resting-state connectivity for VC, including increased connectivity in the posterior insula and decreased connectivity in the precuneus with several other brain areas, while no significant differences between PTSD and VC groups were observed. Because there was no significant difference in spatial smoothness or TSNR of functional images between veterans and NC groups, observed connectivity differences cannot be attributed to scan parameter difference. Most of these findings were consistent with previous observations of abnormal brain activation patterns among people with PTSD in both task-based and resting-state fMRI studies. The current results also extended previous findings by indicating such abnormalities were seen in region-by-region resting-state functional connectivity.

The analysis revealed decreased functional connectivity between the parahippocampal and the occipital visual cortex regions for PTSD compared to NC (Fig. 2A). A correlation between PTSD symptom severity and decreased functional connectivity between the parahippocampal region and the anterior insula was also observed (Fig. 3A). Similar dissociation between the hippocampal memory area and sensorimotor and SN areas has been observed during PTSD-related flashbacks (Whalley et al., 2013). Whalley et al. (2013) indicated that PTSD patients showed hyperactive sensorimotor regions, including visual cortices and hypoactive memory-associated regions (e.g., parahippocampal gyrus), during a trauma cue-elicited flashback experience. This dissociation is consistent with the dual representation theory of PTSD (Brewin et al., 2010). According to the theory, episodic memory has dual representations of context (C-reps) supported by the medial temporal regions, and low-level sensation (S-reps) supported by sensory and interoceptive cortical areas. These representations are associated with each other for a memory of common events, while the C-reps for a memory of a traumatic event could be weakened or lost. This hypothesis is supported by evidence that potentiated amygdala function as well as suppressed hippocampal function was seen under high-level stress situations (Brewin et al., 2010; Elzinga and Bremner, 2002; Payne et al., 2006). The dual representation theory suggests that abnormal memory representation for a traumatic event has strong S-reps without associated C-reps, which underlies symptoms of re-experiencing and hyperarousal. The current results extended this evidence by indicating that resting-state functional connectivity between C-reps and S-reps regions was decreased in PTSD. This suggests that the neurobiological dissociation thought to underlie dual memory representations may be present at rest as well as during cued memory retrieval.

The current results also showed that the PTSD group had decreased functional connectivity across the lateral frontal areas and the SMA with the SN (Fig. 2B, D, E, F) as well as decreased connectivity between the vmPFC and the left middle frontal gyrus that was correlated with PTSD symptom severity (Fig. 3B). A large literature has indicated that lateral frontal regions, vmPFC, and SMA are associated with emotion regulation functions, including reappraisal of emotional stimuli (Johnstone et al., 2007; Kalisch, 2009; Kohn et al., 2014; New et al., 2009; Wager et al., 2008). Decreased activation of these regions in response to emotional stimuli or emotion regulation tasks among people with PTSD has been reported (Aupperle et al., 2012; Blair et al., 2013; Hayes et al., 2012; Patel et al., 2012; van Rooij et al., 2014). Yin et al. (2011) showed that resting-state ALFF at the right medial frontal gyrus was correlated with PTSD symptom severity. A meta-analysis of regional resting-state activation (Koch et al., 2016) also indicated lowered resting-state activity at the middle frontal gyrus for PTSD. In contrast to hypoactive prefrontal emotion-regulating areas, a hyperactive SN is one of the prevalent brain abnormalities observed among

people with PTSD in emotion-related tasks (Hayes et al., 2012; Lanius et al., 2015; Patel et al., 2012). A study of resting-state functional connectivity at the anterior insula (Sripada et al., 2012) also indicated that PTSD had increased anterior insula connectivity with SN regions but decreased connectivity with DMN regions, including the medial PFC. The current results of hypoconnectivity between the lateral prefrontal and SN regions are consistent with these previous reports of aberrant brain activations for PTSD.

Notably, the lowered functional connectivity of the lateral frontal areas was lateralized to the left hemisphere in the current results. Systematic review of brain activation patterns observed during cognitive reappraisal to regulate emotional experience among healthy individuals (Ochsner et al., 2012) suggested that there are two different tactics of reappraisal, reinterpretation and distancing. Their meta-analysis indicated that the regions involved in reinterpretation appear to be more strongly left-lateralized in prefrontal and temporal cortices, whereas regions involved in distancing appear to be more strongly right-lateralized in prefrontal cortex and parietal regions. The left-lateralized hypoconnectivity in the current results, therefore, might suggest that PTSD patients had reduced reinterpretation function compared to distancing. Distancing function, however, could be highly variable across PTSD patients. There is a subtype of PTSD patients with dissociation symptoms (Lanius et al., 2006; Lanius et al., 2005; Nicholson et al., 2015; Nicholson et al., 2016) who show depersonalization and derealization responses to emotional or trauma-related stimuli and could be involuntary distancing to regulate emotional arousal. In the current study, only 9 of the 35 PTSD subjects reported mild dissociation symptoms. Due to the small number of subjects and mild symptoms, we could not evaluate the difference between PTSD subtypes. Future studies are needed to examine differences in resting-state connectivity between subtypes of PTSD.

Increased functional connectivity at the posterior insula was observed among PTSD patients (Fig. 2C) as well as among VC subjects (Fig. 4C, F) but in more areas for VC than PTSD. Similar differences in resting-state insula activity were reported in a meta-analysis of resting-state regional activity (Wang et al., 2016), which found that trauma-exposed controls had higher regional resting-state activity in the right posterior insula compared to people with PTSD. Zhang et al. (2016) reported hypoconnectivity in PTSD at the right posterior insula with the left inferior parietal lobe and the postcentral gyrus. A negative correlation between hyperarousal symptoms and connectivity between the posterior insula and the SN was also reported (Tursich et al., 2015), suggesting greater connectivity of the posterior insula is associated with lower PTSD symptom levels. Consistent with these findings, greater pre-treatment insula gray matter density predicts better response to psychotherapy (Colvonen et al., 2017; Nardo et al., 2010). These findings suggest that greater functional connectivity and volume of the posterior insula could contribute to the alleviation of PTSD symptom. As the insula is thought to support internal representations of emotional states (Craig, 2003), the heightened activity and connectivity at this region might possibly help to accommodate internal emotional states of trauma experience.

Veteran controls also showed reduced connectivity at the precuneus (Fig. 4B, E, G). Patel et al. (2012) showed that the precuneus was hyperactive for PTSD, while most other DMN regions were hypoactive in PTSD in their meta-analysis of functional brain activation studies for PTSD. Cwik et al. (2016) also showed that for acute stress disorder patients the right medial precuneus response to trauma-related pictures was positively correlated with later development of PTSD symptoms. It has been suggested that the precuneus subserves consciousness and self-reflection (Vogt and Laureys, 2005). The dual representation theory (Brewin et al., 2010) suggests precuneus activity triggers top-down retrieval of S-reps with translation into a personally relevant (e.g. egocentric) perspective. It has also been suggested that decreased precuneus function is associated with efforts to terminate self-reflection of aversive sensations (Vogt and Laureys, 2005; Whalley et al., 2013). The

decreased connectivity at the precuneus for VC, therefore, might reflect effort to terminate self-reflection of aversive sensations, such as S-reps of traumatic memory.

Veteran controls also had decreased resting-state functional connectivity between the vmPFC and lingual gyrus (Fig. 4A) and between the left middle frontal and the left postcentral regions (Fig. 4D). It is possible that these reductions in connectivity are effects of traumatization and therefore are comparable to people with PTSD. Several remitted morbidities might also affect the alterations observed among VCs, although we did not observe systematic differences between VCs with and without remitted morbidity for these connectivity findings (Supplementary Fig. S3). It is possible that the abnormalities observed among VCs are due to war deployment, military training, or adaptive changes to traumatic experiences, or that they reflect an innate resilience factor. Future studies that employ longitudinal designs are needed to distinguish the cause of altered resting-state functional connectivity among war-deployed veterans without PTSD.

The current results did not show significant differences in resting-state functional connectivity between the PTSD and VC groups. We note that this result does not necessarily indicate that PTSD and VC groups had the same connectivity patterns. Statistically, a non-significant result does not mean equivalence of the groups. This non-significant result could be due to substantial variability in the VC group, which included individuals with remitted morbidity. However, even when we excluded VC subjects with morbidity history from the analysis, we still did not find significantly different connectivity between the PTSD and VC groups. This suggests that either morbidity history was not a sole reason for variability or that reduced statistical power due to smaller sample sizes negated the benefit of reducing variability within a group. Limited sensitivity of MDMR analysis, as discussed below, could also affect the non-significant result. Accordingly, we cannot draw inferences about the equivalence of the PTSD and VC groups based on this non-significant result, particularly in light of different patterns of connectivity alteration in the PTSD and VC groups compared to the NC group in the current results and previous research that demonstrated connectivity differences between people with PTSD and trauma-exposed controls.

Variability in morbidity and trauma is typical among war-deployed veterans. Even within PTSD patients, expression of the disorder is highly heterogeneous, making it difficult to find a single diagnostic marker of the disorder (Zoladz and Diamond, 2013). Importantly, the current results do not suggest homogeneous abnormality either for the PTSD or VC groups, but suggest average differences between groups. While such between-group designs continue to contribute to our limited understanding of the neuropathology of mental disorders, variability within a diagnostic group needs to be included in analyses in accord with the research domain criteria (RDoC) (Cuthbert, 2014) for further understanding the disorder.

It is also warranted to address a limitation of MDMR analysis. The current analysis did not observe a significant effect in the amygdala, where many studies have indicated abnormality in PTSD (Shin et al., 2006). Whole-brain analyses often do not observe abnormalities in amygdala activity, whereas region of interest (ROI) analyses do observe such abnormalities (Hayes et al., 2012). A meta-analysis (Hayes et al., 2012) including only whole-brain analyses did not find amygdala abnormality for PTSD, while an analysis including ROI analyses found amygdala hyperactivity for PTSD. One reason for the absence of amygdala abnormalities in the current results, therefore, could be its small effect size. Limited sensitivity of MDMR analysis, however, could also be a reason for this result. MDMR analysis evaluates between-subject distance of connectivity maps, and this distance measure could be insensitive to a change in a small region because it summarizes the differences in a large dimensional connectivity map into one measure. Non-significant results in MDMR, therefore, should not be interpreted as indication of a negative result. The distance measure of the MDMR also introduces another limitation, that is, a distance measure reflects

only a size of difference and is not sensitive to how connectivity maps differ. This means that a similar distance value could come from different patterns of connectivity alteration. As the current results demonstrated that not all the seed locations identified with MDMR showed significant group differences in the post-hoc analysis, significant group effects in the MDMR do not necessarily indicate common differences in the group. Post-hoc analysis that investigates what differences contribute to the MDMR measure is needed for correct interpretation of MDMR results.

5. Conclusions

Connectome-wide investigation of altered resting-state functional connectivity for war veterans with PTSD revealed hypoconnectivity between the parahippocampus gyrus and the visual cortex as well as across the lateral prefrontal and vmPFC with the SN regions. These alterations were consistent with previous observations of abnormalities in the emotion-regulation circuit and further support dissociated memory representation in PTSD. The current results extended these findings by indicating that such abnormality also appears to be present in resting-state region-by-region functional connectivity. The analysis also revealed increased connectivity with posterior insula and decreased connectivity with precuneus among veterans without PTSD, with the later suggesting adaptive alteration to suppress traumatic memory. While all the reasons for these observed alterations are not yet clear, the comprehensive exploration via MDMR analysis enabled these findings and offers potential targets for future research. Although we should recognize limitations in sensitivity and interpretation, hypothesis-free exploratory analysis with MDMR connectome-wide investigation yielded valuable information that complements existing hypothesis-driven analyses.

Acknowledgements

This research was supported by W81XWH-12-1-0697 award from the U.S. Department of Defense, the Laureate Institute for Brain Research, and the William K. Warren Foundation. The data of non-trauma exposed healthy males were provided by NIMH/NIH grant R01 MH098099. A part of this study was presented at 2017 annual meeting of the International Society for Magnetic Resonance in Medicine and at 2017 annual meeting of the Organization of Human Brain Mapping.

Appendix A. Supplementary data

Supplementary data to this article can be found online at <https://doi.org/10.1016/j.nicl.2017.10.032>.

References

- American Psychiatric Association, 2000. Diagnostic and Statistical Manual of Mental Disorders DSM-IV-TR, Fourth edition. American Psychiatric Publishing, Washington, DC (Text Revision).
- Anderson, M.J., 2001. A new method for non-parametric multivariate analysis of variance. *Austral Ecol.* 26, 32–46.
- Aupperle, R.L., Melrose, A.J., Stein, M.B., Paulus, M.P., 2012. Executive function and PTSD: disengaging from trauma. *Neuropharmacology* 62, 686–694.
- Avants, B.B., Epstein, C.L., Grossman, M., Gee, J.C., 2008. Symmetric diffeomorphic image registration with cross-correlation: evaluating automated labeling of elderly and neurodegenerative brain. *Med. Image Anal.* 12, 26–41.
- Birn, R.M., Smith, M.A., Jones, T.B., Bandettini, P.A., 2008. The respiration response function: the temporal dynamics of fMRI signal fluctuations related to changes in respiration. *NeuroImage* 40, 644–654.
- Blair, K., Vythilingam, M., Crowe, S., McCaffrey, D., Ng, P., Wu, C., Scaramozza, M., Mondillo, K., Pine, D., Charney, D., 2013. Cognitive control of attention is differentially affected in trauma-exposed individuals with and without post-traumatic stress disorder. *Psychol. Med.* 43, 85–95.
- Blake, D., Weathers, F., Nagy, L., Kaloupek, D., Charney, D., Keane, T., 1995. Clinician-Administered PTSD Scale for DSM-IV (CAPS-DX). National Center for Posttraumatic Stress Disorder, Behavioral Science Division, Boston VA Medical Center, Boston, MA.
- Blanchard, E.B., Jones-Alexander, J., Buckley, T.C., Forneris, C.A., 1996. Psychometric properties of the PTSD checklist (PCL). *Behav. Res. Ther.* 34, 669–673.

- Bonne, O., Gilboa, A., Louzoun, Y., Brandes, D., Yona, I., Lester, H., Barkai, G., Freedman, N., Chisin, R., Shalev, A.Y., 2003. Resting regional cerebral perfusion in recent posttraumatic stress disorder. *Biol. Psychiatry* 54, 1077–1086.
- Brewin, C.R., 2011. The nature and significance of memory disturbance in posttraumatic stress disorder. *Annu. Rev. Clin. Psychol.* 7, 203–227.
- Brewin, C.R., Gregory, J.D., Lipton, M., Burgess, N., 2010. Intrusive images in psychological disorders: characteristics, neural mechanisms, and treatment implications. *Psychol. Rev.* 117, 210–232.
- Brown, V.M., LaBar, K.S., Haswell, C.C., Gold, A.L., McCarthy, G., Morey, R.A., 2014. Altered resting-state functional connectivity of basolateral and centromedial amygdala complexes in posttraumatic stress disorder. *Neuropsychopharmacology* 39, 351–359.
- Calhoun, V.D., Adali, T., 2012. Multisubject independent component analysis of fMRI: a decade of intrinsic networks, default mode, and neurodiagnostic discovery. *IEEE Rev. Biomed. Eng.* 5, 60–73.
- Colvonen, P.J., Glassman, L.H., Crocker, L.D., Buttner, M.M., Orff, H., Schiehr, D.M., Norman, S.B., Afari, N., 2017. Pretreatment biomarkers predicting PTSD psychotherapy outcomes: a systematic review. *Neurosci. Biobehav. Rev.* 75, 140–156.
- Craig, A.D., 2003. Interoception: the sense of the physiological condition of the body. *Curr. Opin. Neurobiol.* 13, 500–505.
- Cuthbert, B.N., 2014. The RDoC framework: facilitating transition from ICD/DSM to dimensional approaches that integrate neuroscience and psychopathology. *World Psychiatry* 13, 28–35.
- Cwik, J.C., Sartory, G., Nuyken, M., Schürholt, B., Seitz, R.J., 2016. Posterior and prefrontal contributions to the development posttraumatic stress disorder symptom severity: an fMRI study of symptom provocation in acute stress disorder. *Eur. Arch. Psychiatry Clin. Neurosci.* 1–11.
- Eklund, A., Nichols, T.E., Knutsson, H., 2016. Cluster failure: why fMRI inferences for spatial extent have inflated false-positive rates. *Proc. Natl. Acad. Sci. U. S. A.* 113, 7900–7905.
- Elzinga, B.M., Bremner, J.D., 2002. Are the neural substrates of memory the final common pathway in posttraumatic stress disorder (PTSD)? *J. Affect. Disord.* 70, 1–17.
- Filippini, N., MacIntosh, B.J., Hough, M.G., Goodwin, G.M., Frisoni, G.B., Smith, S.M., Matthews, P.M., Beckmann, C.F., Mackay, C.E., 2009. Distinct patterns of brain activity in young carriers of the APOE-epsilon4 allele. *Proc. Natl. Acad. Sci. U. S. A.* 106, 7209–7214.
- First, M.B., Spitzer, R.L., Miriam, G., Williams, J.B.W., 1996. Structured Clinical Interview for DSM-IV Axis I Disorders, Clinician Version (SCID-CV). American Psychiatric Press, Inc., Washington, D.C.
- Fonzo, G.A., Simmons, A.N., Thorp, S.R., Norman, S.B., Paulus, M.P., Stein, M.B., 2010. Exaggerated and disconnected insular-amygdalar blood oxygenation level-dependent response to threat-related emotional faces in women with intimate-partner violence posttraumatic stress disorder. *Biol. Psychiatry* 68, 433–441.
- Fornito, A., Zalesky, A., Breakspear, M., 2013. Graph analysis of the human connectome: promise, progress, and pitfalls. *NeuroImage* 80, 426–444.
- Friedman, L., Glover, G.H., 2006. Reducing interscanner variability of activation in a multicenter fMRI study: controlling for signal-to-fluctuation-noise-ratio (SFNR) differences. *NeuroImage* 33, 471–481.
- Friedman, L., Glover, G.H., Krenz, D., Magnotta, V., 2006. Reducing inter-scanner variability of activation in a multicenter fMRI study: role of smoothness equalization. *NeuroImage* 32, 1656–1668.
- Friston, K., 1994. Functional and effective connectivity in neuroimaging: a synthesis. *Hum. Brain Mapp.* 2, 56–78.
- Glover, G.H., Li, T.Q., Ress, D., 2000. Image-based method for retrospective correction of physiological motion effects in fMRI: RETROICOR. *Magn. Reson. Med.* 44, 162–167.
- Hamilton, M., Schutte, N., Malouff, J., 1976. Hamilton anxiety scale (HAMA). Sourcebook of adult assessment: applied clinical. *Psychology* 154–157.
- Hayes, J.P., Hayes, S.M., Mikes, A.M., 2012. Quantitative meta-analysis of neural activity in posttraumatic stress disorder. *Biol. Mood Anxiety Disord.* 2, 1–13.
- Hoge, C.W., Auchterlonie, J.L., Milliken, C.S., 2006. Mental health problems, use of mental health services, and attrition from military service after returning from deployment to Iraq or Afghanistan. *JAMA* 295, 1023–1032.
- Jiang, Q., Ahmed, S., 2009. An analysis of correlations among four outcome scales employed in clinical trials of patients with major depressive disorder. *Ann. General Psychiatry* 8, 4.
- Jo, H.J., Saad, Z.S., Simmons, W.K., Milbury, L.A., Cox, R.W., 2010. Mapping sources of correlation in resting state FMRI, with artifact detection and removal. *NeuroImage* 52, 571–582.
- Johnstone, T., van Reekum, C.M., Urry, H.L., Kalin, N.H., Davidson, R.J., 2007. Failure to regulate: counterproductive recruitment of top-down prefrontal-subcortical circuitry in major depression. *J. Neurosci.* 27, 8877–8884.
- Kalisch, R., 2009. The functional neuroanatomy of reappraisal: time matters. *Neurosci. Biobehav. Rev.* 33, 1215–1226.
- Kennis, M., Rademaker, A.R., van Rooij, S.J., Kahn, R.S., Geuze, E., 2015. Resting state functional connectivity of the anterior cingulate cortex in veterans with and without post-traumatic stress disorder. *Hum. Brain Mapp.* 36, 99–109.
- Koch, S.B., van Zuiden, M., Nawijn, L., Frijling, J.L., Veltman, D.J., Olff, M., 2016. Aberrant resting-state brain activity in posttraumatic stress disorder: a meta-analysis and systematic review. *Depress. Anxiety* 33, 592–606.
- Kohn, N., Eickhoff, S.B., Scheller, M., Laird, A.R., Fox, P.T., Habel, U., 2014. Neural network of cognitive emotion regulation—an ALE meta-analysis and MACM analysis. *NeuroImage* 87, 345–355.
- Lanius, R.A., Williamson, P.C., Bluhm, R.L., Densmore, M., Boksman, K., Neufeld, R.W., Gati, J.S., Menon, R.S., 2005. Functional connectivity of dissociative responses in posttraumatic stress disorder: a functional magnetic resonance imaging investigation. *Biol. Psychiatry* 57, 873–884.
- Lanius, R.A., Bluhm, R., Lanius, U., Pain, C., 2006. A review of neuroimaging studies in PTSD: heterogeneity of response to symptom provocation. *J. Psychiatr. Res.* 40, 709–729.
- Lanius, R.A., Frewen, P.A., Tursich, M., Jetly, R., McKinnon, M.C., 2015. Restoring large-scale brain networks in PTSD and related disorders: a proposal for neuroscientifically-informed treatment interventions. *Eur. J. Psychotraumatol.* 6, 27313.
- Lei, D., Li, K., Li, L., Chen, F., Huang, X., Lui, S., Li, J., Bi, F., Gong, Q., 2015. Disrupted functional brain connectome in patients with posttraumatic stress disorder. *Radiology* 276, 818–827.
- Liberzon, I., Sripada, C.S., 2008. The functional neuroanatomy of PTSD: a critical review. *Prog. Brain Res.* 167, 151–169.
- Maier, W., Buller, R., Philipp, M., Heuser, I., 1988. The Hamilton Anxiety Scale: reliability, validity and sensitivity to change in anxiety and depressive disorders. *J. Affect. Disord.* 14, 61–68.
- Menon, V., Uddin, L.Q., 2010. Saliency, switching, attention and control: a network model of insula function. *Brain Struct. Funct.* 214, 655–667.
- Misaki, M., Suzuki, H., Savitz, J., Drevets, W.C., Bodurka, J., 2016. Individual variations in nucleus accumbens responses associated with major depressive disorder symptoms. *Sci Rep* 6, 21227.
- Montgomery, S.A., Asberg, M., 1979. A new depression scale designed to be sensitive to change. *Br. J. Psychiatry* 134, 382–389.
- Nardo, D., Hogberg, G., Looi, J.C., Larsson, S., Hallstrom, T., Pagani, M., 2010. Gray matter density in limbic and paralimbic cortices is associated with trauma load and EMDR outcome in PTSD patients. *J. Psychiatr. Res.* 44, 477–485.
- New, A.S., Fan, J., Murrough, J.W., Liu, X., Liebman, R.E., Guise, K.G., Tang, C.Y., Charney, D.S., 2009. A functional magnetic resonance imaging study of deliberate emotion regulation in resilience and posttraumatic stress disorder. *Biol. Psychiatry* 66, 656–664.
- Nicholson, A.A., Densmore, M., Frewen, P.A., Theberge, J., Neufeld, R.W., McKinnon, M.C., Lanius, R.A., 2015. The dissociative subtype of posttraumatic stress disorder: unique resting-state functional connectivity of basolateral and centromedial amygdala complexes. *Neuropsychopharmacology* 40, 2317–2326.
- Nicholson, A.A., Sapru, I., Densmore, M., Frewen, P.A., Neufeld, R.W., Theberge, J., McKinnon, M.C., Lanius, R.A., 2016. Unique insula subregion resting-state functional connectivity with amygdala complexes in posttraumatic stress disorder and its dissociative subtype. *Psychiatry Res.* 250, 61–72.
- Ochsner, K.N., Silvers, J.A., Buhle, J.T., 2012. Functional imaging studies of emotion regulation: a synthetic review and evolving model of the cognitive control of emotion. *Ann. N. Y. Acad. Sci.* 1251, E1–24.
- Patel, R., Spreng, R.N., Shin, L.M., Girard, T.A., 2012. Neurocircuitry models of post-traumatic stress disorder and beyond: a meta-analysis of functional neuroimaging studies. *Neurosci. Biobehav. Rev.* 36, 2130–2142.
- Payne, J.D., Jackson, E.D., Ryan, L., Hoscheidt, S., Jacobs, J.W., Nadel, L., 2006. The impact of stress on neutral and emotional aspects of episodic memory. *Memory* 14, 1–16.
- Pitman, R.K., Rasmusson, A.M., Koenen, K.C., Shin, L.M., Orr, S.P., Gilbertson, M.W., Milad, M.R., Liberzon, I., 2012. Biological studies of post-traumatic stress disorder. *Nat. Rev. Neurosci.* 13, 769–787.
- Power, J.D., Schlaggar, B.L., Petersen, S.E., 2015. Recent progress and outstanding issues in motion correction in resting state fMRI. *NeuroImage* 105, 536–551.
- Reimherr, F.W., Martin, M.L., Eudicone, J.M., Marchant, B.K., Tran, Q.V., Pikalov, A., Marcus, R.N., Berman, R.M., Carlson, B.X., 2010. A pooled MADRS/IDS cross-correlation analysis: clinician and patient self-report assessment of improvement in core depressive symptoms with adjunctive aripiprazole. *J. Clin. Psychopharmacol.* 30, 300–305.
- Ruggiero, K.J., Del Ben, K., Scotti, J.R., Rabalais, A.E., 2003. Psychometric properties of the PTSD checklist-civilian version. *J. Trauma. Stress.* 16, 495–502.
- Satterthwaite, T.D., Cook, P.A., Bruce, S.E., Conway, C., Mikkelsen, E., Satchell, E., Vandekar, S.N., Durbin, T., Shinohara, R.T., Sheline, Y.L., 2015. Dimensional depression severity in women with major depression and post-traumatic stress disorder correlates with fronto-amygdalar hypoconnectivity. *Mol. Psychiatry* 21, 894–902.
- Shehzad, Z., Kelly, C., Reiss, P.T., Cameron Craddock, R., Emerson, J.W., McMahon, K., Copland, D.A., Castellanos, F.X., Milham, M.P., 2014. A multivariate distance-based analytic framework for connectome-wide association studies. *NeuroImage* 93 (Pt 1), 74–94.
- Shin, L.M., Rauch, S.L., Pitman, R.K., 2006. Amygdala, medial prefrontal cortex, and hippocampal function in PTSD. *Ann. N. Y. Acad. Sci.* 1071, 67–79.
- Sripada, R.K., King, A.P., Welsh, R.C., Garfinkel, S.N., Wang, X., Sripada, C.S., Liberzon, I., 2012. Neural dysregulation in posttraumatic stress disorder: evidence for disrupted equilibrium between salience and default mode brain networks. *Psychosom. Med.* 74, 904–911.
- Tursich, M., Ros, T., Frewen, P.A., Kluetsch, R.C., Calhoun, V.D., Lanius, R.A., 2015. Distinct intrinsic network connectivity patterns of post-traumatic stress disorder symptom clusters. *Acta Psychiatr. Scand.* 132, 29–38.
- van Rooij, S.J., Rademaker, A.R., Kennis, M., Vink, M., Kahn, R.S., Geuze, E., 2014. Impaired right inferior frontal gyrus response to contextual cues in male veterans with PTSD during response inhibition. *J. Psychiatry Neurosci.* 39, 330–338.
- van Wingen, G.A., Geuze, E., Caan, M.W., Kozicz, T., Olabarriaga, S.D., Denys, D., Vermetten, E., Fernandez, G., 2012. Persistent and reversible consequences of combat stress on the mesofrontal circuit and cognition. *Proc. Natl. Acad. Sci. U. S. A.* 109, 15508–15513.
- Vogt, B.A., Laureys, S., 2005. Posterior cingulate, precuneal and retrosplenial cortices: cytology and components of the neural network correlates of consciousness. *Prog. Brain Res.* 150, 205–217.
- Wager, T.D., Davidson, M.L., Hughes, B.L., Lindquist, M.A., Ochsner, K.N., 2008.

- Prefrontal-subcortical pathways mediating successful emotion regulation. *Neuron* 59, 1037–1050.
- Wang, T., Liu, J., Zhang, J., Zhan, W., Li, L., Wu, M., Huang, H., Zhu, H., Kemp, G.J., Gong, Q., 2016. Altered resting-state functional activity in posttraumatic stress disorder: a quantitative meta-analysis. *Sci Rep* 6, 27131.
- Weathers, F.W., Litz, B.T., Herman, D.S., Huska, J.A., Keane, T.M., 1993. The PTSD Checklist (PCL): reliability, validity, and diagnostic utility. In: Annual Convention of the International Society for Traumatic Stress Studies, (San Antonio, TX).
- Weathers, F.W., Keane, T.M., Davidson, J.R., 2001. Clinician-administered PTSD scale: a review of the first ten years of research. *Depress. Anxiety* 13, 132–156.
- Whalley, M.G., Kroes, M.C., Huntley, Z., Rugg, M.D., Davis, S.W., Brewin, C.R., 2013. An fMRI investigation of posttraumatic flashbacks. *Brain Cogn.* 81, 151–159.
- Winkler, A.M., Ridgway, G.R., Webster, M.A., Smith, S.M., Nichols, T.E., 2014. Permutation inference for the general linear model. *NeuroImage* 92, 381–397.
- Yin, Y., Li, L., Jin, C., Hu, X., Duan, L., Eyler, L.T., Gong, Q., Song, M., Jiang, T., Liao, M., Zhang, Y., Li, W., 2011. Abnormal baseline brain activity in posttraumatic stress disorder: a resting-state functional magnetic resonance imaging study. *Neurosci. Lett.* 498, 185–189.
- Zang, Y., Jiang, T., Lu, Y., He, Y., Tian, L., 2004. Regional homogeneity approach to fMRI data analysis. *NeuroImage* 22, 394–400.
- Zhang, Y., Xie, B., Chen, H., Li, M., Guo, X., Chen, H., 2016. Disrupted resting-state insular subregions functional connectivity in post-traumatic stress disorder. *Medicine (Baltimore)* 95, e4083.
- Zhu, H., Qiu, C., Meng, Y., Cui, H., Zhang, Y., Huang, X., Zhang, J., Li, T., Gong, Q., Zhang, W., Lui, S., 2015. Altered spontaneous neuronal activity in chronic post-traumatic stress disorder patients before and after a 12-week paroxetine treatment. *J. Affect. Disord.* 174, 257–264.
- Zoladz, P.R., Diamond, D.M., 2013. Current status on behavioral and biological markers of PTSD: a search for clarity in a conflicting literature. *Neurosci. Biobehav. Rev.* 37, 860–895.
- Zou, Q.H., Zhu, C.Z., Yang, Y., Zuo, X.N., Long, X.Y., Cao, Q.J., Wang, Y.F., Zang, Y.F., 2008. An improved approach to detection of amplitude of low-frequency fluctuation (ALFF) for resting-state fMRI: fractional ALFF. *J. Neurosci. Methods* 172, 137–141.

**Automatic cardiac cycle determination directly from EEG-fMRI data
by multi-scale peak detection method**

Chung Ki Wong¹, Qingfei Luo¹, Vadim Zotev¹, Raquel Phillips¹, Kam Wai Clifford Chan², Jerzy Bodurka^{1,3,4#}

¹Laureate Institute for Brain Research, Tulsa, OK, USA; ²School of Electrical and Computer Engineering, University of Oklahoma-Tulsa, Tulsa, OK, USA; ³Stephenson School of Biomedical Engineering, University of Oklahoma, Norman, OK, USA; ⁴Center for Biomedical Engineering, University of Oklahoma, Norman, OK, USA.

[#]corresponding author: Jerzy Bodurka

Email: jbodurka@laureateinstitute.org

Address: Laureate Institute for Brain Research

6655 South Yale Avenue

Tulsa, OK 74136

-

Highlights:

Novel algorithm for automatic cardiac cycle detection directly from EEG-fMRI

Algorithm largely improved cardioballistic artifact (BCG) cycle detection in EEG-fMRI

High detection accuracy achieved without using external ECG recordings

Make possible to automate BCG artifact removal from large EEG-fMRI datasets.

Abstract

Background:

In simultaneous EEG-fMRI, identification of the period of cardioballistic artifact (BCG) in EEG is required for the artifact removal. Recording the electrocardiogram (ECG) waveform during fMRI is difficult, often causing inaccurate period detection.

New Method:

Since the waveform of the BCG extracted by independent component analysis (ICA) is relatively invariable compared to the ECG waveform, we propose a multiple-scale peak-detection algorithm to determine the BCG cycle directly from the EEG data. The algorithm first extracts the high contrast BCG component from the EEG data by ICA. The BCG cycle is then estimated by band-pass filtering the component around the fundamental frequency identified from its energy spectral density, and the peak of BCG artifact occurrence is selected from each of the estimated cycle.

Results:

The algorithm is shown to achieve a high accuracy on a large EEG-fMRI dataset. It is also adaptive to various heart rates without the needs of adjusting the threshold parameters. The cycle detection remains accurate with the scan duration reduced to half a minute.

Comparison with Existing Method:

The algorithm is shown to give a higher detection accuracy than the commonly used cycle detection algorithm *fmrib_qrsdetect* implemented in EEGLAB.

Conclusions:

The achieved high cycle detection accuracy of our algorithm without using the ECG waveforms makes possible to create and automate pipelines for processing large EEG-fMRI datasets, and virtually eliminates the need for ECG recordings for BCG artifact removal

1 Introduction

Electroencephalography (EEG) and functional magnetic resonance imaging (fMRI) provide noninvasive techniques to investigate brain states and activities. EEG records the electrical activity from cerebral cortex with a high temporal resolution. fMRI commonly measures the blood oxygen level of the brain with a high spatial resolution. Multimodal brain imaging with simultaneous recordings of EEG and fMRI combines the advantages of high temporal EEG resolution and high spatial fMRI resolution (Mulert and Lemieux, 2010), and has become an important tool to study brain spatial and temporal dynamics (Yuan et al., 2012; Zotev et al., 2016).

Because of the strong static and varying gradient magnetic fields, the EEG data acquired simultaneously with fMRI suffers inevitably from two artifacts: the magnetic resonance (MR) gradient artifact and the cardioballistic (BCG) artifact. The MR artifact originates from the time varying gradient field during image acquisition. With MRI hardware improvements, the MR artifact is strictly periodic with the fMRI repetition time, and hence it can be efficiently removed from the EEG data using the average artifact subtraction (AAS) method (Allen et al., 2000). On the other hand, the BCG artifact is caused by the movements of the electrodes or subject due to pulsatile scalp, or by the movement of conductive blood related to the cardiac cycle (Yan et al., 2010; Mullinger et al., 2013). While the waveform of the BCG artifact exhibits distinct pulse features related to the cardiac cycle, the features vary considerably in shape, amplitude and scale over time.

Common algorithms for the BCG artifact removal include reference-based methods that form artifact templates based on reference signals. The reference signals, for example, can be acquired by electrocardiogram (ECG) (Allen et al., 1998), head motion estimation using adaptive filtering techniques (Bonmassar et al., 2002), and the insulating reference layer that is isolated from the EEG signals (Chowdhury et al., 2014). Recently a reference-free method was also introduced to model and remove the BCG artifact by harmonic basis and harmonic regression (Krishnaswamy et al., 2016). On the other hand, the BCG artifact can be removed by component analysis, such as optimal basis set (OBS) (Niazy et al., 2005), independent component analysis (ICA) (Bell and Sejnowski, 1995; Srivastava et al., 2005; Mantini et al., 2007), and wavelet transform (Kim et al.,

2004; Wan et al., 2006). While using ICA alone may give suboptimal performance in the BCG artifact removal because of the non-stationary BCG nature (Debener et al., 2007), applications of AAS (Allen et al., 1998) or OBS followed by ICA can reduce the BCG artifact significantly (Debener et al., 2007; Vanderperren et al., 2010). The AAS and OBS subtractions remain to be the most widely used methods for the BCG artifact removal in EEG simultaneously acquired with fMRI.

The AAS and OBS algorithms require the detection of the BCG cycles in order to form the artifact subtraction templates. Thus the effectiveness of the BCG artifact correction using these algorithms depends on the accurate detection of the BCG cycles. QRS complex in the ECG waveform reflects the depolarization of the right and left ventricles and is the most prominent feature of the ECG waveform. The QRS complex, in particular the peak of the R wave in the complex, has been used for the determination of the cardiac cycles outside an MRI scanner. In simultaneous EEG-fMRI experiments, the ECG recording is commonly used to acquire the BCG cycle. Because of the strong fields in fMRI, the waveform of the ECG is prone to artifacts, sensitive to the probe design and position, and varies substantially across subjects. While the accuracy of the automatic QRS detection of ECG acquired outside an MRI scanner is very robust and reaches over 99% (Christov 2004), the period detection of ECG acquired in fMRI, which largely depends on its waveform, lacks robustness and was shown to have a much lower accuracy (Iannotti et al., 2015). Since an accurate BCG cycle detection is the basis of a proper removal of the BCG artifact from the EEG data, a robust detection algorithm is critical for the possibility of automatic pipeline for EEG preprocessing.

As compared to that of the ECG recordings during fMRI, the waveforms of the BCG components in the EEG data are relatively invariable. The BCG components can be extracted from the EEG data by ICA (Srivastava et al., 2005; Mantini et al., 2007; McMenamin et al., 2010), and utilized for the BCG cycle determination. Recently, pulse artifact detection and correction based directly on the EEG data were proposed (Luo et al., 2015; Iannotti et al., 2015; Wong et al., 2016). These works extracted the pulse artifact from the EEG data by ICA (Luo et al., 2015; Wong et al., 2016) or by the signal difference between the electrodes on the

left and right hemispheres (Iannotti et al., 2015). As ICA is capable of separating the artifacts, such as the BCG, muscle, blink and saccade artifacts, from each other (McMenamin et al., 2010), it provides a robust way to extract the BCG component with a relatively invariable waveform. This is particularly important for an accurate BCG cycle detection in the automatic processing of a large EEG dataset simultaneously acquired with fMRI. On the other hand, the commonly used algorithm for the automatic cycle detection of the ECG acquired in fMRI (Niazy et al., 2005; Debener et al., 2007; Luo et al., 2015; Iannotti et al., 2015) was developed for the R-peak detection of the ECG acquired outside an MRI scanner (Christov 2004). Since the waveforms of the ECG vary substantially inside the scanner and the algorithm sets no limits to the detected cycle duration for individual subjects, multiple detections in one cycle or detections with significant missing cycles are observed (Fig. 1a). When large EEG datasets are considered, tremendous efforts are needed for the correction of the detected cycles, which prohibits any automation and makes the automatic processing virtually impossible.

The BCG-related independent components (IC_{bcg}) can be automatically identified by the mean power spectral density, topographical map, and signal contribution of the component (Wong et al., 2016). Based on the automatic identification of the IC_{bcg} , we propose a novel automatic multiple-scale peak detection algorithm applied directly to the IC_{bcg} for the BCG cycle determination. The algorithm involves peak detections in two band-pass filtering steps. In the first step, the BCG component is band-pass filtered for the estimation of the BCG cycle, with the band-pass frequencies chosen around the fundamental frequency automatically identified from the energy spectral density of the IC_{bcg} . The second step selects the peak of the pulse artifact occurrence, which follows closely the R-peak of ECG, from each of the estimated cycle. The proposed algorithm limits the number of peaks to be detected in each BCG cycle, and significantly improves the detection accuracy by avoiding the double cycle detection or massively missing the peaks. The proposed algorithm also utilizes the relatively invariable waveform of the automatically identified BCG component from ICA to provide a direct measurement of the BCG cycle from the EEG data without using an external ECG recording.

2 Methods

2.1 Data Acquisition

The study was conducted at the Laureate Institute for Brain Research. The research protocol was approved by the Western Institutional Review Board (IRB). Forty-eight subjects (31 PTSD patients and 17 healthy controls, mean age 32 ± 7 years, all male) participated in the study. Simultaneous EEG-fMRI was recorded on each subject over three scanning sessions. Each session included two resting scans. Out of the 48 subjects, 8 subjects had only 5 resting scans, and 1 subject had 7 resting scans. In total, there were 281 resting scans. Each scan lasted for 8 min 46 s.

The EEG-fMRI experiments were conducted on a 3 tesla MR750 MRI scanner (GE Healthcare, Waukesha, WI) with a standard 8-channel receive-only head coil. A single-shot gradient-echo EPI sequence with Sensitivity Encoding (SENSE) was employed for fMRI. The following EPI imaging parameters were used: TR/TE=2000/30 ms, FOV=240 mm, 34 axial slices per volume, slice thickness=2.9 mm, slice gap=0.5 mm, 96×96 acquisition matrix, SENSE acceleration factor $R=2$, flip angle= 90° , sampling bandwidth=250 kHz. Three EPI volumes (6 s) were excluded from the data analysis to allow the fMRI signal to reach steady state. The EPI images were reconstructed into a 128×128 matrix, so the resulting fMRI voxel size was $1.875 \times 1.875 \times 2.9 \text{ mm}^3$. Physiological pulse oximetry and respiration waveforms were also acquired with fMRI.

The EEG recordings were performed simultaneously with fMRI using a 32-channel MR-compatible EEG system (Brain Products GmbH). The EEG signals were measured using 31 electrodes relative to the common reference (FCz). One electrode was placed at the subject's back for the recording of the ECG. The EEG signals were acquired with 16-bit 5 kS/s sampling providing 0.2 ms temporal and 0.1 μV measurement resolution, and hardware-filtered between 0.016 Hz (10 s time constant) and 250 Hz during the acquisition.

2.2 EEG data preprocessing

The algorithm was implemented in MATLAB (MathWorks, Inc.). The MR gradient artifacts were corrected using OBS (*fmrib_fastr.m* implemented in EEGLAB) (Allen et al., 2000; Delorme and Makeig, 2004; Niazy et al., 2005). The EEG data were then band-pass filtered between 0.1 Hz and 70 Hz and downsampled to 250 S/s. Band-rejection filters (1 Hz bandwidth) were applied to remove harmonics of the fMRI slice selection frequency (17 Hz), as well as the AC power line artifact at 60 Hz, and a vibration artifact at 26 Hz. The ICA was performed on the preprocessed EEG data using the Infomax algorithm (Bell and Sejnowski, 1995) implemented in EEGLAB to extract 31 independent components (ICs) from the 31 EEG channels.

2.3 Automatic identification of the BCG components from the EEG data

We have recently developed an algorithm to automatically identify the cardioballistic artifact ICs (IC_{bcg}) related to head motions by analyzing the features of the power spectral density, topographic map and signal contributions of the IC_{bcg} (Wong et al., 2016). We argued in Wong et al., 2016 that, by adequately choosing the features and adjusting the threshold parameters, the algorithm can be extended to identify also the non-motion related IC_{bcg} , which is associated with a less restricted set of selection criteria, such as smaller signal contribution, larger spectral power at the harmonic frequencies of the BCG, and exhibition of either unilateral or opposite polarity topography. In this paper, the IC_{bcg} was automatically identified based on the algorithm described in Wong et al., 2016, with the algorithm extended to selecting both motion and non-motion related IC_{bcg} . This was achieved by modifying the conditions and threshold parameters in the analyses of the power spectral density, topographic map, and IC_{bcg} signal contribution as described in Appendix A.

2.4 Selection of the BCG component for cycle determination

Because of the non-stationary nature of the cardioballistic artifact, several IC_{bcg} components were usually identified in each scan. The peak contrast of the IC_{bcg} defined in the following was used to select the IC_{bcg} for the BCG cycle detection.

The IC_{bcg} typically exhibits distinct peaks caused by cardiac pulsations. Analyzing the peak contrast of the IC_{bcg} aims to select the IC_{bcg} with the most distinct peak features for the cardiac cycle determination. To calculate the contrast, the IC_{bcg} is first band-pass filtered between 1 Hz and the slice acquisition frequency, normalized using its standard deviation, and multiplied by a sign to ensure the pulsation peaks to point upward. The sign is taken as positive (or negative) if the average values of IC_{bcg} that lie between $[1, 4]$ is greater (or smaller) in magnitude than that lie between $[-4, -1]$. Then the values of the IC_{bcg} greater than 4 are capped at 4 to minimize the motion artifact in the contrast calculation. The processed IC_{bcg} as described above is now denoted by $f(t)$.

It is noted that the distinctness of the peak features in some IC_{bcg} varies during the scan. Therefore the IC_{bcg} contrast is analyzed over local time segments. Divide the scan time into N_T time segments of 4 s duration. The peak contrast of the IC_{bcg} is defined by the average peak to background ratio over all the time segments as

$$C = \frac{1}{N_T} \sum_{j=1}^{N_T} \frac{\langle f_j^{(pk)} \rangle - \langle f_j^{(bg)} \rangle}{\Delta f_j^{(bg)}} . \quad (1)$$

Here $\langle f_j^{(pk)} \rangle$ is the average of $f_j^{(pk)}$ with $f_j^{(pk)} = \{x: x \in \text{the top } 10^{\text{th}} \text{ percentile of the peak amplitude of } f(t) \text{ in the } j^{\text{th}} \text{ time segment}\}$, and $\langle f_j^{(bg)} \rangle$ and $\Delta f_j^{(bg)}$ are the mean and standard deviation of $f_j^{(bg)}$ with $f_j^{(bg)} = \{x: x \in \text{the lower } 90^{\text{th}} \text{ percentile of } f(t) \text{ in the } j^{\text{th}} \text{ time segment}\}$. The IC_{bcg} with the highest peak contrast C is selected for the BCG cycle determination. Now the selected IC_{bcg} is denoted by $F(t)$. Fig. 2a shows examples of the contrast C and the corresponding $F(t)$. The contrasts of the selected IC_{bcg} from the 281 scans are plotted in Fig. 2b.

2.5 Cardiac cycle determination by multi-scale peak detection algorithm

The multiple-scale peak detection algorithm was originally proposed for the peak-to-peak cardiac cycle determination in ECG (Wong et al., 2014). Here the algorithm was refined for the detection directly from the BCG data. The algorithm includes two steps of band-pass filtering. In Step 1 (Section 2.5.2), the selected IC_{bcg}

$(F(t))$ is band-pass filtered ($F_{bp1}(t)$) for the estimation of the cardiac cycle. In order to find the band-pass frequencies adaptive to individual subject, the energy spectral density of the IC_{bcg} ($S(\nu)$) and its smoothed form ($S'(\nu)$) are first evaluated (Section 2.5.1). In Step 2 (Section 2.5.3), $F(t)$ is band-pass filtered and smoothed ($F_{bp2}(t)$) for the peak-to-peak cycle determination. The peaks of the artifact occurrence caused by the cardiac pulsations are selected from each of the estimated cycle found in Step 1. At the end of each step, the detected cycles are adjusted if they exceed the threshold values determined by the reference frequencies acquired from $S(\nu)$. The detailed graphical representation of the algorithm of this paper is sketched in Fig. 3.

2.5.1 Determination of the smoothed energy spectral density and band-pass frequencies

For the BCG cycle estimation, the selected IC_{bcg} is first rectified by setting the negative values to zero before the band-pass filtering. The purpose of the rectification process is to remove the noisy negative part of IC_{bcg} so that the cycle estimation is based primarily on the peaks of the artifact occurrences. It should be noted that, although the rectification process introduces slope discontinuity to the function, the Fourier transform of the IC_{bcg} , and hence the energy spectrum calculation, are only affected at high frequencies, but not in the frequency range of the cardioballistic artifact.

To prevent the Fourier transform of a non-negative function from divergence at the zero frequency, the mean of the rectified IC_{bcg} is removed in the energy spectrum calculation. Denote the resulting IC_{bcg} by $F'(t)$. The energy spectral density of $F'(t)$ is defined by

$$S(\nu) = |\tilde{F}'(\nu)|^2, \quad (2)$$

where $\tilde{F}'(\nu)$ is the Fourier transform of $F'(t)$. Consider the Hann window centered at $t = 0$ (Oppenheim et al., 1999),

$$h(t) = \begin{cases} 0.5 \left[1 - \cos \frac{2\pi \left(\frac{t_h}{2} + t \right)}{t_h} \right] & \text{for } |t| \leq \frac{t_h}{2}, \\ 0 & \text{for } |t| > \frac{t_h}{2} \end{cases}, \quad (3)$$

where $t_h = 16$ s, the smoothed energy spectral density ($S'(\nu)$) is obtained by convolving $S(\nu)$ with the Fourier transform of the Hann window ($\tilde{h}(\nu)$). Typical $S(\nu)$ and $S'(\nu)$ are shown in Figs. 3a and 4. From the smoothed spectrum $S'(\nu)$, the fundamental frequency (ν_0) and the second harmonic frequency (ν_1) of the subject's heart rate are identified. The band-pass filtering frequencies of Step 1 ($[\nu_{bp1,L}, \nu_{bp1,U}]$) are then chosen from the local minima around the identified fundamental frequency in $S'(\nu)$ (Fig. 3a), with the conditions $\nu_{bp1,L} > 0.5$ Hz and $\nu_{bp1,U} < \nu_1$. Finally, three reference frequencies ($\nu_{ref,1}, \nu_{ref,2}, \nu_{ref,3}$) are selected from $S(\nu)$ for cycle adjustment. The evaluation details of the above frequencies ($\nu_{bp1,L}, \nu_{bp1,U}, \nu_0, \nu_1, \nu_{ref,1}, \nu_{ref,2}, \nu_{ref,3}$) are given in Appendix B. The threshold time durations derived from these frequencies to be used in Sections 2.5.2 and 2.5.3 are defined by

$$\Delta_j = \frac{1}{\nu_{ref,j}}, \quad \text{for } j = 1, 2, 3, \quad (4a)$$

$$\Delta_0 = \frac{1}{\nu_0}, \quad (4b)$$

$$\Delta_L = \frac{1}{\nu_{bp1,L}}. \quad (4c)$$

2.5.2 Estimation of the BCG cycle

This step aims to estimate the cycle interval of the BCG component. In this step, the IC_{bcg} is rectified by setting the negative values to zero. The intensity of the rectified function is band-pass filtered ($F_{bp1}(t)$) within the frequency range $[\nu_{bp1,L}, \nu_{bp1,U}]$, and normalized using the standard deviation. Typical waveforms of $F_{bp1}(t)$ are plotted in Figs. 3b and 5. As shown in the figures, $F_{bp1}(t)$ can be used to estimate the cardiac cycle, in each of which the peak of the BCG artifact occurrence is selected.

The time interval of the i^{th} estimated cycle of $F_{bp1}(t)$ is defined by

$$R_{bp1,i} = [t_i^{(bp1)}, t_{i+1}^{(bp1)}], \quad (5)$$

where $t_i^{(\text{bp1})}$ is initially taken at the local minima of $F_{\text{bp1}}(t)$ (Fig. 3b, left column). The time interval is adjusted if they exceed the threshold time limits Δ_3 and Δ_L . Denote all the peaks of $F_{\text{bp1}}(t)$ by $\{t_{p,i}\}$, and the local minima of $F_{\text{bp1}}(t)$ by $\{t_{v,i}\}$, where $t_{p,i} \in R_{\text{bp1},i}$ and $t_{v,i} < t_{p,i} < t_{v,i+1}$. An extra cycle is detected in $R_{\text{bp1},i}$ if the following two conditions are satisfied: (i) the peak rise from the surrounding minima is small as compared to the previous cycles, with either a short time difference from the neighboring peak (Eq. (6a) or (6b)), or a short time difference between the surrounding minima (Eq. (6c)); (ii) the time difference between the surrounding neighbor peaks is insufficiently long to have two cycles (Eq. (6d)). The conditions are summarized in the following:

$$F_{\text{bp1}}(t_{p,i}) - F_{\text{bp1}}(t_{v,i}) < \varepsilon r_{i,\text{ave}}, \quad \text{and} \quad t_{p,i} - t_{p,i-1} < \Delta_3, \quad (6a)$$

$$F_{\text{bp1}}(t_{p,i}) - F_{\text{bp1}}(t_{v,i+1}) < \varepsilon r_{i,\text{ave}}, \quad \text{and} \quad t_{p,i+1} - t_{p,i} < \Delta_3, \quad (6b)$$

$$\min[F_{\text{bp1}}(t_{p,i}) - F_{\text{bp1}}(t_{v,i}), F_{\text{bp1}}(t_{p,i}) - F_{\text{bp1}}(t_{v,i+1})] < \varepsilon r_{i,\text{ave}}, \quad \text{and} \quad t_{v,i+1} - t_{v,i} < \Delta_3, \quad (6c)$$

$$t_{p,i+1} - t_{p,i-1} < \Delta_L, \quad (6d)$$

where $r_{i,\text{ave}}$ is the average peak rise from the surrounding minima over the past 10 cycles, and ε is chosen to be 0.2. The first condition (Eq. (6a), (6b) or (6c)) indicates the exceptionally small peak rise and short cycle detected at $t_{p,i}$, which suggests the possibility of an extra cycle detection. The second condition further suggests that only one cardiac cycle should be found in between $t_{p,i-1}$ and $t_{p,i+1}$. When an extra cycle is recognized in $F_{\text{bp1}}(t)$, the extra cycle is not counted, but is absorbed into the neighboring cycles according to the conditions of Eqs. (6a)–(6c) (Fig. 3b, right column). The new cycle boundary is taken to be the temporal location of the extra peak in the fusion process.

2.5.3 Peak-to-peak cardiac cycle detection of the BCG component

In this step, the peak-to-peak cardiac cycle is determined. The IC_{bcg} is smoothed ($F_{\text{bp2}}(t)$) by band-pass filtering between 1 Hz and the MR slice acquisition frequency ($\nu_{\text{MR}} = 17$ Hz), and normalized within each time

interval $R_{bp1,i}$ using the standard deviation of $F_{bp2}(t)$ in $R_{bp1,i}$. Typical waveforms of $F_{bp2}(t)$ are plotted in Figs. 3c and 5. As shown in the figures, several peaks are usually found in one interval. For one interval at a time, for instance the interval $R_{bp1,i}$, the peak of the BCG artifact occurrence ($t_i^{(bp2)}$) that follows closely the R-peak of ECG is selected. Then the selection process will proceed to the next interval $R_{bp1,i+1}$.

The peak-to-peak cardiac cycles of $F_{bp2}(t)$ are defined by $\{t_i^{(bp2)}\}$. For the selection of $t_i^{(bp2)}$ in $R_{bp1,i}$, the interval $R_{bp1,i}$ is first aligned with each of the past N_c intervals $R_{bp1,j}$ ($j = i-1, \dots, i-N_c$) by maximizing the correlation of $F_{bp2}(t)$ in $R_{bp1,i}$ and $R_{bp1,j}$. After the alignment, the time offset $t_{c,j}$ of the peak $t_j^{(bp2)}$ from the lower bound of the previous interval $R_{bp1,j}$ as measured from the lower bound of the current interval $R_{bp1,i}$ is given by

$$t_{c,j} = t_{b_i} + t_j^{(bp2)} - t_{b_j} - \operatorname{argmax}_{\tau_j} \langle F_{bp2}(t_{b_j} + t + \tau_j) F_{bp2}(t_{b_i} + t) \rangle_t. \quad (7)$$

Here $t_{b_i} = t_i^{(bp1)}$ and $t_{b_j} = t_j^{(bp1)}$ are the lower bounds of the intervals $R_{bp1,i}$ and $R_{bp1,j}$, and $\langle \dots \rangle_t$ denotes the average of the enclosed function over t . Then the reference point for the selection of $t_i^{(bp2)}$ is defined by the average of $t_{c,j}$

$$t_c = \frac{1}{N_c} \sum_{j=i-1, \dots, i-N_c} t_{c,j}.$$

In this paper, $N_c = 10$ past cycles is used. For the peak selection in the first 10 cycles, N_c is set to the number of available past cycles. Denote all the peaks of $F_{bp2}(t)$ by $\{t_{p,i}\}$. The peak $t_i^{(bp2)}$ is selected from $\{t_{p,i}\}$ based on the following criteria:

$$t_i^{(bp2)} = \operatorname{argmin}_{t_{p,i} \in R_{bp1,i}} |t_{p,i} - t_c|, \quad (8a)$$

$$t_i^{(bp2)} = \operatorname{argmax}_{t_{p,i} \in R_{bp1,i}} \{F_{bp2}(t_{p,i})\}, \quad (8b)$$

$$t_i^{(bp2)} = \operatorname{argmax}_{t_{p,i} \in R_{bp1,i}} \{r(t_{p,i})\}, \quad (8c)$$

$$F_{\text{bp}2}(t_i^{(\text{bp}2)}) \geq \langle F_{\text{bp}2}(t) \rangle + a \Delta F_{\text{bp}2}(t), \quad \text{or} \quad r(t_i^{(\text{bp}2)}) \geq \langle r(t_{p,i}) \rangle + a \Delta r(t_{p,i}), \quad (8d)$$

where

$$r(t_{p,i}) = F_{\text{bp}2}(t_{p,i}) - \min_{t \in [t_{p,i} - \Delta t, t_{p,i} + \Delta t]} F_{\text{bp}2}(t) \quad (8e)$$

is the largest amplitude difference in the time range $[t_{p,i} - \Delta t, t_{p,i} + \Delta t]$, $\Delta t = 50$ ms is the approximate width of the peak of the artifact occurrence, and $a = 2$. Again $\langle F_{\text{bp}2}(t) \rangle$ and $\Delta F_{\text{bp}2}(t)$ denote the average and standard deviation of $F_{\text{bp}2}(t)$ over time t , and $\langle r(t_{p,i}) \rangle$ and $\Delta r(t_{p,i})$ denote the average and standard deviation of $r(t_{p,i})$ over peak time $\{t_{p,i}\}$. In some local time segments of the IC_{bcg} with low contrast, no peak satisfies all the criteria in Eq. (8). In such a case, $t_i^{(\text{bp}2)}$ is selected based on the restricted set of criteria in the following order until the peak is found: (i) Eqs. (8a)–(8c); (ii) Eqs. (8a), (8d); (iii) Eq. (8b) or (8c) that gives the closer $t_i^{(\text{bp}2)}$ to t_c . It should be noted that Eq. (8a) is not applicable to the selection of the first peak ($t_1^{(\text{bp}2)}$) in $R_{\text{bp}1,1}$ as no past interval is defined for $t_1^{(\text{bp}2)}$. In this case, $t_1^{(\text{bp}2)}$ is selected based on the criteria in the following order: (i) Eqs. (8b)–(8d); (ii) Eqs. (8b), (8d); (iii) Eqs. (8c), (8d); (iv) Eq. (8b).

At the end of Step 2, the detected peaks ($\{t_i^{(\text{bp}2)}\}$) are validated or adjusted one peak at a time by comparing the duration $t_i^{(\text{bp}2)} - t_{i-1}^{(\text{bp}2)}$ with the time limits Δ_1 , Δ_2 , and Δ_3 defined in Eq. (4). The durations Δ_1 and Δ_3 are used to set the upper and lower limits for the detected cycles. A cycle duration that exceeds such limits indicates a missing cycle, extra cycle, or false cycle detection. For the cycle adjustment, the peak is re-selected from the time interval $R_{\text{adj},i}$ based on Eq. (8), and the correlation of $F_{\text{bp}2}(t)$ in Eq. (7) is calculated using the updated ranges $R_{\text{adj},i}$ ($R_{\text{adj},j}$) instead of $R_{\text{bp}1,i}$ ($R_{\text{bp}1,j}$), with the lower bound t_{b_i} (t_{b_j}) of $R_{\text{adj},i}$ ($R_{\text{adj},j}$) updated correspondingly. While the updated ranges $R_{\text{adj},j} = [t_j^{(\text{bp}2)} - \frac{\Delta_0}{2}, t_j^{(\text{bp}2)} + \frac{\Delta_0}{2}]$ are taken to be centered around the previously detected peaks, the range $R_{\text{adj},i}$ depends on the types of the false detections, which are discussed in details in Appendix C and summarized in Table 1.

After the peaks $\{t_i^{(\text{bp2})}\}$ are validated or adjusted, the peak-to-peak cycles of the IC_{bcg} ($\{t_i^{(\text{IC})}\}$) are obtained by searching for the corresponding peaks of $F_{\text{bp2}}(t)$ in $F(t)$, where

$$t_i^{(\text{IC})} = \operatorname{argmax}_{t_{p,i} \in [t_i^{(\text{bp2})} - \Delta_{\text{MR}}, t_i^{(\text{bp2})} + \Delta_{\text{MR}}]} F(t_{p,i}), \quad (9a)$$

$$\Delta_{\text{MR}} = \frac{1}{\nu_{\text{MR}} - 0.5 \text{ Hz}}, \quad (9b)$$

$\{t_{p,i}\}$ denote all the peaks in $F(t)$, and $\nu_{\text{MR}} = 17 \text{ Hz}$ is the fMRI slice acquisition frequency used in experiments. The 0.5 Hz in Eq. (9b) is used to account for the width of the band-rejection filter after the MRI gradient artifact correction.

2.5.4 Summary of steps

In this section, the proposed multiple-scale peak detection algorithm detects the BCG artifact cycle directly from the BCG component ($F(t)$).

In Sections 2.5.1, the algorithm evaluates the energy spectral density of the rectified IC_{bcg} after having the mean removed, and smooths the spectrum by convolving it with the Fourier transform of the Hann window. From the energy spectral density ($S(\nu)$) and the corresponding smoothed form ($S'(\nu)$), this step outputs the band-pass frequencies ($\nu_{\text{bp1,L}}, \nu_{\text{bp1,U}}$) for the IC_{bcg} cycle estimation, the reference frequencies ($\nu_{\text{ref,1}}, \nu_{\text{ref,2}}, \nu_{\text{ref,3}}$) for the cycle adjustments, and the fundamental frequency (ν_0) of the heart rate of the subject.

In Section 2.5.2, the algorithm evaluates $F_{\text{bp1}}(t)$ by band-pass filtering the intensity of the rectified IC_{bcg} within the frequency range $[\nu_{\text{bp1,L}}, \nu_{\text{bp1,U}}]$, and identifies the peak-to-peak cycles of $F_{\text{bp1}}(t)$. After the cycles are adjusted using the frequencies $\nu_{\text{ref,3}}$ and $\nu_{\text{bp1,L}}$, this step outputs the estimated cycle intervals of the IC_{bcg} $\{R_{\text{bp1},i}: [t_i^{(\text{bp1})}, t_{i+1}^{(\text{bp1})}]\}$, within each of these intervals the peak of the BCG artifact occurrence is selected.

In Section 2.5.3, the algorithm smooths the IC_{bcg} ($F_{\text{bp2}}(t)$) by band-pass filtering it between 1 Hz and the MR slice acquisition frequency (17 Hz). For one cycle interval $[t_i^{(\text{bp1})}, t_{i+1}^{(\text{bp1})}]$ at a time, the algorithm selects

the peak of the BCG artifact occurrence ($t_i^{(\text{bp}2)}$) in $F_{\text{bp}2}(t)$ based on the peak amplitude and the average of the past peak locations after the interval $[t_i^{(\text{bp}1)}, t_{i+1}^{(\text{bp}1)}]$ is aligned with the past cycle intervals by maximizing the correlations between them. After the cycles are validated or adjusted using the frequencies $\nu_{\text{ref},1}$, $\nu_{\text{ref},2}$, $\nu_{\text{ref},3}$ and ν_0 , this step outputs the peak-to-peak cycles of the IC_{bcg} $\{t_i^{(\text{IC})}\}$, which are the corresponding peaks of $F_{\text{bp}2}(t)$ in $F(t)$.

2.6 Evaluation of cycle detection results

The automatically detected peaks of the IC_{bcg} were compared to the correct peak timings ($\{t_{i,\text{corr}}^{(\text{IC})}\}$), which were acquired in reference to both the IC_{bcg} and ECG waveforms by semi-automatic search with subsequent manual inspection. The detected peak is deemed to be correctly identified (a true positive detection) when the difference between the timings of the detected peak and the correct peak is less than the given resolution (δ). A false positive detection refers to a falsely detected peak, and a false negative detection refers to an undetected peak. For the peak comparisons, two resolutions $\delta = 10$ ms and 58.8 ms were used. The 58.8 ms resolution was used in order to exclude the detection error originated from the amplitude fluctuations in the IC_{bcg} induced by MRI gradients (17 Hz).

To evaluate the peak detection accuracy, the sensitivity (S_e), specificity (S_p) and F_1 -score were used:

$$S_p = \frac{\text{TP}}{\text{TP} + \text{FP}}, \quad (10a)$$

$$S_e = \frac{\text{TP}}{\text{TP} + \text{FN}}, \quad (10b)$$

$$F_1 = \frac{\text{TP}}{\text{TP} + 0.5 (\text{FP} + \text{FN})}, \quad (10c)$$

where TP, FP and FN stand for the numbers of true positive, false positive and false negative peak detections.

When the peak detection shifts slightly from the true peak, the single detection error will be counted twice in Eq. (10) through FP and FN. To avoid double counting the error in the evaluation, the shifted false positive (SP) and shifted false negative (SN) detections were introduced (Dotsinsky and Stoyanov, 2004; Christov 2004). A shifted false positive is defined when the false detection falls within 200 ms earlier than the true peak, and a shifted false negative is defined when the false detection falls within 200 ms afterward. With SP and SN taken into account, the sensitivity, specificity and F_1 -score (Eq. (10)) become

$$S_p' = \frac{TP}{TP + FP' + SP}, \quad (11a)$$

$$S_e' = \frac{TP}{TP + FN' + SN}, \quad (11b)$$

$$F_1' = \frac{TP}{TP + 0.5 (FP' + SP + FN' + SN)}, \quad (11c)$$

where $FP' = FP - SP - SN$ and $FN' = FN - SP - SN$ are the numbers of false positive and false negative detections with SP and SN excluded.

Finally, the detection accuracy of *fmrib_qrsdetect.m* on the ECG and IC_{bcg} cycles were evaluated for comparisons. It is noted in some scans that, since the amplitudes of the R-peaks are comparable to the surrounding background amplitude, the R-peaks are not distinctly observed in the waveform of the ECG (Fig. 1a: (S8)). For the scans with distinctly (or indistinctly) observable R-peaks, the correct peak timings of the ECG cycles ($\{t_{i,corr}^{(ECG)}\}$) were taken at the R-peak (or T-peak, c.f. Fig.1a: (S8)) locations. Also as shown in Fig. 1, *fmrib_qrsdetect.m* does not often pick the R-peak (or artifact occurrence peak) locations in the cycle detections of the ECG (or IC_{bcg}). In order to compare the detected ECG (or IC_{bcg}) cycles using *fmrib_qrsdetect.m* with the correct peak timings $\{t_{i,corr}^{(ECG)}\}$ (or $\{t_{i,corr}^{(IC)}\}$), the detected cycles were first aligned to $\{t_{i,corr}^{(ECG)}\}$ (or $\{t_{i,corr}^{(IC)}\}$) by maximizing the correlation between them.

3 Results

The introduced multiple-scale peak detection algorithm was applied to 281 resting scans from 48 subjects. The first 6 s of the scan and the time segments with unrecognizable ECG or IC_{bcg} waveforms caused by subject motions were removed from the peak comparisons, giving a data length of 40.22 hours.

Fig. 1a shows ECG data exemplars from eight subjects (S1-S8), and illustrates the failure of the ECG cycle detection (black crosses) using the cycle detection algorithm (*fmrib_qrsdetect.m*) implemented in EEGLAB (Christov 2004; Kim et al., 2004; Niazy et al., 2005; Delorme and Makeig 2004). Multiple detections in one cycle or detections with significant missing cycles are found in several scans. Also it is noted that the detected cycles do not always fall consistently to a fixed location relatively to the R-peak locations (Fig. 1a: (S2), (S7)). For example, in (S2) of Fig. 1a, the detections fall either at the peak location or afterward. In case when there is incorrect cycle detection, there is an ambiguity in the choice of the corrected cycle. Improved results are found when *fmrib_qrsdetect.m* is applied to the IC_{bcg} (red crosses, Fig. 1b), but the detected cycles still do not fall consistently to a fixed location relative to the R-peak locations. Fig. 5 shows the results of the significantly improved BCG peak detection (the same data exemplar as in Fig. 1) by the proposed algorithm. The detected peaks are shown to follow closely the R peaks of the ECG, and our algorithm correctly detects the peaks despite the vast variations of the ECG waveforms.

The cycle detection accuracy of the proposed algorithm is now evaluated by the specificity, sensitivity and F_1 -score (Eq. (10)). Figs. 6a and 6b plot the F_1 -score of the detected cycles against the IC_{bcg} contrast (C) with the comparison resolutions $\delta = 10$ ms and 58.8 ms. As shown in the figures, the detection accuracy increases with C as expected. The results for the 48 subjects in 281 scans are listed in Table 2. For the 281 scans with $\delta = 10$ ms, the overall TP = 153019, FP = 648, FN = 911, $S_p = 99.58\%$, $S_e = 99.41\%$ and $F_1 = 99.49\%$. With $\delta = 58.5$ ms, the overall TP = 153050, FP = 617, FN = 880, $S_p = 99.60\%$, $S_e = 99.43\%$ and $F_1 = 99.51\%$. With the shifted false positive and shifted false negative detections taken into account, the F_1 -score calculated by Eq. (11) with $\delta = 10$ ms is plotted against the IC_{bcg} contrast (C) in Fig. 6c. The overall TP = 153019, FP' =

297, SP = 174, FN' = 560, SN = 177, $S_p' = 99.69\%$, $S_e' = 99.52\%$ and $F_1' = 99.61\%$. Importantly, the results of the propose cycle detection algorithm are comparable to the ECG cycle detection outside the scanner (Christov, 2004).

For comparisons, the detection accuracy of *fmrib_qrsdetect.m* on the ECG and IC_{bcg} cycles are evaluated. With the resolution $\delta = 10$ ms, the detection accuracies of *fmrib_qrsdetect.m* on the ECG and IC_{bcg} cycles are respectively given by (TP = 97987, FP = 55534, FN = 55867, $S_p = 63.83\%$, $S_e = 63.69\%$, $F_1 = 63.76\%$) and (TP = 126657, FP = 27680, FN = 27273, $S_p = 82.07\%$, $S_e = 82.28\%$, $F_1 = 82.17\%$). The detection accuracies increase with the lower resolution $\delta = 58.8$ ms: (TP = 150989, FP = 2532, FN = 2865, $S_p = 98.35\%$, $S_e = 98.14\%$, $F_1 = 98.24\%$) for the ECG cycle detection and (TP = 149657, FP = 4680, FN = 4273, $S_p = 96.97\%$, $S_e = 97.22\%$, $F_1 = 97.10\%$) for the IC_{bcg} cycle detection. The resolution of the cycle detection is low because of the inconsistent positions of the detected cycles relative to the R-peak locations. It should be noted that *fmrib_qrsdetect.m* gains in accuracy with a lower resolution but it does not benefit from the cleaner BCG waveforms as manifested in the high resolution case. The detection accuracies using *fmrib_qrsdetect.m* with $\delta = 58.8$ ms are summarized in Table 3. The total false positive and false negative detections of the ECG and IC_{bcg} cycles are about 3.5 and 5.7 times of our proposed algorithm.

The calculations were carried out in a workstation with dual Intel® Xeon® CPU E5-2620 at 2.00 GHz and 16 GB memory. The proposed algorithm takes about 4.2 s to detect 406 cardiac cycles in a 526 s duration, and the computational time (T_{cal}) of the algorithm increases linearly with the heart rate (L) (Fig. 7a).

4 Discussions

We have introduced a novel multi-scale peak detection method for automatic and accurate cardiac cycle determination directly from EEG data acquired concurrently with fMRI without the need for ECG recordings. High cardiac cycle detection accuracies are achieved based on the relatively invariable waveform of the IC_{bcg}.

Fig. 2a shows the selected IC_{bcg} according to Eq. (1) and the corresponding contrast (C). Distinct peaks can usually be observed in the entire IC_{bcg} time course when $C \geq 6$. The contrasts of the selected IC_{bcg} from 281 scans are plotted in Fig. 2b. In more than three quarters of scans, the contrasts are larger than 6.5. The high contrasts of the IC_{bcg} warrant the relatively invariable IC_{bcg} waveforms, and thus the high peak detection accuracies.

The performance of the proposed algorithm is analyzed with different hearts rates and scan durations. Fig. 7b plots the distribution of the mean heart rate (L) of each scan. The measured heart rates of 281 scans range widely from 44 to 93 bpm. In Fig. 7c, the fundamental frequency (ν_0) identified from the smoothed spectrum is plotted against the mean heart rate. The figure shows that the identified ν_0 agrees well with the measured heart rate. By using the identified ν_0 to estimate the cardiac cycles, the proposed peak detection algorithm is accurate and adaptive to various heart rates without the needs of adjusting threshold parameters.

When the scan duration is reduced, the total time period with head motions becomes comparable to the total scan duration. In the analysis of the algorithm performance with reduced scan duration, the motion time segments of the IC_{bcg} are masked to zero in the energy spectrum calculation in order to separate the effect of the reduced scan duration from that of the head motions. Fig. 7d shows the detection accuracy of the scans with different reduced durations. The detection remains accurate provided that the scan duration is sufficiently long. When the scan duration is reduced to 16.252 seconds, F_1 decreases significantly in one scan due to the inaccurate cycle estimation. Nevertheless, for all scan durations, the average F_1 over the 281 scans is larger than 98.6% (red line, Fig. 7d), and $F_1 > 95.8\%$ in more than 95% of the scans with scan durations 24.376 seconds or longer (blue line, Fig. 7d).

5 Conclusions

A multiple-scale peak detection algorithm is developed to robustly and accurately measure the cardiac cycle directly from the EEG data acquired simultaneously with fMRI, without the need of an external ECG recording. To extract the cardioballistic (BCG) component from the EEG data, independent component analysis is performed. The BCG component with the highest contrast is selected for the peak-to-peak cycle detection. The peak detection algorithm involves two band-pass filtering steps. The first step estimates the cardiac cycle by band-pass filtering the BCG component around the fundamental frequency identified from the energy spectral density. The second band-pass filtering step smooths the BCG component and selects the peak of BCG artifact occurrence from each of the estimated cycle. The detected cycles are adjusted if they exceed the threshold values determined by the reference frequencies acquired from the energy spectral density.

The multiple-scale peak detection algorithm is shown to give a higher detection accuracy than the commonly used cycle detection algorithm implemented in EEGLAB. More importantly, the algorithm achieves a high accuracy on a large EEG-fMRI dataset, and is adaptive to various heart rates without the needs of adjusting the threshold parameters. The achieved high detection accuracy makes possible to create and automate pipelines for processing a large EEG-fMRI dataset. The proposed algorithm utilizes the relatively invariable waveform of the BCG component to detect the artifact occurrence directly from the EEG data. It simplifies EEG-fMRI experiments by virtually eliminating the need to place the ECG electrode on subject's chest or back for the BCG artifact correction,

Acknowledgements

This work was supported by US Department of Defense award W81XWH-12-1-0607.

Appendix

A. Details of the modified automatic BCG components identification from the EEG data in Section 2.3

To identify both the motion and non-motion related IC_{bcg} , we have modified the algorithm described in our previous work (Wong et al., 2016). Following the original work, the modified algorithm identifies the IC_{bcg} by analyzing the features of the power spectral density, topographic map and signal contributions.

A.1 Power spectral density analysis

In the power spectral density analysis, the power spectral density of the independent component (IC) is evaluated over 2.048 s time windows with 1.024 s overlap in decibel scale. The spectrum is divided into the frequency ranges of the cardioballistic artifact (CB: 2–7 Hz) and neuronal signal (NR: 8–12 Hz). For the spectrum of an IC_{bcg} , large peaks are observed in the CB and NR frequency ranges. The peaks in the NR range of the IC_{bcg} spectrum are originated from the harmonic frequencies of the cardioballistic artifact rather than the alpha rhythm of the brain. To distinguish the IC_{bcg} from the neuronal signal component, comparable spectrum amplitudes in the CB and NR frequency ranges are required for an IC_{bcg} .

The peak rise in the CB frequency range (r_{cb}) is defined by the average amplitude difference from the surrounding minima. An NR peak is defined as the maximum power in the NR range. To obtain the full rise of the NR peak, the frequency range $[\nu_{l<}, \nu_{nr}]$ if $\nu_{l<}$ exist, or $[8 \text{ Hz}, \nu_{nr}]$ if $\nu_{l<}$ does not exist, is used, where ν_{nr} is the NR peak frequency, and $\nu_{l<}$ is the frequency at the local minimum immediately below 8 Hz. The full rise of the NR peak (r_{nr}) is taken as the amplitude difference between the NR peak and the minimum point of the above frequency range. Denote the spectrum amplitudes in the CB and NR ranges by S_{cb} and S_{nr} . The selection criteria for both the motion and non-motion related IC_{bcg} are given by (i) $\max(r_{cb}) > 0.2 S_0$; and either (ii) $r_{nr} \leq \frac{1}{3} S_0$, (iii) $\max(r_{cb}) > r_{nr} - 3$, or (iv) $\max(S_{cb}) > \max(S_{nr}) - 3$ and $\text{mean}(S_{cb}) - S_{min} > \frac{1}{3} r_{nr}$. Here S_0 is the normalization scale of the spectrum calculated by the difference between the maximum and minimum amplitudes below 4 Hz, and S_{min} is the spectrum baseline taken at the minimum amplitude below the NR peak frequency. Condition (i) defines the large peak features required in the CB frequency range for an IC_{bcg} . Condition (ii) defines the amplitude of a small NR peak rise. Conditions (iii) and (iv) define the comparable

spectrum amplitudes required in the CB and NR frequency ranges of an IC_{bcg} spectrum if Condition (ii) is not satisfied.

A.2 Topographic map analysis

The spatial projection of an IC onto the EEG channel space forms a topographic map. The topographic map of an IC is computed by spatially interpolating the spatial projection vector of the IC using the MATLAB function `griddata()`. While a motion-related IC_{bcg} exhibits opposite polarity in the topographic map, an IC_{bcg} generally exhibits unilateral or opposite polarity topography (McMenamin et al., 2010; Zotev et al., 2012). In the case of unilateral polarity topography, the polarity region is located at the rear part of the head.

In the topographic map analysis, the values and radius of the topographic map are normalized to unity. Two sets of polarity regions (primary and secondary polarity regions) are defined. The primary (secondary) polarity regions are the connected map areas with map values larger than 0.3 (0.1). Neutral regions are defined by the remaining non-polarity areas, and polarity arc regions are the overlapping polarity regions with the topographic map boundary (width = 0.2). The notations are defined as follow: A_{\pm} and N_{\pm} (or A_{\pm}' and N_{\pm}') are the total areas and numbers of the primary (or secondary) polarity regions, η_{\pm} (or η_{\pm}') are the numbers of the primary (or secondary) polarity arc regions, Θ_{\pm}' are the areas of the secondary polarity arc regions, and N_0 is the number of neutral region with map magnitude smaller than 0.3. For the identification of both motion or non-motion related IC_{bcg} , topographies with either one unilateral polarity region or two opposite polarity regions that lie on the edge of the topographic map are selected. Suppose the total area of the positive primary polarity region is larger than the negative counterpart, or vice versa, i.e., $A_{+} > A_{-}$. The selection criteria are given by the following: (i) $N_0 \leq 1$; (ii) N_{\pm} or $N_{\pm}' = 1$, η_{\pm} or $\eta_{\pm}' = 1$; (iii) $N_{\mp} = \eta_{\mp} = 1$, or $N_{\mp} = \eta_{\mp} = 0$ with the non-zero primary region centered at the rear part of the head; (iv) $A_{\pm}' > 0.25$; $\Theta_{\pm}' > 0.25$. Condition (i) requires no more than one neutral region in the topographic map of an IC_{bcg} . Condition (ii) requires that, if $A_{+} > A_{-}$ (or $A_{-} > A_{+}$), only one positive (or negative) polarity region and polarity arc region is allowed in the IC_{bcg} topographic map.

For $A_+ > A_-$ (or $A_- > A_+$), Condition (iii) refers to either the opposite polarity topography with one negative (or positive) primary polarity region and polarity arc region, or the unilateral polarity topography with none negative (or positive) primary polarity region. In the latter case, the center of the positive (or negative) primary polarity region is located at the rear part of the head. Condition (iv) sets the minimum areas of the secondary polarity region and polarity arc region for the topographic map of an IC_{bcg} .

A.3 Signal contribution analysis

An IC_{bcg} can be recognized by the distinct peaks in the time course caused by cardiac pulsations. Removing the contribution of the IC_{bcg} from the EEG signal leads to a steady signal reduction at the pulsation peaks. While removing a motion-related IC_{bcg} leads to significant signal reductions at multiple channels far away from the pivot point of the head, removing a non-motion related IC_{bcg} may result in a smaller signal reduction at any EEG channel. In the analysis of the signal contribution, the average positive and negative magnitudes of the reduced signal when an IC is removed are compared with the original signal.

The comparisons between the original and reduced signal are made separately in two sets of comparison time periods $\{T_{+k}\}$ and $\{T_{-k}\}$, where $k = 1, 2, \dots$. Denote the original EEG signal and the reduced signal at the j^{th} channel by $V_j(t)$ and $V_j'(t)$. The comparison time period T_{+k} (T_{-k}) is the k^{th} time segment in which the IC is larger (smaller) than $F_0 + 0.1\sigma_{F0}$ ($F_0 - 0.1\sigma_{F0}$), and also $V_{j0} - 4\sigma_{Vj,\min}(\tau) \leq V_j(t) \leq V_{j0} + 4\sigma_{Vj,\min}(\tau)$, where F_0 and σ_{F0} are the mean and standard deviation of the IC, V_{j0} is the mean of $V_j(t)$, and $\sigma_{Vj,\min}(\tau) = \min(\text{std}(V_j(t), t \in [0, \tau]), \text{std}(V_j(t), t \in [\tau, 2\tau]), \dots)$ is the minimum standard deviation of $V_j(t)$ over time windows of size τ ($\tau = 10$ s). The purpose of setting the limits ($V_{j0} \pm 4\sigma_{Vj,\min}(\tau)$) to the EEG signal in the comparison time periods ($\{T_{\pm k}\}$) is to avoid including the time moments with rapid head motions in $\{T_{\pm k}\}$. The average magnitudes of $V_j(t)$ and $V_j'(t)$ over the comparison time periods $\{T_{\pm k}\}$ are given by $\alpha_{j\pm}$ and $\alpha_{j\pm}'$. For the purpose of BCG cycle detection, either a motion or non-motion related IC_{bcg} is selected. The selection criteria are given by the following: for any channel j , (i) $0.5 (\alpha_{j+}'/\alpha_{j+} + \alpha_{j-}'/\alpha_{j-}) < c_2$; and (ii) $\min(\alpha_{j+}'/\alpha_{j+}, \alpha_{j-}'/\alpha_{j-}) < c_7$, where $(c_2, c_7) = (0.97, 0.95)$.

B. Determination of the fundamental, first harmonic, band-pass filtering, and reference frequencies from $S(\nu)$ and $S'(\nu)$

The lowest heart rate among subjects is assumed to be 0.5 Hz (30 heart beats per minute (bpm)). For the evaluations of $\nu_{\text{bp1,L}}$, $\nu_{\text{bp1,U}}$, ν_0 , ν_1 , $\nu_{\text{ref,1}}$, $\nu_{\text{ref,2}}$, and $\nu_{\text{ref,3}}$, $S(\nu)$ and $S'(\nu)$ are normalized to unity in the frequency range [0.5, 8] Hz. The fundamental frequency is searched from the range between 30 bpm and 120 bpm. Among the peaks within the range, the frequency of the one with the largest $S'(\nu)$ is selected as the fundamental frequency ν_0 .

The band-pass frequencies of Step 1 ($\nu_{\text{bp1,L}}$, $\nu_{\text{bp1,U}}$) are initially taken as $\nu_{v,-1}$ and $\nu_{v,1}$, where $\nu_{v,-1}$ and $\nu_{v,1}$ are the frequencies of the adjacent local minima of ν_0 . Let $\nu_{v,-1} > \nu_{v,-2} > \dots > \nu_{v,-N_l}$ be the N_l local minimum frequencies smaller than ν_0 , $\nu_{v,1} < \nu_{v,2} < \dots < \nu_{v,N_r}$ be the N_r local minimum frequencies larger than ν_0 , and $\nu_{p,j}$ be the frequency of the j^{th} peak with $\nu_{v,j} < \nu_{p,j} < \nu_{v,j+1}$ for $j \leq -2$, and $\nu_{v,j-1} < \nu_{p,j} < \nu_{v,j}$ for $j \geq 2$, and $\nu_{p,\pm 1} = \nu_0$, then the value of $\nu_{\text{bp1,L}}$ is updated from $\nu_{v,j}$ to $\nu_{v,k}$ if

$$S'(\nu_{p,k}) < S'(\nu_{p,j}), \quad (\text{B.1a})$$

$$S'(\nu_{v,k}) < S'(\nu_{v,j}), \quad (\text{B.1b})$$

$$S'(\nu_{p,k}) \geq 0.15 S'(\nu_0), \quad (\text{B.1c})$$

and

$$\nu_{p,k} > 0.5 \text{ Hz}, \quad (\text{B.2})$$

where $k = j - 1 = -2, -3, \dots$. The update of $\nu_{\text{bp1,L}}$ stops when any of the condition in Eqs. (B.1) and (B.2) becomes invalid.

On the other hand, the frequency $\nu_{\text{bp1,U}}$ is updated with an upper limit imposed by the second harmonic frequency (ν_1), which is found within the frequency range determined by $\nu_{\text{bp1,U}}$. Thus the two frequencies,

$\nu_{\text{bp1,U}}$ and ν_1 , are evaluated and updated simultaneously. The width of the fundamental frequency peak is given by

$$\Delta \nu_0 = \nu_{\text{bp1,U}} - \nu_{\text{bp1,L}}, \quad (\text{B.3})$$

where $\nu_{\text{bp1,U}}$ is initially taken as $\nu_{v,1}$. The second harmonic frequency is searched from the peaks that lie within the frequency range R_{ν_1} , where

$$R_{\nu_1} = [\max(2\nu_0 - 0.5\Delta\nu_0, \nu_{\text{bp1,U}}), \min(2\nu_0 + 0.5\Delta\nu_0, 2.5\nu_0)]. \quad (\text{B.4})$$

Until at least a peak is found in R_{ν_1} , R_{ν_1} extends continually from both ends by $0.05\Delta\nu_0$ until the limits $\nu_{\text{bp1,U}}$ and $2.5\nu_0$ are reached. Then ν_1 is selected from the largest peak in R_{ν_1} , such that

$$\nu_1 = \operatorname{argmax}_{\nu \in R_{\nu_1}} S'(\nu). \quad (\text{B.5})$$

Similar to the search of $\nu_{\text{bp1,L}}$, the search of $\nu_{\text{bp1,U}}$ is updated from $\nu_{v,j}$ to $\nu_{v,k}$, where $k = j + 1 = 2, 3, \dots$, together with the simultaneous update of ν_1 (Eqs. (B.3)–(B.5)), if

$$\nu_{v,k} < \nu_1, \quad (\text{B.6})$$

and Eq. (B.1) are satisfied. The update stops when any of the condition in Eqs. (B.1) and (B.6) becomes invalid.

Three reference frequencies ($\nu_{\text{ref},1}$, $\nu_{\text{ref},2}$, $\nu_{\text{ref},3}$) are determined from $S(\nu)$ for the cycle adjustment at the end of each band-pass filtering step. The frequencies $\nu_{\text{ref},1}$ and $\nu_{\text{ref},3}$ are used to set the upper and lower limits for the detected cycles, and $\nu_{\text{ref},2}$ is used together with $\nu_{\text{ref},3}$ to distinguish an incorrect cycle detection from an extra cycle detection. For $\nu_{\text{ref},1}$ and $\nu_{\text{ref},3}$, the frequencies are chosen to minimize the mean value of $S(\nu)$ over the frequency window R_{ν_i} , where

$$\nu_{\text{ref},1} = \operatorname{argmin}_{\nu_i} \{ \langle S(\nu) \rangle_{\nu \in R_{\nu_i}} \}, \quad (\text{B.7a})$$

$$R_{\nu_i} = [\nu_i - \delta\nu, \nu_i + \delta\nu], \quad (\text{B.7b})$$

$$0.5 \text{ Hz} + \delta\nu < \nu_i \leq \nu_{\text{bp1,L}}, \quad (\text{B.7c})$$

and

$$\nu_{\text{ref},3} = \operatorname{argmin}_{\nu_i} \left\{ \langle S(\nu) \rangle_{\nu \in R_{\nu_i}} \right\}, \quad (\text{B.8a})$$

$$R_{\nu_i} = [\nu_i - \delta\nu, \nu_i + \delta\nu], \quad (\text{B.8b})$$

$$\nu_{\text{bp1,U}} \leq \nu_i < \nu_1 - \frac{1}{2} \Delta \nu_0 - \delta\nu. \quad (\text{B.8c})$$

In Eqs. (B.7) and (B.8), the center of the window (ν_i) sweeps through the range of Eqs. (B.7c) and (B.8c) with a frequency step 0.05 Hz, and a window width $\delta\nu = 0.05$ Hz. Finally, $\nu_{\text{ref},2}$ is chosen to be

$$\nu_{\text{ref},2} = 0.5 (\nu_{\text{ref},1} + \nu_0). \quad (\text{B.9})$$

C. Details of the cycle adjustment at the end of the second band-pass filtering step

A missing cycle in interval $R_{\text{bp2},i}$ is detected when

$$t_i^{(\text{bp2})} - t_{i-1}^{(\text{bp2})} > \Delta_1. \quad (\text{C.1})$$

In this case, an extra peak is added in the interval $R_{\text{adj},i} = [t_{i-1}^{(\text{bp2})} + \Delta_3, t_i^{(\text{bp2})}]$ (1st rows of Fig. 3c and Table 1).

On the other hand, when the time separation between two peaks is smaller than Δ_3 , i.e.,

$$t_i^{(\text{bp2})} - t_{i-1}^{(\text{bp2})} < \Delta_3, \quad (\text{C.2})$$

an incorrect peak is expected if the following equation holds:

$$t_{i+1}^{(\text{bp2})} - t_i^{(\text{bp2})} > \Delta_2, \quad \text{or} \quad t_{i-1}^{(\text{bp2})} - t_{i-2}^{(\text{bp2})} > \Delta_2, \quad (\text{C.3a})$$

$$t_{i+1}^{(\text{bp2})} - t_{i-2}^{(\text{bp2})} \geq 2.5 \Delta_0. \quad (\text{C.3b})$$

Eq. (C.3) suggests the higher possibility of detecting three cycles in $[t_{i-2}^{(\text{bp2})}, t_{i+1}^{(\text{bp2})}]$ than two cycles. In this case,

the interval $R_{\text{adj},i}$ is determined by d_1 and d_2 , where $d_1 = t_i^{(\text{bp2})} - t_{i-2}^{(\text{bp2})}$ and $d_2 = t_{i+1}^{(\text{bp2})} - t_{i-1}^{(\text{bp2})}$. If $d_1 < d_2$

(case (i)), the peak at $t_i^{(\text{bp2})}$ is removed, and replaced by the peak re-selected from $R_{\text{adj},i} = [t_{i-1}^{(\text{bp2})} + \Delta_3, t_{i+1}^{(\text{bp2})}]$

(2nd rows of Fig. 3c and Table 1). If $d_1 > d_2$ (case (ii)), the peak at $t_{i-1}^{(\text{bp2})}$ is removed, and replaced by the peak

re-selected from $R_{\text{adj},i} = [t_{i-2}^{(\text{bp2})} + \Delta_3, t_{i-1}^{(\text{bp2})}]$ (3rd rows of Fig. 3c and Table 1). Finally, if Eq. (C.2) holds but

Eq. (C.3) does not, an extra cycle is encountered (4th rows of Fig. 3c and Table 1). In this case, the peaks in $R_{adj,i} = [t_{i-2}^{(bp2)} + \Delta_3, t_{i+1}^{(bp2)}]$ are re-analyzed, and the peak, $t_{i-1}^{(bp2)}$ or $t_i^{(bp2)}$, is removed if it is not re-selected.

References

- Allen P.J., Polizzi G., Krakow K., Fish D.R., Lemieux L., 1998. Identification of EEG events in the MR scanner: the problem of pulse artifact and a method for its subtraction. *Neuroimage* 8, 229–239.
- Allen P.J., Josephs O., Turner R., 2000. A method for removing imaging artifact from continuous EEG recorded during functional MRI. *Neuroimage* 12, 230–239.
- Bell A.J., Sejnowski T.J., 1995. An information-maximization approach to blind separation and blind deconvolution. *Neural Comput.* 7, 1129–1159.
- Bonmassar G., Purdon P.L., Jaaskelainen I.P., Chiappa K., Solo V., Brown E.N., Beliveau J.W., 2002. Motion and ballistocardiogram artifact removal for interleaved recording of EEG and EPs during MRI. *Neuroimage* 16, 1127–1141.
- Chowdhury M.E.H., Mullinger K.J., Glover P., Bowtell R., 2014. Reference layer artefact subtraction (RLAS): a novel method of minimizing EEG artefacts during simultaneous fMRI. *Neuroimage* 84, 307–319.
- Christov I.I., 2004. Real time electrocardiogram QRS detection using combined adaptive threshold. *BioMed. Eng. Online* 3, 28.
- Debener S., Strobel A., Sorger B., Peters J., Kranczioch C., Engel A.K., Goebel R., 2007. Improved quality of auditory event-related potentials recorded simultaneously with 3-T fMRI: removal of the ballistocardiogram artefact. *Neuroimage* 34, 587–597.
- Delorme, A., Makeig, S., 2004. EEGLAB: an open source toolbox for analysis of single-trial EEG dynamics including independent component analysis. *J. Neurosci. Methods* 134, 9–21.
- Dotsinsky I., Stoyanov T., 2004. Ventricular beat detection in single channel electrocardiograms. *BioMed. Eng. OnLine* 3, 3.
- Iannotti G.R., Pittau F., Michel C.M., Vulliemoz S., Grouiller F., 2015. Pulse artifact detection in simultaneous EEG-fMRI recording based on EEG map topography. *Brain Topography* 28, 21–32.

- Kim K.H., Yoon H.W., Park H.W., 2004. Improved ballistocardiac artifact removal from the electroencephalogram recorded in fMRI. *J. Neurosci. Methods* 135, 193–203.
- Krishnaswamy P., Bonmassar G., Poulsen C., Pierce E.T., Purdon P.L., Brown E.N., 2016. Reference-free removal of EEG-fMRI ballistocardiogram artifacts with harmonic regression. *Neuroimage* 128, 398–412.
- Luo Q., Huang X., Wong C.-K., Zotev V., Bodurka J., 2015. Ballistocardiogram artifact removal in EEG-fMRI without ECG recording: ICA-based optimal basis set. Presented at 21st Annual Meeting of the Organization for Human Brain Mapping, 1925.
- Mantini D., Perrucci M.G., Cugini S., Ferretti A., Romani G.L., Del Gratta C., 2007. Complete artifact removal for EEG recorded during continuous fMRI using independent component analysis. *Neuroimage* 34, 598–607.
- McMenamin B.W., Shackman A.J., Maxwell J.S., Bachhuber D.R.W., Koppenhaver A.M., Greischar L.L., Davidson R.J., 2010. Validation of ICA-based myogenic artifact correction for scalp and source-localized EEG. *NeuroImage* 49, 2416–2432.
- Mullinger K.J., Havenhand J., Bowtell R., 2013. Identifying the sources of the pulse artefact in EEG recordings made inside an MR scanner. *Neuroimage* 71, 75–83.
- Niazy R.K., Beckmann C.F., Iannetti G.D., Brady J.M., Smith S.M., 2005. Removal of fMRI environment artifacts from EEG data using optimal basis sets. *Neuroimage* 28, 720–737.
- Oppenheim A.V., Schaffer R.W., Buck J.R., 1999. *Discrete-Time Signal Processing*. Upper Saddle River, NJ: Prentice Hall, 1999, p. 468.
- Srivastava G., Crottaz-Herbette S., Lau K.M., Glover G.H., Menon V., 2005. ICA-based procedures for removing ballistocardiogram artifacts from EEG data acquired in the MRI scanner. *Neuroimage* 24, 50–60.
- Vanderperren K., De Vos M., Ramautar J.R., Novitskiy N., Mennes M., Asseconci S., Vanrumste B., Stiers P., Van den Bergh B.R., Wagemans J., Lagae L., Sunaert S., Van Huffel S., 2010. Removal of BCG artifacts from EEG recordings inside the MR scanner: a comparison of methodological and validation-related aspects. *Neuroimage* 50, 920–934.
- Wan X., Iwata K., Riera J., Ozaki T., Kitamura M., Kawashima R., 2006. Artifact reduction for EEG/fMRI recording: Nonlinear reduction of ballistocardiogram artifacts. *Clin. Neurophysiol.* 117, 668–680.
- Wong C.K., Zotev V., Misaki M., Phillips R., Luo Q., Bodurka J., 2016. An automatic EEG-assisted retrospective motion correction for fMRI (aE-REMCOR). *Neuroimage* 129, 133–147.

- Wong C.K., Zotev V., Yuan H., Bodurka J., 2014. Cardiac cycle detection in EEG with residual MRI gradient artifact by multiple-scale peak detection. Presented at the 20th Meeting of Organization of Human Brain Mapping, 2262.
- Yan W.X., Mullinger K.J., Geirsdottir G.B., Bowtell R., 2010. Physical modeling of pulse artefact sources in simultaneous EEG/fMRI. *Human Brain Mapping* 31, 604–620.
- Yuan H., Zotev V., Phillips R., Drevets W.C., Bodurka J., 2012. Spatiotemporal dynamics of the brain at rest — Exploring EEG microstates as electrophysiological signatures of BOLD resting state networks. *Neuroimage* 60, 2062–2072.
- Zotev V., Yuan H., Phillips R., Bodurka J., 2012. EEG-assisted retrospective motion correction for fMRI: E-REMCOR. *NeuroImage* 63, 698–712.
- Zotev V., Yuan H., Misaki M., Phillips R., Young K.D., Feldner M.T., Bodurka J., 2016. Correlation between amygdala BOLD activity and frontal EEG asymmetry during real-time fMRI neurofeedback training in patients with depression, *Neuroimage Clin* 11, 224–238.

Table 1: Range of $R_{\text{adj},i}$ in the correlation calculations of Eq. (7).

Conditions	$R_{\text{adj},i}$	Index j of $R_{\text{adj},j}$
Eq. (C.1), (Fig. 3c, 1 st row)	$[t_{i-1}^{(\text{bp}2)} + \Delta_3, t_i^{(\text{bp}2)}]$	$j = \begin{cases} i-2, \dots, i-N_c-1, & \text{if } i > N_c+2; \\ 1, \dots, N_c, & \text{otherwise.} \end{cases}$
Eqs. (C.2), (C.3), $d_1 < d_2$ (Fig. 3c, 2 nd row)	$[t_{i-1}^{(\text{bp}2)} + \Delta_3, t_{i+1}^{(\text{bp}2)}]$	$j = \begin{cases} i-1, \dots, i-N_c, & \text{if } i > N_c+1; \\ 1, \dots, N_c, & \text{otherwise.} \end{cases}$
Eqs. (C.2), (C.3), $d_1 > d_2$ (Fig. 3c, 3 rd row)	$[t_{i-2}^{(\text{bp}2)} + \Delta_3, t_{i-1}^{(\text{bp}2)}]$	$j = \begin{cases} i-2, \dots, i-N_c-1, & \text{if } i > N_c+2; \\ 1, \dots, N_c, & \text{otherwise.} \end{cases}$
Eq. (C.2), not Eq. (C.3) (Fig. 3c, 4 th row)	$[t_{i-2}^{(\text{bp}2)} + \Delta_3, t_{i+1}^{(\text{bp}2)}]$	$j = \begin{cases} i-2, \dots, i-N_c-1, & \text{if } i > N_c+2; \\ 1, \dots, N_c, & \text{otherwise.} \end{cases}$

Here $\Delta_3 = \frac{1}{\nu_{\text{ref},3}}$, $d_1 = t_i^{(\text{bp}2)} - t_{i-2}^{(\text{bp}2)}$, $d_2 = t_{i+1}^{(\text{bp}2)} - t_{i-1}^{(\text{bp}2)}$, and $N_c = 10$ past cycles were used for the correlation calculations.

Table 2: Cycle detection results of the 48 subjects in 281 scans by applying the proposed algorithm on IC_{bcg}.

ID	Results of IC _{bcg} cycle detection ($\delta = 10$ ms)						Results of IC _{bcg} cycle detection ($\delta = 58.8$ ms)					
	TP	FP	FN	S_p (%)	S_e (%)	F_1 -score (%)	TP	FP	FN	S_p (%)	S_e (%)	F_1 -score (%)
1	3095	9	18	99.71%	99.42%	99.57%	3095	9	18	99.71%	99.42%	99.57%
2	2594	4	4	99.85%	99.85%	99.85%	2594	4	4	99.85%	99.85%	99.85%
3	3124	17	17	99.46%	99.46%	99.46%	3125	16	16	99.49%	99.49%	99.49%
4	3919	16	18	99.59%	99.54%	99.57%	3919	16	18	99.59%	99.54%	99.57%
5	3308	16	27	99.52%	99.19%	99.35%	3309	15	26	99.55%	99.22%	99.38%
6	2997	13	22	99.57%	99.27%	99.42%	2997	13	22	99.57%	99.27%	99.42%
7	3313	2	5	99.94%	99.85%	99.89%	3313	2	5	99.94%	99.85%	99.89%
8	2743	14	18	99.49%	99.35%	99.42%	2743	14	18	99.49%	99.35%	99.42%
9	4196	18	23	99.57%	99.45%	99.51%	4196	18	23	99.57%	99.45%	99.51%
10	3136	4	6	99.87%	99.81%	99.84%	3136	4	6	99.87%	99.81%	99.84%
11	3091	15	20	99.52%	99.36%	99.44%	3091	15	20	99.52%	99.36%	99.44%
12	2887	34	44	98.84%	98.50%	98.67%	2891	30	40	98.97%	98.64%	98.80%
13	3557	4	6	99.89%	99.83%	99.86%	3557	4	6	99.89%	99.83%	99.86%
14	3058	13	13	99.58%	99.58%	99.58%	3059	12	12	99.61%	99.61%	99.61%
15	2705	1	3	99.96%	99.89%	99.93%	2705	1	3	99.96%	99.89%	99.93%
16*	2953	14	21	99.53%	99.29%	99.41%	2953	14	21	99.53%	99.29%	99.41%
17	3828	65	91	98.33%	97.68%	98.00%	3830	63	89	98.38%	97.73%	98.05%
18*	3068	8	11	99.74%	99.64%	99.69%	3068	8	11	99.74%	99.64%	99.69%
19	3043	2	6	99.93%	99.80%	99.87%	3043	2	6	99.93%	99.80%	99.87%
20	3246	53	58	98.39%	98.24%	98.32%	3246	53	58	98.39%	98.24%	98.32%
21	3913	9	12	99.77%	99.69%	99.73%	3914	8	11	99.80%	99.72%	99.76%
22*	3246	26	39	99.21%	98.81%	99.01%	3250	22	35	99.33%	98.93%	99.13%
23	2799	19	33	99.33%	98.83%	99.08%	2800	18	32	99.36%	98.87%	99.12%
24	2640	6	18	99.77%	99.32%	99.55%	2641	5	17	99.81%	99.36%	99.59%
25	3208	17	26	99.47%	99.20%	99.33%	3211	14	23	99.57%	99.29%	99.43%
26	3640	7	10	99.81%	99.73%	99.77%	3640	7	10	99.81%	99.73%	99.77%
27	3404	7	11	99.79%	99.68%	99.74%	3404	7	11	99.79%	99.68%	99.74%
28*	2320	11	15	99.53%	99.36%	99.44%	2320	11	15	99.53%	99.36%	99.44%
29	3015	1	1	99.97%	99.97%	99.97%	3015	1	1	99.97%	99.97%	99.97%
30	2919	23	34	99.22%	98.85%	99.03%	2924	18	29	99.39%	99.02%	99.20%
31*	3188	2	4	99.94%	99.87%	99.91%	3188	2	4	99.94%	99.87%	99.91%
32	4051	25	30	99.39%	99.26%	99.33%	4052	24	29	99.41%	99.29%	99.35%
33**	4830	2	3	99.96%	99.94%	99.95%	4830	2	3	99.96%	99.94%	99.95%
34	3323	6	8	99.82%	99.76%	99.79%	3323	6	8	99.82%	99.76%	99.79%
35	3423	5	7	99.85%	99.80%	99.83%	3423	5	7	99.85%	99.80%	99.83%
36	3230	17	37	99.48%	98.87%	99.17%	3230	17	37	99.48%	98.87%	99.17%
37	2905	10	11	99.66%	99.62%	99.64%	2905	10	11	99.66%	99.62%	99.64%
38	3368	7	8	99.79%	99.76%	99.78%	3370	5	6	99.85%	99.82%	99.84%
39	3875	22	27	99.44%	99.31%	99.37%	3876	21	26	99.46%	99.33%	99.40%
40	3172	4	5	99.87%	99.84%	99.86%	3173	3	4	99.91%	99.87%	99.89%
41	2852	15	11	99.48%	99.62%	99.55%	2852	15	11	99.48%	99.62%	99.55%
42	2998	3	8	99.90%	99.73%	99.82%	2999	2	7	99.93%	99.77%	99.85%
43	3248	6	14	99.82%	99.57%	99.69%	3248	6	14	99.82%	99.57%	99.69%
44	2295	17	29	99.26%	98.75%	99.01%	2295	17	29	99.26%	98.75%	99.01%
45*	2772	13	18	99.53%	99.35%	99.44%	2772	13	18	99.53%	99.35%	99.44%
46*	2729	13	19	99.53%	99.31%	99.42%	2729	13	19	99.53%	99.31%	99.42%
47	3032	12	13	99.61%	99.57%	99.59%	3032	12	13	99.61%	99.57%	99.59%
48*	2763	21	29	99.25%	98.96%	99.10%	2764	20	28	99.28%	99.00%	99.14%
Total	153019	648	911	99.58%	99.41%	99.49%	153050	617	880	99.60%	99.43%	99.51%

TP: number of true positive detections; FP: number of false positive detections; FN: number of false negative detections.

$S_p = TP/(TP + FP)$ is the specificity. $S_e = TP/(TP + FN)$ is the sensitivity.

The results were calculated with the comparison resolutions $\delta = 10$ ms and 58.8 ms.

* (or **) indicates that the subject had participated 5 (or 7) resting scans. Other subjects had participated 6 resting scans.

Table 3: Cycle detection results of the 48 subjects in 281 scans by applying *fmrrib_qrsdetect.m* on ECG andIC_{beg}.

ID	Results of ECG cycle detection ($\delta = 58.8$ m)						Results of IC _{beg} cycle detection ($\delta = 58.8$ m)					
	TP	FP	FN	S_p (%)	S_e (%)	F_1 -score (%)	TP	FP	FN	S_p (%)	S_e (%)	F_1 -score (%)
1	3068	16	43	99.48%	98.62%	99.05%	3040	49	73	98.41%	97.65%	98.03%
2	2571	5	28	99.81%	98.92%	99.36%	2573	341	25	88.30%	99.04%	93.36%
3	3111	43	30	98.64%	99.04%	98.84%	3089	40	52	98.72%	98.34%	98.53%
4	3905	19	32	99.52%	99.19%	99.35%	3787	122	150	96.88%	96.19%	96.53%
5	3302	8	31	99.76%	99.07%	99.41%	3268	22	67	99.33%	97.99%	98.66%
6	2985	17	30	99.43%	99.00%	99.22%	2965	41	54	98.64%	98.21%	98.42%
7	3308	0	10	100.00%	99.70%	99.85%	3290	16	28	99.52%	99.16%	99.34%
8	2724	18	34	99.34%	98.77%	99.05%	2677	51	84	98.13%	96.96%	97.54%
9	4100	102	119	97.57%	97.18%	97.38%	4157	39	62	99.07%	98.53%	98.80%
10	3123	17	17	99.46%	99.46%	99.46%	3123	2	19	99.94%	99.40%	99.66%
11	3047	49	63	98.42%	97.97%	98.20%	3048	56	63	98.20%	97.97%	98.09%
12	2847	67	80	97.70%	97.27%	97.48%	2852	73	79	97.50%	97.30%	97.40%
13	3550	0	14	100.00%	99.61%	99.80%	3347	539	216	86.13%	93.94%	89.86%
14	3053	6	18	99.80%	99.41%	99.61%	2873	625	198	82.13%	93.55%	87.47%
15	2692	2	17	99.93%	99.37%	99.65%	2695	1	13	99.96%	99.52%	99.74%
16*	2909	35	65	98.81%	97.81%	98.31%	2889	66	85	97.77%	97.14%	97.45%
17	3796	486	120	88.65%	96.94%	92.61%	3713	175	206	95.50%	94.74%	95.12%
18*	3051	6	29	99.80%	99.06%	99.43%	3050	21	29	99.32%	99.06%	99.19%
19	3010	21	39	99.31%	98.72%	99.01%	3015	13	34	99.57%	98.88%	99.23%
20	3259	25	40	99.24%	98.79%	99.01%	2967	303	337	90.73%	89.80%	90.26%
21	3890	13	36	99.67%	99.08%	99.37%	3872	27	53	99.31%	98.65%	98.98%
22*	2892	288	396	90.94%	87.96%	89.42%	3160	82	125	97.47%	96.19%	96.83%
23	2704	100	129	96.43%	95.45%	95.94%	2734	80	98	97.16%	96.54%	96.85%
24	2618	29	38	98.90%	98.57%	98.74%	2621	15	37	99.43%	98.61%	99.02%
25	3202	16	25	99.50%	99.23%	99.36%	3138	61	96	98.09%	97.03%	97.56%
26	3615	12	36	99.67%	99.01%	99.34%	3612	16	38	99.56%	98.96%	99.26%
27	3329	27	80	99.20%	97.65%	98.42%	3349	40	66	98.82%	98.07%	98.44%
28*	2299	345	34	86.95%	98.54%	92.38%	2286	38	49	98.36%	97.90%	98.13%
29	3004	2	11	99.93%	99.64%	99.78%	2971	31	45	98.97%	98.51%	98.74%
30	2883	15	67	99.48%	97.73%	98.60%	2885	50	68	98.30%	97.70%	98.00%
31*	3157	5	38	99.84%	98.81%	99.32%	3161	24	31	99.25%	99.03%	99.14%
32	4047	15	25	99.63%	99.39%	99.51%	3952	76	129	98.11%	96.84%	97.47%
33**	4784	29	50	99.40%	98.97%	99.18%	4655	269	178	94.54%	96.32%	95.42%
34	3300	2	25	99.94%	99.25%	99.59%	3276	40	55	98.79%	98.35%	98.57%
35	3414	4	15	99.88%	99.56%	99.72%	3280	13	150	99.61%	95.63%	97.58%
36	3173	55	96	98.30%	97.06%	97.68%	3129	103	138	96.81%	95.78%	96.29%
37	2727	91	187	96.77%	93.58%	95.15%	2848	23	68	99.20%	97.67%	98.43%
38	3351	12	24	99.64%	99.29%	99.47%	3334	18	42	99.46%	98.76%	99.11%
39	3854	33	43	99.15%	98.90%	99.02%	3768	117	134	96.99%	96.57%	96.78%
40	3144	17	31	99.46%	99.02%	99.24%	3144	16	33	99.49%	98.96%	99.23%
41	2817	21	45	99.26%	98.43%	98.84%	2814	206	49	93.18%	98.29%	95.67%
42	2973	16	28	99.46%	99.07%	99.27%	2971	9	35	99.70%	98.84%	99.26%
43	3219	18	38	99.44%	98.83%	99.14%	3201	45	61	98.61%	98.13%	98.37%
44	2279	27	40	98.83%	98.28%	98.55%	2149	161	175	93.03%	92.47%	92.75%
45*	2761	12	26	99.57%	99.07%	99.32%	2744	32	46	98.85%	98.35%	98.60%
46*	2725	5	23	99.82%	99.16%	99.49%	2588	141	160	94.83%	94.18%	94.50%
47	2894	147	153	95.17%	94.98%	95.07%	2898	286	147	91.02%	95.17%	93.05%
48*	2523	234	267	91.51%	90.43%	90.97%	2699	66	93	97.61%	96.67%	97.14%
Total	150989	2532	2865	98.35%	98.14%	98.24%	149657	4680	4273	96.97%	97.22%	97.10%

TP: number of true positive detections; FP: number of false positive detections; FN: number of false negative detections.
 $S_p = TP/(TP + FP)$ is the specificity. $S_e = TP/(TP + FN)$ is the sensitivity.

The results were calculated with the comparison resolution $\delta = 58.8$ ms.

* (or **) indicates that the subject had participated 5 (or 7) resting scans. Other subjects had participated 6 resting scans.

Figure captions

Figure 1: Automatically detected cardiac cycles by applying *fmrib_qrsdetect.m* on (a) ECG (black crosses) and (b) the selected BCG-related independent component (IC_{bcg}) (red crosses). The same scans for eight representative subjects S1–S8 were used in (a) and (b). Red line: ECG; blue line: IC_{bcg} ; blue dots: correct peak timing for the ECG recording ($\{t_{i,corr}^{(ECG)}\}$); green dots: correct peak timing of the BCG artifact occurrence ($\{t_{i,corr}^{(IC)}\}$). In the plots, IC_{bcg} and ECG are normalized using their respective standard deviations. Note that the ECG waveforms vary substantially across subjects.

Figure 2: (a) Selected IC_{bcg} ($F(t)$) (black line) and its contrast (C) for subjects S6, S9–S11; (b) distribution of the selected IC_{bcg} contrast in 281 scans. In (a), the red line is the ECG. $F(t)$ and ECG are normalized using their respective standard deviations.

Figure 3: Schematic of the proposed automatic BCG cycle detection algorithm. The algorithm includes (a) the evaluations of the frequencies $\nu_{bp1,L}$, $\nu_{bp1,U}$, ν_0 , ν_1 , $\nu_{ref,1}$, $\nu_{ref,2}$, $\nu_{ref,3}$ from $S(\nu)$ and $S'(\nu)$ (Section 2.5.1, Appendix B); (b) the estimation of the cardiac cycle $\{R_{bp1,i}\}$ (Section 2.5.2); and (c) the peak-to-peak cycle determination $\{t_i^{(bp2)}\}$ (Section 2.5.3). In (a), black line: $S'(\nu)$; green line: $S(\nu)$. In (b), blue line: $F(t)$; cyan line: $F_{bp1}(t)$; red line: ECG. $F_{bp1}(t)$ is calculated by band-pass filtering $F(t)$ in $[\nu_{bp1,L}, \nu_{bp1,U}]$. The black crosses indicate the peaks of $F_{bp1}(t)$ in $R_{bp1,i}$. The black dashed lines mark the cycle intervals $\{R_{bp1,i}\}$. The left and right columns of (b) show the detected $\{R_{bp1,i}\}$ before and after the cycle adjustment (Eq. (6)) using Δ_L and $\Delta_{ref,3}$ (Eq. (4)). The black arrows indicate the merging of two intervals. The alternate shaded and white regions in the right column of (b) and left column of (c) mark the cycle intervals $\{R_{bp1,i}\}$ in each of which the peak of artifact occurrence is selected. In (c), black line: $F_{bp2}(t)$; cyan line: $F_{bp1}(t)$; red line: ECG. The black dashed lines mark the detected peak-to-peak cycles of $F_{bp2}(t)$ ($\{t_i^{(bp2)}\}$). The left and right columns of (c) show the

cycles $\{t_i^{(\text{bp2})}\}$ before and after the cycle adjustment according to Eqs. (C.1)–(C.3) and Table 1 using Δ_0 , $\Delta_{\text{ref},1}$, $\Delta_{\text{ref},2}$, $\Delta_{\text{ref},3}$ (Eq. (4)). The black arrows indicate the range $R_{\text{adj},i}$, in which a peak is added or re-selected. The red dashed lines mark the lower bound t_{b_i} of $R_{\text{adj},i}$. In (b) and (c), $F(t)$, $F_{\text{bp1}}(t)$ and ECG are normalized by their standard deviations, and $F_{\text{bp2}}(t)$ is piecewise normalized within each interval $\{R_{\text{bp1},i}\}$ using the standard deviation as described in Section 2.5.3.

Figure 4: Smoothed energy spectral density of the selected IC_{bcg} ($S'(\nu)$) for the same eight subjects S1–S8 shown in Figs. 1 and 5. The original energy spectral density ($S(\nu)$) is plotted in green line. $S'(\nu)$ and $S(\nu)$ are normalized to unity within [0.5 Hz, 8 Hz]. The pair of magenta circles indicates the frequency range of the first band-pass filtering step (Section 2.5.1). The blue triangles are the reference frequencies used for the adjustments of the detected cycles at the end of each band-pass filtering step (Sections 2.5.2 and 2.5.3). The red and black crosses respectively mark the fundamental and second harmonic frequencies.

Figure 5: Detected peak-to-peak cycles using the multiple-scale peak detection algorithm for the same representative subjects S1–S8 shown in Figs. 1 and 4. Black line: $F_{\text{bp2}}(t)$; blue line: $F(t)$; cyan line: $F_{\text{bp1}}(t)$; and red line: ECG. The black and blue circles are respectively the detected peaks of $F_{\text{bp2}}(t)$ and $F(t)$, i.e., $\{t_i^{(\text{bp2})}\}$ and $\{t_i^{(\text{IC})}\}$. The blue dots are the correct peak timing of the BCG artifact ($\{t_{i,\text{corr}}^{(\text{IC})}\}$). $F(t)$, $F_{\text{bp1}}(t)$ and ECG are normalized by their standard deviations, and $F_{\text{bp2}}(t)$ is piecewise normalized within each interval $\{R_{\text{bp1},i}\}$ using the standard deviation as described in Section 2.5.3. Note that the black and blue lines almost overlap with each other. The delay of the IC_{bcg} peaks ($\{t_{i,\text{corr}}^{(\text{IC})}\}$) from the ECG R-peaks ($\{t_{i,\text{corr}}^{(\text{ECG})}\}$) for subjects S1–S7 can be estimated by maximizing the correlation between them, and are given by 208, 108, 196, 212, 200, 92 and 152 ms. For subject S8, the delay of the IC_{bcg} peaks from the ECG T-peaks is 8 ms.

Figure 6: Plots of (a)–(b) F_1 -score of the detected cardiac cycles (Eq. (10)) and (c) F_1 -score of the detected cardiac cycles with the shifted false positive and shifted false negative detections taken into account (F_1') (Eq. (11)) against the IC_{bcg} contrast (C) for 281 scans. In (a) and (c), the comparison resolution is $\delta = 10$ ms. In (b), $\delta = 58.8$ ms. The black lines are the power fit trends.

Figure 7: Performance of the proposed algorithm for different hearts rates and scan durations. (a) Plot of calculation time (T_{cal}) against mean heart rate (L) for all scans. (b) Distribution of the mean heart rate (L) of the scans. (c) Plot of the fundamental frequency (ν_0) against the mean heart rate (L) for all scans. (d) Semi-log plot of F_1 against different scan durations for 281 scans. In (a), the red line is the linear fit of T_{cal} versus L . In (c), the grey area shows the standard deviation of the heart rate of each scan. The red line plots $\nu_0 = L$. In (d), the reduced scan duration is taken from the beginning portions of the scans after the first 6 s segment is removed. The scan durations considered in the plot are 16.252, 24.376, 32.5, 48.752, 65, 97.5, 130, 195, 260, 325, 390, 455, 520 s. The results are calculated by Eq. (10) with the comparison resolution $\delta = 10$ ms. The red and blue lines represent the mean and top 95th percentile of F_1 for a given scan duration. The dotted area is plotted in an enlarged scale in the inset.

Figure 1
[Click here to download high resolution image](#)

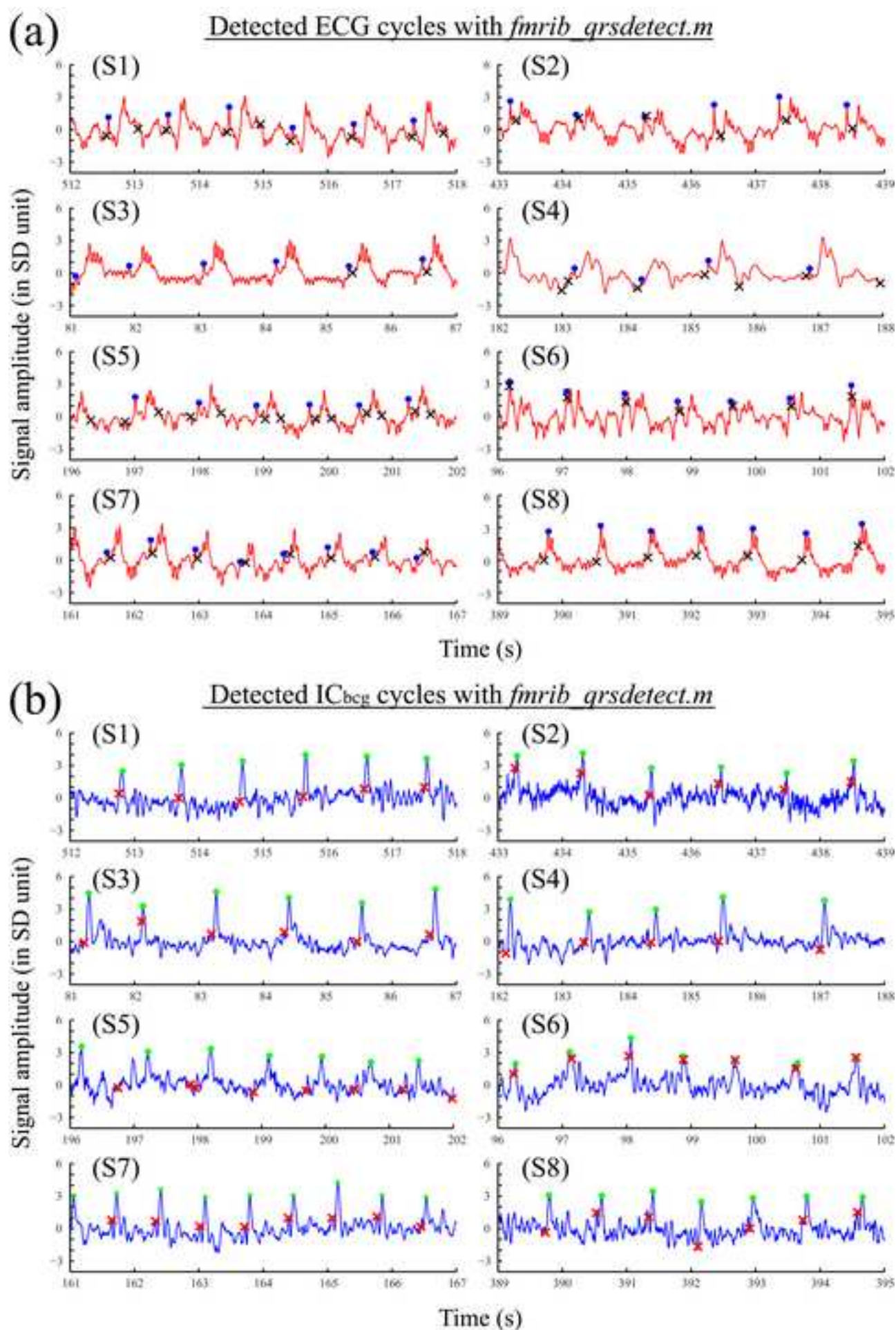
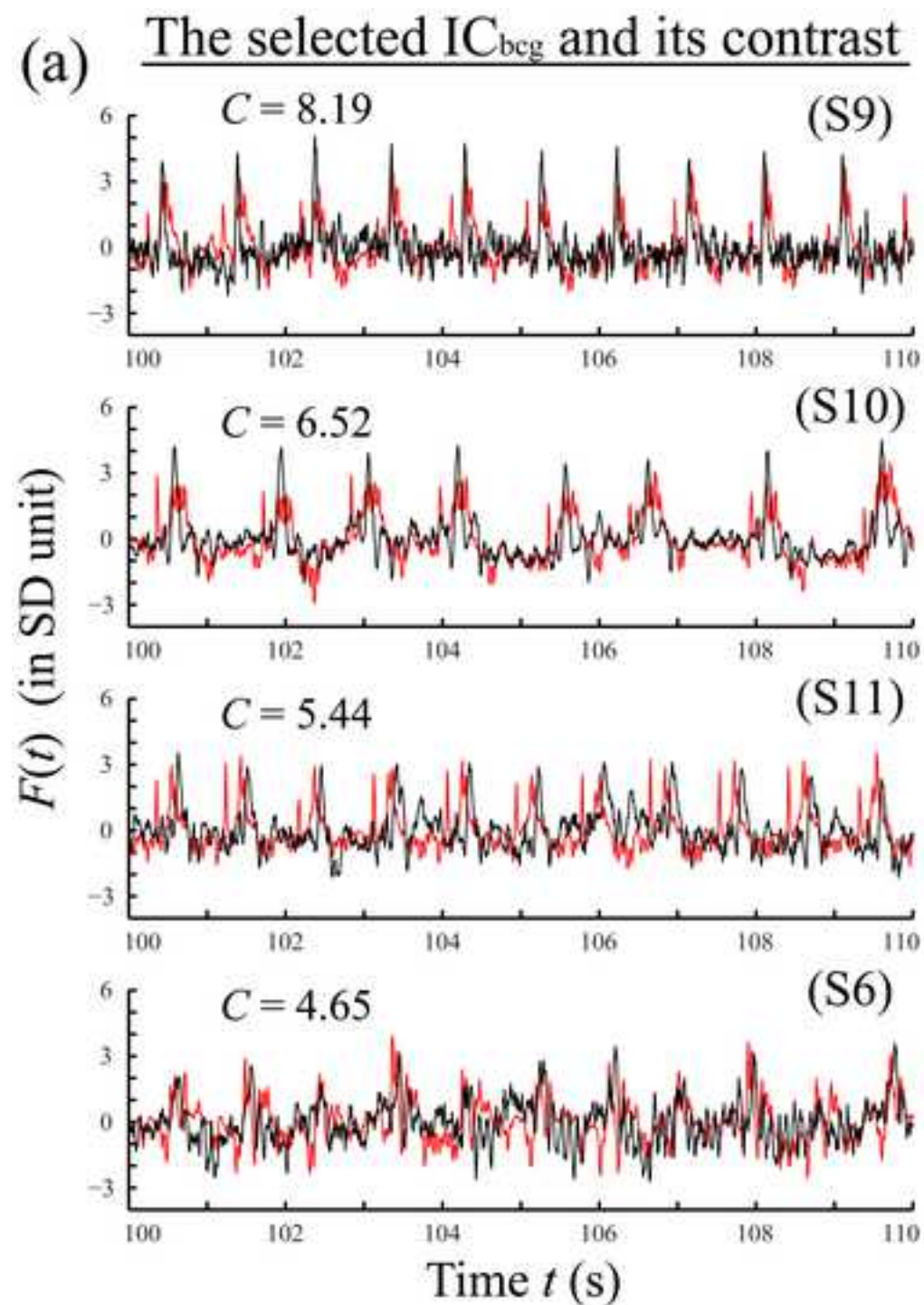


Figure 2
[Click here to download high resolution image](#)



Contrast distribution in all scans

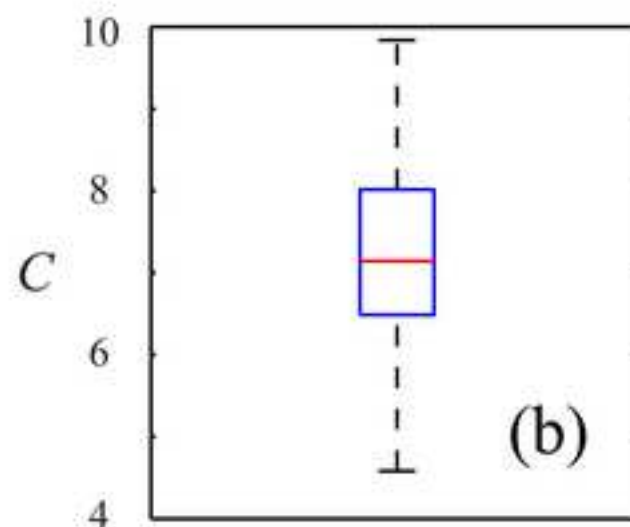


Figure 3

[Click here to download high resolution image](#)

Schematic of the automatic BCG cycle detection algorithm

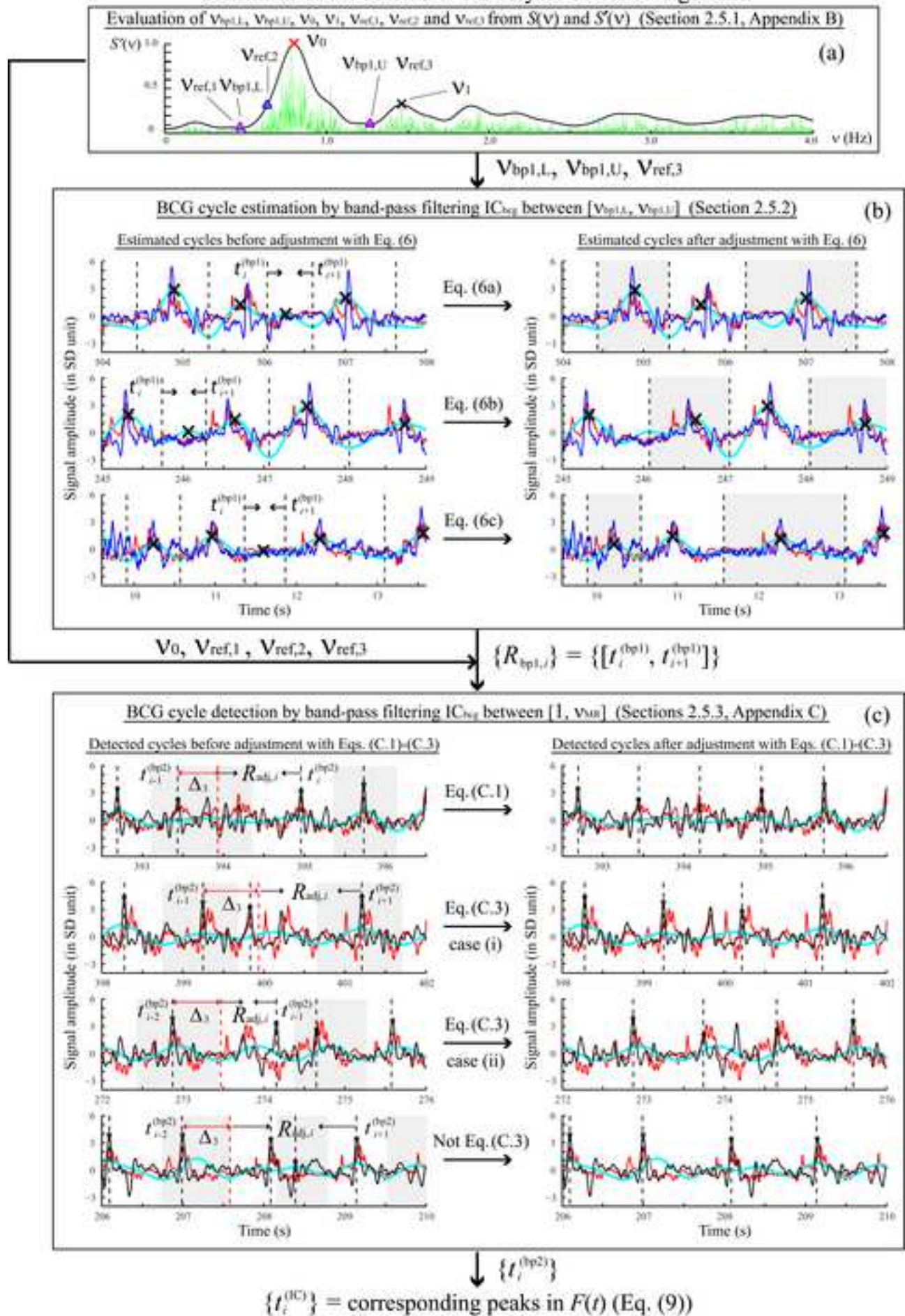


Figure 4
[Click here to download high resolution image](#)

Smoothed energy spectral density $S'(\nu)$

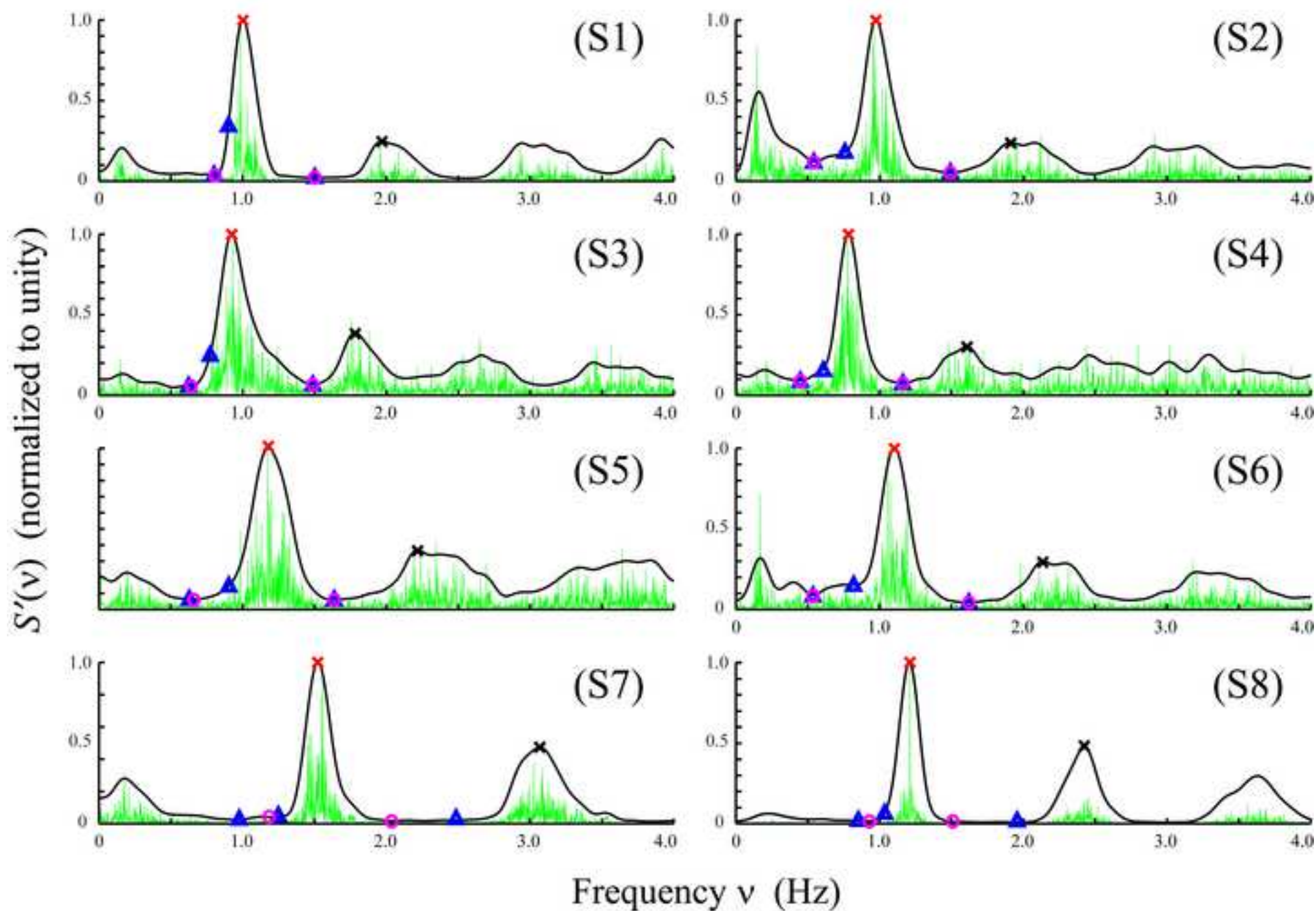


Figure 5
[Click here to download high resolution image](#)

Detected cardiac cycles of $F_{bp2}(t)$

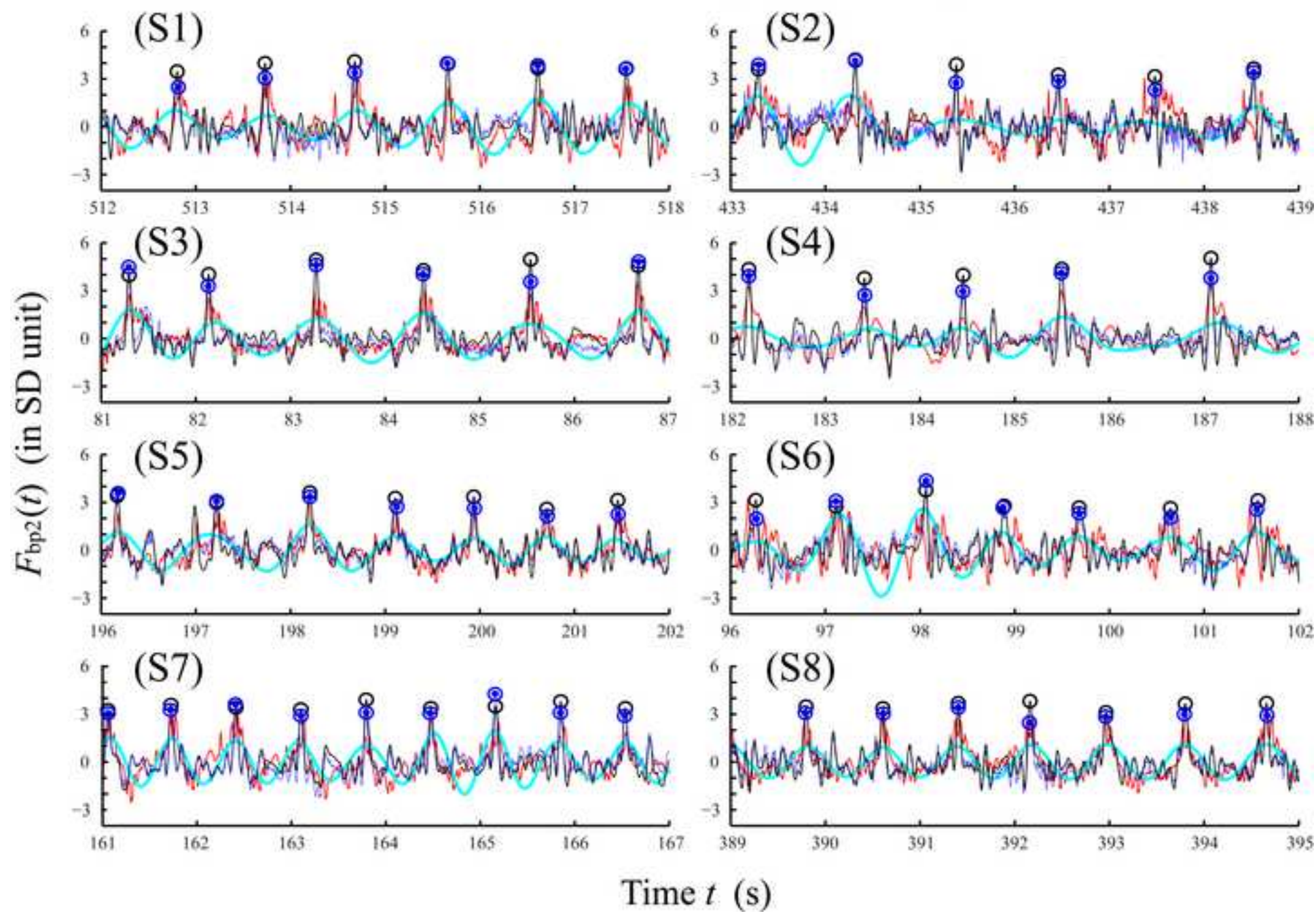


Figure 6
[Click here to download high resolution image](#)

F_1 and F_1' of the detected cardiac cycles

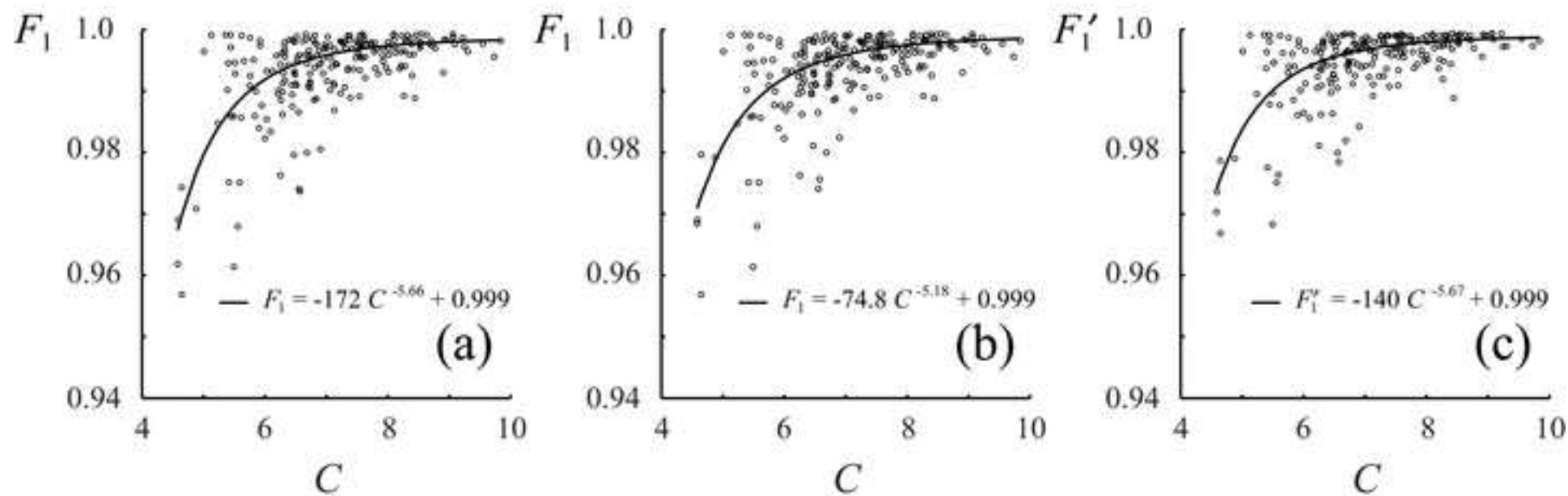
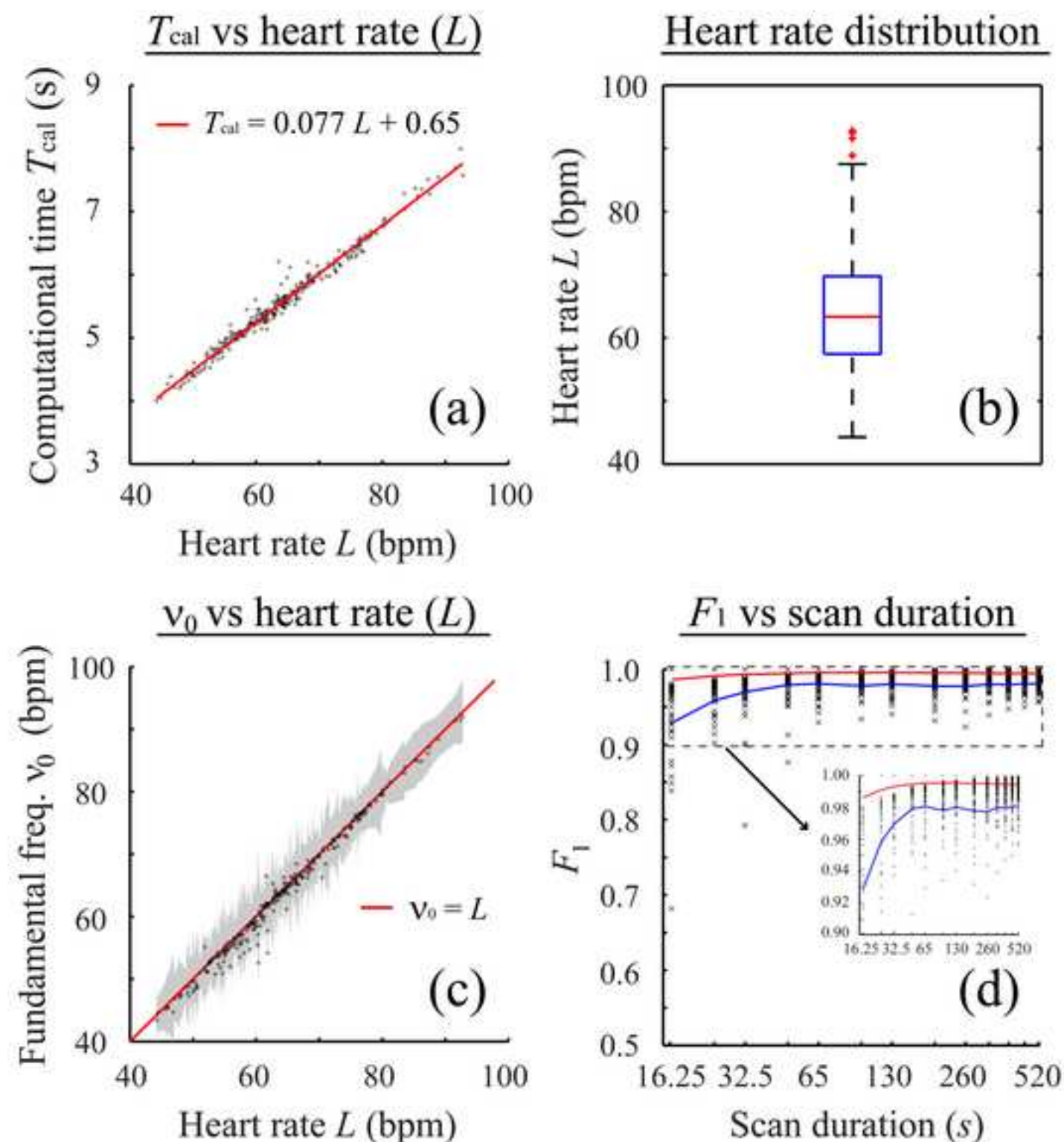


Figure 7
[Click here to download high resolution image](#)

Performance for different heart rates and scan durations



Tracking Resting State Connectivity Dynamics in Veterans with PTSD

Han Yuan^{1,2,3}, Raquel Phillips³, Chung-Ki Wong³, Vadim Zotev³, Masaya Misaki³, Brent Wurfel^{3,4},
Frank Krueger^{3,5}, Matthew Feldner⁶, Jerzy Bodurka^{1,2,3#}

¹Stephenson School of Biomedical Engineering, University of Oklahoma, Norman, OK, USA

²University of Oklahoma Institute for Biomedical Engineering, Science and Technology, Norman,
OK, USA

³Laureate Institute for Brain Research, Tulsa, OK, USA

⁴Laureate Psychiatric Clinic and Hospital, Tulsa, OK, USA

⁵School of Systems Biology, George Mason University, Fairfax, VA, USA

⁶Department of Psychological Science, University of Arkansas, Fayetteville, AR, USA

[#]Corresponding author:

Jerzy Bodurka (jbodurka@laureateinstitute.org, +1 918-502-5101)

Laureate Institute for Brain Research, 6655 S. Yale Avenue, Tulsa, OK 74136-3326

Abstract

Posttraumatic stress disorder (PTSD) is a trauma- and stressor-related disorder that may emerge following a traumatic event. Neuroimaging studies have shown evidence of functional abnormality in many brain regions and systems affected by PTSD. Exaggerated threat detection associated with abnormalities in the salience network, as well as abnormalities in executive functions involved in emotions regulations, self-referencing and context evaluation processing are broadly reported in PTSD. Here we aimed to investigate the behavior and dynamic properties of fMRI resting state networks in combat-related PTSD, using a novel, multimodal imaging approach. Simultaneous electroencephalography (EEG) and functional magnetic resonance imaging (fMRI) was employed to measure neurobiological brain activity among 36 veterans with combat-related PTSD and 20 combat-exposed veterans without PTSD. Based on the recently established method of measuring temporal-independent EEG microstates, we developed a novel strategy to integrate EEG and fMRI by quantifying the fast temporal dynamics associated with the resting state networks. We found distinctive occurrence rates of microstates associated with the dorsal default mode network and salience networks in the PTSD group as compared with control. Furthermore, the occurrence rate of the microstate for the dorsal default mode network was positively correlated with PTSD severity, whereas the occurrence rate of the microstate for the anterior salience network was negatively correlated with hedonic tone reported by participants with PTSD. Our findings reveal a novel aspect of abnormal network dynamics in combat-related PTSD and contribute to a better understanding of the pathophysiology of the disorder. Simultaneous EEG and fMRI will be a valuable tool in continuing to study the neurobiology underlying PTSD.

Keywords:

Posttraumatic stress disorder, Combat Veterans, Simultaneous EEG and fMRI, Resting state networks,
Functional connectivity, Temporal independent EEG microstates

INTRODUCTION

Posttraumatic stress disorder (PTSD) is a psychiatric disorder that may emerge following a traumatic event (American Psychiatric Association [APA], 2013). It is a chronic and debilitating psychiatric disorder with characteristic symptoms of hypervigilance and hyperarousal, emotional numbing, dissociation, negative alterations in cognitions, and re-experiencing phenomena (APA, 2013; Kessler, 2000). PTSD is common following combat experiences at military deployments, particularly those in Iraq and Afghanistan (Hoge et al., 2004). The neuropathophysiology of PTSD have become investigated in neuroimaging studies. Functional magnetic resonance imaging (fMRI) studies have reported functional abnormalities in cortical and subcortical circuits involving the amygdala, insula, ventromedial prefrontal cortex (vmPFC), anterior cingulate cortex (ACC) and hippocampus (Pitman et al., 2012; Shin and Liberzon, 2010). Activation patterns of these discrete anatomical entities in response to emotion elicitations, such as the presentation of traumatic event cues, have been the focus of examination. However, it is not clear whether the abnormal patterns observed in the neural circuits are specific to reactivity to experimental emotion elicitations or if they reflect more general functional abnormalities. Therefore, identifying dysregulated patterns of resting state functional connectivity (Fox and Raichle, 2007; Greicius et al., 2009), which is examined in the absence of external tasks, may provide valuable insights into the pathophysiology of PTSD.

Resting state functional connectivity (RSFC) refers to correlations in hemodynamic activity levels among different brain regions, suggesting synchronization of neural activation of those regions during rest (Greicius et al., 2009). The organization of the connectivity is structured as a set of resting state networks (RSNs; Biswal et al., 1995; Fox and Raichle 2007), and regions within a RSN shows spontaneous and coherent activities. The alterations in two specific networks may underlie PTSD: the default mode network (DMN; Bluhm et al., 2009; Daniels et al., 2011; Shin et al., 2009; Lanius et al.,

2010; Lui et al. 2009, Shin et al., 2009), and the salience network (SN; Daniels et al., 2010; Sripada et al., 2012b). To date, many studies examining integrity of network connectivity in PTSD have investigated the effect of combat exposure. However, the findings have been elusive. Conflicting results of these studies have largely depended on the selection of a control group. Alterations in resting state networks, or connectivity, have been reported in PTSD compared to non-trauma-exposed controls (Daniels et al., 2010), or a combination of trauma-exposed and non-trauma-exposed controls (Kennis et al., 2016; Sripada et al. 2012a). Sampling both combat-exposed and civilian controls obfuscates understanding if PTSD-related differences are specific to PTSD or due to combat exposure or even being in the military more generally. In this regard, a study by DiGangi et al. (2016) examined details in three groups, i.e. veterans with combat-related PTSD, combat-exposed controls without PTSD and never-traumatized healthy controls, and compared their resting state functional connectivity. Differences associated with PTSD were only observed in comparison with the civilian control, but not in comparison with combat-exposed veterans. Thus, it remains unclear whether abnormality of resting state networks is best attributed to military status, combat exposure, or PTSD.

The goal of the current study was to test whether RSFC differs between combat-exposed veterans with, as compared to without, PTSD. This method allows for ruling out the effects of being in the military generally, and combat exposure specifically. We employed a novel multimodal imaging approach using simultaneous electroencephalography (EEG) and fMRI to study activity in the resting state networks. The measurement of neural activity via fMRI, as done in prior work, is relatively limited in terms of understanding temporal dynamics of neural activity because the BOLD signal relies on a relatively slow hemodynamic response. In contrast, EEG is much more sensitive to the temporal dynamics of neural activity because it captures fast neuronal events that evolve on the scale of milliseconds. Neuroimaging with integrated and combined EEG-fMRI has been suggested to offer new

insights in the study of functional connectivity because it offers both high spatial resolution of fMRI and the high temporal resolution of EEG (He et al., 2008). In order to examine resting state network activity, a new method by Yuan et al. (2012) has demonstrated that temporal independent EEG microstates (EEG-ms) can be obtained from resting state EEG acquired concurrently with fMRI. It was further showed that EEG-ms form direct electrophysiological signatures to the canonical resting state networks measured by resting state fMRI in both spatial and temporal domains (Yuan et al. 2012 and 2016). This study examined EEG-ms associated with the resting state networks of relevance to PTSD — default mode network and the salience network. We proposed a new strategy to quantify the fast temporal dynamics of DMN, and SN functional connectivity in terms of EEG-ms **occurrence rate**. We hypothesized to observe abnormalities in the electrophysiological signatures of the two resting state networks, default-mode network and salience network, between the PTSD group and the combat control group.

METHODS

Participants

The study was approved by the Western Institutional Review Board (IRB). All study procedures were carried out in accordance with the principles expressed in the Declaration of Helsinki. Thirty-six male, unmedicated veterans aged 18 to 55 years with combat-related PTSD according to the Diagnostic and Statistical Manual of Mental Disorders— Fourth Edition Text Revision (DSM-IV-TR, APA, 2000) participated. Twenty male, combat-exposed, medically and psychiatrically healthy male veterans who did not meet diagnostic criteria of PTSD or any other Axis I psychiatric disorder were also recruited as combat-exposed controls (CEC). Participants, recruited from the community, underwent medical and psychiatric screening evaluations at the Laureate Institute for Brain Research. PTSD diagnoses were

determined with the Clinician Administered PTSD Scale (CAPS), which is a gold standard for diagnosing PTSD (Blake et al., 1990, 1995; Weathers et al., 2001), delivered by interviewers trained in the administration of the interviewer. Participants were also administered the Structural Clinical Interview for DSM-IV Disorders, the PTSD Checklist military version (PCL-M; Weathers et al., 1991), Hamilton Anxiety Rating Scale (HARS; Hamilton, 1959), the Snaith-Hamilton Pleasure Scale (SHAPS; Snaith et al., 1995), the Montgomery–Åsberg Depression Rating Scale (MADRS; Montgomery & Åsberg, 1979) and the Hamilton Depression Rating Scale (HDRS; Hamilton, 1960).

Exclusion criteria included general MRI exclusions, psychosis, current or past history of schizophrenia, schizoaffective disorder, bipolar disorder, or dementia, moderate to severe traumatic brain injury, serious suicidal ideation, major medical or neurological disorders, and exposure to any medication likely to influence cerebral function or blood flow within three weeks (eight weeks for fluoxetine), as well as meeting DSM-IV criteria for substance abuse or substance dependence (other than nicotine) within 3 months prior to screening. After receiving a complete explanation of the study procedures, all participants provided written informed consent as approved by the Western Institutional Review Board. Participants received financial compensation for their participation.

Data Acquisition

Simultaneous EEG and fMRI data were acquired in all study participants. MRI scans were completed at the Laureate Institute for Brain Research on General Electric Discovery MR750 whole-body 3 Tesla MRI scanners (GE Healthcare, USA) with standard 8-channel receive-only head coils. Resting-state fMRI data were acquired using a single-shot gradient-recalled EPI sequence with Sensitivity Encoding (SENSE). The resting state session lasts for a total of 8 minutes and 46 seconds when participants were instructed to keep their eyes open and fixed on a white cross in front of a gray background. The

following EPI imaging parameters were used: FOV/slice = 240/2.9 mm, axial slices per volume = 34, acquisition matrix = 96×96, repetition time/echo time (TR/TE) = 2000/30 ms, SENSE acceleration factor R = 2 in the phase encoding (anterior-posterior) direction, flip angle = 90°, sampling bandwidth = 250 kHz. The EPI images were reconstructed into a 128×128 matrix, in which the resulting fMRI voxel volume was 1.875×1.875×2.9mm³. Additional structural MRI were collected using a T1-weighted magnetization-prepared rapid gradient-echo (MPRAGE) sequence with SENSE. The following parameters were set for structural MRI: FOV = 240 mm, axial slices per slab = 128, slice thickness = 1.2 mm, image matrix = 256×256, TR/TE = 5/1.9 ms, acceleration factor R = 2, flip angle = 10°, delay/inversion time TD/TI = 1400/725 ms, sampling band-width = 31.2 kHz.

Simultaneous EEG signals were recorded using MRI-compatible BrainAmp MR Plus amplifiers (Brain Products GmbH, Munich, Germany). Thirty-one channels of EEG at the standard 10-20 positions were acquired, with a reference to the FCz position. The electrodes covered the whole brain with an inter-electrode distance of ~ 5 cm. One additional electrode of electrocardiogram was also acquired for the purpose of correcting the pulse artifacts (Allen et al., 1998). All electrodes were well prepared and maintained with impedance below 10 kΩ throughout the recording. SyncBox device (Brain Products GmbH, Munich, Germany) was set up for synchronizing the internal sampling clock of the EEG amplifier with the MRI scanner 10MHz master clock signal for the purpose of removing the gradient artifacts (Allen et al., 2000; Mandelkow et al., 2006). The signals were recorded at a sampling frequency of 5000 Hz with an analog filter (from 0.016 to 250 Hz) and a resolution of 0.1μV.

Additional auxiliary data included respiration and cardiac pulses recorded by a pneumatic respiration belt and a photoplethysmograph, respectively, for correcting the physiological noise in resting state fMRI data. The recording of the cardiac pulse and respiratory data was synchronized with the fMRI data acquisition. Both waveforms were sampled at a frequency of 50 Hz.

EEG Processing

Preprocessing of the EEG data corrected the artifacts due to simultaneous recording with MRI scanning, i.e. the gradient artifacts and the pulse artifacts, using the average subtraction method (Allen et al., 1998; Allen et al., 2000) implemented in BrainVision Analyzer software (Brain Products GmbH, Munich, Germany). Residual pulse artifacts were removed by using the independent component analysis (ICA) implemented in the EEGLAB toolbox (<http://sccn.ucsd.edu/eeglab/>). In some participants, an EEG channel with extreme noises was disregarded and then interpolated by an average of neighbor channels. The de-noised data were subsequently band-pass filtered from 1 Hz to 70 Hz, downsampled to 250 Hz, and re-referenced to the common average reference.

After preprocessing, temporal independent EEG microstates (EEG-ms) were derived using the method described in Yuan et al. (2012). Briefly, the EEG topographies were extracted at the local peaks of global field power, pooled across all sessions and further segregated into temporal independent patterns in a data driven manner by ICA, namely the temporal independent EEG microstates. The number of independent components (ICs) in microstates was chosen to be 30, i.e. the maximum number of channels commonly available among all participants. Components related to nuisance processes (i.e., eye movement, residual pulse artifact and muscle artifact) were further excluded. The temporal independent EEG-ms were separately analyzed for the PTSD and CEC groups. Then the microstates of the PTSD group were matched to each of those in the CEC group by selecting the one with the highest spatial correlation coefficient. A back-projection was performed to obtain time courses associated with each EEG-ms, resulting in continuous time series as the original EEG data. Furthermore, the time series were normalized using a winner-take-all approach, i.e. a microstate was assigned to a time point based on which microstate has the maximal absolute intensity value. The resulted time series of a EEG-ms are

composed of series of zeros and ones, with the value of ones at time points when the absolute intensity value of the particular microstate exceeded those of all other microstates. The time course describes the temporal dynamics of the EEG-ms dominating the momentary EEG topographies over other microstates. The occurrence rate of a EEG-ms was calculated as the summation of the time series of the EEG-ms divided by the duration of the period of time, indicating how frequent the EEG-ms dominates the momentary EEG topographies over other microstates.

The occurrence rate of EEG-ms was calculated for each subject, compared across groups, and examined in relation to clinical ratings. Group-level comparison between PTSD and CEC was performed on the occurrence rate of the EEG-ms, using a two-sample, unpaired t-test assuming unequal variance.

fMRI Processing

The fMRI data preprocessing was performed using the Analysis of Functional NeuroImages software (AFNI, <http://afni.nimh.nih.gov/>) (Cox 1996). Preprocessing of the resting state fMRI data steps include removal of the first five volumes of each run, respiration- and cardiac-induced noise reduction using RETROICOR (Glover et al., 2000), slice timing and rigid-body motion correction, spatial smoothing with a Gaussian kernel (FWHM = 6 mm), and temporal filtering with a bandpass filter (0.01 ~ 0.1 Hz). Further processing removed the low-frequency changes in respiration volume and motion as nuisances in the regression (Birn et al., 2006). Spatial co-registration and normalization was conducted by converting fMRI data in the original individual space to a common anatomical space defined in the Talairach and Tournoux template brain (Talairach and Tournoux 1988) with aid of the Advanced Normalization Tools (<http://www.picsl.upenn.edu/ANTS/>).

After preprocessing, resting state networks of the fMRI were obtained using a spatial ICA implemented in the MELODIC (multivariate exploratory linear optimized decomposition into independent components) tool in the FSL software (Beckmann et al., 2005). The order of independent components (ICs) was determined to be 30, as consistent with EEG and also consistent with other fMRI studies of RSN (Damoiseaux et al., 2006; Smith et al., 2010). The intensity values in each map of each participant were constructed via dual regression (Filippini et al., 2009; Veer et al., 2010), resulting in subject-specific spatial maps of z-scores. Voxel-wise comparison between the PTSD and CEC groups was performed using an unpaired, two-sample t test. The significance criterion for thresholding was set at $p_{\text{corrected}} < 0.05$ determined using the AFNI program 3dClustSim. In addition, an averaged map across all individuals was calculated and thresholded at the value of 2 (Damoiseaux et al., 2006).

Multi-Modal Analysis

In order to identify the RSNs associated the EEG-ms, we compared the time courses of the EEG-ms associated with the dynamics of whole-brain fMRI time series. Firstly, to accommodate the dramatically different temporal scales of multimodal EEG and fMRI data, the time courses of the EEG-ms were convolved with a double-gamma hemodynamic response function (HRF) (Friston et al., 1998) and then down-sampled to TR, resulting in EEG-ms-informed regressors. The microstate that is related to a resting state network is determined by integrating the EEG-ms-informed regressors in a general linear model (GLM) analysis using a mixed-effect model. EEG-ms-informed statistical maps were created by showing voxels where the time courses of BOLD signals significantly co-varied with the time courses of EEG-ms-informed regressors. The significance criterion for thresholding was set at $p_{\text{corrected}} < 0.05$ determined using the AFNI program 3dClustSim.

The EEG-ms-informed maps were compared with the resting state networks calculated from fMRI. A Pearson's correlation coefficient was calculated between a EEG-ms-informed map and all maps of fMRI RSNs. A particular EEG microstate of interest is associated with a RSN, by selecting and designating the RSN that has the highest spatial correlation with the EEG-ms-informed map. Then the selected fMRI RSNs from our data were compared with 14 template RSNs reported in Shirer et al. (2012). Since the templates were in binary numbers, the selected fMRI RSN maps were thresholded following the procedure described in Shirer et al. (2012). Dice coefficient for a pair of maps in binary values was calculated. An fMRI RSN was labeled with the template RSN that has the highest dice coefficient. Correspondingly, an EEG-informed network matched with the fMRI RSN was also designated with the same label.

RESULTS

Thirty-six PTSD veterans and twenty CEC veterans were included in the current analysis. Table 1 lists the demographic and clinical characteristics of the participants of the current study.

[Insert Table 1 here]

A series of ten temporal independent microstates were identified in the groups of PTSD and CEC veterans (Fig. 1). Nine out of the 10 microstates highly resemble those found in our previous study (MS1, MS2, MS4, MS5, MS6, MS7, MS8, MS9 and MS10 in Yuan et al. 2012). Remarkably, the microstates in the current study are obtained from a low-density cap with only 30 EEG channels and from eyes-open resting state. Among the common patterns observed in the healthy participants, the microstates MS1, MS6, MS7, MS8, and MS9 shows patterns in the parietal and occipital cortex. The

microstates MS2 and MS4 shows strong patterns in the sensorimotor cortex, while microstate MS5 was dominated by temporal-parietal sources. A unique microstate MS11 was identified in the current study, featuring a bilateral pattern with sources originated from the junction of posterior and temporal areas.

[Insert Figure 1 here]

As the dynamics of the temporal independent microstates were reconstructed from EEG time series, their signatures at a time scale of millisecond could be examined. Among these EEG-ms, three microstates demonstrated distinctive differences in their fast-evolving dynamics. The EEG-ms that differed between PTSD and CEC groups are marked by dashed lines in Fig. 1. The occurrence rate of these three microstates showed significant difference between groups. For microstates MS1 and MS11, the PTSD group showed significantly higher occurrence rate than the control group, whereas for microstate MS 10, the PTSD group showed a lower occurrence rate. All other microstates failed to demonstrate group-level difference between PTSD and CEC in terms of their occurrence rate.

To further explore the neuronal substrates of these three signature microstates, the temporal dynamics of the microstate were compared with the time courses of BOLD signals after convolving with the impulse hemodynamic response function. Regions where BOLD and EEG microstate time series are correlated were identified using a general linear model, resulting in EEG-ms-informed networks. The EEG-informed networks were then compared with the resting state network calculated from fMRI data. The selected fMRI RSN from our data were further compared with 14 template RSN from Shirer et al. (2012). The fMRI RSN and their corresponding EEG-ms-informed network were designated with the same label of best-matched template RSN. The dorsal default model network (dDMN) was therefore identified associated with one of the EEG microstates, MS1 (Fig. 2). Importantly, the occurrence rate of

the dDMN-associated EEG microstates shows distinctive temporal dynamics between CEC and PTSD groups (i.e., higher in the PTSD group). Moreover, the occurrence rate of the EEG-ms was also linearly related to the scores of PCL-M scores in the PTSD group, indicating that more severe PTSD symptoms are associated with faster dynamics of the dDMN network. While functional MRI was able to pinpoint the anatomical regions of DMN, simultaneous EEG offers fast temporal dynamics that facilitate relating them to the severity of symptoms. Regarding dorsal DMN, the comparison between the fMRI RSN found in our data and the template RSN is shown in Supplemental Fig. S1.

[Insert Figure 2 here]

Two other microstates MS 10 and MS11, were also found to be associated with distinctive dynamics between PTSD and CEC groups. Interestingly, both MS10 and MS11 identified a similar network, involving bilateral insular, the cingulate cortex and the medial temporal cortex. MS10 (Fig. 3) appears to engage the anterior salience network (aSN) that includes the anterior insular, dorsal anterior cingulate/paracingulate cortex, and the medial thalamus. By the way of comparison, MS11 (Fig. 4) is related to the posterior salience network (pSN) that includes the posterior insular region and dorsal anterior cingulate cortex. However, the temporal dynamics of MS10 and MS11 show importantly different characteristics. For MS11, the PTSD group showed significantly higher occurrence rate than the control group, whereas for microstate MS 10, the PTSD group showed lower occurrence rate. Furthermore, the dynamics of MS10 was found to negatively correlate with SHAPS scores across the individual subjects, which assess hedonic experience or positive valence. Therefore, in the PTSD group, participants with higher level of hedonic tone are associated with lower occurrence rate of the anterior salience network. The dynamics of MS11 did not show any significant linear trend between the

occurrence rate and the level of symptoms ($p > 0.05$ for both PCL-M and SHAPS scores). For anterior and posterior salience networks, the comparison between the fMRI RSN found in our data and the template RSN is shown in Supplemental Figures S2 and S3.

[Insert Figure 3 here]

[Insert Figure 4 here]

Furthermore, our analysis evaluated the group-level difference in the three fMRI RSNs between PTSD and CEC. Using similar statistical criteria for thresholding the EEG-ms-informed networks, no regions with significant difference between PTSD and CEC groups were identified in the fMRI RSN maps. To illustrate the comparison, representative images of the group mean for PTSD and CEC are shown in Supplemental Fig. S4.

DISCUSSIONS

We investigated and compared the electrophysiological signatures of hemodynamic RSNs in male veterans with and without combat related PTSD. To our knowledge, this is the first examination of resting state networks in PTSD using a multimodal concurrent EEG-fMRI approach and also controls for combat exposure. We proposed a new strategy to integrate EEG and fMRI by quantifying the fast temporal dynamics associated with the resting state networks. Results show that in three fMRI derived resting state networks, namely dorsal DMN as well as anterior and posterior SNs networks, the temporal dynamics as characterized and measured by EEG, differ as a function of PTSD. The electrophysiological correlates – temporal independent EEG microstates associated with the DMN and anterior and posterior SNs - show aberrant occurrence rate in PTSD. In particular, the occurrence rate of the DMN is higher in PTSD and positively correlated with the score of PTSD severity. In contrast, the occurrence rate of the

anterior SN is lower in PTSD and negatively correlated with the score of hedonic tone or degree of pleasantness.

Multiple brain regions have been depicted in the imaging studies of PTSD, as patterns of activations during tasks of symptom provocation. Hyperactivity of limbic brain regions (e.g., amygdala, insula) and hypo-activity of brain areas involved in emotional regulation (e.g., ventromedial prefrontal cortex [vmPFC], dorsal anterior cingulate cortex [dACC]) have been observed, suggesting insufficient top-down modulation of limbic regions (especially the amygdala) by the prefrontal cortex (Rauch et al., 2006; Liberzon and Sripada, 2007; Pitman et al., 2012). In addition, fMRI imaging of RSFC or RSN has become a useful tool in the investigation of the neurobiological mechanism of PTSD, as the disease shows symptoms of re-experiencing the traumatic events, avoidance and hyperarousal at resting state. Patterns of connectivity between the PTSD-implicated regions could give new information on the neural basis of PTSD, and on mechanisms of PTSD symptom development.

Multimodal imaging using simultaneous EEG and fMRI has been recently exploited in studying the mechanisms or functions of the RSNs in the human brain (Mantini et al., 2007; Britz et al., 2010; Musso et al., 2010; Deco et al., 2011; Yuan et al., 2012). The simultaneously acquired EEG data provides high-temporal resolution to capture the millisecond-level recordings of neural activity (Yuan et al., 2011, 2012, 2016), physiological noise (Yuan et al., 2013), or head movement (Zotev et al., 2012, Wong et al., 2016). The temporal independent EEG-ms (Yuan et al., 2012) have been discovered and shown to be coupled to the temporal dynamics of BOLD RSNs. More intriguingly, the source generators of the temporal independent EEG microstates have been reconstructed using EEG source imaging and shown to spatially match eight of the resting state networks established in fMRI studies (Yuan et al., 2016). Taken together, the temporal independent EEG-ms are electrophysiological correlates to specific resting state networks, both in their spatial patterns and temporal dynamics. In our current study, we capitalize

on the rich temporal information obtained from the EEG and investigate how PTSD relates to temporal electrophysiological signatures in two hemodynamic RSNs of interest, the DMN and the SN.

During rest, disrupted connectivity within the DMN has been reported in PTSD due to traumatic life events (Bluhm et al., 2009; Shin et al., 2009; Daniels et al., 2011) and the related psychiatric problem of acute stress disorder (Lui et al. 2009; Lanius et al., 2010). Most studies examining integrity of DMN connectivity in PTSD have focused on civilian trauma; however, less is known about the effect of combat-related trauma. To date, only a few studies have examined network-level alternations in combat-related PTSD (Daniels et al., 2010; Sripada et al. 2012; Kennis et al., 2015; DiGangi et al., 2016); and the findings have been inconclusive. Sripada et al. (2012) reported that PTSD veteran participants showed reduced coupling within DMN, as compared to a combination of combat-exposed controls and healthy community controls. However, the way of using a combined cohort of combat and civilian controls raise concern of whether the observed difference is evident in comparison to combat exposed veterans without PTSD, or just to the healthy civilians. In this regard, a study by DiGangi et al. (2016) examined details of DMN connectivity in three groups: veterans with combat-related PTSD, combat-exposed controls without PTSD and never-traumatized healthy controls and compared their resting state functional connectivity. Difference in DMN associated with PTSD was found only in comparison with the civilian control but not in the comparison with combat-exposed veterans. Thus, it remains unclear whether the abnormality of resting state networks is due to the experience of trauma, or the pathology of PTSD. Another independent study by Kennis et al., (2015) investigated the ACC cortex, a key component of DMN, and found out specific difference in connectivity between veterans with combat-related PTSD and combat exposed controls. As compared to the PTSD group or the healthy control group, combat controls showed increased left rostral ACC connectivity with the precentral gyrus, extending into the medial frontal gyrus, suggesting a protective mechanism unique to the combat

controls in the connectivity between rostral ACC and precentral gyrus. Nonetheless, in the examination of connectivity with regard to the perigenual ACC (pgACC; i.e. part of the **dorsal** DMN), no difference was reported between PTSD and combat veterans; whereas as compared to the healthy controls, veterans with and without PTSD showed reduced functional connectivity of the pgACC with the supramarginal gyrus (SMG) and middle temporal gyrus (MTG). Nonetheless, it remains unclear to what level does the connectivity in the DMN differs between combat PTSD and combat-exposed control.

In this study, we compared veterans with war-related PTSD and combat-exposed veterans without PTSD. Results suggested *increased* **occurrence rate** of DMN-related electrophysiological states in the veterans with PTSD as compared to the veteran controls. The EEG microstate MS1 was observed to be the electrophysiological correlate of regions including the precuneus, the medial prefrontal gyrus (MPFC) and the bilateral dorsal lateral PFC, which constitutes the key nodes of the DMN (Buckner et al., 2008). The precuneus is involved in autobiographical memory and is also related to self-referential processing (Lou et al., 2004; Cavanna and Trimble, 2006; Yuan et al., 2014). Furthermore, precuneus activity has been related to trauma memory generalization (Hayes et al., 2011), and flashbacks (Whalley et al., 2013). Thus, alterations in the precuneus are associated with PTSD and may potentially be related to altered memory- and self-referential processes, such as memory deficits, intrusions or flashbacks. These findings altogether suggest that the DMN is disturbed in PTSD.

Our observation regarding *increased* DMN temporal dynamics is in line with previous task-based studies of PTSD patients which report increased connectivity within DMN-related regions (Daniels et al., 2010). An analysis of the whole brain RSFC network topology associated with combat-related PTSD revealed the abnormally increased connectivity of the precuneus within the DMN (Kennis et al., 2015). Furthermore, our investigation extended prior work by examining the DMN using a multimodal approach and showed increased temporal dynamics within the PTSD group. Moreover, the temporal

dynamics in PTSD appear positively correlated with PTSD severity. As PTSD severity increased, the occurrence of electrophysiological states (e.g. EEG-ms) associated with the DMN were higher, suggesting a neuroimaging metric that has potential as a biomarker of symptom severity.

The salience network (Seeley et al., 2007) has also been another focus in the neuroimaging studies of PTSD. The SN consists of dorsal anterior cingulate (dACC) and orbital frontoinsula cortices with robust connectivity to subcortical and limbic structures. Further delineation of the salience network resulted in two sub-networks, the anterior SN and the posterior SN (Shirer et al., 2012). Studies of SN have suggested it plays in detecting and orienting to salient stimuli (Dosenbach et al., 2007; Sridharan et al., 2008), emotional control (Seeley et al., 2007), cognitive control (Menon and Uddin, 2010), and error processing (Ham et al., 2013). In particular, the intrinsic functional connectivity of the dACC node of the SN has been associated with anxiety ratings in the healthy population (Seeley et al., 2007).

Alterations in the SN that are associated with PTSD, however, have been investigated in a limited number of studies. The insula and amygdala have been found to be hyperactive in PTSD (Shin and Liberzon, 2010; Etkin et al., 2007) and are involved in the SN (Cauda et al., 2011). Reduced ACC resting state functional connectivity with the thalamus, amygdala, posterior cingulate cortex (PCC)/precuneus, and prefrontal regions has been reported in PTSD versus non-trauma-exposed controls (Kennis et al., 2015; Daniels et al., 2010), trauma-exposed controls (Sripada et al., 2012a; Yin et al., 2011) or both (Kennis et al., 2016; Sripada et al., 2012b). As discussed above, using a control group of non-trauma-exposed civilian or a combination of combat-exposed and non-combat-exposed controls raises methodological concerns and limits the interpretation of the findings.

Our results found distinct PTSD-related signatures for the anterior SN and the posterior SN. The microstate MS10 was observed to be the electrophysiological correlate of the anterior SN, which includes the anterior insular, dorsal anterior cingulate/paracingulate cortex, and the medial thalamus. In

contrast, MS11 is related to the posterior **saliency** network that includes the posterior insular region and dACC. The delineation of anterior and posterior SN has been documented in data-driven studies of resting-state fMRI data (Shirer et al., 2012) and tractography-based studies of diffusion tensor imaging data (Figley et al., 2015). However, the functional relevance of the subnetworks of the SN is not yet fully delineated. Our study compared the temporal dynamics of the EEG microstates associated with the anterior and posterior SN: *decreased* temporal dynamics in the anterior SN, yet *increased* dynamics in the posterior SN, were observed in PTSD. These results suggest an antagonist relationship between the anterior and posterior SN in PTSD. More interestingly, the dynamics of the anterior SN is related to the hedonic tone of the participants. The PTSD group was found to have significantly higher hedonic tone than the controls, and correspondingly the PTSD participants show a significantly lower **occurrence rate** EEG-ms associated with anterior SN. In line with the group-level finding, at an individual level in the PTSD group, the higher the score of hedonic tone is, the less frequently the anterior SN EEG-ms occurs. These results suggest that activity of the SN is disturbed in among people with PTSD while at rest, and are consistent with work documenting abnormal functioning of the emotion regulation network in this population.

Moreover, the SN is thought to play a critical role modulating and regulating the balance between DMN and central-executive network (CEN) activity (Bressler and Menon, 2010). **Our study found that the temporal dynamics of DMN and SN show antagonist features.** Whereas the temporal dynamics of DMN become more frequently dominant in PTSD, the states of the anterior SN go in an opposite, diminishing direction. Interestingly, the exaggerated DMN dynamics are positively associated with the severity of PTSD symptoms whereas the diminishing states of the anterior SN are negatively associated with the hedonic tone across PTSD individuals. Moreover, the posterior SN has been also delineated in

our findings. Although the states of the posterior SN show higher **occurrence rate** in the PTSD than the CEC group, it remains still unclear about the functional underpinning of the posterior SN.

Our results show the merit of multimodal imaging in studying the neural mechanism of PTSD. The current results confirmed our previous findings that temporal independent microstates are electrophysiological correlates of distinct RSNs, as shown here in two independent cohorts of adult participants (combat-exposed healthy males without, and males with combat-related PTSD). We provided novel evidence that temporal dynamics of large-scale DMN and SNs, reflected by associated EEG-ms, differentiate the PTSD and combat-exposed controls groups. By relating to other studies on EEG microstate (Lehmann et al., 1987; Koenig et al., 2002), we have previously proposed that these miniature brain states of temporal independent EEG microstates **represent putative neuronal events in the form of** spatially and temporally synchronized neuronal activity (Yuan et al., 2016). The spontaneous brain network activity may be driven by synchronized burst-type neural events (~40 ms, EEG-ms physiologically relevant time scale), which can be separated into temporally independent processes representing functional RSNs. In such a framework, the EEG-ms and RSNs may refer to the common building blocks of brain spontaneous neuronal activity. More importantly, the concept of the microstate introduces new ways to dictate the dynamics of resting state brain activity (Khanna et al., 2015). The temporal dynamics of EEG microstates, such as **occurrence rate or duration of states**, are found to be altered in panic disorder (Kikuchi et al., 2011), schizophrenia (Kindler et al., 2011), and dementia (Nishida et al., 2013; Hatz et al., 2015; Grieder et al., 2016). Here, our results documented that temporal independent EEG microstates associated with DMN, and SNs are altered in combat-related PTSD.

Our findings revealed that the temporal dynamics of the DMN- and SN-associated EEG-ms are associated with PTSD severity and hedonic tone, respectively, suggest that such neuroimaging metrics

may be used as PTSD-related biomarkers. While future investigations on such neuroimaging metrics are warranted to fully characterize their relevance to psychopathology of PTSD, and to clinically relevant outcome measures, EEG-ms have potentials in facilitating the diagnosis and prognosis of PTSD. Furthermore, since EEG-ms is related to the level of disease severity, it may be used as an evaluation biomarker in determining the effectiveness of an intervention or treatment. A relevant work from our group showed that the EEG microstates exploited in the current study can also be constructed from EEG alone data (Yuan et al., 2016). The temporal independent microstates based on stand-alone EEG data may be able to provide more portable and less expensive way for researching novel interventions for PTSD. Another potential use of EEG-ms is as neurofeedback training for user to alleviate the symptom via a learning by biofeedback approach (Zotев et al., 2014). Since instrumentation for EEG-based neurofeedback is considerably affordable and portable, it opens another avenue of use for the EEG-ms.

Conclusion

Our study employed a novel approach to study the fast dynamics of resting state networks associated with PTSD by using simultaneous EEG and fMRI. To our knowledge, this study for the first time showed differences in the fast temporal dynamics of dorsal default mode network, anterior and posterior salience networks, comparing veterans with combat-related PTSD to combat-exposed veteran controls without PTSD. The occurrence rate of the EEG microstates associated with the default mode network was higher in PTSD than control, and positively associated with the severity of PTSD symptoms. The occurrence rate of the electrophysiological state associated with the anterior salience network was lower in PTSD than control, and negatively associated with the hedonic tone in PTSD participants. Our findings contribute new information to our understanding of the neural mechanisms of PTSD, and further suggest that a disruption in emotion generation and regulation circuits plays a crucial role and

contributes to the pathophysiology of PTSD. Moreover, the study suggests that multimodal neuroimaging yields valuable information about large-scale neural activity at high temporal as well as high spatial resolution and is a useful technology for understanding neuropsychiatric disorders.

Acknowledgements

This work was supported by the W81XWH-12-1-0697 grant from the U.S. Department of Defense. The authors thank all staff members at Laureate Institute for Brain Research, Matthew Meyer, M.D., and William Yates, M.D. for conducting psychiatric interviews, Tim Collins, Lisa Kinyon, and Megan Cole for administering clinical interviews and assessments, and Julie Owen, Julie Crawford, Leslie Walker, and Tressia Lewis for helping with MRI scanning. The funding agencies were not involved in the design of experiment, data collection and analysis, interpretation of results and preparation and submission of the manuscript. The authors declare that they have no conflict of financial interest.

Table 1

Demographical and clinical characteristics of PTSD group and combat exposed control (CEC) group.

Characteristic	PTSD (n=36)	CEC (n=20)
Age (Mean \pm SD Years)	32 \pm 7	34 \pm 9
PCL-M (Mean \pm SD) ***	42.9 \pm 14.6	18.4 \pm 2.2
CAPS (Mean \pm SD) ***	54.0 \pm 18.5	4.7 \pm 5.1
SHAPS (Mean \pm SD) ***	29.9 \pm 5.7	23.5 \pm 5.8
HARS (Mean \pm SD) ***	15.3 \pm 6.2	2.6 \pm 3.5
HDRS (Mean \pm SD) ***	14.3 \pm 5.6	2.6 \pm 3.7
MADRS (Mean \pm SD) ***	17.2 \pm 8.2	2.1 \pm 3.8

PTSD: post-traumatic stress disorder.

CAPS: Clinician Administered PTSD Scale.

PCL-M: the PTSD Checklist, military version.

HARS: Hamilton Anxiety Rating Scale.

HDRS: Hamilton Depression Rating Scale.

SHAPS: the Snaith-Hamilton Pleasure Scale.

MADRS: the Montgomery–Åsberg Depression Rating Scale.

SD: standard derivation.

*** indicates significant difference between PTSD and HC ($p < 0.001$).

Figure Captions

Figure 1. Microstates identified in CEC and PTSD groups. The pairs of microstates in dashed lines show distinct features between CEC and PTSD groups.

Figure 2. **Dorsal** Default Mode Network. Analysis of temporal dynamics identified that microstate MS1 (A) is related to an EEG-informed Network (C) which resembles the fMRI **dorsal** Default Mode Network (D), showing at positions $z=4, 21$ and 32 (B). (E) **Occurrence rate** of microstate MS1 differs between CEC and PTSD groups ($p = 0.02$). (F) In all thirty-six PTSD individuals, the **occurrence rate** of microstate MS1 is positively correlated to the score of symptom severity measured by PCL-M ($r = 0.51$, $p = 0.004$).

Figure 3. Anterior Salience Network. Analysis of temporal dynamics identified that microstate MS10 (A) is related to an EEG-informed network (C) which resembles the fMRI Anterior Salience Network (D), showing at positions $z=2, 16$ and 44 (B). (C) **Occurrence rate** of microstate MS10 differs between CEC and PTSD groups ($p = 0.03$). (D) In the PTSD individuals, the **occurrence rate** of microstate MS10 is inversely correlated to the score of hedonic tone measured by the Snaith-Hamilton Pleasure Scale (SHAPS) ($r = -0.46$, $p = 0.006$).

Figure 4. Posterior Salience Network. Analysis of temporal dynamics identified that microstate MS11 (A) is related to an EEG-informed network (C) which resembles the fMRI Posterior Salience Network (D), showing at positions $z=2, 10$ and 32 (B). (C) **Occurrence rate** of microstate MS11 significantly differs between CEC and PTSD groups ($p = 0.0004$). Among the PTSD individuals, neither the score of PTSD severity or the score of hedonic tone was correlated with the **occurrence rate** of microstate MS11.

References:

- American Psychiatric Association, 2000. Diagnostic and Statistical Manual of Mental Disorders, 4th ed. Text revision (DSM-IV-TR). American Psychiatric Press, Washington, DC.
- American Psychiatric Association, 2013. Diagnostic and Statistical Manual of Mental Disorders, 5th ed. (DSM-5). American Psychiatric Press, Washington, DC.
- Allen P.J., Polizzi G., Krakow K., Fish D.R., Lemieux L. 1998. Identification of EEG events in the MR scanner: the problem of pulse artifact and a method for its subtraction. *Neuroimage* 8:229–239.
- Allen P.J., Josephs O., Turner R. 2000. A method for removing imaging artifact from continuous EEG recorded during functional MRI. *Neuroimage* 12:230–239.
- Beckmann CF, DeLuca M, Devlin JT, Smith SM. 2005. Investigations into resting-state connectivity using independent component analysis. *Philos Trans R Soc Lond B Biol Sci.* 360:1001-1013.
- Bell, A.J. and Sejnowski, T.J. 1995. An information-maximization approach to blind separation and blind deconvolution. *Neural Computation* 7:1129-1159.
- Birn RM, Diamond JB, Smith MA, Bandettini PA. 2006. Separating respiratory-variation-related fluctuations from neuronal-activity-related fluctuations in fMRI. *Neuroimage.* 31:1536-1548.
- Biswal, B., Yetkin, F.Z., Haughton, V.M., Hyde, J.S. 1995. Functional connectivity in the motor cortex of resting human brain using echo-planar MRI. *Magn. Reson. Med.* 34:537-541.
- Blake, D.D., Weathers, F.W., Nagy, L.M., Kaloupek, D.G., Klauminzer, G., Charney, D.S., Keane, T.M. 1990. A clinician rating scale for assessing current and lifetime PTSD: the CAPS-1. *Behav. Ther.* 13:187-188.
- Blake, D., Weathers, F., Nagy, L., Kaloupek, D., Gusman, F., Charney, D., Keane, T. 1995. The development of a clinician-administered PTSD scale. *J Traumatic Stress* 8:75-90.
- Bressler, S. L., and Menon, V. 2010. Large-scale brain networks in cognition: emerging methods and

principles. *Trends Cogn. Sci.* 14:277–290.

Brown, V.M., LaBar, K.S., Haswell, C.C., Gold, A.L., Mid-Atlantic MIRECC Workgroup, McCarthy, G., Morey, R.A. 2014. Altered resting-state functional connectivity of basolateral and centromedial amygdala complexes in posttraumatic stress disorder. *Neuropsychopharmacology* 39(2):351-359.

Bluhm, R.L., Williamson, P.C., Osuch, E.A., Frewen, P.A., Stevens, T.K., Boksman, K., Neufeld, R.W., Théberge, J., Lanius, R.A. 2009. Alterations in default mode network connectivity in posttraumatic stress disorder related to early-life trauma. *J. Psychiatric Neurosci* 34(3):187-194.

Britz, J., Van De Ville, D., Michel, C.M. 2010. BOLD correlates of EEG topography reveal rapid-state network dynamics. *Neuroimage* 52(4):1162-1170.

Buckner, R.L., Andrews-Hanna, J.R., Schacter, D.L. 2008. The brain default network: anatomy, function, and relevance to disease. *Ann NY Acad Sci* 1124:1-38.

Cauda, F., D'Agata, F., Sacco, K., Duca, S., Geminiani, G., Vercelli, A. 2011. Functional connectivity of the insula in the resting brain. *Neuroimage*. 55:8–23.

Cavanna, A.E., Trimble, M.R. 2006. The precuneus: a review of its functional anatomy and behavioural correlates. *Brain* 129(3): 564–583.

Cox, R.W. 1996. AFNI: software for analysis and visualization of functional magnetic resonance neuroimages. *Comput. Biomed. Res.* 29:162-173.

Chen, A.C., Etkin, A. 2013. Hippocampal network connectivity and activation differentiates post-traumatic stress disorder from generalized anxiety disorder. *Neuropsychopharmacology* 38(10):1889-1898.

Damoiseaux, J.S., Rombouts, S.A., Barkhof, F., Scheltens, P., Stam, C.J., Smith, S.M., Beckmann, C.F. 2006. Consistent resting-state networks across healthy subjects. *Proc. Natl. Acad. Sci.* 103:13848-13853.

Daniels, J.K., McFarlane, A.C., Bluhm, R.L., Moores, K.A., Clark, C.R., Shawn, M.E., Williamson, P.C., Densmore, M., Lanius, R.A. 2010. Switching between executive and default mode networks in

posttraumatic stress disorders: alterations in functional connectivity. *J. Psychiatry Neurosci* 35(4):258-266.

Daniels, J.K., Frewen, P., McKinnon, M.C., Lanius, R.A., Default mode alterations in posttraumatic stress disorder related to early-life trauma: a developmental perspective. 2011. *J Psychiatry Neurosci*. 36:56–9.

Daniels, J.K., McFarlane, A.C., Bluhm, R.L., Moores, K.A., Clark, C.R., Shaw, M.E., Williamson, P.C., Densmore, M., Lanius, R.A. 2010. Switching between executive and default mode networks in posttraumatic stress disorder: alterations in functional connectivity. *J Psychiatry Neurosci*. 35:258–66.

Deco G1, Jirsa VK, McIntosh AR. 2011. Emerging concepts for the dynamical organization of resting-state activity in the brain. *Nat Rev Neurosci* 12(1):43-56.

DiGangi, J.A., Tadayyon, A., Fitzgerald, D.A., Rabinak, C.A., Kennedy, A., Klumpp, H., Rauch, S.A., Phan, K.L. 2016. Reduced default mode network connectivity following trauma. *Neurosci Lett* 615:37-43.

Dosenbach, N.U., Fair, D.A., Miezin, F.M., Cohen, A.L., Wenger, K.K., Dosenbach, R.A., Fox, M.D., Snyder, A.Z., Vincent, J.L., Raichle, M.E., Schlaggar, B.L., Petersen, S.E. 2007. Distinct brain networks for adaptive and stable task control in humans. *Proc Natl Acad Sci U S A*. 104:11073–8.

Etkin, A., Wager, T.D. 2007. Functional neuroimaging of anxiety: a meta-analysis of emotional processing in PTSD, social anxiety disorder, and specific phobia. *Am J Psychiatry*. 164:1476–88.

Figley TD, Bhullar N, Courtney SM, Figley CR. 2015. Probabilistic atlases of default mode, executive control and salience network white matter tracts: an fMRI-guided diffusion tensor imaging and tractography study. *Front Hum Neurosci*. 9:585.

Filippini, N., MacIntosh, B.J., Hough, M.G., Goodwin, G.M., Frisoni, G.B., Smith, S.M., Matthews, P.M., Beckmann, C.F., Mackay, C.E., 2009. Distinct patterns of brain activity in young carriers of the APOE-epsilon4 allele. *Proc. Natl. Acad. Sci. U. S. A*. 106, 7209–7214.

- Fox, M.D. and Raichle, M.E., 2007. Spontaneous fluctuations in brain activity observed with functional magnetic resonance imaging. *Nature Reviews.Neuroscience* 8:700-711.
- Friston KJ, Fletcher P, Josephs O, Holmes A, Rugg MD, Turner R. 1998. Event-related fMRI: Characterizing differential responses. *Neuroimage*. 7:30-40.
- Glover, G.H., Li, T.Q., Ress, D., 2000. Image-based method for retrospective correction of physiological motion effects in fMRI: RETROICOR. *Magn. Reson. Med.* 44:162-167.
- Greicius, M.D., Supekar, K., Menon, V., Dougherty R.F. 2009. Resting-state functional connectivity reflects structural connectivity in the default mode network. *Cereb Cortex* 19(1):72-78.
- Grieder M, Koenig T, Kinoshita T, Utsunomiya K, Wahlund LO, Dierks T, Nishida K. Discovering EEG resting state alterations of semantic dementia. *Clin Neurophysiol.* 2016 May;127(5):2175-81.
- Ham, T., Leff, A., de Boissezon, X., Joffe, A., and Sharp, D. J. 2013. Cognitive control and the salience network: an investigation of error processing and effective connectivity. *J. Neurosci.* 33: 7091–7098.
- Hamilton, M., 1959. The assessment of anxiety states by rating. *Br. J. Med. Psychol.* 32:50-55.
- Hamilton, M., 1960. A rating scale for depression. *J. Neurol. Neurosurg. Psychiatry* 23:56-62.
- Hatz F, Hardmeier M, Benz N, Ehrensperger M, Gschwandtner U, Rüegg S, Schindler C, Monsch AU, Fuhr P. Microstate connectivity alterations in patients with early Alzheimer's disease. *Alzheimers Res Ther.* 2015 Dec 31;7:78.
- Hayes, J.P., LaBar, K.S., McCarthy, G., Selgrade, E., Nasser, J., Dolcos, F., Morey, R.A., 2011. Reduced hippocampal and amygdala activity predicts memory distortions for trauma reminders in combat-related PTSD. *J. Psychiatr. Res.* 45(5):660–669.
- He, B.J., Snyder, A.Z., Zempel, J.M., Smyth, M.D., Raichle, M.E., 2008. Electrophysiological correlates of the brain's intrinsic large-scale functional architecture. *Proc. Natl. Acad. Sci.* 105:16039-16044.

- Hoge, C.W., Castro, C.A., Messer, S.C., McGurk, D., Cotting, D.I., Koffman, R.L. 2004. Combat duty in Iraq and Afghanistan, mental health problems, and barriers to care. *N Engl J Med* 351:13–22.
- Kennis, M., van Rooij, S.J., van den Heuvel, M.P., Kahn, R.S., Geuze, E. 2015. Functional network topology associated with posttraumatic stress disorder in veterans. *Neuroimage Clin.* 10:302-309.
- Kennis, M., Rademaker, A.R., van Rooij, S.J., Kahn, R.S., Geuze, E. 2015. Resting state functional connectivity of the anterior cingulate cortex in veterans with and without post-traumatic stress disorder. *Hum Brain Mapp* 36(1):99-109.
- Kessler, R.C., *Posttraumatic stress disorder: the burden to the individual and to society.* *J Clin Psychiatry*, 2000. 61(suppl 5): p. 4-12.
- Lanius, R.A., Bluhm, R.L., Coupland, N.J., Hegadoren, K.M., Rowe, B., Theberge, J., Neufeld, R.W., Williamson, P.C., Brimson, M. 2010. Default mode network connectivity as a predictor of post-traumatic stress disorder symptom severity in acutely traumatized subjects. *Acta Psychiatr Scand.* 121:33–40.
- Laird, A.R., Eickhoff, S.B., Li, K., Glahn, D.C., Fox, P.T. 2009. Investigating the functional heterogeneity of the default mode network using coordinate-based meta-analytic modeling. *J. Neurosci* 29(46):14496-14505.
- Li, Y.O., Adali, T., Calhoun, V.D. 2006. Sample dependence correction for order selection in FMRI analysis. *Proc. ISBI*.
- Liberzon, I., Sripada, C.S., 2007. The functional neuroanatomy of PTSD: a critical review. *Prog. Brain Res.* 167:151–169.
- Lou, H.C., Luber, B., Crupain, M., Keenan, J.P., Nowak, M., Kjaer, T.W., Sackeim, H.A., Lisanby, S.H. 2004. Parietal cortex and representation of the mental Self. *Proc Acad Sci USA* 101(17):6827-6832.
- Lui, S., Huang, X., Chen, L., Tang, H., Zhang, T., Li, X., Li, D., Kuang, W., Chan, R.C., Mechelli, A., Sweeney, J.A., Gong, Q. 2009. High-field MRI reveals an acute impact on brain function in survivors of the magnitude 8.0 earthquake in China. *Proc Natl Acad Sci U S A.* 106:15412-15417;

- Mandelkow, H., Halder, P., Boesiger, P., Brandeis, D., 2006. Synchronization facilitates removal of MRI artefacts from concurrent EEG recordings and increases usable bandwidth. *NeuroImage* 32:1120-1126.
- Mantini, D., Perrucci, M.G., Del Gratta, C., Romani, G.L., Corbetta, M., 2007. Electrophysiological signatures of resting state networks in the human brain. *Proc. Natl. Acad. Sci.* 104:13170-13175.
- Menon, V., and Uddin, L. Q. 2010. Saliency, switching, attention and control: a network model of insula function. *Brain Struct. Funct.* 214:655–667.
- Montgomery, S.A., Asberg, M., 1979. A new depression scale designed to be sensitive to change. *Br. J. Psychiatry* 134, 382-389.
- Musso, F., Brinkmeyer, J., Mobascher, A., Warbrick, T., Winterer, G. 2010. Spontaneous brain activity and EEG microstates. A novel EEG/fMRI analysis approach to explore resting-state networks. *Neuroimage* 52(4):1149-1161.
- Nishida K, Morishima Y, Yoshimura M, Isotani T, Irisawa S, Jann K, Dierks T, Strik W, Kinoshita T, Koenig T. EEG microstates associated with salience and frontoparietal networks in frontotemporal dementia, schizophrenia and Alzheimer's disease. *Clin Neurophysiol.* 2013 Jun;124(6):1106-14.
- Pitman, R.K., Rasmusson, A.M., Koenen, K.C., Shin, L.M., Gilbertson, M.W., Milad, M.R., Liberzon, I. 2012. Biological studies of post-traumatic stress disorder. *Nat Rev Neurosci* 13(11):769-787.
- Rissanen, J., 1983. A universal prior for integers and estimation by minimum description length. *Ann Statistics* 11:416–431.
- Rauch, S.L., Shin, L.M., Phelps, E.A., 2006. Neurocircuitry models of posttraumatic stress disorder and extinction: human neuroimaging research-past, present, and future. *Biol. Psychiatry* 60(4):376–382.
- Seeley, W.W., Menon, V., Schatzberg, A.F., Keller, J., Glover, G.H., Kenna, H., Reiss, A.L., Greicius, M.D. 2007. Dissociable intrinsic connectivity networks for salience processing and executive control. *J Neurosci* 27(9):2349-2356.

Shin, L.M., Lasko, N.B., Macklin, M.L., Karpf, R.D., Milad, M.R., Orr, S.P., Goetz, J.M., Fischman, A.J., Rauch, S.L., Pitman, R.K.. 2009. Resting metabolic activity in the cingulate cortex and vulnerability to posttraumatic stress disorder. *Arch Gen Psychiatry*. 66:1099–107.

Shin, L.M., Liberzon, I., 2010. The neurocircuitry of fear, stress, and anxiety disorders. *Neuropsychopharmacol*. 35:169-191.

Shirer, W. R., Ryali, S., Rykhlevskaia, E., Menon, V., and Greicius, M. D. 2012. Decoding subject-driven cognitive states with whole-brain connectivity patterns. *Cereb. Cortex* 22:158–165.

Snaith, R.P., Hamilton, M., Morley, S., Humayan, A., Hargreaves, D., Trigwell, P., 1995. A scale for the assessment of hedonic tone: the Snaith-Hamilton Pleasure Scale. *Br. J. Psychiatry* 167:99-103.

Sridharan, D., Levitin, D.J., Menon, V. 2008. A critical role for the right fronto-insular cortex in switching between central-executive and default-mode networks. *Proc Natl Acad Sci U S A*. 105:12569–74.

Sripada, R.K., King, A.P., Welsh, R.C., Garfinkel, S.N., Wang, X., Sripada, C.S., Liberzon, I., 2012a. Neural dysregulation in posttraumatic stress disorder: evidence for disrupted equilibrium between salience and default mode brain networks. *Psychosom Med*. 74(9):904-911.

Sripada, R.K., King, A.P., Garfinkel, S.N., Wang, X., Sripada, C.S., Welsh, R.C., Liberzon, I., 2012b. Altered resting-state amygdala functional connectivity in men with posttraumatic stress disorder. *J. Psychiatry Neurosci*. 37(4):241-249.

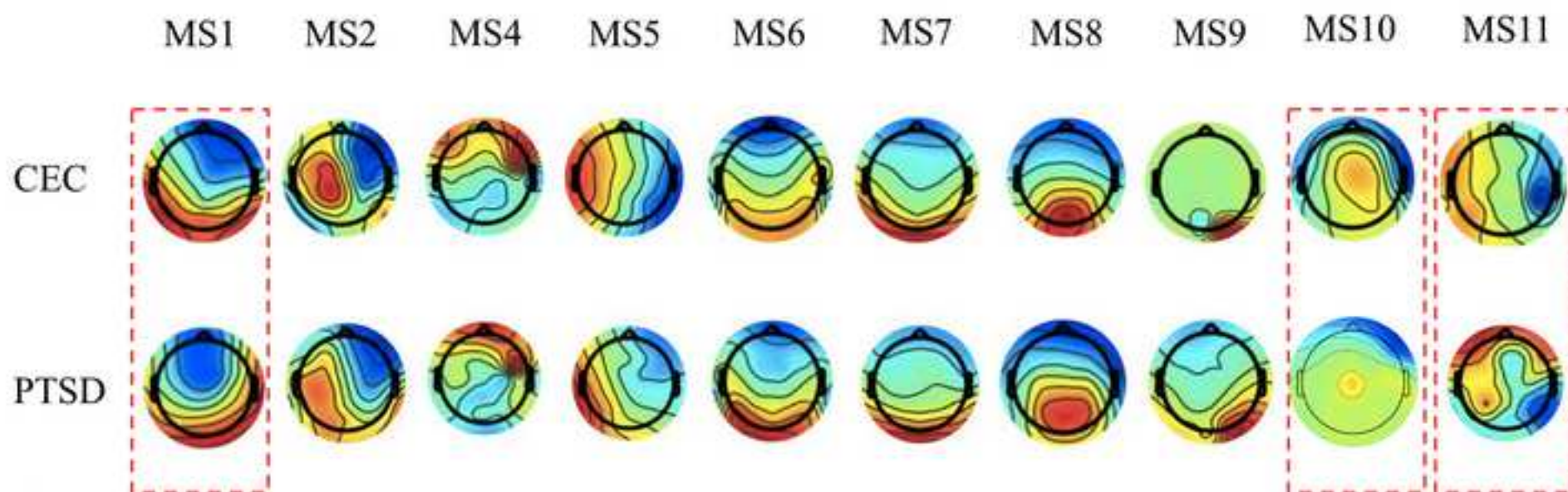
Talairach, J. and Tournoux, P. 1988. Co-planar stereotaxic atlas of the human brain. 3-dimensional proportional system: An approach to cerebral imaging.

Veer, I.M., Beckmann, C.F., van Tol, M.J., Ferrarini, L., Milles, J., Veltman, D.J., Aleman, A., van Buchem, M.A., van der Wee, N.J., Rombouts, S.A., 2010. Whole brain resting-state analysis reveals decreased functional connectivity in major depression. *Front. Syst. Neurosci.*, 4. pii: 41.

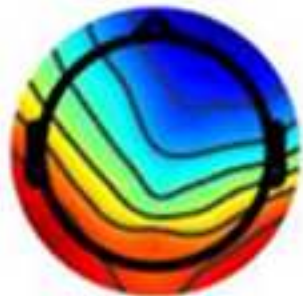
Whalley, M.G., Kroes, M.C.W., Huntley, Z., Rugg, M.D., Davis, S.W., Brewin, C.R., 2013. An fMRI investigation of posttraumatic flashbacks. *Brain Cogn*. 81 (1):151–159.

- Weathers, F.W., Huska, J., Keane, T.M., 1991. The PTSD Checklist Military Version (PCL-M). National Center for PTSD, Boston, MA.
- Weathers, F., Keane, T., Davidson, J. 2001. Clinician-administered PTSD Scale: A review of the first ten years. *Depression and Anxiety* 13:132-156.
- Wong, C.K., Zotev, V., Misaki, M., Phillips, R., Luo, Q., Bodurka, J. 2016. Automatic EEG-assisted retrospective motion correction for fMRI (aE-REMCOR). *Neuroimage* 129:133-147.
- Yin, Y., Jin, C., Hu, X., Duan, L., Li, Z., Song, M., Chen, H., Feng, B., Jiang, T., Jin, H., Wong, C., Gong, Q., Li, L., 2011. Altered resting-state functional connectivity of thalamus in earthquake-induced posttraumatic stress disorder: a functional magnetic resonance imaging study. *Brain Res.* 1411:98–107.
- Yuan, H., Perdoni, C., Yang, L., He, B. 2011. Differential electrophysiological coupling for positive and negative BOLD responses during unilateral hand movements. *J Neurosci.* 31:9585-9593.
- Yuan H., Zotev V., Phillips R., Drevets W.C., Bodurka J., 2012. Spatiotemporal dynamics of the brain at rest — Exploring EEG microstates as electrophysiological signatures of BOLD resting state networks. *Neuroimage* 60:2062–2072.
- Yuan, H., Zotev, V., Phillips, R., Bodurka, J. 2013. Correlated slow fluctuations in respiration, EEG, and BOLD fMRI. *Neuroimage* 1:79:81-93.
- Yuan, H., Young, K.D., Phillips, R., Zotev, V., Misaki, M., Bodurka, J. 2014. Resting-state functional connectivity modulation and sustained changes after real-time functional magnetic resonance imaging neurofeedback training in depression. *Brain Connect* 4(9):690-701.
- Yuan, H., Ding, L., Zhu, M., Zotev, V., Phillips, R., Bodurka, J., 2016. Reconstructing Large-Scale Brain Resting-State Networks from High-Resolution EEG: Spatial and Temporal Comparisons with fMRI. *Brain Connect* 6(2):122-35.
- Zotev, V., Phillips, R., Yuan, H., Misaki, M., Bodurka, J., 2014. Self-regulation of human brain activity using simultaneous real-time fMRI and EEG neurofeedback. *Neuroimage* 85(3):985-95.

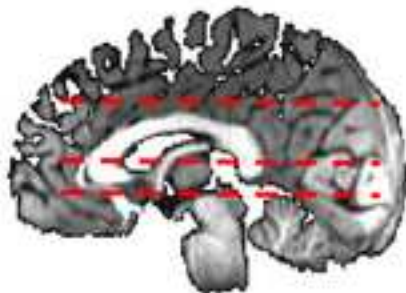
9. Figure 1
[Click here to download high resolution image](#)



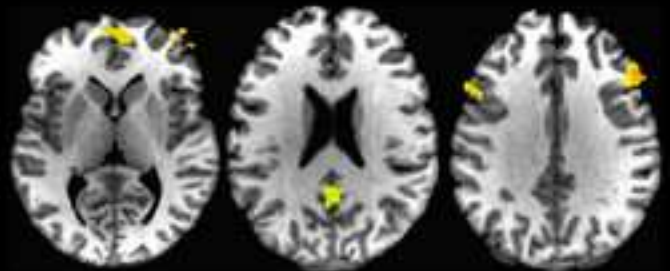
(A) EEG MS1



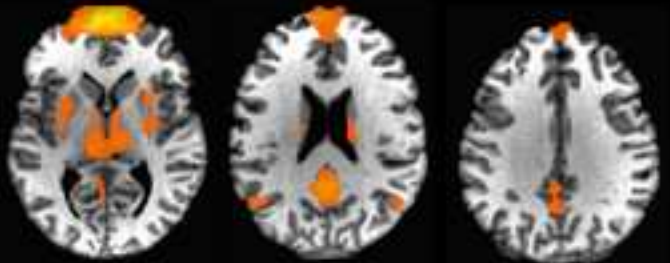
(B) Z = 4, 21, 32



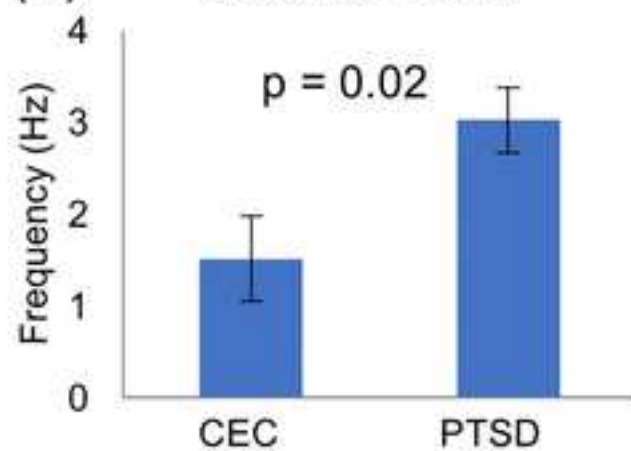
(C) MS1-informed Network



(D) Default Mode Network



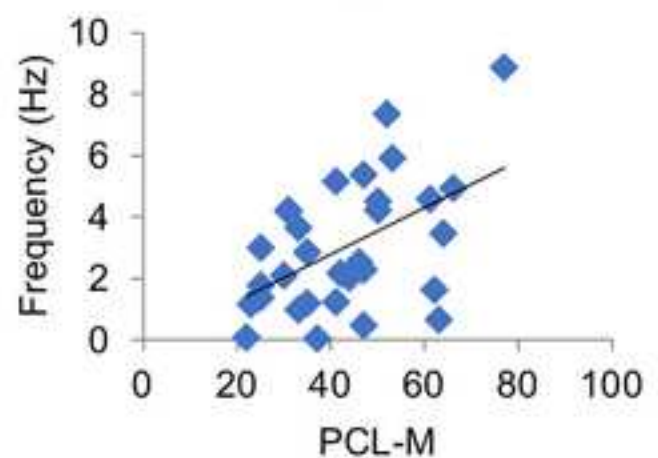
(E) CEC vs. PTSD

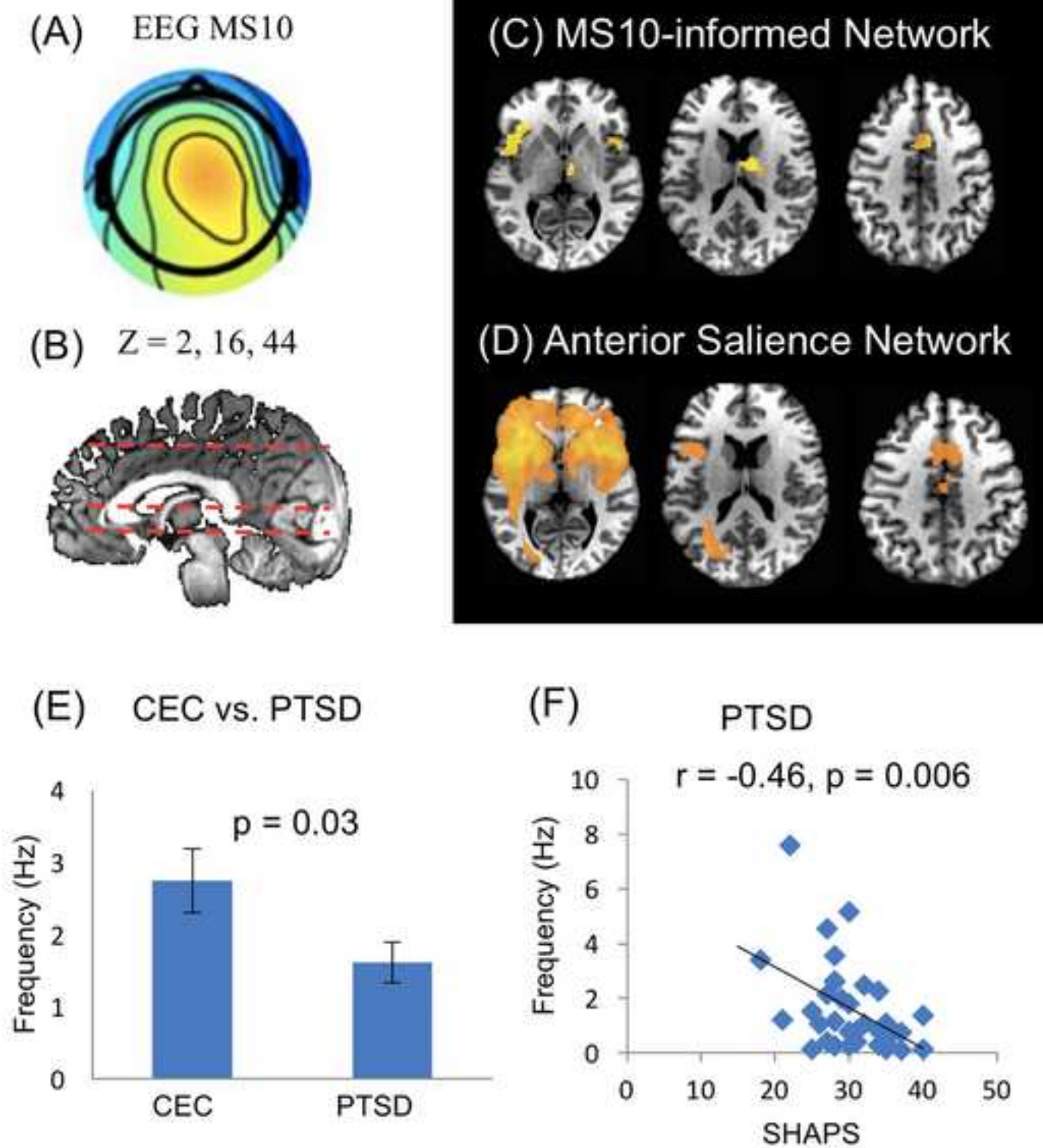


(F)

PTSD

$r = 0.51, p = 0.004$





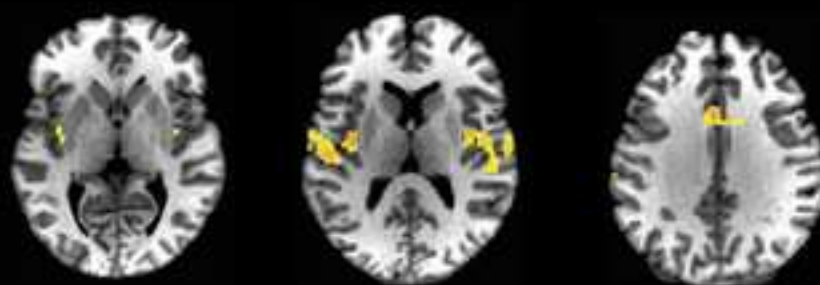
(A) MS11



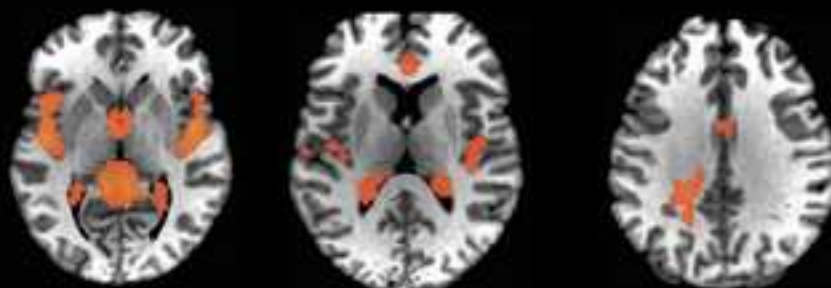
(B) $Z = 2, 10, 32$



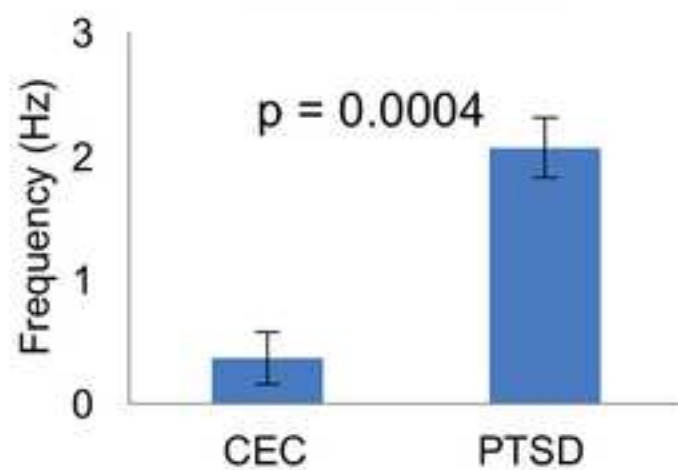
(C) MS11-informed Network



(D) Posterior Saliience Network



(E) CEC vs. PTSD



Supplementary Material to:

Tracking Resting State Connectivity Dynamics in Veterans with PTSD

Han Yuan, Raquel Phillips, Chung-Ki Wong, Vadim Zotev, Masaya Misaki, Brent Wurfel,

Frank Krueger, Matthew Feldner, Jerzy Bodurka

Supplemental Figures:

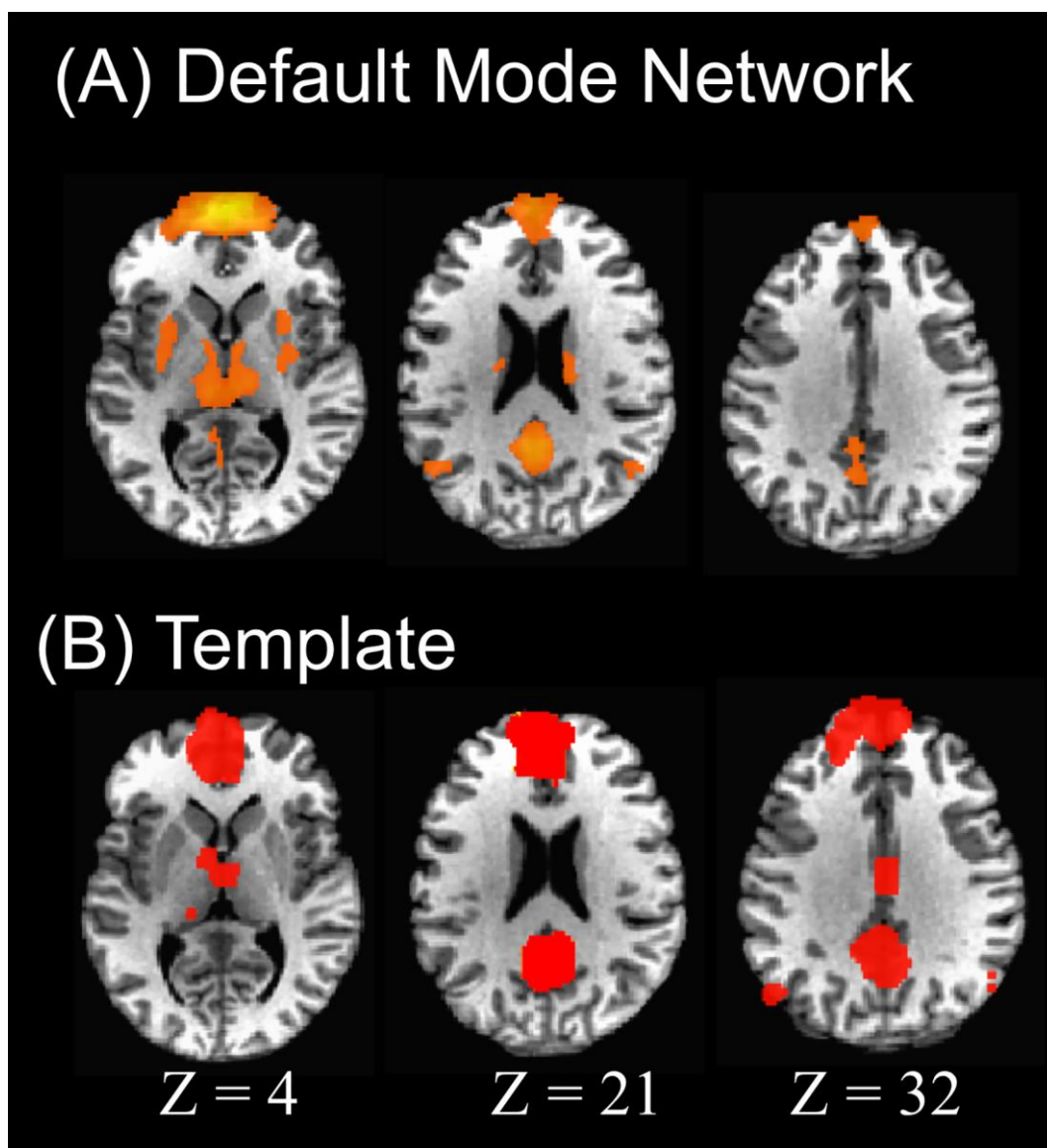


Figure S1. An fMRI RSN obtained from current study was matched to a template RSN of dorsal default mode network.

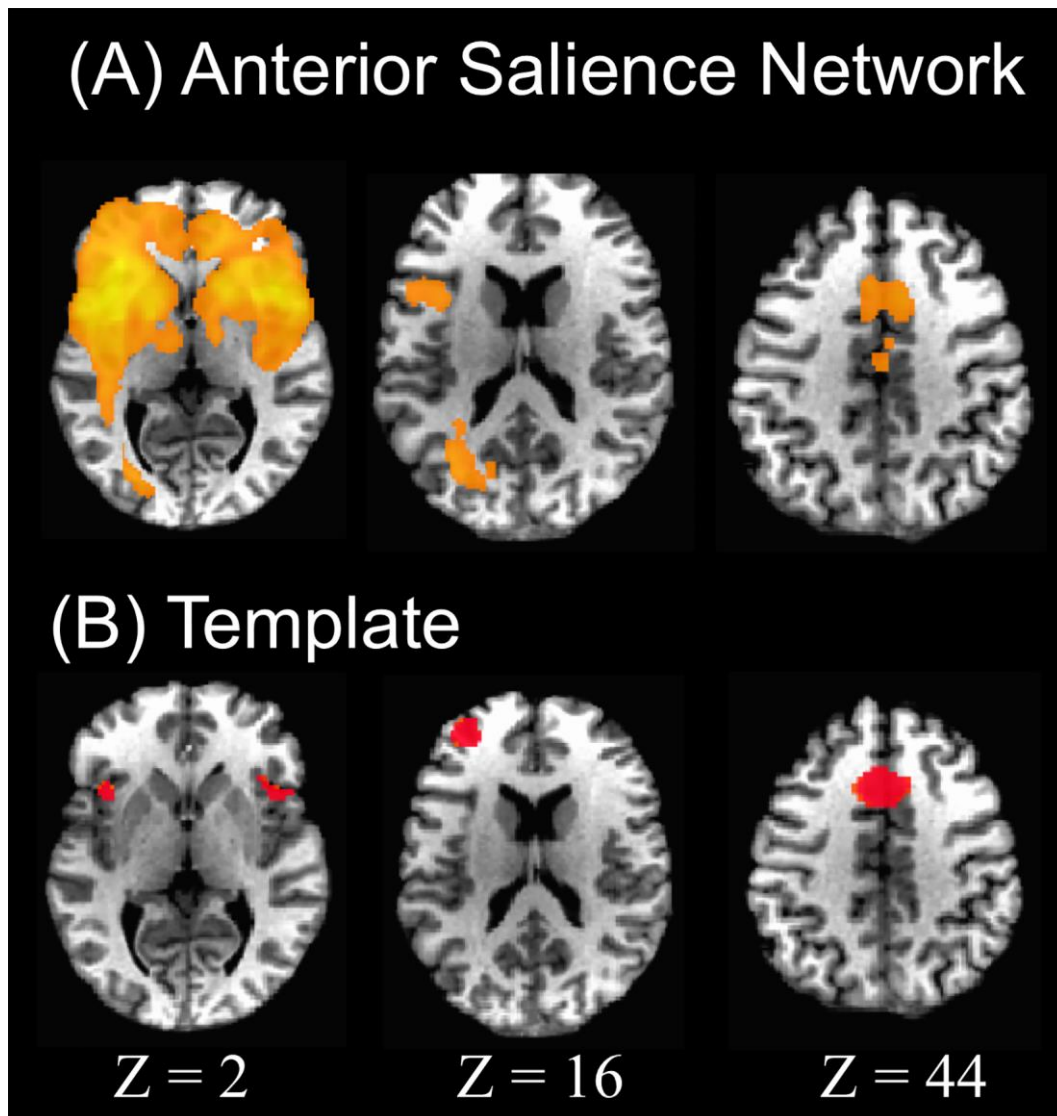


Figure S2. An fMRI RSN obtained from current study was matched to a template RSN of anterior salience network.

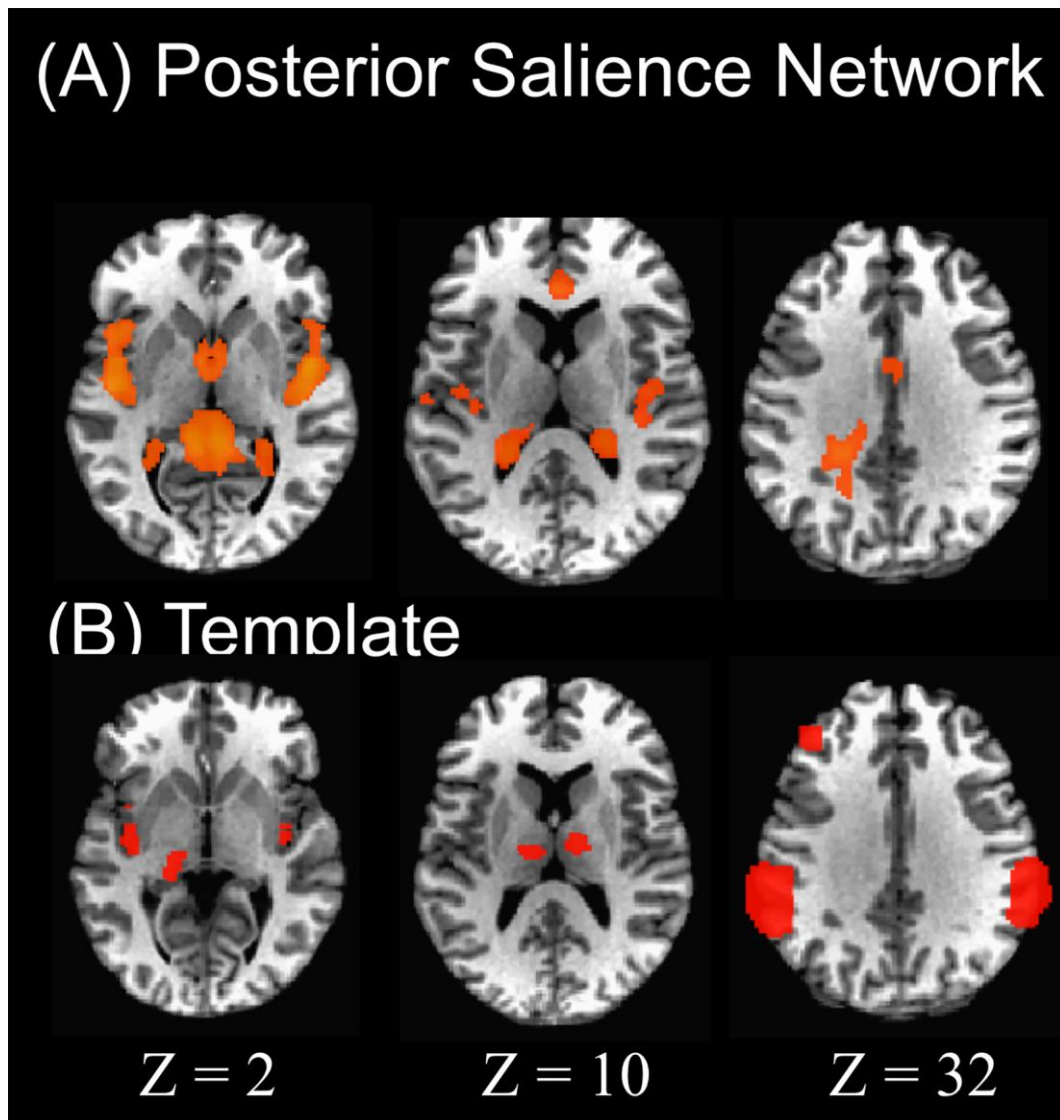


Figure S3. An fMRI RSN obtained from current study was matched to a template RSN of posterior saliience network.

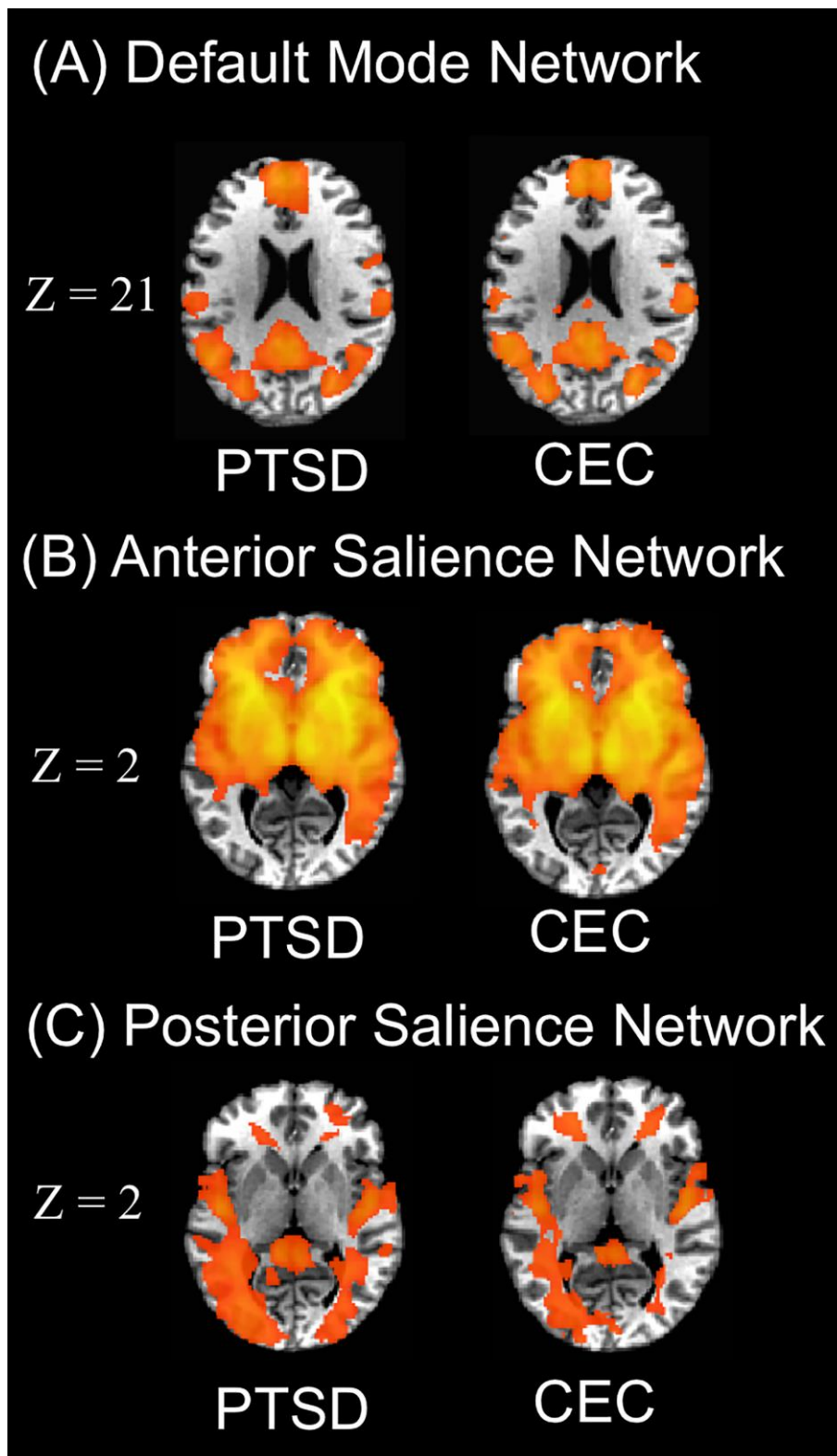


Figure S4. Group average images of RSNs in PTSD and CEC, threshold at $p < 0.01$ (uncorrected). No regions with significant difference between PTSD and CEC groups were identified at $p_{\text{corrected}} < 0.05$.

Real-time fMRI neurofeedback training of amygdala activity with simultaneous EEG in veterans with combat-related PTSD

Vadim Zotev¹, Raquel Phillips¹, Masaya Misaki¹, Chung Ki Wong¹, Brent E. Wurfel^{1,2}, Frank Krueger³, Matthew Feldner⁴, and Jerzy Bodurka^{1,5#}

¹ Laureate Institute for Brain Research, Tulsa, OK, United States

² Laureate Psychiatric Clinic and Hospital, Tulsa, OK, United States

³ School of Systems Biology, George Mason University, Fairfax, VA, United States

⁴ Dept. of Psychological Science, University of Arkansas, Fayetteville, AR, United States

⁵ Stephenson School of Biomedical Engineering, University of Oklahoma, Tulsa, OK, United States

Word count: 6,967

Number of figures: 9

Number of tables: 4

[#]Corresponding author

E-mail address: jbodurka@laureateinstitute.org

Abstract

Posttraumatic stress disorder (PTSD) is a chronic and disabling neuropsychiatric disorder characterized by insufficient top-down modulation of amygdala activity by the prefrontal cortex. Real-time fMRI neurofeedback (rtfMRI-nf) is an emerging method with potential for modifying amygdala-prefrontal cortex interactions. We report the first controlled emotion self-regulation study in veterans with combat-related PTSD utilizing rtfMRI-nf of amygdala activity. The study included three rtfMRI-nf training sessions wherein brain activity was simultaneously monitored via electroencephalography (EEG) and fMRI. PTSD severity was assessed before and after the training using the Clinician-Administered PTSD Scale (CAPS). Our results showed that PTSD patients in the experimental group (EG, $n=20$) learned to upregulate BOLD activity of the left amygdala (LA) using the rtfMRI-nf during a happy emotion induction task. PTSD patients in the control group (CG, $n=11$) were provided with a sham rtfMRI-nf. The EG participants who completed the study showed a significant reduction in total CAPS ratings, including significant reductions in avoidance and hyperarousal symptoms. They also exhibited a significant reduction in comorbid depression severity. Overall, 80% of the EG demonstrated clinically meaningful reductions in CAPS ratings, compared to 38% in the CG. During the first rtfMRI-nf session, the EG achieved a significant increase in the blood-oxygenation-level-dependent (BOLD) signal in the LA. Functional connectivity of the LA with the orbitofrontal cortex and the dorsolateral prefrontal cortex was enhanced during the rtfMRI-nf training, and these enhancements significantly and positively correlated with the CAPS ratings. Left-lateralized enhancement in upper alpha EEG coherence also exhibited a significant positive correlation with CAPS scores. Our findings demonstrated that rtfMRI-nf of amygdala activity has the potential to correct the amygdala-prefrontal functional connectivity deficiencies observed in PTSD and rtfMRI-nf can be seen as a promising technique for enhancing PTSD treatments.

Keywords: PTSD, combat trauma, neurofeedback, real-time fMRI, EEG-fMRI, amygdala, prefrontal cortex, orbitofrontal cortex, functional connectivity, EEG coherence

1. Introduction

Posttraumatic stress disorder (PTSD) is a chronic and disabling neuropsychiatric disorder with lasting negative effects on personal well-being and high economic costs to society (Kessler, 2000). Among veterans with PTSD who receive trauma-focused treatment, such as cognitive processing therapy or prolonged exposure therapy, only 50% to 70% achieve clinically meaningful symptom improvement, and as many as 66% retain their PTSD diagnosis after treatment (Steenkamp et al., 2015).

Treatment of PTSD is complicated by the fact that this disorder afflicts functions of several brain systems (Liberzon & Abelson, 2016). First, abnormalities in the salience network (SN) are associated with exaggerated threat detection. This network includes the amygdala, the insula, the dorsal anterior cingulate cortex (dACC), and other regions. Second, abnormal functioning of the executive function/emotion regulation (EF/ER) system leads to cognitive and emotion regulation impairments. This system includes regions of the prefrontal cortex (PFC): the dorsolateral PFC (DLPFC), the ventrolateral PFC (VLPFC), and the medial PFC (MPFC). The MPFC, in turn, includes the ventromedial PFC (VMPFC), the dorsomedial PFC (DMPFC), the orbitofrontal cortex (OFC), and encompasses the anterior/rostral ACC (rACC), and other regions. Third, functional deficiencies in the brain circuits involved in contextual processing (CP) lead to difficulties in threat discrimination. These circuits include the hippocampus, the thalamus, the locus coeruleus, and the MPFC areas (Liberzon & Abelson, 2016).

Functional neuroimaging studies of emotional processing have demonstrated prominent involvement of the above-mentioned brain systems (SN, EF/ER, CP) in the neurobiology of PTSD (e.g., Etkin & Wager, 2007; Lanius et al., 2006; Patel et al., 2012; Shin & Liberzon, 2010). In particular, numerous studies have shown hyperactivity of the amygdala and hypoactivity of the PFC regions during

emotional processing in PTSD patients compared to control participants (e.g., Etkin & Wager, 2007). This finding is often interpreted as indicating an insufficient top-down regulation of amygdala activity by the PFC. It also suggests that functional connectivity between the amygdala and the PFC is abnormally reduced in PTSD. Among the PFC regions, the OFC, along with the rACC and the subgenual ACC (sgACC), has the densest neuronal connections to the amygdala (Ghashghaei et al., 2007). The lateral OFC (LOFC, BA 47, part of the VLPFC, as well as lateral BA 11) and the medial OFC (MOFC, BA 11, part of the MPFC adjacent to the VMPFC) play important roles in emotion regulation and reward/punishment guided learning (Kringelbach & Rolls, 2004; Ochsner et al., 2002; Rushworth et al., 2011). Abnormalities in the LOFC and MOFC functions are observed in anxiety disorders (Milad & Rauch, 2007), including hypoactivity of these regions in PTSD (Lanius et al., 2006; Patel et al., 2012).

Real-time fMRI neurofeedback (rtfMRI-nf) is a promising neuromodulation technique that allows for non-invasive training of volitional modulation of blood-oxygenation-level-dependent (BOLD) activity of small, precisely defined regions deep inside the brain (e.g., Birbaumer et al., 2013; Sulzer et al., 2013; Thibault et al., 2016; Weiskopf, 2012). We have shown previously that rtfMRI-nf of amygdala activity enhanced both functional and effective connectivity between the amygdala and the PFC (Zotev et al., 2011, 2013). This is not surprising because rtfMRI-nf training involves goal-oriented behavior that engages the EF/ER system (Zotev et al., 2016). With the amygdala as the target region, the rtfMRI-nf training can enhance top-down modulation of amygdala activity by the EF/ER. Notably, rtfMRI-nf of amygdala activity has been shown to reduce depressive symptoms in patients with major depressive disorder (MDD; Young et al., 2017; Zotev et al., 2016). In addition, EEG recordings during the rtfMRI-nf procedure revealed left-lateralized enhancement in EEG coherence that positively correlated with

depression severity (Zotev et al., 2016). These findings suggest that rtfMRI-nf of amygdala activity can correct (reverse) the functional connectivity abnormalities observed in MDD, and, possibly, other neuropsychiatric disorders.

Two recent pilot studies explored the feasibility of using rtfMRI-nf of amygdala activity for the treatment of PTSD. The first pilot study included 10 PTSD patients who learned during one rtfMRI-nf session to downregulate BOLD activity of the bilateral amygdala using rtfMRI-nf while viewing personalized trauma words (Nicholson et al., 2017). Increased activation in the DLPFC and LOFC, as well as enhanced fMRI connectivity of the amygdala with the DLPFC and DMPFC, were observed during the rtfMRI-nf task compared to a control task (Nicholson et al., 2017). However, changes in PTSD severity were not assessed in this study. The second pilot study included three combat veterans with chronic PTSD, who were asked to downregulate BOLD activity of the bilateral amygdala after listening to a personal trauma-based audio script (Gerin et al., 2016). After three rtfMRI-nf sessions, two participants showed clinically meaningful reductions in PTSD severity. Increased resting fMRI connectivity of the amygdala with the MOFC and rACC/sgACC was observed after the training (Gerin et al., 2016). Overall, both studies had limited statistical power due to small samples. Moreover, neither study included a control group, so specificity of the reported effects to the amygdala-based rtfMRI-nf could not be verified.

Here, we report the results from the first rtfMRI-nf study of emotion self-regulation in a sufficiently large group of veterans with combat-related PTSD ($n=31$ across an experimental [EG] and control group [CG]: EG, $n=20$, CG, $n=11$). Moreover, this study involved a significant enhancement of the assessment of the effects of the rtfMRI-nf procedure by simultaneously measuring neurobiological activity via fMRI and EEG. PTSD participants learned to upregulate BOLD activity of the left amygdala (LA) using

rtfMRI-nf while performing a positive emotion induction task introduced earlier (Zotev et al., 2011). We tested the following hypotheses: neurofeedback-naïve participants receiving the LA-based rtfMRI-nf would i) be able to significantly increase BOLD activity of the LA during the training; ii) report clinically meaningful reductions in PTSD severity; iii) evidence enhanced fMRI connectivity between the LA and key PFC regions involved in emotion regulation, even after controlling for comorbid depression; and iv) evidence EEG-measured effects of the rtfMRI-nf training will be observed in simultaneously recorded EEG data.

2. Methods

2.1. Study overview

The study was conducted at the Laureate Institute for Brain Research and approved by the Western Institutional Review Board (IRB). All study procedures were carried out in accordance with the principles expressed in the Declaration of Helsinki.

The study included eight sessions (visits), illustrated schematically in Fig. 1A. The visits were typically scheduled one week apart. Each visit involved a psychological evaluation by a licensed psychiatrist in addition to experimental procedures.

Visit 1 included an initial assessment. It included administration of the following tests: the Edinburgh Handedness Inventory (EHI, Oldfield, 1971), the Family Interview for Genetic Studies (FIGS, Maxwell, 1992), the Fagerström Test for Nicotine Dependence (FTND, Fagerström, 1978), the Hollingshead Four-factor Index of Socioeconomic Status (SES, Hollingshead, 1975), the Quick Inventory of Depressive Symptomatology (QIDS, Rush et al., 2000), and the 21-item Hamilton Depression Rating Scale (HDRS, Hamilton, 1960).

Visit 2 included the initial assessment of PTSD severity by means of the Clinician-Administered PTSD Scale for DSM-IV (CAPS; Blake et al., 1990; Weathers et al., 2001). The CAPS was administered by trained raters blinded to the group participants were assigned to. It also included completion of the 20-item Toronto Alexithymia Scale (TAS-20; Bagby et al., 1994), and the Emotion Contagion Scale (EC; Doherty, 1997).

Visit 3 included the emotional counting Stroop task (ecStroop; Whalen et al., 2006) with simultaneous fMRI, and the Script-Driven Imagery Procedure (SDIP; Pitman et al., 1987) with the Responses to Script-Driven Imagery Scale (RSDI; Hopper et al., 2007). At the beginning of the visit, the HDRS, the Montgomery-Asberg Depression Rating Scale (MADRS; Montgomery & Asberg, 1979), the PTSD Checklist Military Version (PCL-M; Weathers et al., 1991), the Hamilton Anxiety Rating Scale (HARS; Hamilton, 1959), and the Snaith-Hamilton Pleasure Scale (SHAPS; Snaith et al., 1995) were administered. The Profile of Mood States (POMS; McNair et al., 1971) and Visual Analog Scales (VAS) ranging from 0 (*not at all*) to 10 (*extremely*) for happy, restless, sad, anxious, irritated, drowsy, and alert states were completed by participants both before and after the ecStroop and the SDIP procedures.

Visits 4, 5, and 6 were the neurofeedback training sessions, which involved the rtfMRI-nf with simultaneous EEG procedure, illustrated in Fig. 1B. At the beginning of each session, the HDRS, the MADRS, the HARS, the PCL-M, and the SHAPS scales were administered. The POMS and the VAS were completed both before and after the rtfMRI-nf procedure in each visit.

Visit 7 included the same tests and procedures as Visit 3.

Visit 8 included the final assessments of PTSD severity using the CAPS.

2.2. Participants

Participants provided a written informed consent as approved by the IRB. They met the *Diagnostic and Statistical Manual of Mental Disorders-Fourth Edition Text Revision* (DSM-IV-TR) (American Psychiatric Association, 2000) criteria for PTSD. All the subjects were male and had PTSD related to combat trauma as their primary diagnosis. They received monetary compensation for their participation in the study.

Participants were randomly assigned to either the experimental group (EG) or the control group (CG) at approximately a 2:1 ratio and they were blinded to group status. During the rtfMRI-nf training sessions (visits 4, 5, 6), the EG was provided with rtfMRI-nf based on BOLD activity of the LA (Zotev et al., 2011). The CG was provided with control rtfMRI-nf based on BOLD activity of a brain region, presumably not involved in emotion processing (Zotev et al., 2011). Selection of the target regions for rtfMRI-nf is described in detail below.

Table 1 reports main characteristics of the EG and CG groups. In the EG, 20 participants completed the first rtfMRI-nf session (visits 1-4), and 15 of them completed the whole study (visits 1-8, Fig. 1A). In the CG, 11 subjects completed the first rtfMRI-nf session, and 8 of them completed the whole study. There were no significant group differences in age, CAPS, PCL-M, HDRS, or MADRS ratings at baseline.

2.3. Experimental protocol

The experimental protocol for each rtfMRI-nf session (Fig. 1B) was similar to the one we employed previously in rtfMRI-nf studies with healthy participants (Zotev et al., 2011, 2014) and MDD patients (Young et al., 2017; Zotev et al., 2016). Prior to each rtfMRI-nf session, a participant was given detailed

instructions that included an overview of the experiment and an explanation of each experimental task. The participant was asked to think of and write down three happy autobiographical memories, keeping them private. It was suggested that he use those three memories at the beginning of the rtfMRI-nf training to evaluate their effects, and then explore various other happy autobiographical memories as the training progressed to enhance happy emotion and improve rtfMRI-nf performance.

Each rtfMRI-nf session included seven fMRI runs (Fig. 1B), and each run lasted 8 min 46 s. During the initial and final Rest runs, participants were asked to relax and rest while looking at a fixation cross. The five task runs – the Practice run, Run 1, Run 2, Run 3, and the Transfer run – consisted of alternating 40-s long blocks of Happy Memories, Count, and Rest conditions (Fig. 1B). The real-time GUI display screens for these conditions are shown schematically in Fig. 1C. Each condition was specified by visual cues that included a colored square with the condition name at the center of the screen and a text line at the top of the screen. For the Happy Memories condition blocks, participants were instructed to feel happy by evoking and contemplating happy autobiographical memories while simultaneously trying to raise the variable-height red rtfMRI-nf bar on the screen to the target level of the blue bar (Fig. 1C, left). The red bar height was updated every 2 s, and was also indicated by the red numeric value shown above the bar (Fig. 1C, left). For the Count condition blocks, the subjects were instructed to mentally count back from 300 by subtracting a given integer as shown on the screen (Fig. 1C, middle). For the Rest condition blocks, participants were asked to rest and let their minds wander while looking at the screen (Fig. 1C, right).

During the four rtfMRI-nf runs (Practice, Runs 1-3), participants performed the three experimental tasks as indicated by the GUI display screens shown in Fig. 1C. The target level for the rtfMRI-nf (blue bar in Fig. 1C, left) was fixed during each run, but was raised in a linear fashion across the four nf runs.

It was set to 0.5%, 1.0%, 1.5%, and 2.0% for the Practice run, Run 1, Run 2, and Run 3, respectively (see Fig. 3A below). During the Practice run, participants were given an opportunity to become familiar with (or refresh knowledge of) the rtfMRI-nf procedure and to consider the emotional impact of the three happy autobiographical memories they had prepared. During the Transfer run, the participants performed the same tasks as during the preceding nf runs, except that no bars were shown on the screen during the Happy Memories conditions, and the text line read “As Happy as possible”. The Transfer run was included to evaluate whether participants’ learned ability to control BOLD activity of the target ROI generalized beyond the actual rtfMRI-nf training when the nf information was no longer provided. The Count conditions involved counting back from 300 by subtracting 3, 4, 6, 7, and 9 for the Practice run, Run 1, Run 2, Run 3, and the Transfer run, respectively. After each experimental run with the Happy Memories task, a participant was asked to verbally rate his performance on a scale from 0 (*not at all*) to 10 (*extremely*) by answering two questions: “How successful were you at recalling your happy memories?” and “How happy are you right now?”.

2.4. Regions of interest

The rtfMRI-nf procedure was based on the target region-of-interest (ROI) approach we employed previously (Zotev et al., 2011, 2016). Two target ROIs were defined as 14-mm diameter spheres in the stereotaxic array of Talairach and Tournoux (Talairach & Tournoux, 1988). The target ROI centered at (−21, −5, −16) in the left amygdala (LA) region (Fig. 2A) was used for the EG. The target ROI centered at (−42, −48, 48) in the left horizontal segment of the intraparietal sulcus (LHIPS) region (Fig. 2B) was used for the CG. The specified ROI centers were selected based on quantitative meta-analyses of functional neuroimaging studies investigating the role of the amygdala in emotion processing (Sergeier

et al., 2008) or the role of the HIPS in number processing (Dehaene et al., 2003). During the experiment, these target ROIs were transformed from the Talairach space to each participant's individual fMRI (EPI) image space and used to provide rt-fMRI-nf signal depending on the group. For offline fMRI data analysis, the left amygdala (LA) and the right amygdala (RA) ROIs (Fig. 2C) were defined anatomically as the amygdala regions specified in the Talairach-Tournoux brain atlas in AFNI (Cox, 1996; Cox & Hyde, 1997).

2.5. Data acquisition

All experiments were conducted on the General Electric Discovery MR750 3T MRI scanner with a standard 8-channel receive-only head coil (Fig. 2D). A single-shot gradient echo EPI sequence with FOV/slice=240/2.9 mm, $TR/TE=2000/30$ ms, flip angle=90°, 34 axial slices per volume, slice gap=0.5 mm, SENSE $R=2$ in the phase encoding (anterior-posterior) direction, acquisition matrix 96×96, sampling bandwidth=250 kHz, was employed for fMRI. Each fMRI run lasted 8 min 46 s and included 263 EPI volumes (the first three EPI volumes were included to allow the fMRI signal to reach a steady state and were excluded from data analysis). Physiological pulse oximetry and respiration waveforms were recorded simultaneously with fMRI. The EPI images were reconstructed into a 128×128 matrix, resulting in $1.875 \times 1.875 \times 2.9$ mm³ fMRI voxels. A T1-weighted 3D MPRAGE sequence with FOV/slice=240/1.2 mm, $TR/TE=5.0/1.9$ ms, $TD/TI=1400/725$ ms, flip angle=10°, 128 axial slices per slab, SENSE $R=2$, acquisition matrix 256×256, sampling bandwidth=31.2 kHz, scan time=4 min 58 s, was used for structural imaging. It provided high-resolution anatomical brain images with $0.94 \times 0.94 \times 1.2$ mm³ voxels.

EEG recordings were performed simultaneously with fMRI (Fig. 2D) using a 32-channel MR-compatible EEG system from Brain Products, GmbH. The EEG system clock was synchronized with the

MRI scanner 10 MHz clock using the Brain Products' SyncBox device. EEG data were acquired with 0.2 ms temporal and 0.1 μ V measurement resolution (16-bit 5 kS/s sampling) in 0.016...250 Hz frequency band with respect to FCz reference. All technical details of the EEG-fMRI system configuration and data acquisition were reported previously (Zotев et al., 2012). Similar to our recent study (Zotев et al., 2016), the EEG recordings in the present work were passive, i.e. no EEG information was used in real time as part of the experimental procedure.

2.6. Real-time data processing

The rtfMRI-nf was implemented using the custom real-time fMRI system utilizing real-time functionality of AFNI (Cox, 1996; Cox & Hyde, 1997) as described previously (Zotев et al., 2011). A high-resolution MPRAGE anatomical brain image and a short EPI dataset (5 volumes) were acquired prior to each rtfMRI-nf session. The last volume in the EPI dataset was used as a reference EPI volume defining the subject's individual EPI space. The LA and LHIPS target ROIs, defined in the Talairach space (Fig. 2A,B) were transformed to the individual EPI space using the MPRAGE image data. The resulting ROIs in the EPI space contained approximately 140 voxels each. During the subsequent fMRI runs (Fig. 1B), the AFNI real-time plugin was used to perform volume registration of each acquired EPI volume to the reference EPI volume (motion correction) and export mean values of fMRI signals for these ROIs in real time. The custom developed GUI software was used to further process the exported fMRI signal values and display the ongoing rtfMRI-nf information (Fig. 1C). The rtfMRI signal for each Happy Memories condition was computed as a percent signal change relative to the baseline obtained by averaging fMRI signal values for the preceding Rest condition block (Fig. 1B). A moving average of the current and two preceding rtfMRI signal values was computed to reduce effects of fMRI noise and physiological artifacts (Zotев et al., 2011). This average value was used to set the height of the red

rtfMRI-nf bar (Fig. 1C) every $TR=2$ s.

2.7. fMRI data analysis

In this work our analysis focuses on the first neurofeedback training session (Visit 4) to evaluate and understand effect of rtfMRI-nf in neurofeedback-naïve PTSD individuals before examining effects across multiple sessions. Offline analysis of the fMRI data was performed in AFNI as described in detail in *Supplementary material* (S1.1). The analysis involved fMRI pre-processing with despiking, cardiorespiratory artifact correction (Glover et al., 2000), slice timing correction, and volume registration. A general linear model (GLM) analysis with Happy Memories and Count block-stimulus conditions was applied to the preprocessed fMRI data. Average GLM-based fMRI percent signal changes were computed for the LA and RA ROIs, shown in Fig. 2C.

2.8. fMRI connectivity analysis

Analysis of fMRI functional connectivity for the LA as the seed region was performed within the GLM framework. The fMRI data were bandpass filtered between 0.01 Hz and 0.08 Hz. The six fMRI motion parameters were similarly filtered. The LA ROI (Fig. 2C) was transformed to each subject's individual high-resolution anatomical image space, and then to the individual EPI image space. The LA ROI in the EPI space included ~100 voxels. In addition, 10-mm-diameter ROIs were defined within the left and right frontal white matter (WM) and within the left and right ventricle cerebrospinal fluid (CSF). These ROIs were defined using individual high-resolution anatomical brain maps and similarly transformed. The resulting ROIs in the individual EPI space were used as masks to obtain average time courses for the LA, left and right WM, and left and right CSF regions. The GLM-based functional connectivity analysis was conducted for each task run using the 3dDeconvolve AFNI program. The -

censor option was used to restrict the analysis to the Happy Memories condition blocks in each run. The GLM model included the time course of the LA ROI as the stimulus (seed) regressor. Nuisance covariates included five polynomial terms, time courses of the six fMRI motion parameters (together with the same time courses shifted by one TR), time courses of the left and right WM and CSF ROIs to reduce physiological noise [Jo et al., 2010], and step functions to account for the breaks in the data between the Happy Memories condition blocks. Each GLM analysis provided R^2 -statistics and t -statistics maps for the stimulus regressor term, which we used to compute the correlation coefficient for each voxel. The correlation coefficient maps were Fisher r -to- z normalized, transformed to the Talairach space, and re-sampled to $2 \times 2 \times 2$ mm³ isotropic voxel size. The resulting individual LA functional connectivity maps were spatially smoothed (5 mm FWHM) and submitted to group analyses.

Group analysis of fMRI connectivity for one task run, e.g. the Practice run, was performed using the 3dttest++ AFNI program. The analysis included three covariates: the CAPS ratings, the HDRS ratings, and the average individual fMRI connectivity of the LA with central white matter. The last covariate accounted for residual spurious LA connectivity effects caused, for example, by head motion. The central white matter mask was defined using the standard AFNI white matter mask in the Talairach space (TT_wm), that was re-sampled to $2 \times 2 \times 2$ mm³ voxels, subjected to three-step erosion, and limited to $15 < z < 35$ mm slab. The individual-subject LA connectivity values for the same run were averaged within this mask to yield a single covariate value for each subject. Centering of the three covariates was performed within the 3dttest++ program by subtraction of their means. The LA fMRI connectivity vs CAPS correlation effect was the main effect of interest. The statistical results were corrected for multiple comparisons by controlling the family-wise-error (FWE). The correction was based on Monte Carlo simulations implemented in the AlphaSim AFNI program.

Analysis of fMRI connectivity enhancement across the four neurofeedback runs was conducted as follows. An fMRI connectivity slope (FCS) was defined for each voxel as a slope of a linear trend in fMRI connectivity with the LA seed ROI across the Happy Memories conditions in the four rtfMRI-nf runs (Practice, Run 1, Run 2, Run 3), as illustrated in Fig. 3B. The LA fMRI connectivity maps in the Talairach space for the four rtfMRI-nf runs were concatenated, and the 3dTfitter AFNI program was used to carry out a voxel-wise linear trend analysis, yielding the FCS map for each subject. Group analysis on the FCS data was performed using the 3dttest++ AFNI program. The analysis included three covariates: CAPS ratings, HDRS ratings, and the average individual LA FCS for central white matter. The last covariate was computed using the same white matter mask as described above, and accounted for spurious LA connectivity trends across the four runs. The FCS vs CAPS correlation effect and the mean FCS effect were the main effects of interest. The statistical results were corrected for multiple comparisons by controlling the FWE as explained above.

2.9. EEG data analysis

Offline analysis of EEG data, acquired simultaneously with fMRI, was performed using BrainVision Analyzer 2.1 software (Brain Products, GmbH) as described in detail in *Supplementary material* (S1.2). Removal of EEG artifacts was based on the average artifact subtraction and independent component analysis (Bell & Sejnowski, 1995; McMenamin et al., 2010). Channel Cz was selected as a new reference, and FCz was restored as a regular channel. Following the artifact removal, data from 29 EEG signal channels were down sampled to 8 ms temporal resolution. The upper alpha EEG band was defined individually for each participant as [IAF...IAF+2] Hz, where IAF is the individual alpha peak frequency. The IAF was determined by inspection of average EEG spectra for the occipital and parietal EEG channels across the Rest condition blocks in the four rtfMRI-nf runs (Fig. 1B).

2.10. EEG coherence analysis

EEG coherence analysis was conducted separately for the Rest and Happy Memories conditions in each of the four rtfMRI-nf runs (Fig. 1B). The analysis included a segmentation with 4.096 s intervals (with exclusion of bad intervals, see S1.2), a complex FFT with 0.244 Hz spectral resolution, and the Coherence transform implemented in the Analyzer 2.1. A coherence value for signals from two EEG channels at a given frequency was computed as the squared magnitude of their cross spectrum value normalized by their power spectrum values at the same frequency ('magnitude-squared coherence' method). An average coherence value for the upper alpha band [IAF...IAF+2] Hz was then computed for each channel pair.

Analysis of EEG coherence enhancement across the four neurofeedback runs was performed as follows. An EEG coherence slope (ECS) was defined for each channel pair as a slope of a linear trend in the upper alpha EEG coherence changes between the Rest and Happy Memories conditions across the four rtfMRI-nf runs (Practice, Run 1, Run 2, Run 3), as illustrated in Fig. 3C. Analysis of partial correlations between the ECS values and the CAPS ratings, controlling for HDRS ratings, was performed using the `partialcorr()` function in MATLAB. To alleviate the multiple comparisons problem, average ECS values were computed for previously defined groups of fronto-temporal EEG channels (Zotev et al., 2016), and their partial correlations with the CAPS ratings were evaluated.

2.11. Statistical tests

Inferential statistical analyses were performed in IBM SPSS Statistics 20. Correction for multiple comparisons was based on controlling the false discovery rate (FDR q), which was computed by applying the 3dFDR AFNI program to a column of uncorrected p -values from multiple tests. Partial

correlation analyses were conducted using MATLAB Statistics toolbox.

3. Results

3.1. Psychological measures

Changes in PTSD severity and comorbid depression severity for the PTSD veterans who completed the study are reported in Table 2. The initial and final CAPS ratings were assessed during visits 2 and 8, respectively (Fig. 1A). The initial and final HDRS ratings were determined during visits 3 and 7, respectively. The participants in the EG showed a significant reduction in the total CAPS ratings after the study (EG: $t(14)=-3.69$, $p<0.0024$, $q<0.004$), with significant reductions in sub-scores for avoidance symptoms (EG: $t(14)=-3.78$, $p<0.0020$, $q<0.004$) and hyperarousal symptoms (EG: $t(14)=-2.54$, $p<0.024$, $q<0.030$). The EG participants also exhibited a significant reduction in the HDRS ratings (EG: $t(14)=-4.61$, $p<0.0004$, $q<0.002$).

The participants in the CG also showed a nonsignificant reduction in total CAPS ratings (CG: $t(7)=-1.75$, $p<0.124$, $q<0.207$). The corresponding reductions in avoidance symptoms (CG: $t(7)=-1.95$, $p<0.092$, $q<0.207$) and HDRS ratings (CG: $t(7)=-2.28$, $p<0.056$, $q<0.207$) were also nonsignificant.

In the EG, 12 participants out of 15 (80%) demonstrated clinically meaningful reductions in CAPS ratings (by 10 points or more). In the CG, 3 subjects out of 8 (or 38%) showed clinically meaningful CAPS reductions. However, no significant difference in the CAPS rating changes (final vs initial) was observed between the two groups (EG vs CG: $t(21)=-0.90$, $p<0.377$). Similarly, the HDRS rating changes (final vs initial) showed no significant group difference (EG vs CG: $t(21)=-0.22$, $p<0.825$).

3.2. Amygdala BOLD activity

Figure 4 shows results of the offline fMRI activation analysis for the LA and RA ROIs (Fig. 2C). The results are for the first rtfMRI-nf session (visit 4; EG: $n=20$; CG: $n=11$). The LA BOLD activity levels for the Happy Memories conditions for the EG (H vs R, Fig. 4A, left) were significant for Run 3 (R3: $t(19)=3.03$, $p<0.007$, $q<0.035$) and for the Transfer run (TR: $t(19)=2.63$, $p<0.017$, $q<0.042$). There was no significant difference in the LA activity between these two runs (TR vs R3: $t(19)=-1.33$, $p<0.199$). The RA BOLD activity levels for the EG (H vs R, Fig. 4A, right) were significant for Run 3 (R3: $t(19)=3.04$, $p<0.007$, $q<0.034$) and trended toward significance after correction for the Transfer run (TR: $t(19)=2.24$, $p<0.037$, $q<0.093$). Similar to the LA, there was no significant difference in the RA activity between these two runs (TR vs R3: $t(19)=-1.16$, $p<0.259$). For the CG, BOLD activity levels for either the LA or the RA were not significant (Fig. 4B).

To compare the neurofeedback effects between the EG and CG groups, we examined average individual BOLD activity levels across the three rtfMRI-nf training runs (Run1, Run 2, Run 3). For the average LA BOLD activity levels, Levene's test for equality of variances suggested that variances differed between the groups ($F=4.79$, $p<0.037$). An independent-samples t -test with Welch-Satterthwaite adjustment indicated that the average LA BOLD activity levels were significantly higher for the EG than for the CG ($t(28.18)=2.38$, $p<0.024$, equal variances not assumed). For the average RA BOLD activity levels, variances did not differ between the groups ($F=0.14$, $p<0.908$). The difference in the average RA BOLD activity levels between the EG and the CG trended toward significance ($t(29)=1.76$, $p<0.088$).

3.3. Amygdala connectivity during Practice

All fMRI connectivity and EEG coherence results reported below correspond to the first rtfMRI-nf session (Fig. 1A, visit 4). The initial CAPS ratings (visit 2) and initial HDRS ratings (visit 3) were used

in partial correlation analyses.

Figure 5 shows whole-brain group statistical maps of the correlation between the LA fMRI connectivity during Happy Memories conditions in the Practice run and CAPS ratings for the EG. Data from $n=19$ EG participants were included in the analysis. One outlier EG participant, whose initial CAPS rating was much higher (CAPS=95) than the rest of the EG subjects, was excluded from the analysis to avoid biasing the group results. The group statistical maps in Fig. 5 were thresholded at $t=\pm 2.95$ (uncorr. $p<0.01$) and clusters containing at least 75 voxels (FWE corr. $p<0.05$) are shown in the figure. The cluster properties are described in Table 3. The results in Fig. 5 and Table 3 demonstrate that, at the beginning of the training, fMRI connectivity with the LA showed *negative* correlations with PTSD severity for many prefrontal brain regions, particularly the LOFC, the MOFC, the rACC, and the DLPFC. For the CG, the correlations during the Practice run are similar to those for the EG in Fig. 5.

The negative correlation effects mapped in Fig. 5 are illustrated in Figure 6. Note that several other regions exhibited *positive* correlations between their fMRI connectivity with the LA and CAPS ratings, but the corresponding clusters were not large enough to survive the whole-brain FWE correction. For example, these regions included the left caudate at $(-19, -25, 20)$ ($t=5.21$, 62 vox.), the right mediodorsal nucleus (MD) of the thalamus at $(3, -16, 15)$ ($t=5.46$, 26 voxels), the right amygdala at $(25, -7, -20)$ ($t=5.00$, 24 voxels), the right precuneus (PCun, BA 39) at $(27, -57, 31)$ ($t=4.24$, 22 voxels), the left precuneus (BA 7) at $(-25, -61, 31)$ ($t=4.24$, 22 voxels). The correlation effects for the R MD and the R PCun are also illustrated in Fig. 6.

3.4. Amygdala connectivity enhancement

Figure 7 exhibits whole-brain group statistical maps of the correlation between the LA fMRI

connectivity slope (FCS) across Happy Memories conditions in the four rtfMRI-nf runs (Fig. 3B) and CAPS ratings. The results are for the same EG participants ($n=19$) as in Figs. 5 and 6. The maps in Fig. 7 were thresholded at $t=\pm 2.95$ (uncorr. $p<0.01$) and clusters containing at least 81 voxels (FWE corr. $p<0.025$) are shown in the figure. The cluster properties are specified in Table 4. The table also includes statistical results for the mean FCS effect, thresholded and clustered in the same way (FWE corr. $p<0.025$, to account for testing the two effects). The mean FCS effect was obtained in the same group analysis and corresponds to the mean values of the covariates (CAPS ratings, HDRS ratings, LA FCS for white matter). The results in Fig. 7 and Table 4 demonstrate that the fMRI connectivity enhancement (FCS) with the LA during the training exhibited *positive* correlations with PTSD severity for several prefrontal regions, including the LOFC and the DLPFC. The left DLPFC also showed a significant fMRI connectivity enhancement with the LA that was independent of the CAPS and HDRS variability (the mean FCS effect, Table 4). For the CG, no significant positive FCS vs CAPS correlations or mean FCS effects were found within the PFC.

The positive correlation effects mapped in Fig. 7 are illustrated in Figure 8. Note that several other regions that showed negative correlations in Figs. 5 and 6 exhibited positive correlations between the FCS and CAPS, but the corresponding clusters did not survive the whole-brain FWE correction. For example, these regions included the right LOFC at (55, 25, -1) ($t=5.22$, 68 voxels), the left MOFC at (-1, 39, -15) ($t=3.99$, 25 voxels). Furthermore, some regions showed *negative* correlations between the FCS and CAPS, such as the right precuneus/posterior cingulate at (23, -62, 25) ($t=-3.71$, 39 voxels). The correlation effects for these regions are also illustrated in Fig. 8.

3.5. EEG coherence enhancement

Figure 9 demonstrates correlations between the EEG coherence slope (ECS) for the upper alpha

EEG band across the four rtfMRI-nf runs (Fig. 3C) and CAPS ratings for the EG. The EEG recordings were conducted simultaneously with fMRI (Fig. 2D). Data from 18 EG participants were included in the ECS vs CAPS correlation analysis, with the same outlier excluded as described above along with a second participant whose data were excluded due to excessive EEG-fMRI artifacts. According to Fig. 9A, the ECS exhibited positive correlations ($r(15) > 0$, $p < 0.05$, uncorr.) with CAPS ratings for many EEG channel pairs, particularly those involving frontal and left temporal (T7) EEG channels. (Negative correlations, $r(15) < 0$, did not reach the $p < 0.05$ statistical threshold). This correlation effect is illustrated in Fig. 9B for one channel pair. Following our previous work (Zotey et al., 2016), we defined average ECS for 10 pairs of fronto-temporal EEG channels on the left, ECS(L), and for 10 corresponding channel pairs on the right, ECS(R), as detailed in Fig. 9C,D. The ECS(L) demonstrated a significant *positive* correlation with CAPS ratings (Fig. 9C). The average ECS laterality, ECS(L)–ECS(R), showed a positive correlation with CAPS that trended toward significance (Fig. 9E).

4. Discussion

This study employed rtfMRI-nf of left amygdala activity while recalling happy autobiographical memories to investigate the clinical potential of training veterans with combat-related PTSD to regulate amygdala hemodynamic activity. After three rtfMRI-nf training sessions, the EG participants who completed the study ($n=15$) showed a significant reduction in PTSD severity. This reduction was largely due to a reduction in avoidance symptoms, with only a moderately significant reduction in hyperarousal symptoms and a nonsignificant reduction in reexperiencing symptoms. Remarkably, the reduction in comorbid depression severity was even more robust. Previous studies have linked depression to deficient approach motivation (e.g., Henriques & Davidson, 2000; McFarland et al., 2006; Trew, 2011). Thus, the reduction in depression severity could conceivably be associated with an enhancement in approach

motivation (though approach tendencies were not directly assessed in the present study). This reasoning suggests that the strongest neuropsychological effects of the rtfMRI-nf training in PTSD veterans may occur along the approach-avoidance (motivational) dimension. This would be consistent with a stronger engagement of the EF/ER system during the rtfMRI-nf task.

Among the EG, 80% of the participants who completed the study achieved clinically meaningful reductions in PTSD severity (10 CAPS points or more). This symptom improvement rate is higher than in veterans with PTSD undergoing cognitive therapies (Steenkamp et al., 2015). It is consistent with preliminary work on amygdala rtfMRI-nf, in which two PTSD veterans out of three showed clinically meaningful PTSD symptom improvements (Gerin et al., 2016). However, 38% of the participants in the CG who completed the study also demonstrated clinically meaningful reductions in PTSD severity, despite receiving the sham rtfMRI-nf. This symptom improvement may be attributable to placebo effects, as well as to positive effects of regular interactions with the clinical assessment personnel.

The EG participants who completed the first rtfMRI-nf training session ($n=20$) were able to significantly increase LA BOLD activity during the Happy Memories conditions in Run 3 and in the Transfer run. This suggests participants gradually learned to upregulate LA activity as the training progressed. Importantly, the LA BOLD activity levels averaged across the three rtfMRI-nf training runs (Runs 1-3) were significantly higher for the EG than for the CG. However, the PTSD patients in the EG only achieved mean LA activity levels for individual runs in the range from 0.1% to 0.2% (Fig. 4A). This is lower than the 0.2% to 0.3% mean LA activity range for MDD patients who followed the same protocol in our previous study (Zotev et al., 2016). This suggests that the effects of this neurofeedback

protocol may be smaller when completed by people with PTSD and therefore a larger sample is needed to reach comparable statistical power (Desmond & Glover, 2002).

Functional connectivity of the LA during the Happy Memories conditions in the Practice run of the first rtfMRI-nf session served as an estimate of the task-specific LA connectivity at the beginning of the training. During this run, the participants were exposed to the rtfMRI-nf for the first time and did not yet know how to effectively control the rtfMRI-nf signal. The results in Fig. 5 and Table 3 demonstrate negative correlations between the LA fMRI connectivity and the initial CAPS ratings for many prefrontal regions, including the LOFC (BA 47, 11), MOFC (BA 11), DLPFC (BA 9, 8), VLPFC (BA 45), medial frontopolar cortex (BA 9), and rACC (BA 24). These results are consistent with the PFC hypoactivity pattern previously observed among people with PTSD (e.g., Etkin & Wager, 2007; Lanius et al., 2006; Patel et al., 2012). At the same time, the LA connectivity with several brain regions, including the right amygdala, the right MD, and the bilateral precuneus (BA 39, 7), exhibited positive, though smaller, correlations with the CAPS ratings (Sec. 3.3, Fig. 6). Parietal regions, including the precuneus and the inferior parietal lobule, are known to be hyperactive together with the amygdala in PTSD (e.g., Etkin & Wager, 2007; Lanius et al., 2006; Patel et al., 2012). Our results suggest that fMRI connectivity between the amygdala and regions of the autobiographical memory recall system (MD, precuneus) is increased in PTSD not only during recollection of traumatic events, but also during retrieval of happy autobiographical memories.

The main result of the present work is the observation of the significant *positive* correlations between PTSD severity and the LA fMRI connectivity enhancement (FCS) for several PFC regions during the rtfMRI-nf training. This positive FCS vs CAPS correlation effect is observed for the left

LOFC (BA 47, 11), bilateral DLPFC (BA 9), and left precentral gyrus (BA 4) for the EG (Fig. 7, Table 4). Positive, though less robust, correlation effects were also observed for the right LOFC (BA 47) and the left MOFC (BA 11), as illustrated in Fig. 8. Such positive correlations suggest that the patients with more severe PTSD (higher CAPS ratings) showed more positive changes in the LA connectivity with these PFC regions as the rtfMRI-nf training progressed. For the right precuneus, the corresponding LA connectivity changes were more negative (Fig. 8). Therefore, the results in Figs. 7 and 8 demonstrate correction (at least partial) of the LA fMRI connectivity deficiencies specific to PTSD and evident in Figs. 5 and 6. Furthermore, the EG participants exhibited a significant mean FCS effect in the left DLPFC (BA 9) (Table 4). This effect indicates a significant fMRI connectivity enhancement between the LA and the left DLPFC across the rtfMRI-nf runs, independent of the PTSD and depression severity (and corresponding to the mean CAPS and HDRS ratings for the EG). This finding is generally consistent with the positive group-average fMRI connectivity changes between the amygdala and the DL/DMPFC during the rtfMRI-nf task reported by Nicholson and colleagues (2017).

EEG recordings performed simultaneously with fMRI allowed us to investigate electrophysiological correlates of the rtfMRI-nf training. We examined variations in EEG coherence, which is an EEG measure of functional connectivity, across the four rtfMRI-nf runs. The average enhancement in upper alpha EEG coherence for the fronto-temporal EEG channels on the left, ECS(L), significantly correlated with PTSD severity for the EG (Fig. 9C). Note that this positive ECS vs CAPS correlation effect is directly related to the positive FCS vs CAPS correlation effect in Fig. 7 and Table 4. Indeed, four out of five clusters in Fig. 7 appear within the left PFC. Stronger functional connectivities among these PFC regions and the LA likely result in stronger coherences for EEG signals measured above these regions.

Importantly, the enhancements in functional connectivity that accompany the rtfMRI-nf training may therefore be observable in both fMRI and EEG domains.

Interestingly, the map of ECS vs CAPS correlation effects in the EEG channel space (Fig. 9A) is similar to the map of ECS vs HDRS correlation effects in our recent MDD study (Zotev et al., 2016). However, the average ECS laterality, ECS(L)–ECS(R), exhibited a less significant positive correlation with the CAPS ratings (Fig. 9E) than the ECS(L) (Fig. 9C). This trend is different from that in our MDD study, in which the ECS laterality showed a more significant correlation with the MDD patients' HDRS ratings than the ECS(L) (Zotev et al., 2016).

The reported study has several limitations. First, the rtfMRI-nf procedure did not include any personalized trauma-related content. Second, the study design focused on the correction of aberrant emotion regulation in PTSD but did not explicitly target other symptoms of PTSD, such as reexperiencing or avoidance. Third, the rtfMRI-nf task involved upregulation of the amygdala activity in order to help people learn to control amygdala activity, while the amygdala is usually hyperactive during emotional processing in PTSD. Nevertheless, our experimental results suggest people suffering from combat-related PTSD can learn to influence amygdala BOLD activity using rtfMRI-nf and doing so may have clinical benefits.

5. Conclusion

Our study demonstrated that rtfMRI-nf of amygdala activity to enhance emotion regulation ability may be beneficial to veterans with combat-related PTSD. Our fMRI and EEG results independently suggest that the rtfMRI-nf training has the potential to correct the amygdala-PFC functional connectivity deficiencies specific to PTSD. The most significant PTSD-specific enhancements in fMRI connectivity

between the LA and the PFC were observed for the LOFC and DLPFC regions, which are parts of the EF/ER system. Because activities of these cortical regions can be probed using EEG, a carefully designed EEG-nf procedure may complement the rtfMRI-nf of the amygdala.

Acknowledgments

This work was supported by the W81XWH-12-1-0697 grant from the U.S. Department of Defense. The authors thank all staff members at Laureate Institute for Brain Research, Matthew Meyer, M.D., and William Yates, M.D. for conducting psychiatric interviews, Tim Collins, Lisa Kinyon, and Megan Cole for administering clinical interviews and assessments, and Julie Owen, Julie Crawford, Leslie Walker, and Tressia Lewis for helping with MRI scanning. We would like to also thank Dr. Robert Störmer, Dr. Patrick Britz, and Dr. Mario Bartolo of Brain Products, GmbH for their help and technical support.

References

- American Psychiatric Association, 2000. Diagnostic and Statistical Manual of Mental Disorders, 4th ed. text rev. (DSM-IV-TR). American Psychiatric Press, Washington, DC.
- Bagby, R.M., Parker, J.D.A., Taylor, G.J., 1994. The twenty-item Toronto Alexithymia Scale – I. Item selection and cross-validation of the factor structure. *J. Psychosom. Res.* 38, 33-40.
- Bell, A.J., Sejnowski, T.J., 1995. An information-maximization approach to blind separation and blind deconvolution. *Neural Comput.* 7, 1129-1159.
- Birbaumer, N., Ruiz, S., Sitaram, R., 2013. Learned regulation of brain metabolism. *Trends Cogn. Sci.* 17, 295-302.
- Blake, D.D., Weathers, F.W., Nagy, L.M., Kaloupek, D.G., Klauminzer, G., Charney, D.S., Keane, T.M., 1990. A clinician rating scale for assessing current and lifetime PTSD: the CAPS-1. *Behav. Ther.* 13, 187-188.

- Cox, R.W., 1996. AFNI: software for analysis and visualization of functional magnetic resonance neuroimages. *Comput. Biomed. Res.* 29, 162-173.
- Cox, R.W., Hyde, J.S., 1997. Software tools for analysis and visualization of fMRI data. *NMR Biomed.* 10, 171-178.
- Dehaene, S., Piazza, M., Pinel, P., Cohen, L., 2003. Three parietal circuits for number processing. *Cogn. Neuropsychol.* 20, 487–506.
- Desmond, J.E., Glover, G.H., 2002. Estimating sample size in functional MRI (fMRI) neuroimaging studies: statistical power analyses. *J. Neurosci. Meth.* 118, 115-128.
- Doherty, R.W., 1997. The emotion contagion scale: a measure of individual differences. *J. Nonverb. Behav.* 21, 131-154.
- Etkin, A., Wager, T.D., 2007. Functional neuroimaging of anxiety: a meta-analysis of emotional processing in PTSD, social anxiety disorder, and specific phobia. *Am. J. Psychiatry* 164, 1476-1488.
- Fagerström, K.O., 1978. Measuring degree of physical dependency to tobacco smoking with reference to individualization of treatment. *Addict. Behav.* 3, 235-241.
- Gerin, M.I., Fichtenholtz, H., Roy, A., Walsh, C.J., Krystal, J.H., Southwick, S., Hampson, M., 2016. Real-time fMRI neurofeedback with war veterans with chronic PTSD: a feasibility study. *Front. Psychiatry* 7, 111 (1-11).
- Ghashghaei, H.T., Hilgetag, C.C., Barbas, H., 2007. Sequence of information processing for emotions based on the anatomic dialogue between prefrontal cortex and amygdala. *NeuroImage* 34, 905-923.
- Glover, G.H., Li, T.Q., Ress, D., 2000. Image-based method for retrospective correction of physiological motion effects in fMRI: RETROICOR. *Magn. Reson. Med.* 44, 162-167.
- Hamilton, M., 1959. The assessment of anxiety states by rating. *Br. J. Med. Psychol.* 32, 50-55.
- Hamilton, M., 1960. A rating scale for depression. *J. Neurol. Neurosurg. Psychiatry* 23, 56-62.

- Henriques, J.B., Davidson, R.J., 2000. Decreased responsiveness to reward in depression. *Cogn. Emotion* 14, 711-724.
- Hollingshead, A.B., 1975. Four factor index of social status. Yale University, Department of Sociology.
- Hopper, J.W., Frewen, P.A., Sack, M., Lanius, R.A., van der Kolk, B.A., 2007. The Responses to Script-Driven Imagery Scale (RSDI): assessment of state posttraumatic symptoms for psychobiological and treatment research. *J. Psychopathol. Behav. Assess.* 29, 249-268.
- Jo, H.J., Saad, Z.S., Simmons, W.K., Milbury, L.A., Cox, R.W., 2010. Mapping sources of correlation in resting state fMRI, with artifact detection and removal. *NeuroImage* 52, 571-582.
- Kessler, R. C., 2000. Posttraumatic stress disorder: the burden to the individual and to society. *J Clin Psychiatry* 61 Suppl 5, 4-12; discussion 13-4.
- Kringelbach, M.L., Rolls, E.T., 2004. The functional neuroanatomy of the human orbitofrontal cortex: evidence from neuroimaging and neuropsychology. *Progr. Neurobiol.* 72, 341-372.
- Lanius, R.A., Bluhm, R., Lanius, U., Pain, C., 2006. A review of neuroimaging studies in PTSD: heterogeneity of response to symptom provocation. *J. Psychiat. Res.* 40, 709-729.
- Liberzon, I., Abelson, J.L., 2016. Context processing and the neurobiology of post-traumatic stress disorder. *Neuron* 92, 14-30.
- Maxwell, M.E., 1992. Family Interview for Genetic Studies (FIGS). National Institute of Mental Health, Washington, DC.
- McFarland, B.R., Shankman, S.A., Tenke, C.E., Bruder, G.E., Klein, D.N., 2006. Behavioral activation system deficits predict the six-month course of depression. *J. Affect. Disord.* 91, 229-234.
- McMenamin, B.W., Shackman, A.J., Maxwell, J.S., Bachhuber, D.R.W., Koppenhaver, A.M., Greischar, L.L., Davidson, R.J., 2010. Validation of ICA-based myogenic artifact correction for scalp and source-localized EEG. *NeuroImage* 49, 2416-2432.

- McNair, D.M., Lorr, M., Droppleman, L.F., 1971. Profile of Mood States. Educational and Industrial Testing Service, San Diego.
- Milad, M.R., Rauch, S.L., 2007. The role of the orbitofrontal cortex in anxiety disorders. *Ann. N.Y. Acad. Sci.* 1121, 546-561.
- Montgomery, S.A., Asberg, M., 1979. A new depression scale designed to be sensitive to change. *Br. J. Psychiatry* 134, 382-389.
- Nicholson, A.A., Rabellino, D., Densmore, M., Frewen, P.A., Paret, C., Kluetsch, R., Schmahl, C., Théberge, J., Neufeld, R.W.J., McKinnon, M.C., Reiss, J., Jetly, R., Lanius, R.A., 2017. The neurobiology of emotion regulation in posttraumatic stress disorder: amygdala downregulation via real-time fMRI neurofeedback. *Hum. Brain. Mapp.* 38, 541-560.
- Ochsner, K.N., Bunge, S.A., Gross, J.J., Gabrieli, J.D.E., 2002. Rethinking feelings: an fMRI study of the cognitive regulation of emotion. *J. Cogn. Neurosci.* 14, 1215-1229.
- Oldfield, R.C., 1971. The assessment and analysis of handedness: the Edinburgh inventory. *Neuropsychologia* 9, 97-113.
- Patel, R., Spreng, R.N., Shin, L.M., Girard, T.A., 2012. Neurocircuitry models of posttraumatic stress disorder and beyond: a meta-analysis of functional neuroimaging studies. *Neurosci. Biobehav. Rev.* 36, 2130-2142.
- Pitman, R.K., Orr, S.P., Forgue, D.F., de Jong, J.B., Claiborn, J.M., 1987. Psychophysiologic assessment of posttraumatic stress disorder imagery in Vietnam combat veterans. *Arch. Gen. Psychiatry* 44, 970-975.
- Rush, A.J., Carmody, T.J., Reimnitz, P.E., 2000. The Inventory of Depressive Symptomatology (IDS): clinician (IDS-C) and self-report (IDS-SR) ratings of depressive symptoms. *Int. J. Methods Psychiatr. Res.* 9, 45-59.
- Rushworth, M.F.S., Noonan, M.P., Boorman, E.D., Walton, M.E., Behrens, T.E., 2011. Frontal cortex

and reward-guided learning and decision-making. *Neuron* 70, 1054-1069.

Sergerie, K., Chochol, C., Armony, J.L., 2008. The role of the amygdala in emotional processing: a quantitative meta-analysis of functional neuroimaging studies. *Neurosci. Biobehav. Rev.* 32, 811–830.

Shin, L.M., Liberzon, I., 2010. The neurocircuitry of fear, stress, and anxiety disorders. *Neuropsychopharmacol.* 35, 169-191.

Snaith, R.P., Hamilton, M., Morley, S., Humayan, A., Hargreaves, D., Trigwell, P., 1995. A scale for the assessment of hedonic tone: the Snaith-Hamilton Pleasure Scale. *Br. J. Psychiatry* 167, 99-103.

Steenkamp, M.M., Litz, B.T., Hoge, C.W., Marmar, C.R., 2015. Psychotherapy for military-related PTSD. A review of randomized clinical trials. *J. Am. Med. Assoc.* 314, 489-500.

Sulzer, J., Haller, S., Scharnowski, F., Weiskopf, N., Birbaumer, N., Blefari, M.L., Bruehl, A.B., Cohen, L.G., deCharms, R.C., Gassert, R., Goebel, R., Herwig, U., LaConte, S., Linden, D., Luft, A., Seifritz, E., Sitaram, R., 2013. Real-time fMRI neurofeedback: progress and challenges. *NeuroImage* 76, 386-399.

Talairach, J., Tournoux, P., 1988. *Co-Planar Stereotaxic Atlas of the Human Brain*. Thieme Medical Publishers, New York.

Thibault, R.T., Lifshitz, M., Raz, A., 2016. The self-regulating brain and neurofeedback: experimental science and clinical promise. *Cortex* 74, 247-261.

Trew, J.L., 2011. Exploring the roles of approach and avoidance in depression: an integrative model. *Clin. Psychol. Rev.* 31, 1156-1168.

Weathers, F.W., Huska, J., Keane, T.M., 1991. *The PTSD Checklist Military Version (PCL-M)*. National Center for PTSD, Boston, MA.

Weathers, F.W., Keane, T.M., Davidson, J.R.T., 2001. Clinician-Administered PTSD Scale: a review of the first ten years of research. *Depress. Anxiety* 13, 132-156.

- Weiskopf, N., 2012. Real-time fMRI and its application to neurofeedback. *NeuroImage* 62, 682-692.
- Whalen, P.J., Bush, G., Shin, L.M., Rauch, S.L., 2006. The emotional counting Stroop: a task for assessing emotional interference during brain imaging. *Nat. Protocols* 1, 293-296.
- Young, K.D., Siegle, G.J., Zotev, V., Phillips, R., Misaki, M., Yuan, H., Drevets, W.C., Bodurka, J., 2017. Randomized clinical trial of real-time fMRI amygdala neurofeedback for major depressive disorder: effects on symptoms and autobiographical memory recall. *Am. J. Psychiatry* 174, 748-755.
- Zotev, V., Krueger, F., Phillips, R., Alvarez, R.P., Simmons, W.K., Bellgowan, P., Drevets, W.C., Bodurka, J., 2011. Self-regulation of amygdala activation using real-time fMRI neurofeedback. *PLoS ONE* 6, e24522 (1-17).
- Zotev, V., Yuan, H., Phillips, R., Bodurka, J., 2012. EEG-assisted retrospective motion correction for fMRI: E-REMCOR. *NeuroImage* 63, 698-712.
- Zotev, V., Phillips, R., Young, K.D., Drevets, W.C., Bodurka, J., 2013. Prefrontal control of the amygdala during real-time fMRI neurofeedback training of emotion regulation. *PLoS ONE* 8, e79184 (1-14).
- Zotev, V., Phillips, R., Yuan, H., Misaki, M., Bodurka, J., 2014. Self-regulation of human brain activity using simultaneous real-time fMRI and EEG neurofeedback. *NeuroImage* 85, 985-995.
- Zotev, V., Yuan, H., Misaki, M., Phillips, R., Young, K.D., Feldner, M.T., Bodurka, J., 2016. Correlation between amygdala BOLD activity and frontal EEG asymmetry during real-time fMRI neurofeedback training in patients with depression. *NeuroImage: Clin.* 11, 224-238.

Table 1. Main characteristics of the experimental and control groups. Numbers of participants who started the study (and completed the first rtfMRI-nf session) and those who completed the whole study are specified for each group. Mean PTSD and depression severity ratings are also included. Abbreviations: CAPS – Clinician-Administered PTSD Scale; PCL-M – PTSD CheckList Military Version; HDRS – Hamilton Depression Rating Scale; MADRS – Montgomery-Asberg Depression Rating Scale.

Measure	Experimental group (EG)		Control group (CG)	
	Started mean (SD)	Completed mean (SD)	Started mean (SD)	Completed mean (SD)
Participants	20	15	11	8
Age	31 (6)	31 (5)	34 (8)	37 (8)
CAPS	51.3 (13.9)	40.6 (17.9)	57.0 (24.1)	53.8 (22.3)
PCL-M	44.7 (10.8)	36.3 (11.9)	47.2 (17.8)	40.5 (19.6)
HDRS	16.8 (5.8)	11.1 (5.5)	14.7 (8.6)	11.1 (5.8)
MADRS	20.7 (8.9)	13.9 (10.0)	17.1 (12.9)	14.3 (9.4)

Table 2. Changes in PTSD and depression severity ratings for participants who completed the study. Mean rating values at the beginning of the study (initial) and at the end of the study (final) are included, and their statistical changes (final vs initial) within each group are specified. Abbreviations: CAPS – Clinician-Administered PTSD Scale; HDRS – Hamilton Depression Rating Scale.

Rating	Initial mean (SD)	Final mean (SD)	Change <i>t</i> -score#	Change <i>p</i> -value [<i>q</i>]
Experimental group (EG, <i>n</i>=15)				
CAPS	54.9 (13.6)	40.6 (17.9)	−3.69	0.0024 [0.004]*
Reexperiencing symptoms	11.1 (5.8)	9.1 (6.6)	−1.56	0.142 [0.142]
Avoidance symptoms	21.8 (7.4)	14.0 (9.4)	−3.78	0.0020 [0.004]*
Hyperarousal symptoms	22.0 (4.7)	17.5 (7.2)	−2.54	0.024 [0.030]*
HDRS	17.3 (6.5)	11.1 (5.5)	−4.61	0.0004 [0.002]*
Control group (CG, <i>n</i>=8)				
CAPS	62.3 (20.9)	53.8 (22.3)	−1.75	0.124 [0.207]
Reexperiencing symptoms	15.8 (6.3)	13.5 (8.4)	−1.41	0.203 [0.254]
Avoidance symptoms	24.6 (11.5)	18.0 (13.1)	−1.95	0.092 [0.207]
Hyperarousal symptoms	21.9 (4.6)	22.3 (4.5)	0.30	0.776 [0.776]
HDRS	16.8 (8.5)	11.1 (5.8)	−2.28	0.056 [0.207]

t(14) for the EG, *t*(7) for the CG.

* FDR *q*<0.05 for the five tests.

Table 3. Statistical data for the correlation between the fMRI connectivity of the left amygdala during the Happy Memories conditions in the Practice run and PTSD severity (CAPS). Location of the point with the peak group *t*-score and the number of voxels are specified for each cluster obtained after FWE correction for multiple comparisons.

Region	Laterality	<i>x, y, z</i> (mm)	<i>t</i> -score	Size (voxels)
Frontal Lobe				
Lateral orbitofrontal cortex (BA 47)	R	51, 23, -8	-9.50	646
Dorsolateral prefrontal cortex (BA 9)	L	-33, 51, 24	-5.45	306
Lateral orbitofrontal cortex (BA 11)	L	-31, 41, -11	-6.77	288
Medial frontal polar cortex (BA 9)	R	9, 61, 30	-6.91	252
Ventrolateral prefrontal cortex (BA 45)	L	-55, 21, 12	-6.85	188
Dorsolateral prefrontal cortex (BA 8)	R	21, 43, 42	-6.70	181
Superior frontal gyrus (BA 8)	L	-7, 31, 48	-5.62	158
Medial orbitofrontal cortex (BA 11)	R	1, 33, -22	-5.55	125
Medial orbitofrontal cortex (BA 11)	R	5, 20, -20	-7.34	84
Temporal Lobe				
Middle temporal gyrus (BA 21)	R	67, -19, -12	-5.98	325
Middle temporal gyrus (BA 20)	R	57, -43, -12	-5.94	92
Limbic Lobe				
Anterior cingulate cortex (BA 24)	R	3, 37, 9	-5.76	127
Sub-lobar Regions				
Insula (BA 13)	L	-35, 21, 0	-4.79	144

Notations: BA – Brodmann areas; L – left; R – right; *x, y, z* – Talairach coordinates; FWE corrected $p < 0.05$ (Size – cluster size, minimum 75 voxels for uncorr. $p < 0.01$).

Table 4. Statistical data for the correlation between the fMRI connectivity slope (FCS) for the left amygdala and PTSD severity (CAPS), as well as for the mean FCS effect. Location of the point with the peak group *t*-score and the number of voxels are specified for each cluster obtained after FWE correction for multiple comparisons.

Region	Laterality	<i>x, y, z</i> (mm)	<i>t</i> -score	Size (voxels)
FCS vs CAPS correlation effect				
Lateral orbitofrontal cortex (BA 11)	L	-23, 47, -12	5.19	219
Dorsolateral prefrontal cortex (BA 9)	R	15, 37, 39	4.65	116
Dorsolateral prefrontal cortex (BA 9)	L	-35, 25, 26	5.45	110
Lateral orbitofrontal cortex (BA 47)	L	-43, 17, -6	4.69	106
Precentral gyrus (BA 4)	L	-49, -11, 50	5.76	84
Mean FCS effect				
Dorsolateral prefrontal cortex (BA 9)	L	-55, 9, 30	4.68	250
Inferior temporal gyrus (BA 20)	L	-55, -37, -16	6.35	93
Superior temporal gyrus (BA 22)	R	55, -7, -2	4.64	81

Notations: BA – Brodmann areas; L – left; R – right; *x, y, z* – Talairach coordinates; FWE corrected $p < 0.025$ (Size – cluster size, minimum 81 voxels for uncorr. $p < 0.01$).

Figure captions

Figure 1. Overview of the emotion self-regulation study utilizing real-time fMRI neurofeedback (rtfMRI-nf) of the amygdala in veterans with combat-related PTSD. **A)** The study included eight sessions (visits) with three rtfMRI-nf training sessions (visits 4, 5, 6) and two PTSD symptom assessment (CAPS) sessions (visits 2, 8). **B)** Experimental protocol for one rtfMRI-nf session. It consisted of seven runs, each lasting 8 min 46 s. It included two Rest runs, four rtfMRI-nf runs – Practice, Run 1, Run 2, Run 3, and a Transfer run without nf. The names of the seven runs are abbreviated in the figures below as RE, PR, R1, R2, R3, TR, and RE, respectively. The experimental runs (except the Rest) consisted of 40-s long blocks of Happy Memories, Count, and Rest conditions (abbreviated as H, C, and R, respectively). **C)** Real-time GUI display screens for the Happy Memories, Count, and Rest conditions. The rtfMRI-nf signal is displayed during the Happy Memories conditions as the variable-height red bar. The red bar height represents real-time fMRI activity of the target ROI and is updated every 2 s. The blue bar height specifies a target level for the rtfMRI-nf signal and is raised from run to run.

Figure 2. Regions of interest employed in real-time fMRI data processing and offline fMRI data analyses. **A)** Spherical 14-mm diameter target ROI in the left amygdala (LA) region used to provide rtfMRI-nf for the experimental group (EG). **B)** Spherical 14-mm diameter target ROI in the left horizontal segment of the intraparietal sulcus (LHIPS) region used to provide sham rtfMRI-nf for the control group (CG). **C)** Left amygdala (LA) and right amygdala (RA) ROIs defined anatomically as the amygdala regions specified in the co-planar stereotaxic atlas of the human brain by Talairach and Tournoux. These ROIs were used in the offline fMRI data analyses. The ROIs are projected in the figure onto the standard TT_N27 template in the Talairach space. Following the radiological notation, the left hemisphere (L) is shown to the reader's right. **D)** A 32-channel MR-compatible EEG system from Brain Products, GmbH was used to perform EEG recordings during fMRI.

Figure 3. Analyses of linear trends in functional connectivity measures across neurofeedback runs. **A)** The target level for the rtfMRI-nf (blue bar in Fig. 1C) was raised in a linear fashion across the four

rtfMRI-nf runs (Practice, Run 1, Run 2, Run 3) in each neurofeedback session (Fig. 1B). **B)** Definition of the fMRI connectivity slope (FCS). It is defined, for each fMRI voxel, as a slope of a linear trend in fMRI connectivity with the seed ROI across the Happy Memories conditions in the four rtfMRI-nf runs. **C)** Definition of the EEG coherence slope (ECS). It is defined, for each pair of EEG channels, as a slope of a linear trend in upper alpha EEG coherence changes between the Rest and Happy Memories conditions across the four rtfMRI-nf runs.

Figure 4. BOLD activity of the amygdala during the first rtfMRI-nf session. **A)** Average fMRI percent signal changes for the left amygdala (LA, left) and the right amygdala (RA, right) ROIs for the experimental group (EG). Each bar represents a mean GLM-based fMRI percent signal change for the corresponding ROI (Fig. 2C) with respect to the Rest baseline for the Happy Memories (H vs R) or Count (C vs R) conditions in a given run, averaged across the group. The error bars are standard errors of the means (sem) for the group averages. The experimental runs and condition blocks are depicted schematically in Fig. 1B. Significance of the H vs R results is specified after FDR correction for testing the data for five runs. **B)** Corresponding average fMRI percent signal changes for the control group (CG).

Figure 5. Statistical maps of the correlation between the fMRI connectivity of the left amygdala (LA) during the Happy Memories conditions in the Practice run and PTSD severity (CAPS) for the experimental group (EG). The correlation is a voxel-wise partial correlation with CAPS ratings controlled for comorbid depression severity (HDRS) ratings and average individual LA connectivity with white matter. The maps are FWE corrected and projected onto the standard anatomical template TT_N27 in the Talairach space, with 3 mm separation between axial slices. The number adjacent to each slice indicates the z coordinate in mm. The left hemisphere (L) is to the reader's right. The green crosshairs mark the center of the LA target ROI (Fig. 2A). Peak t -statistics values for the correlation effect and the corresponding cluster properties are specified in Table 3.

Figure 6. Illustration of the correlation effects between the LA fMRI connectivity during the Happy Memories conditions in the Practice run and PTSD severity (CAPS) for the EG. Each plot shows an average correlation effect for a 10-mm diameter ROI centered at a specified location. The correlation is

a partial correlation with CAPS ratings controlled for HDRS ratings and average individual LA connectivity with white matter ($n=19$, $df=15$). The results for the R LOFC, L LOFC, R MOFC, and L DLPFC correspond to those reported in Fig. 5 and Table 3. The results for the R MD and R PCun are included to illustrate existence of positive correlations between the LA fMRI connectivity and PTSD severity (see text). Abbreviations: LOFC – lateral orbitofrontal cortex, MOFC – medial orbitofrontal cortex, DLPFC – dorsolateral prefrontal cortex, MD – mediodorsal nucleus of the thalamus, PCun – precuneus.

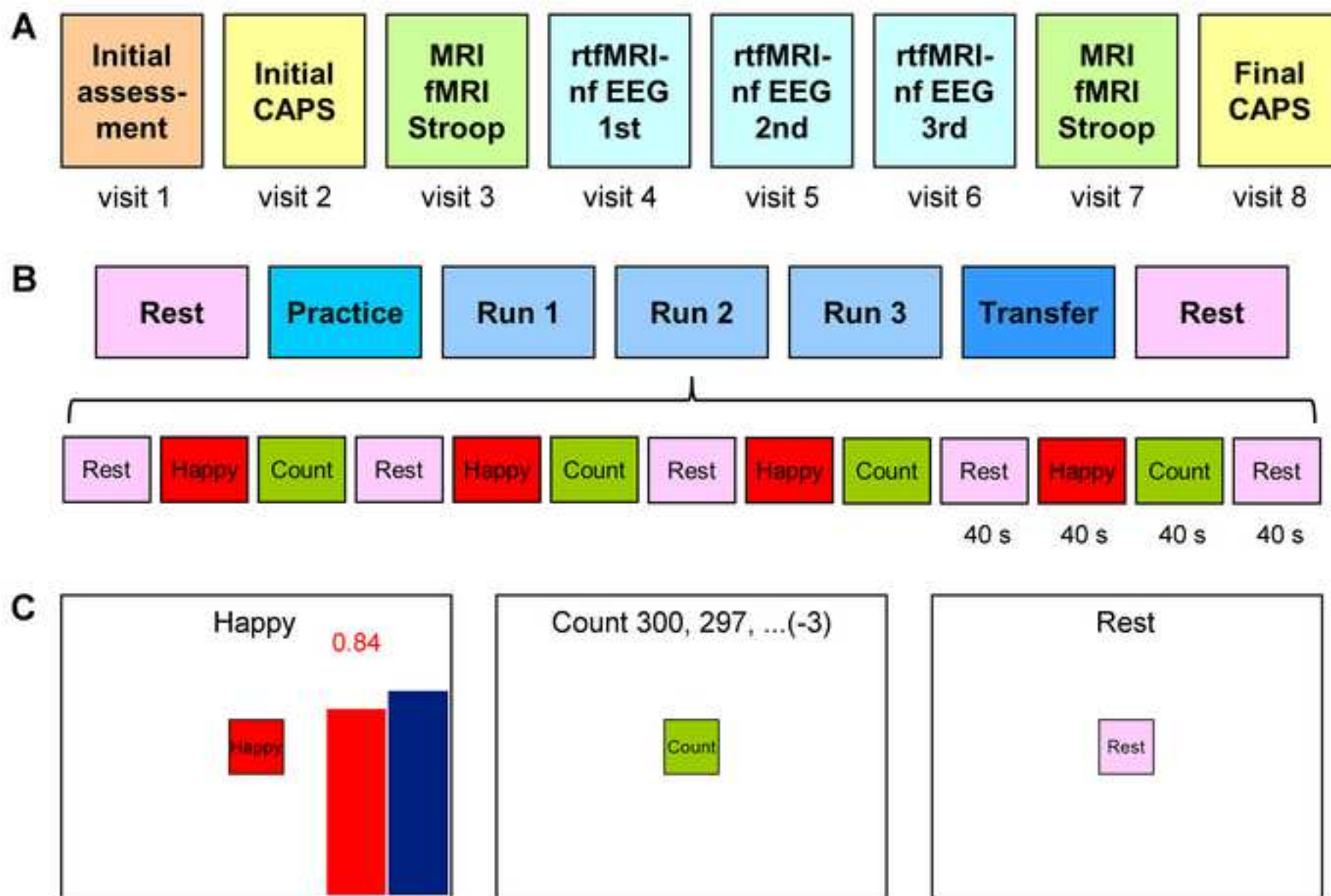
Figure 7. Statistical maps of the correlation between the fMRI connectivity slope (FCS) for the left amygdala (LA) and PTSD severity (CAPS) for the experimental group (EG). The FCS is defined in Fig. 3B. The correlation is a voxel-wise partial correlation with CAPS ratings controlled for comorbid depression severity (HDRS) ratings and average individual LA FCS for white matter. The maps are FWE corrected and projected onto the TT_N27 template, with 3 mm separation between axial slices. The number adjacent to each slice indicates the z coordinate in mm. The left hemisphere (L) is to the reader's right. The green crosshairs mark the center of the LA target ROI (Fig. 2A). Peak t -statistics values for the correlation effect and the corresponding cluster properties are specified in Table 4.

Figure 8. Illustration of the correlation effects between the LA FCS and PTSD severity (CAPS) for the EG. Each plot shows an average correlation effect for a 10-mm diameter ROI centered at a specified location. The correlation is a partial correlation with CAPS ratings controlled for HDRS ratings and average individual LA FCS for white matter ($n=19$, $df=15$). The results for the L LOFC (BA 11), L LOFC (BA 47), and L DLPFC correspond to those reported in Fig. 7 and Table 4. The results for the R LOFC, L MOFC, and R PCun are included for comparison with the corresponding results in Figs. 5,6 (see text). The abbreviations are the same as in Fig. 6.

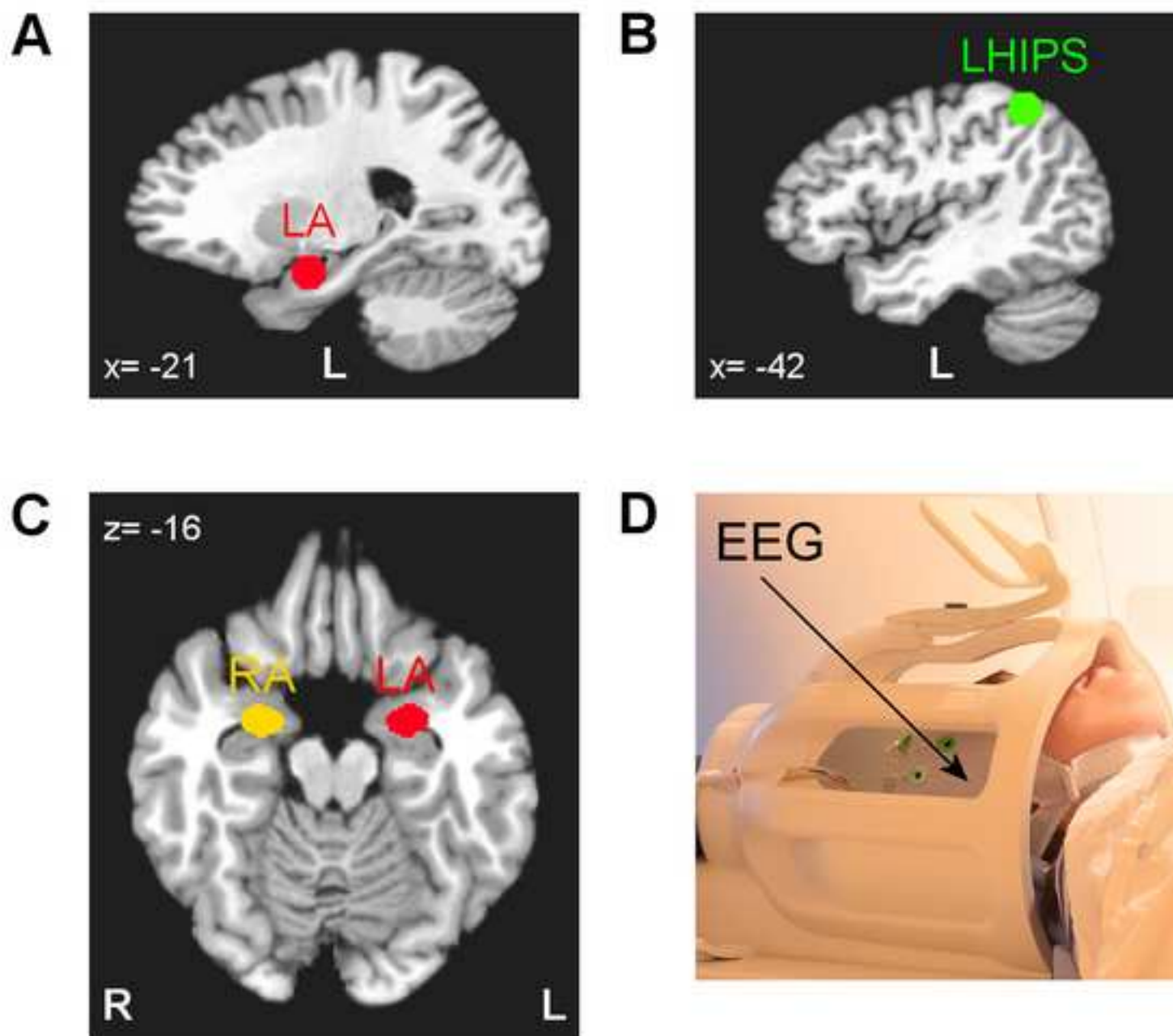
Figure 9. Correlation between the EEG coherence slope (ECS) in the upper alpha band and PTSD severity (CAPS) for the experimental group (EG). The ECS is defined in Fig. 3C. The correlation for each EEG channel pair (or average across multiple channel pairs) is a partial correlation with CAPS ratings controlled for comorbid depression severity (HDRS) ratings ($n=18$, $df=15$). **A)** Red segments denote EEG channel pairs for which the ECS vs CAPS correlations are positive ($r(15)>0$, $p<0.05$,

uncorr.). **B)** Example of such correlation for one channel pair. **C)** Significant correlation between the ECS(L), i.e. the average ECS for 10 pairs of fronto-temporal EEG channels on the left, and CAPS ratings. **D)** Lack of correlation between the ECS(R), i.e. the average ECS for 10 pairs of corresponding fronto-temporal EEG channels on the right, and CAPS ratings. **E)** Correlation between the average ECS laterality, ECS(L)–ECS(R), and CAPS ratings.

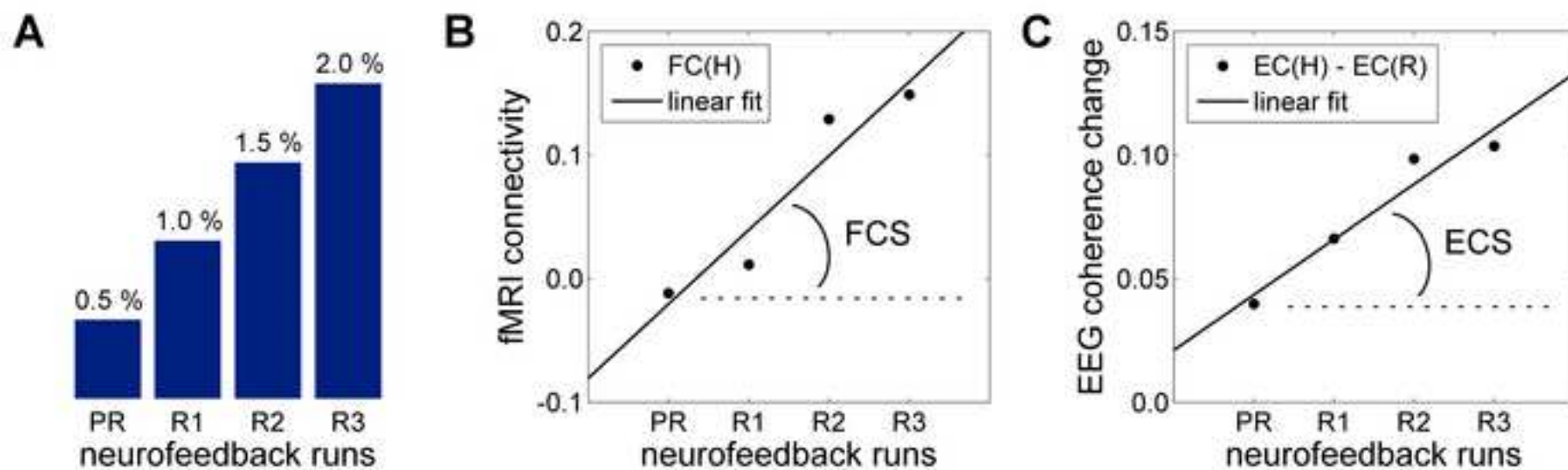
9. Figure 1
[Click here to download high resolution image](#)



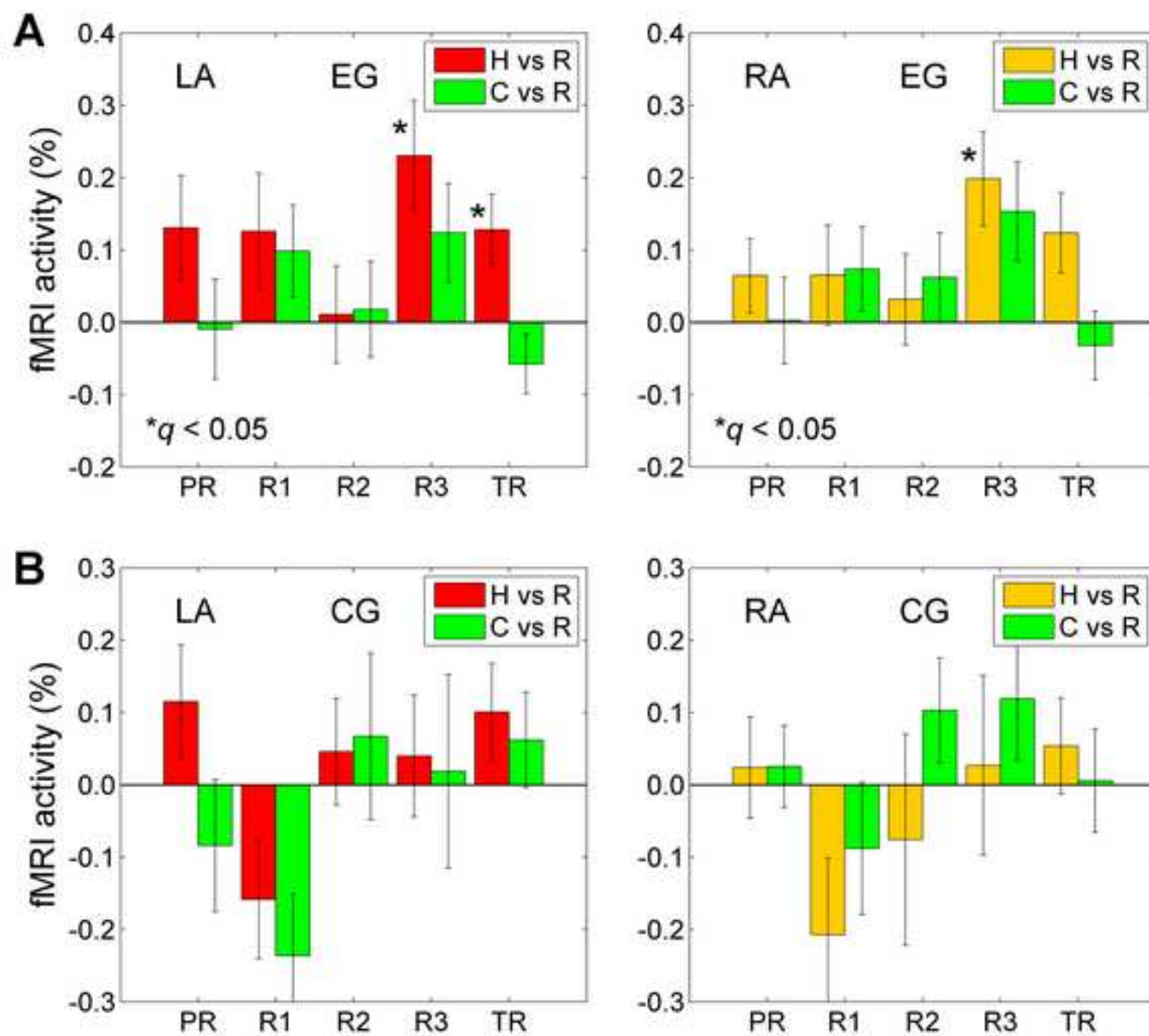
9. Figure 2
[Click here to download high resolution image](#)



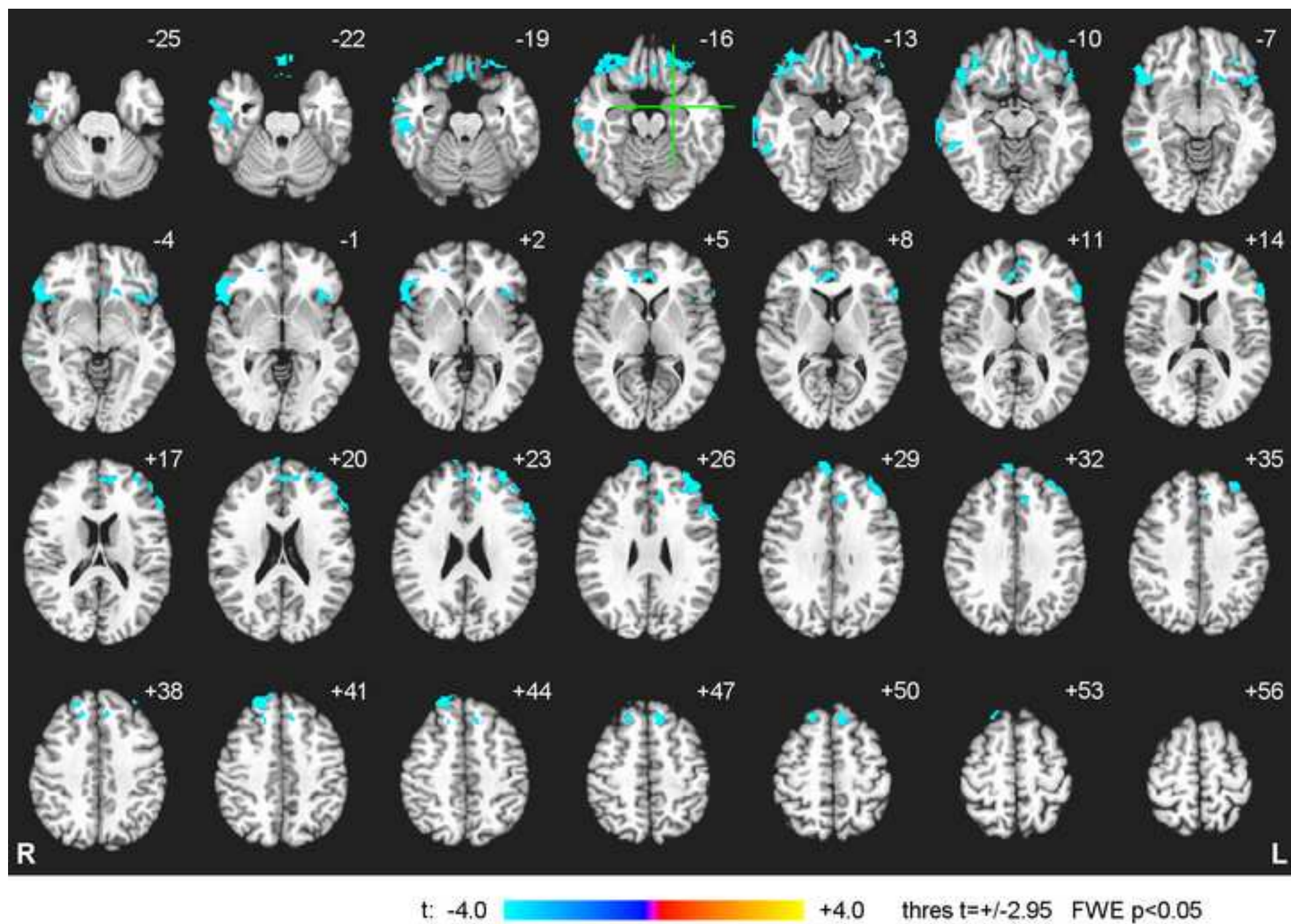
9. Figure 3
[Click here to download high resolution image](#)



9. Figure 4
[Click here to download high resolution image](#)

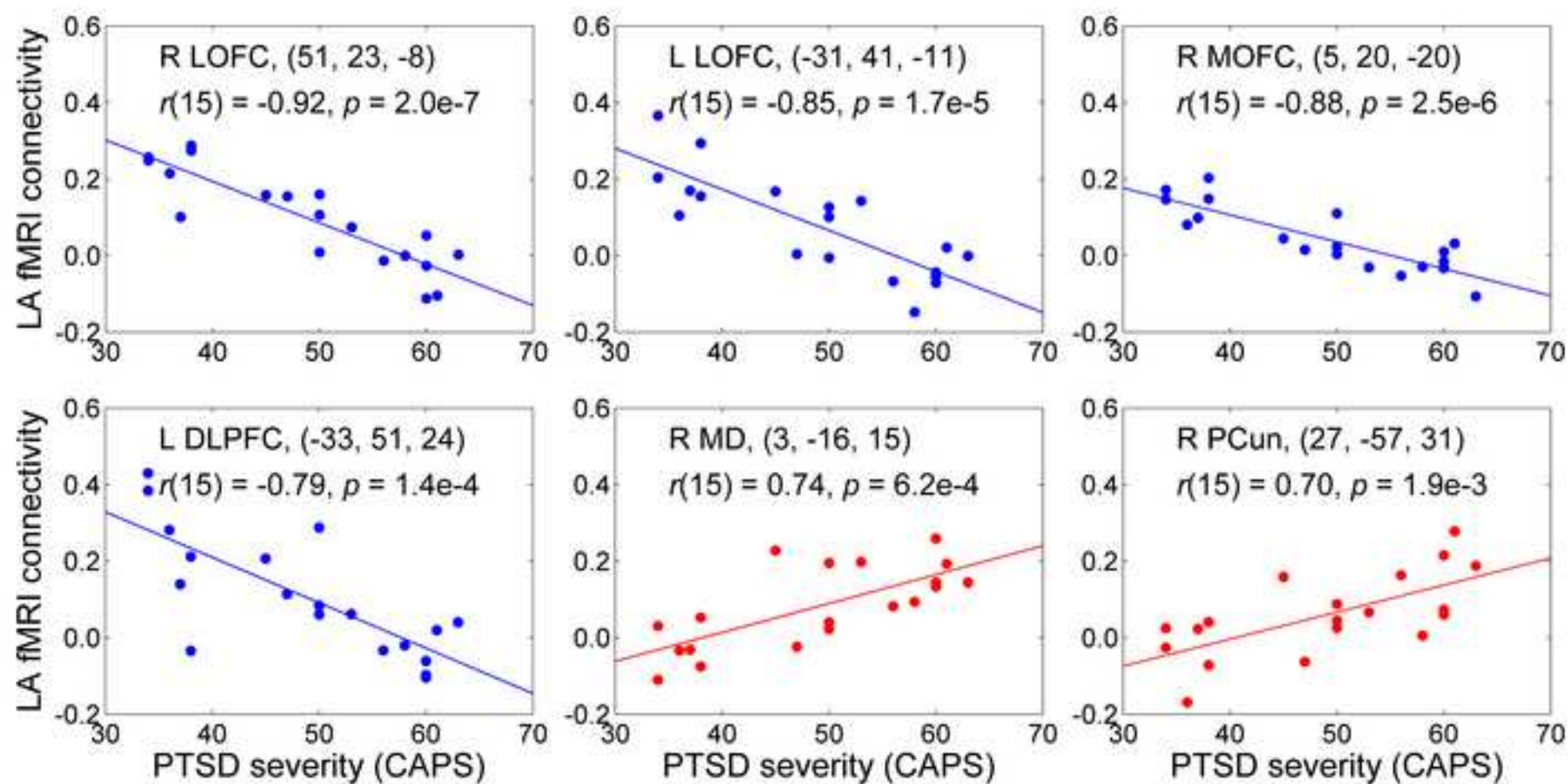


9. Figure 5
[Click here to download high resolution image](#)

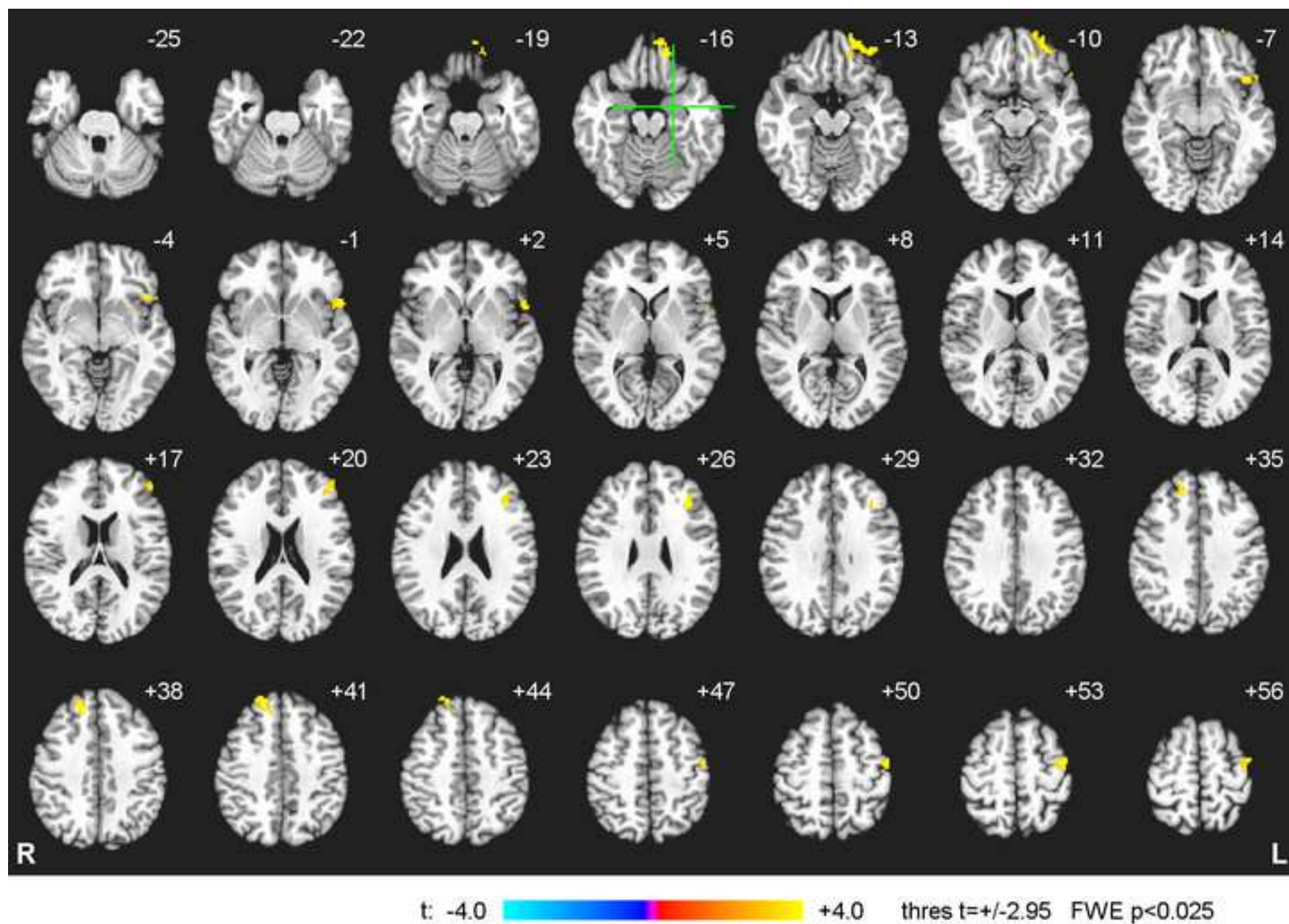


9. Figure 6

[Click here to download high resolution image](#)

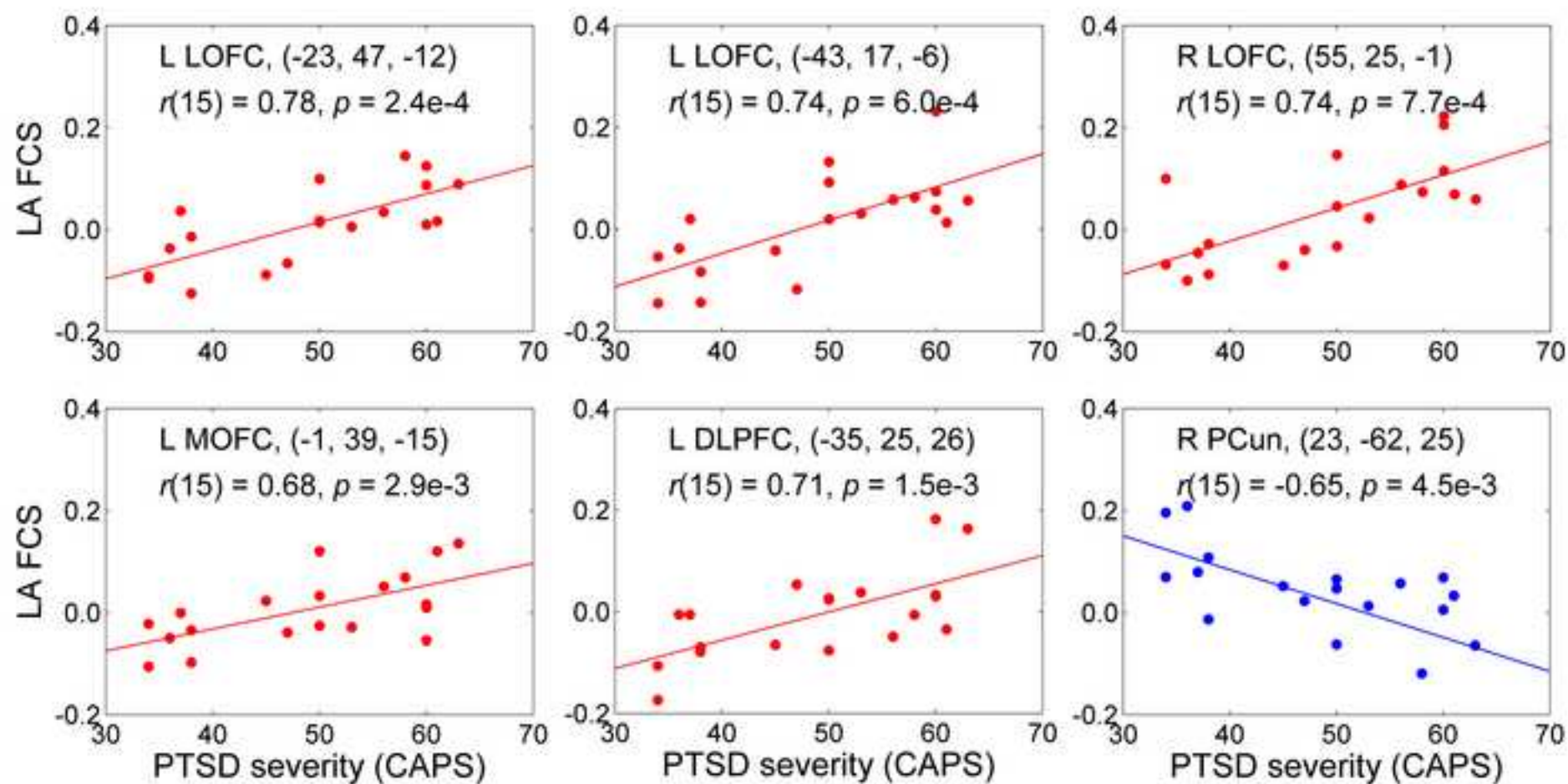


9. Figure 7
[Click here to download high resolution image](#)

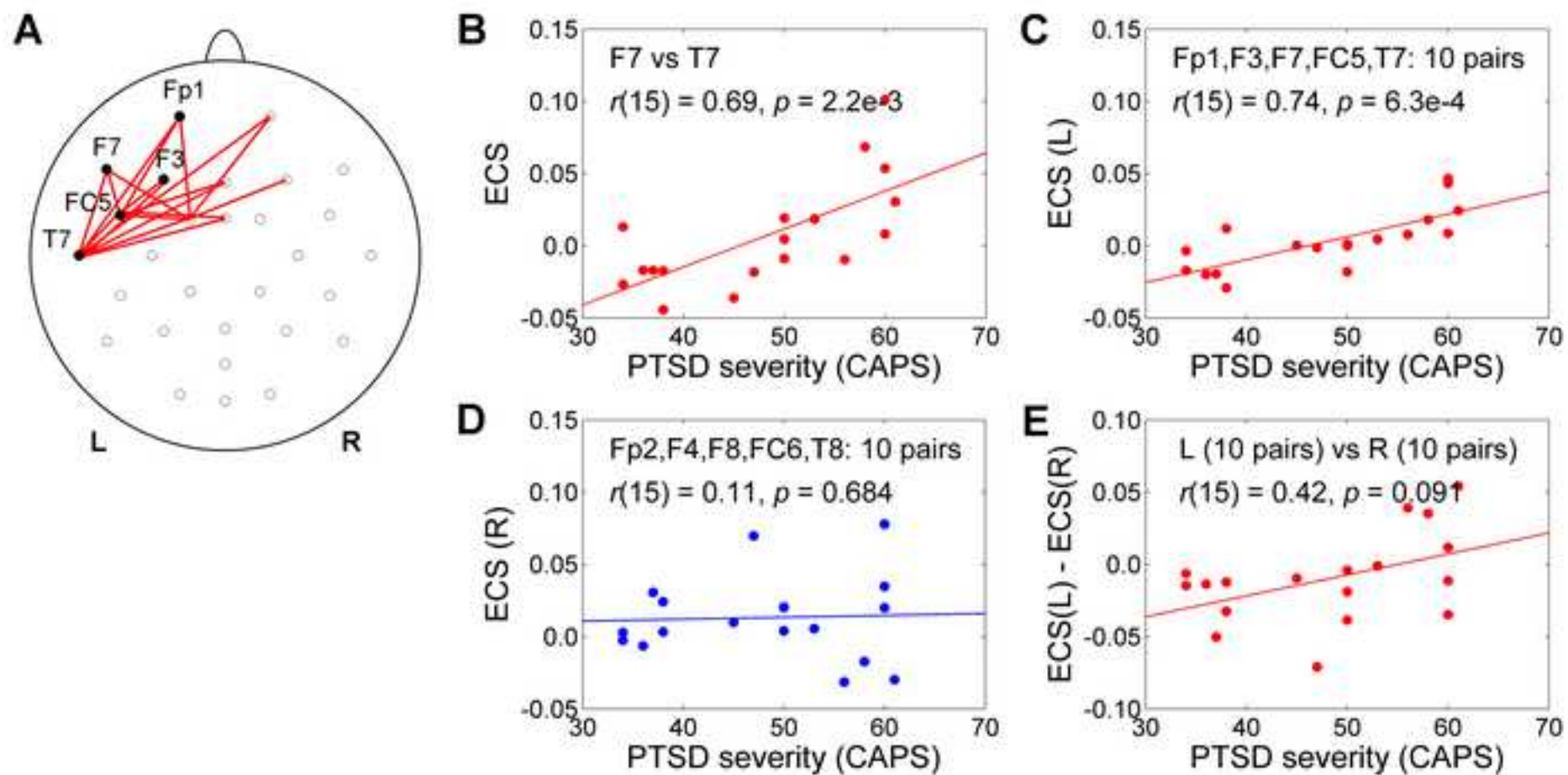


9. Figure 8

[Click here to download high resolution image](#)



9. Figure 9
[Click here to download high resolution image](#)



Supplementary Material

“Real-time fMRI neurofeedback training of the amygdala activity with simultaneous EEG in veterans with combat-related PTSD” by V. Zotev et al.

S1.1. fMRI data analysis

Offline analysis of the fMRI data was performed in AFNI [Cox, 1996; Cox & Hyde, 1997]. Pre-processing of single-subject fMRI data included despiking using the 3dDespike AFNI program and correction of cardiorespiratory artifacts using the AFNI implementation of the RETROICOR method [Glover et al., 2000]. Further fMRI pre-processing involved slice timing correction and volume registration of all EPI volumes acquired in the experiment using the 3dvolreg AFNI program with two-pass registration. The last volume of the short EPI dataset acquired immediately after the high-resolution anatomical (MPRAGE) brain image was used as the registration base.

The fMRI activation analysis was performed using the standard general linear model (GLM) approach. It was conducted for each of the five task fMRI runs (Fig. 1B) using the 3dDeconvolve AFNI program. The GLM model included two block-design stimulus condition terms, Happy Memories and Count (Fig. 1B), represented by the standard block-stimulus regressors in AFNI. A general linear test term was included to compute the Happy vs Count contrast. Nuisance covariates included the six fMRI motion parameters and five polynomial terms for modeling the baseline. GLM β coefficients were computed for each voxel, and average percent signal changes for Happy vs Rest, Count vs Rest, and Happy vs Count contrasts were obtained by dividing the corresponding β values ($\times 100\%$) by the β value for the constant baseline term. The resulting fMRI percent signal change maps for each run were transformed to the Talairach space by means of the @auto_tlrc AFNI program using each subject's high-resolution anatomical brain image as the template.

Average individual BOLD activity levels for the left and right amygdala were computed in the offline analysis for the LA and RA ROIs, exhibited in Fig. 2C. The ROIs were defined anatomically as specified in the AFNI implementation of the Talairach-Tournoux brain atlas. The voxel-wise fMRI percent signal change data from the GLM analysis, transformed to the Talairach space, were averaged within the LA and RA ROIs and used as GLM-based measures of these regions' BOLD activities.

S1.2. EEG data analysis

Removal of MR and cardioballistic (CB) artifacts was based on the average artifact subtraction method implemented in BrainVision Analyzer 2.1 (Brain Products, GmbH). The MR artifact template was defined using MRI slice markers recorded with the EEG data. After the MR artifact removal, the EEG data were bandpass filtered between 0.5 and 80 Hz (48 dB/octave) and downsampled to 250 S/s sampling rate (4 ms interval). The fMRI slice selection frequency (17 Hz) and its harmonics were removed by band rejection filtering. The CB artifact template

was determined from the cardiac waveform recorded by the ECG channel, and the CB artifact to be subtracted was defined, for each channel, by a moving average over 21 cardiac periods. Intervals with strong motion artifacts were not included in the CB correction.

Following the MR and CB artifact removal, the EEG data from the five task runs (Fig. 1B) were concatenated to form a single dataset. The data were carefully examined, and intervals exhibiting significant motion or instrumental artifacts (“bad intervals”) were excluded from the analysis. Channel Cz was selected as a new reference, and FCz was restored as a regular channel.

An independent component analysis (ICA) was performed over the entire dataset with exclusion of the bad intervals. This approach ensured that independent components (ICs) corresponding to various artifacts were identified and removed in a consistent manner across all five runs. Channels TP9 and TP10 were excluded from the ICA and further analysis, because their signals are very sensitive to head and jaw movements, producing large artifacts. The Infomax ICA algorithm (Bell & Sejnowski, 1995), implemented in BrainVision Analyzer 2.1, was applied to the data from 29 EEG channels and yielded 29 ICs. Time courses, spectra, topographies, and kurtosis values of all the ICs were carefully analyzed (see e.g. McMenamin et al., 2010 and supplement therein) to identify various artifacts, as well as EEG signals of neuronal origin, with particular attention to the alpha and theta EEG bands. After all the ICs had been classified, an inverse ICA transform was applied to remove the identified artifacts from the EEG data. Following the ICA-based artifact removal, the EEG data were low-pass filtered at 40 Hz (48 dB/octave) and down sampled to 125 S/s (8 ms interval). Because many artifacts had been already removed using the ICA, the data were examined again, and new bad intervals were defined to exclude remaining artifacts.

Real-time fMRI amygdala neurofeedback positive emotional training normalized resting-state functional connectivity in combat veterans with and without PTSD: a connectome-wide investigation

Masaya Misaki¹, Raquel Phillips¹, Vadim Zotev¹, Chung Ki Wong¹, Brent E. Wurfel^{1,2}, Frank Krueger³, Matthew Feldner⁴, and Jerzy Bodurka^{1,5#}

¹Laureate Institute for Brain Research, Tulsa, OK, United States

²Laureate Psychiatric Clinic and Hospital, Tulsa, OK, United States

³Neuroscience Dept., George Mason University, Fairfax, VA, United States

⁴Dept. of Psychological Science, University of Arkansas, Fayetteville, AR, United States

⁵Stephenson School of Biomedical Engineering, University of Oklahoma, Norman, OK, United States

[#]Corresponding author:

Jerzy Bodurka (jbodurka@laureateinstitute.org, +1 918-502-5101)

Laureate Institute for Brain Research, 6655 S. Yale Avenue, Tulsa, OK 74136-3326

Abstract

Self-regulation of brain activation using real-time functional magnetic resonance imaging neurofeedback (rtfMRI-nf) is an emerging approach for treating mood and anxiety disorders. However, the action mechanism of rtfMRI-nf in symptom improvement remains unclear. The effect of neurofeedback training on resting-state functional connectivity warrants investigation as changes in spontaneous brain activation could reflect the association between sustained symptom relief and brain alteration. In the current study, combat veterans with posttraumatic stress disorder (PTSD) and without PTSD were trained to increase a feedback signal reflecting left amygdala activity while recalling positive autobiographical memories. Abnormal PTSD connectivity at the baseline session was identified by a data-driven, connectome-wide approach using a multivariate distance matrix regression (MDMR) analysis that examines comprehensive whole-brain voxel-by-voxel connectivity. The rtfMRI-nf training effect on these abnormal connectivities was examined by longitudinal linear mixed-effect model analysis. In addition, a longitudinal MDMR analysis was performed to examine connectome-wide neurofeedback training effects beyond those associated with effects on abnormal baseline connectivity.

Results showed significant PTSD symptom reduction in the PTSD group after training, but not in the control group that received sham feedback from the horizontal part of the intraparietal sulcus, which is not implicated in emotional processing. Abnormal resting-state connectivity for combat veterans with and without PTSD was normalized after the training. Those included hypoconnectivities between the left amygdala and the left ventrolateral prefrontal cortex (vlPFC) and between the supplementary motor area (SMA) and the dorsal anterior cingulate cortex (dACC). The increase of SMA-dACC connectivity was associated with PTSD symptom reduction. Longitudinal MDMR analysis revealed a connectivity change between the precuneus and the left superior frontal cortex. The increase of this connectivity was associated with a decrease in hyperarousal symptoms.

These results indicated that the rtfMRI-nf training effect was not limited to a feedback target region and symptom relief could be mediated by brain modulation in several regions other than a feedback target area.

Keywords: combat veterans, neurofeedback, amygdala, positive memories, prefrontal cortex, precuneus

Highlights

- fMRI neurofeedback training effect on resting-state connectivity was examined
- Left amygdala activity was trained to increase with positive memory
- Neurofeedback normalized altered connectivity in veterans with and without PTSD
- PTSD symptoms reduced significantly after training
- Connectivity-symptom association was seen in mPFC and precuneus

1. Introduction

Neurofeedback training with real-time functional magnetic resonance imaging (rtfMRI-nf) enables self-regulation of brain activation by presenting ongoing brain activation measured with the blood oxygenation level dependent (BOLD) signal (Weiskopf, 2012). Emerging evidence suggests clinical utility of self-regulation of brain activation with rtfMRI-nf training. deCharms et al. (2005) conducted a pioneering study of the clinical application of rtfMRI-nf, which demonstrated that training to reduce rostral anterior cingulate cortex (rACC) activity with rtfMRI-nf could reduce chronic pain symptoms. Subsequently, studies have applied rtfMRI-nf training to various neurological and psychiatric disorders, including chronic tinnitus (Haller et al., 2010), schizophrenia (Ruiz et al., 2011), Parkinson's disease (Subramanian et al., 2011), spider phobia (Zilverstand et al., 2015), cigarette smoking (Hartwell et al., 2016), borderline personality disorder (Paret et al., 2016a), and mood and anxiety disorders (Scheinost et al., 2013), including major depressive disorder (MDD) (Hamilton et al., 2016; Linden et al., 2012; Young et al., 2017a; Young et al., 2017b; Young et al., 2014; Zotev et al., 2016) and posttraumatic stress disorder (PTSD) (Gerin et al., 2016; Nicholson et al., 2017).

These studies demonstrated that participants can learn to self-regulate feedback target regions as a result of rtfMRI-nf training. Symptom reduction effects, however, have not been consistent and the associations between therapeutic and neurobiological effects are not clear yet. A systematic review of neurofeedback treatment studies (Thibault et al., 2016) raised several arguments regarding neurofeedback specificity (whether the observed treatment effect is a result of neurofeedback-dependent brain modulation or the mental strategy used in the training) and sustainability (how long and how much of the trained brain modulation effect on symptom treatment continues after the neurofeedback training). They highlighted that several non-specific factors, such as positive expectancies (placebo effect) and spontaneous remission, need to be ruled out to confirm therapeutic utility of neurofeedback training

(Thibault et al., 2016). Accordingly, more research for possible action mechanisms of the neurofeedback brain modulation and how it impacts psychiatric symptoms is necessary.

Resting-state fMRI functional connectivity (Friston, 1994) has potential for elucidating mechanisms underlying rtfMRI-nf therapeutic effects. This measure evaluates correlations among BOLD signals during rest. Such spontaneous brain activation could reflect a generalized effect of neurofeedback training that is not limited to a trained context and could be associated with sustained treatment effects. In fact, the effects of neurofeedback training with fMRI and/or EEG are not limited to a training task, but have been observed on resting-state functional connectivity as well (Kluetsch et al., 2014; Kopel et al., 2016; Nicholson et al., 2016; Scheinost et al., 2013; Yuan et al., 2014).

Studies also showed that neurofeedback training effects are not restricted to a neurofeedback target region. Scheinost et al. (2013) examined the effect of rtfMRI-nf training to reduce orbitofrontal cortex (OFC) activity while viewing contamination-associated stimuli among people with contamination anxiety. They found changes in connectivity in many brain regions, including reduced connectivity with limbic structures and increased connectivity in the dorsolateral prefrontal cortex. Subjective evaluation of control over anxiety was negatively correlated with bilateral OFC activation and positively correlated with right lateral parietal activation. Emmert et al. (2016) also reported a broad effect of the training in a meta-analysis of rtfMRI-nf training studies. These results suggest symptom reduction may be due to neurobiological changes beyond a targeted region of neurofeedback. The effect of training, therefore, needs to be examined across the whole-brain to elucidate the neurobiological basis of the therapeutic effect.

For whole-brain comprehensive functional connectivity analysis, a connectome-wide association approach has been proposed (Shehzad et al., 2014). This approach uses a nonparametric multivariate analysis of variance called multivariate distance matrix regression (MDMR). This enables comprehensive search in whole-brain voxel-by-voxel connectivity without *a priori* definition of a seed

region (Anderson, 2001). Satterthwaite et al. (2015) used this method to find the resting-state functional connectivity that was associated with depression and anxiety symptoms among women with MDD and PTSD. They found that decreased connectivities between the amygdala and the dorsolateral prefrontal cortex (dlPFC), the ACC, and the anterior insula were correlated with depression symptom severity.

The current study performed a left amygdala-focused rtfMRI-nf training for combat veterans with and without PTSD to investigate the training effects on resting-state functional connectivity and how such effects were related to PTSD symptom reduction. Participants were trained to increase the feedback signal by recalling positive autobiographical memory. A connectome-wide approach was used for comprehensive investigation of the training effect on whole-brain voxel-by-voxel connectivity and its association with change in PTSD symptoms.

Pathological hyperactivity of the amygdala is consistently observed for PTSD patients, both in response to negative stimulus presentation (Etkin and Wager, 2007; Fonzo et al., 2010; Hayes et al., 2012; Patel et al., 2012; Pitman et al., 2012; Rauch et al., 2000; Shin et al., 2006; Simmons et al., 2011; St Jacques et al., 2011) and at rest (Koch et al., 2016; Wang et al., 2016). Gerin et al. (2016) and Nicholson et al. (2017) performed amygdala-focused rtfMRI-nf training among people with PTSD to suppress amygdala activity. In contrast, participants in the current study were trained to increase amygdala activity using positive autobiographical memory recall. A meta-analysis (Lindquist et al., 2016) demonstrated that the amygdala response is valence-general; it responds to both positive and negative stimulus presentations. Basic, animal research (Kim et al., 2017) has documented that distinct populations of central amygdala neurons mediate mouse appetitive behaviors. In fact, our previous study using the same rtfMRI-nf training approach to enhance amygdala response to positive memory recall among people with MDD (Young et al., 2017b) demonstrated symptom reduction resulting from the procedure. These results suggest that enhancing positive emotion by increasing amygdala activity has potential for reducing PTSD symptoms.

This report focused on changes in resting-state functional connectivity resulting from the rtfMRI-nf training among combat veterans with and without PTSD. Brain activation during the training sessions will be reported separately. We hypothesized that the rtfMRI-nf amygdala positive emotional training will restore and normalize at least some of observed and reported aberrant resting state functional connectivities in PTSD. A series of analyses were done for the resting-state functional connectivity at the baseline and post-training sessions. First, we analyzed connectivity with the left amygdala region of interest (ROI), which was the feedback target region, and demonstrated abnormal connectivity at baseline. Then changes in abnormal connectivity resulting from the training, as well as its association with symptom change, were examined. A whole-brain search for training effects on left amygdala connectivity was also performed. Second, training effects on abnormal connectivity that were identified in the previous connectome-wide analysis (Misaki et al., under review) and their associations with symptom change were examined. Finally, a connectome-wide training effect analysis was conducted to identify the effect outside of abnormal connectivity. For this analysis, we developed a longitudinal MDMR that enabled comprehensive examination of training effects and associations with symptom change in whole brain voxel-by-voxel connectivity.

2. Materials and methods

2.1. Participants

Forty male U.S. military combat veterans with PTSD, 21 male U.S. military combat veterans without PTSD (veteran control, VC), and 28 non-trauma-exposed male controls (NC) participated in the baseline resting-state fMRI scan session. See supplementary material “Veteran participants” section for details regarding recruitment and inclusion/exclusion criteria. NC subjects were sampled from male participants in another study (Misaki et al., 2016) and were matched to the veteran group in terms of age and head motion during scanning sessions.

RtfMRI-nf training was performed only for veteran participants. Thirty PTSD and 17 VC participants completed 3 sessions of rtfMRI-nf training and the post-training resting-state scan session. PTSD participants were randomly assigned to the experimental group (PTSD-exp) where they received left amygdala rtfMRI-nf (N=21) or to the control group (PTSD-ctrl) where they received rtfMRI-nf from the left horizontal segment of the intraparietal sulcus (N=9). All VC participants were in the experimental group (VC-exp). Participants with excessive head motion (more than 40 censored volumes, see fMRI data processing section below for details) were excluded from the analysis. Five PTSD and three VC participants in the baseline session and an additional three PTSD and three VC participants who completed the post-training-session were excluded from the analysis. One VC participant did not complete the last neurofeedback session but performed the post-training resting-state scan. This participant was included in the analysis because the training effect on resting-state functional connectivity for this participant was not significantly different from others. Table 1 shows the number of participants analyzed in the baseline and the post-training session, respectively, with means and standard deviations of age and head motion estimates during the resting-state scan. Motion size is a mean L2-norm of frame-wise displacement evaluated at realignment procedure in the fMRI image preprocessing. There were no significant differences in age (Baseline: $F(2,78)=1.388$, $p=0.256$, Post-training: $F(2,30)=1.791$, $p=0.184$) and motion (Baseline: $F(2,78)=1.292$, $p=0.281$, Post-training: $F(2,30)=0.404$, $p=0.671$) between groups in either session.

Table 1. Participant demographics

	N	Baseline			Post-training		
		Age	Motion		N	Age	Motion
PTSD	35	32±7	0.061±0.026	exp	16	30±6	0.052±0.027
				ctrl	6	31±9	0.062±0.033
VC	18	33±10	0.065±0.024	exp	11	36±1	0.051±0.022
NC	28	29±11	0.055±0.017				

2.2. RtfMRI-nf training schedule

Veteran groups participated in 7-days of rtfMRI-nf training sessions. Details of the training schedule at each visit are provided in the “Schedules of real-time fMRI neurofeedback (rtfMRI-nf) training” section of the supplementary material. Resting-state scans at the 2nd and 6th visits were analyzed as the baseline and the post-training scans in the current report. No rtfMRI-nf training was performed at these visits and the resting-state scan was performed before any other task runs to avoid contamination from another task. The mean interval between the last training session (Visit 5) and the post-training resting-state scan (Visit 6) was 11 days ($SD=6$ days). The mean interval between the last training session (Visit 5) and the follow-up assessment (Visit 7) was 15 days ($SD=7$ days).

The rtfMRI-nf training was performed at the 3rd, 4th, and 5th visits. In the training session, subjects were asked to increase the neurofeedback signal by recalling positive autobiographical memories. The feedback signal was extracted from the left amygdala for the experimental group and from the left horizontal segment of the intraparietal sulcus for the control group. Participants were instructed to retrieve positive memories while attempting to increase the feedback signal presented on a screen via a bar. Each neurofeedback run consisted of alternating 40s blocks of rest, feedback (happy memory retrieval), and count (backward from 300 by a given one-digit integer) conditions. Each rtfMRI-nf session consisted of four fMRI runs, each lasting 8min 46s; a practice run, three training runs, and a final transfer run in which no neurofeedback information was provided. Further details of the

experimental procedures were described previously (Bodurka and Bandettini, 2008; Zotev et al., 2011) and in the “Visits 3–5: Real-Time fMRI Neurofeedback Training” section of the supplementary material.

The Clinician-Administered PTSD Scale (CAPS) for DSM-IV (Blake et al., 1995) and the PTSD Checklist - Military Version (PCL-M) (Weathers et al., 1993) were used to identify PTSD diagnosis and to measure symptom levels. The CAPS is considered a gold standard for diagnosing PTSD (Blake et al., 1995; Weathers et al., 2001) and yields symptom severity scores for each of the PTSD symptom clusters, including criterion B (reexperiencing), criterion C (avoidance), and criterion D (hyperarousal) symptoms. The CAPS was administered at the first and the last visits by a research staff member trained to mastery in administration of the interview. The PCL-M was administered at the 2nd and 6th visits. Depression and anxiety symptoms were also measured at the 2nd and 6th visits by the Montgomery-Åsberg Depression Rating Scale (MADRS) (Montgomery and Åsberg, 1979) and the Hamilton Anxiety Scale (HAM-A) (Hamilton et al., 1976), respectively.

2.3. MRI measurement

Data from resting-state sessions completed at the 2nd and 6th visits were analyzed as the baseline and post-training sessions, respectively. During resting-state fMRI scans, participants were instructed not to move and to relax and rest while looking at a fixation cross on a screen in the scanner. Magnetic resonance imaging was conducted on a 3 tesla MR750 MRI scanner (GE Healthcare, Milwaukee, WI) equipped with 32-channel receive-only head array coils (GE Healthcare, Nova Medical, Wilmington, MA). A single-shot gradient-recalled echo-planner imaging (EPI) sequence with sensitivity encoding (SENSE) was used for fMRI with imaging parameters of TR=2000ms, TE=30ms, FA=90°, FOV=240mm, 34 axial slices with 2.9mm thickness with 0.5mm gap, matrix=96×96, SENSE acceleration factor R=2. The EPI images were reconstructed into a 128×128 matrix resulting 1.875×1.875×3.4mm³ voxel volume. The resting fMRI run time was 6min 50s (205 volumes). Physiological pulse oximetry and respiration waveforms were simultaneously recorded (40Hz). A

photoplethysmograph with an infrared emitter placed under the pad of a participant's finger was used for pulse oximetry, and a pneumatic respiration belt was used for respiration measurements.

T1-weighted MRI images were acquired for anatomical reference with magnetization-prepared rapid gradient-echo (MPRAGE) sequence (FOV=240×192mm, matrix=256×256, 120 axial slices, slice thickness=0.9mm, 0.9375×0.9375×0.9mm³ voxel volume, TR=5ms, TE=2.0ms, R=2, flip angle=8°, delay time=1400ms, inversion time=725ms, sampling bandwidth=31.2kHz, scan time=5min 40s).

2.4. MRI image processing

The same image processing procedure as in Misaki et al. (under review) was used. Here is the reproduction of its description. Analysis of Functional NeuroImages (AFNI) software (<http://afni.nimh.nih.gov/afni/>) was used for image processing. The `afni_proc.py` command was used to make a data processing script. Initial five volumes were excluded from analysis. Outlier time points were replaced with interpolation (despike). RETROICOR (Glover et al., 2000) and respiration volume per time (RVT) correction (Birn et al., 2008) were applied to remove cardiac- and respiration-induced noise in the BOLD signal. Slice-timing differences were corrected by aligning to the first slice. Motion correction was applied by aligning all functional volumes to the first volume. Nonlinear warping to the MNI template brain with resampling to 2mm³ voxels was done with the Advanced Normalization Tools (ANTs) software (Avants et al., 2008) (<http://stnava.github.io/ANTs/>). We used the non-linearly aligned and averaged MNI152 brain provided with the FSL package (<https://fsl.fmrib.ox.ac.uk/fsl/fslwiki>) as a template. Spatial smoothing (4mm FWHM) and scaling to percent change were applied to the data.

Further noise reduction was applied by regressing out three principal components of the ventricle signal, local white matter average signal (ANATICOR) (Jo et al., 2010), 12 motion parameters (3 shift and 3 rotation parameters with their temporal derivatives), and low-frequency fluctuation (3rd-order Legendre polynomial model) from the signal time course. White matter and ventricle masks were extracted using FreeSurfer 5.3 (<http://surfer.nmr.mgh.harvard.edu/>) from the anatomical image of

individual subject and then warped to the normalized fMRI image space. Any fMRI time point with large motion (more than 0.25mm frame-wise displacement (FD)) along with the following point was censored within the regression (Power et al., 2015). FD was calculated by the L2-norm of frame-wise displacement that was evaluated at the realignment for motion correction.

2.5. Amygdala ROI analysis

Left amygdala (LA) region of interest (ROI) was anatomically defined using the Jülich histological atlas on MNI template brain (Eickhoff et al., 2005) provided with the FSL package. Voxels with larger than 50% probability of the left amygdala region were extracted. The first principal component of voxel's resting-state signal time-course was used as a seed time-course. The sign of the principal component signal was adjusted to make its correlation with the mean signal to be positive. The signal was extracted from a fully processed image (after regressing out noise components). Pearson's correlations between the seed time-course and time-courses in all other brain voxels were calculated and applied Fisher's z-transform ($z = \text{arctanh}(r)$, where r is correlation coefficient) to make a connectivity map. This map was subject to the following group analyses.

The baseline abnormality of the LA connectivity was examined by linear model analysis with group (PTSD, VC, NC), age, and motion size as predictor variables. The statistical parametric map for the group contrast was thresholded by $p < 0.005$ voxel-wise and family-wise error correction by cluster-extent $p < 0.016$ ($= 0.05/3$ for Bonferroni correction of three group comparisons). A cluster-extent threshold was evaluated by permutation test with 10,000 repetitions (Eklund et al., 2016).

The rtfMRI-nf training effect was examined by linear mixed-effect (LME) model analysis for longitudinal design. The LME model included fixed effects of session (baseline, post-training), group (PTSD-exp, PTSD-ctrl, VC-exp), session by group interaction, age, and motion size and a random effect of the subject on intercept. The LME analysis was performed with R language and environment for statistical computing (R Core Team, 2017) with nlme package (Pinheiro et al., 2017). This analysis was

done for the abnormal connectivity identified in the baseline analysis. Post-hoc test of LME to test the session effect in each group was done with Dunnett's multiple comparison method using critical values from multivariate t -distribution with lsmeans package in R (Lenth, 2016). This multiple comparison method was used for all post-hoc tests of LME in this study and all reported p -values for the post-hoc test of LME were corrected.

The training effect on left amygdala connectivity was also examined in whole-brain voxels. The LME analysis was performed for all connectivities between the left amygdala and whole-brain voxels. The statistical parametric maps for the main effect of session and the interaction between session and group was thresholded by $p < 0.005$ voxel-wise and family-wise error correction by cluster-extent $p < 0.05$. Since permutation test for the LME analysis was computationally too expensive, we used an improved cluster-size simulation with 3dClustSim in AFNI (Cox et al., 2017). The new approach used an improved spatial autocorrelation function to simulate the null distribution of cluster size that remedies the false positive problem (Cox et al., 2017). We also examined an LME model with additional regressors of symptom change and its interaction with session and group as fixed effects to search for an LA connectivity change that was associated with symptom change. The analysis for symptom association was done separately for each symptom measure only with the PTSD groups.

2.6. MDMR analysis for baseline abnormality

Misaki et al. (under review) performed MDMR analysis to investigate comprehensive voxel-wise resting-state connectivity alteration between the PTSD, VC, and NC groups. The current study used the same data as the baseline and examined changes in these abnormal connectivities as a result of the rtfMRI-nf training. The analysis procedure was described in Misaki et al. (under review) in detail and it is reproduced in the supplementary material, "Baseline MDMR analysis to identify abnormal resting-state functional connectivity" section. This analysis identified connectivity alterations in the PTSD and

VC groups compared to NC. The same LME models as in the LA ROI analysis were used to examine the training effect on these altered connectivities.

2.7. Longitudinal MDMR for the connectome-wide training effect

A longitudinal MDMR analysis was performed for a comprehensive investigation of the training effect that was not limited to the abnormal connectivity at baseline. The longitudinal MDMR included the connectivity maps before and after the training for each subject. The distance matrix of these maps was the dependent variable in the MDMR. The design matrix was made following a longitudinal design example in Winkler et al. (2014) (example 6 in the appendix of Winkler et al. (2014)). This design matrix included session, group (PTSD-exp, PTSD-ctrl, VC-exp), session by group interaction, age, and motion size. In addition, a subject-wise factor variables were included in the design matrix. These regressors had 1 at a pair of a same subject's samples and 0 for the others. This could regress out subject-wise average effect, so that the longitudinal analysis could find the session and the group effect on within-subject connectivity difference. Exchangeability block of permutation test in the MDMR was defined for each subject. That is, permutation was performed within a subject to randomize session order and then subject blocks were randomly permuted.

We found this design matrix was rank-deficient due to collinearity between the subject-wise regressors and age and motion regressors, which made the MDMR estimation unstable. We solved this problem by orthogonalizing the design matrix using singular value decomposition (SVD) (Mandel, 1982). The design matrix was decomposed to $X = USV^T$ using SVD. V^T is a transpose of V . MDMR analysis can be described as $G = X\beta = USV^T\beta = U\alpha$, where G is a centered negative distance matrix ($G = CAC$, where $C = (I - \frac{1}{n}11^T)$, $A = (-\frac{1}{2}d_{ij}^2)$, n is the number of subjects, I is the $n \times n$ identity matrix and 1 is a vector of n 1s (Shehzad et al., 2014)) and $\alpha = SV^T\beta$. This transformation improved the stability of the analysis because columns of U are orthogonal to each other. Pseudo- F value can be

evaluated by $F = \frac{\text{tr}(HG)/(m-1)}{\text{tr}[(I-H)G]/(n-m)}$, where $H = UU^T$. MDMR evaluates an individual effect of regressor using a partial design matrix, X_N , which is a design matrix excluding effects of interest columns.

Pseudo- F value of the effect of interest is obtained by $F_I = \frac{\text{tr}(H_I G)/m_I}{\text{tr}[(I-H)G]/(n-m)}$, where $H_I = H - H_N$,

$H_N = U_N U_N^T$, $U_N S_N V_N^T = \text{SVD}(X_N)$, and m_I is the number of effects of interest regressors. We note that this procedure with SVD is equivalent to the original MDMR when the design matrix X is full-rank.

The processed resting-state fMRI image was down-sampled to 4mm^3 voxels to apply longitudinal MDMR. Significance of the pseudo- F value was evaluated by permutation test with 10,000 repeats and thresholded by $p < 0.005$ voxel-wise and family-wise error correction by cluster-extent $p < 0.05$. Cluster-extent threshold was evaluated by permutation test. The regions with a significant main effect of interest (sum of the effects of session, group, and the session by group interaction) in the MDMR were used as seed regions for post-hoc connectivity analysis.

A seed-based post-hoc analysis for the significant regions with the MDMR was done in the original resolution images. Seed regions were placed at a peak location of the significant cluster in the MDMR statistical map for the main effect of interest. Peak coordinates in each significant cluster separated by at least 30mm were extracted. Seed area was a 6mm-radius sphere centered at the peak coordinates of the MDMR statistical map. Mean signal time-course of the seed area was used as a reference signal to calculate correlations with other voxels. The statistical test of the post-hoc analysis was the same as in the LA ROI analysis using LME and 3dClustSim. We also performed a longitudinal MDMR analysis with additional regressors of symptom change and its interaction with session and group to examine an association between connectivity change and symptom change. The analysis for symptom association was done separately for each symptom measure only with the PTSD groups.

3. Results

3.1. Symptom measure

Table 2 shows symptom levels at the baseline and the post-training sessions for the veterans listed in Table 1. Post-training CAPS scores were not available for five PTSD-exp, one PTSD-ctrl, and one VC participants. LME longitudinal analysis showed a significant main effect of session on CAPS total scores ($p=0.004$ with Wald tests (Pinheiro et al., 2017)), CAPS Criterion C subscale (sub-C; $p=0.020$), CAPS Criterion D subscale (sub-D; $p=0.004$), PCL-M total symptom scores ($p=0.005$), MADRS ($p=0.012$), and HAM-A ($p=0.005$). Post-hoc analysis of session effects for each group indicated that significant symptom reduction was seen only for the PTSD-exp group in all measures except CAPS Criterion B subscale scores (reexperiencing symptoms).

Table 2: Symptom measures at baseline and post-training sessions

	Baseline		Post-training		
	PTSD	VC	PTSD-exp	PTSD-ctrl	VC-exp
CAPS (total)	55.2±18.4	4.8±4.9	38.2±19.8***	50.8±30.1	2.0±2.3
CAPS (sub-B)	13.2±7.1	0.2±0.8	7.5±6.1	11.2±10.3	0.2±0.6
CAPS (sub-C)	20.1±9.6	0.8±2.2	14.7±11.0**	17.6±18.1	0.8±1.7
CAPS (sub-D)	21.9±5.3	3.9±3.9	15.9±7.6**	22.0±6.0	1.0±2.2
PCL-M	48.0±14.2	19.6±2.6	36.0±12.8*	45.0±23.5	18.1±1.4
MADRS	20.4±9.6	1.4±1.8	12.8±8.4**	14.0±9.7	0.7±1.0
HAM-A	18.2±7.8	1.9±1.5	10.4±6.0**	14.5±6.7	1.1±1.4

Means and standard deviations of symptom measures at the baseline and the post-training sessions. CAPS: Clinician-Administered PTSD Scale; CAPS (sub-B): CAPS Criterion B subscale, re-experiencing symptoms; CAPS (sub-C): CAPS Criterion C subscale, avoidance and numbing symptoms; CAPS (sub-D): CAPS Criterion D subscale, hyperarousal symptoms; PCL-M: MADRS: Montgomery-Åsberg Depression Scale; HAM-A: Hamilton Anxiety Rating Scale. * ($p<0.05$), ** ($p<0.005$), and *** ($p<0.001$) indicate corrected p -values of symptom change between the baseline and the post-training sessions.

3.2. Left amygdala connectivity

The PTSD group had significantly lower connectivity between the left amygdala and the left ventrolateral prefrontal cortex (vlPFC) than the NC group at baseline (Fig. 1). This connectivity was significantly increased after the training only for the PTSD-exp group (Fig. 1). Longitudinal LME analysis with a post-hoc test of the mean connectivity between the left amygdala seed and the voxels in the cluster of significantly altered connectivity showed a significant effect of session only for the PTSD-exp group ($t(29)=2.554$, corrected $p=0.047$). This connectivity change, however, was not significantly associated with symptom change. A whole-brain analysis for left amygdala connectivity with or without an effect of symptom change found no connectivity that was significantly associated with session and symptom change.

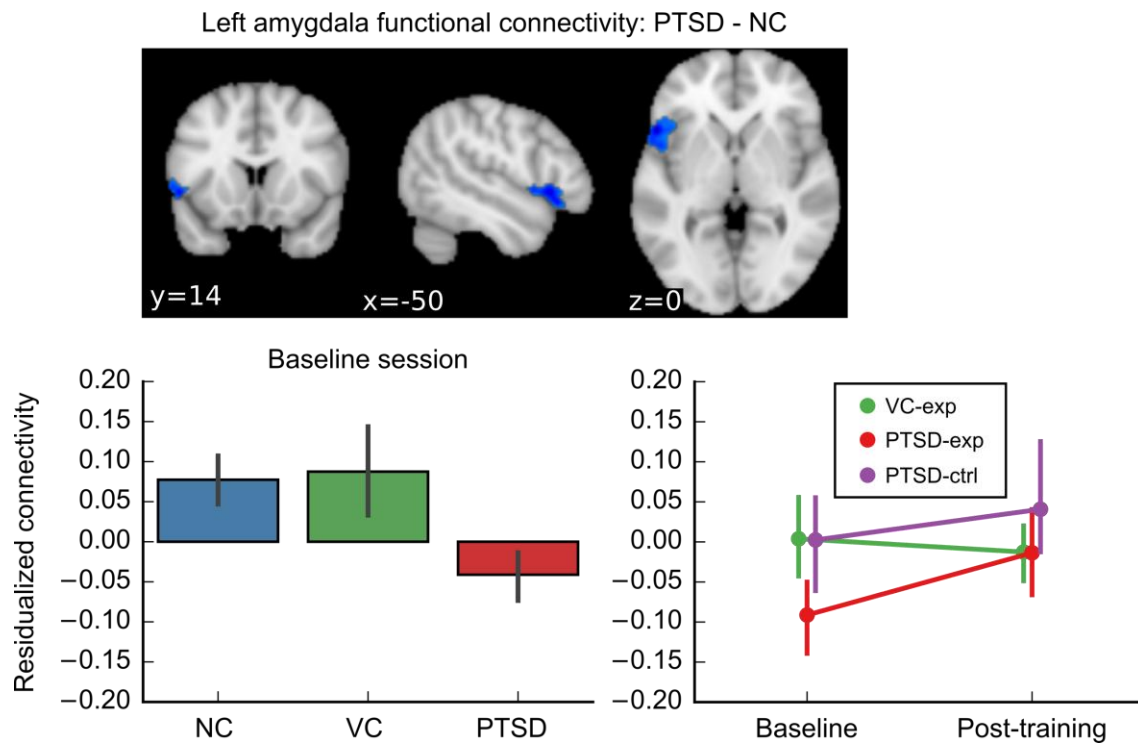


Figure 1. The region with significantly lower functional connectivity from the left amygdala ROI at the baseline session and its change between the sessions. Graphs show the group means and its 95% confidence intervals. Connectivity values are z-transformed correlation coefficients residualized with regard to age and motion.

3.3. Training effects on abnormal resting-state functional connectivity

Misaki et al. (under review) reported altered resting-state functional connectivities for the PTSD and VC groups compared to the NC group using a connectome-wide analysis. Supplementary tables S2 and S3 show lists of those altered connectivities. Here we investigated change in these abnormal connectivities after the neurofeedback training.

Figure 2A shows connectivity that had been altered in the PTSD group at baseline and changed significantly after training. Connectivity between the supplementary motor area (SMA) and the dorsal anterior cingulate cortex (dACC) was significantly lower in the PTSD group compared to the NC group at baseline. This connectivity was significantly increased after training only for the PTSD-exp group. Longitudinal LME analysis with a post-hoc test for the mean connectivity between the seed (SMA) and the voxels in the altered connectivity cluster showed a significant effect of session only for the PTSD-exp group ($t(29)=2.770$, corrected $p=0.028$), and this connectivity increase was significantly associated with a decrease of PCL-M in the PTSD-exp group (Fig. 2B, $t(15)=-3.092$, corrected $p=0.007$).

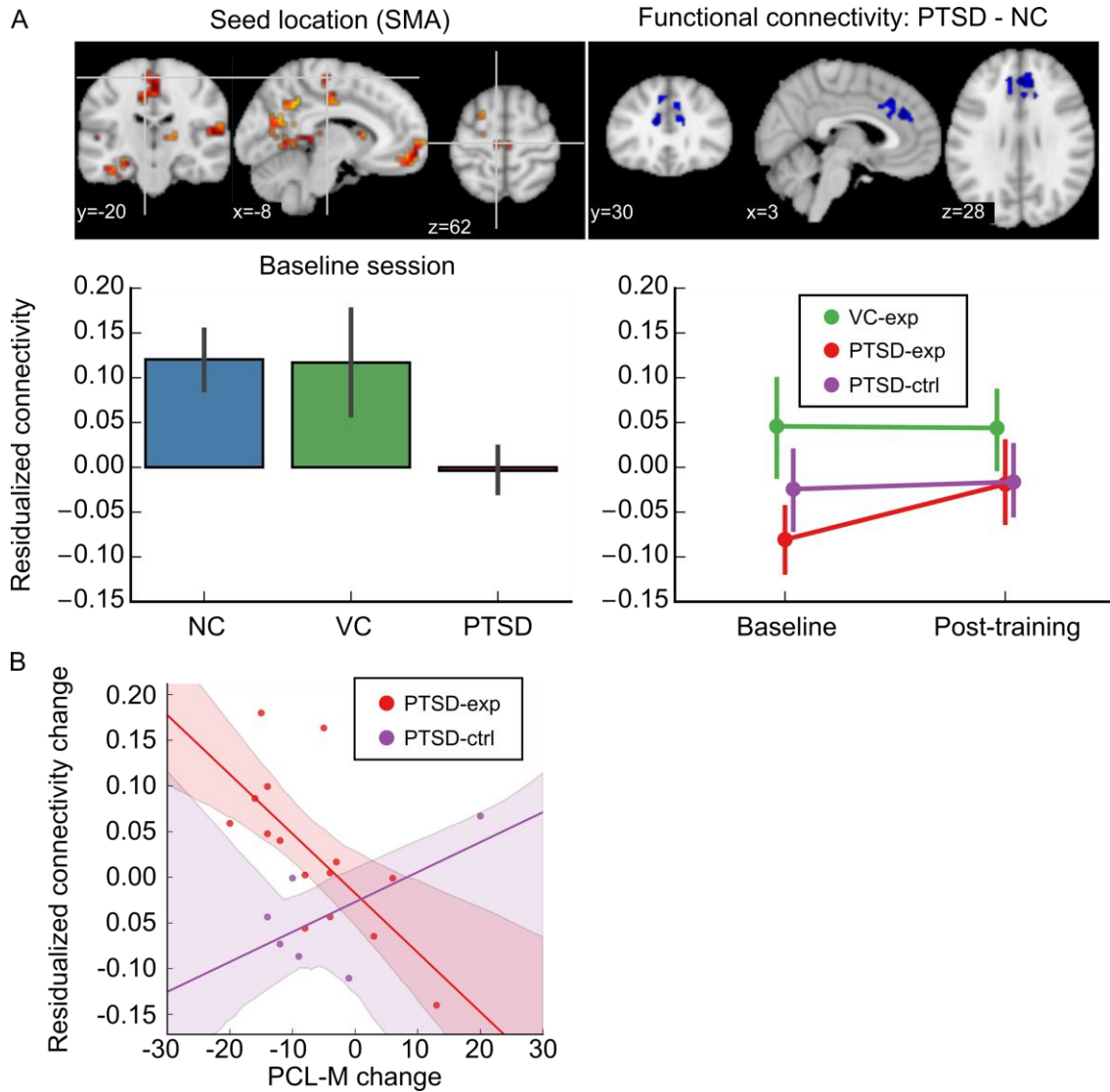


Figure 2. Training effect on abnormal connectivity for PTSD. A. Upper panels show seed location identified with MDMR (upper left) and abnormal connectivity region found in a post-hoc analysis of PTSD–NC contrast (upper right). Lower panels show mean connectivity between the seed and the voxels in the cluster of significantly altered connectivity at the baseline. The connectivity value was a z-transformed correlation with regressing out age and motion effects. Error bars show 95% confidence interval of the mean value. B. Association between the PCL-M score change and the connectivity change for PTSD participants are shown with fitted lines. Shadow around the line indicates the 95% confidence intervals of a fitted line. The connectivity change is the change in z-transformed correlations with regressing out age and motion effects.

Figure 3 shows connectivity that had been altered for the VC group at baseline and significantly changed after training. Connectivity between the left superior frontal region and the precuneus and the supramarginal gyrus was significantly lower for the VC group compared to the NC group at baseline

(Fig. 3A). This connectivity was significantly increased after training only for the VC-exp group. Longitudinal LME analysis with a post-hoc test for the mean connectivity between the seed (left superior frontal region) and the voxels in the cluster of significantly altered connectivity showed a significant effect of session only for the VC-exp group ($t(29)=3.518$, corrected $p=0.004$). The bilateral insula regions showed hyperconnectivity with several brain areas (see supplementary table S3 for details) at the baseline session (Fig. 3B, 3C). These connectivities were significantly decreased after training for the VC-exp group. Longitudinal LME analysis with a post-hoc test for the mean connectivity between the seed and the voxels in the clusters of significantly altered connectivity showed a significant effect of session for the VC-exp group ($t(29)=-3.990$, corrected $p=0.001$ and $t(29)=-3.485$, corrected $p=0.005$ for the left and right insula seed, respectively). The PTSD-ctrl group also showed a significant decrease of left insula connectivity after training ($t(29)=-3.156$, corrected $p=0.011$). Fig. 3B indicated that the PTSD-ctrl group had hyperconnectivity in the left insula at baseline that was similar to the VC group. For the PTSD-ctrl group, the decrease in this connectivity was associated with a decrease in CAP sub-D (hyperarousal) symptoms (Fig. 3B, $t(10)=2.754$, corrected $p=0.020$).

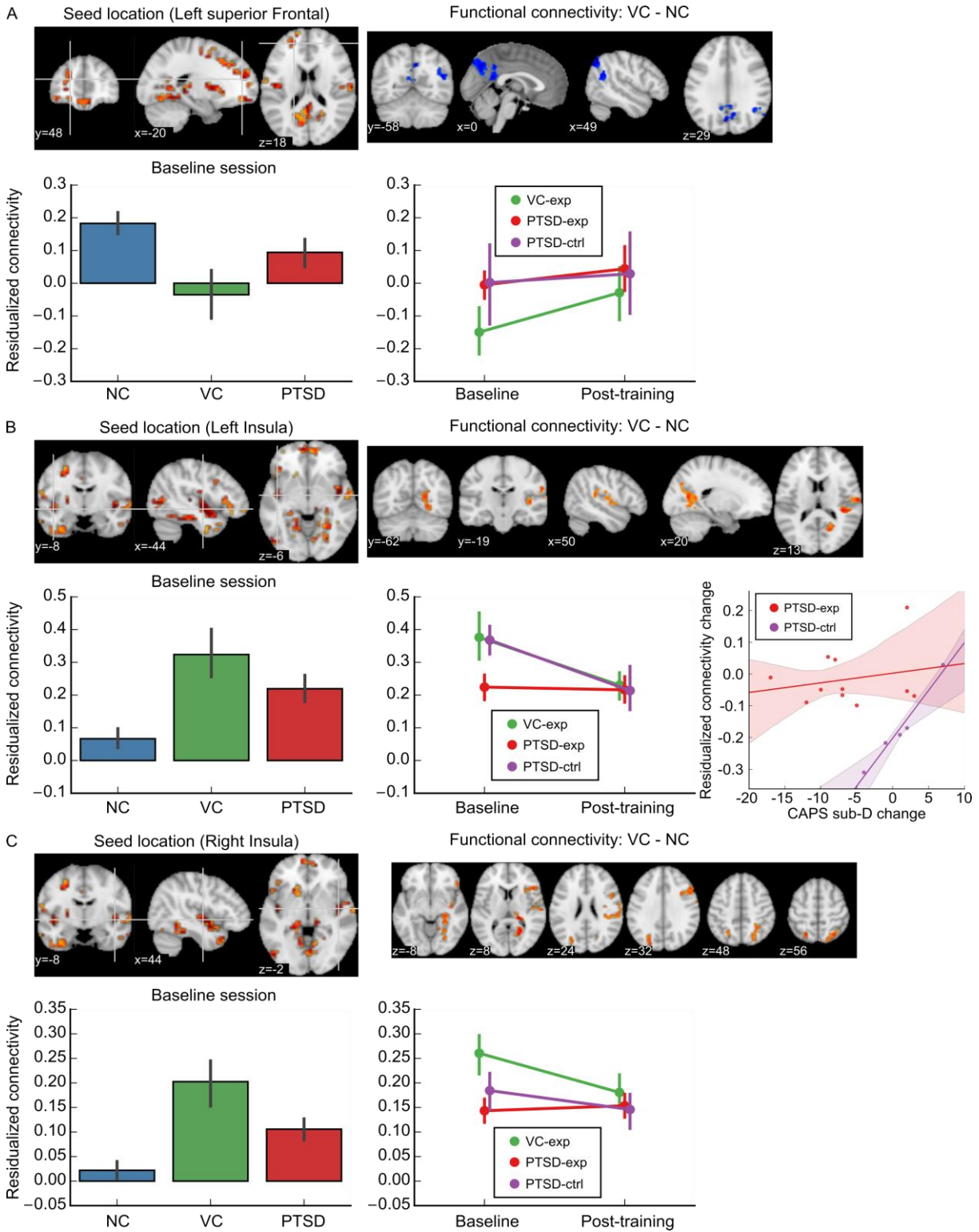


Figure 3: Training effect on abnormal connectivity for VC. For each panel A, B, and C, seed location (upper left) was identified with MDMR analysis and altered connectivity region (upper right) found in a post-hoc analysis of VC–NC contrast. Bar and line plots show mean connectivity between the seed and the voxels in the cluster of significantly altered connectivity at baseline. The connectivity value was a z-transformed correlation with regressing out age and motion effects. Error bars show the 95% confidence interval of the mean value.

3.4. Longitudinal MDMR for connectome-wide training effect

No significant effect of session or interaction between session and group was observed in the longitudinal MDMR analysis when no symptom change was included in the model. When the change in CAPS sub-D (hyperarousal) scores was included in the analysis, longitudinal MDMR found a significant cluster in the right precuneus region for the sum of effect of interest (Fig. 4).

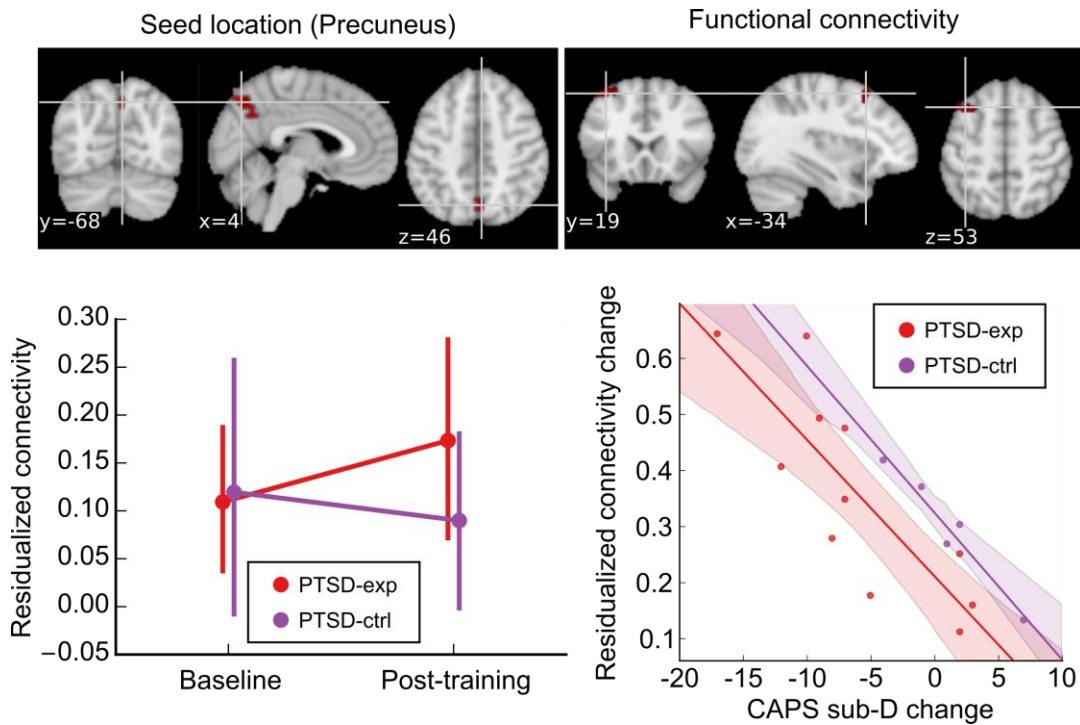


Figure 4: Training effect on resting-state functional connectivity identified with longitudinal MDMR. Upper panels show seed location (upper left) identified with longitudinal MDMR and abnormal connectivity region (upper right) found in a post-hoc LME analysis for the interaction between the CAPS sub-D score change and the session. The bottom left panel shows mean connectivity between the seed and the voxels in a significant cluster. The connectivity value was z-transformed correlation with regressing out age and motion effects. Error bars show 95% confidence interval of the mean value. The bottom right panel shows the association between the CAPS sub-D change and the connectivity change for PTSD participants. The shadow around the line indicates the 95% confidence interval of a fitted line. The connectivity change is the difference in the z-transformed correlations with regressing out age and motion effects.

The post-hoc LME analysis for the functional connectivity from this region revealed a significant interaction between session and CAPS sub-D score change in the connectivity between the precuneus and the left superior frontal region (Fig. 4). The increase in this connectivity was significantly associated

with a decrease in CAPS sub-D (hyperarousal) symptoms for the PTSD-exp group ($t(10)=-4.192$, $p=0.002$). The PTSD-ctrl group showed a similar trend, but the association was not statistically significant ($t(10)=-2.015$, $p=0.072$).

4. Discussion

RtfMRI-nf training for increasing left amygdala activity by recalling positive autobiographical memory reduced PTSD symptoms as well as depression and anxiety symptoms among veterans with combat-related PTSD. Comprehensive investigation of training effects on resting-state functional connectivity revealed that changes in connectivity were observed both in left amygdala connectivity as well as in the SMA, ACC, insula, precuneus, and prefrontal regions. These changes were in the direction of normalizing abnormal connectivity. Connectivity increases between the SMA and the dACC and between the precuneus and the left superior frontal gyrus were associated with a decrease in PTSD symptoms measured by PCL-M and CAPS sub-D, respectively.

The PTSD group evidenced hypoconnectivity between the left amygdala and the vIPFC region compared to the NC group at baseline. Amygdala hyperactivity both at rest (Koch et al., 2016; Wang et al., 2016; Yan et al., 2013) and during negative emotion-inducing tasks (Etkin and Wager, 2007; Fonzo et al., 2010; Hayes et al., 2012; Patel et al., 2012; Pitman et al., 2012; Rauch et al., 2000; Shin et al., 2006; Simmons et al., 2011; St Jacques et al., 2011) has been consistently reported for PTSD. This hyperactivity suggests failure of emotion regulation that could be instantiated by hypoconnectivity between the amygdala and the prefrontal emotion-regulation regions, including the ventromedial PFC (vmPFC) (Hayes et al., 2012; Patel et al., 2012) and medial prefrontal cortex (mPFC) (Jin et al., 2014). Brown et al. (2014) also reported decreased resting-state functional connectivity between the right basolateral amygdala (BLA) complex and the left inferior frontal gyrus for PTSD compared to trauma-exposed controls. The vIPFC has been linked to emotion regulation in many studies (Buhle et al., 2014;

Frank et al., 2014; Kohn et al., 2014; Ochsner and Gross, 2005; Zilverstand et al., 2017). Taken together, the hypoconnectivity between the amygdala and the vIPFC was consistent with prior research suggesting dysfunction of emotion regulation in PTSD related to deficient prefrontal activity and its hypoconnectivity with the amygdala. Recovery of this connectivity after training suggests that such emotion regulation functioning could be improved by amygdala-focused neurofeedback training of positive emotion up-regulation.

This connectivity change may be more pronounced in emotion enhancement training rather than emotion suppression training. Ellard et al. (2017) indicated that amygdala-vIPFC connectivity was increased during emotion acceptance and decreased during emotion suppression among people with anxiety disorders. Fonzo et al. (2017) investigated a difference between responders and non-responders to exposure therapy for PTSD in baseline brain response to emotion reactivity and emotion reappraisal tasks. They found that treatment response was associated with high brain activation during an emotion-reactivity task but not associated with an emotion-reappraisal task. This suggests that the treatment effect was not mediated by a reappraisal of emotion, but by accepting and habituating to emotion. Our approach that trained subjects to enhance positive emotion did not involve efforts to suppress emotion and, indeed, significant symptom reduction was observed. Taken together, these results suggest that neurofeedback procedures that involve emotion enhancement might be more effective for PTSD treatment than those that involve emotion suppression training.

While connectivity of the left amygdala was normalized by the training, this change was not associated with PTSD symptom change. The connectivity change that was associated with symptom relief was seen in the connectivity between the SMA and the dACC. The increase in this connectivity was significantly correlated with a decrease in PCL-M scores. SMA and premotor regions have been consistently implicated as central nodes of the emotion regulatory network (Buhle et al., 2014; Frank et al., 2014; Kohn et al., 2014). Etkin et al. (2011) suggested that the dorsal-caudal part of the ACC and

medial PFC are involved in both expression and reappraisal of negative emotion. Bonini et al. (2014) used intracerebral electroencephalography to investigate SMA function in an action monitoring task. They indicated that SMA is a center of performance monitoring that detects errors in action and sends signals to other mPFC and ACC regions to drive action correction. Ellard et al. (2017) also showed that dACC activation was increased during emotion acceptance. Taken together, the lowered connectivity between the SMA and dACC at baseline for PTSD might be associated with a deficit in emotion representation and emotion monitoring. Its recovery resulting from training could be associated with normalization of this function. The current training approach, which encourages subjects to repeatedly recall memories that elicit positive emotion, may normalize neurobiological mechanisms involved in emotion representation.

Another connectivity change that was associated with symptom relief was between the precuneus and the left superior frontal gyrus. The increase in this connectivity was associated with the decrease in CAPS sub-D scores (hyperarousal symptoms). This association was discovered in the longitudinal MDMR analysis and no significant abnormality was found at baseline. The precuneus has been implicated in memory retrieval (Brewin et al., 2010). A meta-analysis (Ochsner et al., 2012) indicated consistent left superior frontal activity in emotion regulation tasks. The increase of this connectivity, therefore, might be due to repetitive positive memory retrieval during the training. Interestingly, the increase in this connectivity was associated with a decrease in PTSD symptoms, while previous studies indicated abnormal hyperactivity in the precuneus among people with PTSD (Etkin and Wager, 2007; Lanius et al., 2006; Morey et al., 2008; Patel et al., 2012; Rabellino et al., 2015). Cwik et al. (2016) reported a positive correlation between the precuneus response to trauma-related pictures and subsequent PTSD symptom severity in acute stress disorder patients. Also, paroxetine treatment for PTSD has been shown to decrease resting-state amplitude of low-frequency fluctuation in the precuneus (Zhu et al., 2015). Collectively, these results suggest that elevated precuneus activity in PTSD is a

pathological brain alteration. Although the increase of connectivity between the precuneus and the superior frontal region could potentially enhance precuneus activity, this connectivity change was not associated with symptom increases, but rather decreases. This increase in connectivity might be associated with better control of precuneus activity or the pathological hyperactivity of the precuneus was specific to negative memory so that connectivity enhancement with positive memory retrieval may not have enhanced the abnormal activity.

The increase of precuneus connectivity after the training was also observed for the VC group. The VC group showed hypoconnectivity in the precuneus at baseline (Misaki et al., under review). It has been suggested that decreased precuneus activation is associated with efforts to terminate self-reflection of aversive sensations (Vogt and Laureys, 2005; Whalley et al., 2013). The decreased connectivity in the precuneus for the VC group, therefore, could be adaptive in that it promotes healthy recovery by effectively suppressing retrieval of traumatic memories. The recovery of this connectivity might be considered a side effect of repetitive memory retrieval training. Importantly, however, no symptom change was seen for the VC group after the training. This also suggests that the increase of the precuneus connectivity did not enhance pathological activation.

Connectivity normalization for the VC group was also seen in the bilateral insula regions. The VC group had hyperconnectivity in these regions at baseline that was normalized after the training. These insula regions were more posterior areas than the anterior insula, which has been consistently reported as hyperactive among people with PTSD (Pitman et al., 2012; Wang et al., 2016; Whalley et al., 2013). While the mid-to-posterior insula is a region implicated in proprioceptive sensation (Craig, 2003; Menon and Uddin, 2010), its abnormality among people with PTSD has also been reported. Tursich et al. (2015) showed that connectivity between the posterior insula and the salience network was negatively correlated with PTSD hyperarousal symptom severity. Zhang et al. (2016) reported decreased connectivity between the right posterior insula and the left inferior parietal lobe and the postcentral

gyrus in PTSD. The VC group had increased insula connectivity that was opposite to this abnormality in PTSD so that this connectivity alteration in the VC group might be considered an adaptive change. This connectivity was normalized after the training. The change of connectivity in the posterior insula region with neurofeedback training was also reported in other rtfMRI-nf studies. Scheinost et al. (2013) performed rtfMRI-nf training for subjects with significant contamination anxiety to reduce orbitofrontal cortex activation while viewing a contamination-related image. They found reduced connectivity in the bilateral mid and posterior insula after training. Nicholson et al. (2017) trained PTSD patients to reduce amygdala activity during a symptom provocation task and found a negative correlation between bilateral insula activation and state dissociation scores at a transfer run. These indicated that mid and posterior insula regions are not specifically representing proprioceptive internal stimulation, but may also be responsive to emotional and cognitive tasks. As the decrease in left insula connectivity was also seen for the PTSD-sham group (Fig. 3B), this change might not be specifically associated with the neurofeedback signal but a general effect of emotion elicitation training. Although the implication of normalizing insula hyperconnectivity for the VC group is not clear yet, it is important that no exacerbation of PTSD symptoms was observed for the VC participants and even a correlated symptom reduction was seen for the PTSD-sham group (Fig. 3B).

Several limitations in the study merit comment. The number of PTSD-ctrl participants who completed the training sessions was small compared to the PTSD-exp group. While we observed significant symptom reductions only for the PTSD-exp group, the non-significant result for the PTSD-ctrl could be due to its small sample size. Despite random assignment, we also found large baseline differences between the PTSD-exp and the PTSD-ctrl groups in connectivity (e.g. Fig. 3B). Due to these limitations, inferences regarding the specificity of training effects resulting from left amygdala-focused neurofeedback remain tentative. We also did not consider individual variability of training success in the training sessions for the resting-state analysis. Including such variability might improve the sensitivity of

the analysis to detect the effect of training on resting-state connectivity. We note, however, that since the treatment effect could be associated with brain regions other than the neurofeedback target region, training success might not be defined only by the regulation of the feedback target region.

We should also note limited sensitivity of the MDMR analysis. While the ROI analysis for left amygdala connectivity detected significant hypoconnectivity for PTSD at baseline, this was not detected in the MDMR analysis. Also, significant connectivity changes that were detected when we focused on abnormal connectivities at baseline were not detected by the longitudinal MDMR. These dissociations suggest limited sensitivity of the MDMR analysis. This was partly due to a conservative statistical thresholding for whole-brain multiple testing correction. Limited sensitivity was also due to an MDMR analysis mechanism. The MDMR evaluates between-subject distance of connectivity maps and this distance measure could be relatively insensitive to connectivity change between small regions because it summarizes the differences in a large dimensional connectivity map into one measure. The distance measure is also insensitive to how connectivity maps differ so that the same distance could be derived from different changes in connectivity patterns. These limitations could explain the dissociation between the results of ROI-based analysis and MDMR analysis. We need to note that a non-significant result of MDMR should not be interpreted as strong evidence of a negative finding.

5. Conclusions

The effect of rtfMRI-nf training to increase left amygdala activity with positive memory retrieval on resting-state functional connectivity was not restricted to the feedback target region, but also observed in multiple connectivities that were associated with emotion regulation and memory retrieval, including the lateral prefrontal cortex, SMA, dACC, precuneus, and posterior insula regions. A connectome-wide approach using MDMR enables exploratory analysis of connectivity. Despite the limited sensitivity of MDMR, this approach is promising for connectome-wide investigation of training effects on brain functional connectivity.

PTSD patients showed significant symptom reduction after the training that suggests potential utility of amygdala neurofeedback training using positive emotion enhancement techniques.

Interestingly, the symptom reduction did not appear due to a connectivity change in the amygdala, but rather connectivities between the SMA and dACC and between the precuneus and the left anterior frontal region. This suggests neurofeedback effects may be due to a larger brain network than only the targeted region.

The connectivity changes observed in this study might involve correcting emotion representation and memory retrieval. Such an effect could be promoted by positive emotion enhancement training rather than suppressing or reappraising negative emotions. Many rtfMRI-nf treatment studies have focused on suppressing abnormal activity (Gerin et al., 2016; Hamilton et al., 2016; Linden et al., 2012; Nicholson et al., 2017; Paret et al., 2016b; Scheinost et al., 2013; Zilverstand et al., 2015). However, promoting positive emotional experience might help correct abnormal emotion representation and could have the same, if not more of, a therapeutic effect in treating the biological underpinnings of dysregulated emotion and mood disorder symptoms (Young et al., 2017a; Young et al., 2017b). Future development of rtfMRI-nf training methods may benefit from further testing of training approaches that promote healthy emotional brain responses rather than suppress abnormal responses.

Acknowledgement

This research was supported by W81XWH-12-1-0697 award from the U.S. Department of Defense, the Laureate Institute for Brain Research (LIBR), and the William K. Warren Foundation. The data of non-trauma exposed healthy males were provided by NIMH/NIH grant R01 MH098099. The funding agencies were not involved in the design of experiment, data collection and analysis, interpretation of results and preparation and submission of the manuscript. The authors thank all LIBR staff members, Matthew Meyer, M.D., and William Yates, M.D. for conducting psychiatric interviews, Tim Collins, Lisa Kinyon, and Megan Cole for administering clinical interviews and assessments, and Julie Owen, Julie Crawford, Leslie Walker, and Tressia Lewis for helping with MRI scanning. A part of this study was presented at 2017 annual meeting of the International Society for Magnetic Resonance in Medicine and at 2017 annual meeting of the Organization of Human Brain Mapping. The authors declare that they have no conflict of financial interest.

References

- Anderson, M.J., 2001. A new method for non - parametric multivariate analysis of variance. *Austral ecology* 26, 32-46.
- Avants, B.B., Epstein, C.L., Grossman, M., Gee, J.C., 2008. Symmetric diffeomorphic image registration with cross-correlation: evaluating automated labeling of elderly and neurodegenerative brain. *Med Image Anal* 12, 26-41.
- Birn, R.M., Smith, M.A., Jones, T.B., Bandettini, P.A., 2008. The respiration response function: the temporal dynamics of fMRI signal fluctuations related to changes in respiration. *Neuroimage* 40, 644-654.
- Blake, D., Weathers, F., Nagy, L., Kaloupek, D., Charney, D., Keane, T., 1995. Clinician-Administered PTSD Scale for DSM-IV (CAPS-DX). National Center for Posttraumatic Stress Disorder, Behavioral Science Division, Boston VA Medical Center, Boston, MA.
- Bodurka, J., Bandettini, P.A., 2008. Real-time software for monitoring MRI scanner operation. 14th Annual Meeting of the Organization for Human Brain Mapping, Melbourne, Australia, p. S85.
- Bonini, F., Burle, B., Liegeois-Chauvel, C., Regis, J., Chauvel, P., Vidal, F., 2014. Action monitoring and medial frontal cortex: leading role of supplementary motor area. *Science* 343, 888-891.
- Brewin, C.R., Gregory, J.D., Lipton, M., Burgess, N., 2010. Intrusive images in psychological disorders: characteristics, neural mechanisms, and treatment implications. *Psychol Rev* 117, 210-232.
- Brown, V.M., LaBar, K.S., Haswell, C.C., Gold, A.L., McCarthy, G., Morey, R.A., 2014. Altered resting-state functional connectivity of basolateral and centromedial amygdala complexes in posttraumatic stress disorder. *Neuropsychopharmacology* 39, 351-359.
- Buhle, J.T., Silvers, J.A., Wager, T.D., Lopez, R., Onyemekwu, C., Kober, H., Weber, J., Ochsner, K.N., 2014. Cognitive reappraisal of emotion: a meta-analysis of human neuroimaging studies. *Cereb Cortex* 24, 2981-2990.
- Cox, R.W., Chen, G., Glen, D.R., Reynolds, R.C., Taylor, P.A., 2017. FMRI Clustering in AFNI: False-Positive Rates Redux. *Brain Connect* 7, 152-171.

- Craig, A.D., 2003. Interoception: the sense of the physiological condition of the body. *Curr Opin Neurobiol* 13, 500-505.
- Cwik, J.C., Sartory, G., Nuyken, M., Schürholt, B., Seitz, R.J., 2016. Posterior and prefrontal contributions to the development posttraumatic stress disorder symptom severity: an fMRI study of symptom provocation in acute stress disorder. *Eur Arch Psychiatry Clin Neurosci*, 1-11.
- deCharms, R.C., Maeda, F., Glover, G.H., Ludlow, D., Pauly, J.M., Soneji, D., Gabrieli, J.D., Mackey, S.C., 2005. Control over brain activation and pain learned by using real-time functional MRI. *Proc Natl Acad Sci U S A* 102, 18626-18631.
- Eickhoff, S.B., Stephan, K.E., Mohlberg, H., Grefkes, C., Fink, G.R., Amunts, K., Zilles, K., 2005. A new SPM toolbox for combining probabilistic cytoarchitectonic maps and functional imaging data. *Neuroimage* 25, 1325-1335.
- Eklund, A., Nichols, T.E., Knutsson, H., 2016. Cluster failure: Why fMRI inferences for spatial extent have inflated false-positive rates. *Proc Natl Acad Sci U S A* 113, 7900-7905.
- Ellard, K.K., Barlow, D.H., Whitfield-Gabrieli, S., Gabrieli, J.D., Deckersbach, T., 2017. Neural Correlates of Emotion Acceptance Versus Worry or Suppression in Generalized Anxiety Disorder. *Soc Cogn Affect Neurosci*.
- Emmert, K., Kopel, R., Sulzer, J., Brühl, A.B., Berman, B.D., Linden, D.E.J., Horovitz, S.G., Breimhorst, M., Caria, A., Frank, S., Johnston, S., Long, Z., Paret, C., Robineau, F., Veit, R., Bartsch, A., Beckmann, C.F., Van De Ville, D., Haller, S., 2016. Meta-analysis of real-time fMRI neurofeedback studies using individual participant data: How is brain regulation mediated? *Neuroimage* 124, Part A, 806-812.
- Etkin, A., Egner, T., Kalisch, R., 2011. Emotional processing in anterior cingulate and medial prefrontal cortex. *Trends Cogn Sci* 15, 85-93.
- Etkin, A., Wager, T.D., 2007. Functional neuroimaging of anxiety: a meta-analysis of emotional processing in PTSD, social anxiety disorder, and specific phobia. *Am J Psychiatry* 164, 1476-1488.

- Fonzo, G.A., Goodkind, M.S., Oathes, D.J., Zaiko, Y.V., Harvey, M., Peng, K.K., Weiss, M.E., Thompson, A.L., Zack, S.E., Lindley, S.E., Arnow, B.A., Jo, B., Gross, J.J., Rothbaum, B.O., Etkin, A., 2017. PTSD Psychotherapy Outcome Predicted by Brain Activation During Emotional Reactivity and Regulation. *Am J Psychiatry*, appiajp201716091072.
- Fonzo, G.A., Simmons, A.N., Thorp, S.R., Norman, S.B., Paulus, M.P., Stein, M.B., 2010. Exaggerated and disconnected insular-amygdalar blood oxygenation level-dependent response to threat-related emotional faces in women with intimate-partner violence posttraumatic stress disorder. *Biological Psychiatry* 68, 433-441.
- Frank, D.W., Dewitt, M., Hudgens-Haney, M., Schaeffer, D.J., Ball, B.H., Schwarz, N.F., Hussein, A.A., Smart, L.M., Sabatinelli, D., 2014. Emotion regulation: quantitative meta-analysis of functional activation and deactivation. *Neurosci Biobehav Rev* 45, 202-211.
- Friston, K., 1994. Functional and effective connectivity in neuroimaging: A synthesis. *Hum. Brain Mapp.* 2, 56-78.
- Gerin, M.I., Fichtenholtz, H.P., Roy, A., Walsh, C.J., Krystal, J.H., Southwick, S., Hampson, M.P., 2016. Real-time fMRI neurofeedback with war veterans with chronic PTSD: a feasibility study. *Front Psychiatry* 7, 111.
- Glover, G.H., Li, T.Q., Ress, D., 2000. Image-based method for retrospective correction of physiological motion effects in fMRI: RETROICOR. *Magn Reson Med* 44, 162-167.
- Haller, S., Birbaumer, N., Veit, R., 2010. Real-time fMRI feedback training may improve chronic tinnitus. *Eur Radiol* 20, 696-703.
- Hamilton, J.P., Glover, G.H., Bagarinao, E., Chang, C., Mackey, S., Sacchet, M.D., Gotlib, I.H., 2016. Effects of salience-network-node neurofeedback training on affective biases in major depressive disorder. *Psychiatry Res* 249, 91-96.
- Hamilton, M., Schutte, N., Malouff, J., 1976. Hamilton anxiety scale (HAMA). *Sourcebook of Adult Assessment: Applied Clinical Psychology*, 154-157.
- Hartwell, K.J., Hanlon, C.A., Li, X., Borekardt, J.J., Canterberry, M., Prisciandaro, J.J., Moran-Santa Maria, M.M., LeMatty, T., George, M.S., Brady, K.T., 2016. Individualized real-time fMRI

neurofeedback to attenuate craving in nicotine-dependent smokers. *J Psychiatry Neurosci* 41, 48-55.

Hayes, J.P., Hayes, S.M., Mikedis, A.M., 2012. Quantitative meta-analysis of neural activity in posttraumatic stress disorder. *Biol Mood Anxiety Disord* 2, 1-13.

Jin, C., Qi, R., Yin, Y., Hu, X., Duan, L., Xu, Q., Zhang, Z., Zhong, Y., Feng, B., Xiang, H., Gong, Q., Liu, Y., Lu, G., Li, L., 2014. Abnormalities in whole-brain functional connectivity observed in treatment-naïve post-traumatic stress disorder patients following an earthquake. *Psychol Med* 44, 1927-1936.

Jo, H.J., Saad, Z.S., Simmons, W.K., Milbury, L.A., Cox, R.W., 2010. Mapping sources of correlation in resting state fMRI, with artifact detection and removal. *Neuroimage* 52, 571-582.

Kim, J., Zhang, X., Muralidhar, S., LeBlanc, S.A., Tonegawa, S., 2017. Basolateral to Central Amygdala Neural Circuits for Appetitive Behaviors. *Neuron* 93, 1464-1479 e1465.

Kluetsch, R.C., Ros, T., Theberge, J., Frewen, P.A., Calhoun, V.D., Schmahl, C., Jetly, R., Lanius, R.A., 2014. Plastic modulation of PTSD resting-state networks and subjective wellbeing by EEG neurofeedback. *Acta Psychiatr Scand* 130, 123-136.

Koch, S.B., van Zuiden, M., Nawijn, L., Frijling, J.L., Veltman, D.J., Olff, M., 2016. Aberrant Resting-State Brain Activity in Posttraumatic Stress Disorder: A Meta-Analysis and Systematic Review. *Depress Anxiety*.

Kohn, N., Eickhoff, S.B., Scheller, M., Laird, A.R., Fox, P.T., Habel, U., 2014. Neural network of cognitive emotion regulation--an ALE meta-analysis and MACM analysis. *Neuroimage* 87, 345-355.

Kopel, R., Emmert, K., Scharnowski, F., Haller, S., Ville, D.V.D., 2016. Distributed patterns of brain activity underlying real-time fMRI neurofeedback training. *IEEE Transactions on biomedical engineering* PP, 1-1.

Lanius, R.A., Bluhm, R., Lanius, U., Pain, C., 2006. A review of neuroimaging studies in PTSD: heterogeneity of response to symptom provocation. *J Psychiatr Res* 40, 709-729.

Lenth, R.V., 2016. Least-squares means: the R package lsmeans. *J Stat Softw* 69, 1-33.

- Linden, D.E.J., Habes, I., Johnston, S.J., Linden, S., Tatineni, R., Subramanian, L., Sorger, B., Healy, D., Goebel, R., 2012. Real-Time Self-Regulation of Emotion Networks in Patients with Depression. *PLoS ONE* 7, e38115.
- Lindquist, K.A., Satpute, A.B., Wager, T.D., Weber, J., Barrett, L.F., 2016. The Brain Basis of Positive and Negative Affect: Evidence from a Meta-Analysis of the Human Neuroimaging Literature. *Cereb Cortex* 26, 1910-1922.
- Mandel, J., 1982. Use of the Singular Value Decomposition in Regression Analysis. *The American Statistician* 36, 15-24.
- Menon, V., Uddin, L.Q., 2010. Saliency, switching, attention and control: a network model of insula function. *Brain Struct Funct* 214, 655-667.
- Misaki, M., Phillips, R., Zotev, V., Wong, C.K., Wurfel, B.E., Krueger, F., Feldner, M., Bodurka, J., under review. Connectome-wide investigation of altered resting-state functional connectivity in war veterans with and without posttraumatic stress disorder.
- Misaki, M., Suzuki, H., Savitz, J., Drevets, W.C., Bodurka, J., 2016. Individual Variations in Nucleus Accumbens Responses Associated with Major Depressive Disorder Symptoms. *Sci Rep* 6, 21227.
- Montgomery, S.A., Åsberg, M., 1979. A new depression scale designed to be sensitive to change. *Br J Psychiatry* 134, 382-389.
- Morey, R.A., Petty, C.M., Cooper, D.A., Labar, K.S., McCarthy, G., 2008. Neural systems for executive and emotional processing are modulated by symptoms of posttraumatic stress disorder in Iraq War veterans. *Psychiatry Res* 162, 59-72.
- Nicholson, A.A., Rabellino, D., Densmore, M., Frewen, P.A., Paret, C., Kluetsch, R., Schmahl, C., Theberge, J., Neufeld, R.W., McKinnon, M.C., Reiss, J., Jetly, R., Lanius, R.A., 2017. The neurobiology of emotion regulation in posttraumatic stress disorder: Amygdala downregulation via real-time fMRI neurofeedback. *Hum Brain Mapp* 38, 541-560.
- Nicholson, A.A., Ros, T., Frewen, P.A., Densmore, M., Theberge, J., Kluetsch, R.C., Jetly, R., Lanius, R.A., 2016. Alpha oscillation neurofeedback modulates amygdala complex connectivity and arousal in posttraumatic stress disorder. *Neuroimage Clin* 12, 506-516.

- Ochsner, K.N., Gross, J.J., 2005. The cognitive control of emotion. *Trends Cogn Sci* 9, 242-249.
- Ochsner, K.N., Silvers, J.A., Buhle, J.T., 2012. Functional imaging studies of emotion regulation: a synthetic review and evolving model of the cognitive control of emotion. *Ann N Y Acad Sci* 1251, E1-24.
- Paret, C., Kluetsch, R., Zaehring, J., Ruf, M., Demirakca, T., Bohus, M., Ende, G., Schmahl, C., 2016a. Alterations of amygdala-prefrontal connectivity with real-time fMRI neurofeedback in BPD patients. *Soc Cogn Affect Neurosci* 11, 952-960.
- Paret, C., Ruf, M., Gerchen, M.F., Kluetsch, R., Demirakca, T., Jungkunz, M., Bertsch, K., Schmahl, C., Ende, G., 2016b. fMRI neurofeedback of amygdala response to aversive stimuli enhances prefrontal-limbic brain connectivity. *Neuroimage* 125, 182-188.
- Patel, R., Spreng, R.N., Shin, L.M., Girard, T.A., 2012. Neurocircuitry models of posttraumatic stress disorder and beyond: a meta-analysis of functional neuroimaging studies. *Neurosci Biobehav Rev* 36, 2130-2142.
- Pinheiro, J., Bates, D., DebRoy, S., Sarkar, D., R Core Team, 2017. nlme: Linear and Nonlinear Mixed Effects Models. R package version 3.1-131.
- Pitman, R.K., Rasmusson, A.M., Koenen, K.C., Shin, L.M., Orr, S.P., Gilbertson, M.W., Milad, M.R., Liberzon, I., 2012. Biological studies of post-traumatic stress disorder. *Nat Rev Neurosci* 13, 769-787.
- Power, J.D., Schlaggar, B.L., Petersen, S.E., 2015. Recent progress and outstanding issues in motion correction in resting state fMRI. *Neuroimage* 105, 536-551.
- R Core Team, 2017. R: A Language and Environment for Statistical Computing. R Foundation for Statistical Computing, Vienna, Austria. URL <https://www.r-project.org/>.
- Rabellino, D., Tursich, M., Frewen, P., Daniels, J., Densmore, M., Théberge, J., Lanius, R., 2015. Intrinsic Connectivity Networks in post - traumatic stress disorder during sub - and supraliminal processing of threat - related stimuli. *Acta Psychiatr Scand* 132, 365-378.

- Rauch, S.L., Whalen, P.J., Shin, L.M., McInerney, S.C., Macklin, M.L., Lasko, N.B., Orr, S.P., Pitman, R.K., 2000. Exaggerated amygdala response to masked facial stimuli in posttraumatic stress disorder: a functional MRI study. *Biological Psychiatry* 47, 769-776.
- Ruiz, S., Lee, S., Soekadar, S.R., Caria, A., Veit, R., Kircher, T., Birbaumer, N., Sitaram, R., 2011. Acquired self-control of insula cortex modulates emotion recognition and brain network connectivity in schizophrenia. *Hum Brain Mapp*.
- Satterthwaite, T.D., Cook, P.A., Bruce, S.E., Conway, C., Mikkelsen, E., Satchell, E., Vandekar, S.N., Durbin, T., Shinohara, R.T., Sheline, Y.I., 2015. Dimensional depression severity in women with major depression and post-traumatic stress disorder correlates with fronto-amygdalar hypoconnectivity. *Mol Psychiatry*.
- Scheinost, D., Stoica, T., Saksa, J., Papademetris, X., Constable, R.T., Pittenger, C., Hampson, M., 2013. Orbitofrontal cortex neurofeedback produces lasting changes in contamination anxiety and resting-state connectivity. *Transl Psychiatry* 3, e250.
- Shehzad, Z., Kelly, C., Reiss, P.T., Cameron Craddock, R., Emerson, J.W., McMahon, K., Copland, D.A., Castellanos, F.X., Milham, M.P., 2014. A multivariate distance-based analytic framework for connectome-wide association studies. *Neuroimage* 93 Pt 1, 74-94.
- Shin, L.M., Rauch, S.L., Pitman, R.K., 2006. Amygdala, medial prefrontal cortex, and hippocampal function in PTSD. *Ann N Y Acad Sci* 1071, 67-79.
- Simmons, A.N., Matthews, S.C., Strigo, I.A., Baker, D.G., Donovan, H.K., Motezadi, A., Stein, M.B., Paulus, M.P., 2011. Altered amygdala activation during face processing in Iraqi and Afghanistani war veterans. *Biol Mood Anxiety Disord* 1, 6.
- St Jacques, P.L., Botzung, A., Miles, A., Rubin, D.C., 2011. Functional neuroimaging of emotionally intense autobiographical memories in post-traumatic stress disorder. *J Psychiatr Res* 45, 630-637.
- Subramanian, L., Hindle, J.V., Johnston, S., Roberts, M.V., Husain, M., Goebel, R., Linden, D., 2011. Real-time functional magnetic resonance imaging neurofeedback for treatment of Parkinson's disease. *J Neurosci* 31, 16309-16317.

- Thibault, R.T., Lifshitz, M., Raz, A., 2016. The self-regulating brain and neurofeedback: Experimental science and clinical promise. *Cortex* 74, 247-261.
- Tursich, M., Ros, T., Frewen, P.A., Kluetsch, R.C., Calhoun, V.D., Lanius, R.A., 2015. Distinct intrinsic network connectivity patterns of post-traumatic stress disorder symptom clusters. *Acta Psychiatrica Scand* 132, 29-38.
- Vogt, B.A., Laureys, S., 2005. Posterior cingulate, precuneal and retrosplenial cortices: cytology and components of the neural network correlates of consciousness. *Prog Brain Res* 150, 205-217.
- Wang, T., Liu, J., Zhang, J., Zhan, W., Li, L., Wu, M., Huang, H., Zhu, H., Kemp, G.J., Gong, Q., 2016. Altered resting-state functional activity in posttraumatic stress disorder: A quantitative meta-analysis. *Sci Rep* 6, 27131.
- Weathers, F.W., Keane, T.M., Davidson, J.R., 2001. Clinician-administered PTSD scale: a review of the first ten years of research. *Depress Anxiety* 13, 132-156.
- Weathers, F.W., Litz, B.T., Herman, D.S., Huska, J.A., Keane, T.M., 1993. The PTSD Checklist (PCL): Reliability, validity, and diagnostic utility. annual convention of the international society for traumatic stress studies, San Antonio, TX. San Antonio, TX.
- Weiskopf, N., 2012. Real-time fMRI and its application to neurofeedback. *Neuroimage* 62, 682-692.
- Whalley, M.G., Kroes, M.C., Huntley, Z., Rugg, M.D., Davis, S.W., Brewin, C.R., 2013. An fMRI investigation of posttraumatic flashbacks. *Brain Cogn* 81, 151-159.
- Winkler, A.M., Ridgway, G.R., Webster, M.A., Smith, S.M., Nichols, T.E., 2014. Permutation inference for the general linear model. *Neuroimage* 92, 381-397.
- Yan, X., Brown, A.D., Lazar, M., Cressman, V.L., Henn-Haase, C., Neylan, T.C., Shalev, A., Wolkowitz, O.M., Hamilton, S.P., Yehuda, R., 2013. Spontaneous brain activity in combat related PTSD. *Neuroscience Letters* 547, 1-5.
- Young, K.D., Misaki, M., Harmer, C.J., Victor, T., Zotev, V., Phillips, R., Siegle, G.J., Drevets, W.C., Bodurka, J., 2017a. Real-Time Functional Magnetic Resonance Imaging Amygdala Neurofeedback Changes Positive Information Processing in Major Depressive Disorder. *Biol Psychiatry*.

Real-time fMRI amygdala neurofeedback positive emotional training normalized resting-state functional connectivity in combat veterans with and without PTSD: a connectome-wide investigation by Misaki et al.

Supplementary materials

Table of Contents

Veteran participants	2
Supplementary table S1	3
Schedules of real-time fMRI neurofeedback (rtfMRI-nf) training	4
Visit 1: Consent and Baseline	4
Visits 2 and 6: Pre-Neurofeedback MRI, fMRI, and Behavioral Tasks	4
Visits 3–5: Real-Time fMRI Neurofeedback Training	5
Visit 7: Follow-Up	5
Compensation	5
Baseline MDMR analysis to identify abnormal resting-state functional connectivity	6
Supplementary table S2	8
Supplementary table S3	9
References	10

Veteran participants

Participants were adult (age 18 to 55 years) male U.S. military combat veterans. Veterans, largely from recent conflicts including OEF/OIF/OND, were recruited from eastern and central Oklahoma as well as northwest Arkansas. Potential subjects who called the Laureate Institute for Brain Research (LIBR) in response to advertisements and flyers underwent a brief telephone screen. During the telephone screen, basic demographic information was collected and an MRI safety screen was performed to determine whether the potential subject was eligible for MRI imaging. In addition, a brief medical questionnaire was administered to rule out history of any major medical conditions, such as stroke or head trauma, that would make the potential subject ineligible for studies at the LIBR. Individuals who are deemed eligible based on the telephone screen were then scheduled for an in-person screening evaluation.

Inclusion Criteria. Subjects (i) had to be able to give written informed consent prior to participation and (ii) have not had taken psychotropic medication within 3 weeks, or 8 weeks for fluoxetine (note that people will not be discontinued from effective medication for purposes of the study). Many psychotropic medications have been shown to alter the reactivity of the amygdala to a variety of emotional stimuli, and thus would introduce potential confounds in the fMRI data.

Exclusion Criteria. Volunteers were excluded from participating for the following reasons: (i) a clinically significant or unstable cardiovascular, pulmonary, endocrine, neurological, or gastrointestinal illness or unstable medical disorder; (ii) meeting DSM-IV criteria for substance abuse or substance dependence (other than nicotine) within 3 months prior to screening; (iii) endorsing suicidal intent or a suicide attempt within the preceding three months; (iv) current or past history of schizophrenia, schizoaffective disorder, bipolar disorder, or dementia; (v) moderate to severe traumatic brain injury (history of traumatic brain injury was identified via the Brief Traumatic Brain Injury Screen and, as recommended by the Defense and Veterans Brain Injury Center, and followed by a clinician interview to validate the screen and determine if the injury was mild, defined as loss of consciousness or altered mental status, which did not result in exclusion from the study, or moderate to severe, which did result in exclusion from the study) and (vi) inability to complete an MRI scan due to claustrophobia or general MRI exclusions (e.g. shrapnel inside body). Subjects with vision and/or hearing loss severe enough to interfere with testing and subjects not fluent in English were also excluded.

Supplementary table S1. Session schedule

Visit	1. Consent	2. Pre-NF	3. rtfMRI-nf 1	4. rtfMRI-nf 2	5. rtfMRI-nf 3	6. Post-NF	7. Follow-Up
Clinical ratings	CAPS	HDRS, MADRS, HAM-A	HDRS, MADRS, HAM-A	HDRS, MADRS, HAM-A	HDRS, MADRS, HAM-A	HDRS, MADRS, HAM-A	CAPS
Self-ratings	TAS, EC	PCL-M, SHAPS, VAS, POMS	PCL-M, SHAPS, VAS, POMS	PCL-M, SHAPS, VAS, POMS	PCL-M, SHAPS, VAS, POMS	PCL-M, SHAPS, VAS, POMS	-
MRI	-	High-resolution T1- and T2-weighted structural MRI; fMRI: Rest ×2, ecStroop ×4	Structural MRI; rtfMRI-nf: Rest, Practice, NF ×3, Transfer, Rest	Structural MRI; rtfMRI-nf: Rest, Practice, NF ×3, Transfer, Rest	Structural MRI; rtfMRI-nf: Rest, Practice, NF ×3, Transfer, Rest	High-resolution T1- and T2-weighted structural MRI; fMRI: Rest ×2, ecStroop ×4	-
Post-scan self-ratings	-	VAS, POMS	VAS, POMS, NF debrief	VAS, POMS, NF debrief	VAS, POMS, NF debrief	VAS, POMS	-

Note: CAPS=Clinician-Administered PTSD Scale, EC=Emotional Contagion Scale, ecStroop=Emotional Counting Stroop task, HAM-A=Hamilton Anxiety Rating Scale, HDRS=Hamilton Depression Rating Scale, MADRS= Montgomery-Åsberg Depression Rating Scale, NF=neurofeedback, PCL-M=PTSD Checklist military version, POMS=Profile of Mood States, SDIP=Script-Driven Imagery Procedure, SHAPS=Snaith-Hamilton Pleasure Scale, TAS=Toronto Alexithymia Scale, VAS=Visual Analog Scales

Schedules of real-time fMRI neurofeedback (rtfMRI-nf) training

Visit 1: Consent and Baseline. See Table S1 for an overview of the assessment schedule. After obtaining written informed consent from the subject, a clinician administered the CAPS to measure PTSD symptom severity at baseline. The subjects also completed two questionnaires, the Toronto Alexithymia and Emotional Contagion (TAS and ECS) scales, as well as a questionnaire to select relevant positively and negatively valenced words that were used in an emotional counting Stroop (ecStroop) task. Finally, a clinician worked with the subject to develop personalized scripts for one neutral and one traumatic memory to be used in a script-driven imagery procedure.

Visits 2 and 6: Pre-Neurofeedback MRI, fMRI, and Behavioral Tasks. First, a clinician completed ratings of the subjects' depression and anxiety symptoms using the HDRS, MADRS, and HAM-D. Then the subject completed questionnaires measuring PTSD and anhedonia symptoms as well as mood with the PCL-M, SHAMS, VAS, and POMS. On Visit 2 (Pre-Neurofeedback), subjects practiced performing the ecStroop task in our mock scanner. The mock scanner is a scale model of an MRI scanner that includes a moving table, a mock head coil with a mirror and projector system similar to the one in our MRI environment, and a sound system capable of mimicking the sound of an MRI sequence. The mock scanner was used to allow subjects to acclimate themselves to the physical, visual, and aural restrictions of the scanner outside of the strong magnetic field.

On both visits 2 and 6, subjects underwent high-resolution structural MRI scans, two eyes-open resting fMRI scans, and four runs of the ecStroop task. In this task the subject was asked to count the number of times a word appeared on the screen. Each word was classified by valence: negative, positive, or neutral. During visit 1, the subjects rated the relevance of a list of negatively valenced words and a list of positively valenced words. Only the 80 most relevant negative words and 80 most relevant positive words were used in the task. Each of the positive and negative words was matched with a neutral word for length, concreteness, and frequency of use in the English language. Half of the words were used in the pre-neurofeedback session and the other half in the post-neurofeedback session (i.e., 40 negative words, 40 positive words, and 80 neutral words per session). The neutral words corresponding to these negative and positive words were used in the same session. Within each session there were four task runs, each run was composed of 205 trials, each trial lasted 2000 ms, and thus each run lasted 6 minutes 50 seconds. Forty-five of the trials were fixation trials; for those trials the subject was presented with a fixation cross for 2000ms. The first five trials of each run were always fixation trials to allow the fMRI signal to reach steady state. The other 40 fixation trials were interspersed with the 160 counting trials. For the first 500ms of a counting trial the subject was presented with a fixation cross. For the following 1500ms the subject was presented with a word repeated one, two, three, or four times. The subject indicated how many words he counted on the screen using a four-button response device accessible by his dominant hand. Each of the 40 negative, 40 positive, and 80 neutral words were presented once in each of the four runs, and each word was repeated a different number of times in each run. Trial order was determined using the FreeSurfer sequence optimizer optseq2.

Following the MRI session, subjects again completed the POMS and the VAS before completing a well-established script-driven imagery procedure (SDIP) (Badour and Feldner, 2013; Lang et al., 1983; Pitman et al., 1987). During the SDIP, participants' respiration, heart rate, and skin conductance were recorded by pneumatic belt around the abdomen, pulse oximeter on the finger, and two electrodermal activity electrodes placed the first and second fingers, respectively, using a BIOPAC MP150 (BIOPAC Systems, Inc.). An experimenter worked with each participant to generate individualized scripts of an affectively neutral event (e.g., mowing the lawn) and a script describing the index traumatic event identified during the CAPS. As done previously (e.g., Pitman et al., 1987), a checklist of specific bodily sensations (e.g., racing heart) was administered to participants during script generation to assist in identifying sensations present during the event and incorporating them into the scripts. Participants were also asked to include sensory details of the experience (e.g., sights, sounds, smells). A male experimenter then used this information to create an individualized 30s audio script for each event. The SDIP began with a 10min imaginal rehearsal, during which a recorded male voice instructed the subject to imagine a series of scenes as vividly as

possible. The scenes included positive, neutral, and negative narratives. There was then a five-minute resting baseline measurement. Following the resting baseline, the subject filled in the POMS and VAS. The subject then listened to their personalized neutral and traumatic event scripts, respectively. These 30s scripts were recorded by the same male speaker from the imaginal rehearsal in a neutral tone of voice describing, in the second person present tense, the neutral and traumatic memories previously described by the subject. Following each script, the subject filled out the RSDI, POMS, and VAS.

Visits 3–5: Real-Time fMRI Neurofeedback Training. On each of the real-time fMRI neurofeedback (rtfMRI-nf) training visits, a clinician completed ratings of subjects' depression and anxiety symptoms using the HDRS, MADRS, and HAM-D. Then, subjects completed questionnaires measuring PTSD and anhedonia symptoms as well as mood with the PCL-M, SHAMS, VAS, and POMS. Next, subjects completed the rtfMRI-nf with passive 32-channel EEG recordings. During the rtfMRI-nf session subjects will undergo a Rest run, a Practice run, 3 training runs (Runs 1–3) followed by a 'Transfer' run, and a second Rest run. Each run lasted 8-min, 40-sec (Fig. 2). During the first and the last Rest runs (RE), a resting state paradigm was employed; subjects were instructed to clear their minds and not think of anything in particular while fixating on the display screen. All other runs consisted of a series of 40s blocks of Rest, Count, and Happy Memories tasks. During the Rest condition the subjects were instructed to clear their minds and try to not think of their happy memories. The Rest blocks were used as the baseline for the neurofeedback signal. During the Count conditions subjects were instructed to mentally count backward from 300 by a given integer. This second control condition was used to allow additional time for the amygdala to deactivate. During the Happy Memories condition subjects were instructed to recall positive autobiographical memories that were specific and vivid while trying control a dynamic red neurofeedback bar. The subjects were also shown a static blue bar that served as a target level. For subjects in the experimental and trauma control groups, the neurofeedback signal was derived from activity in subjects' left amygdala, while for subjects in the control group (CG), the signal was derived from activity in the left HIPS, a region putatively uninvolved in emotion regulation. In the Practice run, subjects were instructed to practice recalling three different prepared happy autobiographical memories during the first three Happy Memories conditions and to practice with whichever of the three worked best during the fourth Happy Memories condition. During the subsequent three training runs subjects were instructed to use any positive autobiographical memory that was working well for the task. The target level was raised in a linear fashion across the nf runs (Practice, Runs 1–3) to introduce a linear trend in the targeted connectivity strength across the runs. Finally, during the Transfer run, subjects were instructed to perform the same task as during the neurofeedback training, but no nf information was provided for the blocks of the Happy Memories condition. The Transfer runs allowed for assessment of the transfer of the learned control over neurobiological activity (i.e., whether, after nf training, the training effect generalized to situations where no feedback was available). After the training, subjects completed the VAS, POMS, and a debriefing form about what memories and strategies they used during the neurofeedback.

Visit 7: Follow-Up. During the final follow-up visit, a clinician re-administered the CAPS. Participants also completed questionnaires about their participation in the study to collect information about ways we could improve recruitment and retention of veterans for the study.

Compensation. All subjects received monetary compensation for their time. The compensation rate was \$25 per half hour for time spent in the MRI scanner and time spent preparing the EEG cap. The rate was \$10 per half hour for other activities, including questionnaires, clinical interviews, and the script-driven imagery procedure. As our recruitment catchment area was large and some participants drove hundreds of miles to the LIBR to participate in the multi-visit study, subjects also received \$50 gift cards for a local gas station and convenience store chain on visits 1 and 7.

Baseline MDMR analysis to identify abnormal resting-state functional connectivity

Multivariate distance matrix regression (MDMR) analysis was applied to investigate resting-state connectivity alteration between PTSD, VC, and NC groups. The analysis procedure and its results have been reported in (Misaki et al., under review). This supplementary material is a reproduction of it.

The processed resting-state fMRI image was downsampled to 4mm^3 voxels. Only the voxels in gray matter regions were extracted from the down-sampled image. This masking resulted in extracting 18,693 voxels that were subject to the MDMR analysis. We followed the procedure introduced in Shehzad et al. (2014) for the MDMR analysis, which is briefly reproduced here. In each voxel, a connectivity map from that voxel to all other voxels was made with Pearson's correlations between signal time-courses of the voxels. The dependent variable of MDMR is a distance matrix of the connectivity maps between subjects. The distance of the maps between subject i and j , (d_{ij}) was calculated with Euclidean distance of Fisher's z-transformed connectivity maps. The MDMR analysis evaluates the association between the distance matrix (dissimilarities of connectivity maps across subjects) and the predictor variables in the design matrix, X , using a pseudo- F value statistic, $F = \frac{\text{tr}(HG)/(m-1)}{\text{tr}[(I-H)G]/(n-m)}$, where $H = X(X^T X)^{-1} X^T$ is the hat matrix that maps response values (G) to the fitted value space, m is the number of columns in X , and tr is the trace of matrix. G is the mean-centered distance matrix as $G = CAC$, where $C = (I - \frac{1}{n} \mathbf{1}\mathbf{1}^T)$, $A = (-\frac{1}{2} d_{ij}^2)$, n is the number of subjects, I is the $n \times n$ identity matrix and $\mathbf{1}$ is a vector of n 1s. In the current study, the design matrix X included two columns of group factors for PTSD and VC, in which 1 indicated PTSD and 0 others, and 1 indicated VC and 0 others, respectively. This coding means that NC group is a reference group and the effects of PTSD and VC relative to NC were evaluated. X also included columns of age and motion size (average FD) as nuisance variables as well as all 1s for the intercept. Individual effect of regressors was estimated using a partial design matrix. Hat matrix with effects of no interest regressors was subtracted from the full hat matrix as $H_I = H - H_N$, where $H_N = X_N(X_N^T X_N)^{-1} X_N^T$, and X_N is a design matrix only with age, motion, and intercept columns. Pseudo- F value for the sum of the effect of interest, namely the main effect of the group difference, was then calculated as $F_I = \frac{\text{tr}(H_I G)/(m_I)}{\text{tr}[(I-H)G]/(n-m)}$, where $m_I (=2)$ is the number of the effect of interest regressors.

Statistical tests for the pseudo- F value were performed with a permutation test. Nuisance regressors in the permutation test need to be handled differently from the regressors of interest because the effect of interest should be evaluated after excluding nuisance effects. We used the Smith procedure (Winkler et al., 2014), in which regressors of interest were orthogonalized with regard to nuisance regressors and then the orthogonalized regressors of interest were permuted randomly. 10,000 random permutations were performed in the analysis.

These procedures were repeated for all voxels as a seed, and pseudo- F values (with respective p -values) were mapped onto the brain to make a statistical parametric map. We used a computationally efficient method introduced by Shehzad et al. (2014), in which evaluations for all voxels of all permutations were performed in one-time matrix multiplication. The MDMR statistical map was thresholded with voxel-wise $p < .005$, and then with cluster-size corrected $p < .05$. Cluster-size corrected p -value was evaluated with the same permutation procedure as the voxel-wise evaluation to avoid an inflated false positive rate (Eklund et al., 2016).

The post-hoc analysis was performed with the original resolution whole-brain functional images (not restricted to gray matter). Seed regions were placed at peak locations of the significant clusters in the MDMR statistical map of the group main effect. Peak coordinates in each significant cluster separated by at least 30mm were extracted. Seed area was a 6mm-radius sphere centered at the peak coordinates of the MDMR statistical map. Average signal time-course of the seed area was used as a reference signal to calculate correlations with other voxels. Fisher's z-transformation was applied to the correlation coefficient to make a connectivity map for each subject. A voxel-wise general linear model analysis was performed for the connectivity map with the same design matrix as the MDMR analysis. t -value maps of each group contrast, PTSD-NC, VC-NC, and PTSD-VC, were

calculated and thresholded with voxel-wise $p < .005$ and cluster-size corrected $p < .016$ for multiple testing of three groups. Cluster-size corrected p -value was evaluated with the permutation test (10,000 permutations) using the Smith procedure (Winkler et al., 2014).

Supplementary table S2 (reproduced from Misaki et al. (under review))

Table S2 includes peak locations and statistical values of post-hoc analyses for connectivity differences between the PTSD and NC groups. Local maximum positions separated by at least 30 mm were extracted from significant clusters. Cluster-size *p*-values were evaluated by permutation test with 10,000 random permutations. L: left, R: right, SMA: supplementary motor area, BA: Brodmann area.

Seed location (MNI, x, y, z mm)	Peak location (MNI, mm)			Brain region	<i>t</i> (PTSD – NC)	Cluster size (2mm ³ voxel)	Cluster-size <i>p</i> -value
	x	y	z				
A. L Parahippocampal (-36, -16, -26)	-34	-44	-22	L Fusiform	-5.658	1216	.0021
	-56	-74	10	L Middle Temporal	-4.149		
	38	-44	-22	R Fusiform	-6.015	976	.0030
	52	-80	-8	R Middle Occipital	-4.693		
	0	-46	14	R Posterior Cingulate	-5.285	513	.0122
B. L SMA (-8, -20, 62)	14	34	20	R Anterior Cingulate	-5.262	735	.0042
	-38	18	6	L Anterior Insula	-4.979	461	.0128
C. L Insula (-44, -8, -6)	18	-40	46	R Middle Cingulate	4.403	527	.0135
D. L Inferior Frontal (-52, 20, 2)	8	-8	52	R SMA	-5.451	1402	.0008
	-32	0	54	L Middle Frontal (BA6)	-4.209		
E. L Middle Frontal (-32, 12, 26)	-30	6	30	L Inferior Frontal (BA44)	-4.649	714	.0068
	-48	6	0	L Frontal Operculum (BA44)	-4.315		
F. L Superior Frontal (-24, 28, 34)	-12	32	34	L Medial Frontal	-5.051	1297	.0018
	-10	-6	46	L Middle Cingulate	-4.311		
	-38	-2	10	L Insula	-5.742	1190	.0022
	-26	26	8	L Anterior Insula	-5.342		
	56	18	8	R Inferior Frontal (BA45)	-5.472	1182	.0022

Supplementary table S3 (reproduced from Misaki et al. (under review))

Table S3 includes peak locations and statistical values of post-hoc analyses of connectivity differences between the VC and NC groups. Local maximum positions separated by at least 30 mm were extracted from significant clusters. Cluster-size *p*-values were evaluated by permutation test with 10,000 random permutations. L: left, R: right.

Seed location (MNI, x, y, z mm)	Peak location (MNI, mm)			Brain region	<i>t</i> (VC-NC)	Cluster size (2mm ³ voxel)	Cluster-size <i>p</i> -value
	x	y	z				
A. R Lingual (4, -68, 2)	10	62	8	R vmPFC	-5.569	628	.0062
B. L Superior Frontal (-20, 48, 18)	4	-62	40	R Precuneus	-4.948	1151	.0016
	54	-66	38	R Inferior Parietal	-4.903	521	.0161
C. L Insula (-44, -8, -6)	46	-18	4	R Insula	5.333	768	.0057
	24	-58	-2	R Lingual	5.623	564	.0127
	14	-84	24	R Cuneus	4.280		
D. L Middle Frontal (-24, 0, 46)	-44	-22	58	L Postcentral	-5.024	577	.0089
E. R Transverse Temporal (56, -24, 10)	6	-64	26	R Precuneus	-4.783	551	.0152
F. R Insula (44, -8, -2)	64	-16	18	R Postcentral	4.992	1561	.0005
	52	22	34	R Middle Frontal	4.862		
	46	-4	-18	R Middle Temporal	4.519		
	20	-64	10	R Calcarine	5.736	611	.0066
	-22	-62	54	L Superior Parietal	4.904	552	.0086
	48	24	10	R Inferior Frontal	4.789	513	.0111
	24	-72	52	R Superior Parietal	4.551	495	.0126
	20	-32	8	R Thalamus	5.728	470	.0143
G. L Superior Temporal (-48, -24, 6)	-4	-54	34	L Precuneus/PCC	-4.292	563	.0147

References

- Badour, C.L., Feldner, M.T., 2013. Trauma-related reactivity and regulation of emotion: associations with posttraumatic stress symptoms. *J Behav Ther Exp Psychiatry* 44, 69-76.
- Eklund, A., Nichols, T.E., Knutsson, H., 2016. Cluster failure: Why fMRI inferences for spatial extent have inflated false-positive rates. *Proc Natl Acad Sci U S A* 113, 7900-7905.
- Lang, P.J., Levin, D.N., Miller, G.A., Kozak, M.J., 1983. Fear behavior, fear imagery, and the psychophysiology of emotion: the problem of affective response integration. *J Abnorm Psychol* 92, 276-306.
- Misaki, M., Phillips, R., Zotev, V., Wong, C.K., Wurfel, B.E., Krueger, F., Feldner, M., Bodurka, J., under review. Connectome-wide investigation of altered resting-state functional connectivity in war veterans with and without posttraumatic stress disorder.
- Pitman, R.K., Orr, S.P., Foa, E.B., de Jong, J.B., Claiborn, J.M., 1987. Psychophysiologic assessment of posttraumatic stress disorder imagery in Vietnam combat veterans. *Arch Gen Psychiatry* 44, 970-975.
- Shehzad, Z., Kelly, C., Reiss, P.T., Cameron Craddock, R., Emerson, J.W., McMahon, K., Copland, D.A., Castellanos, F.X., Milham, M.P., 2014. A multivariate distance-based analytic framework for connectome-wide association studies. *Neuroimage* 93 Pt 1, 74-94.
- Winkler, A.M., Ridgway, G.R., Webster, M.A., Smith, S.M., Nichols, T.E., 2014. Permutation inference for the general linear model. *Neuroimage* 92, 381-397.

1 **Dynamical Hurst Analysis Identifies EEG Channel**

2 **Differences between PTSD and Healthy Controls**

3 Bahareh Rahmani^{1,2,**}, Chung Ki Wong^{3*}, Payam Norouzzadeh^{4*}, Jerzy Bodurka^{3,5}, B. A.
4 McKinney²

5 ¹Mathematics and Computer Science Department, Fontbonne University, Saint Louis, MO, 63105

6 ²Tandy School of Computer Science, University of Tulsa, Tulsa, OK, USA

7 ³Laureate Institute for Brain Research (LIBR), Tulsa, OK, USA

8 ⁴Helmerich Advanced Technology Research Center, Oklahoma State University, Tulsa, Oklahoma, USA

9 ⁵College of Engineering, University of Oklahoma, Tulsa, OK, USA

10

11 *Chung Ki Wong and Payam Norouzzadeh contributed equally to this work.

12

13 ** Corresponding author

14 E-mail: Brahmani@fontbonne.edu

Abstract

We employ a time-dependent Hurst analysis to identify EEG signals that differentiate between healthy controls and combat-related PTSD subjects. The Hurst exponents, calculated using a rescaled range analysis, demonstrate a significant differential response between healthy and PTSD samples which may lead to diagnostic applications. To overcome the non-stationarity of EEG data, we apply an appropriate window length wherein the EEG data displays stationary behavior. We then use the Hurst exponents for each channel as hypothesis test statistics to identify differences between PTSD cases and controls.

Our study included a cohort of 12 subjects with half healthy controls. PTSD cases have bigger Hurst exponent than healthy controls in channel F3. Our results indicate that F3 may be a useful channel for diagnostic applications of Hurst exponents in distinguishing PTSD and healthy subjects.

Keywords: Hurst exponent, EEG, Stationary.

Introduction

EEG (Electroencephalogram) signal measures voltage temporal variations, which reflect brain neuronal electrical activity¹. The EEG signals contain relevant dynamic information about the brain's electrophysiological activity. Thus, prediction and modeling EEG signals is an important area of biological and biomedical research.^{2,3} EEG signals feature non-linear and non-stationary pseudo oscillatory behavior characterizing spontaneous brain oscillations such as alpha waves. To extract important features of EEG for the diagnosis of different diseases, advanced signal processing techniques are required. There are various states and conditions that influence the signals - such as sleep, epilepsy, reflexology, drugs/anesthesia, diabetes, meditation, experiencing emotions, listening to music - as well as artifacts that influence the signals.⁴ Long-term and short-term characteristics of EEG time series have been investigated in biological applications,⁵ and EEG time series have been studied to identify affected regions of the brain in disease, such as epilepsy.⁶

In the current study, EEG was employed to study time-series differences related to post-traumatic stress disorder (PTSD). In a study of the dynamical complexity of EEG time series in 27 PTSD and 14 healthy people. Jeong-Ho Chae et al. (2004) found reduced complexity in channels Fp1, F8, C4, P4, T3, T4, T5, T6 and O1 for PTSD cases.⁷ Another group calculated non-linear independence (NI) values of EEG data of 16 channels corresponding to 18 pairs of PTSD and healthy controls. They showed that, in PTSD patients NI factors increase in channels F3, F7, C3, T5, P3 and decrease in channels F4, C4, P4, and O2.⁸ In five case studies, Rutter (2014) determined diagnosed channels: F3, F4, C3, C4, P3, P4, Fz, Cz, and Pz as the most influenced ones by the disorder⁹.

There have been several studies on the application of Hurst exponent to investigate the EEG signals¹⁰. Hurst exponent is a measure of the long-memory properties of the signals.^{11,12} In this study, we aim to explore the possibility of developing a Hurst exponent-based method for feature selection of channels that may be important for prediction. We hypothesize that the long memory of the EEG signals in the PTSD and healthy control groups differentiate each other. To this end, we investigate the long-memory properties of the EEG data by applying the time dependent Hurst analysis using the rescaled range (R/S) technique.

The manuscript is organized as follow. First, the EEG data are described statistically. Next, the theoretical approach of the Hurst exponent calculation including the R/S analysis method and the importance of stationary data are explained. Finally, the results are presented and discussed.

Material and Methods

EEG data were collected at the Laureate Institute for Brain Research as part of a simultaneous EEG and fMRI study¹³ conducted on individuals with combat-related PTSD and healthy controls. The study research protocol was approved by the Western Institutional Review Board. Human research was conducted according to the principles expressed in the Declaration of Helsinki.

1. Data description

Six PTSD individuals and six healthy controls (mean age = 27 ± 5 years, all male) were involved in this study. For each subject, EEG signals from 31 channels (Fp1, Fp2, F3, F4, C3, C4, P3, P4, O1, O2, F7, F8, T7, T8, P7, P8, Fz, Cz, Pz, Oz, FC1, FC2, CP1, CP2, FC5, FC6, CP5, CP6, TP9, TP10, POz) were recorded with the ground and reference electrodes positioned at AFz and FCz. One channel was placed at subject's back to measure electrocardiogram. The EEG signals were

79 recorded at a sampling rate of 5000 samples/s and a resolution of 0.1 μ V. The EEG preprocessing
80 was carried out in the proprietary software BrainVision Analyzer2 (Brain Products, GmbH). For
81 further analysis we used EEGLAB software (<http://sccn.ucsd.edu/eeglab>^{Ref.a}). The original data is
82 attached in supplementary materials.

83
84 For the EEG preprocessing, MRI gradient artifact and cardioballistic (BCG) artifact were removed
85 using the template subtraction method^{17,18}. After the gradient artifact removal, the EEG data was
86 down sampled to 250 samples/s (4 ms temporal resolution) and low-pass filtered to 40Hz. Residual
87 cardio ballistic artifact, as well as blink and saccade artifacts, were removed using independent
88 component analysis (ICA). PTSD subjects move a lot during the fMRI scan. We ignored the time
89 periods with subject head motions for further analysis. In the experiment, the scan lasted for 526
90 s. The first 6 second was removed for steady state signals. There were 130,000 time points in each
91 channel. For the analysis, we included only 50,000 data points by selecting the first available
92 50,000 points without subject motion. Provided that there are sufficient EEG data points to reach
93 stationarity, using fewer data points does not affect the results statistically but decreases the
94 calculation time.

95 For the Hurst analysis, we calculated the temporal changes in the preprocessed data. As we find in
96 the results, the Hurst exponent differentiates most strongly between healthy and PTSD subjects for
97 the F3 channel. Thus, we summarize the statistics of the F3 channel data for all subjects (Table 1).
98 Note that positive skewness and kurtosis of the EEG data are found for both groups of subjects.
99 The positive skewness indicates the asymmetrical distribution of the EEG signal amplitude with a
100 long tail to the right. Furthermore, the positive kurtosis suggests that the distribution about the
101 mean is more peaked than a Gaussian distribution. EEG time-series distributions for channel F3

Commented [c1]: No need to emphasize "original" here, since the analysis on the filtered preprocessed data is never presented in this work

for each subject is shown in Fig.1. The distribution of the other channels is given in supplementary materials, Appendix I.

Table 1: Summary of EEG statistics for all subjects for channel F3.

Subject	Mean	Std.	Skewness	Kurtosis
Healthy	28.9012	5.9296	0.0737	2.5290
PTSD	32.0050	2.6315	0.0398	3.1504

Fig 1: EEG time series distribution for channel F3 for 12 subjects.

2. Theoretical approach

2.1. R/S analysis

R/S method was employed to estimate the Hurst exponent of time series as a measure of the long-range correlation¹⁴. This method can be described by the following steps:

Step 1: Calculate the logarithmic retunes of detrended time series with length $N = r - 1$, where t is the length of original time series.

$$N_i = \log \left(\frac{t_{i+1}}{t_i} \right) \quad i = 1, 2, \dots, r - 1 \quad (1)$$

Step 2: Split the time series into m adjoining subsets S_j of length n , where $m \times n = N$, and $j = 1, 2, \dots, m$. The segments of each subset calls N_k , with $k = 1, 2, \dots, n$. The average of each subset S_j is counted by:

$$M_j = \frac{1}{n} \sum_{k=1}^n N_{k,j} \quad (2)$$

Step 3: Calculate the addition of deviation from the average for each subset of S_j as:

$$X_{k,j} = \sum_{i=1}^k (N_{i,j} - M_j), \quad k = 1, 2, \dots, n \quad (3)$$

Step 4: The mean relative range of any single subset which surf the time series is calculated as:

$$R_{I_j} = \max(X_{k,j}) - \min(X_{k,j}), \quad 1 < k < n \quad (4)$$

Step 5: In this step, standard deviation of each subgroup is considered:

$$S_{I_j} = \sqrt{\frac{1}{n} \sum_{k=1}^n (N_{k,j} - M_j)^2}. \quad (5)$$

125 Step 6: The range R_{I_j} of each subset rescaled by the related standard deviation S_{I_j} . Therefore, the average
126 R/S measures for each window with length n is:

127
$$(R/S)_n = \frac{1}{m} \sum_{j=1}^m \left(\frac{R_{I_j}}{S_{I_j}} \right). \quad (6)$$

128 All above steps should be repeated for different time periods.

129 Step 7: Plot $\log(R/S)_n$ versus $\log(n)$. The slope of this graph shows the Hurst exponents H .¹⁵

130 Hurst values could be calculated using Rescaled range formula estimated by above steps.

131
$$RR = (2^{(2H-1)} - 1) \times n^H \quad (7)$$

132 Where H the Hurst exponent for each EEG is signal and n is the number of data points^{16,17,18}

133 2.2. Stationarity of data

134 A time series is considered stationary when its statistical properties such as mean, variance,
135 autocorrelation, etc., are constant over time. In terms of probability, if the probability distribution
136 function of a time series does not change with time, it can be considered as a stationary process.^{19,20}
137 In practice, most of statistical forecasting methods are based on the assumption that the time series
138 can be rendered approximately stationary through the use of mathematical transformations.

139
140 R/S method estimates reliable Hurst exponents only for stationary time series while EEG signals
141 present strong non-stationary characteristics.²¹ Thus, to investigate the dynamical Hurst exponents
142 of EEG signals the issue of non-stationarity of data should be resolved.²² To this end, one
143 possibility is to process the data within a window that is large enough so that the data statistically
144 behave like a stationary time series. This approach would be beneficial only if the statistical
145 properties of data such as mean, standard deviation, etc. saturate over an increasing time scale. In
146 this study, we use the variation of standard deviation versus time (Fig. 2) to estimate the window
147 width that best fulfills the stationary criterion. Standard deviation to find the best stationary point
148 for all channels is coming in supplementary material, Appendix II.

Commented [c2]: This sentence is unclear and grammatically wrong

149

150 **Fig 2: Standard deviation of the EEG data against length.**

151 **3. Results and discussions**

152 Positive skewness and kurtosis indicate deviations from Gaussian distribution. Our statistical
153 inferences demonstrate that the EEG data are strongly non-Gaussian (Table 1). To prepare the data
154 for the estimation of the Hurst exponent, the data are segmented according to the saturation
155 window length as explained Section 2.2 The saturation window length or, as we call it, the
156 stationary point for each EEG signal is to be determined by calculating the signal standard
157 deviation versus time for all 31 channels of all twelve subjects.

158

159 Figure 2 depicts the variation of the standard deviation over time for channel F3 for each of the 12
160 subjects. Each curve corresponds to a healthy or PTSD subject with 49 windows each with 1000
161 data. The **closest power of 2** for the stationary point is plotted in dotted line. Our results show that,
162 although for many EEG signals the standard deviation saturates over a few thousand data points,
163 the largest saturation point that is large enough for both the original and filtered data to be
164 considered stationary equals 32768 (or 131 second).

165

166 The EEG data can be considered stationary within the window length of 32,768 points. Next we
167 perform the Hurst exponent calculations within moving windows of this length for all EEG
168 channels and subjects. The moving window is defined in such a way that the window of data slides
169 over the time series each time with the original beginning 1,000 data points removed and the next
170 1,000 new data points updated at the end of the window For 50,000 data points considered in each
171 EEG channel, there are almost 17,000 moving windows, and hence, 17,000 Hurst exponents.

Commented [c3]: I had expressed this before, and would like to emphasize this again.

Please correct the dotted line in your figure:
The dotted line for
 $2^{15}=32768$
should be closer to the 30,000 than the 40,000 tick label

Commented [c4]: see previous comment

The Hurst exponents calculated for the representative channel F3 from the preprocessed data are presented in Fig 3. This figure shows that all subjects, healthy or PTSD, possess Hurst exponents with highly persistent behavior ($H > 0.5$). The high Hurst exponent values are indicative of the existence of strong correlation in the data, which leads to long-term memory of the data. The Hurst exponent separation between healthy and PTSD subjects is small for channel F3, but there is a statistically significant difference between the groups (Table 2). We used a Mann-Whitney U test to investigate the null hypothesis of no difference in the Hurst exponent between PTSD and control groups. The p-value of F3 reaches statistical significance after a strict Bonferroni adjustment for multiple-testing (adjusted p-value is .004).

Table 2: Significant unadjusted p-value calculated by Mann-Whitney U test for difference of Hurst exponent between PTSD and healthy control for F3 channel.

	data	Hurst of data	Mean Hurst PTSD	Mean Hurst Healthy
F3	2.17E-05	0.000129901	0.9572	0.9234

Our findings suggest that the F3 channel discriminates between PTSD and healthy controls based on the Hurst exponent. The relevance of channel F3 to PTSD is consistent with other reports [8,9]. Non-linear independence (NI) values of PTSD and Healthy controls calculated by J. Kim and collaborators show that in PTSD patients NI factors increases in channel F3.⁸ In five case studies, Rutter (2014) determined F3 as one of the most influenced diagnosed channel by the disorders.⁹ F3 is located in the frontal region of brain, which is related to emotion recognition responsibilities. Furthermore, it involves the tasks of judgment, planning, sustained attention, inhibition of responses, verbal episodic memory retrieval, problem solving, sequencing, and deducing facts to conclusions. Changes in the EEG alpha band have been investigated in multiple studies.^{23,24,25,26;} however, we did not find a significant difference between PTSD and healthy subjects in the Hurst exponent for the EEG alpha band. The readers may find the Hurst exponents of all the channels in the supplementary material, Appendix III.

Fig 3: Hurst exponent distribution.

Acknowledgments.

The authors would like to acknowledge Bill White for his helps in programming and Tandy supercomputing center for many hours of computing time and supports.

This research was supported in part by W81XWH-12-1-0697 grant from the US Department of Defense to JB and CKW.

Author Contributions

BR: conceived the ideas of the paper, analyzed the data and wrote the paper. CKW: collected and pre-processed the data. PN: analyzed the data and contributed in analysis tools, writing and programming. JB: provided the data and supervised the biological and statistical approaches. BM: supervised the computational and statistical approaches. All authors commented on this paper.

1. **Niedermeyer E, da Silva FL.** Electroencephalography: Basic Principles, Clinical Applications, and Related Fields. Lippincott Williams & Wilkins. ISBN, 2004; 0-7817-5126-8.
2. **Zaremba W.** Modeling the variability of EEG/MEG data through statistical machine learning, Master's thesis in mathematics, University of Warsaw, 2012.
3. **Coben R, Evansn JR.** neurofeedback and neuromodulation techniques and applications, Elsevier, 2011.
4. **Lopes da Silva F.** EEG – fMRI Physiological Basis, Technique, and Applications, Springer, 2010; 19-38.
5. **Ingber L.** Statistical mechanics of neocortical interactions: Training and testing canonical momenta indicators of EEG. Mathematical Computer Modelling. Volume 27. Number 3. 1998; 33-64.
6. **Abou-Khalil B, Musilus,** Atlas of EEG & Seizure Semiology. Elsevier, 2006.
7. **Chaea J, Jeongb J, B. Petersonc, Kima D, Bahka W, Juna T, et all.** Dimensional complexity of the EEG in patients with posttraumatic stress disorder, Psychiatry Research: Neuroimaging Volume 131, Issue 1, 30 May 2004;79–89.
8. **Kim J, Chae J, Ko H, Latchoumane CV, Banerjee A, Mandell DJ, et all.** Hemispheric asymmetry in non-linear interdependence of EEG in post-traumatic stress disorder, Psychiatry and Clinical Neurosciences 2012; 66: 87–96.

9. **Rutter P.** Five case studies using live z- score training percent-z ok on individuals diagnosed with PTSD, *NeuroConnections*, 2012.
10. **Subha DP, Joseph PK, Acharya R, Lim CM.** EEG Signal Analysis: A Survey, *J Med Syst* , 2010;34:195–212.
11. **Hurst HE, Black RP, Simaika YM.** Long-term storage: an experimental study. London: Constable, 1965.
12. **Hurst HE.** Long term storage capacity of reservoirs. *Trans. Am. Soc. Eng.* 1951;116: 770–799.
13. **Mulert C, Lemieux L.** EEG-fMRI: Physiological Basis, Technique, and Applications. Springer-Verlag, Berlin Heidelberg, Eds., 2010.
14. **Fan J.** Rescaled Range Analysis in Higher Dimensions, *Research Journal of Applied Sciences, Engineering and Technology* 5(18): 4489-4492, 2013.
15. **Jokic-Begic N, Begic D,** Quantitative electroencephalogram (qEEG) in combat veterans with post-traumatic stress disorder (PTSD). *Nord J Psychiatry.* 2003;57(5):351–355.
16. **Norouzzadeh P, Jafari GR.** Application of multifractal measures to Tehran price index, *Physica A*, 2005, Volume 356, 609–627.
17. **Voss J.** Rescaled Range Analysis: A Method for Detecting Persistence, Randomness, or Mean Reversion in Financial Markets, CFA institute, 2013.
18. **Rose O.** Estimation of the Hurst Parameter of Long Range Dependent Time Series, University of Wurzburg, Research Report Series, 1996.
19. **Nason GP.** Wavelet Methods in Statistics with R, Springer, Chapter 11, 2008.
20. **Norouzzadeh P, Rahmani B, Norouzzadeh MS** Forecasting smoothed non-stationary time series using genetic algorithms, *International Journal of Modern Physics C*, 2007.
21. **Korolev VY, Skvortsova NN.** Stochastic Models of Structural Plasma Turbulence, Walter de Gruyter, 2006.
22. **Morales R, Di Matteo T, Gramatica R, Aste T.** Dynamical Hurst exponent as a tool to monitor unstable periods in financial time series, *arXiv:1212.3195v2*. 2013.
23. **Wahbeh H, Oken BS.** Peak High-Frequency HRV and Peak Alpha Frequency Higher in PTSD, *Appl Psychophysiol Biofeedback.* 2013 Mar;38(1): 57–69.
24. **Rabe S, Beauducel A, Zollner T, Maercker A, Karl A,** Regional brain electrical activity in posttraumatic stress disorder after motor vehicle accident. *J Abnorm Psychol.* 2006;115(4):687–698.
25. **Jokic-Begic N, Begic D,** Quantitative electroencephalogram (qEEG) in combat veterans with post-traumatic stress disorder (PTSD). *Nord J Psychiatry.* 2003;57(5):351–355.
26. **Metzger LJ, Paige SR, Carson MA, et al.** PTSD arousal and depression symptoms associated with increased right-sided parietal EEG asymmetry. *J Abnorm Psychol.* 2004;113(2): 324–329.

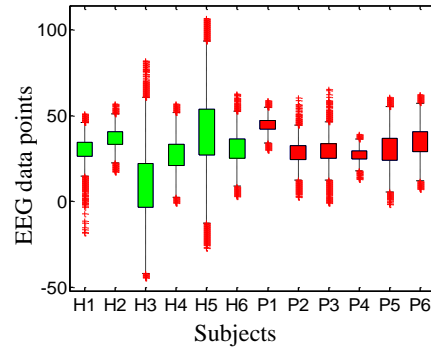


Fig 1: EEG time-series distributions for channel F3 for each subject. The red box plots represent PTSD and green box plots represent healthy controls.

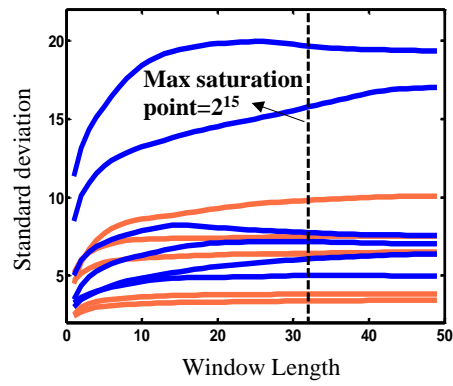


Fig 2: Standard deviation of the EEG data against length: 6 PTSD subjects (orange) and 6 healthy controls (blue) of channel F3.

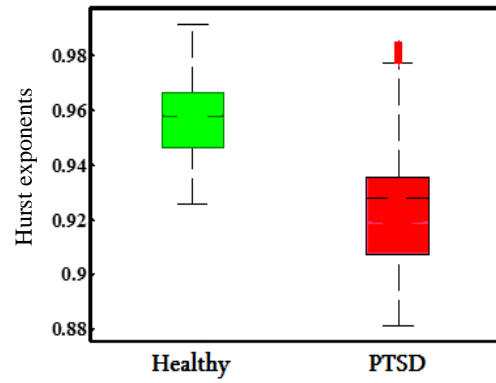


Fig 3: Hurst exponent distribution: 6 Healthy controls (green box) and 6 PTSD cases (red box) of channel F3